UNIVERSITY OF GENOA
Department of Civil, Chemical and Environmental Engineering (DICCA)
PhD Program in Civil, Chemical and Environmental Engineering
Curriculum in Structural and Geotechnical Engineering, Mechanics and Materials - Cycle XXXIV

Doctoral Dissertation

SEISMIC FRAGILITY CURVES ACCOUNTING FOR SITE AND SOIL STRUCTURE INTERACTION EFFECTS ON URM BUILDINGS

Andrea Brunelli

September, 2022

SEISMIC FRAGILITY CURVES ACCOUNTING FOR SITE AND SOIL STRUCTURE INTERACTION EFFECTS ON URM BUILDINGS

BY

ANDREA BRUNELLI

Dissertation discussed in partial fulfillment of
the requirements for the Degree of

DOCTOR OF PHILOSOPHY

in Civil, Chemical and Environmental Engineering
curriculum in Structural and Geotechnical Engineering, Mechanics and Materials
Department of Civil, Chemical and Environmental Engineering (DICCA)
University of Genoa, Italy

September, 2022

Scientific Supervisors

Serena Cattari, Associate Professor
Department of Civil, Chemical and Environmental Engineering (DICCA),
University of Genoa, Genoa, Italy
Filomena de Silva, RTD-A
Department of Civil, Architectural and Environmental Engineering,
University of Naples Federico II, Naples, Italy

External Reviewers:

Emmanouil Rovithis, Researcher
Institute of Engineering Seismology and Earthquake Engineering (ITSAK),
Thessaloniki, Greece
Romeu da Silva Vicente, Associate Professor
Civil engineering, UA,
University of Aveiro, Aveiro, Portugal

Examination Committee:

Luisa Pagnini, Associate Professor
Department of Civil, Chemical and Environmental Engineering (DICCA),
University of Genoa, Genoa, Italy
Antonio Formisano, Associate Professor
Department of Civil, Architectural and Environmental Engineering,
University of Naples Federico II, Naples, Italy
Filippo Santucci De Magistris, Full Professor
Department DiBT, Structural and Geotechnical Dynamics Lab. StreGa,
University of Molise, Italy

ABSTRACT

Significant site-amplification effects have been observed in various historic centers following the recent seismic events in Italy (e.g., L'Aquila 2009, Emilia 2012, Central Italy 2016-17), but also examples of Soil Foundation Structure (SFS) interaction in ordinary unreinforced masonry (URM) buildings. In the past, SFS interaction effects were usually considered for masonry buildings only in slender or massive URM monumental structures. Following the latest observed evidence, this research aims to further investigate the role of site amplification and SFS interaction in the seismic response of URM residential structures. The final goal is to provide an effective procedure to consider these effects in large-scale risk assessment as well.

The first part of the research validated the numerical approach to analyze the SFS interaction by reproducing the seismic response of the Visso school affected by the earthquake sequence in central Italy. This school constituted a very emblematic case study, since it was permanently monitored by the Italian Department of Civil Protection and suffered very severe damage, allowing validation even in a highly nonlinear phase.

The procedure is based on the decoupled approach. Therefore, the input motion of the foundation is calculated from the site response analyses and the structural performance is analyzed through a structural model with springs at the base and characterized by equivalent damping. This school's validated procedure and numerical model were exploited to derive fragility curves that include site effects and SFS interaction under different subsurface conditions. The predicted damage probability was also compared with the results obtained from different amplifications of the simplified Code-compliant approach.

Finally, the research was further generalized by considering multiple building types and different soil profiles. The structural types were inspired by the most frequent building types in the municipality of Visso, consisting of aggregate masonry structures.

The set of derived fragility curves was finally applied to an urban scale to develop damage scenarios. In particular, the resulting damage under ground motion of the Central Italy earthquake was compared with that observed and predicted by existing faster and less accurate approaches, to assess the potential of the developed tools also to support possible future large-scale mitigation policies.

INDEX

CHAPTER 1

Introduction: motivations and overview on the thesis structure

The research is motivated by the fact that numerous URM buildings are founded on shallow soft covers which amplify the seismic motion and affect the structural response through soil-foundation-structure (SFS) interaction. The studies about the last Italian earthquakes (e.g. Sextos et al. (2018); Sorrentino et al. (2019); Stewart et al. (2018); Chieffo and Formisano (2020); Brando et al. (2020)) highlighted the relevance of such effects especially for small historical centres, since they are often built in geomorphologic context prone to topographic and soil stratigraphic effects and are characterized by high vulnerability factors. The latter arise because the built environment is usually the result of a process of building growth across centuries, leading to buildings in aggregate with interacting units characterized by different materials and irregularity in elevation. Despite the relevance of the topic, the attempts in the literature to provide tools to address the seismic assessment of URM buildings in such conditions are still very few. In the following some basic theoretical aspects are quickly recalled in order to thus illustrate the hypotheses adopted in this study.

Site effects are the amplification of the seismic waves propagating from the bedrock through a soft soil deposit that modified the seismic waves up to ground surface (i.e. soil response at free-field conditions). In addition, the kinematic interaction between the embedded masonry foundation and the surrounding soil may modify free-field input due to the stiffness of the foundation (see Kim and Stewart (2003)). Simultaneously, the structure transfers to its base inertial forces and moments which make foundations sway and rock. These latter affect the structural response in terms of displacements and accelerations, as well as by increasing the period and damping due to the additional energy dissipated by wave radiation and soil hysteresis.

Such effects can be studied through:

- uncoupled approaches, in which the system is analysed by decoupling the kinematic from the inertial interaction with the so-called ‘substructure method’;
- coupled approaches, in which all the effects of the interaction can be evaluated simultaneously, by performing dynamic analyses on a model including soil, foundation and structure.

In this work, the uncoupled approach (see Mylonakis et al. (1997); Kaynia (2021)) is adopted with the aim of developing fragility curves suitable to support risk analyses also at large scale, i.e. balancing reliability and computational effort. Accordingly, the input motion is calculated through seismic response analyses and the interaction between the soil and the structure is considered in the analysis through a compliant base model endowed with springs, whose stiffness is properly calibrated through the impedance functions proposed by Gazetas (1991) and Pais and Kausel (1988). The kinematic interaction was neglected because the thesis is focused on masonry ordinary buildings, generally characterized by shallow foundations which are poorly affected by such effect. Moreover, the nonlinear behavior of URM buildings is described according to the equivalent frame approach by adopting the Tremuri software package (Lagomarsino et al. (2013)), particularly suitable in terms of computational effort to perform extensive nonlinear dynamic analyses, which constitute the main numerical tool which the research is based on. Both isolated and aggregated URM buildings are considered in the research, also addressing some tricky issues from the modelling point of view as reported in detail in the following.

All case studies are inspired by URM buildings of historical centre of Visso, a very emblematic case hit by the Central Italy 2016/2017 earthquake that is adopted also as a validation tool at different

scales (i.e. that of the single building and the urban one).
Figure 1.1 illustrates the workflow of the research and the corresponding structure of chapters.
Each chapter corresponds to a journal paper or a contribution to international conference: Chapter §2 in Brunelli et al. (2021a), Chapter §3 in Brunelli et al. (2022a) and Chapter §4.1 in Brunelli et al. (2021b)), already published; Chapter §4.2 in Angiolilli et al. (2022a) under review; Chapter §5 in Brunelli et al. (2022b) under review. The contents of the thesis are integrated by additional data and interpretations deepening reported in Annex section; some of annexes summarizes further contributions to international conference (e.g. Annex A.4.2a published in Brunelli et al. (2022c)). Some chapters of the thesis do not exactly match the published papers because suggestions from the dissertation reviewers were taken on board and offered further improvement to the work presented here. Each Chapter starts with a brief summary of motivations and main results achieved in the corresponding step of the research, followed by the corresponding publication.
In the first step of the research (as show in the first box of Figure 1.1), the attention was focused on the numerical simulation of the real response of the Pietro Capuzi school of Visso (MC) subjected to the Central Italy 2016/2017 seismic sequence, for which evidence of SFS interaction effects have been highlighted (Ferrero et al. (2020); Brunelli et al. (2021a)). This part of the research is illustrated in Chapter §2. This first part of the report aims to provide and verify a simplified but rigorous approach to implement the soil-foundation-structure interaction for a URM building. To do this, it was necessary to calibrate the substructure considering the role of the soil.
The school building was permanently monitored by the Department of Civil Protection and was inspected by University of Genoa after the Central Italy sequence hence the following relevant data were available: a detailed geometric and technological survey; the dynamic pre-event identification based on Ambient Vibration Tests; all the main recordings of the seismic sequence in various points of the structure; the damage pattern reconstruction; the soil profile and geotechnical characterization. Two numerical models have been developed: a fixed base (FB) and a compliant base (CB) model. In the latter case, the role of the soil is taken into account by inserting springs under each foundation pier. These are characterized by five degrees of freedom (only the rotation around the vertical axis was neglected). These springs were calibrated on basis on the real part of the impedance function by Gazetas (1991). The imaginary part of the impedances is used to estimate the dashpots coefficients. Since the introduction of dashpots is not possible in the Tremuri software, the Replacement Oscillator (RO) (based on the formula of Maravas et al. (2014)) was used to estimate the damping equivalent to the contributions of the structural viscous damping (set to 3%), the radiative damping of the foundation and the hysteretic damping mobilized in the soil by the foundation motion. This total equivalent damping was implemented in the numerical model as a Rayleigh damping. The model was calibrated in the elastic field against the experimental data available before the seismic sequence. The simulation of the structural behaviour under white noise and the seismic sequence confirmed that the CB model reproduced more successfully the actual response not only in terms of natural frequencies and vibration modes (i.e. in linear field) but also in term of damage pattern, accelerations in various control points and activated inertial forces (i.e. in strong nonlinear field). From the results shown in this chapter, it is observed that the effects of SFS interaction in the dynamic response of the structure is important when the structure is still undamaged. Conversely the effect of the extensive structural damage likely induced by strong motions prevails with respect to that of the SFS interaction.

In Chapter §3, further insight on the variability of results was obtained regarding: a) the formulation adopted for computing the impedance functions; b) the approach adopted to compute the equivalent damping through the RO. For the first aim a), the formulation proposed by Pais and Kausel (1988) was explored together with that of Gazetas (1991); while, for the second one b), three alternative proposals (Maravas et al. (2014); Givens et al. (2016)) were considered that also allows to include the hysteresis contribution associated to the nonlinear response of the soil.

CHAPTER 2 and CHAPTER 3

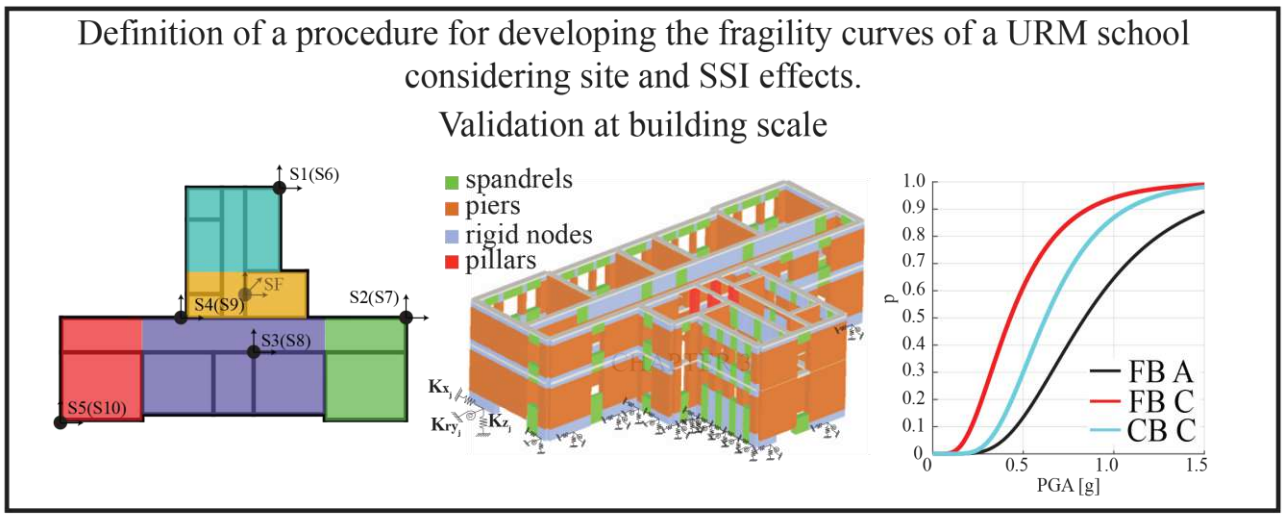

CHAPTER 4

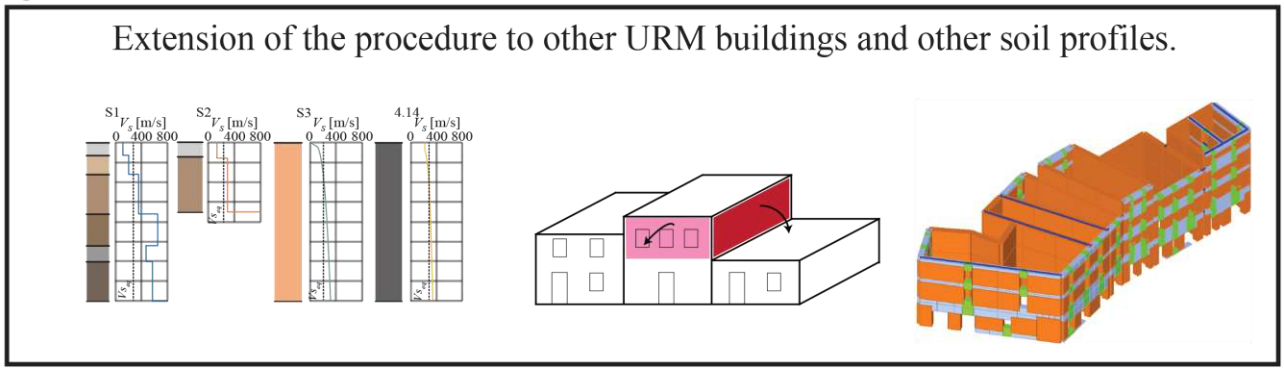

CHAPTER 5

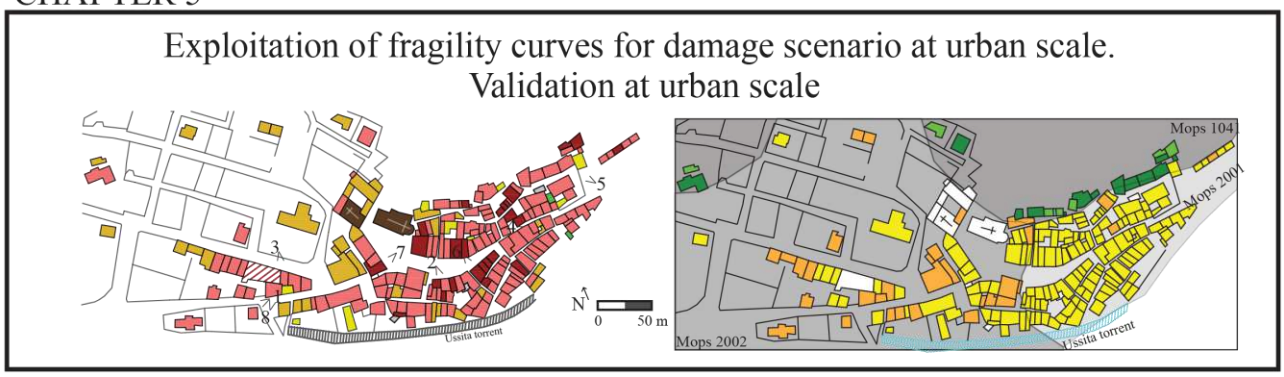

Figure 1.1. Research workflow and structure of chapters

The results about the case study highlighted that there are no marked differences in the simulation of the real response of the school of Visso between the two formulations of the impedances and between the three for the RO.

The biggest differences are seen when considering the soil hysteretic damping, which leads to a closer match with observations and a general beneficial effect for the structural response by reducing the severity of damage in the structural elements. These results oriented the final modelling hypotheses (for the soil and the structure) to be considered in the development of fragility curves. In particular, fragility curves were evaluated considering:

- (i) the FB model on soil type A corresponding to a stiff rock outcrop;

- (ii) the FB model on soil type C reproduced through the soil profile and properties below the school of Visso;
- (iii) the CB model again on soil C neglecting the soil hysteresis in the equivalent damping of RO;
- (iv) and finally, the CB model on soil C including the soil hysteresis (this model is named in the following adding "βs").

According to the hypothesis (i) site amplification of the seismic motion crossing soft soil layers are considered in the fragility curves through standard corrective coefficients. Conversely, in the hypothesis (ii), site amplifications are directly evaluated through seismic response analyses; these results are very useful to be compared with the results of approach (i) and thus assess the reliability of more simplified approaches. Finally, modelling assumptions (iii) and (iv) of the procedure explicitly account for both site effects and SFS interaction.

The fragility curves have been defined by performing nonlinear dynamic analyses according to a cloud approach (considering for some recordings a small scaling factor). In particular, a total of 136 events has been considered as representative of a seismic event recorded on a stiff rock outcrop. More specifically, signals were selected as recorded by stations located on soil characterized by shear velocity $V_{S,30}$ greater than 700 m/s. These signals have been directly adopted to perform the analyses in case (i). Then, local seismic response analyses have been performed through the STRATA software (Kottke and Rathje (2008)) by propagating these signals through the stratigraphy representative of that characterizing the Visso's school, to obtain the motions to be applied in cases from (ii) to (iv). Through the site response analysis, the freefield accelerograms, the shear stiffness and the damping mobilized in the soil by each event were obtained. The shear stiffness attained in each event constituted the input to properly calibrate the springs in the CB model; analogously, the damping mobilized was used to recalculate the equivalent damping of the RO. According to this procedure, the models for performing the analyses in cases (ii), (iii) and (iv) were set.

In order to evaluate the two parameters that define the fragility curve (i.e. the median value (IM_{50}) of the intensity measure that produces the attainment of a given damage level in the structure and its dispersion), the analyses were grouped according to the maximum damage produced in the building. To this aim, results of nonlinear dynamic analyses were processed according to a multiscale approach that, starting from the original proposal made by Lagomarsino and Cattari (2015a), was further developed to be consistent with the five levels of damage (DL) adopted in the macroseismic EMS98 scale (see Grünthal (1998)) (DL1 ÷ 5).

In particular, the attainment of damage level was monitored through variables at two different scales: the wall scale (to check the spreading of damage along different elements) and the global scale (through thresholds set on the pushover curve). Several Intensity Measures (IM) were considered: Peak Ground Acceleration (PGA); Spectral acceleration in correspondence of the initial period of the building ($Sa(T_1)$); Cumulative Absolute Velocity (CAV) calculated in the significant duration of the event (i.e. for that interval of the event that brings values of Arias Intensity (AI) between 5% and 95%); Housner Intensity (IH) calculated in three ranges of period variation (i.e. 0.1-0.5s, 0.4-0.8s and 0.7-1.1s, the same adopted in 3rd level seismic microzonation studies of Italy). The results highlighted that the IMs associated to the lowest dispersion (i.e. those associated to the best correlation with the structural response) were the PGA, the $Sa(T_1)$ and the IH calculated between 0.1-0.5s which is the range of periods of the building under examination. That was confirmed for all considered cases from (i) to (iv). The comparison between the results of FB models on soil A (i) and C (ii) respectively, confirmed the role of site amplification producing a high damage probability for the building.

Then, the results derived from fragility curves of models on soil C (ii,iii,iv) were compared with those obtained by using the fragility curve of case (i). In the latter case, the intensity measure used to enter in the curve was amplified through the corrective coefficients proposed in the Italian Code (NTC (2018)) to account in an approximate way for the site stratigraphic amplification phenomena. Consistently with the flat site morphology, topographical effects were neglected. The comparison of results highlighted that the simplified approach by Codes may produce not conservative outcomes,

especially when the structural response attains high damage level which are the most interesting for the seismic design and assessment of existing buildings to the Life Safety Condition. Only in the case of CB C model with the hysteresis of the soil (case iv), values comparable to those of the standard are obtained, if the $Sa(T_1)$ is considered as IM. Moreover, results highlighted that explicitly accounting for the SFS Interaction (cases iii and iv) in general is beneficial for the structure limiting the extent of damage, in particular under higher IMs. These results are reported in Brunelli et al. (2022a). The research in Chapter §3 investigates the approach by comparing the results with other codes besides the Italian one, referring to Eurocode 8 (CEN (2004), ASCE7 (2016)), and the New Zealand code (NZS (2017)).
Then, in Chapter 4 the aforementioned results were extended by considering various soil profiles and additional structural types (as show in the second box of Figure 1.1).

More specifically, as the first aspect concerns, the same analyses were repeated on the same structural model inspired by the Visso's school but on three additional soil profiles made of fine- or coarse-grained soil with compatible values of V_{S30} The trend in the comparisons between fixed base and compliant base models is confirmed, but with different amount of dispersions at high damage levels due to the different nonlinear soil response among the selected profiles. This aspect is reported in Chapter §4.1. In particular, three other soils were considered: the one representative of the historic center of Visso (calibrated in Annex A4.1a), one of homogenous clay and one of homogeneous gravel.

Then, as the second aspect concerns, the procedure to simulate SFS interaction effects described and validated in Chapters §2 and §3 for the school of Visso has applied to two aggregates, inspired by the typical features of the buildings in the historical centre of Visso (Figure 1.2).
Indeed, studies that explicitly consider fragility curves for aggregate masonry buildings are quite rare in the literature (e.g. Angiolilli et al. (2021); Battaglia et al. (2021); Penna et al. (2022a)). In most cases, aggregate buildings are considered in a simplified way (Formisano et al. (2015); Formisano (2017); Chieffo and Formisano (2020); Romis et al. (2021); Formisano et al. (2022)). This research instead attempts to propose a procedure able to explicitly quantify specific vulnerability factors that characterize them.

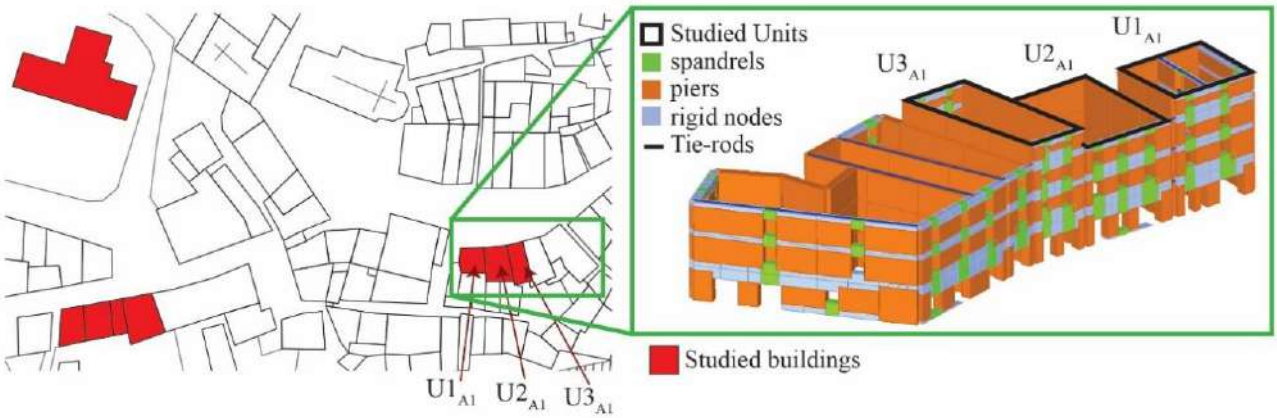

Figure 1.2. Identification of buildings by which the archetypes are inspired and 3D equivalent frame model of the aggregate.

As originally proposed in Angiolilli et al. (2021), in this research, the in-plane (IP) response of the buildings was simulated through nonlinear dynamic analyses performed on a 3D equivalent frame model of the structure.
The interaction effect among adjacent units has been modelled through the insertion of elastic truss elements and fictitious floors between the units; these elements allow the opening between buildings

only along their longitudinal direction. To quantify such interaction effect on the IP response, each structural unit has been also investigated as isolated. Moreover, also the pounding effect was considered in determining the actual damage level of each structural unit. More details on this last aspect are provided in Chapter 4.2. The results of the various units associated to the IP response and for the different soils are reported in Annex A 4.2b. These results show the variability of the behavior as a function of the characteristics of the structural unit (period, resistant area, etc.) and the amplification of the soil. Also for these units a comparison of the results obtained with those of a simplified code approach was carried out.
The out-of-plane (OOP) mechanisms were also analysed, by adopting the rigid-block assumption and considering as seismic input the accelerations derived from the global 3D model. In this manner, while the IP and OOP responses are analysed in a separate way, their interaction is included in a simplified way. The individuation of the walls susceptible to overturning was defined based on building geometry, opening layout, constructive details and restraints given by the structure. In particular, it was reasonable to consider the OOP mechanisms involving only the tympanum and upper level as well as the two upper levels of the external façades, because of the wall slenderness and the amplification phenomena generally occurred for the upper building levels.
As for the Visso's school, a validation of the simulated response of one of these aggregates has been carried out through the comparison with the actual damage occurred during the Central Italy 2016-2017 earthquake. Such results are reported in Annex A4.2a and Annex A4.2b. Such validation was executed by also considering the modification of the seismic motion along the valley of Visso through 2D site response analyses (see Annex A4.2a).

Then the fragility curves of the selected archetypes were derived according to the proposed procedure. With the final goal of assessing damage scenario at urban scale (last step of the research depicted in the last box of Figure 1.1), fragility curves on specific archetypes were generalized to be representative of building classes with homogeneous behaviour. Thus:

- based on the evidence provided by examined structures, corrective modifiers have been defined to account in a simplified way for the OOP response and the SFS interaction;
- the dispersion of fragility curves has been increased to account also for the possible uncertainty on the mechanical parameters. Moreover, the combination of results associated to various structural units allowed an estimate also of the building-to-building variability.

This part of the research is illustrated in Chapter 5. At urban scale, the validation of the procedure is performed by comparing the damage observed in Visso after the Central Italy earthquake to that estimated through FB C or CB C fragility curves which account for site effects and site effects/SFS interaction, respectively. Furthermore, the results obtained for the FB A model were compared with other fragility curves available in the literature for fixed-base structures (da Porto et al. (2021); Penna et al. (2022a)). In fact, most fragility curves are derived by neglecting site effects and soil foundation structure interaction effects (e.g., Mosoarca et al. (2020)). To date, only the first effect (Formisano et al. (2021); Ademovic et al. (2022)) is considered by entering in the fragility curves with an amplified value of the intensity measure.
Results showed a good match even if the latter have large dispersions. This underlines the potential to customize the fragility curves for the buildings under investigation.

Finally, the set of developed fragility curves has been applied to derive damage scenario at urban scale and compare it with the observed one and the obtainable economic effects were compared.

CHAPTER 2

Real-scale observations and developed procedure for the numerical simulation of site and SFS interaction

Summary:
This chapter is published in Brunelli et al. (2021a) and investigates the numerical simulation of the seismic response of a URM school in Visso to the Central Italy 2016/17 seismic sequence. In particular, the role played by site amplification and SFS interaction in the real seismic response of the examined URM building is analysed. This case study can be considered a unicum due to the numerous data available, including an in-depth knowledge of the geometric survey and construction details. In fact, this building was monitored by the OSS (Seismic Observatory of Structures) of the Italian Civil Protection Department which installed a system of ten bi-directional accelerometers on two levels and one three- directional accelerometer at the base of the structure. Therefore, both a pre-event dynamic identification and the recordings during the main events of the Central Italy 2016/17 seismic sequence are available. Moreover, an accurate survey of the damage was available after each earthquake. Thanks to such data, it was also possible to perform a very accurate comparison on the damage after each seismic event. The signal recorded at the base of the school was applied as input motion to both a fixed-base and a compliant-base structural model. The comparisons between the observed and simulated response revealed an influence of SFS interaction under both white noise and strong motions. The successful match between observations and simulations in terms of fundamental period, floor acceleration, localization and intensity of the cumulated damage was intended as a detailed validation of the conceived procedure for:

- *the calibration of the base spring in the compliant base model;*
- *the quantification and the application of the equivalent damping ratio;*
- *legitimating the negligibility of the kinematic interaction;*
- *the structural modelling strategy with reference to the global in-plane response.*

published in *Bulletin of Earthquake Engineering* **19**, 1181-1211.
DOI: 10.1007/s10518-020-00980-3

NUMERICAL SIMULATION OF THE SEISMIC RESPONSE AND SOIL-STRUCTURE INTERACTION FOR A MONITORED MASONRY SCHOOL BUILDING DAMAGED BY THE 2016 CENTRAL ITALY EARTHQUAKE

Andrea Brunelli[1], Filomena de Silva[2], Annachiara Piro[2], Fulvio Parisi[2], Stefania Sica[3], Francesco Silvestri[2], Serena Cattari[1]

[1]University of Genova, Genoa, Italy
andrea.brunelli@edu.unige.it, serena.cattari@unige.it

[2]University of Naples Federico II, Naples, Italy
(filomena.desilva, annachiara.piro, fulvio.parisi, francesco.silvestri)@unina.it

[3]University of Sannio, Benevento, Italy
stefsica@unisannio.it

Abstract:

Despite significant research advances on the seismic response analysis, there is still an urgent need for validation of numerical simulation methods for prediction of earthquake response and damage. In this respect, seismic monitoring networks and proper modelling can further support validation studies, allowing more realistic simulations of what earthquakes can produce.

This paper discusses the seismic response of the "Pietro Capuzi" school in Visso, a village located in the Marche region (Italy) that was severely damaged by the 2016-2017 Central Italy earthquake sequence. The school was a two-story masonry structure founded on simple enlargements of its load-bearing walls, partially embedded in the alluvial loose soils of the Nera river. The structure was monitored as a strategic building by the Italian Seismic Observatory of Structures (OSS), which provided acceleration records under both ambient noise and the three mainshocks of the seismic sequence. The evolution of the damage pattern following each one of the three mainshocks was provided by on-site survey integrated by OSS data. Data on the dynamic soil properties was available from the seismic microzonation study of the Visso village and proved useful in the development of a reliable geotechnical model of the subsoil. The equivalent frame approach was adopted to simulate the nonlinear response of the school building through both fixed-base and compliant-base models, to assess the likely influence of soil-structure interaction on the building performance. The ambient noise records allowed for an accurate calibration of the soil-structure model. The seismic response of the masonry building to the whole sequence of the three mainshocks was then simulated by nonlinear time history analyses by using the horizontal accelerations recorded at the underground floor as input motions. Numerical results are validated against the evidence on structural response in terms of both incremental damage and global shear force–displacement relationships. The comparisons are satisfactory, corroborating the reliability of the compliant-base approach as applied to the equivalent frame model and its computational efficiency to simulate the soil-foundation-structure interaction in the case of masonry buildings.

Keywords: monitored structures, URM buildings, seismic response, equivalent frame modelling, soil-structure interaction

1. INTRODUCTION

Seismic events that hit Italy in the last 20 years produced not only dramatic social and economic consequences, but also major data to understand various engineering issues (Dolce and Di Bucci (2017)). In 2002, Molise earthquake caused the collapse of San Giuliano di Puglia school, highlighting the significant role of site amplification on damage to buildings and strategic structures (e.g., Puglia et al. (2013)) and promoting national research programs to assess their safety level and support the updating of building codes (Dolce et al. (2019a)). L'Aquila earthquake in 2009 demonstrated the role of near-fault seismic motion and vulnerability of non-structural components in losses, providing unique data supporting the reconstruction process (Di Ludovico et al. (2017a, b)). In 2012, Emilia earthquake pointed out the existence of soil liquefaction hazard in Italy (Lai et al. (2015)) and its potential damage to buildings and provided data on the seismic response of specific assets particularly spread in that area, such as fortresses (Cattari et al. (2014); Parisi and Augenti (2013a)) or industrial buildings (Bournas et al. (2014)). During 2016 and 2017, the historical seismicity of Italy was further marked by a sequence of strong earthquakes that hit the central regions of the country, causing once again heavy damages and loss of life. Those earthquakes struck numerous historical urban centres, involving an area even larger than those mentioned above and producing cumulative damage particularly to unreinforced masonry (URM) constructions (Di Ludovico et al. (2019)).

Focusing on the 2016-2017 Central Italy earthquake, reports (GEER (2016); GEER (2017)) and papers (e.g. Sextos et al. (2018); Stewart et al. (2018); Sorrentino et al. (2019)) following post-earthquake field missions highlighted a distinct variability of damage throughout the affected area, due to site-by-site differences in structural vulnerability and local amplification of seismic ground motion produced by subsoil response. A significant amount of accurate data collected during and after seismic events on real buildings, in terms of seismic motion, structural features and soil properties, were useful to minimize the uncertainties involved in the validation process of predictive models. Within this context, since 1993 the Italian Department of Civil Protection through the OSS (acronym of the Italian name "Osservatorio Sismico delle Strutture") installed a network of permanent seismic monitoring systems on public buildings, bridges and dams (Dolce et al. (2017)), particularly those located in highly hazardous areas.

This paper presents a numerical simulation and validation study for a real masonry structure monitored by OSS through permanent accelerometers, which were able to record its motion under both weak-to-strong earthquakes and ambient noise (ReLUIS (2018a); Cattari et al. (2019a)). The case-study building is an URM school located in Visso village, which was settled in a depressed area between the Nera and Ussita rivers of the Marche region, very close to the epicentres of 26th October and 30th October 2016 earthquakes (see Figure 2.1a). The school was progressively damaged under the mainshocks of the Central Italy seismic sequence, resulting in a severe damage accumulation that motivated its demolition.

Several factors make the Visso school an interesting, if not even singular, case study according to the following remarks:

- Monitoring data on the seismic behaviour of a real building that developed a strong nonlinear response is available for a detailed validation of numerical models. This is an almost unique occurrence, being the amount and accuracy of the digital data recorded comparable only to that typically produced by shaking table tests, which however necessarily imply simplifications with respect to the prototype testing (e.g. Senaldi et al. (2020); Magenes et al. (2014); Pitilakis et al. (2018a)).
- The building had a T-shaped plan that is a recurrent characteristic of Italian school buildings, typically producing an irregular seismic response, damage concentrations or even a premature collapse (see e.g. Augenti and Parisi (2010)).

- The building was accurately inspected after the last mainshock occurred in 2016, but data related to previous shocks was collected as well, allowing damage accumulation to be assessed in terms of location, typology, and incremental severity rating.
- The main periods obtained from the interpretation of the dynamic structural behaviour under ambient noise (Cattari et al. (2019a); Lorenzoni et al. (2019)) resulted unexpectedly high, evidencing possible effects of the inertial interaction with the soft foundation soil (Cattari et al. (2019b); Ferrero et al. (2020)). The available strong motion records represent a unique chance to observe such effects on a real case study, overcoming the physical limitations or the unavoidable assumptions that usually characterize both laboratory and field tests on simplified prototypes (e.g. Gajan and Kutter (2008); Tileylioglu et al. (2011); Jabary and Madabushi (2017); Pitilakis et al. (2018b); Star et al. (2019)). Moreover, until today most of evidences or studies on soil structure interaction on URM structures were focused on slender or monumental buildings (e.g. Karatzetzou et al. (2015); de Silva et al. (2018); de Silva (2020)).

In this study, the potential effects of soil-foundation-structure (SFS) interaction are examined through a compliant-base numerical model, which was characterized through experimental investigations performed on the structure (Section 2) and the soil (Section 3). The dynamic response of the school was compared to the results of the on-site dynamic identification (Section 4). Then, the seismic response of the building was simulated through nonlinear time history analyses on both fixed-base (FB) and compliant-base (CB) models under the sequence of the mainshocks (Section 5), recorded at the underground level of the school. The simulated response through the FB and CB models was compared to the observed behaviour, first at a *local* scale (i.e. motion recorded by single sensors) and thereafter as a *global* performance. The scope of such a comparison was twofold: (i) to assess the capability of equivalent frame models to reproduce the observed cumulative damage, and (ii) to evaluate the potential impact of soil-structure interaction on nonlinear behaviour and damage of the URM buildings through CB models.

2. MAIN FEATURES OF THE CASE STUDY AND DAMAGE

The school masonry building was located in the region of the Central Italy seismic sequence. Figure 2.1a shows the position of epicentres of the three mainshocks that struck Central Italy in 2016, with moment magnitude M_W equal to 6.0, 5.9 and 6.5 on 24th August, 26th October and 30th October, respectively (hereafter tagged as E1, E2 and E3). Figure 2.1b shows the location of the Visso village in a depressed area at the confluence of the alluvial valleys of Nera and Ussita rivers. The soil fundamental frequency identified from ambient noise recorded in the middle of the depression falls in the typical range of the predominant frequencies of URM buildings (i.e. 2 to 5 Hz). Moving toward the valley borders, higher soil frequency values are caused by a shallower bedrock.

The effect of the variable bedrock depth on the site response is reflected by the amplification factors of spectral accelerations at periods between 0.1 s and 0.5 s (see contours re-drawn in Figure 2.1b as resulting from the seismic microzonation studies of the village), which are representative of the seismic response of most URM buildings in that area. In fact, the highest amplification values involve almost the whole valley (except the North-West border), consistently with the distribution of the observed damage. As an example, Figure 2.1c shows three different damage levels detected on various buildings in three different zones of Visso. Collapses (see left-hand side picture) and huge damages (see central picture) occurred in the most recently urbanized area, which was settled in the middle of the valley where loose soil deposits reach their maximum thickness. By contrast, more ancient buildings laying closer to the valley edges, i.e. where the geological bedrock outcrops, survived the seismic sequence with none-to-slight damage (see right-hand side picture in Figure 2.1c).

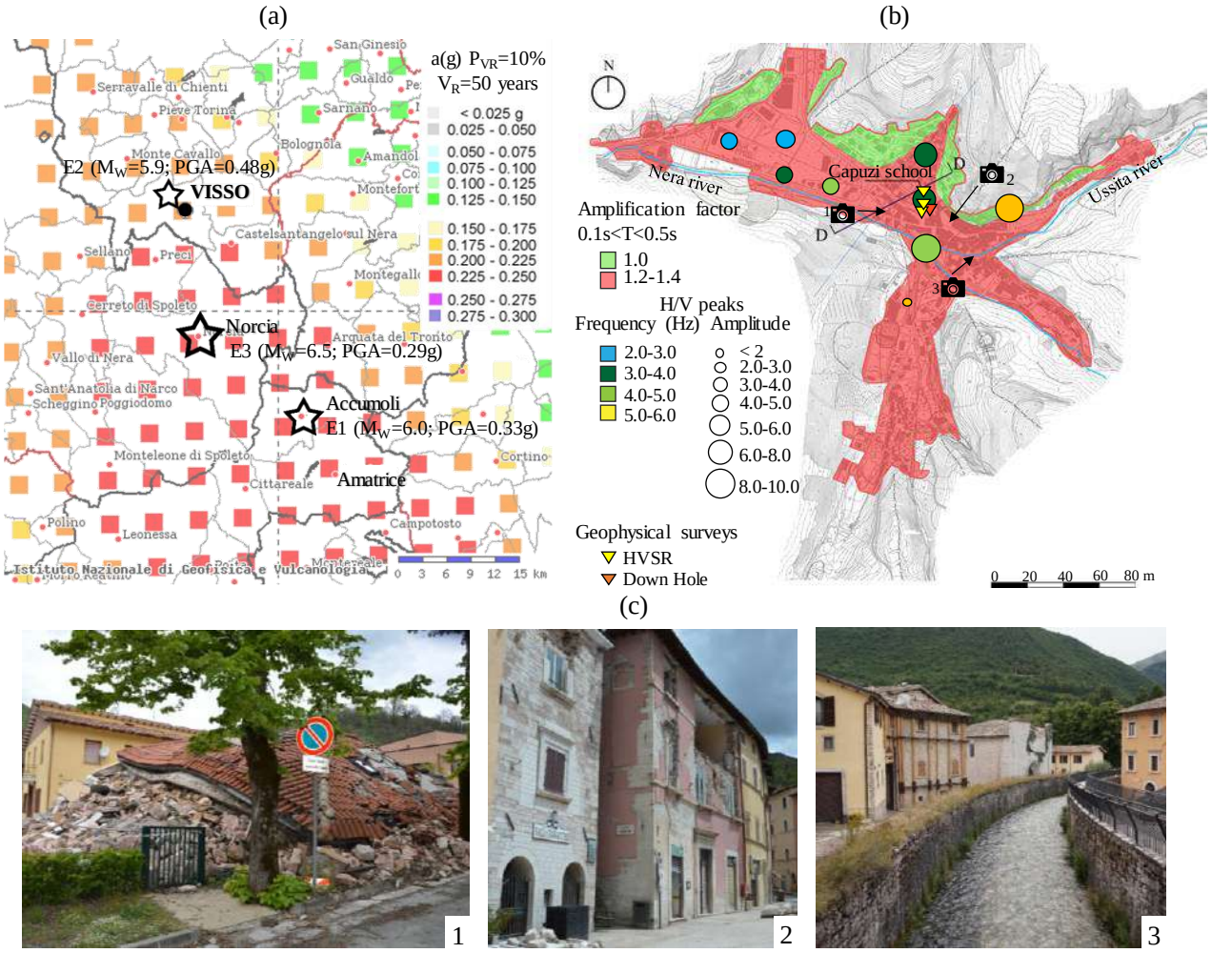

Figure 2.1. (a) Location of the 2016 seismic events vs. the Italian hazard map in terms of peak ground acceleration with a probability of exceedance equal to 10% in 50 years; (b) amplification factors estimated in Visso for buildings with periods between 0.1 s and 0.5 s and H/V peaks (MZS3 (2018)); (c) pictures of differently damaged buildings after event E3.

Figure 2.1b also indicates the position of the case study analysed in this paper: the "Pietro Capuzi" school, which was built around 1930 and extended over a 620 m^2 floor surface with T shape (Figure 2.2a). The building consisted of two stories above ground and an attic covered by a pitched timber roof. The load-bearing walls were characterized by a two-leaf stone masonry with a rather regular bond scheme; there were also four internal pillars made of brick masonry. Floor diaphragms were composed by a mixed concrete-masonry system, with an exception for the attic floor system that was made of iron beams and thin, hollow clay bricks. The timber roof was a typical "Piemontese" type system, with the covering consisting of hollow flat tiles and a thin reinforced concrete (RC) slab. The foundation system was barely an enlargement of the load-bearing walls, slightly embedded in the soil, except for the North-East side where there was a partially underground additional storey. After the 1997-1998 Umbria-Marche earthquake sequence, the building was subjected to seismic retrofitting that mainly consisted of: mortar injections through some internal load-bearing walls; insertion of some tie-rods; improvement of roof-to-wall connections; and partial replacement of the timber roof structure, the latter deteriorated due to aging. The position of most of those retrofitting interventions is shown in Figure 2.2a. More details can be found in Cattari et al. (2019a) and de Silva et al. (2019).

The municipality decided to demolish the building due to the severe damage observed after event E3, including the partial collapse of a façade that contributed to that of the upper floors (Figure 2.2b). Damage was firstly produced by shock E1 and was further aggravated by shocks E2 and E3. Figures

2c and 2d show the cumulative damage to two different piers that suffered an in-plane shear failure mode.

A detailed description of the building structure and damage observed after each single earthquake is included in the ReLUIS – Task 4.1 Workgroup report (ReLUIS (2018a)). Figure 2.3 summarizes the damage level attained by each wall (DL_W) after the three mainshocks, which was rated as follows: DL0-1: none to negligible; DL2: moderate; DL3: severe; DL4: very severe to near collapse; DL5: collapse.

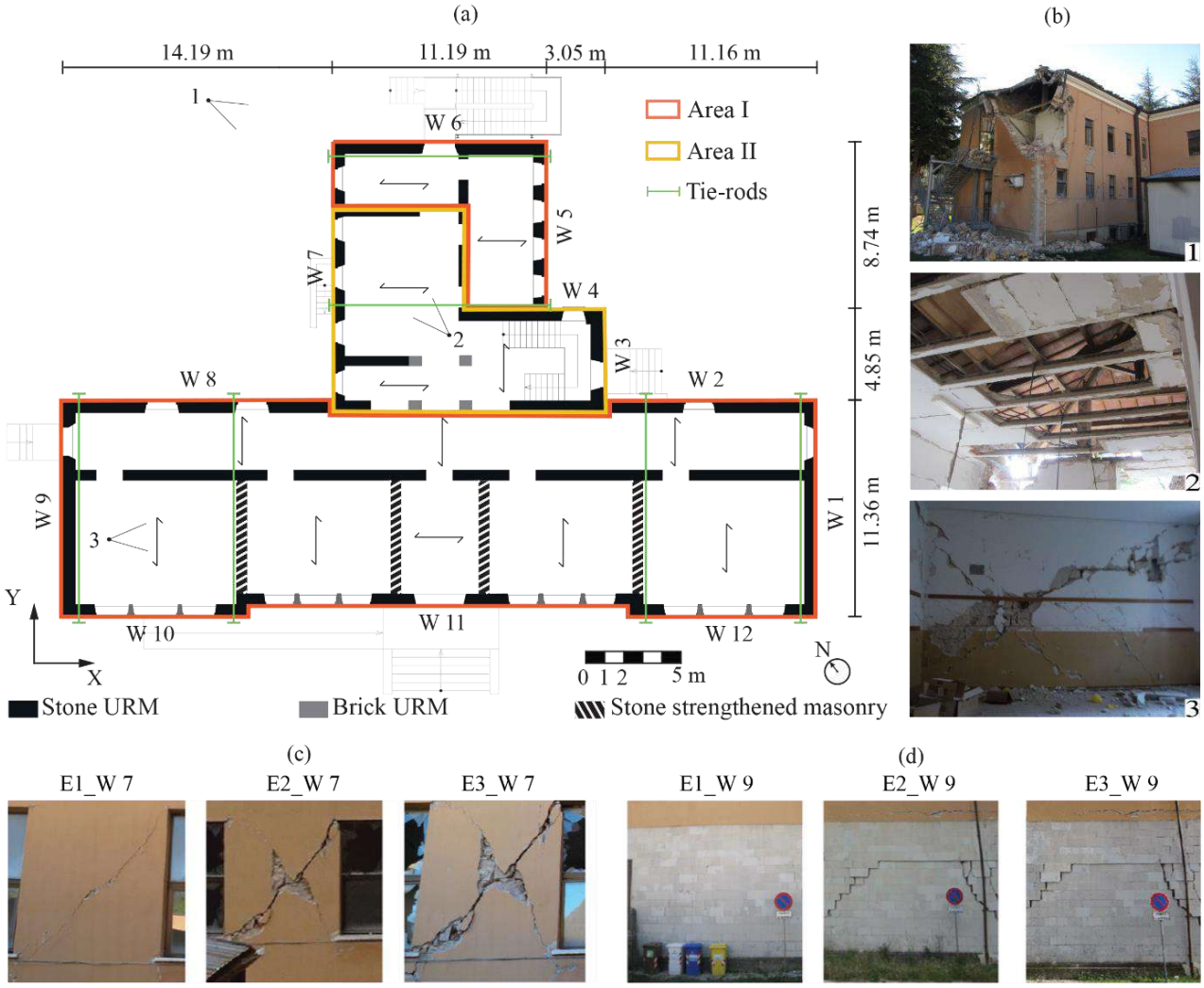

Figure 2.2. (a) Plan view of the building; (b) damage to different structural components (walls and diaphragms) observed after event E3; (c) cumulative damage observed on a pier of load-bearing wall W7; (d) cumulative damage observed on a pier of load-bearing wall W9.

A damage level DL_E was firstly assigned to the single structural elements in terms of type and severity of failure, based on the interpretation of photos made available by OSS thanks to various investigators after the first two mainshocks (E1 and E2) and the direct on-site survey carried out by the University of Genova (ReLUIS (2018a)) after the third mainshock (E3). Then, the overall damage level DL_W at wall scale was computed as weighted average of the levels DL_E assigned to the individual piers of the wall under consideration, by assuming their sectional areas as weights. In such a way, single damage peaks in some piers are lost, but a more effective overview of damage at building scale is provided. That computation considered only piers because of their primary importance in the seismic resistance of URM buildings, like the Pietro Capuzi school, which have strong spandrels due to the systematic presence of RC tie beams. The final step of damage assessment

was aimed at transforming the DL_W value into a synthetic information to map the damage distribution over the building plan, as shown in Figure 2.3. For each wall, the DL_W value was converted into an integer degree (as depicted in Figure 2.3) by conventionally assuming a binominal distribution, leading to the following ranges: 0–0.7 for DL0; 0.7–1.6 for DL1; 1.6–2.5 for DL2; 2.5–3.4 for DL3; 3.4–4.3 for DL4; 4.3–5 for DL5. Figure 2.3 provides evidence of significant damage accumulation with the highest damage severity occurred along Y rather than X direction. The collapse of diaphragms was surveyed after mainshock E3, but it probably occurred during mainshock E2, together with the activation of the out-of-plane collapse mechanism of load-bearing wall W6. Apart the activation of that local mechanism (also probably favoured by the accumulated damage), the seismic behaviour of the building was dominated by the in-plane response of walls.

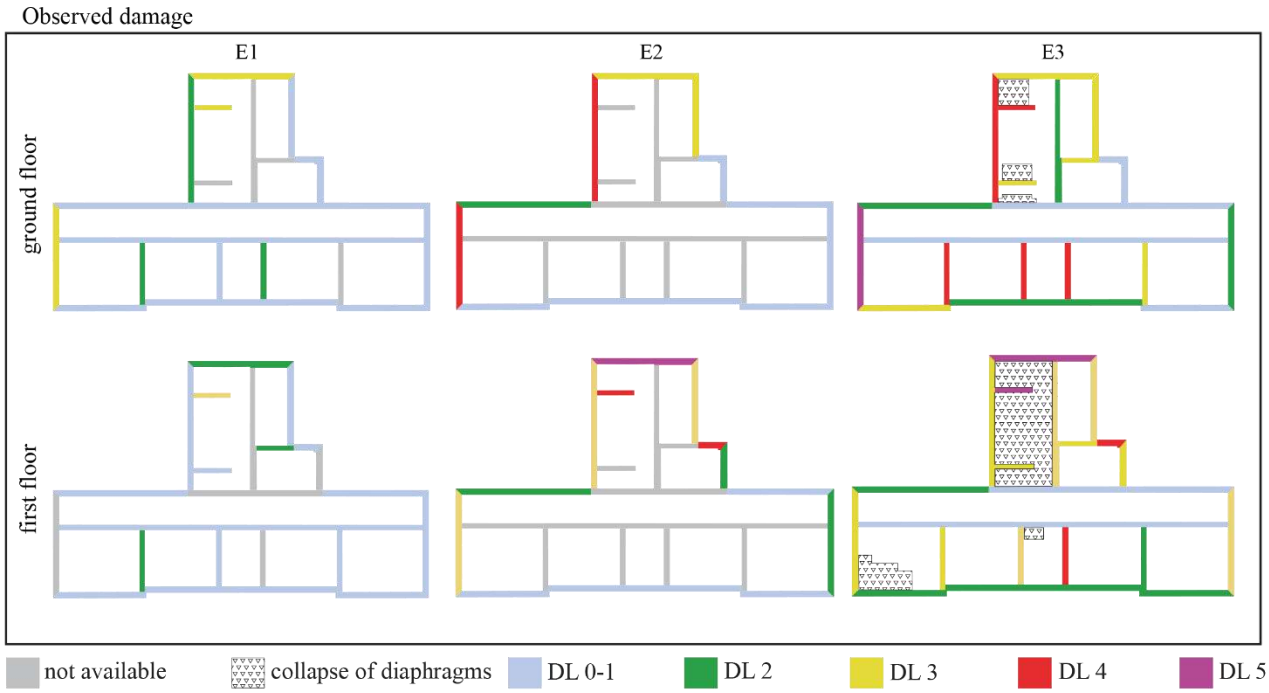

Figure 2.3. Reconstruction of the cumulative damage suffered by the load-bearing walls after the three mainshocks E1, E2 and E3. For E2, photos were available only for exterior walls.

3. GEOTECHNICAL SUBSOIL MODEL AND SEISMIC SITE RESPONSE

The geological section drawn in Figure 2.4a shows the location of the school in the middle of the valley, above an almost 40-m-thick layer of loose soil deposits covering the geological bedrock made of Scaglia Variegata and Scaglia Cinerea.

The soil closely below the Pietro Capuzi school was investigated through a borehole drilled down to 35 m and a down-hole test performed during the seismic microzonation study of the Visso village (MZS3 (2018)). In the frame of the ReLUIS research activities (ReLUIS (2018a)), the OSS made available the data of a MASW test committed by the Italian Civil Protection Department when the monitoring system was installed. Figures 2.4c and 2.4d show the layered soil profile and the associated values of shear wave velocity V_S, respectively. The predominance of a sandy gravel layer (SG), covered and locally interbedded by clayey silt (CS) and silty clay (SC) lenses, was recognized. Both DH and MASW tests reveal that the V_S of the SG deposit increases with depth, exceeding the V_S values measured in the fine-grained lenses.

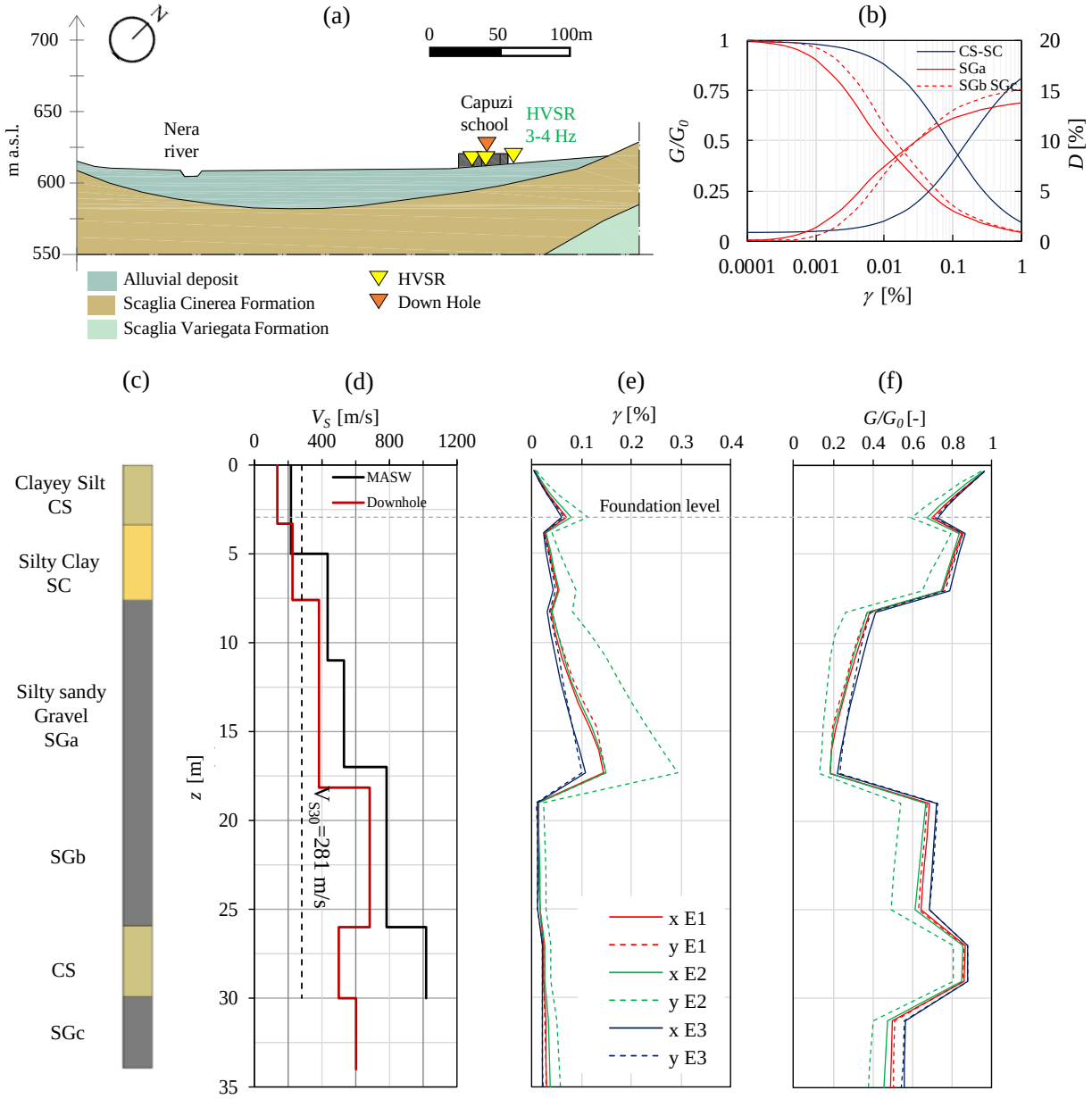

Figure 2.4. (a) Geological cross section of the Visso village area (modified after Sextos et al. (2018)); (b) variation of normalized shear stiffness and damping ratio with shear strain; (c) soil layering; (d) V_S profiles measured by DH and MASW tests; (e,f) back-figured profiles of shear strain and normalized stiffness mobilized along the building plan directions under the three mainshocks.

The one-dimensional seismic response of the subsoil profile under the three mainshocks of the Central Italy sequence was investigated through the EERA numerical code (Bardet et al. (2000)).

Table 2.1 summarizes physical and mechanical soil properties assigned to each layer (ReLUIS (2018b)): the values of V_S derive from the downhole test, whereas those of unit weight (γ), Poisson's ratio (ν) and shear wave velocity of the bedrock half-space were inferred from measurements on similar materials collected and adopted during the seismic microzonation study (MZS3 (2018)). In the same table, z_{min} and z_{max} indicate the minimum and maximum depths of each soil layer, whereas G stands for the initial shear modulus of soil. As a matter of fact, neither P-wave measurements nor laboratory tests were included in the investigations at this site.

A strain-dependent visco-elastic behaviour was assigned to all materials except for the bedrock,

through the curves in Figure 2.4b that reproduce the decay of the shear modulus normalized with respect to its small-strain value (G/G_0) and the increase of the damping ratio (D) with the shear strain amplitude (γ).

The curves adopted for the fine-grained soils (CS, SC) were obtained on the basis of a comprehensive model calibrated on the results of laboratory tests, which were performed on comparable materials in the seismic microzonation studies for Central Italy (ReLUIS (2018c); Ciancimino et al. (2019)). The functional expressions of the curves were defined assuming a plasticity index equal to 17%, based on laboratory tests on samples taken on site.

The G/G_0-γ curves obtained by Liao et al. (2013), through laboratory tests on silty sandy gravel samples consolidated at confining stress σ'_c = 52 kPa and σ'_c = 207 kPa, were associated to the shallower SGa and deeper SGb and SGc layers, respectively, in order to reproduce the dependence of nonlinear soil behaviour on the lithostatic stress. The corresponding D-γ curves were calculated by applying the Ramberg and Osgood (1943) model and the Masing (1926) criteria to the above G/G_0-γ curves taken from the literature.

Table 2.1: Physical and mechanical properties of soils.

	z_{min} (m)	z_{max} (m)	γ (kN/m^3)	V_S (m/s)	G_0 (MPa)	ν
CS_a	0	3.2	20	136	38	0.4
SC_b	3.2	8	20	226	104	0.4
SG_a	8	18	21	383	314	0.3
SG_b	18	26	21	683	999	0.3
CS_b	26	30	20	500	510	0.4
SG_c	30	40	21	602	776	0.3
Bedrock	40	–	22	1300	3790	–

A validation of the soil model is reported by Cattari et al. (2019b), who demonstrated that the resonance frequency characterizing the dynamic response of the one-dimensional soil model under a low-amplitude input motion is very close to the value measured on site (MZS3 (2018); Gaudiosi et al. (2016)) by interpreting noise records through horizontal-to-vertical spectral ratio (HVSR in Figure 2.4a).

In this study, the accelerograms recorded at the underground floor during the E1, E2 and E3 seismic events were deconvolved to the bedrock depth. The analyses were performed through the linear equivalent approach, in which materials are assumed to be visco-elastic with shear stiffness and damping ratio iteratively updated according to the strain level achieved in each soil layer throughout the shaking time history. In these deconvolution analyses, the accelerograms recorded at the underground floor level were assumed to be representative of the free-field motion.

Figures 2.4e and 2.4f show the profiles of both shear strain and normalized shear modulus provided by the deconvolution of the ground motions recorded under the three main events along the two directions, i.e. X and Y. The profile in Figure 2.4e shows larger shear strains along the Y-direction, particularly during event E2 that was the mainshock with the closest epicentre to Visso (see Figure 2.1a). In the shallowest fine soil layers, the reduction of shear modulus with the mobilized strain is moderate ($G/G_0 > 0.6$), and even in the underlying gravel the shear strain is well below 1%. Consequently, soil plastic straining in free-field conditions is not expected to have occurred.

Figure 2.5a compares the response spectra (for 5% structural damping) obtained from the accelerograms recorded at the base of the school against those provided by the Italian Building Code (NTC (2018)) for soil type C, being V_{S30} = 281 m/s as shown in Figure 2.4d. Two return periods were considered, i.e. T_R = 475 years (adopted for ordinary buildings) and T_R = 712 years (corresponding to highly important buildings such as schools). The same comparison is reported in Figure 2.5b between the spectra at the bedrock depth resulting from the deconvolution and the reference code spectrum corresponding to a rock outcrop (type A ground, T_R = 475 years). The vertical lines plotted in Figure

2.5 indicate the fundamental periods estimated for the school from the ambient vibration measurements before the seismic events (T_x and T_y, see Section 4.3) and for the subsoil (T_{soil}).
The comparison highlights that the spectral accelerations predicted by NTC (2018) are generally lower than those recorded on site, especially under the strongest event E2; such a phenomenon was already recognized in epicentral area (Iervolino et al. (2019)). Peaks of the recorded spectra occur at periods longer than those measured at school under ambient noise. Indeed, resonance might have occurred due to the close values of soil and structural periods, leading the school to suffer the spectral accelerations mostly amplified by site- effects. Moreover, the plausible increase of the fundamental period of the structure in its damaged state could have enhanced these effects.

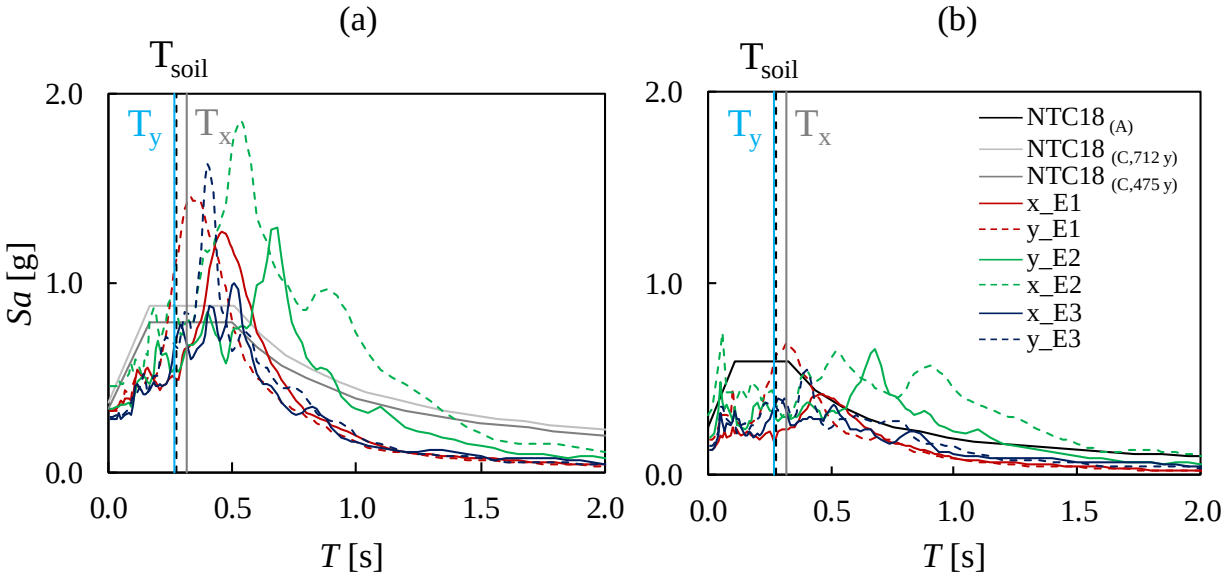

Figure 2.5. Acceleration response spectra specified by the Italian National Technical Code versus (a) spectra derived from seismic motion recorded at school building and (b) spectra back-figured through deconvolution.

4. SETTING AND CALIBRATION OF THE NUMERICAL SFS INTERACTION MODEL

4.1. Equivalent frame building model

The structural knowledge acquired from survey, together with some pre-existing results regarding the mechanical properties of masonry (ReLUIS (2018a); Cattari et al. (2019a)), permitted the authors to develop a 3D model of the structure based on the equivalent frame approach. This choice is justified by the regular pattern of wall openings in Pietro Capuzi school and by the evidence on the actual response, with cracks mainly developed in piers and spandrels as assumed by the equivalent frame idealization that concentrates the nonlinear response in those elements of load-bearing masonry walls (see e.g. Parisi and Augenti (2013b)).

The structural model was realized with the Tremuri software package (Lagomarsino et al. (2013)) that is particularly effective in performing nonlinear dynamic analyses (Cattari et al. (2018)). In the capacity model, both pier and spandrel panels were idealized through nonlinear beams with lumped inelasticity, whereas floor diaphragms were modelled as 3- or 4-node finite elements with linear orthotropic membrane formulation in plane stress conditions. The in-plane behaviour of the diaphragms and the out-of-plane response of walls were not considered, assuming a global building response mainly governed by the in-plane behaviour of walls. This assumption is consistent with the main behaviour exhibited by the building (as described in Section 2) and rigorous at least until the mainshock E2 that activated a local mechanism only in the rear body, that is, in a small portion of the building.

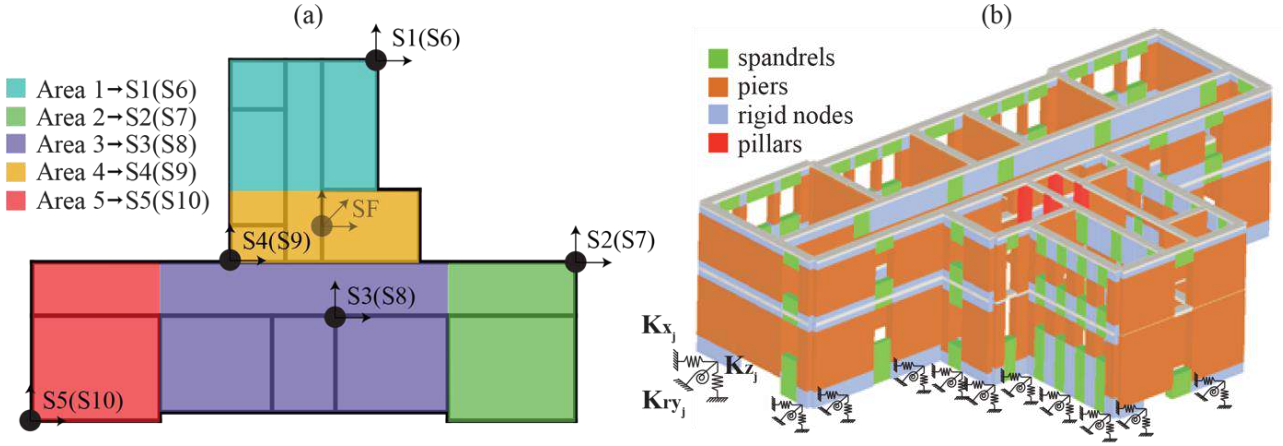

Figure 2.6. (a) Plan position of accelerometers installed by OSS and area attributed to each sensor (SF is the sensor located at the basement level, while brackets indicate sensors located at the first floor); (b) 3D equivalent frame model with springs implemented in the CB model.

The–dimensions of–piers and spandrels were assumed on basis of the criteria proposed by Lagomarsino et al. (2013); the accuracy of this choice was directly validated, since the actual pattern of seismic damage was observed on the Pietro Capuzi school. The role of other possible epistemic uncertainties in the modelling process was already deepened in Cattari et al. (2019a), leading to the following assumptions: length of RC beams intermediates between that of the opening span and the distance between two consecutive nodes; effective height of piers of the ground level varying with the actual foundation level; attic and roof modelled as equivalent mass. The RC beams are modelled according to a lumped plasticity approach by considering the flexural behaviour as ductile while the shear one as brittle; the strength criteria usually proposed also in Standards to interpret these failure mechanisms are implemented in the Tremuri software. A detailed illustration of the modelling strategy for RC beams is contained in Cattari and Lagomarsino (2013).

Two structural models were analysed in the paper, i.e. a fixed-base (FB) model and a compliant-base (CB) model in which the soil-foundation impedance was simulated with equivalent linear springs at the base of each pier (see Figure 2.6b). The underground story located in Area II (see Figure 2.2a) was not explicitly modelled, but its presence was taken into account in the computation of the spring stiffness, as described in Section 4.2.

A full factorial analysis was carried out to assess the role of aleatory uncertainties on mechanical properties of the masonry typologies detected in the structure and on the diaphragm stiffness. The following variables or groups of variables have been singled out:

- X_1 – Young's and shear moduli of the unreinforced masonry (E_{URM1}, G_{URM1});
- X_2 – Young's and shear moduli of the strengthened masonry (E_{URM2}, G_{URM2});
- X_3 – Shear modulus of the equivalent membrane assumed for diaphragms of floor level 1 ($G_{D,1}$);
- X_4 – Shear modulus of the equivalent membrane assumed for diaphragms of floor level 2 ($G_{D,2}$).

For the groups X_1 and X_2, the variables were considered as fully correlated to each other, by assuming a fixed ratio between them (G = E/3, i.e. uncompressible material) as proposed also in the Italian Building Code Commentary (MIT (2019)). This deepening permitted the definition of the more plausible combination of values (i.e. minimum, maximum or another) to be assumed for the aleatory variables for reproduction of target frequencies identified on site. The results are in the following illustrated only referring to the FB model, having checked that substantially analogous conclusions could have obtained from CB model.

Figure 2.7 shows the range of variation assumed in the factorial analysis-for the variables which has been selected to be compatible with the reference interval proposed in the Italian Building Code Commentary (MIT (2009), then recently updated into MIT (2019)) for the "cut stone masonry with good bonding". The range of variation also accounts for some modification coefficients proposed in

(MIT (2019)) to consider beneficial effects of construction features on mechanical properties of masonry (e.g. the presence of good-quality mortar joints or transverse connections). The maximum value assumed for strengthened masonry (URM2) is higher than that of unreinforced masonry (URM1), being the former strengthened by a mortar injection intervention. The shear stiffness properties of floor diaphragms (X_3, X_4) were assumed to be compatible with those of a RC slab with thickness equal to 0.05 m. Then, the apparently huge range of variation accounted for both the possible effects of material degradation and quality of floor-to-wall connections. Conversely, the brick masonry type was assumed as deterministic since it characterizes very few elements in the buildings (not able to significantly influence the overall response); the values are consistent with the mean value of the range of variation proposed in the Italian Building Code Commentary (MIT (2019)) amplified by 1.5, in order to consider the presence of a good-quality mortar.

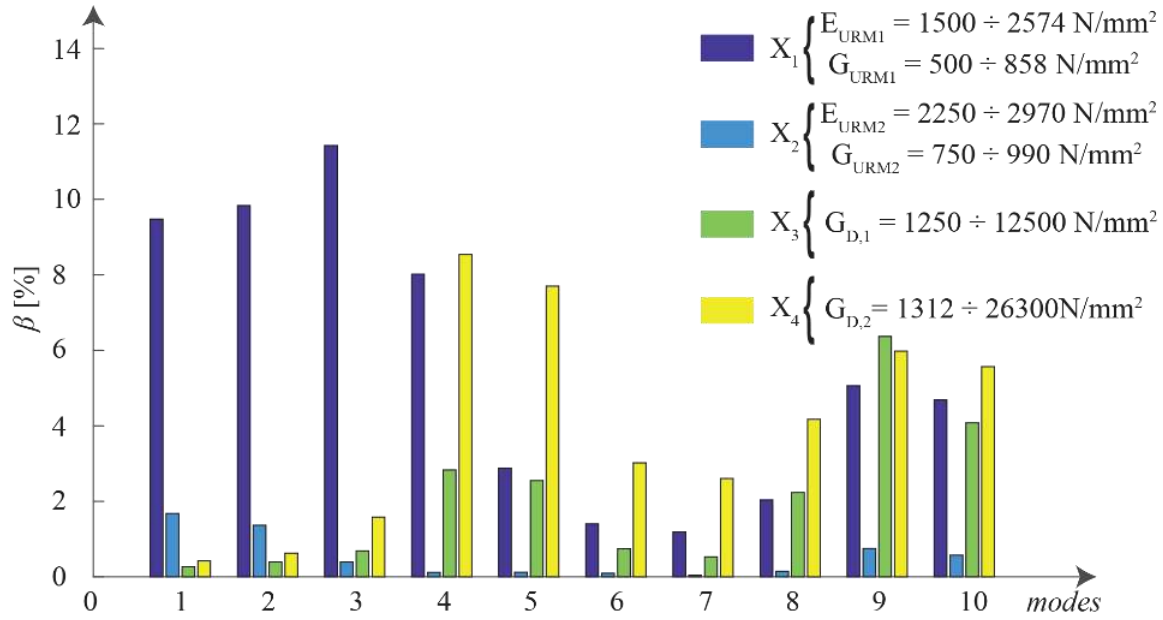

Figure 2.7. Results of the full factorial analysis carried out in phase B of the calibration process and ranges of variation assumed for the aleatory variables.

Figure 2.7 also summarizes the results of the full factorial analysis in terms of variable β_i, expressed as follows:

$$\beta_i = (\boldsymbol{Z}^T\boldsymbol{Z})^{-1}\boldsymbol{Z}^T\boldsymbol{Z} \qquad (2.1)$$

where:

- **Z** is the matrix of normalized variables (i.e. by assigning -1 and +1 to the minimum and maximum value attributed to each variable, as reported in Figure 2.7);
- **T** is the array collecting the structural response parameters, in this case the periods associated with the first 10 modes.

These results highlight that X_1 group significantly affects the first three vibration modes that mainly activated the flexural behaviour of walls (in X and Y directions). By contrast, the role of diaphragms at the first floor level (X_3 group) and second floor level (X_4 group) becomes more significant for the highest and intermediate vibration modes, respectively.

On such a basis, a final reference model was set up, through which the SFS interaction phenomena were investigated by considering both the FB and CB models and the final refinement of aleatory variables was carried out. In particular, Table 2.2 outlines the values of the stiffness properties adopted in the models, which were calibrated to achieve a satisfactory agreement of the simulated dynamic behaviour of the structure against the observations, as illustrated in Section 4.3 and in Cattari et al. (2019b). For both masonry types URM1 and URM2, the maximum value of the initial range of

variation was assumed. Moreover, the values assigned to the URM1 are also compatible - even higher - with some results of double flat-jack tests performed on the structure by OSS before the seismic events (ReLUIS (2018a)).
Table 2.2 also shows the strength parameters adopted in nonlinear dynamic analyses. In the nonlinear field, the response of piers and spandrels (in orange and green respectively in Figure 2.6b) was simulated through the piecewise-linear formulation proposed by Cattari and Lagomarsino (2013) and illustrated in Figure 2.8. The constitutive law allows for describing the nonlinear response until very severe damage levels at element scale (i.e. DL_E from 1 to 5) through progressive strength degradation corresponding to assigned drift values. The values assumed for the latter drifts and the corresponding strength decay are consistent with experimental data in the literature (Vanin et al. (2017); Graziotti et al. (2012); Beyer and Dazio (2012)). The hysteretic response is formulated through a phenomenological approach (see Cattari and Lagomarsino (2013); Lagomarsino (2015)) to capture the differences among the possible failure modes (flexural type - Figure 2.8a, shear type –Figure 2.8b, or even hybrid) and the different response of piers (Figures 2.8a and 2.8b) and spandrels (Figure 2.8c).

Table 2.2: Mechanical parameters adopted for piers and spandrels.

	E (MPa)	G (MPa)	τ_0 (MPa)	f_m (MPa)	G_D (MPa)	E_D (MPa)
X_1 - cut stone	2574	858	0.096	4.94		
X_2 - strengthened cut stone	2970	991	0.111	5.70		
brick masonry	2701	901	0.114	4.80		
X_3 - diaphragms @ floor level 1					12500	60000*
X_4 - diaphragms @ floor level 2**					26125	14641

τ_0: diagonal shear strength of masonry under zero confining stress; f_m: uniaxial compression strength of masonry; E_D: Young's modulus in the main orientation of diaphragm.

* Equivalent value, the factorization of which by the equivalent thickness assumed for the membrane allows the reproduction of the overall axial stiffness of the diaphragm, considering also the contribution from other floor components (e.g. beams).

** Equivalent values also accounting for the stiffening contribution provided by the roof (not explicitly modelled but included in the model as equivalent mass and stiffness).

As far as the strength criteria concern, the flexural behaviour was interpreted according to those proposed in NTC (2018), whereas the shear behaviour according to the diagonal cracking failure mode proposed by Turnšek and Sheppard (1980) (proposed as reference in MIT (2019) for existing masonry). In the case of spandrels, the development of a strut mechanism was assumed likely to occur due to the presence of RC tie beams and it was interpreted according to the criterion proposed in NTC (2018). Strength parameters are consistent for the masonry typology that characterized the building and are compatible with those proposed in the Italian Building Code Commentary (MIT (2019)). They were set to the same reference value (mean eventually amplified by some modification factors) similarly to what defined for the Young's and shear moduli, as resulting from the calibration process in the elastic phase. Strength values are also consistent with some evidences from experimental results available in the literature (Vanin et al. (2017); Kržan et al. (2015)). Indeed, it is evident that also the strength parameters reported in Table 2.2 and the factors that characterize the nonlinear behaviour shown in Figure 2.8 should be considered as uncertain variables.

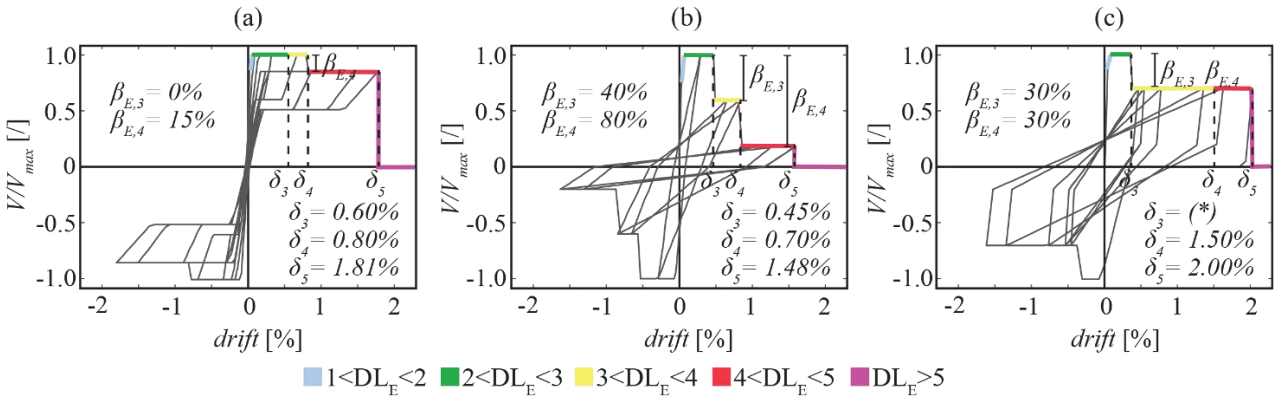

Figure 2.8. Backbone and hysteretic response of masonry elements: (a) piers under flexure; (b) piers under shear; (c) spandrels. In (c) δ_3 was defined starting from drift corresponding to the yielding point of the element and assuming a ductility factor equal to 4, similarly to what suggested in Beyer and Mangalathu (2014).

Despite this, they were considered as deterministic properties in the nonlinear dynamic analyses described in Section 5. The motivation behind that choice was to carry out a blind prediction similarly to what a common and expert analyst can do by calibrating the model against on-site dynamic identification data and then by defining the other parameters through expert judgment. In engineering practice, it is indeed not possible to make further modelling refinements in the absence of evidence from the actual response, as that kind of data is typically not available to professionals.

4.2. Setting of foundation impedance functions

Following the so-called 'substructure approach' (e.g. Wolf (1985); Mylonakis et al. (2006)), the soil-structure interaction should be modelled accounting for both 'kinematic' and 'inertial' mechanisms. As usually suggested in the literature for shallow foundations (e.g. Elsabee and Morray (1977); Kim and Stewart (2003); Conti et al. (2017)), the kinematic interaction can be neglected, being the stiffness of masonry foundations comparable to that of the surrounding soil (Pitilakis and Karatzetzou (2015)) and the embedment of load-bearing walls relatively low. Consequently, SFS interaction analysis was reduced to the inertial mechanisms only.

In the substructure approach, the dynamic soil compliance is represented through springs and dashpots assigned to the base of the structural model. The relevant dynamic stiffness and damping properties are respectively based on the real and imaginary parts of the impedance functions (Gazetas (1991)). The reliability of such a soil-structure model was already assessed for URM buildings by de Silva et al. (2018) and Piro et al. (2020) against predictions of more refined numerical methods, in which a unique soil-foundation-structure continuum system was simulated.

Since the adopted structural software package is not capable to implement base-supporting dashpots, the radiation damping was implemented in the nonlinear analyses through the procedure described in Section 5.1, whereas only the real part of dynamic soil compliance was considered at this stage of the work. The latter was computed for each degree of freedom of the foundation piers through the formulas proposed by Gazetas (1991) for a rectangular rigid foundation embedded in an elastic half-space. To get consistency between the structural and geotechnical models, the foundation length was defined by adding the half-length of the spandrel panel to the size of the load-bearing wall. Moreover, an enlargement of 0.15 m at each side of the load-bearing wall was considered, leading to a foundation width equal to 0.90 m. The value of the embedment was set to 0.6 m for Area I and 2.95 m for Area II, where the underground level was present (see Figure 2.2a).

For the dynamic impedance computation, the assumption of a homogeneous half-space for the subsoil is reliable enough. In fact, the depth - where the uppermost stiff layer is intercepted (around 18 m below the ground level, as shown in Figure 2.4c) - is much higher than that affecting the foundation motion, which is approximately equal to once to twice its width (Stewart et al. (2003); Mylonakis et

al. (2006)).
In the ambient noise records adopted for the dynamic identification analysis (Section 4.3), a full contact was supposed between the foundation and surrounding soil, where small strain levels are expected to be mobilized. For the same reason, in such analyses the static stiffness was computed considering the small-strain shear stiffness (G_0) derived from the mean shear wave velocity measured in the shallowest 3 m of the first soil layer, corresponding to the depth of the soil volume expected to affect the foundation motion (de Silva (2020)). Each dynamic impedance component turned out approximately equal to the corresponding static stiffness, since the frequency-dependent dynamic stiffness coefficients associated to the experimental fundamental frequency were close to unity. The results of the deconvolution analyses reported in Section 3 revealed that the strain levels mobilized in the shallowest soil layer are significantly lower than those associated with the plastic behaviour. Accordingly, it appeared reasonable to exclude soil plasticity without neglecting nonlinear effects. Thus, the soil nonlinearity was considered by computing the impedance functions through a 'degraded' stiffness value (G_{deg}) consistent with the shear strain levels induced in the soil by the three mainshocks. From the seismic response analyses, a mean shear stiffness G_{deg} = 26.25 MPa resulted as mobilized in the shallowest 3 m of subsoil, corresponding to about 70% of G_0.
The impedance values relevant to axial (K_z), swaying (K_x, K_y) and rocking ($K_{r,x}$, $K_{r,y}$) foundation motion components were computed considering the variability of the pier length with the position in the building. Table 2.3 summarizes the mean value (μ) and the coefficient of variation (CoV) of the data computed in Areas I and II of the structure, accounting for the different depths of the embedment. In Area II, the embedment depth induces a significant increase of the mean values along with a decrease of the statistical variation, more apparently for the rocking stiffness terms.

Table 2.3: Mean value and coefficient of variation of the real part of the impedance functions of load-bearing walls adopted in the dynamic identification procedure and in the back-analysis of the recorded seismic response.

	Area I			Area II		
	Impedances w.r.t. G_0	Impedances w.r.t. G_{deg}		Impedances w.r.t. G_0	Impedances w.r.t. G_{deg}	
	μ	μ	CoV	μ	μ	CoV
K_x (MN/m)	296	211	0.32	794	565	0.21
K_y (MN/m)	409	292	0.45	669	478	0.12
K_z (MN/m)	518	369	0.44	1200	858	0.41
$K_{r,x}$ (MNm)	351	249	1.85	2275	1614	0.08
$K_{r,y}$ (MNm)	279	200	1.38	4163	2979	0.58

4.3. Numerical model assessment through dynamic identification data

The dynamic identification data herein adopted as target for the calibration were available from the studies carried out by other researchers involved in the ReLUIS Workgroup (2018a), thanks to the data on ambient noise tests provided by OSS (e.g. as reported in Lorenzoni et al. (2019)). Indeed, the interpretation of the recordings turned out to be quite complex, providing distinct results from different teams involved in such research. Despite that, the different results agree on the fact the first modal shape suggests a combined effect of torsional and flexural behaviour along the Y direction, whereas the second mode reflects a significant torsional component and the third mode a purely flexural behaviour along the X direction.

The differences between the two available interpretations were investigated by computing the Modal Assurance Criterion (MAC) between the first three modal shapes; in particular, those identified by OSS (solution $\boldsymbol{\Psi_2}$, available from ReLUIS (2018a)) and those obtained by the research group from the University of Padua (solution $\boldsymbol{\Psi_1}$, available from Lorenzoni et al. (2019)) have been

assumed as reference. As well known, the MAC index increases from zero to unity as the match improves. Figure 2.9a shows the results, highlighting a significant uncertainty on the second modal shape.

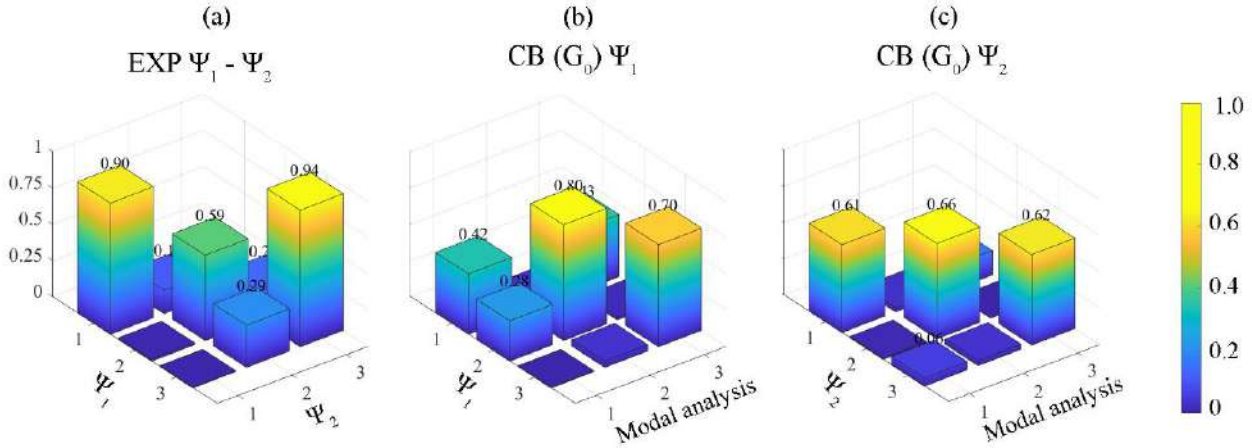

Figure 2.9. MAC matrix between: (a) two alternative interpretations of experimental data (Ψ_1 or Ψ_2); the CB model against the (b) Ψ_1 and (c) Ψ_2 interpretations of experimental data.

The left part of Table 2.4 summarizes the experimental periods associated with the first three modes. The experimental periods appear to be significantly affected by the interaction with the soil being significantly higher than those expected for a URM building characterized by the structural details and the geometrical configuration of Pietro Capuzi school when assumed fixed at the base (as discussed for example in Graziotti et al. (2019) and Ferrero et al. (2020)).

Table 2.4: Reference values of periods estimated through ambient noise measurements (ReLUIS (2018a)) and modal analysis results for numerical models.

	Periods from experimental identification		Dynamic properties from the numerical models set by using Tremuri software			
	$\boldsymbol{\Psi}_1$	$\boldsymbol{\Psi}_2$	FB	CB (G_0)	FB participating mass	
	T (s)	T (s)	T (s)	T (s)	M_X (%)	M_Y (%)
1st mode	0.294	0.315	0.174	0.258	2	67
2nd mode	0.258	0.267	0.163	0.244	1	20
3rd mode	0.203	0.247	0.148	0.218	85	0

Figure 2.10 shows the natural periods identified from the ambient noise records compared to those resulting from modal analysis of both the FB and CB equivalent frame models adopted in this study and based on the material properties characterized as described in Sections 4.1 and 4.2. For the CB model, only the springs resulting from the adoption of G_0 were assumed as reference, since nonlinearity is not expected to be induced by ambient noise. The numerical values are also reported in the right-hand side of Table 2.4 together with the estimates of the participating mass from the FB model.

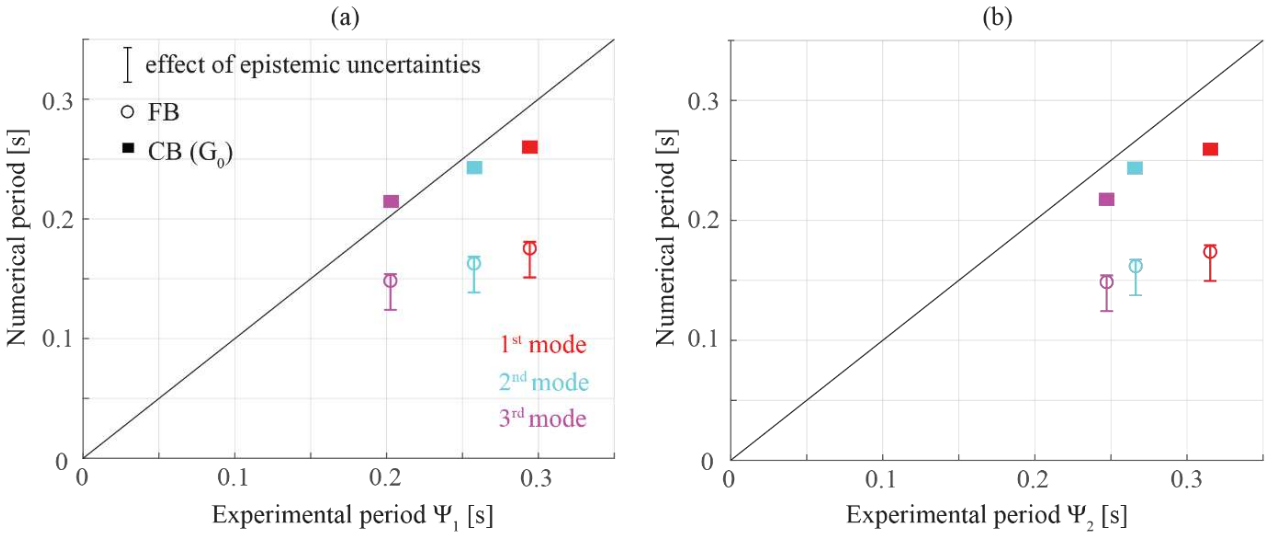

Figure 2.10. Comparison between the experimental and numerical periods according to (a) Ψ_1 and (b) Ψ_2.

The plots in Figures 2.10a and 2.10b show that the periods predicted by the CB model are much closer to the target experimental values with respect to those relevant to the FB-model, that conversely are too short for all the first three modes identified by both $\boldsymbol{\Psi_1}$ and $\boldsymbol{\Psi_2}$. Also the sensitivity to the epistemic uncertainties examined in Cattari et al. (2019) on the FB model (shown by the whisker symbols in Figures 2.10a and 2.10b) and an alteration of the values of aleatory variables are not enough to explain such a high mismatch of the fixed-base modelling, unless making unrealistic assumptions as also discussed by Ferrero et al. (2020). This result indicates a significant effect of SFS interaction on the building dynamic response, in agreement with some evidence from the survey at the scale of the whole historical centre (Sextos et al. (2018)) and from other numerical simulations (Ferrero et al. (2020)).

A final model assessment is further provided by Figure 2.9, showing even the MAC values obtained by comparing the numerical modal shapes to their experimental counterparts, i.e. CB model with impedance based on G_0 versus $\boldsymbol{\Psi_1}$ or $\boldsymbol{\Psi_2}$ in Figures 2.9b and 2.9c, respectively. Even though the relevant MAC values are not very close to unity, the calibration can be considered globally satisfactory, also taking into account the aforementioned huge uncertainty in the interpretation of experimental data.

5. NUMERICAL SIMULATION OF SEISMIC RESPONSE

For simulating the seismic performance of the Pietro Capuzi school to the series of strong-motion events (E1, E2, E3), the sequence of acceleration time histories recorded along both horizontal directions X and Y at the basement together with the vertical component were applied to nonlinear EF models with both fixed and compliant base.

While the dissipation associated with the nonlinear response of URM panels was directly considered through the hysteretic formulation introduced in Section 4.1, the soil-footing radiation damping was approximately introduced by calibrating the equivalent viscous damping of the well-known Rayleigh formulation through the method described in (Section 5.1).

The results of the nonlinear dynamic analyses are reported in the subsequent sections, where different types of comparisons are presented as follows:

- at the *local scale* (Section 5.2), in terms of acceleration time histories recorded by each single sensor versus those resulting from the analyses at the same points;
- at the *global scale* (Section 5.3), in terms of activated inertia forces versus the average top displacement, attributing to each sensor a pertinent mass estimated from the model;

- in terms of *damage mechanisms* (Section 5.4), to assess the accuracy of the model also in describing the main failure modes observed and their localization.

5.1. Evaluation of SFS interaction effects through the replacement oscillator

The total horizontal displacement of a structure on soft soil can be expressed as the sum of three contributions, with the first one associated with the oscillation of the structure (i.e. soil assumed as rigid) and the others associated with the swaying and rocking oscillations of the base (i.e. structure assumed as rigid). From such a conceptual basis, Maravas et al. (2014) demonstrated that the fundamental period $\tilde{T}$ and the total damping $\tilde{\zeta}$ of an equivalent single-degree-of-freedom (SDOF) system (the so-called 'replacement oscillator'), characterized by the same total displacement of an actual soil-structure system, can be obtained from the real and imaginary parts of the following equation:

$$\frac{\tilde{T}^2(1-2i\tilde{\zeta})}{1+4\tilde{\zeta}^2} = \frac{T_x^2(1-2i\zeta_x)}{1+4\zeta_x^2} + \frac{T_\theta^2(1-2i\zeta_\theta)}{1+4\zeta_\theta^2} + \frac{T_c^2(1-2i\zeta)}{1+4\zeta^2} \quad (2.2)$$

where:

- T_c is the oscillation period of the structure in the fixed-base conditions;
- ζ is the structural viscous damping ratio;
- T_x and T_θ are the uncoupled (fictitious) natural periods of the system under swaying and rocking oscillation of the base, respectively, they can be derived from the equation of Wolf (1985):

$$T_X = \frac{2\pi}{\omega_x} \; and \; T_\theta = \frac{2\pi}{\omega_\theta} \quad (2.3\text{-}2.4)$$

where

$$\omega_x = \sqrt{\frac{K_x}{M}} \; and \; \omega_\theta = \sqrt{\frac{K_\theta}{h^2 M}} \quad (2.5\text{-}2.6)$$

with M the mass of the structure and K_x and K_θ the real part of the impedances of the foundation.

- ζ_x and ζ_θ are energy loss coefficients relevant to the swaying and rocking modes calculated as the ratio of the imaginary part to twice the real part of the two components of the foundation impedances.

T_c increases with the ratio between the mass and the lateral stiffness of the FB structure. Since the impedances are frequency-dependent, Eq. (2.2) needs to be solved iteratively until the resulting $\tilde{T}$ is equal to the value adopted for the computation of the impedance functions. This approach was applied to the case-study building by firstly approximating the structure through a SDOF system with viscous damping ratio $\zeta = 3\%$ and dynamic properties associated with the first vibration modes of the FB configuration, as resulting from the modal analysis (see Table 2.4). Being the replacement oscillator motion expressed in terms of horizontal in-plane displacement, reference was made to the first and third vibration modes, neglecting the second one, identified as mainly torsional and with lower participating mass (see Section 4.3).

The SDOF system was therefore considered to be placed on a foundation characterized by the sum of the impedances of the Y-oriented load-bearing walls to evaluate the SFS interaction effects on the first mode. Similarly, the sum of the impedances of the X-oriented load-bearing walls was considered in the approximation regarding the third mode of vibration.

Consistently with the approaches described in Section 4.2, the soil shear stiffness was assumed equal to the following values:

- the small-strain value (G_0), to predict the fundamental periods provided by on-site dynamic identification;
- $G_{deg} = 0.7G_0$, to approximate the nonlinear seismic response under the strong-motion records.

In this latter case, the footing might even detach from the soil. Thus, two extreme hypotheses were formulated, i.e. full connection and total loss of lateral soil-foundation contact.

The good performance of the introduction of the mean mobilized shear modulus (instead of G0) within the embedment depth for the derivation of impedance functions of the foundation has also been proved in the recent studies of Di Laora and Rovithis (2015) and Stacul et al. (2022) dealing with the seismic response of pile foundations in a wide range of shear strains developed in the surrounding soil. It is considered useful to use the Gdeg also for surface foundations.
The values of period and damping ratio resulting for all the analysed cases are reported in Table 2.5, where the symbol $\tilde{\zeta}_m$ indicates the mean total damping ratio mobilized by the 1st and 3rd modes.

Table 2.5: Frequency and damping ratio predicted by the replacement oscillator*.

	$\tilde{T}$ (s)		$\tilde{\zeta}$ (%)		
	1st Mode	3rd Mode	1st Mode	3rd Mode	Mean
G_0	0.23	0.20	4.28	7.75	6.01
G_{deg} & S-F full contact	0.24	0.22	4.97	9.65	7.31
G_{deg} & S-F detachment	0.28	0.24	4.01	6.11	5.06

*S and F indicate the soil and foundation, respectively.

Assuming the small-strain soil stiffness (G_0), the periods predicted by the replacement oscillator are very close to those resulting from numerical analyses (see right-hand side of Table 2.5), with a difference equal to -12% for the 1st mode and only -6% for the 3rd mode. It is noted that the 1st mode is partially torsional and consequently more difficult to be reproduced through the simplified replacement oscillator approach. An expected period elongation occurs if the soil stiffness degradation and soil-footing detachment are incorporated.

Being the radiation damping proportional to the dimension of the soil-footing contact area, higher values of $\tilde{\zeta}$ result for the 3rd mode, since the X-oriented load-bearing walls participating to such a structural motion are longer than those oriented along Y direction, involved in the 1st mode. For the same reason, the loss of soil-foundation contact produces a reduction of $\tilde{\zeta}$.
In order to account for both structural and foundation radiation damping, the nonlinear analyses under the three mainshocks were then performed by assigning an additional Rayleigh damping ratio to the EF model, calibrated to be almost constant in the frequency range from 1.41 Hz to 3.45. The upper bound of such a range is equal to the initial main vibration frequency of the CB model, whereas the lower bound was set to include the expected frequency reduction associated with the structural damages, i.e. $1.41 = 3.45/(6)^{1/2}$, where 6 is the ductility factor. A value of $\tilde{\zeta}$ = 6% was inferred from the replacement oscillator model as an intermediate estimate between those computed by assuming G_{deg} in both contact conditions (7.31 and 5.06 in Table 2.5).

5.2. Comparisons at local scale: recorded versus numerical accelerations at sensor locations

The model capability to reproduce the seismic response of different parts of the building was quantitatively evaluated through the covariance (CoV) between the numerical accelerogram and the signal recorded by all the available sensors. The CoV computation was repeated also by considering a time lag and then by assuming as reference the highest value obtained. Figure 2.11a highlights the time lag associated with the CoV values shown in Figure 2.11b expressed as *n* times a conventional

reference time τ = 0.024s (corresponding to the sampling time of the signal). Indeed, apart very few cases (e.g. sensor #6), the time shift is not decisive in improving the agreement and in all cases can be considered very small compared to the main periods of the structure. Therefore, the time shift has a negligible effect. In Figure 2.11b, the outcome of the numerical-experimental comparison is tagged in green, yellow and red according to high, moderate and low agreement levels, which were defined in terms of CoV ranges as CoV ≥ 0.7, 0.4 ≤ CoV < 0.7 and CoV < 0.4, respectively.

(a)

Sensor (see Figure 2.6a)	FB							CB						
	ground floor				1st floor			ground floor				1st floor		
	E1	E2	E3		E1	E2	E3	E1	E2	E3		E1	E2	E3
1	+1τ	+1τ	0	6	+2τ	+2τ	+2τ	0	+1τ	-1τ	6	0	+3τ	0
2	0	0	+2τ	7	-1τ	0	+2τ	-2τ	-1τ	0	7	-2τ	-1τ	0
3	0	0	+2τ	8	0	0	+2τ	-1τ	-1τ	0	8	-1τ	-1τ	0
4	0	0	+2τ	9	0	0	+2τ	-2τ	-1τ	0	9	-2τ	-1τ	0
5	-1τ	0	+2τ	10	0	+1τ	+4τ	-1τ	-1τ	0	10	-3τ	-1τ	+1τ
1	-2τ	-4τ	-4τ	6	-1τ	-3τ	+4τ	-2τ	-2τ	-1τ	6	-2τ	-1τ	+4τ
2	-4τ	-4τ	-3τ	7	-4τ	-4τ	-2τ	-4τ	-4τ	-3τ	7	-4τ	-4τ	-2τ
3	-1τ	-2τ	-1τ	8	-2τ	-3τ	+1τ	-2τ	-2τ	-2τ	8	-3τ	-2τ	+1τ
4	-1τ	-3τ	-1τ	9	-1τ	0	+3τ	-1τ	-1τ	-1τ	9	-2τ	0	+1τ
5	0	0	+2τ	10	0	+1τ	+2τ	0	+1τ	-1τ	10	-1τ	+1τ	0

(b)

	FB							CB						
	ground floor				1st floor			ground floor				1st floor		
	E1	E2	E3		E1	E2	E3	E1	E2	E3		E1	E2	E3
1	75	63	67	6	77	49	60	1	91	68	63	6	85	60	44
2	81	65	53	7	86	77	65	2	84	87	82	7	84	87	79
3	88	81	73	8	86	81	72	3	86	91	87	8	82	86	85
4	89	68	68	9	86	81	75	4	85	77	87	9	82	86	84
5	69	66	52	10	65	65	57	5	71	77	72	10	68	70	71
1	57	41	21	6	56	44	17	1	76	76	40	6	73	68	59
2	27	18	8	7	36	18	10	2	46	64	57	7	51	58	54
3	70	70	47	8	74	60	42	3	86	84	75	8	89	81	76
4	75	67	40	9	80	56	43	4	87	87	70	9	88	75	81
5	72	49	36	10	77	51	39	5	80	73	63	10	79	71	55

X

Y

CoV ≥ 70% 40 % ≤ CoV < 70% CoV < 40%

Figure 2.11. Numerical-experimental matching of accelerations at each sensor expressed in terms of (a) time lag and (b) CoV (indicated as percentage) for all selected mainshocks, floor levels, building plan directions and equivalent frame models.

Even if both models provide a fair agreement during the first mainshock, the CB model reproduces the best overall consistency over all three mainshocks, significantly improving the response simulation of the Y component of sensor #2. For some measurement locations, the CoV values associated with the FB and CB models gradually reduce starting from the mainshock E2 and E3, respectively. Referring to the CB model, the increase in the mismatch is particularly evident for both components of sensor #1 and appreciable for the Y component of further sensors located at the ground floor. To explain such a result, it is worth to recall that during the mainshock E2 the following damage occurrences were detected (see Figures 2.2 and 2.3): (i) a local collapse mechanism activated on Wall 6 where sensor #1 was placed; and (ii) a significant damage – reaching collapse – reasonably involved the floors of Area I. As a matter of fact, both failures cannot be captured by the numerical model, which neglects the out-of-plane response of URM walls and assumes a linear behaviour of the floor diaphragms. Despite the above approximations, the general agreement between numerical results and monitoring data appears satisfactory.

The evolution of the school response along the two horizontal directions of the building plan was investigated in detail through a time-frequency analysis using the Stockwell transform (see e.g. Sundar (2019)). That transform was carried out on the recorded acceleration time histories (including the input motion) and those obtained from numerical simulations through the FB and CB models. Figure 2.12a shows the time-frequency contours relevant to the motion along X direction, using data from sensor #8 installed at the centre of the first floor and poorly affected by the local failure of curtain walls. The visual comparison between the contours obtained from the time-frequency analysis shows a good overall agreement of both numerical models with the on-site recorded data, evidencing a more significant high-frequency content in the response of the FB model.

The frequency response was analytically assessed by computing the mean predominant frequency of the experimental records and numerical results throughout the significant duration ($D_{5\text{-}95}$) of each one of the three mainshocks and during the 'quiet' pauses between two subsequent events. The latter intervals are indicated in Figure 2.12b with reference to the time history and cumulative Arias

intensity (normalised to its final maximum value for each event) of the X-acceleration recorded at the underground level of the school, i.e. that applied as input motion in the simulations. Figures 2.12c and 2.12d compare the resulting frequencies, clearly highlighting a satisfactory agreement with the experimental data during the three mainshocks (full markers). On the other hand, differences are recognized during the quiet intervals between the earthquakes (hollow markers), where motion tends to a free vibration and the response of the FB model resets to higher frequency values.
The vertical dashed lines in Figures 2.12c and 2.12d indicate the mean predominant frequencies of the input motions, again computed in the time-window of the significant duration ($D_{5\text{-}95}$).
For each event, full markers remain close to the associated vertical line, indicating that the seismic response of both the real structure and the numerical model is controlled by the frequency content of the strong input motion. Such an effect is clearly recognized during the first event (E1) in both directions and the following earthquakes (E2 and E3) along the X direction. As a matter of fact, the lower frequency response along the Y direction could have been induced by a higher amount of structural permanent damage along that direction, detected during the in-situ survey (see Section 2, Figures 2.2 and 2.3), as further discussed in Section 5.4. Furthermore, the reduction of experimental and numerical frequency in the quiet intervals between the couples of mainshocks (E1, E2) and (E2, E3) as well as after mainshock E3 confirms the structural stiffness degradation related to damage accumulation and progression of nonlinear response (de Silva et al. (2019)). As a further corroboration of the relevance of soil-structure interaction, the degradation in the experimental frequency is better captured by the numerical CB model with respect to its FB counterpart.

5.3. Comparisons at global scale: inertia forces

Figure 2.13 shows the experimental building response and the numerical simulations by the FB and CB models under the three mainshocks, in terms of horizontal components of base shear (V) versus the average top displacement (d) of the building.
The experimental behaviour was evaluated by approximating the building as an equivalent multi-degree-of-freedom (MDOF) system, having the amount of DOFs equal to the number of stories. The base shear V was computed as total inertia force at the base of the structure, i.e. the sum of recorded accelerations multiplied by corresponding inertia masses. These latter were estimated on the basis of the tributary floor area of each sensor, as shown in Figure 2.6a (see also Cattari et al. (2019a)). Similarly, the top displacement d was computed as weighted average of the nodal displacements on roof level, assuming inertia masses as weights. Starting from the mainshock E2, recordings of sensor #6 were not considered, since its response was affected by the activation of the local mechanism in Wall 6. It is worth recalling that the analyses were performed under the sequence of three mainshock signals. Nonetheless, the force–displacement curves in Figure 2.13 are plotted for each mainshock for sake of clearness.

The experimental increase of both displacement amplitude and energy dissipated in the hysteresis loops highlights a progressive development of the nonlinear response of the school building, which was more pronounced in the Y direction. Such unbalanced structural behaviour can be explained by the stronger ground motion recorded starting from the mainshock E2 along the Y direction (see Figure 2.5) and is consistent with the uneven evolution of observed damage discussed in Section 2 (see Figure 2.3). In fact, Figure 2.3 allows deducing that, moving from the mainshock E1 to E2, the damage to the load-bearing walls oriented in the X direction mostly moved from DL0-1 to DL2 (in few cases from DL2/3 to DL4/5). By contrast, most walls oriented in the Y direction experienced a damage transition from either DL0-1 to DL3 or DL2 to DL4.
The numerical results show that the difference between the FB and CB models is less evident than in the elastic field (as discussed in Section 4.3), since the effect of nonlinear structural response prevails on soil-structure interaction. In the case of CB model, a slight overestimation of top displacement can be observed in the X direction after mainshock E1. This can be explained by the lower value of equivalent damping ratio adopted in the simulation with respect to the value predicted by the

replacement oscillator approach (see Table 2.5). Along the Y direction, both models tend to overestimate the peak displacement even during mainshock E1. Thereafter, the FB model strongly overestimates the top displacement, due to the apparent attainment of the collapse condition in piers that were only partially damaged in the reality (see also Figure 2.16b in the following Section 5.4). In this respect, the simulation results of the CB model are more consistent with the recorded response. The hysteresis loops produced by mainshock E3 (characterized by a lower intensity than E2; see also Figure 2.5) indicate that the numerical models tend to underestimate a bit the response. This can be due to a slight model deficiency to reproduce the effects of damage accumulation (as pointed out by Figure 2.17 passing from E2 to E3). Despite this, results appear quite satisfactory, particularly for the CB model.

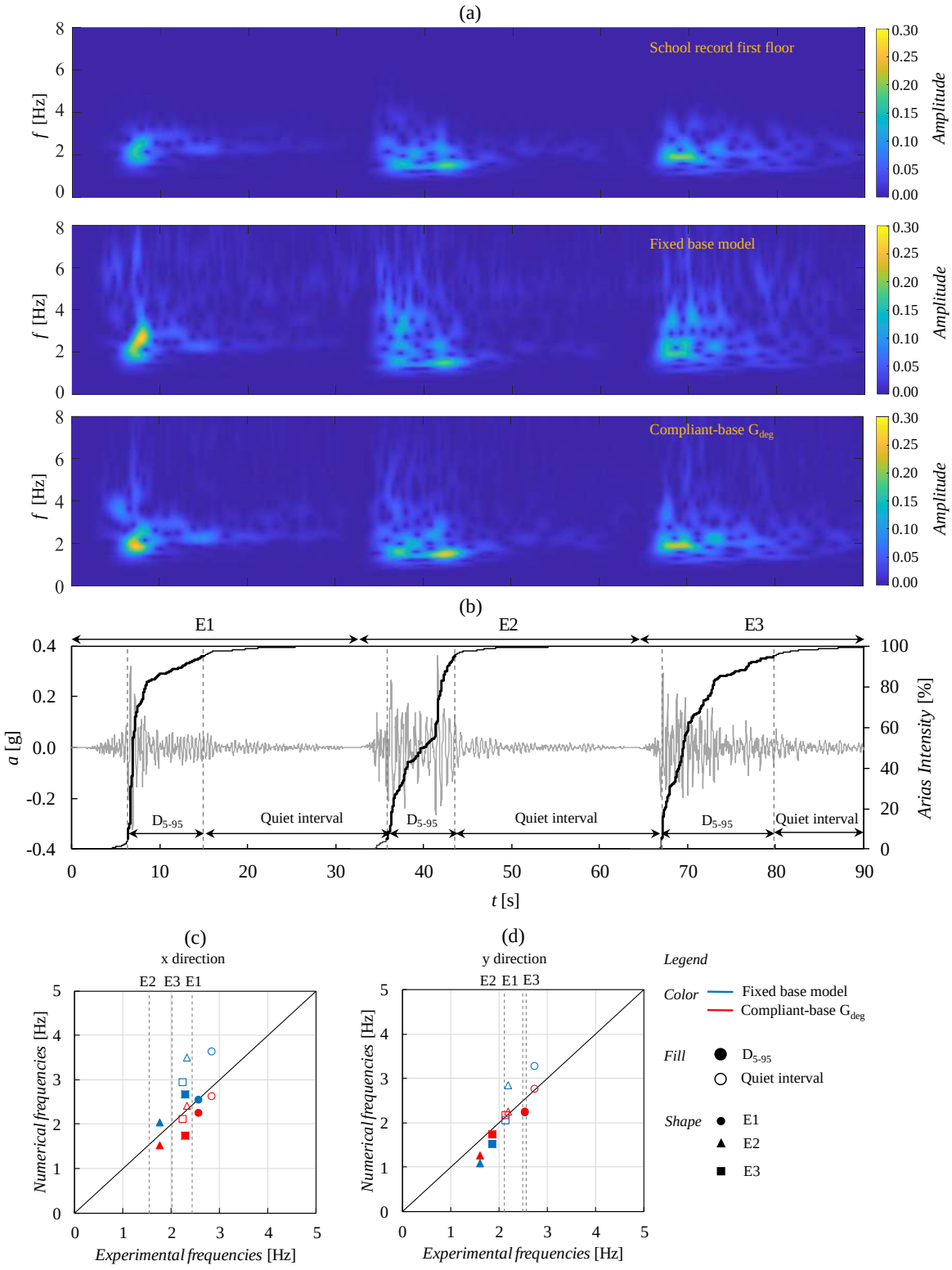

Figure 2.12. (a) Stockwell transform of the X-acceleration recorded on site by sensor #8 and simulated through the FB and CB models; (b) time histories of the X-acceleration and normalised Arias intensity recorded at the underground level of the school during the Central Italy seismic sequence; (c,d) comparison between the experimental and numerical frequencies during the three mainshocks along X and Y directions.

5.4. Real versus simulated damage

The comparison between recorded and numerical data in terms of damage was carried out at different scales, to verify the following validation aspects:

- for each pier element, the ability of the numerical simulation to capture the failure mode (i.e. flexural, shear or hybrid, herein respectively abbreviated as F, S and H), the damage level and its evolution during the seismic sequence (Figures 2.14 and 2.15);
- at wall scale, the correspondence in the prevailing activated in-plane mechanism (Figure 2.16);
- at building scale, the overall consistency in the extension and damage level throughout several load-bearing walls and parts of the structure (Figure 2.17).

Figures 14 and 15 summarize how the data from numerical simulations were post-processed, considering Wall 7 oriented in the Y direction as an example. The damage level (Figure 2.14a) and failure modes (Figure 2.14b) were firstly compared for each pier element and mainshock. Then, consistently with the observed damage (see Section 2), the reference damage level of the wall was computed as the average value of the piers weighted by their gross sectional area (Figure 2.14c). The comparison in Figure 2.14a shows a more satisfactory agreement between damage simulated by the CB model and damage observed after the whole sequence. Figure 2.14b shows that, whatever the base condition, both models predict the occurrence of the flexural failure mode more frequently than in reality. Finally, Figure 2.14c suggests that both numerical models tend to overestimate the damage severity at the wall scale under the mainshock E1, with the CB model better predicting the subsequent cumulated damage at both floor levels.

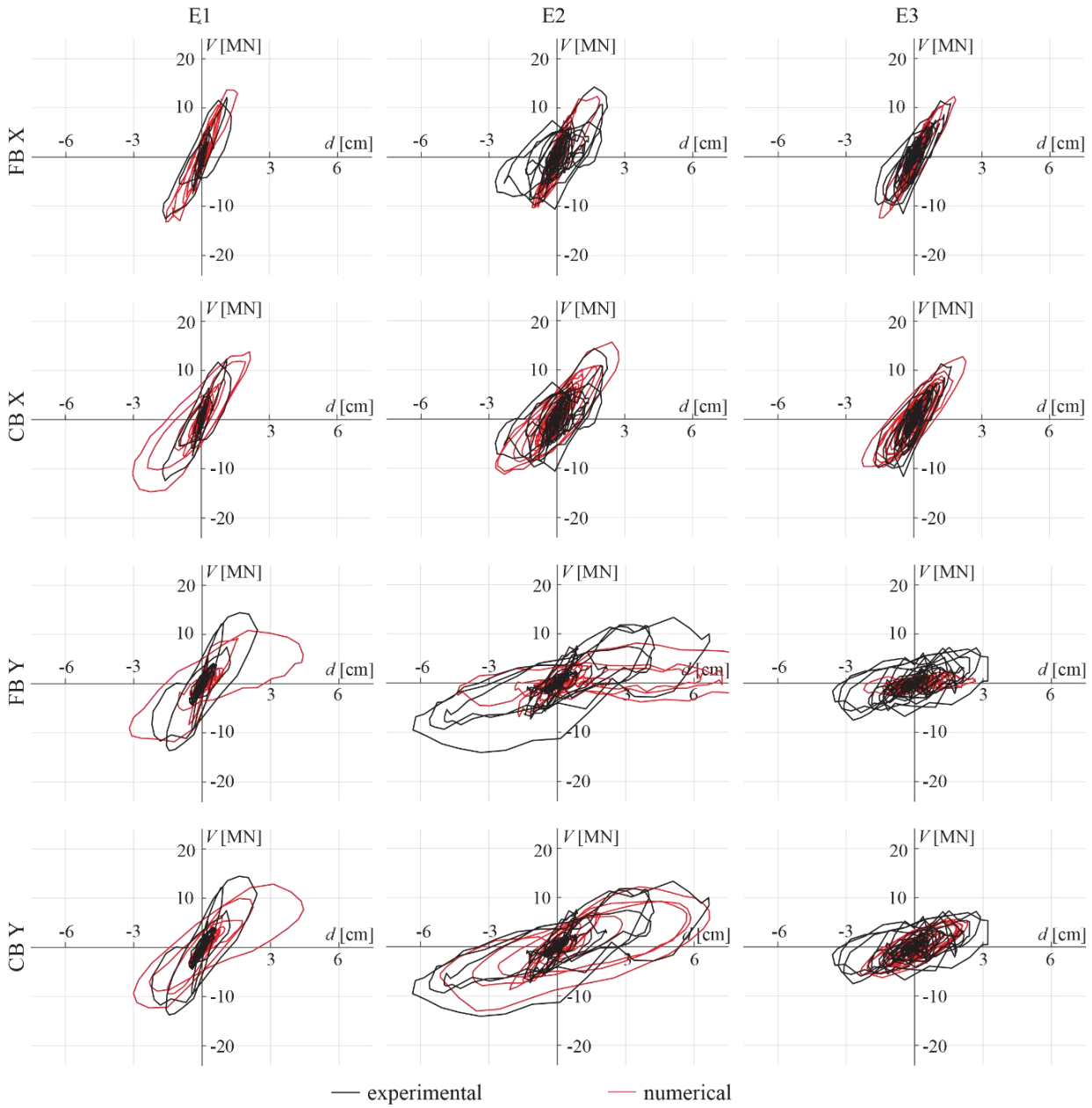

Figure 2.13. Comparison between experimental and numerical base shear–top displacement curves (numerical curves derived from nonlinear time histories under the sequence of consecutive mainshock records).

Figure 2.15 shows a detailed, element-by-element comparison between the observed and simulated damage to Wall 7 after mainshock E3, considering the numerical results associated with the CB model. Such a comparison shows a good agreement on the distribution of failure modes activated throughout the wall, with a higher overall damage at ground floor. As expected, a higher damage level affects piers rather than spandrels, being these latter strengthened by the RC tie beams.

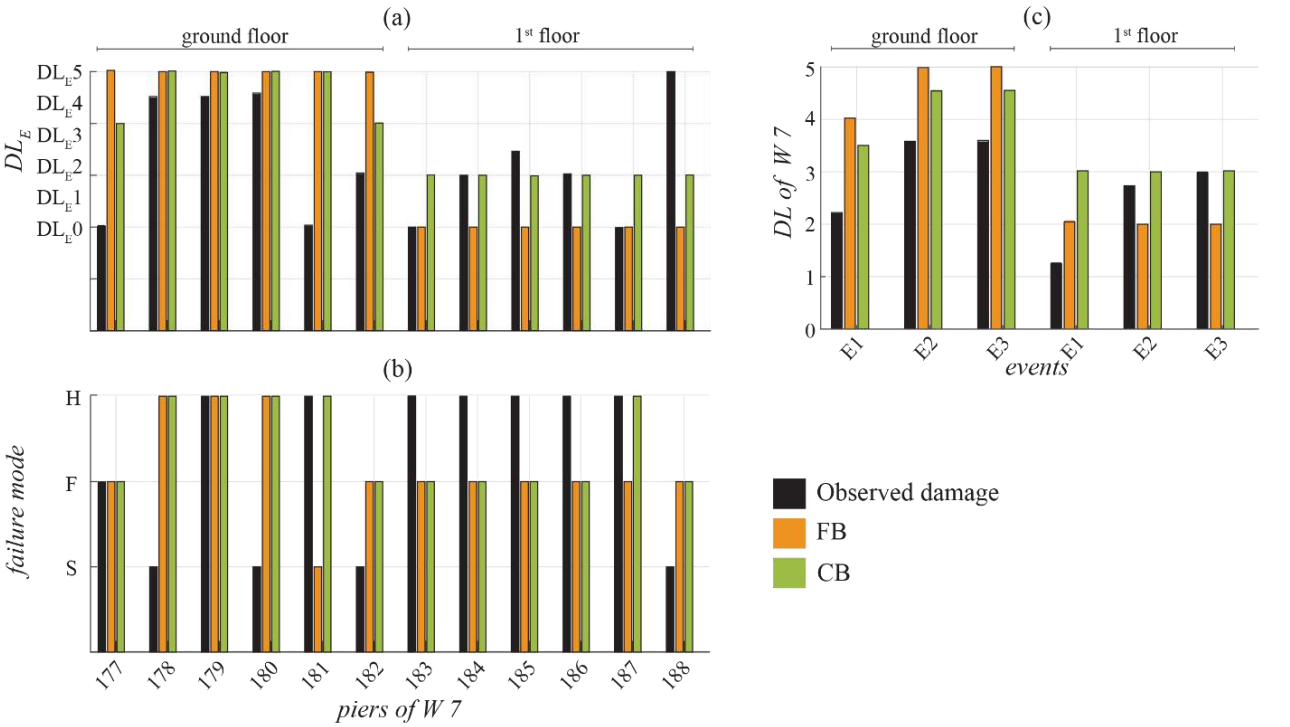

Figure 2.14. Damage comparison at single element scale in terms of (a) severity and (b) failure mode after mainshock E3 (F = flexural, S = shear, H = hybrid; for the element numbering refer to Figure 2.15). (c) Damage level computed at wall scale.

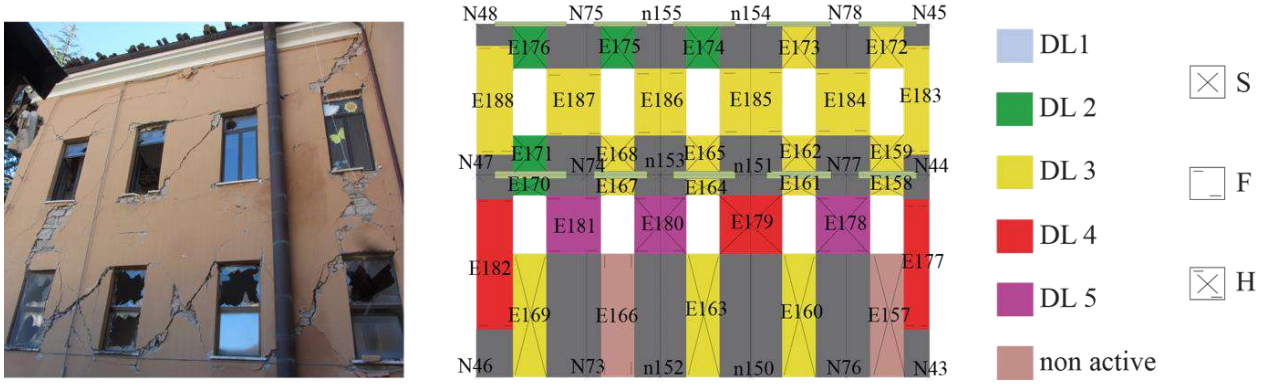

Figure 2.15. Comparison between observed and simulated damage on CB model for Wall 7 after mainshock E3.

Figure 2.16 shows an overview of the damage level simulated at scale of each wall after mainshock E3. In general, a quite overall good agreement can be observed but, on average, the FB model is too over-conservative at the ground floor and the numerical simulations overestimate the damage at the first floor. Overall, the CB model is found to allow the best simulation of the observed damage.

Finally, Figure 2.17 depicts the cumulative rate of pier damage ($CD_{DLi,piers}$), computed as the percentage of piers that reached or exceeded a given DL, weighted by the corresponding gross sectional area, as originally proposed by Lagomarsino and Cattari (2015a). The damage evolution was reconstructed also for the observed damage, as reported in Section 2. It is worth to recall that the increase of the observed damage moving from mainshock E2 to E3 is affected by more uncertainty with respect to that related to the transition from mainshock E1 to E3, due to less accurate information available after mainshock E2.

Notwithstanding the already mentioned inconsistency about the initial overestimation of damage following mainshock E1, the models appear able to satisfactorily reproduce the subsequent accumulation. In general, it can be observed that both numerical models tend to overestimate the

occurrence of moderate damage (i.e. DL2), whereas a quite good agreement is found for the higher severity degrees (i.e. DL3 through to DL5), particularly for the CB model at the end of seismic sequence. Indeed, it should be recalled that a reliable assignment of DL2 at the pier scale is more difficult to make in reality, being that damage level associated with the attainment of a yielding condition that is complex to be detected by visual inspection.

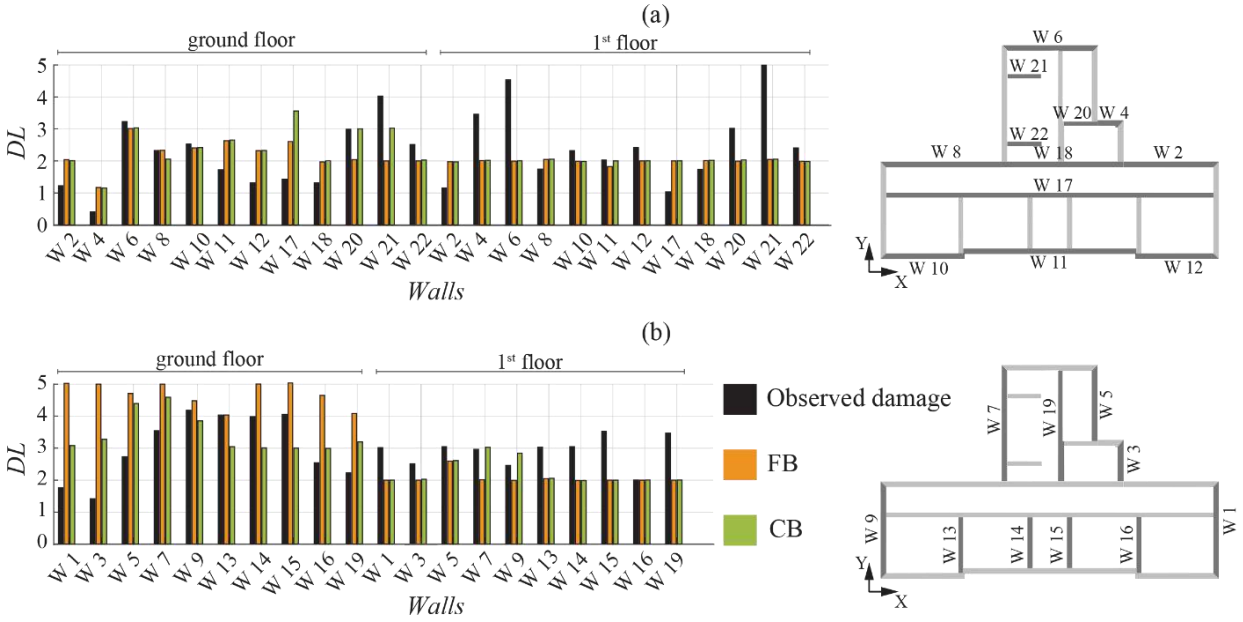

Figure 2.16. Comparison between simulated and observed damage levels after mainshock E3 for load-bearing walls oriented along (a) X and (b) Y directions.

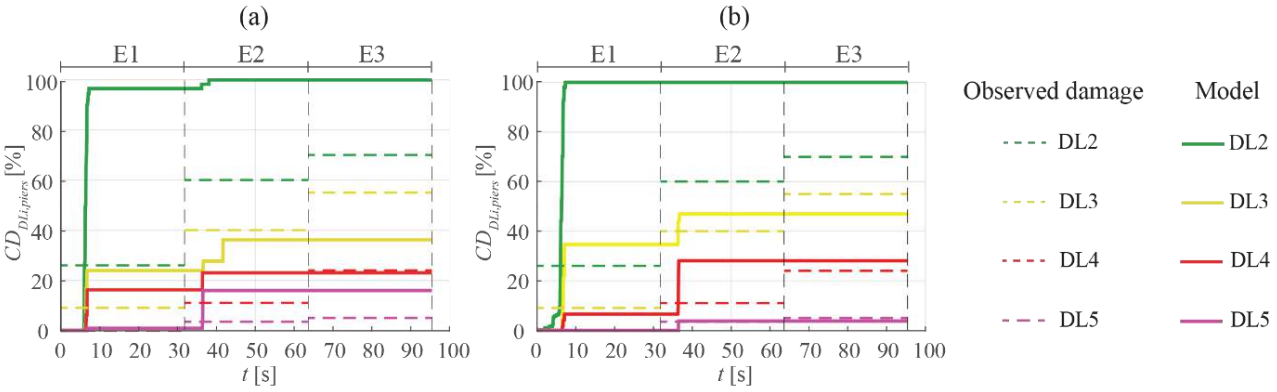

Figure 2.17. Comparison between the cumulative rate of pier damage as simulated and observed after each mainshock: (a) FB model; (b) CB model.

6. CONCLUSIONS

The paper investigated the seismic response of the Pietro Capuzi school in Visso, which was monitored during the 2016-2017 Central Italy earthquake sequence. The school represented almost a *unicum* for the amount of data available not only on the structural response but also on the soil characterization. The availability of both qualitative information on damage accumulation phenomena (as reconstructed by photos and in-situ surveys) and quantitative data (as provided by the permanent monitoring system) formed a valuable and indispensable source for a comprehensive validation of equivalent frame models with and without consideration of soil-foundation-structure interaction.

The fundamental periods of the structure, as identified from the interpretation of ambient noise measurements, resulted very close to the soil predominant period, evidencing that the spectral accelerations affecting the building performance are those mostly amplified by the soil. Such an occurrence, together with the intensity and frequency content of the seismic events, justified the high damage level observed on the school structure, which did not present significant deficiencies nor vulnerability factors (apart the in-plan irregularity) from a structural point of view.

Nonlinear time history analyses were performed by applying the accelerograms recorded at the school basement to fixed-base (FB) and compliant-base (CB) three-dimensional models of the building, which were developed according to the equivalent frame approach. Periods and modal shapes of both models were compared to the results of the on-site dynamic identification of the school. The comparison revealed a strong influence of the soil compliance in the linear range, so that the match between experimental and numerical frequencies is much better in the case of the CB model.

Conversely, the nonlinear response of the FB and CB models is more similar during the three strong motions, because (i) the mobilization of structural nonlinearity prevails on the soil-structure interaction effects and (ii) the seismic structural response is mainly governed by the frequency content of the input motions. As a matter of fact, more significant differences between the responses of the two models were recognized through a time-frequency analysis during the low-amplitude stages of the input motions. Both the experimental and numerical predominant periods of the school increase over time, highlighting a stiffness degradation of the structure and the relevant progression of nonlinear response, as proven by the damage accumulation detected by the in-situ survey.

It must be underlined that the soil-structure model was calibrated in the linear regime due to the availability of dynamic identification data, whereas nonlinear analyses were performed as a ‘blind prediction’. In fact, nonlinear material properties, such as the masonry strength and the strain-dependency of soil stiffness and damping, were set on the basis of reference literature data, without altering or back-figuring them in order to achieve the best match with the experimental records. This choice firstly reflects the will to test the effectiveness of the equivalent frame modelling in a representative application as it might be managed by a common, even if expert, analyst. The simulation demonstrates satisfactory results, validating the accuracy of such a structural modelling strategy that is widespread in engineering practice. Moreover, the uncoupled approach based on proper impedance functions appeared quite promising to simulate the SFS interaction, if carefully calibrated by duly considering soil nonlinearity and radiation damping. As a perspective, coupled advanced approaches accounting for the explicit modelling of the soil as a continuum will be very useful to confirm the role of SFS interaction and to corroborate the use of more simplified strategies, such as the uncoupled approach, also in the case of URM buildings.

CHAPTER 3

Derivation of fragility functions for URM school

Summary:
Starting from the modelling strategies validated in Chapter §2, Chapter §3 investigates the influence of the variability of the mechanical parameters controlling the response of the soil-foundation system on the response of the compliant-base model of the school of Visso.
In particular, the two most widespread approaches, i.e. Gazetas (1991) and Pais and Kausel (1988), and all the analytical formulations reported by Givens et al. (2016) were checked for the calibration of the impedance functions and the equivalent damping ratio. They were calibrated according to the stiffness and damping ratio mobilized into the soil by weak to strong motions, to check their sensitivity to the development of soil nonlinearity. The sensitivity analysis revealed that the different approaches poorly influence the model response, while the most influencing parameter is the soil hysteretic damping, which reduces the damage and provided an improvement in the match with the real behaviour of the case study at hand.
For this reason, the fragility curves of the school were extensively developed accounting for the site and SFS interaction effects and with the contribution of soil hysteresis. The damage predicted by the so computed fragility curves was compared with that obtained by entering in the fragility curves of the fixed base structure by simply amplifying the intensity measure to account for site effects through the amplification factors provided by Codes This chapter is published by Brunelli et al. (2022a). The complete selection used as input motion of nonlinear dynamic analyses to generate the fragility curves is attached as supplementary material to Brunelli et al. (2022a). The same is here attached at the end of Chapter §3.

published in *Soil Dynamics and Earthquake Engineering* **154**(4), 107125.
DOI:10.1016/j.soildyn.2021.107125

SITE EFFECTS AND SOIL-FOUNDATION-STRUCTURE INTERACTION: DERIVATION OF FRAGILITY CURVES AND COMPARISON WITH CODES-CONFORMING APPROACHES FOR A MASONRY SCHOOL

Andrea Brunelli[1], Filomena de Silva[2], Serena Cattari[1]
[1]University of Genova, Genoa, Italy
andrea.brunelli@edu.unige.it, serena.cattari@unige.it

[2]University of Naples Federico II, Naples, Italy
filomena.desilva@unina.it

Abstract:

The paper investigates the role of site-amplification and soil-foundation-structure (SFS) interaction on the seismic response of masonry structures. The aim is twofold: i) to quantify the potential impact of such effects on fragility curves numerically derived through nonlinear dynamic analyses; and to verify the reliability of conventional code-conforming approaches. These goals are pursued by referring to a prototype masonry building inspired by a school whose response was proven to be affected by SFS interaction during the Central Italy 2016/2017 earthquake. The 3D structural model was generated through the equivalent frame approach, able to simulate the in-plane nonlinear response and the hysteretic behaviour of masonry panels. The model was firstly fully restrained at its base to simulate the fixed-base conditions and then endowed with springs simulating the soil compliance. To account for the energy dissipated by the foundation, the latter model was characterized by a damping ratio higher than that assumed for the fixed base. The sensitivity of the structural response to various formulations of the soil-foundation stiffness and damping was investigated. Nonlinear dynamic analyses were performed on both models, firstly, under the acceleration time histories of 49 natural earthquakes recorded on stiff rock outcrop, and, then, propagated through a site response analysis in a 1D soil model reproducing the actual soil profile under the examined school. The resulting fragility curves confirmed the expected negative impacts of site amplification, while highlighted a potential beneficial role of the SFS interaction enhanced by soil hysteresis. In the latter case, the probability of failure reduces more significantly at severe and very severe to near collapse damage levels. Finally, the average damage associated with the fragility curves calculated in this study was compared with that obtained from the fragility curves of a fixed base system in which site effects are considered through the conventional coefficients proposed in three different international Standards. The comparison highlighted that, when only site effects are considered, the code-approach underestimates the damage up to three damage levels. The beneficial effect of the SFS interaction reduces this gap but a difference of one/two damage levels still results.

Keywords: seismic site amplification, soil-structure interaction, fragility curves, masonry structures, foundation damping ratio, nonlinear dynamic analyses, code previsions.

1 INTRODUCTION

Evidence from past earthquakes has already highlighted the detrimental effects of site-amplification in the damage of existing unreinforced masonry (URM) buildings (see Sextos et al. (2018); Sorrentino et al. (2019); Stewart et al. (2018); Chieffo and Formisano (2020); Brando et al. (2020)). Together with this evidence at large scale or on huge building stocks, numerical studies on refined models constitute a valuable source: i) to integrate the knowledge and better understand the phenomenon; ii) to assess the reliability of more simplified practice-oriented approaches, as those implemented in Codes; iii) to explicitly investigate the effects of the soil-foundation-structure (SFS) inertial interaction. As known, such effects mainly consist of: a) the elongation of the natural period with respect to the fixed base condition; ii) and the generation of the radiation and hysteretic damping. They respectively account for the energy dissipated by the wave scattering from the foundation and for the hysteresis of the soil beneath the foundation. Within the field of risk analyses addressed to support mitigation policies, the development of fragility curves including also such effects turns out to be very useful. That represents the main goal of the paper.

While various literature works already addressed these issues for reinforced concrete (see Rajeev and Tesfamariam (2012); Karapetrou et al. (2015); Mitropoulou et al. (2016); Oz et al. (2020); Karapetrou et al. (2013); Tomeo et al. (2018); Petridis and Pitilakis (2020)) or steel structures (see Mashhadi et al. (2021); Hamidia et al. (2021); Homaei (2021)), very few are those dealing with URM buildings. Moreover, the latter ones are mostly focused to slender structures (like as towers (e.g. Casolo et al. (2017); de Silva (2020)) or minarets (e.g. Bayraktar and Hökelekli (2020)), massive monumental assets (like as fortresses Karatzetzou et al. (2015) or Fathi et al. (2020)) or infrastructures (like as masonry bridges Güllü and Jaf (2016)) rather than ordinary buildings which this paper focuses on. Moreover, the works available on ordinary URM buildings are mainly based on an empirical approach calibrated on observed data (Peduto et al. (2019); Chieffo and Formisano (2020)), while the attempts addressed to investigate the issue through the execution of nonlinear dynamic analyses (NLDA) on URM structures founded on piles (Cavalieri et al. (2020) or shallow foundations (Brunelli et al. (2021a)) are quite recent.

Only a few of the above-referenced studies (Karapetrou et al. (2013); Karapetrou et al. (2015); Tomeo et al. (2018); Petridis and Pitilakis (2020); de Silva (2020)) proposes fragility curves derived from coupled analyses, i.e. in which structure and soil are modelled together to directly account for both site amplification and SFS interaction. Due to the huge computational effort of the coupled approach, in most cases the inertial effects of SFS interaction are modelled by restraining the structural base through springs and dashpots simulating the soil reaction to the foundation motion. The spring behaviour can be modelled as elastic (Karapetrou et al. (2013); Mitropoulou et al. (2016); Oz et al. (2020); Petridis and Pitilakis (2020)) or elastic-plastic (Rajeev and Tesfamariam (2012); Tomeo et al. (2018); Mashhadi et al. (2021); Hamidia et al. (2021); Homaei (2021)). The compliant-base models are excited by seismic motions recorded on stiff rock outcrops (Rajeev and Tesfamariam (2012); Tomeo et al. (2018); Oz et al. (2020); Mashhadi et al. (2021); Hamidia et al. (2021); Homaei (2021)) or amplified by coefficients to account for the site effects (see Mitropoulou et al. (2016)). The ground motion is calculated through site response analyses by Karapetrou et al. (2013) and Petridis and Pitilakis (2020).

Within this context and with the aim of contributing to fill this gap, in the paper fragility curves are developed referring to a prototype URM structure inspired by the "Pietro Capuzi" school in Visso (MC, Italy). The school constitutes a quite emblematic benchmark since it was monitored by the Italian Seismic Observatory of Structures (Dolce et al. (2017)). Thus, recordings under the three mainshocks of the 2016-2017 Central Italy earthquake and a quite accurate reconstruction of the actual damage are available from numerous accelerometers installed on the building. Nowadays the school has been demolished due to the very severe damage occurred, but the records are still available under request to the Italian Department of Civil Protection and the structural details are available from other research projects (Cattari et al. (2019a); Cattari and Magenes (2022)).

The selection of this case study is further motivated since previous literature works (Brunelli et al. (2021a); Dolce et al. (2017); Cattari et al. (2019a); Cattari and Magenes (2022); Ferrero et al. (2020)) proved that its actual seismic response during the Central Italy 2016-2017 earthquake has been affected by both site amplification and SFS interaction. In this paper the numerical model validated by Brunelli et al. (2021a) becomes the tool to perform a huge amount of NLDA and pursue the aforementioned widest goals. Among all the possible strategies discussed in D'Altri et al. (2020), the structural model was generated through the equivalent frame approach which is reliable in describing the seismic response of URM buildings dominated by the in-plane global response and characterized by a quite regular pattern of openings (see for example Penna et al. (2016); Marino et al. (2019a)) such as the examined one. Moreover, the equivalent frame approach is computationally efficient in executing a large set of NLDA (see for example Cattari et al. (2018)).
As usual in the literature for shallow foundations (see Kramer (1996)) and confirmed by several numerical studies on the kinematic interaction factors (Conti et al. (2017)), the foundation input motion is assumed to be coincident with the free field signal resulting from 1D site response analysis. Hence the latter has been applied to the base of the structural model. The effect of the inertial SFS interaction has been introduced by equipping the model base endowed with springs and assigning a damping ratio higher than that typically assumed for the fixed base structures. Many works (one for all Gazetas (2015)) have recognized the contribution of the foundation damping ratio to dissipate the seismic energy and numerous analytical formulas have been proposed for its quantification (Veletsos and Nair (1975); NIST (2012); Maravas et al. (2014)). Although the latter has been theoretically compared by Givens et al. (2016), the sensitivity of numerical results to their different predictions has never been checked against data recorded on a complex SFS system, like the case study at hand. For this reason, i) different impedance functions (Pais and Kausel (1988); Gazetas (1991)) to calibrate the stiffness of the base springs and ii) different formulas to estimate the foundation damping ratio have been adopted in this study, as illustrated in sections 5.2 and 5.3, respectively.
The proposed fragility curves were derived by calculating the free field motion through linear equivalent site response analyses. This allowed to accurately account for site effects and to calibrate the spring stiffness and the foundation damping in a more refined way, *i.e.* based on the stiffness and damping mobilized in the foundation soil during each earthquake. In particular, the soil hysteretic damping was included in the computation of the impedance functions while only the radiation component is generally considered in the existing literature. Besides the compliant-base model, also the response of a fixed-base one has been examined under the same selection of accelerograms, either propagated along the 1D soil profile or not. The comparison among the resulting fragility curves were used to assess the site effects due to the soil stratigraphic amplification. Similarly, the comparison among the fragility curves of the fixed-base model and that of the model on springs allowed to assess the potential effect of SFS interaction. All the results were finally exploited to assess the accuracy of practice-oriented approaches as those recommended in Codes (see Italian code NTC (2018); Eurocode CEN (2004); American code ASCE7 (2016); New Zeland code NZS (2017)) which are based on the use of conventional amplification factors to account for the site effects.

2 METHOD OF ANALYSIS

Figure 3.1 shows the three main paths adopted for the derivation of fragility curves:

- the black one defined as FB A case, that is the fixed base (FB) structural model investigated by NLDA performed with records of natural earthquakes selected to be representative of the rock soil;
- the red one defined as FB C case, according to which the fixed base structural model is analyzed under accelerograms derived through the linear-equivalent one-dimensional seismic response analyses of the soil profile below the school (belonging to the class soil C according to the classification by Codes (NTC (2018); CEN (2004));
- the cyan one defined as CB C case, in which the SFS interaction was considered by analyzing the compliant base (CB) model under the same free field input motions adopted in the FB C case.

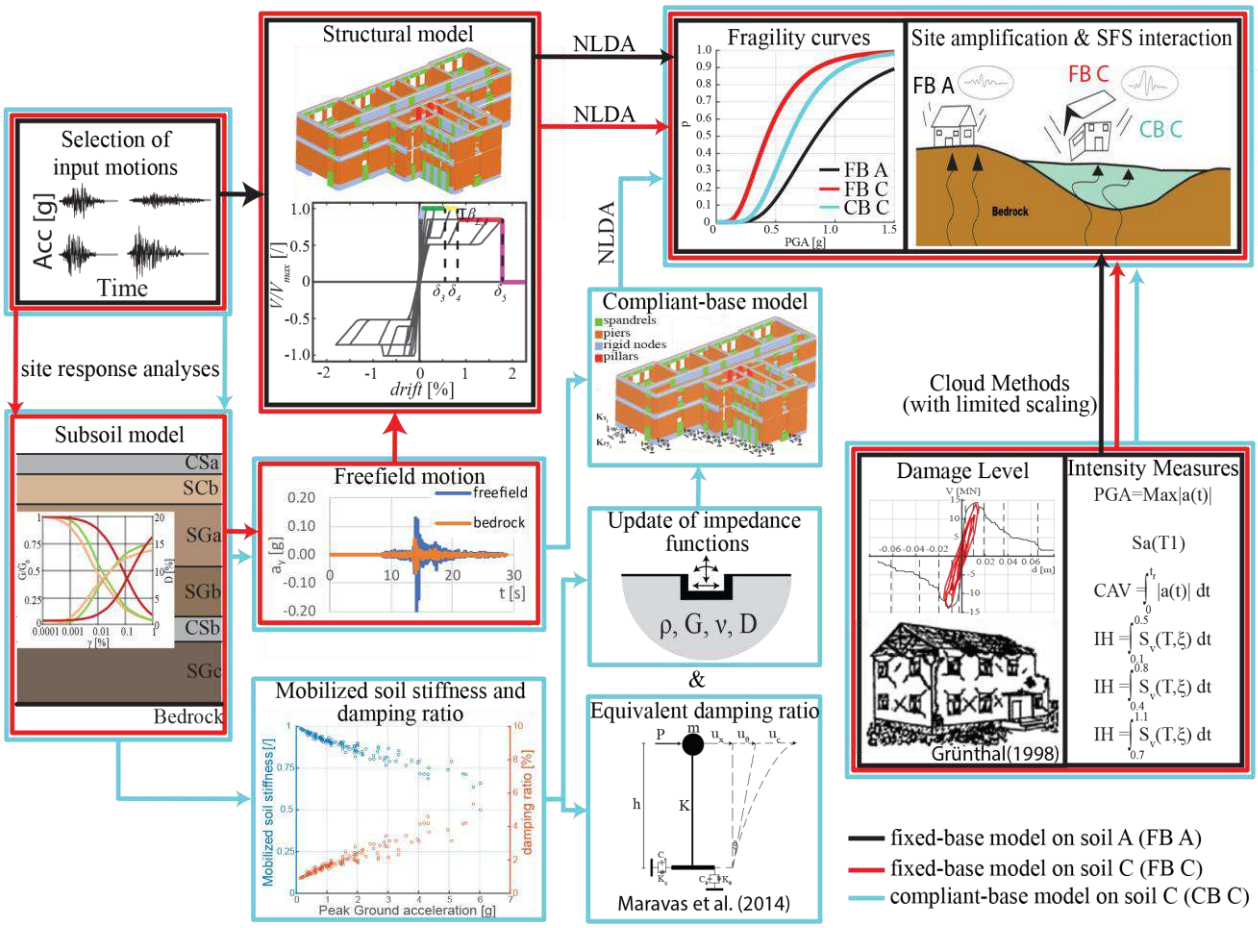

Figure 3.1. Outline of the procedure adopted.

Whatever it is the followed path, it is necessary to establish:

i. the Intensity Measures (IM) adopted to describe the seismic input motion;
ii. the approach to synthetically interpret the huge amount of data on the structural response, derived from each NLDA, and to associate to each record the attainment of a specific damage level;
iii. the approach to fit the data and finally derive the fragility curves.

As far the issue (i) concerns, among the possible alternatives (Bommer et al. (2004); Douglas et al. (2015)), the following IMs have been used in this study: the peak ground acceleration (PGA); the spectral acceleration ($Sa(T_1)$); the cumulative absolute velocity (CAV); and the Housner P-Velocity Spectrum Intensity computed in the range of periods from 0.1 to 0.5 s ($IH_{0.1\ 0.5}$). The integral parameters allowed to also consider the frequency content and the duration of the records in addition to the amplitude. These selected IMs are consistent with various studies on URM buildings (Cattari et al. (2018); Zucconi et al. (2020); Mouyiannou and Rota (2017)) and, in the recent work by Kita et al. (2020), they have been proved to be very effective within a huge set of more than other forty parameters.

The NS and the EW horizontal components of the selected natural events were applied simultaneously and parallel to the X and Y directions of the model, respectively (see Figure 3.2). The analyses were then repeated by switching the components, so that the NS was applied parallel to Y and EW parallel to X. Since the two components were applied simultaneously, the geometrical mean of the PGA and the $Sa(T_1)$ associated to the predominant period along the X and Y directions of the numerical model, was used as IM. Of course, the elongation of the period induced by the SFS interaction makes the $Sa(T_1)$ of the CB C model different from that of the FB C case, while the PGA is obviously the same for the two models.

As far the issue (ii) concerns, a multiscale approach has been adopted with the final aim of interpreting

the simulated structural response through a synthetic parameter consisting of the global damage level (DL). The latter has been defined to be conceptually consistent with the five ones defined by the EMS98 scale Grünthal (1998), that is DL0 – none, DL1 – negligible, DL2 – moderate, DL3 – severe, DL4 - very severe to near collapse and DL5 - collapse.
In particular, the adopted multiscale approach, similarly to what originally proposed in Lagomarsino and Cattari (2015a), combines two heuristic criteria (see Figure 3.2):

- a first one that refers to the global response scale. It defines proper thresholds of the displacement capacity of the building on the pushover curves estimated from nonlinear static analyses. These thresholds are defined in terms of proper fractions of the overall base shear (V_b), namely: before the attainment of the maximum value ($V_{b,max}$), to define the DL1 (equal to 0.4 $V_{b,max}$) and DL2 (equal to 0.8 $V_{b,max}$); after the attainment of the maximum value, i.e. on the softening phase of the curve, to define the DL3 (equal to a residual capacity equal to 0.8 $V_{b,max}$), DL4 (equal to a residual capacity equal to 0.4 $V_{b,max}$) and DL5 (equal to a residual capacity equal to 0.2 $V_{b,max}$);
- a second one that aims to monitor the spread of damage along the building. It is based on the evaluation of the damage severity and diffusion on vertical walls through the cumulative rate of walls that reached a given DL. More specifically, the attainment of the DL on a wall is checked in terms of the DL_{min} variable, as firstly introduced in Marino et al. (2019b). This variable assigns a damage level to the wall based on the minimum DL attained by all the masonry elements of a certain floor. This allows to overcome the definition of conventional interstory drift thresholds, which are not suited to consider the different damage mechanisms exhibited by structural elements of different slenderness (e.g. if associated to the flexural or shear damage mode). A similar damage-assignment criterion has been recently recommended by the Italian Structural Code (MIT (2019)). The thresholds assumed for the cumulative rate have been defined to be consistent with the linguistic description of the damage grades proposed by the EMS98 (Grünthal (1998)); they are described in more detail in Sivori (2021).

For each record, the worst criterion (i.e. the one that occurs at first) is adopted to assign the final resulting global DL. According to this procedure, results of records can be properly grouped as those associated to the same DL.
Finally, about the issue (iii), a lognormal distribution has been assumed as usual in risk analyses (Baraschino et al. (2019)).
Thus, fragility curves were computed by estimating the probability of exceeding (p_{DLi}) the different damage levels, DLi (i=1…5), given a level of ground shaking quantified through the IM. The p_{DLi} was computed from the lognormal distribution of the IM values causing the i^{th} DL. According to the lognormal model, the fragility curve is expressed by the median value IM_{mi} and the lognormal standard deviation σ, according to equation 3.1:

$$p_{DLi}(DL > DLi|IM) = \Phi\left(\frac{log\,(IM|IM_{mi})}{\sigma}\right) \quad (3.1)$$

where Φ is the standard cumulative probability function.

3 STRUCTURAL FEATURES AND SUBSOIL CONDITIONS OF THE CASE STUDY

The building consisted of two stories above ground and an attic covered by a pitched timber roof. The load-bearing walls were characterized by a two-leaf stone masonry with a rather regular bond scheme. Floor diaphragms were composed by a mixed concrete-masonry system, with an exception for the attic floor system that was made of iron beams and thin hollow clay bricks. The foundation system was barely an enlargement of the load-bearing walls, slightly embedded in the soil, except for the North-East side (Area II in Figure 3.2), where there was a partially underground additional storey. After the 1997-1998 Umbria-Marche earthquake sequence, the building was subjected to seismic retrofitting that mainly consisted of: mortar injections through some internal load-bearing walls; insertion of some tie-rods; improvement of roof-to-wall connections; and partial replacement of the timber roof structure deteriorated due to aging. Many of these interventions are shown in Figure 3.2.

A detailed description of the building structure and the damage observed after each single earthquake is included in Cattari et al. (2019a) and de Silva (2019) and Brunelli et al. (2021a).

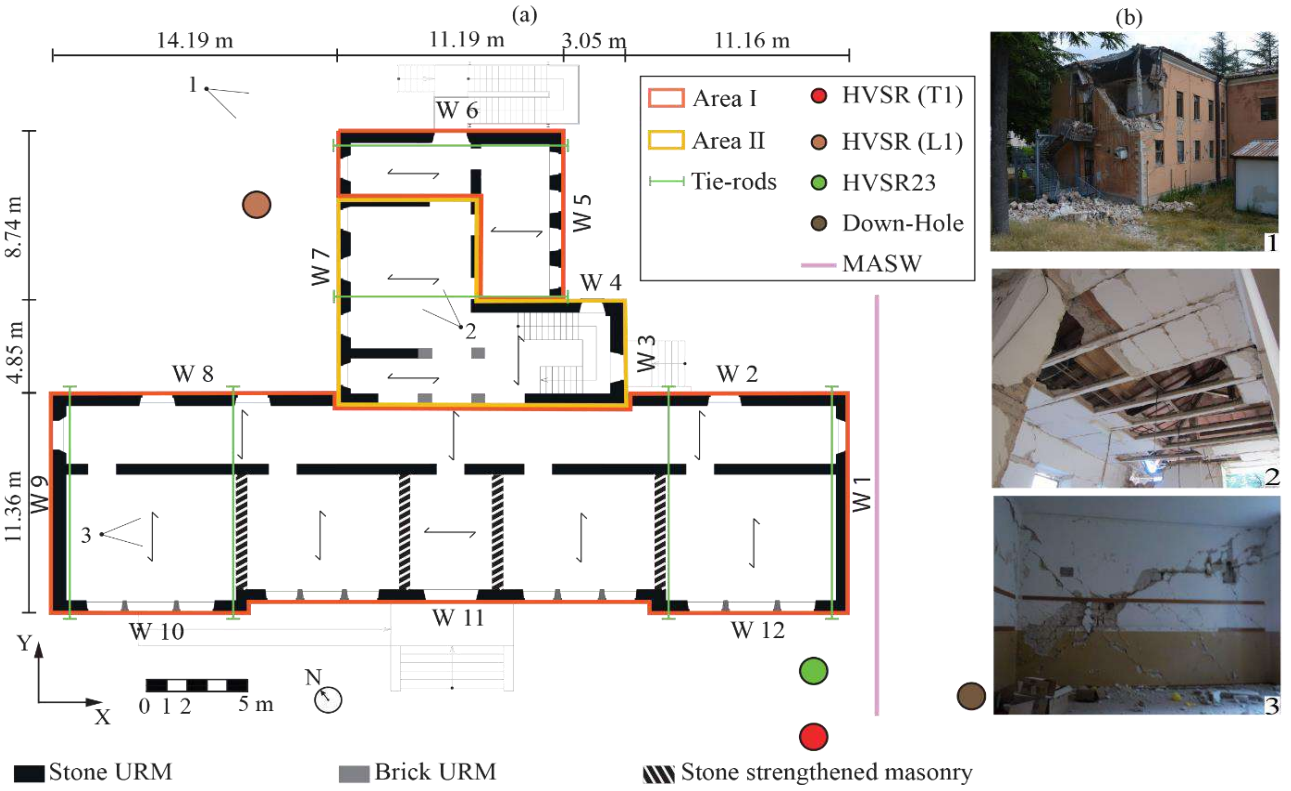

Figure 3.2. (a) Plan view of the building and location of geotechnical surveys; (b) damage to different structural components (walls and diaphragms) observed after event E3.

The building was settled in the middle of a valley, above an almost 40-m-thick layer of loose soil deposits covering the geological bedrock made of Scaglia Variegata and Scaglia Cinerea. The soil closely below the school was investigated through a borehole drilled down to 35 m and a down-hole test performed during the seismic microzonation study of the Visso village (MZS3 (2018)). Moreover, a MASW test was committed by the Italian Civil Protection Department (ReLUIS (2018a)). Figure 3.3a and b show the layered soil profile and the associated values of shear wave velocity V_S, respectively. The predominance of a sandy gravel layer (SG), covered and locally interbedded by clayey silt (CS) and silty clay (SC) lenses, was recognized. As aforementioned, the subsoil is thus classified as C, according to the classification by (NTC (2018); CEN (2004)).

Table 3.1 summarizes the subsoil geotechnical model (Cattari et al. (2019b)). The values of V_S were derived from the down-hole test, whereas those of unit weight (γ), Poisson's ratio (ν) and shear wave velocity of the bedrock half-space were inferred from measurements on similar materials collected and adopted during the seismic microzonation study (MZS3 (2018)). More details on the selection of soil properties are reported in Brunelli et al. (2021a). In the same table, z_{min} and z_{max} indicate the minimum and maximum depth of each soil layer while the column "nonlinear soil response" refers to the curves adopted to reproduce the decay of the shear modulus with respect to its small-strain value (G/G_0) and the increase of the damping ratio (D) with the shear strain amplitude (γ). Indeed, a strain-dependent visco-elastic behaviour was assigned to all materials except for the bedrock. A validation of the soil model is reported in Cattari et al. (2019b).

Table 3.1: Physical and mechanical properties of soils.

	z_{min} (m)	z_{max} (m)	γ (kN/m^3)	V_S (m/s)	ν	Nonlinear soil response
CS_a	0	3.2	20	136	0.4	ReLUIS (2018c); Ciancimino et al. (2019)
SC_b	3.2	8	20	226	0.4	ReLUIS (2018c); Ciancimino et al. (2019)
SG_a	8	18	21	383	0.3	Liao et al. (2013) (σ'_c = 52 kPa)
SG_b	18	26	21	683	0.3	Liao et al. (2013) (σ'_c = 207 kPa)
CS_b	26	30	20	500	0.4	ReLUIS (2018c); Ciancimino et al. (2019)
SG_c	30	40	21	602	0.3	Liao et al. (2013) (σ'_c = 207 kPa)
Bedrock	40	–	22	1300	–	–

σ'_c is the confining stress applied by Liao et al. (2013) during the laboratory tests measuring the hysteretic soil response

4 SITE EFFECTS ON THE SELECTED INPUT MOTIONS

The input motions employed in the seismic analyses were selected from the SIMBAD database (Smerzini and Paolucci (2013); Iervolino et al. (2014)). The selection includes the EW and NS components of accelerations recorded during 49 natural events at stations located on stiff rock outcrop, i.e. Vs_{30} greater than 700 m/s. Since in this study site effects were directly simulated through site response analyses, signals recorded on softer soil were excluded to avoid excessive and unrealistic amplifications. However, some selected signals were scaled to improve the estimate of the dispersion of the fragility curves of fixed base model on soil type A. Table 3.2 groups the adopted input motions according to their scaling factors. For sake of brevity, the magnitude of the selected events, the epicentral distance, the Vs_{30} of the recording stations and the intensity measures of the records are listed in detail in the supplementary material that integrates the contents of the paper.

Table 3.2: Scaling factors applied to obtain the input motions for the seismic analyses.

scaling factor	0.6	0.7	0.75	0.8	0.9	1*	1.1	1.2	1.25	1.3	1.5	1.6	TOT
N of input motions	2	2	24	10	4	98	2	4	24	14	30	2	272

The ground motions on surface were calculated by applying the selected records to the bedrock of the layered soil of Visso, shown in Figure 3.3 (a) together with its V_S profile (b). One dimensional-equivalent linear site response analyses were performed through the STRATA software (Kottke and Rathie (2008). The mesh size, Δ, was calibrated according with the rule $\Delta<V_S/8f_{max}$ proposed by Kuhlemeyer and Lysmer (1973). This rule allows the frequency content of the selected input motion to reliably propagate through the layered soil up to f_{max} = 25 Hz. Figure 3.3 shows the results in terms of: strain profile (c), profiles of the mobilized shear stiffness normalized with respect to the initial value (d), profile of the mobilized damping ratio (e) and that of the acceleration (f). Grey lines indicate the result of the ith analysis, while the 50th percentile and the 16-84th percentiles are marked through black continuous and dashed lines, respectively. The most significant nonlinear effects are concentrated in the shallowest silty sand gravel layer, being the linear threshold of such coarse-grained soil lower than that of the two upper fine-grained CS and SC layers. Consequently, the decay of G/G_0 at the two foundation levels (z=0.60 m and z=2.95 m in Figure 3.3) ranges between 0.5 and 0.9 (16-84th percentile), while the damping is comprised between 1% and 7%.

Figure 3.4a shows the spectra of the selected records for a damping ratio equal to 5% and Figure 3.4b those resulting on surface from the site response analysis for the same damping ratio. The notable percentiles are marked as for Figure 3.3.

Both Figure 3.3e and Figure 3.4 revealed the huge variability of the PGA and spectral accelerations associated with the fundamental periods of soil (T_{soil}=0.275 s as computed by Cattari et al. (2019b)), and of the structural models placed on fixed base (T_{xFB}=0.148 s T_{yFB}=0.174 s as computed by Brunelli et al. (2021a)), and compliant base (T_{xCB}=0.218 s T_{yCB}=0.258 s as computed by Brunelli et al.

(2021a)). Their mean spectra are lower than the acceleration spectra provided by the Italian Code for soil type A and C and for a probability of exceedance equal to 10% in 50 years. In Figure 3.4, the Code spectrum is overlaid through the red lines.
The response spectra obtained from the accelerograms recorded at the base of the school during the three events of the Central Italy earthquake are superimposed to Figure 3.4b, too. They exceed the Code spectrum and are mostly enveloped by the mean and the 84th percentile spectra resulting from the seismic response analyses for periods higher than 0.2 s.

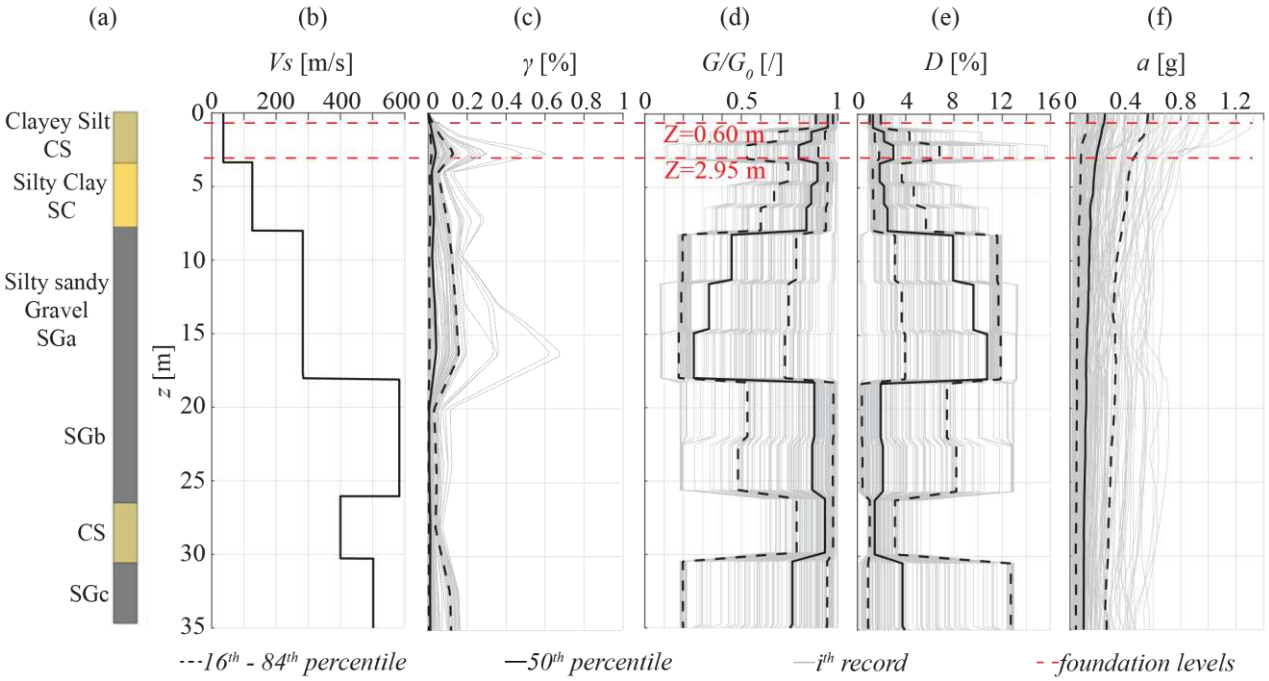

Figure 3.3. (a) soil layering, (b) V_S profiles, (c) strain profile, (d) normalized shear stiffness, (e) damping ratio and (f) PGA, resulting from site response analyses.

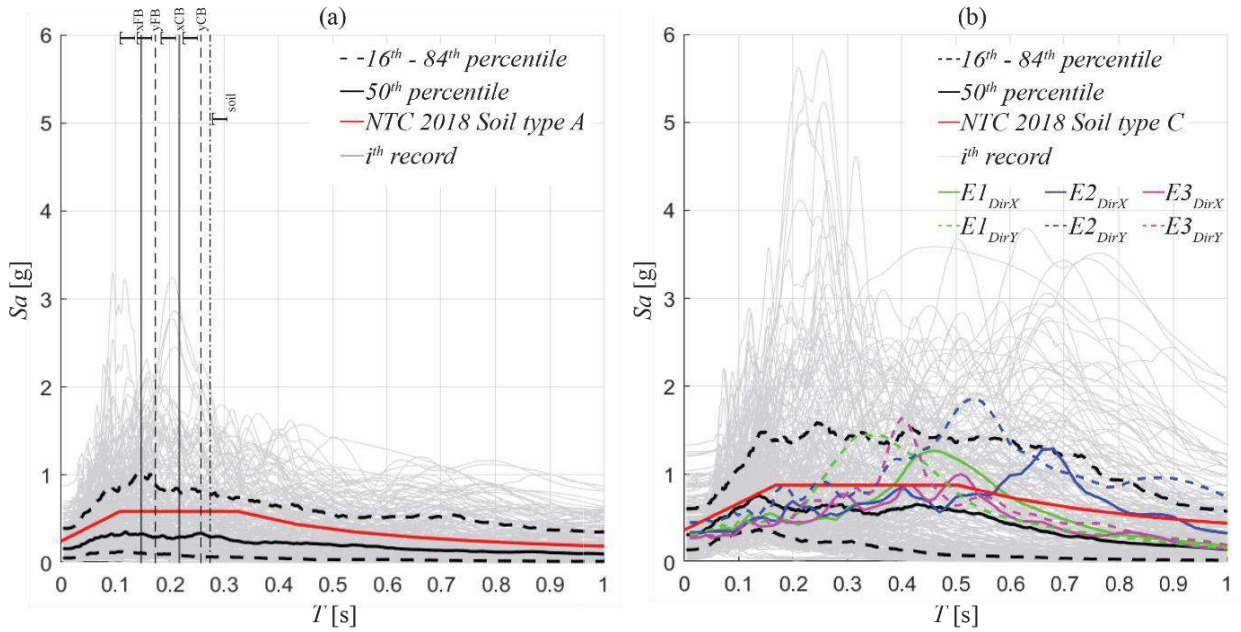

Figure 3.4. Acceleration response spectra of (a) the selected input motions and (b) resulting from site response analyses.

Figure 3.5a plots the amplification factors of the PGA and Figure 3.5b those of the spectral acceleration of the FB and CB model against the PGA and Sa values of the selected records. Both

plots highlight the expected reduction of the amplifications with increasing the amplitude of the input motions. Such effect turns to be beneficial for the structural safety since strong motion events are the less amplified by site effects. Conversely, SFS interaction moves the structural period towards the soil predominant period, where spectral ordinates are maximized. Hence higher spectral accelerations affect the CB model, except for very weak motions (around $Sa(T_1)<0.25g$ in Figure 3.5b).

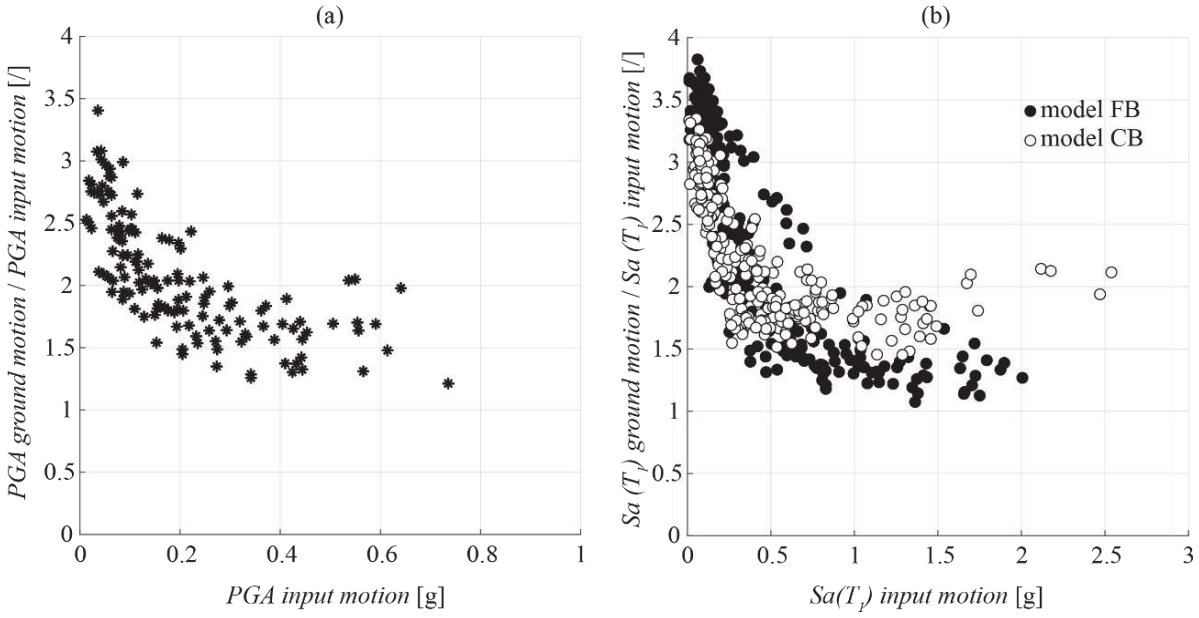

Figure 3.5. Amplification factors of (a) PGA and (b) Sa (T_1).

5 FIXED-BASE AND COMPLIANT-BASE NUMERICAL MODELS

5.1 Equivalent frame model of the selected URM building

Figure 3.6a illustrates the 3D equivalent frame model of the examined case study. The model was realized with the Tremuri software package Lagomarsino et al. (2013) and it was already validated in Brunelli et al. (2021a) by simulating the actual response of the Visso's school caused by the seismic sequence that hit Central Italy in 2016-2017.

According to such a modelling strategy, the nonlinear behaviour is concentrated in masonry panels (piers and spandrels, in orange and green respectively in Figure 3.6) which are identified a priori in each URM wall and are then connected by rigid nodes (in cyan in Figure 3.6). Piers constitute the main vertical structural elements able to equilibrate both vertical and horizontal actions, while spandrels play the main role of connecting piers (like the beams in a corresponding reinforced concrete frame).

More specifically, masonry panels are modelled according to the nonlinear beam piecewise-linear model proposed by Cattari and Lagomarsino (2013). This constitutive law allows for describing the nonlinear response until very severe damage levels at element scale (i.e. $DL_{E,i}$ with i from 1 to 5) through progressive strength degradation ($\beta_{E,i}$) corresponding to assigned drift values (δ_i). The drift thresholds, the strength degradation as well as the parameters that rule the hysteretic response may be differentiated as a function of the most recurring failure modes that characterize URM panels (i.e. flexural, diagonal cracking shear or bed-joint sliding) and as a function of their type (if piers or spandrels).

By way of example, Figure 3.6b illustrates the response of a pier dominated by a shear failure mode. Table 3.3 shows the strength parameters adopted in nonlinear dynamic analyses, that are considered deterministic in this research. These values are consistent with the masonry type that characterized the building. They are compatible with those proposed in the Italian Building Code Commentary (MIT (2019)) and tested in various experimental campaigns (Kržan et al. (2015); Vanin et al. (2017);

Rezaie et al. (2020)). Moreover, their reliability in reproducing the seismic response of the Visso school was already verified in Brunelli et al. (2021a). The maximum shear strength of the panels has been computed according to the strength criteria already corroborated in the literature to interpret the aforementioned failure modes (see Calderini et al. (2009) for a literature review of them).

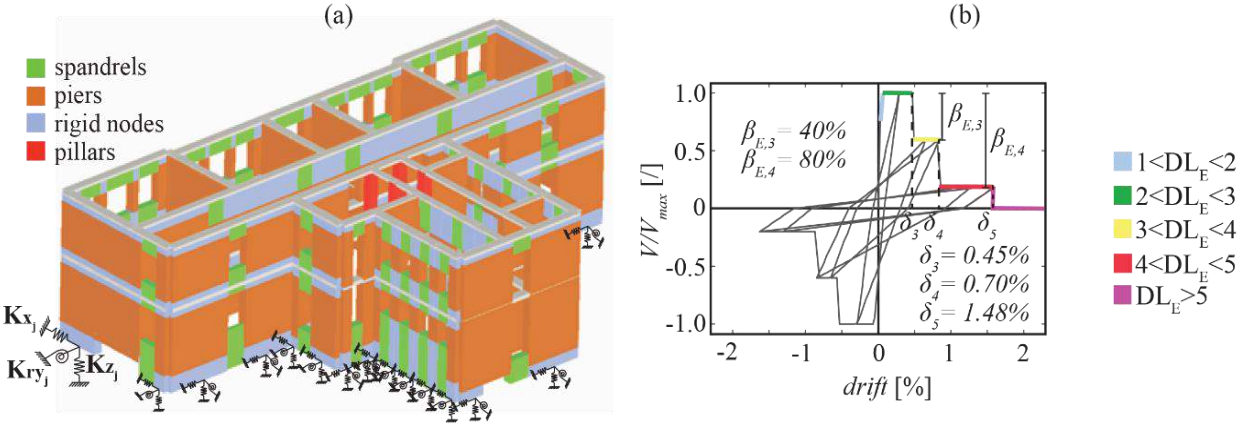

Figure 3.6. (a) 3D equivalent frame model with springs implemented in the CB model, (b) backbone and hysteretic response of masonry elements: piers under shear.

In particular, the flexural behaviour of piers was interpreted according to the criterion proposed in NTC (2018), whereas the shear behaviour according to the diagonal cracking failure mode proposed by Turnšek and Sheppard (1980) (and recommended as reference also in MIT (2019) for existing masonry). In the case of spandrels, the development of a strut mechanism was assumed likely to occur due to the presence of RC tie beams and thus the flexural behaviour was accordingly interpreted according to the criterion proposed in NTC (2018).

Table 3.3: Mechanical parameters adopted for piers and spandrels.

	E (MPa)	G (MPa)	τ_0 (MPa)	f_m (MPa)	G_D (MPa)	E_D (MPa)
cut stone	2574	858	0.096	4.94		
strengthened cut stone	2970	991	0.111	5.70		
brick masonry	2701	901	0.114	4.80		
diaphragms of floor level 1					12500	60000*
diaphragms of floor level 2**					26125	14641

τ_0: diagonal shear strength of masonry under zero confining stress; f_m: uniaxial compression strength of masonry; E_D: Young's modulus in the main orientation of diaphragm

* Equivalent value that allows the reproduction of the overall axial stiffness of the diaphragm, considering the contribution from other diaphragms components (e.g. beams). For the membrane is thus assumed the equivalent thickness equal to 0.05 m.

** Equivalent values also accounting for the stiffening contribution provided by the roof (not explicitly modelled but included in the model as equivalent mass and stiffness).

The nonlinear response of URM panels is analogously simulated in both FB and CB models, but then in the CB model proper springs were inserted under each foundation pier. The calibration of these springs is described in section 5.2. Moreover, since Tremuri software does not allow to put a base dashpot, the damping of the whole SFS system was computed as an equivalent damping ratio, then implemented in the NLDA as a Rayleigh damping ratio (see section 5.3). The equivalent value results from the combination of three contributions: the structural viscous damping; the foundation radiation damping; and the hysteretic soil damping. The radiation damping was computed through the impedance functions, while the hysteretic component was estimated from the seismic response analyses.

5.2 Effect of soil non-linearity and foundation geometry on the selected impedance functions

The soil-foundation impedances of the case study were calibrated according to the two approaches suggested by NIST (2012), i.e. the analytical formula proposed by Pais and Kausel (1988) and Gazetas (1991). Table 3.4 sums up the hypotheses made on the foundation and on the soil by the two formulations. They both assume a rigid and massless foundation placed on the surface or embedded in a homogeneous elastic half-space. Only the Gazetas' approach allows to model the loss of contact between the lateral sides of the foundation and the surrounding soil likely occurring under strong motions. The foundation shape can be either circular or rectangular for Pais and Kausel (1988) while arbitrary for Gazetas (1991).

For the case at hand, the impedances associated to the translational along the horizontal ($\underline{K}_x$) and vertical ($\underline{K}_z$) directions and to the rocking ($\underline{K}_{ry}$) around the axis parallel to the foundation width were computed (see Figure 3.6a). The shape varies from square to rectangular being the foundation length defined by adding the half-length of the spandrel panel to the size of the load-bearing wall. Conversely, the foundation width is constant and equal to 0.90 m; it results from the thickness of the load-bearing wall plus an enlargement of 0.15 m at each side. The value of the embedment was set to 0.6 m for Area I and 2.95 m for Area II in Figure 3.2. To compare the resulting impedances under the same hypotheses, a full soil-foundation contact was assumed in the application of both the approaches.

The half-space shear modulus was set equal to the mean shear modulus mobilized under each input motion up to a depth equal to the foundation width, i.e. 0.95 m below the foundation, and corresponding to the soil volume expected to be affected by the horizontal and rocking foundation motion Gazetas (1983).

The adoption of such linear equivalent approach is reasonable, being the decay of the shear stiffness below the foundation limited (see Section 4 and Figure 3.3b).

The frequency-dependent dynamic coefficients of the impedances were computed as a function of the period computed from the equivalent stiffness, that has been predicted through the formulas reported in the following Section 5.3. The calibration was solved iteratively until the resulting period was equal to the value adopted for the computation of the impedance functions. The soil-fundamental period is slightly higher than the period of the CB model when the springs are calibrated according to the initial soil stiffness. Thus, the impedances are indirectly calibrated around the predominant period of the free field motions (see Figure 3.4).

The real parts of the so computed impedances are the stiffness of the springs placed at the base of the CB model. The imaginary part, which quantifies the radiation damping, was divided by the double of the real part of the impedance to obtain the energy loss coefficients β_x, β_z and β_{ry} (Maravas et al. (2014)). The latter were employed to calculate the equivalent damping ratio of the soil-foundation-structure system, as detailed in the following.

Table 3.4: Hypotheses of the selected formulations on the foundation and soil.

Formulation	Hypothesis on the foundation	Hypothesis on soil behaviour
Pais and Kausel (1988)	Geometry: circular or rectangular. Stiffness: rigid. Mass: none. Depth: any. Contact between soil and foundation sides: full	Homogeneous elastic half-space.
Gazetas (1991)	Geometry: any shape. Stiffness: rigid. Mass: none. Depth: any. Contact between soil and foundation sides: any	Homogeneous elastic half-space

Table 3.5 reports the real part of the impedances and the energy loss coefficients, respectively associated to the three degrees of freedom for the two different foundation depths (z=0.6 m and

z=2.95 m) and to the minimum and maximum length to width ratios (L/B_{min}=1, square, and L/B_{max}=8.13, rectangular).

Table 3.5: Real parts of the impedances and energy loss coefficients associated to the initial value of the soil shear modulus (G_0).

	Formulation	L/B_{min}=1 (square)		L/B_{max} =8.13 (rectangular)	
		z=0.6m	z=2.95m	z=0.6m	z=2.95m
Real K_x	Gazetas (1991)	204	1213	536	2309
[MN/m]	Pais and Kausel (1988)	215	1210	483	2189
Real K_z	Gazetas (1991)	187	977	604	2447
[MN/m]	Pais and Kausel (1988)	199	914	570	2227
Real K_{ry}	Gazetas (1991)	79	401	20809	115118
[MNm]	Pais and Kausel (1988)	98	2964	7504	56826
β_x [%]	Gazetas (1991)	7.53	7.78	13.60	16.26
	Pais and Kausel (1988)	7.91	13.48	15.42	27.04
β_z [%]	Gazetas (1991)	7.58	7.77	19.49	17.46
	Pais and Kausel (1988)	13.29	21.59	28.42	44.79
β_{ry} [%]	Gazetas (1991)	2.13	32.76	negligible	1.35
	Pais and Kausel (1988)	1.69	6.61	negligible	1.23

The real parts of the translational impedances ($\underline{K}_x$ and $\underline{K}_z$) derived from the two approaches are in a fair agreement for L/B_{min}, while values predicted by the Pais and Kausel (1988) formula are slightly lower when L/B is maximum. Higher differences resulted for the real part of the rocking impedance, according to the different ways in which the foundation geometry and depth are accounted for in two approaches. More specifically, the variation of the depth from z=0.6 m to z=2.95 m of the square foundation produces an increase of K_{ry} more significant when the approach by Pais and Kausel is applied (2964 MNm vs 401 MNm). Conversely, higher K_{ry} resulted from the Gazetas (1991) formula for the deeper rectangular shape.

Formulas by Pais and Kausel lead to higher energy loss coefficients in most of the cases. Independently of the approach, β_x and β_z show the expected rise with increasing the soil-footing contact area, i.e. the foundation length or depth. Being the energy loss coefficient proportional to the soil deformability, the stiffer soil, that corresponds to the deeper foundation level, makes the rise slight and produces even a reduction for the vertical component of the rectangular footing in Gazetas (1991). Values associated to the rocking (β_{ry}) are significantly lower than those associated to the translational motions and almost negligible for the rectangular foundation.

For the cases listed in Table 3.5, Figure 3.7 shows the evolution with the normalized shear modulus of the real part of the impedances (a, b, c) and of the energy loss coefficients (d, e, f). They are normalized with respect to the values computed for G_0 and reported in Table 3.5. The expected reduction of the real parts with the decrease of G/G_0 is observed. Such effect is maximized for the deeper rectangular foundation. All the other analysed cases show the same trend independently of the approach (grey vs black indicators) and of the foundation length and depth. Conversely, energy loss coefficients increase with the shear modulus reduction. Such effect is more accentuated when Gazetas formulas are applied to the deeper foundations. The latter is exceeded by the prediction of Pais and Kausel formulas only for the rocking motion (Figure 3.7f).

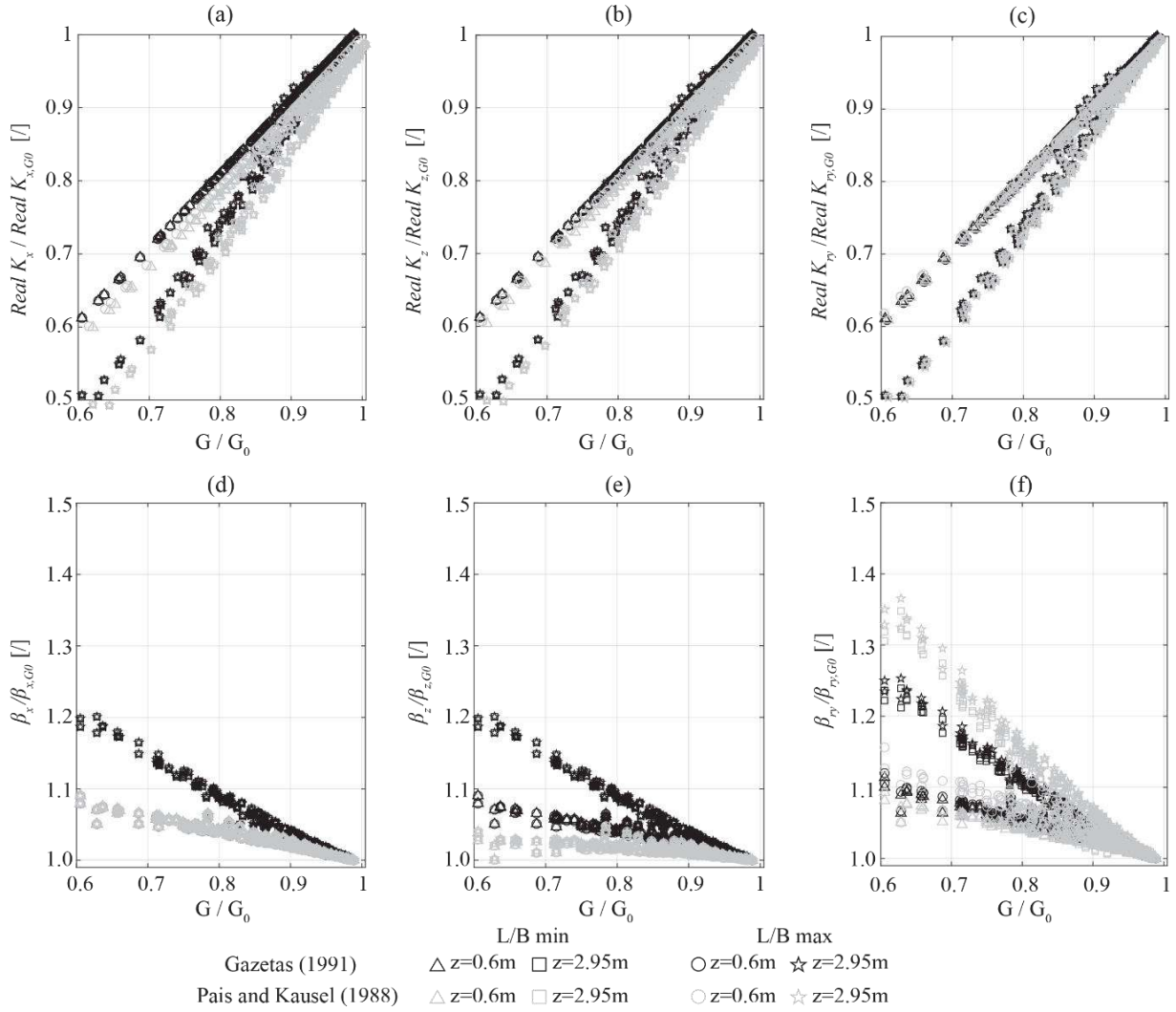

Figure 3.7. Evolution with the normalized shear modulus of the real part of the impedances (a, b, c) and of the energy loss coefficients (d, e, f) associated with the horizontal translation (a, d), vertical translation (b, e) and rocking motion (c, f). Values computed for the maximum and minimum foundation length and depth are reported.

5.3 Evaluation of the damping ratio of the compliant-base model

The stiffness and damping ratio of a compliant base single degree of freedom system is traditionally derived from the following expression:

$$\frac{(1-2i\beta_{eq})}{K_{eq}(1+4\beta_{eq}^2)} = \frac{(1-2i\beta_{fb})}{K(1+4\beta_{fb}^2)} + \frac{(1-2i\beta_x)}{K_x(1+4\beta_x^2)} + \frac{(1-2i\beta_{ry})}{K_{ry}(1+4\beta_{ry}^2)} \quad (3.2)$$

where K_{eq} and β_{eq} are the unknown equivalent stiffness and damping ratio of the SFS system, K and β_{fb} are the lateral stiffness and damping ratio of the fixed base structure. The terms K_x, K_{ry}, β_x and β_{ry} are the real parts and the energy loss coefficients derived from the impedance functions. Such properties are those of a fixed base system with the same displacement of the CB system.
Three different approaches were applied to compute β_{eq}. They are derived from Equation 2 and consist of:

- Approach 1 (A1) obtained by neglecting the second order terms in the denominators and equating the imaginary parts of the left and right sides. Such approach is proposed by NIST (2012) and, under the same hypothesis on the structural damping ratio, leads to the same results of the formulas proposed by Bielak (1971); Roesset (1980); Wolf (1985). The final formula is the easiest to apply because all the terms are real.

- Approach 2 (A2) in which the second order terms in the denominators are neglected. The complex impedances of the foundation are replaced by their moduli in the final formula of β_{eq}, to avoid the calculation with complex contributions. Such approach is reported by Veletsos and Nair (1975); Givens et al. (2016).
- Approach 3 (A3) proposed by Maravas et al. (2014) on basis of the previous study by Avilés and Pérez-Rocha (1996). The equivalent damping ratio β_{eq} results from both the real and the imaginary components without neglecting the second order terms in Equation 2. The same approach was followed to estimate the equivalent period $\tilde{T}$ (from K_{eq} and the structural mass) of the SFS system used to calibrate the impedance functions in Figure 3.7.

The final formulas concerning each of the three approaches are reported by Givens et al. (2016). The two contributions of the foundation in Equation 2 are relevant to the radiation damping associated to the swaying and rocking motions. Actually, energy is dissipated also by the soil hysteresis (β_s) activated by the foundation motions. The relevant damping ratio, β_s, is introduced in A1 as an additional term of the final formula and is summed to the energy loss coefficients in A2 and A3.

The three approaches were applied to compute the equivalent damping ratio mobilized along the X and Y directions of the case-study under each input motion. To this aim, the school building was approximated through a Single Degree of Freedom (SDOF) system with a viscous damping ratio β_{fb}=3% and a lateral stiffness, K, derived from the fundamental periods along the X and Y directions of the fixed base configuration, as resulting from the modal analysis. The terms $\underline{K}_x$, $\underline{K}_{ry}$, β_x and β_{ry} were calculated from the sum of the real and imaginary parts of the impedances of the X-oriented (or Y-oriented) load-bearing walls to compute β_{eq} along the X-direction (or Y-direction). Values of β_s were set equal to the mean hysteretic damping, D, again mobilized up to a depth equal to 0.95 m below the foundation.

The calculation was repeated for each input motion and the values of $\underline{K}_x$, $\underline{K}_{ry}$, β_x, β_{ry} and β_s were consequently updated according to the soil shear stiffness and damping ratio mobilized during each seismic response analysis (see Figure 3.3). In the following, β_{eq} indicates the mean of the values obtained for the two directions assumed as representative of the energy dissipated under each input motion.

Figure 3.8 shows the variation with the normalized shear modulus, G/G_0, of the equivalent damping ratio normalized with respect to the value associated to G_0. Predictions of the three different approaches are compared in Figure 3.8a being equal the formulation of the impedances by Gazetas (1991), while results of A3 changing the formulation of the impedances are compared in Figure 3.8b. Values estimated neglecting the hysteretic damping ratio (acronyms without the subscript β_s in the keys) overlay within the plots. The damping ratios associated to the initial soil shear stiffness used to normalize the data in Figure 3.8a and b are reported in Table 3.6 and Table 3.7, respectively.

Tables and graphs reveal very slight differences between the results of the different analytical approaches and formulations of the impedances. Table 3.6 highlights that the lowest values are estimated with A1, while the highest is relevant to A2 or A3 depending on if β_s is introduced or not. Table 3.7 shows a slight increase of the damping ratio when the Gazetas (1991) formula are applied to the impedance and β_s is neglected. Conversely, the β_{eq} value associated to the Pais and Kausel (1988) impedances is predominant when soil hysteresis is accounted for.

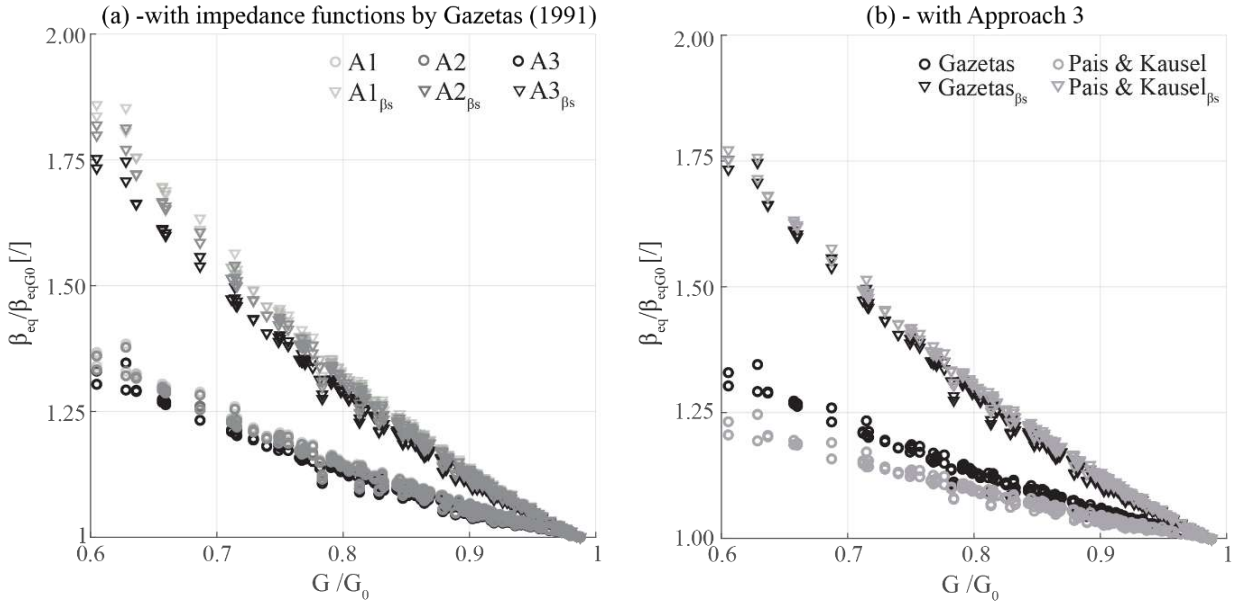

Figure 3.8. Comparisons between the evolution of the normalized equivalent damping ratio with the normalized shear modulus (a) varying the analytical approach and (b) varying the impedance functions.

Table 3.6: Damping ratio associated to the initial soil shear stiffness used to normalize the data in Figure 3.8a.

	A1	A2	A3
No βs	5.57 %	5.78 %	6.00 %
with βs	5.96 %	6.39 %	6.20 %

As expected, the contribution of the hysteretic damping ratio mostly influences the results with reducing G/G_0, as shown in Figure 3.8. Given the hypothesis on β_s, the increase of β_{eq} with reducing the soil stiffness is almost independent of the adopted formulation. The most relevant differences are observed between A1 and A2 or A3 when G/G_0 approaches 0.6 (see Figure 3.8a), as well as between the results obtained by changing the impedance functions and neglecting β_s (see Figure 3.8b).

Table 3.7: Damping ratio associated to the initial soil shear stiffness used to normalized data in Figure 3.8b.

	Gazetas (1991)	Pais and Kausel (1988)
No β_s	6.00 %	5.91 %
with β_s	6.20 %	6.45 %

6 INFLUENCE OF THE SELECTED IMPEDANCE FUNCTIONS ON THE SIMULATION OF THE ACTUAL SEISMIC RESPONSE OF VISSO SCHOOL

Based on results of previous sections, the school response to the Central Italy seismic sequence was simulated by considering four cases, in which the base springs were calibrated respectively according to the impedances by Gazetas (1991) or Pais and Kausel (1988) and including or neglecting the hysteretic soil damping ratio. In all cases, the approach A3 discussed in section 5.3 was followed to compute the equivalent damping ratio β_{eq}.

Thus, the response of these four CB models was compared to the recorded response under the three main events of the 2016 Central Italy seismic sequence, which occurred on the 24th August (E1), 26th October (E2) and 30th October (E3), respectively. To simulate the cumulative effects, the signals recorded at the school base were applied in sequence. The computation of the impedances and of the equivalent damping ratio was executed by setting the soil shear stiffness equal to 26.4 MPa and the hysteretic damping ratio β_s equal to 4.2%, respectively. These values correspond to the mean values mobilized during the three events in a soil volume extending up to 0.95 m below the foundation.

The model capability to reproduce the seismic response at local scale was checked by calculating the covariance (CoV) between the acceleration recorded by the sensors no. 3, 5, 8 and 10 and the

acceleration resulting from the analyses, exactly in the nodes where these sensors were installed in the school (Figure 3.9). While in Brunelli et al. (2021a) the whole set of available sensors was analyzed to verify the reliability of the CB model against that of the FB model, herein this subset of sensors has been selected by way of example to assess the influence of the use of different impedance functions and hypotheses on the foundation damping. The CoV was computed considering a time lag between the recorded and the simulated accelerometers ranging between about ± 0.07 s. Figure 3.9 shows the highest resulting CoV value, even though it is poorly sensitive to the time lag. The agreement is assumed satisfying if CoV is greater than 70%. The actual response is effectively simulated except for the 5-10 alignment in the Y direction at the third event. This mismatch is justified by the fact a significant shear sliding occurred along the wall W9 (see Figure 3.2a), that has produced significant irreversible displacements.

The CoV values obtained from the two different impedance functions are comparable, while a small but systematic improvement is recognized when the hysteretic soil damping ratio is considered. Moreover, independently of the hypotheses on the soil-foundation impedance, the covariance reduces from the first E1 (black markers in Figure 3.9) to the third E3 event (white markers in Figure 3.9). This is true especially along the Y direction. The worsening match after E1 is associated to the inability of the adopted model to reproduce some local collapses occurred in the school during E2, such as the partial overturning of the wall W6 and the partial collapse of some diaphragms, mainly concentrated in Area II (see photos 1 and 2 in Figure 3.2b).

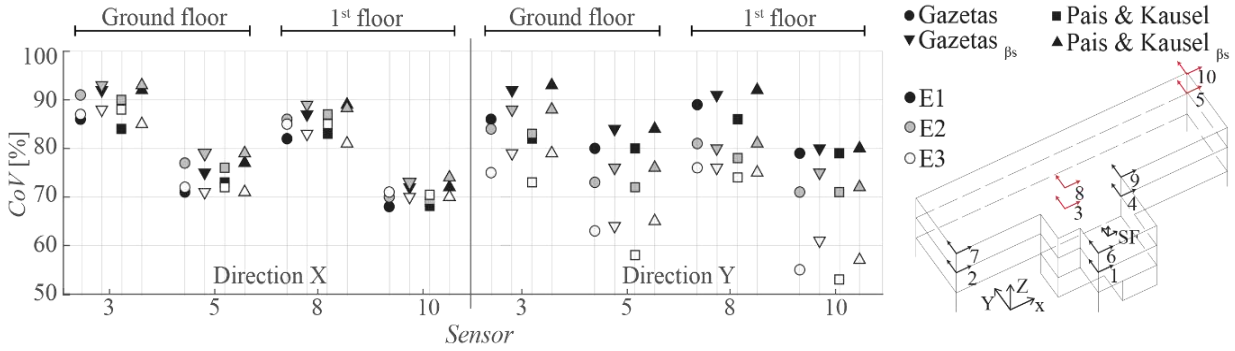

Figure 3.9. Numerical-experimental matching of accelerations at sensors n. 3,5,8 and 10 expressed in terms of CoV (indicated as percentage) for the three mainshocks and location of sensors in the structure.

The performance of each numerical model was then compared to the recorded response in terms of the overall consistency in the extension and severity of damage after the events E2 and E3. The damage induced by E1 was not assumed as reference being lower than that produced by E2 and E3, thus less effective for such a comparison. The evolution of the actual damage from E1 to E3 was reconstructed from the data acquired through in situ surveys and the photos provided by the Department of Civil Protection, as reported in Brunelli et al. (2021a).

Figure 3.10 depicts the maximum value of Cumulative rate of piers Damage ($CD_{DLEi,piers}$), computed as the percentage of piers that reached or exceeded a given DL_E, weighted by the corresponding gross sectional area, as originally proposed by Lagomarsino and Cattari (2015b). For the actual response, values of $CD_{DLEi,piers}$ have been estimated thanks to the accurate reconstruction of the damage aforementioned.

In the models, the attainment of specific damage levels at scale of pier (DL_E) is provided by certain thresholds of drift as illustrated in Figure 3.6b. For each model, only one value of $CD_{DLEi,piers}$ is reported because the damage level reached after E2 and E3 is the same, being the E2 the most severe mainshock. The $CD_{DLi,piers}$ associated to DL3, DL4 and DL5 after E2 and E3 overlays within the same Figure 3.10.

The agreement between the observed and simulated damage is generally satisfying. The actual DL3 is slightly underestimated by the models with soil hysteresis (Gazetas β_s, Pais and Kausel β_s) while DL4 and DL5 are conversely slightly overestimated by the models that neglect such contribution.

Such opposite trend depends on the fact that both impedances and the equivalent damping ratio were calibrated on the mean soil properties mobilized during the three events. A better agreement is expected if the latter are changed according to value effectively mobilized by each event.

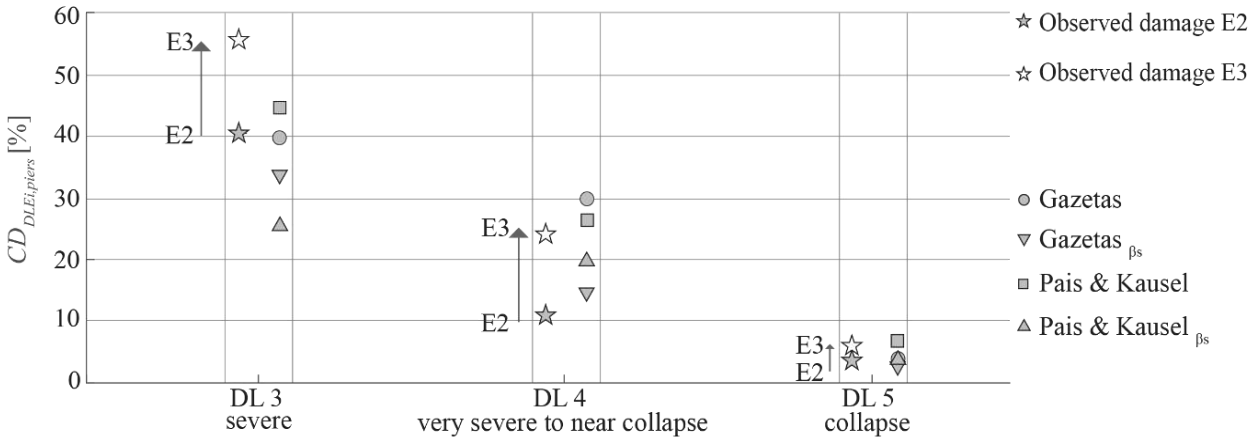

Figure 3.10. Comparisons of the maximum values of the cumulative of pier damage to the variation of impedance formulations.

The comparison shows that the higher differences in the cumulative damage are associated with the hypothesis on the soil hysteretic damping, while the two formulations for the impedances lead to similar results. For this reason, only the formulation by Gazetas with (CB $C_{\beta s}$) or without (CB C) soil hysteresis is discussed for the derivation of fragility curves illustrated in section 7.

7 DERIVATION OF FRAGILITY CURVES

7.1 Overview on the results achieved from NLDA

NLDA provided a huge amount of information on the structural response, that are summarized in the following in terms of damage, before the derivation of fragility curves (Sections 7.2 and 7.3). By way of example, Figure 3.11 shows:

- For the seismic event no.25 (Figure 3.11a), the damage level occurred in the walls oriented in Y direction. The DL of each wall refers to that at the end of the NLDA and it has been assigned on basis on the criteria introduced in Section 2. The damage tends to decrease passing from the FB C to the CB C model, thanks to the beneficial effect of the SFS interaction. Moreover, a further decrease is obtained when the role of the soil hysteresis is accounted for.
- For walls W7 and W10, the recurrence of each DLi (Figure 3.11b) out of the whole set of analyses. The Figure 3.11 statistically confirms the occurrence of lower damage passing from the FB C to the CB C models and, then, from the CB C to the CB $C_{\beta s}$ models.

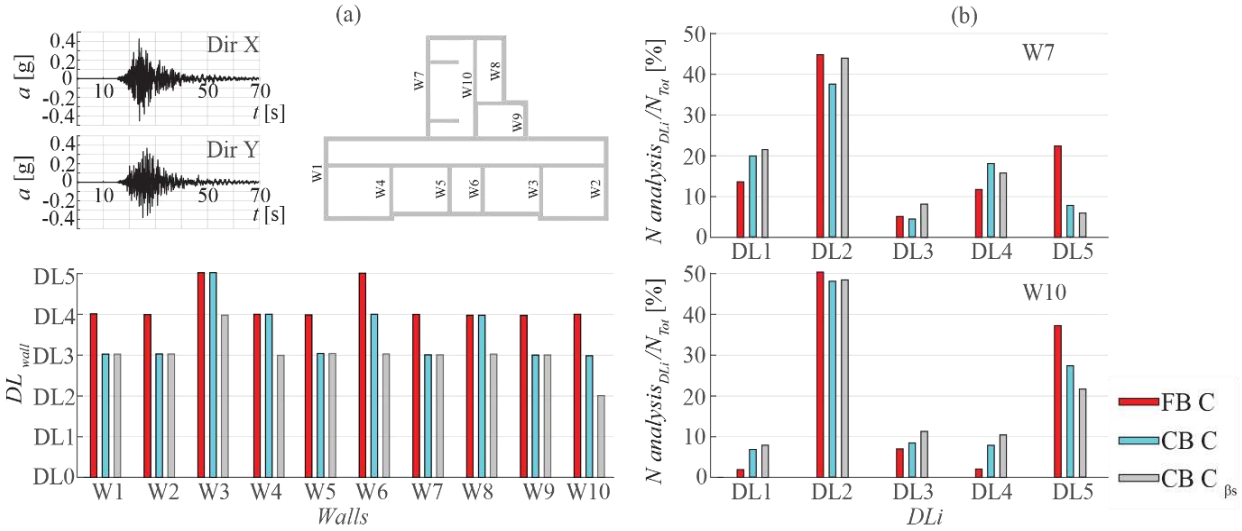

Figure 3.11. (a) Damage levels attained in the models during the numerical simulation of the seismic event no.25; (b) statistical recurrence of the damage level attained in W7 and W10 considering the whole set of analyses.

7.2 Influence of site effects on the fragility curves

Table 3.8 and Table 3.9 report the number of analyses ($N_{records}$), the median value (IM_{50}) and the standard deviation (σ) respectively used to generate the fragility curves of the FB model. The values refer, in Table 3.8, to the model analysed under the input motion (FB A path in section 2) and, in Table 3.9, to that analysed under the free field motion resulting from the site response analyses (FB C path in section 2). As explained in section 2, the IM of the input motion was used to calculate the fragility curves in both cases. The sum of the records producing the different DLs does not match the total number of selected input motions, i.e. 272, because the structure resulted completely safe (i.e. DL0) in some analyses under the lowest input motions.

Only a few analyses, reported in brackets in Table 3.8, mobilized DL3, DL4 and DL5 for the FB A case. Therefore, the initial set of input motions described in section 4 was integrated to obtain a more robust statistic. To this aim, additional natural signals recorded on stiff rock outcrop and collected by Paolucci et al. (2020) were used. However, the updated parameters IM_{50} and σ are comparable with that resulting from the original selection.

For both cases, the comparison of the values reported in Table 3.8 and Table 3.9 reveals that the PGA and the $IH_{0.1\ 0.5}$ are the most efficient IMs, being their σ values the lowest, especially for the highest DLs. However, the σ values associated to $Sa(T_1)$ are substantially comparable, even a bit higher. As expected, the IM_{50}s reduce moving from the FB A to FB C because in the latter case the IM shown in Table 3.9 is amplified due to site effects before the analysis of the structural performance. Figure 3.12 shows the fragility curves calculated in PGA for the two FB models and the five DLs.

Table 3.8: Median value (IM_{50}) and standard deviation (σ) associated with the DLs IMs for the FB A case.

FB A									
	PGA [g]		$Sa(T_1)$ [g]		CAV [m/s]		$IH_{0.1\ 0.5}$ [m]		$N_{records}$
	IM_{50}	σ	IM_{50}	σ	IM_{50}	σ	IM_{50}	σ	
DL1	0.095	0.495	0.178	0.473	1.395	0.703	0.024	0.625	127
DL2	0.274	0.314	0.656	0.391	3.936	0.674	0.093	0.368	92
DL3	0.450	0.219	1.013	0.376	5.870	0.314	0.174	0.186	18 (10)
DL4	0.530	0.191	1.182	0.308	7.672	0.431	0.214	0.176	17 (7)
DL5	0.619	0.219	1.500	0.261	10.102	0.401	0.249	0.221	44 (12)

Table 3.9: Median value (IM_{50}) and standard deviation (σ) associated with the DLs IMs for the FB C case.

FB C	PGA [g]		Sa(T_1) [g]		CAV [m/s]		$IH_{0.1\,0.5}$ [m]		$N_{records}$
	IM_{50}	σ	IM_{50}	σ	IM_{50}	σ	IM_{50}	σ	
DL1	0.051	0.474	0.093	0.335	0.777	0.618	0.012	0.435	54
DL2	0.120	0.430	0.237	0.469	1.633	0.659	0.032	0.497	98
DL3	0.211	0.219	0.433	0.335	2.992	0.531	0.074	0.173	16
DL4	0.240	0.248	0.595	0.338	4.420	0.556	0.094	0.236	28
DL5	0.404	0.329	0.975	0.426	5.922	0.569	0.147	0.330	70

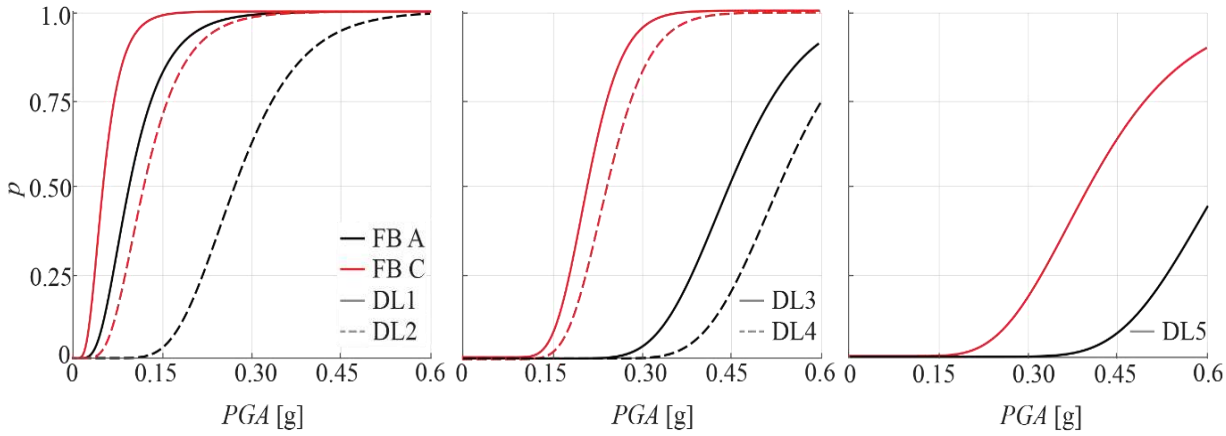

Figure 3.12. Comparisons between the fragility curves obtained respectively by applying to the FB model the inputs selected (A) or those resulting from the site response analyses (C). The represented IM consists of PGA.

7.3 Influence of soil-structure interaction on the fragility curves

Table 3.10 and Table 3.11 report the same parameters shown in Table 3.8 and Table 3.9, but with reference to the fragility curves of the CB C and CB $C_{\beta s}$ models. The curves were again computed by referring to the IM of the selected input motions (see section 2). The comparison among the parameters highlights that soil hysteresis produces an increase of IM_{50}, thus reducing the probability of failure on the building Conversely, its influence on the standard deviation is slight and less clear. The most efficient IMs i.e. those associated with the lowest σ) are the same already discussed in section 7.2.

Table 3.10: Median value (IM_{50}) and standard deviation (σ) associated with the various DLs for the CB C model.

CB C	PGA [g]		Sa(T_1) [g]		CAV [m/s]		$IH_{0.1\,0.5}$ [m]		$N_{records}$
	IM_{50}	σ	IM_{50}	σ	IM_{50}	σ	IM_{50}	σ	
DL1	0.071	0.442	0.101	0.367	0.983	0.521	0.015	0.406	70
DL2	0.143	0.482	0.278	0.492	1.970	0.678	0.043	0.410	86
DL3	0.209	0.262	0.493	0.398	3.555	0.527	0.085	0.225	19
DL4	0.319	0.284	0.738	0.383	6.295	0.603	0.122	0.297	36
DL5	0.463	0.254	0.994	0.467	6.055	0.434	0.167	0.273	38

Table 3.11: Median value (IM_{50}) and standard deviation (σ) associated with the various DLs for the CB $C_{\beta s}$ model.

CB C $_{\beta s}$	PGA [g]		Sa(T_1) [g]		CAV [m/s]		$IH_{0.1\,0.5}$ [m]		$N_{records}$
	IM_{50}	σ	IM_{50}	σ	IM_{50}	σ	IM_{50}	σ	
DL1	0.074	0.406	0.109	0.374	1.045	0.583	0.017	0.380	71
DL2	0.158	0.439	0.317	0.452	2.180	0.680	0.050	0.396	87
DL3	0.242	0.268	0.578	0.413	4.432	0.685	0.097	0.246	22
DL4	0.357	0.274	0.794	0.426	6.067	0.555	0.131	0.299	37
DL5	0.490	0.249	1.065	0.451	6.317	0.452	0.178	0.257	31

Figure 3.13 shows the resulting fragility curves for the different DLi, in terms of both PGA and Sa (T_1). The latter has been preferred to $IH_{0.1\ 0.5}$ since its use is more widespread in engineering applications and, definitely, also in probabilistic hazard assessment. For both IMs, SFS interaction produces a shift of the curve to the right side, enhanced by soil hysteresis. The shift to the right reduces the probability of failure and such beneficial effect is more pronounced for DL3 and DL4. Despite these results, it must be pointed out that the judgement on the potential beneficial effect of SFS interaction cannot be conclusive since the research needs to be extended to additional soil profiles as well as other URM buildings. Indeed, the issue if SFS interaction may produce beneficial or detrimental effects is still debated in the literature. Parametrical studies on more simplified systems demonstrated that both effects may be produced and with a different amount (from negligible to relevant) as a function of the properties of the structure, the soil and the ground motion (Moghaddasi et al. (2011); Khosravikia et al. (2018); Mylonakis and Gazetas (2000)). Moreover, the judgment may change also as a function of the main effect considered (i.e. the ductility, the overall lateral displacement, the internal forces, the overall failure mechanism of the structure, the fragility curve, etc.). In addition, the studies more explicitly focused on URM structures are still very few and limited to specific study-cases that does not allow to generalize any conclusion. In particular, in Fathi et al. (2020) the SFS interaction effects on the out-of-plane behaviour of a massive URM structure have been investigated performing NLDA on a Finite Element Model and confirming that the rate of the increase in the displacement demand and decrease in the acceleration demand depend on the earthquake magnitude and duration. In Karatzetzou et al. (2015), the response of a neoclassical school in Rhodes has been analysed by adopting the equivalent frame model and performing nonlinear static analyses. In that case, the authors evaluated detrimental effect of SFS interaction in one direction, with a strong reduction of the maximum ground acceleration the building can resist, while negligible in the orthogonal one; moreover, they obtained that SFS interaction may produce a strong alteration of the overall failure mechanism predicted by the model. Thus, these studies, even not yet conclusive, highlighted the relevance in accounting for these effects for a more reliable seismic assessment.

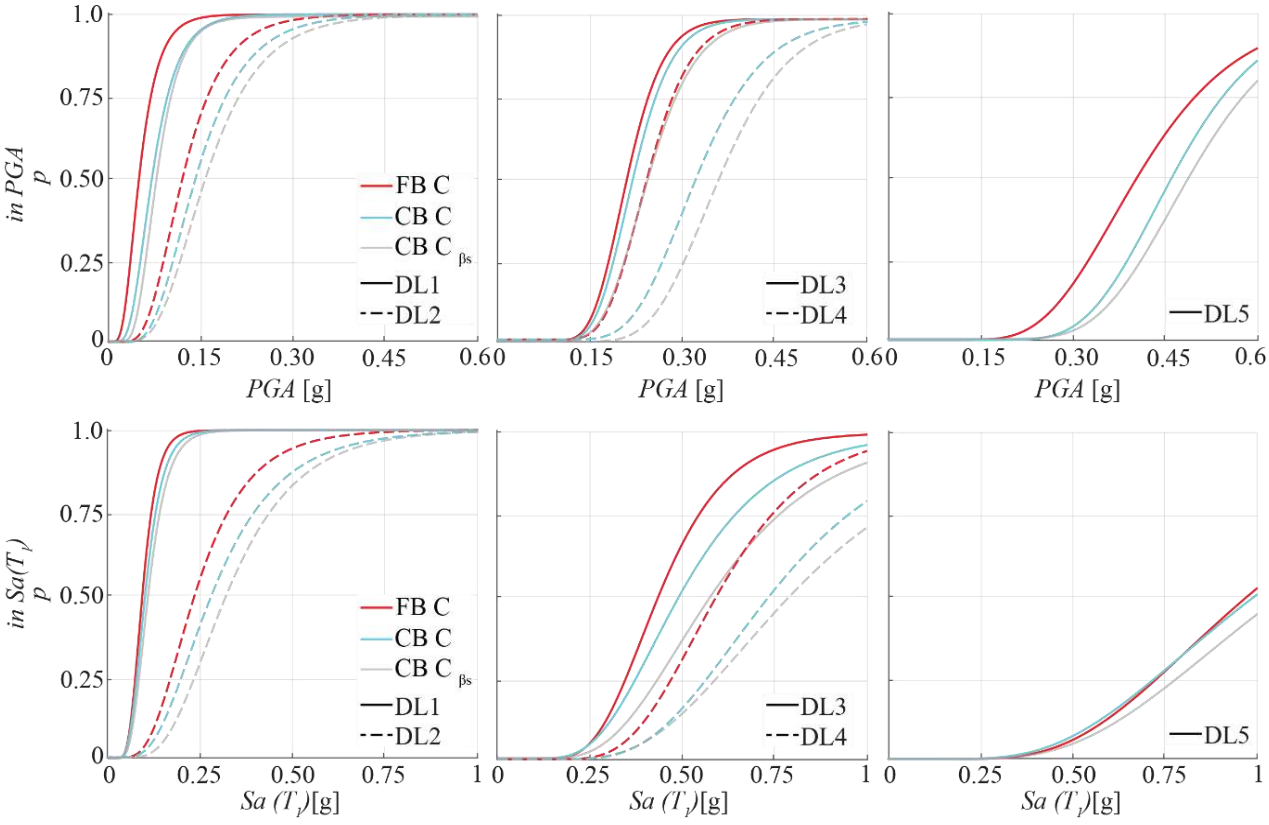

Figure 3.13. Comparisons between the curves obtained from the model on soil C with PGA and Sa (T_1) as IM.

8 COMPARISONS WITH CODES-CONFORMING SIMPLIFIED APPROACHES

In this section, the results achieved from different approaches and various models are quantitatively discussed in terms of average damage (μ_d), as computed through the fragility curves of previous sections and introducing also the simplified approach adopted by Codes to account for site effect. The μ_d parameter is calculated according to the formula in Figure 3.14b as the sum of the probabilities (p_{DLi}) weighted by 0,1,2,3,4 or 5 moving from DL0 to DL5. As an example, Figure 3.14a shows through the vertical line the probabilities of exceeding the various DLs for the PGA expected to occur on a stiff rock outcrop at Visso with a return period of 475 years (PGA_{475}). The reference value of PGA_{475} has been computed according to the Italian seismic hazard map Stucchi et al. (2004). Then, the IM on the abscissa must be properly modified to account for the site amplification. By way of example, in Figure 3.14a, the PGA value is amplified according to the coefficient S_S proposed by the Italian Code (NTC (2018)) which is equal to 1.35. The probability of failure is consequently associated to the modified value, PGA^*_{475}.

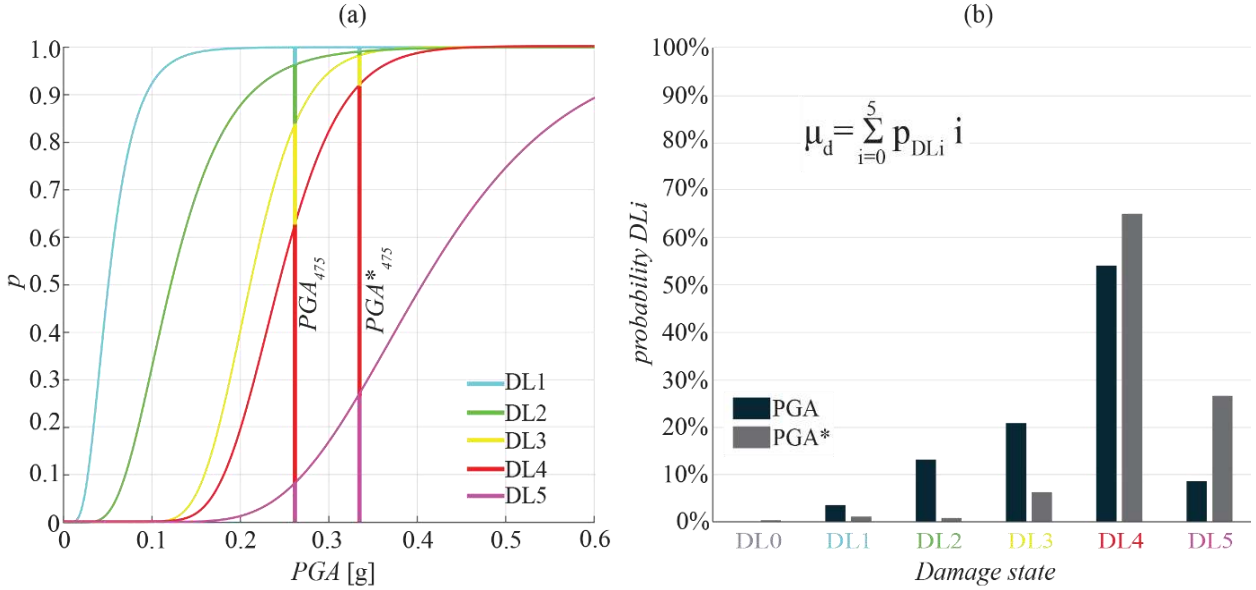

Figure 3.14. (a) Illustrative example of the IM associated to the FB A (PGA_{475}) and FB A-code (PGA^*_{475}) cases, (b) definition of the μ_d with the probability of each DLi calculated with the fragility curve in Figure 3.14a.

The effectiveness of the Code-conforming approach was thus checked by comparing the average damage calculated for the FB A case using such modified intensity measure IM* to that obtained from the direct analysis of the three cases FB C, CB C and CB $C_{\beta s}$. Being the model 3D, the mean IM (or IM*) along the two in-plane dimensions was assumed to enter in the fragility curves.

The simplified procedure proposed in the following four Codes has been considered: the Italian Code (NTC (2018)); the Eurocode 8 (EC8 (2004)); the American Code (ASCE7 (2016)) and the New Zealand Code (NZS (2017)). The site classification for the soil profile below the Visso's school is type C for all Codes except for ASCE7, for which it corresponds to a soil type D. Due to this difference, in the following the IM provided on the stiff rock outcrop is referred as bedrock IM (or IM*) and that estimated on the surface of the soil profile is referred as surface IM (or IM*).

Firstly, the different Codes were examined to compare the modifications introduced in the amplitude and shape of the response spectrum to account for the site effects. Table 3.12 highlights that: the PGA-amplification factor varies with the severity of the event at bedrock for NTC and ASCE7; it assumes two alternative values based on the Magnitude of the surface wave (M_s) according to EC8; and it remains constant for NZS. Moreover, the values assumed by the initial, T_B, and final, T_C, periods of the flat branch of the spectra evolve with the severity of the event for ASCE7 and with M_s for EC8, while do not change in NTC and NZS.

An example of the spectra provided by the different Codes is shown in Figure 3.15 for one component

of two events, which are characterized by different PGA and M_s. In the same figure, the spectral values associated with the FB and CB periods along the X-direction are highlighted; the vertical lines indicate T_B and T_C of the bedrock spectra. The plot confirms the differences among Codes in the definition of the spectral shape and amplitude, both at bedrock and on surface.

Table 3.12: Modifications of the bedrock acceleration response spectra proposed by different Codes to consider site effects in the Visso village.

	Soil type	PGA-amplification coefficient	T_B and T_C
NTC	C	Ranging between 1 and 1.5 according to the bedrock PGA	Constant
EC8	C	1.5 if $M_s < 5.5$ 1.15 if $M_s > 5.5$	T_B=0.1s and T_C = 0.25s if M_s< 5.5 T_B=0.2s and T_C = 0.6s if $M_s > 5.5$
ASCE7	D	Ranging between 1 and 1.6 according to the severity of the event	Variable with the bedrock PGA (about the same)
NZS	C	Constant	Constant

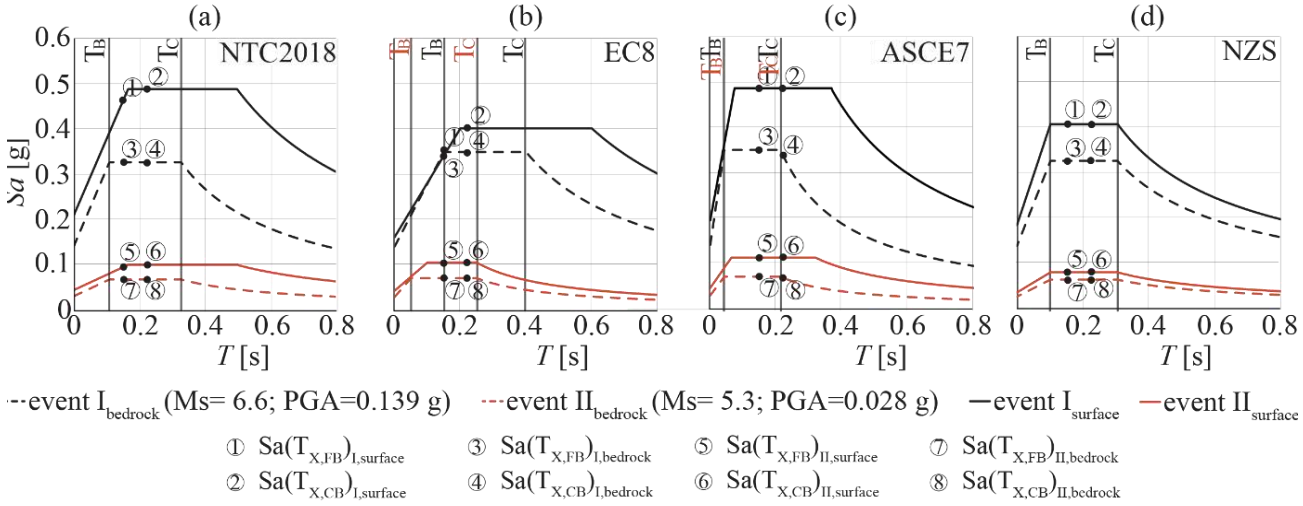

Figure 3.15. Acceleration response spectra defined by NTC (a), EC8 (b), ASCE7 (c) and NZS (d) on soil-type A (or B for ASCE7) and C (or D for ASCE7) and two different values of PGAs.

The calculation of μ_d was repeated by referring to the PGA and Sa(T_1). In the latter case, the spectral acceleration corresponding to the fundamental period of the FB model was adopted to estimate the μ_d of the FB A (in this case Sa*) and FB C cases, while the Sa(T_1) corresponding to the fundamental period of the CB model was used for the CB C and CB $C_{\beta s}$ cases. The reference periods of both the FB and CB models are the initial periods (see Figure 3.4a). Thus, their elongation due to structural damage or soil nonlinearity during each seismic analysis (see Figure 3.3) was not considered. That is consistent with the typical procedure adopted in engineering practice-oriented applications to estimate the seismic damage affecting structures. For the same reason, all the spectra were computed with reference to the conventional damping ratio equal to 5%, independently on the value set for the structural material and on the assumption on the base restraint. As a matter of fact, such choice is conservative because the initial damping ratio of the CB C and CB $C_{\beta s}$ cases is just slightly higher than 5% (see approach A3 in Table 3.6).

When the Code approach was followed, the spectral ordinates on the surface of the Visso soil profile were computed by multiplying the acceleration spectrum of each input motion in Figure 3.4a by the amplification factor (S_{Sa}), defined as the ratio between the spectral ordinates on surface and that at bedrock provided by each Code. Obviously, S_{Sa} coincides with the PGA-amplification factor for a null period. The above mentioned differences in the definition of the spectra (see Figure 3.15) produce a variability of S_{Sa} with the period, the severity of the input motion and the considered Code.

Figure 3.16 compares the μ_d obtained from the numerical analyses and provided by the different Code approach. In particular:

- Each black point represents the μ_d estimated, for each selected input motion, from the fragility curves of the FB C case (ordinates) and from the fragility curve of the FB A case (abscissas), respectively, after the modification of the intensity measure according to the Code, IM*, to include site effects.
- Each grey (or white) point has on the ordinate, the μ_d estimated for each selected input motion from the fragility curves of the CB C (or CB $C_{\beta s}$) case and, on the abscissa, the μ_d estimated from the fragility curves of the FB A case. Consistently with what above discussed, the modification of the IM according to the Code (IM*) to include both site and SFS interaction effects has been applied.

Obviously, the comparison among the Code conforming approach and the CB model is less straightforward with respect to that with the FB C model since Code neglects SFS interaction effects. To try to be even more synthetic in the comparisons, the μ_d value is also converted into an equivalent DL according to the following ranges (Lagomarsino and Giovinazzi (2006)): 0-0.7 for DL0; 0.7-1.6 for DL1; 1.6-2.5 for DL2; 2.5-3.4 for DL3; 3.4-4.3 for DL4; 4.3-5 for DL5.Thus, in Figure 3.16, the square elements are filled in: light grey, if the same DL is estimated by both models/approaches; and progressively darker grey, when the estimation differs of one, two or three DLs.

For NZS, the trend of the results is very similar for the two IMs. This is due to the fact the fixed-base and compliant-base fundamental periods generally fall in the flat branch of the spectrum (i.e. between T_B and T_C, see Figure 3.15), where the amplification factor (S_{Sa}) is constant. Conversely, a scatter is shown by the μ_d-values computed from Sa(T_1) according to NTC and ASCE7, especially for the CB C and CB $C_{\beta s}$ models. This is because their periods are generally out of the range defined by T_B and T_C. Finally, results obtained from EC8 appeared ordered according to the Magnitude of the surface wave of the event, consistently with the different definition of the spectral parameters reported in Table 3.12.

When only site effects are considered, the Code conforming approach appears almost consistent with the prediction of the FB C model for DL0 and DL1, while it underestimates μ_d at the higher DLs, reaching a difference up to three damage levels for EC8 and ASCE7.

SFS interaction reduces the gap between the μ_d estimated through the Code conforming approaches and those estimated by explicitly accounting for site effects joint to SFS interaction (CB C and CB $C_{\beta s}$). Nevertheless, a difference of one DL still results for NTC, EC8 and NZS and up to two DLs for ASCE7 even for CB $C_{\beta s}$. Such underestimation arguably would increase if the increment of damping ratio induced by SFS interaction was considered in the computation of the IM*.

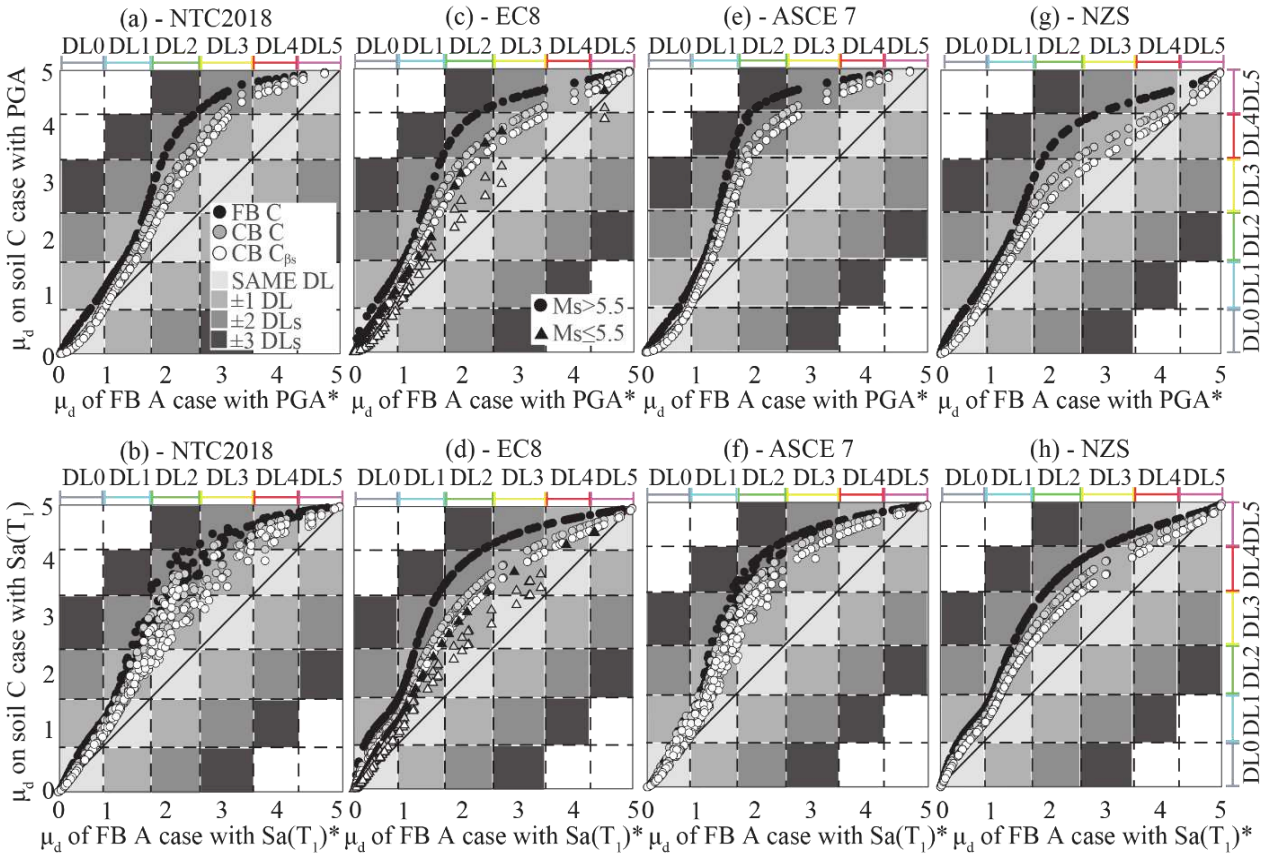

Figure 3.16. Comparison among the $\lceil_d$ resulting for the different analyzed cases from the curves expressed as a function of (a,b,c,d) PGA and (e,f,g,h) Sa(T_1). The PGA* and Sa* amplified according to the coefficients of the (a, b) NTC, (c, d) EC8, (e, f) ASCE7 and (g, h) NZS Code was used in the FB A case.

9 CONCLUSIONS

The paper presents a first attempt to fill the gap present in the literature dealing with numerical fragility curves specifically derived for URM ordinary buildings to account also for the site effects and the SFS interaction.

The selected case study constitutes in the paper the tool to compare and validate different impedance functions as well as different solutions for the foundation damping available in the literature. Such a validation was made possible by the accurate data on actual recordings from the permanent monitoring system and the damage survey after the Central Italy 2016/2017 seismic sequence available for the selected building. It emerged that the impedances by Pais and Kausel (1988) or Gazetas (1991) provide substantially analogous results, while considering or neglecting the hysteretic soil damping may produce more significant alterations. A systematic improvement of the comparison between the simulated and the observed structural behaviour is recognized when the hysteretic soil damping ratio is considered for the case at hand.

This evidence allowed to address the final modelling choices of the equivalent frame model, especially for the compliant base model that has been used in the research to explicitly account for the SFS interaction effects in the derivation of fragility curves through NLDA.

The procedure followed to evaluate the effects of site amplification and SFS interaction is based on a linear equivalent approach to model both the soil response to the seismic waves and the stiffness and damping of the soil-foundation system. Such approach is recognized as reliable if the shear strains in the soil are moderate (approximately lower than 0.1% (Mair (1993)), so that the soil is far from failure and even conservative with respect to the coupled analyses of SFS systems (Karapetrou et al. (2013); Tomeo et al. (2018)). In such cases, the satisfying comparison with the experimental data revealed that also the setting of a Rayleigh damping equivalent to the combination of the viscous

structural damping and the radiation and hysteretic soil-foundation damping is a valid modelling strategy. Moreover, its calibration through the formula based on the replacement oscillator was thought for practical use. Obviously, additional numerical analyses are needed to validate such procedure when the structure cannot be modelled as a SDOF system or the foundation geometry is extremely irregular or the soil profile variable below the building.

The fragility curves of the fixed base model on rock soil (FB A) and the fixed base model on the stratigraphy representative of subsoil under the school (FB C) confirmed, as expected, the potential significant role of the site effects, while the evidence from the compliant model (CB C) highlighted as the soil-structure interaction produces a shift of the curve to the right side enhanced by soil hysteresis. The shift to the right reduces the probability of failure and such beneficial effect is more pronounced for the severe (DL3) and very severe to near collapse (DL4) damage levels.

Among the different intensity measures investigated in the paper, the PGA and the $Sa(T_1)$ revealed as the most efficient IMs. The Housner intensity also appears promising. However, its application in risk analyses addressed to support mitigation policies appears difficult due to the lack of hazard scenarios expressed in terms of $IH_{0.1\ 0.5}$.

Finally, the developed fragility curves have been used to verify the reliability of the Code-conforming approach. To this aim, four national and international Codes have been compared. It emerged that, when only site effects are considered, the Code approach underestimates the damage in any case and up to three DLs for EC8 (2004) and ASCE7 (2016). SFS interaction reduces the gap between the damages estimated through the Code conforming approaches and those estimated in this study by explicitly accounting for site effects joint to SFS interaction. These results highlighted the need of improvements in the Code-conforming approach to avoid excessively unconservative estimates.

Of course, results achieved in the paper will be in the future further integrated accounting for additional soil profiles as well as for other URM buildings, representative also of residential buildings.

Supplementary data of Chapter 3

The data of each signal used are herein reported. In particular, Figure 3.17 summarizes the statistics of the signals used in Chapter 3 and the Table 3.13 collect: (1) Name of record, (2) Magnitude, (3) Vs_{30} of the station' soil expressed in m/s, (4) the epicentral distance in km, (5) scale factor, (6) PGA in g, (7) $Sa(T_1)$ for FB model and (8) CB model in g, (9) CAV in m/s and (10) $IH_{0.1\ 0.5}$ expressed in cm.

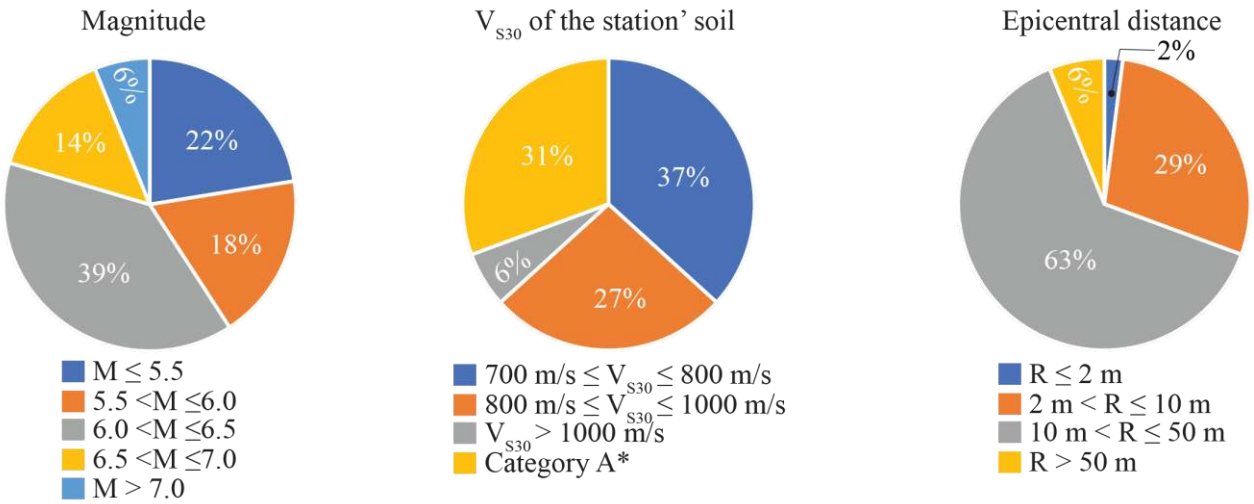

Figure 3.17: Distribution of the real signals (scale factor equal to 1) by magnitude, V_{S30} of recording station, and epicenter distance.

Table 3.13: Data and Input Motion (IM) of the original and scaled selected signals.

	(1)	(2)	(3)	(4)	(5)	(6)		(7)		(8)		(9)		(10)	
						X	Y	X	Y	X	Y	X	Y	X	Y
1	Shimane Hiroshima Border	5.1	929	18.4	1	0.014	0.013	0.016	0.010	0.012	0.011	0.275	0.257	0.002	0.002
2	L'Aquila aftershock	5.1	717	17.9	1	0.016	0.020	0.045	0.056	0.062	0.048	0.356	0.354	0.007	0.007
3	L'Aquila aftershock	5.3	717	13.1	1	0.022	0.024	0.040	0.050	0.052	0.056	0.355	0.421	0.007	0.008
4	L'Aquila aftershock	5	830	5.3	1	0.038	0.031	0.116	0.087	0.082	0.036	0.330	0.334	0.007	0.007
5	Molise_2002	5.7	865	58.3	1	0.039	0.034	0.115	0.139	0.067	0.073	0.772	0.873	0.009	0.010
6	Gran Sasso	5.1	717	12.2	1	0.035	0.041	0.058	0.060	0.076	0.077	0.470	0.645	0.008	0.014
7	L'Aquila aftershock	5.4	717	16.2	1	0.041	0.050	0.072	0.071	0.081	0.085	0.860	0.839	0.012	0.015
8	Irpinia	6.9	1149	23.8	1	0.057	0.056	0.128	0.127	0.158	0.137	2.729	2.364	0.024	0.024
9	Kyushu	5.7	889	27.0	1	0.029	0.064	0.067	0.113	0.067	0.187	0.347	0.403	0.012	0.027
10	Southern Iwate Pref.	5.1	744	25.0	1	0.051	0.068	0.110	0.302	0.097	0.099	0.707	0.802	0.012	0.015
11	Tottori_2000	6.3	650	107.0	1	0.056	0.072	0.082	0.098	0.050	0.048	1.619	1.303	0.006	0.011
12	L'Aquila aftershock	5.1	717	5.5	1	0.050	0.080	0.094	0.079	0.069	0.073	0.572	0.678	0.011	0.012
13	Loma Pietra 2000	6	873	84.1	1	0.079	0.093	0.154	0.142	0.157	0.194	1.508	1.480	0.026	0.025
14	L'Aquila aftershock	5.6	830	5.3	1	0.094	0.076	0.233	0.133	0.275	0.146	0.843	0.861	0.029	0.023
15	Duzce	7.1	719	15.6	1	0.104	0.074	0.188	0.157	0.162	0.216	2.026	1.591	0.030	0.023
16	Southern Italy 1995	5.2	865	27.8	1	0.115	0.111	0.144	0.081	0.210	0.067	0.634	0.651	0.016	0.011
17	Friuli 4th shock	5.9	901	10.0	1	0.102	0.129	0.437	0.352	0.179	0.248	1.475	1.888	0.030	0.035
18	Taiwan_1999	6.2	804	44.7	1	0.177	0.152	0.527	0.299	0.442	0.402	4.086	3.872	0.087	0.063

19	W Tottori Prefecture	6.6	929	24.6	1	0.129	0.186	0.185	0.258	0.112	0.237	4.061	3.439	0.020	0.042
20	Cosenza_1995	5.2	1906	2.4	1	0.186	0.132	0.260	0.188	0.345	0.370	0.988	1.068	0.040	0.045
21	Balkan_1979	6.9	A*	19.7	1	0.214	0.176	0.346	0.634	0.396	0.490	5.173	4.961	0.088	0.099
22	Parkfield_2004	6	906	9.3	1	0.245	0.196	0.427	0.327	0.473	0.269	1.720	1.912	0.076	0.074
23	Northridge	6.7	715	14.7	1	0.289	0.232	0.692	0.844	0.929	0.550	4.776	4.654	0.121	0.115
24	Southern Iwate Prefecture	6.9	744	23.1	1	0.300	0.222	0.821	0.507	0.649	0.535	7.893	8.284	0.093	0.103
25	Kobe_1995	6.9	1043	25.4	1	0.276	0.312	0.452	0.402	0.404	0.503	4.999	4.243	0.095	0.122
26	Anza	5.2	725	14.2	1	0.278	0.315	0.712	0.524	0.770	0.377	0.909	0.870	0.065	0.046
27	L'Aquila mainshock	6.3	717	5.7	1	0.330	0.354	1.027	0.649	0.463	0.656	5.227	5.942	0.095	0.112
28	Aquila_2009	6.3	705	1.8	1	0.330	0.354	1.027	0.649	0.463	0.656	5.744	6.385	0.095	0.112
29	Centro_Italia_2016	6	687	15.3	1	0.359	0.373	0.850	1.227	1.700	1.169	4.158	3.572	0.136	0.116
30	Manjil_1990	7.4	723	21.8	1	0.515	0.497	1.960	1.480	1.354	1.208	17.265	25.150	0.210	0.218
31	Shimane Hiroshima Border	5.1	929	18.4	1	0.013	0.014	0.008	0.011	0.007	0.013	0.257	0.275	0.002	0.002
32	L'Aquila aftershock	5.1	717	17.9	1	0.020	0.016	0.066	0.046	0.035	0.039	0.354	0.356	0.007	0.007
33	L'Aquila aftershock	5.3	717	13.1	1	0.024	0.022	0.053	0.052	0.047	0.041	0.421	0.355	0.008	0.007
34	L'Aquila aftershock	5	830	5.3	1	0.031	0.038	0.079	0.095	0.053	0.039	0.334	0.330	0.007	0.007
35	Molise_2002	5.7	865	58.3	1	0.034	0.039	0.119	0.118	0.103	0.046	0.873	0.772	0.010	0.009
36	Gran Sasso	5.1	717	12.2	1	0.041	0.035	0.071	0.053	0.061	0.039	0.645	0.470	0.014	0.008
37	L'Aquila aftershock	5.4	717	16.2	1	0.050	0.041	0.095	0.070	0.069	0.072	0.839	0.860	0.015	0.012
38	Irpinia	6.9	1149	23.8	1	0.056	0.057	0.108	0.158	0.141	0.185	2.364	2.729	0.024	0.024
39	Kyushu	5.7	889	27.0	1	0.064	0.029	0.090	0.060	0.126	0.120	0.403	0.347	0.027	0.012
40	Southern Iwate Pref.	5.1	744	25.0	1	0.068	0.051	0.201	0.116	0.186	0.068	0.802	0.707	0.015	0.012
41	Tottori_2000	6.3	650	107.0	1	0.072	0.056	0.105	0.075	0.049	0.042	1.303	1.619	0.011	0.006
42	L'Aquila aftershock	5.1	717	5.5	1	0.080	0.050	0.128	0.095	0.075	0.068	0.678	0.572	0.012	0.011
43	Loma Pietra 2000	6	873	84.1	1	0.093	0.079	0.121	0.119	0.123	0.102	1.480	1.508	0.025	0.026
44	L'Aquila aftershock	5.6	830	5.3	1	0.076	0.094	0.197	0.158	0.225	0.336	0.861	0.843	0.023	0.029
45	Duzce	7.1	719	15.6	1	0.074	0.104	0.123	0.234	0.142	0.193	1.591	2.026	0.023	0.030
46	Southern Italy 1995	5.2	865	27.8	1	0.111	0.115	0.143	0.143	0.071	0.139	0.651	0.634	0.011	0.016
47	Friuli 4th shock	5.9	901	10.0	1	0.129	0.102	0.428	0.266	0.315	0.177	1.888	1.475	0.035	0.030
48	Taiwan_1999	6.2	804	44.7	1	0.152	0.177	0.370	0.506	0.326	0.598	3.872	4.086	0.063	0.087
49	W Tottori Prefecture	6.6	929	24.6	1	0.186	0.129	0.295	0.157	0.157	0.087	3.439	4.061	0.042	0.020
50	Cosenza_1995	5.2	1906	2.4	1	0.132	0.186	0.194	0.417	0.264	0.282	1.068	0.988	0.045	0.040
51	Balkan_1979	6.9	A*	19.7	1	0.176	0.214	0.549	0.391	0.425	0.499	4.961	5.173	0.099	0.088
52	Parkfield_2004	6	906	9.3	1	0.196	0.245	0.327	0.396	0.327	0.557	1.912	1.720	0.074	0.076
53	Northridge	6.7	715	14.7	1	0.232	0.289	0.807	1.096	0.895	1.094	4.654	4.776	0.115	0.121
54	Southern Iwate Prefecture	6.9	744	23.1	1	0.222	0.300	0.493	0.696	0.690	0.449	8.284	7.893	0.103	0.093
55	Kobe_1995	6.9	1043	25.4	1	0.312	0.276	0.641	0.391	0.402	0.602	4.243	4.999	0.122	0.095
56	Anza	5.2	725	14.2	1	0.315	0.278	0.644	0.780	0.449	0.585	0.870	0.909	0.046	0.065
57	L'Aquila mainshock	6.3	717	5.7	1	0.354	0.330	0.844	0.803	0.584	0.590	5.942	5.227	0.112	0.095
58	Aquila_2009	6.3	705	1.8	1	0.354	0.330	0.844	0.803	0.584	0.590	6.385	5.744	0.112	0.095
59	Centro_Italia_2016	6	687	15.3	1	0.373	0.359	1.146	1.149	1.606	1.300	3.572	4.158	0.116	0.136
60	Manjil_1990	7.4	723	21.8	1	0.497	0.515	1.531	1.962	1.378	1.214	25.150	17.265	0.218	0.210
61	Molise_2002	5.7	865	58.3	1.75	0.067	0.059	0.202	0.243	0.117	0.127	1.350	1.528	0.016	0.018
62	Irpinia	6.9	1149	23.8	1.75	0.101	0.098	0.224	0.222	0.276	0.240	4.775	4.137	0.041	0.043
63	Duzce	7.1	719	15.6	0.75	0.078	0.055	0.141	0.118	0.122	0.162	1.519	1.193	0.023	0.018
64	Southern Italy 1995	5.2	865	27.8	0.75	0.086	0.083	0.108	0.061	0.158	0.050	0.476	0.488	0.012	0.008
65	Balkan_1979	6.9	A*	19.7	0.7	0.150	0.123	0.242	0.444	0.277	0.343	3.621	3.473	0.062	0.069
66	Southern Iwate Prefecture	6.9	744	23.1	1.25	0.375	0.278	1.026	0.634	0.811	0.668	9.866	10.356	0.117	0.129

67	Kobe_1995	6.9	1043	25.4	0.6	0.165	0.187	0.271	0.241	0.242	0.302	2.999	2.546	0.057	0.073
68	Duzce	7.1	719	15.6	1.75	0.181	0.129	0.328	0.275	0.284	0.378	3.545	2.785	0.053	0.041
69	Southern Italy 1995	5.2	865	27.8	1.25	0.143	0.139	0.180	0.102	0.263	0.084	0.793	0.814	0.020	0.013
70	Tottori_2000	6.3	650	107.0	1.25	0.070	0.090	0.103	0.123	0.063	0.060	2.024	1.628	0.007	0.013
71	Taiwan_1999	6.2	804	44.7	0.6	0.106	0.091	0.316	0.180	0.265	0.241	2.452	2.323	0.052	0.038
72	W Tottori Prefecture	6.6	929	24.6	0.75	0.097	0.139	0.139	0.194	0.084	0.178	3.046	2.579	0.015	0.031
73	Northridge	6.7	715	14.7	1.75	0.505	0.406	1.212	1.477	1.626	0.963	8.358	8.144	0.211	0.201
74	L'Aquila mainshock	6.3	717	5.7	0.6	0.198	0.212	0.616	0.389	0.278	0.394	3.136	3.565	0.057	0.067
75	Centro_Italia_2016	6	687	15.3	1.75	0.629	0.653	1.487	2.146	2.975	2.045	7.276	6.251	0.238	0.203
76	Tottori_2000	6.3	650	107.0	1.75	0.098	0.126	0.144	0.172	0.088	0.084	2.834	2.280	0.010	0.019
77	W Tottori Prefecture	6.6	929	24.6	1.75	0.226	0.325	0.324	0.452	0.195	0.414	7.107	6.018	0.035	0.073
78	Shimane Hiroshima Border	5.1	929	18.4	1.25	0.017	0.017	0.020	0.013	0.015	0.013	0.343	0.321	0.003	0.002
79	L'Aquila aftershock	5.1	717	17.9	1.25	0.020	0.025	0.056	0.070	0.077	0.060	0.446	0.443	0.009	0.009
80	L'Aquila aftershock	5.3	717	13.1	1.25	0.028	0.030	0.050	0.062	0.065	0.070	0.444	0.526	0.008	0.010
81	L'Aquila aftershock	5	830	5.3	1.25	0.047	0.039	0.145	0.109	0.103	0.045	0.412	0.417	0.009	0.008
82	Gran Sasso	5.1	717	12.2	1.25	0.044	0.051	0.072	0.075	0.095	0.096	0.588	0.806	0.010	0.017
83	L'Aquila aftershock	5.4	717	16.2	1.75	0.071	0.087	0.126	0.125	0.141	0.148	1.505	1.468	0.021	0.027
84	Kyushu	5.7	889	27.0	1.75	0.051	0.111	0.117	0.197	0.117	0.328	0.607	0.706	0.022	0.048
85	Southern Iwate Pref.	5.1	744	25.0	1.75	0.089	0.120	0.193	0.528	0.169	0.172	1.237	1.404	0.021	0.027
86	L'Aquila aftershock	5.1	717	5.5	1.25	0.062	0.100	0.117	0.098	0.086	0.092	0.715	0.848	0.014	0.015
87	Loma Pietra 2000	6	873	84.1	0.75	0.059	0.070	0.116	0.107	0.117	0.146	1.131	1.110	0.020	0.019
88	L'Aquila aftershock	5.6	830	5.3	0.75	0.070	0.057	0.174	0.100	0.206	0.109	0.633	0.646	0.022	0.018
89	Friuli 4th shock	5.9	901	10.0	0.75	0.077	0.097	0.328	0.264	0.134	0.186	1.106	1.416	0.023	0.027
90	Cosenza_1995	5.2	1906	2.4	0.75	0.139	0.099	0.195	0.141	0.259	0.277	0.741	0.801	0.030	0.034
91	Parkfield_2004	6	906	9.3	0.6	0.147	0.118	0.256	0.196	0.284	0.161	1.032	1.147	0.045	0.044
92	Anza	5.2	725	14.2	0.75	0.209	0.236	0.534	0.393	0.578	0.283	0.681	0.653	0.049	0.034
93	Aquila_2009	6.3	705	1.8	0.6	0.198	0.212	0.616	0.389	0.278	0.394	3.446	3.831	0.057	0.067
94	Manjil_1990	7.4	723	21.8	0.6	0.309	0.298	1.176	0.888	0.813	0.725	10.359	15.090	0.126	0.131
95	Shimane Hiroshima Border	5.1	929	18.4	1.75	0.024	0.023	0.028	0.018	0.021	0.019	0.481	0.450	0.004	0.003
96	L'Aquila aftershock	5.3	717	13.1	1.75	0.039	0.042	0.071	0.087	0.091	0.098	0.622	0.736	0.012	0.014
97	L'Aquila aftershock	5	830	5.3	1.75	0.066	0.054	0.202	0.152	0.144	0.063	0.577	0.584	0.013	0.012
98	Gran Sasso	5.1	717	12.2	1.75	0.061	0.072	0.101	0.105	0.133	0.134	0.823	1.128	0.014	0.024
99	L'Aquila aftershock	5.1	717	5.5	0.75	0.037	0.060	0.070	0.059	0.052	0.055	0.429	0.509	0.008	0.009
100	Loma Pietra 2000	6	873	84.1	1.75	0.138	0.163	0.270	0.249	0.274	0.340	2.639	2.589	0.046	0.043
101	L'Aquila aftershock	5.6	830	5.3	1.75	0.164	0.133	0.407	0.233	0.481	0.255	1.476	1.508	0.050	0.041
102	Friuli 4th shock	5.9	901	10.0	1.75	0.179	0.226	0.765	0.616	0.312	0.433	2.582	3.304	0.053	0.062
103	Cosenza_1995	5.2	1906	2.4	1.75	0.325	0.231	0.455	0.329	0.603	0.647	1.729	1.868	0.071	0.079
104	Anza	5.2	725	14.2	1.75	0.429	0.460	1.335	0.843	0.602	0.853	7.467	8.300	0.124	0.145
105	Molise_2002	5.7	865	58.3	1.75	0.059	0.067	0.209	0.206	0.181	0.080	1.528	1.350	0.018	0.016
106	Irpinia	6.9	1149	23.8	1.75	0.098	0.101	0.188	0.276	0.246	0.324	4.137	4.775	0.043	0.041
107	Duzce	7.1	719	15.6	0.75	0.055	0.078	0.093	0.175	0.107	0.145	1.193	1.519	0.018	0.023
108	Southern Italy 1995	5.2	865	27.8	0.75	0.083	0.086	0.107	0.108	0.054	0.104	0.488	0.476	0.008	0.012
109	Balkan_1979	6.9	A*	19.7	0.7	0.123	0.150	0.384	0.274	0.298	0.349	3.473	3.621	0.069	0.062
110	Southern Iwate Prefecture	6.9	744	23.1	1.25	0.278	0.375	0.616	0.870	0.863	0.561	10.356	9.866	0.129	0.117
111	Kobe_1995	6.9	1043	25.4	0.6	0.187	0.165	0.384	0.234	0.241	0.361	2.546	2.999	0.073	0.057
112	Duzce	7.1	719	15.6	1.75	0.129	0.181	0.216	0.409	0.249	0.338	2.785	3.545	0.041	0.053
113	Southern Italy 1995	5.2	865	27.8	1.25	0.139	0.143	0.178	0.179	0.089	0.174	0.814	0.793	0.013	0.020
114	Tottori_2000	6.3	650	107.0	1.25	0.090	0.070	0.131	0.093	0.062	0.052	1.628	2.024	0.013	0.007

115	Taiwan_1999	6.2	804	44.7	0.6	0.091	0.106	0.222	0.304	0.195	0.359	2.323	2.452	0.038	0.052
116	W Tottori Prefecture	6.6	929	24.6	0.75	0.139	0.097	0.221	0.118	0.117	0.065	2.579	3.046	0.031	0.015
117	Northridge	6.7	715	14.7	1.75	0.406	0.505	1.412	1.919	1.565	1.914	8.144	8.358	0.201	0.211
118	L'Aquila mainshock	6.3	717	5.7	0.6	0.212	0.198	0.506	0.482	0.350	0.354	3.565	3.136	0.067	0.057
119	Centro_Italia_2016	6	687	15.3	1.75	0.653	0.629	2.005	2.011	2.810	2.275	6.251	7.276	0.203	0.238
120	Tottori_2000	6.3	650	107.0	1.75	0.126	0.098	0.184	0.130	0.086	0.073	2.280	2.834	0.019	0.010
121	W Tottori Prefecture	6.6	929	24.6	1.75	0.325	0.226	0.515	0.275	0.274	0.153	6.018	7.107	0.073	0.035
122	Shimane Hiroshima Border	5.1	929	18.4	1.25	0.017	0.017	0.010	0.014	0.009	0.017	0.321	0.343	0.002	0.003
123	L'Aquila aftershock	5.1	717	17.9	1.25	0.025	0.020	0.082	0.057	0.043	0.049	0.443	0.446	0.009	0.009
124	L'Aquila aftershock	5.3	717	13.1	1.25	0.030	0.028	0.066	0.065	0.059	0.051	0.526	0.444	0.010	0.008
125	L'Aquila aftershock	5	830	5.3	1.25	0.039	0.047	0.099	0.119	0.066	0.049	0.417	0.412	0.008	0.009
126	Gran Sasso	5.1	717	12.2	1.25	0.051	0.044	0.089	0.066	0.077	0.049	0.806	0.588	0.017	0.010
127	L'Aquila aftershock	5.4	717	16.2	1.75	0.087	0.071	0.167	0.123	0.122	0.127	1.468	1.505	0.027	0.021
128	Kyushu	5.7	889	27.0	1.75	0.111	0.051	0.157	0.105	0.221	0.210	0.706	0.607	0.048	0.022
129	Southern Iwate Pref.	5.1	744	25.0	1.75	0.120	0.089	0.352	0.202	0.325	0.119	1.404	1.237	0.027	0.021
130	L'Aquila aftershock	5.1	717	5.5	1.25	0.100	0.062	0.160	0.119	0.093	0.085	0.848	0.715	0.015	0.014
131	Loma Pietra 2000	6	873	84.1	0.75	0.070	0.059	0.091	0.089	0.092	0.076	1.110	1.131	0.019	0.020
132	L'Aquila aftershock	5.6	830	5.3	0.75	0.057	0.070	0.148	0.118	0.169	0.252	0.646	0.633	0.018	0.022
133	Friuli 4th shock	5.9	901	10.0	0.75	0.097	0.077	0.321	0.200	0.237	0.133	1.416	1.106	0.027	0.023
134	Cosenza_1995	5.2	1906	2.4	0.75	0.099	0.139	0.146	0.313	0.198	0.212	0.801	0.741	0.034	0.030
135	Parkfield_2004	6	906	9.3	0.6	0.118	0.147	0.196	0.238	0.196	0.334	1.147	1.032	0.044	0.045
136	Anza	5.2	725	14.2	0.75	0.236	0.209	0.483	0.585	0.336	0.438	0.653	0.681	0.034	0.049
137	Aquila_2009	6.3	705	1.8	0.6	0.212	0.198	0.506	0.482	0.350	0.354	3.831	3.446	0.067	0.057
138	Manjil_1990	7.4	723	21.8	0.6	0.298	0.309	0.918	1.177	0.827	0.729	15.090	10.359	0.131	0.126
139	Shimane Hiroshima Border	5.1	929	18.4	1.75	0.023	0.024	0.015	0.020	0.012	0.023	0.450	0.481	0.003	0.004
140	L'Aquila aftershock	5.3	717	13.1	1.75	0.042	0.039	0.092	0.090	0.082	0.071	0.736	0.622	0.014	0.012
141	L'Aquila aftershock	5	830	5.3	1.75	0.054	0.066	0.138	0.166	0.093	0.068	0.584	0.577	0.012	0.013
142	Gran Sasso	5.1	717	12.2	1.75	0.072	0.061	0.124	0.092	0.108	0.069	1.128	0.823	0.024	0.014
143	L'Aquila aftershock	5.1	717	5.5	0.75	0.060	0.037	0.096	0.071	0.056	0.051	0.509	0.429	0.009	0.008
144	Loma Pietra 2000	6	873	84.1	1.75	0.163	0.138	0.213	0.208	0.215	0.178	2.589	2.639	0.043	0.046
145	L'Aquila aftershock	5.6	830	5.3	1.75	0.133	0.164	0.345	0.276	0.395	0.588	1.508	1.476	0.041	0.050
146	Friuli 4th shock	5.9	901	10.0	1.75	0.226	0.179	0.749	0.466	0.552	0.309	3.304	2.582	0.062	0.053
147	Cosenza_1995	5.2	1906	2.4	1.75	0.231	0.325	0.340	0.729	0.463	0.494	1.868	1.729	0.079	0.071
148	Anza	5.2	725	14.2	1.75	0.460	0.429	1.097	1.044	0.759	0.767	8.300	7.467	0.145	0.124
149	Irpinia	6.9	997	28.3	1	0.096	0.083	0.153	0.139	0.199	0.144	5.509	5.089	0.042	0.036
150	Hector-Mine	7.1	726	26.5	1	0.337	0.266	0.483	0.679	0.980	0.677	7.657	5.229	0.171	0.089
151	South-Iceland	6.5	A*	5.3	1	0.320	0.345	0.712	1.096	0.749	1.014	4.325	4.448	0.155	0.143
152	South-Iceland	6.5	A*	13.2	1	0.126	0.159	0.383	0.563	0.418	0.340	1.523	1.725	0.056	0.059
153	Zarand	6.4	852	20.8	1	0.057	0.099	0.163	0.182	0.128	0.233	1.316	1.590	0.018	0.041
154	Olfus	6.3	A*	9.3	1	0.542	0.335	0.885	0.479	0.749	0.503	3.845	2.655	0.181	0.124
155	Olfus	6.3	A*	9.3	1	0.671	0.477	1.167	0.919	0.892	0.721	5.223	3.756	0.131	0.134
156	Olfus	6.3	A*	9.3	1	0.132	0.106	0.143	0.167	0.203	0.171	1.333	1.618	0.045	0.040
157	L'Aquila-aftershock	5.6	717	9.4	1	0.082	0.090	0.203	0.171	0.170	0.150	1.417	1.223	0.033	0.025
158	Christchurch	6	A*	17.5	1	0.119	0.100	0.418	0.232	0.329	0.154	1.216	1.239	0.047	0.034
159	Meinong	6.4	A*	18.5	1	0.195	0.199	0.341	0.379	0.399	0.456	1.895	2.353	0.088	0.097
160	Norcia	6.5	A*	18.6	1	0.434	0.392	0.923	1.208	1.335	1.239	5.946	5.916	0.181	0.160
161	Norcia	6.5	A*	19.2	1	0.189	0.189	0.428	0.444	0.493	0.502	4.607	4.685	0.064	0.074
162	Norcia	6.5	A*	26.0	1	0.133	0.117	0.326	0.275	0.446	0.297	2.259	1.929	0.047	0.042
163	Norcia	6.5	A*	10.5	1	0.279	0.278	0.522	0.544	0.493	0.527	4.433	4.256	0.106	0.089

164	Norcia	6.5	A*	20.1	1	0.075	0.089	0.123	0.140	0.106	0.080	1.758	1.780	0.016	0.017
165	South-Iceland	6.5	A*	5.3	1	0.472	0.414	1.256	1.203	1.262	1.201	6.328	5.297	0.230	0.193
166	L'Aquila-mainshock	6.3	717	5.7	1	0.631	0.598	1.668	1.659	1.456	1.449	11.099	10.309	0.257	0.242
167	Norcia	6.5	A*	12.0	1	0.614	0.568	1.347	1.516	1.462	1.460	8.051	8.525	0.227	0.267
168	Irpinia	6.9	997	28.3	1	0.083	0.096	0.125	0.133	0.174	0.164	5.089	5.509	0.036	0.042
169	Hector-Mine	7.1	726	26.5	1	0.266	0.337	0.695	0.606	0.755	0.687	5.229	7.657	0.089	0.171
170	South-Iceland	6.5	A*	5.3	1	0.345	0.320	1.260	0.645	1.148	0.849	4.448	4.325	0.143	0.155
171	South-Iceland	6.5	A*	13.2	1	0.159	0.126	0.576	0.363	0.433	0.501	1.725	1.523	0.059	0.056
172	Zarand	6.4	852	20.8	1	0.099	0.057	0.198	0.166	0.155	0.096	1.590	1.316	0.041	0.018
173	Olfus	6.3	A*	9.3	1	0.335	0.542	0.470	0.820	0.476	0.645	2.655	3.845	0.124	0.181
174	Olfus	6.3	A*	9.3	1	0.477	0.671	0.901	1.393	0.805	0.770	3.756	5.223	0.134	0.131
175	Olfus	6.3	A*	9.3	1	0.106	0.132	0.189	0.166	0.243	0.215	1.618	1.333	0.040	0.045
176	L'Aquila-aftershock	5.6	717	9.4	1	0.090	0.082	0.178	0.235	0.130	0.209	1.223	1.417	0.025	0.033
177	Christchurch	6	A*	17.5	1	0.100	0.119	0.219	0.214	0.339	0.234	1.239	1.216	0.034	0.047
178	Meinong	6.4	A*	18.5	1	0.199	0.195	0.390	0.339	0.408	0.458	2.353	1.895	0.097	0.088
179	Norcia	6.5	A*	18.6	1	0.392	0.434	1.193	1.306	1.192	1.425	5.916	5.946	0.160	0.181
180	Norcia	6.5	A*	19.2	1	0.189	0.189	0.592	0.432	0.392	0.626	4.685	4.607	0.074	0.064
181	Norcia	6.5	A*	26.0	1	0.117	0.133	0.276	0.339	0.303	0.328	1.929	2.259	0.042	0.047
182	Norcia	6.5	A*	10.5	1	0.278	0.279	0.554	0.588	0.591	0.441	4.256	4.433	0.089	0.106
183	Norcia	6.5	A*	20.1	1	0.089	0.075	0.181	0.148	0.100	0.072	1.780	1.758	0.017	0.016
184	South-Iceland	6.5	A*	5.3	1	0.414	0.472	1.276	1.248	1.309	1.343	5.297	6.328	0.193	0.230
185	L'Aquila-mainshock	6.3	717	5.7	1	0.598	0.631	1.815	1.535	1.257	1.513	10.309	11.099	0.242	0.257
186	Norcia	6.5	A*	12.0	1	0.568	0.614	1.755	1.741	1.380	1.324	8.525	8.051	0.267	0.227
187	Duzce	7.1	719	15.6	1.25	0.130	0.092	0.234	0.196	0.203	0.270	2.532	1.989	0.038	0.029
188	Southern Italy 1995	5.2	865	27.8	1.5	0.172	0.167	0.216	0.122	0.315	0.101	0.951	0.976	0.023	0.016
189	Balkan_1979	6.9	A*	19.7	0.8	0.171	0.141	0.277	0.507	0.317	0.392	4.138	3.969	0.070	0.079
190	Southern Iwate Prefecture	6.9	744	23.1	0.8	0.240	0.178	0.657	0.406	0.519	0.428	6.314	6.628	0.075	0.082
191	Kobe_1995	6.9	1043	25.4	1.5	0.414	0.467	0.678	0.604	0.605	0.755	7.498	6.365	0.142	0.183
192	Tottori_2000	6.3	650	107.0	1.5	0.084	0.108	0.124	0.147	0.075	0.072	2.429	1.954	0.008	0.016
193	Taiwan_1999	6.2	804	44.7	1.5	0.265	0.228	0.791	0.449	0.663	0.603	6.129	5.809	0.131	0.094
194	W Tottori Prefecture	6.6	929	24.6	1.25	0.161	0.232	0.231	0.323	0.140	0.296	5.077	4.298	0.025	0.052
195	Northridge	6.7	715	14.7	1.5	0.433	0.348	1.039	1.266	1.394	0.825	7.164	6.980	0.181	0.173
196	L'Aquila mainshock	6.3	717	5.7	1.2	0.396	0.424	1.232	0.778	0.556	0.787	6.272	7.131	0.114	0.134
197	Centro_Italia_2016	6	687	15.3	1.5	0.539	0.560	1.275	1.840	2.550	1.753	6.237	5.358	0.204	0.174
198	Taiwan_1999	6.2	804	44.7	1.2	0.212	0.183	0.633	0.359	0.530	0.482	4.904	4.647	0.104	0.075
199	W Tottori Prefecture	6.6	929	24.6	1.5	0.194	0.279	0.277	0.388	0.167	0.355	6.092	5.158	0.030	0.063
200	L'Aquila aftershock	5.1	717	5.5	1.75	0.087	0.141	0.164	0.138	0.121	0.128	1.001	1.187	0.019	0.021
201	Parkfield_2004	6	906	9.3	0.8	0.196	0.157	0.341	0.261	0.379	0.215	1.376	1.529	0.061	0.059
202	Aquila_2009	6.3	705	1.8	0.8	0.264	0.283	0.822	0.519	0.371	0.525	4.595	5.108	0.076	0.089
203	Manjil_1990	7.4	723	21.8	0.8	0.412	0.398	1.568	1.184	1.084	0.966	13.812	20.120	0.168	0.174
204	L'Aquila aftershock	5.3	717	13.1	1.5	0.033	0.036	0.060	0.075	0.078	0.084	0.533	0.631	0.010	0.012
205	L'Aquila aftershock	5	830	5.3	1.5	0.057	0.047	0.174	0.130	0.123	0.054	0.495	0.500	0.011	0.010
206	Gran Sasso	5.1	717	12.2	1.5	0.052	0.062	0.086	0.090	0.114	0.115	0.706	0.967	0.012	0.020
207	L'Aquila aftershock	5.1	717	5.5	1.6	0.080	0.129	0.150	0.126	0.111	0.117	0.915	1.086	0.017	0.019
208	Loma Pietra 2000	6	873	84.1	1.5	0.118	0.139	0.231	0.213	0.235	0.292	2.262	2.220	0.039	0.037
209	L'Aquila aftershock	5.6	830	5.3	1.25	0.117	0.095	0.291	0.166	0.344	0.182	1.054	1.077	0.036	0.029
210	Friuli 4th shock	5.9	901	10.0	1.5	0.153	0.194	0.656	0.528	0.268	0.371	2.213	2.832	0.045	0.053
211	Cosenza_1995	5.2	1906	2.4	1.5	0.279	0.198	0.390	0.282	0.517	0.554	1.482	1.601	0.061	0.068
212	Parkfield_2004	6	906	9.3	0.9	0.221	0.176	0.384	0.294	0.426	0.242	1.548	1.721	0.068	0.066
213	Anza	5.2	725	14.2	1.5	0.417	0.473	1.068	0.785	1.156	0.566	1.363	1.305	0.097	0.069

214	Aquila_2009	6.3	705	1.8	1.3	0.429	0.460	1.335	0.843	0.602	0.853	7.467	8.300	0.124	0.145
215	Manjil_1990	7.4	723	21.8	1.1	0.566	0.547	2.156	1.627	1.490	1.329	18.992	27.665	0.231	0.239
216	Duzce	7.1	719	15.6	1.25	0.092	0.130	0.154	0.292	0.178	0.241	1.989	2.532	0.029	0.038
217	Southern Italy 1995	5.2	865	27.8	1.5	0.167	0.172	0.214	0.215	0.107	0.208	0.976	0.951	0.016	0.023
218	Balkan_1979	6.9	A*	19.7	0.8	0.141	0.171	0.439	0.313	0.340	0.399	3.969	4.138	0.079	0.070
219	Southern Iwate Prefecture	6.9	744	23.1	0.8	0.178	0.240	0.395	0.557	0.552	0.359	6.628	6.314	0.082	0.075
220	Kobe_1995	6.9	1043	25.4	1.5	0.467	0.414	0.961	0.586	0.602	0.903	6.365	7.498	0.183	0.142
221	Tottori_2000	6.3	650	107.0	1.5	0.108	0.084	0.158	0.112	0.074	0.062	1.954	2.429	0.016	0.008
222	Taiwan_1999	6.2	804	44.7	1.5	0.228	0.265	0.555	0.759	0.488	0.896	5.809	6.129	0.094	0.131
223	W Tottori Prefecture	6.6	929	24.6	1.25	0.232	0.161	0.368	0.196	0.196	0.109	4.298	5.077	0.052	0.025
224	Northridge	6.7	715	14.7	1.5	0.348	0.433	1.211	1.644	1.342	1.640	6.980	7.164	0.173	0.181
225	L'Aquila mainshock	6.3	717	5.7	1.2	0.424	0.396	1.012	0.964	0.700	0.708	7.131	6.272	0.134	0.114
226	Centro_Italia_2016	6	687	15.3	1.5	0.560	0.539	1.718	1.724	2.409	1.950	5.358	6.237	0.174	0.204
227	Taiwan_1999	6.2	804	44.7	1.2	0.183	0.212	0.444	0.608	0.391	0.717	4.647	4.904	0.075	0.104
228	W Tottori Prefecture	6.6	929	24.6	1.5	0.279	0.194	0.442	0.235	0.235	0.131	5.158	6.092	0.063	0.030
229	L'Aquila aftershock	5.1	717	5.5	1.75	0.141	0.087	0.224	0.166	0.131	0.118	1.187	1.001	0.021	0.019
230	Parkfield_2004	6	906	9.3	0.8	0.157	0.196	0.261	0.317	0.262	0.445	1.529	1.376	0.059	0.061
231	Aquila_2009	6.3	705	1.8	0.8	0.283	0.264	0.675	0.643	0.467	0.472	5.108	4.595	0.089	0.076
232	Manjil_1990	7.4	723	21.8	0.8	0.398	0.412	1.225	1.570	1.102	0.971	20.120	13.812	0.174	0.168
233	L'Aquila aftershock	5.3	717	13.1	1.5	0.036	0.033	0.079	0.078	0.070	0.061	0.631	0.533	0.012	0.010
234	L'Aquila aftershock	5	830	5.3	1.5	0.047	0.057	0.118	0.142	0.080	0.059	0.500	0.495	0.010	0.011
235	Gran Sasso	5.1	717	12.2	1.5	0.062	0.052	0.106	0.079	0.092	0.059	0.967	0.706	0.020	0.012
236	L'Aquila aftershock	5.1	717	5.5	1.6	0.129	0.080	0.205	0.152	0.119	0.108	1.086	0.915	0.019	0.017
237	Loma Pietra 2000	6	873	84.1	1.5	0.139	0.118	0.182	0.178	0.185	0.153	2.220	2.262	0.037	0.039
238	L'Aquila aftershock	5.6	830	5.3	1.25	0.095	0.117	0.247	0.197	0.282	0.420	1.077	1.054	0.029	0.036
239	Friuli 4th shock	5.9	901	10.0	1.5	0.194	0.153	0.642	0.399	0.473	0.265	2.832	2.213	0.053	0.045
240	Cosenza_1995	5.2	1906	2.4	1.5	0.198	0.279	0.292	0.625	0.397	0.423	1.601	1.482	0.068	0.061
241	Parkfield_2004	6	906	9.3	0.9	0.176	0.221	0.294	0.356	0.295	0.501	1.721	1.548	0.066	0.068
242	Anza	5.2	725	14.2	1.5	0.473	0.417	0.966	1.170	0.673	0.877	1.305	1.363	0.069	0.097
243	Aquila_2009	6.3	705	1.8	1.3	0.460	0.429	1.097	1.044	0.759	0.767	8.300	7.467	0.145	0.124
244	Manjil_1990	7.4	723	21.8	1.1	0.547	0.566	1.684	2.158	1.516	1.336	27.665	18.992	0.239	0.231
245	South-Iceland	6.5	A*	5.3	1.3	0.416	0.449	0.926	1.424	0.974	1.318	5.623	5.782	0.201	0.186
246	South-Iceland	6.5	A*	13.2	1.75	0.221	0.278	0.669	0.986	0.731	0.595	2.665	3.018	0.098	0.104
247	Olfus	6.3	A*	9.3	1.3	0.704	0.436	1.151	0.623	0.973	0.654	4.999	3.452	0.235	0.161
248	Olfus	6.3	A*	9.3	1.3	0.872	0.620	1.517	1.195	1.160	0.938	6.790	4.882	0.171	0.174
249	Meinong	6.4	A*	18.5	1.3	0.564	0.510	1.200	1.571	1.735	1.611	7.730	7.691	0.235	0.208
250	Norcia	6.5	A*	18.6	1.75	0.331	0.330	0.749	0.776	0.862	0.879	8.062	8.198	0.113	0.129
251	Norcia	6.5	A*	19.2	1.75	0.233	0.204	0.570	0.482	0.780	0.520	3.953	3.376	0.083	0.073
252	Norcia	6.5	A*	26.0	1.3	0.363	0.361	0.678	0.708	0.641	0.685	5.763	5.533	0.138	0.116
253	South-Iceland	6.5	A*	5.3	0.75	0.240	0.259	0.534	0.822	0.562	0.761	3.244	3.336	0.116	0.107
254	South-Iceland	6.5	A*	13.2	1.5	0.189	0.238	0.574	0.845	0.627	0.510	2.285	2.587	0.084	0.089
255	Olfus	6.3	A*	9.3	0.75	0.406	0.251	0.664	0.359	0.561	0.377	2.884	1.991	0.136	0.093
256	Olfus	6.3	A*	9.3	0.75	0.503	0.358	0.875	0.689	0.669	0.541	3.918	2.817	0.098	0.101
257	Meinong	6.4	A*	18.5	0.9	0.391	0.353	0.831	1.087	1.201	1.115	5.351	5.325	0.163	0.144
258	Norcia	6.5	A*	18.6	1.3	0.246	0.245	0.556	0.577	0.641	0.653	5.989	6.090	0.084	0.096
259	South-Iceland	6.5	A*	5.3	1.3	0.449	0.416	1.638	0.838	1.493	1.103	5.782	5.623	0.186	0.201
260	South-Iceland	6.5	A*	13.2	1.75	0.278	0.221	1.008	0.634	0.758	0.876	3.018	2.665	0.104	0.098
261	Olfus	6.3	A*	9.3	1.3	0.436	0.704	0.611	1.066	0.619	0.838	3.452	4.999	0.161	0.235
262	Olfus	6.3	A*	9.3	1.3	0.620	0.872	1.172	1.811	1.047	1.001	4.882	6.790	0.174	0.171
263	Meinong	6.4	A*	18.5	1.3	0.510	0.564	1.551	1.698	1.550	1.852	7.691	7.730	0.208	0.235

264	Norcia	6.5	A*	18.6	1.75	0.330	0.331	1.036	0.755	0.686	1.095	8.198	8.062	0.129	0.113
265	Norcia	6.5	A*	19.2	1.75	0.204	0.233	0.484	0.594	0.531	0.574	3.376	3.953	0.073	0.083
266	Norcia	6.5	A*	26.0	1.3	0.361	0.363	0.721	0.764	0.768	0.573	5.533	5.763	0.116	0.138
267	South-Iceland	6.5	A*	5.3	0.75	0.259	0.240	0.945	0.484	0.861	0.636	3.336	3.244	0.107	0.116
268	South-Iceland	6.5	A*	13.2	1.5	0.238	0.189	0.864	0.544	0.649	0.751	2.587	2.285	0.089	0.084
269	Olfus	6.3	A*	9.3	0.75	0.251	0.406	0.353	0.615	0.357	0.484	1.991	2.884	0.093	0.136
270	Olfus	6.3	A*	9.3	0.75	0.358	0.503	0.676	1.045	0.604	0.577	2.817	3.918	0.101	0.098
271	Meinong	6.4	A*	18.5	0.9	0.353	0.391	1.074	1.176	1.073	1.282	5.325	5.351	0.144	0.163
272	Norcia	6.5	A*	18.6	1.3	0.245	0.246	0.770	0.561	0.510	0.813	6.090	5.989	0.096	0.084

CHAPTER 4

Development of fragility curves for the building stock located in the Visso's historical centre

Summary:

Chapter §4 focuses on the response of (4.1) the school model ideally founded on different subsoil profiles and (4.2) different structural configurations isolated or in aggregate. Their contents were respectively published in Brunelli et al. (2021b) and Angiolilli et al. (2022a) (paper under review).

With the final aim to generate fragility curves appliable at urban scale, this chapter was intended to be an intermediate stage of the research investigating if and how site and SFS interaction effects modifies the seismic vulnerability of structures with respect to the typical building-on-rock assumption, when soft subsoil with different nonlinear response (fine vs coarse grained) or masonry structures with different mass, stiffness and "lateral constraints" are considered. The analysed cases were partially inferred from the typical structural typologies and soil profile of Visso, whose calibration for subsoil is reported in Annex A.4.1a. The fragility curves accounting for site effects through seismic response analyses (as detailed in previous chapters) were compared with those derived by applying to the structural model input motions recorded on seismic stations located on soft soil in Annex A.4.1b, revealing a successful match only at low damage levels.

To extend the research also to other URM buildings, other archetypes inspired by the buildings of municipality of Visso were selected. In particular, the historical center is characterized by 85% of masonry buildings, almost of which (93%) are in aggregate. This is a typical feature of the majority of small historical centres both in Italy and Europe. Moreover, the studies available in the literature specifically addressed to investigate their response are very few and the seismic assessment of building in aggregate still represents an open issue. Thus, all these considerations motivated to addressing the research on this typology. Two aggregates were selected.

The validation of the numerical model with and without SFS interaction of one of this aggregate is illustrated in the Annex A.4.2a (Brunelli et al. (2022c)). The numerical model is considered on his real subsoil, which is representative of the soil below the historical center in Visso. The valley effects is also investigated in this Annex, by simulating a 2D subsoil model in collaboration with the research group of University Federico II of Naples. The results showed that in the area of Visso's school there is no variation of 1D results considering the valley effect. This confirms the reliability of results obtained in the previous chapters. Conversely, in the historical centre where the aggregate is located, the valley effect reduces the seismic input. Only considering the valley effect, the comparison between observed and simulated damage was satisfactory.

Section 4.2., that refers to Angiolilli et al. (2022a). focuses on the modelling criteria adopted to simulate the specific key-features of building in aggregate, namely: the interaction effects between adjacent units, including the pounding; the interaction between in-plane response and out-of-plane mechanisms. Obviously, according to the main goal of the research, analyses are carried out both at bedrock and considering site amplification. Various out-of-plane mechanisms (one or two-floor cantilever mechanism of the façade and the overturning of the tympanum (or gable mechanism) are then considered. A specific comparison is given by analysing each structural unit also s isolated in order to assess the effect provided by the restraint of adjacent units. For the examined buildings, the latter effect revealed beneficial.

In Annex A.4.2b, a further aggregate building is considered. While the aggregate presented in chapter §4.2 is characterized by units of 3 or 4 storeys, the additional present units of 2 and 3 storeys. Also

in this case the comparison between the simulated and real damage is reported, highlighting once again as the model with SFS interaction better simulates the real response. In addition, the results obtained in terms of fragility curves varying the soil profile under the aggregate are here reported.

CHAPTER 4.1

Influence of different soil profiles

published in *VIII COMPDYN 28-30 June 2021*, Athens, Greece.
DOI: 10.7712/120121.8732.18903

ON THE SITE-AMPLIFICATION AND SOIL-STRUCTURE INTERACTION IN URM STRUCTURES: USE OF FRAGILITY CURVES TO ASSESS THE SIMPLIFIED CODE-APPROACH

Andrea Brunelli[1], Filomena de Silva[2], Serena Cattari[1]
[1] University of Genoa, Genoa, Italy
andrea.brunelli@edu.unige.it, serena.cattari@unige.it

[2] University of Naples Federico II, Naples, Italy
filomena.desilva@unina.it

Abstract:

The paper investigates the effects of site-amplification and soil-foundation-structure interaction (SFS) on the fragility curves of a real unreinforced masonry (URM) structure. The building is inspired to a school with an irregular T-shape plan and is modelled according to the equivalent frame approach. The structure was ideally placed on a stiff rock outcrop (case FB A) or settled on four different soft soil profiles, including its real foundation subsoil. In the latter cases the base of the structural model was assumed as fixed (FB C) or endowed with springs (CB C) simulating the soil-foundation dynamic impedance. To evaluate the fragility curves, the corresponding structural models were analysed through non-linear dynamic analyses under 136 input motions, propagated in 1D soil models reproducing the selected profiles for FB C and CB C. The results were compared in the paper in terms of:

- *fragility curves calculated for five damage levels (defined to be conceptually consistent with those of the EMS98 scale) and expressed as a function of different intensity measures of the input motion;*
- *average damage derived as a weighted average of the probability of failure associated to all the damage levels.*

The comparison among the results of the different models highlights the expected increase of damage due to site effects and a beneficial effect of soil-structure interaction, mainly due to the increment of damping associated to the additional energy dissipated by the soil-foundation system. Finally, the average damage of FB C and CB C models were compared with those obtained from the fragility curves of a fixed base system in which site effects are considered through the conventional coefficients proposed in Codes (e.g. by the Eurocode 8), that neglect SFS. This latter approach is that followed in the current practice. The comparison demonstrates that the Code-based approach underestimates the fragility especially at high damage levels.

Keywords: seismic site amplification, soil-structure interaction, fragility curves, unreinforced masonry structures, nonlinear dynamic analyses, code prevision.

1. INTRODUCTION

Various reconnaissance studies after seismic events(see Sextos et al. (2018); Sorrentino et al. (2019); Stewart et al. (2018)) as well as more specific studies at scale of whole historical centres (D'Amico and Mucciarelli (2002); Chieffo and Formisano (2020); Brando et al. (2020)) testified as the site-amplification effects (either associated to topographic and soil stratigraphic effects) may play a relevant role, together with their vulnerability, in determining the resulting damage levels on existing unreinforced (URM) masonry. The microzonation studies, developed in various area in Italy after the recent seismic events (e.g. Pagliaroli et al. (2019); Lanzo et al. (2011)) that hit the country, confirmed this potential risk factor.

Together with this evidence at large scale or on huge building stocks, studies based on detailed models of prototype buildings and more refined analyses methods turn out very useful to understand the phenomenon and also deepen the potential effect of the soil-foundation-structure interaction (SFS). In Khosravikia et al. (2018) the topic is treated in a parametric way to attempt in providing a general overview of such effects on various structural typologies (classifiable according to their dynamic behaviour as "stiff" or "flexible") concluding how the SFS may produce either beneficial or detrimental effects. The literature works specifically addressed to URM buildings are still very few, and usually focused to slender structures, like as towers or minarets (e.g. Casolo et al. (2017); de Silva (2020); Bayraktar and Hokelekli (2020)), or massive monumental assets, like as fortresses (e.g. Karatzetzou et al. (2015); Fathi et al. (2020)). A recent very interesting case, that testified the possible role of SFS also on ordinary URM buildings, is constituted by the "Pietro Capuzi" school in Visso (MC, Italy). Being monitored as a strategic building by the Italian Seismic Observatory of Structures (Dolce et al. (2017)), the school response under the three mainshocks of the 2016-2017 Central Italy earthquake was recorded through numerous accelerometers installed in the building as well as the damage after each event was detected through on-site inspections. Although nowadays the school has been demolished due to the very severe damage occurred, all the precious data collected were very useful to validate numerical models and assess the role played by SFS phenomena in the seismic response of the school, like by Ferrero et al. (2020) and Brunelli et al. (2021a).

In particular, in Brunelli et al. (2021a) a compliant-base model has been successfully validated based on these data. This model, that works according to the equivalent frame modelling approach, is the one adopted also for the further developments presented in this paper, which focuses to both the site-amplification due to soil stratigraphic effects and the role played by SFS.

More specifically, the numerical strategy validated in Brunelli et al. (2021a) upon implementing real recordings from the 2016-2017 Central Italy earthquake has been replicated by executing a huge set of nonlinear dynamic analyses (NLDA) with the final aim of developing fragility curves, similarly to what done for example by Chieffo and Formisano (2020), Cavalieri et al. (2020) or Peduto et al. (2019). The model (briefly recalled at §2.3) has been analysed both as fixed at the base (FB) and endowed with springs (CB) simulating the soil-foundation dynamic impedance. NLDA have been performed according to the Cloud Method (see e.g. Jalayer et al. (2017)) with a selection of records extracted from the SIMBAD database in Smerzini and Paolucci (2013) and Iervolino et al. (2014) to be representative of real events recorded on stiff rock outcrop. Then, they have been propagated by considering four different soft soil profiles (§2.1) representative of a class soil C (according to classification adopted in NTC (2018) and CEN (2004)), including the real foundation subsoil of the school (§2.2). Fragility curves are defined assuming a log-normal distribution. The structural response from NLDA is interpreted according to a multiscale approach briefly described at §2, that allows to attribute to each records a damage level, defined to be conceptually consistent with those of the EMS98 scale (Grünthal (1998)). Moreover, different intensity measures of the input motion have been considered in order to assess the sensitivity to the dispersion in the definition of the fragility

curves (§3.1), namely the Peak Ground Acceleration (PGA) and the Spectral Acceleration corresponding to the fundamental period of the structure ($Sa(T_1)$).

Finally, the average damage of FB C and CB C models were compared with those obtained from the fragility curves of a fixed base system in which site effects are considered in a simplified way through the conventional coefficients proposed in Codes (e.g. by the Eurocode 8 (CEN (2004))), that neglect SFS (§3.2). This latter approach is that followed in the current practice. The comparison aims to assess if the current Code-based approach is on the safe side or not, also varying the expected damage level (i.e. the nonlinear phase attained by the structure).

2. METHOD OF ANALYSIS

As introduced at §1, in this study fragility curves of a URM building endowed with shallow foundations were calculated accounting for both the amplification of the ground motion due to site effects and the dynamic SFS interaction. Due to the low foundation embedment, the foundation input motion is expected to be equal to the free field motion, hence the latter was calculated through linear-equivalent one-dimensional site response analyses performed on four soil profiles. The resulting ground motion (illustrated at §2.3) was then used as input motion to perform non-linear dynamic analyses on:

- a fixed base structural model (indicated as FB C in the following);
- a compliant base structural model in which the base of each main wall is equipped with springs (indicated as CB C in the following).

The rich and huge amount of data from each nonlinear dynamic analysis carried out are interpreted according to a multiscale approach with the final aim of interpreting the simulated structural response through a synthetic parameter consisting in the global damage level. The latter has been defined to be conceptually consistent with the five ones defined in the EMS98 scale (see Grünthal (1998)), that is (DLi, i=0…5): DL0 - none; DL1 - negligible; DL2 - moderate; DL3 - severe; DL4 - very severe to near collapse; DL5 - collapse. In particular, the adopted multiscale approach, similarly to what originally proposed in Lagomarsino and Cattari (2015a), combines two heuristic criteria:

- a first one that directly refers to the global response scale, by defining proper thresholds of the displacement capacity of the building on pushover curves estimated from nonlinear static analyses. These thresholds are defined in terms of proper fractions of the overall base shear (V_b): before the attainment of the maximum value ($V_{b,max}$) to define the DL1 (equal to 0.4 $V_{b,max}$) and DL2 (equal to 0.8 $V_{b,max}$); after the attainment of the maximum value, i.e. on the softening phase of the curve, to define the DL3 (corresponding to a residual capacity equal to 0.8 $V_{b,max}$), DL4 (corresponding to a residual capacity equal to 0.4 $V_{b,max}$) and DL5 (corresponding to a residual capacity equal to 0.2 $V_{b,max}$).
- a second, based on the evaluation of damage severity and diffusion on vertical walls, that aims to monitor the spread of damage on the building. To this aim, the cumulative rate of walls that reached a given DL (referring to a gradually increasing damage level) is computed. The attainment of the DL on a wall is checked in terms of the DL_{min} variable firstly introduced in Marino et al. (2019b). This variable replaces the adoption of interstorey drift thresholds at the wall scale and the proposal assigns a damage level to the wall based on the minimum damage level attained by all the elements of a certain floor. This allows overcoming the definition of conventional interstory drift thresholds, which are not suited to take into account the different damage mechanism exhibited by structural elements of different slenderness. A similar damage-assignment criterion has been recently pursued in Italian Structural Code (MIT (2019)). The thresholds assumed for the cumulative rate have been defined to be consistent with the description of the damage grades of buildings proposed by Grünthal (1998); they are described in more detail in Sivori (2021) and Cattari and Angiolilli (2022).

According to this procedure, results of records can be properly grouped as those associated to the same resulting global DL.

Then, fragility curves were computed by estimating the probability of exceeding, p_{DLi}, the different damage levels, DLi, given a level of ground shaking quantified through the intensity measure, IM. The p_{DLi} was computed from the lognormal distribution of *IM* causing the i^{th} DL and characterized by the median value IM_{mi} and the lognormal standard deviation σ:

$$p_{DLi}(DL > DLi|IM) = \Phi\left(\frac{\log IM|IM_{mi}}{\sigma}\right) \quad (4.1.1)$$

where Φ is the standard cumulative probability function.
Among possible intensity measures reported in Boomer et al. (2004), in this study, the peak ground acceleration, PGA, and the spectral acceleration, $Sa(T_1)$ referred to the bedrock input motion were used as IM. This choice is consistent with various studies on URM buildings (see Zucconi et al. (2020); Mouyiannou and Rota (2017); Cattari et al. (2018)). In particular, the geometrical mean of the PGA and the $Sa(T_1)$ associated to the predominant period along the X and Y directions of the numerical model was used. Since an elongation of the periods is expected for the compliant base models, the $Sa(T_1)$ of the CB C case differs from those of the FB C case, while the PGA is obviously the same for the two models.
On basis of this procedure, the fragility curves resulting from the FB C model account only for site effects, while those of the CB C model consider both the site and SFS effects. Both cases have been then compared with the fragility curves of the same structure ideally placed on a stiff rock outcrop. The latter were obtained by analyzing the behavior of the fixed-base model subjected to the input motions representative of the bedrock condition (namely the FB A case in the following).

2.1. Analysed soil profiles

To study the influence of the soil stiffness on the results of FB C and CB C cases, four soil profiles were selected. The criterion adopted for the selection is that based on an equivalent shear wave velocity up to the bedrock depth, V_{Seq}, falling in the range of class C (as defined by NTC (2018); CEN (2004)). The first profile (S1) is the actual soil below the "Pietro Capuzi" School of Visso, i.e. a sandy gravel layer (SG), covered and locally interbedded by clayey silt (CS) and silty clay (SC) lenses. The stiffness profile was measured through a MASW test (ReLUIS (2018c)) and several down-hole tests (MZS3 (2018)). The on-site measured free field frequency obtained from HVSR tests allowed the back-calculation of the bedrock depth equal to 40 m. The shear wave velocity, V_S, is variable with depth with an equivalent value up to the bedrock equal to 281m/s. Additional details on the geotechnical characterization of this soil profiles are reported in Brunelli et al. (2021a).

The second profile (S2) is representative of the soil profile in the historic centre of Visso (see Figure 4.1.1). Information on such soil profile were collected during the third level microzonation studies MZS3 (2018). The bedrock at a depth varies between 15-18 m and the profile in the centre of the valley is made of clayey silt for the first 4 m, overlaying a 11 m thick sandy gravel layer. In lack of direct measurements, V_S was obtained through correlations between Vs and the number of blows of SPT tests done in the borehole (B). In particular, three SPT tests were assumed as reference executed at a depth of 1.9 m in CS and 4.4 and 8.9 m in SG, respectively (see B6 and B4 in Figure 4.1.1).
These correlations were calibrated on subsoil profiles all around the world; hence their reliability for the subsoil of Visso was firstly checked against the outcomes of the Down-hole tests. To this aim, 40 correlations for coarse-grained soil and 50 correlations for fine-grained soil (the full list is in the Annex 4.1a) were applied to the number of blows of SPT tests executed in the sandy gravel in the borehole close to the school, identified as DH1 in Figure 4.1.1, as well as in the clayey silt in the shallowest zone of B11 and B12. The tests used in the calibration are in Figure 4.1.1 coloured in red instead the unused tests are in black.

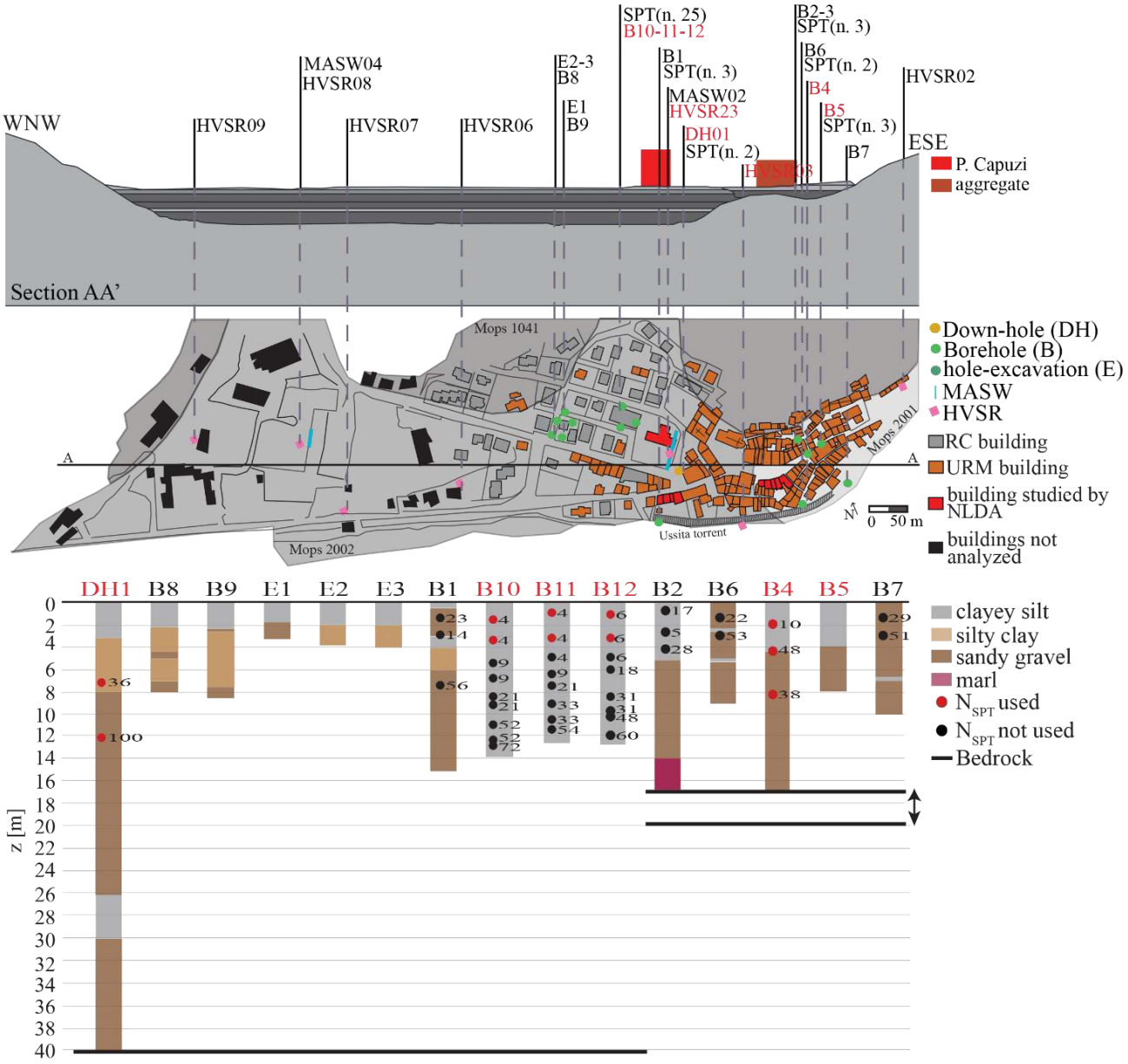

Figure 4.1.1. Tests carried out in Visso during the surveys carried out by MZS3 (2018).

Such validation is reported in Annex 4.1a. The most successful correlations in the validation were used to characterize S2. In particular, the correlations by Imai and Yoshimura (1970) and Lee (1992) were used for CS, leading to the same V_S=162 m/s, and by Ohta and Goto (1978) for SG, leading to V_S=337 m/s. The consequent equivalent V_S up to the bedrock depth is V_{Seq}= 272 m/s. Finally, two other ideal clay (S3) and gravel (S4) profiles were considered, these are calibrated to have the Vs_{eq} closed to the first two soil profiles. This is useful for studying the variation in response with soils with similar Vs_{eq} but different stratigraphies. Soil S3 and S4 is calibrated with the bedrock placed at a depth of 40 m. In both cases Vs increases with depth. Its profile was calculated through the empirical laws by d'Onofrio and Silvestri (2001) for S3 and by Hardin and Kalinski (2005) for S4, respectively. The resulting Vs_{eq} are 200 and 279 m/s, which are similar, as wanted, to those of S1 and S2.
Figure 4.1.2a summarizes the four soil and V_S profiles while Figure 4.1.2b reports their amplification functions (FA). The latter have been calculated through a linear site response analysis performed by using the STRATA software (Kottke and Rathje (2008)). An initial damping of 5% is assumed in this analysis. As highlighted by the resulting natural frequencies, there is a significant variety among the

responses of the different soil profiles.

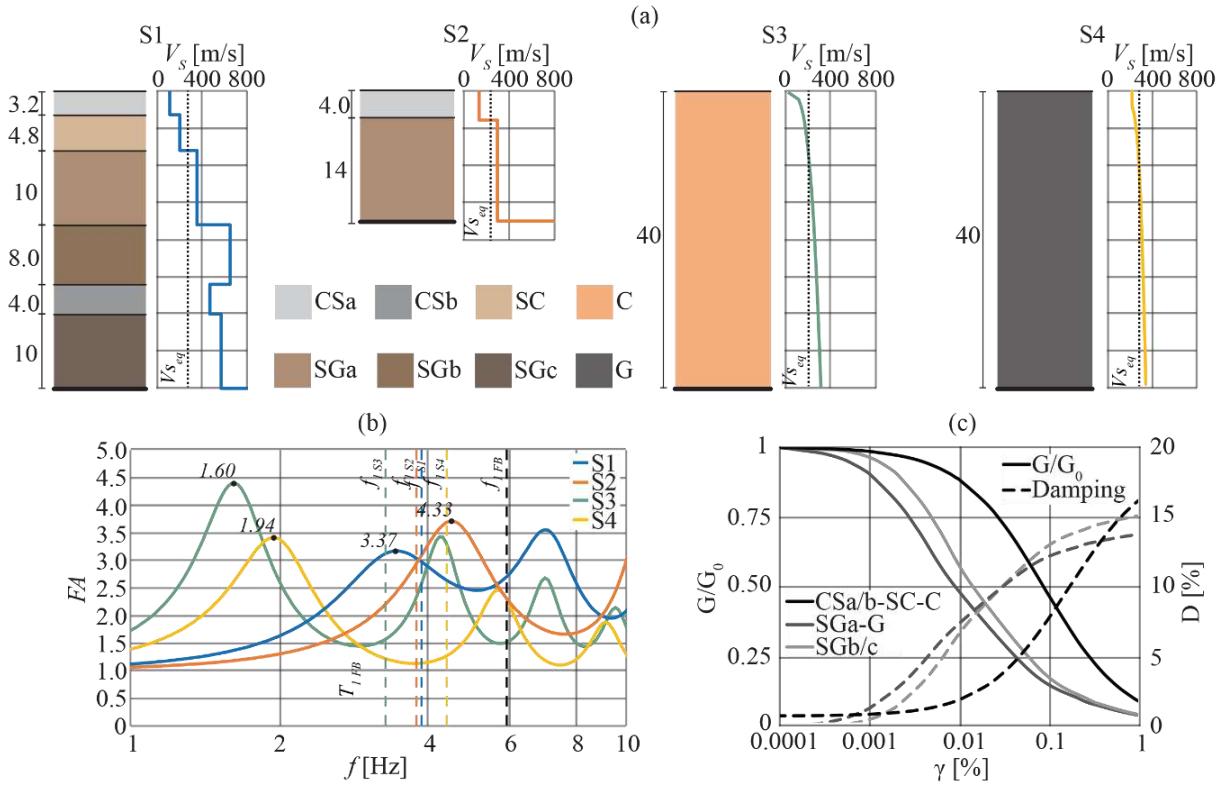

Figure 4.1.2. (a) layer with profile Vs; (b) FA of the four soil profiles and (c) decay curves of the soils considered.

Finally, Figure 4.1.2c shows the variation of the normalized shear modulus (G/G_0) and the damping ratio (D) with the shear strain (γ) adopted in the linear equivalent site response analyses executed with the records of real earthquakes and performed again in the STRATA software. The curves adopted for the fine-grained soils ((CS, SC)) in S1, S2 and S3 were obtained based on a comprehensive model calibrated by ReLUIS (2018c) and Ciancimino et al. (2019) on the results of laboratory tests on comparable materials. The G/G_0-γ curves obtained by Liao et al. (2013), through laboratory tests on silty sandy gravel samples different confining stress were associated to the sandy gravel soil in S1, S2 and S4. The corresponding D-γ curves were calculated by applying the model by Ramber and Osgood (1943) and the Masing criteria (Masing (1926)) to the G/G_0-γ curves.

2.2. Results of site response analyses under records of real earthquakes

Figure 4.1.3 shows the acceleration time histories of the input motions employed to analyse the site effects in the four soil profiles described in §2.1. They were chosen from the Selected Input Motions for Displacement-Based Assessment and Design (SIMBAD) database (Smerzini and Paolucci (2013); Iervolino et al. (2014)).

The selection includes the EW (Channel 1 (C1)) and NS (Channel 2 (C2)) components of accelerations recorded during 49 natural events at stations located on stiff rock outcrop, *i.e.* Vs_{30} greater than 700 m/s. Some selected signals were slightly scaled to achieve the desired variability of the intensity measures to be used in the construction of the fragility curves of the FB A.

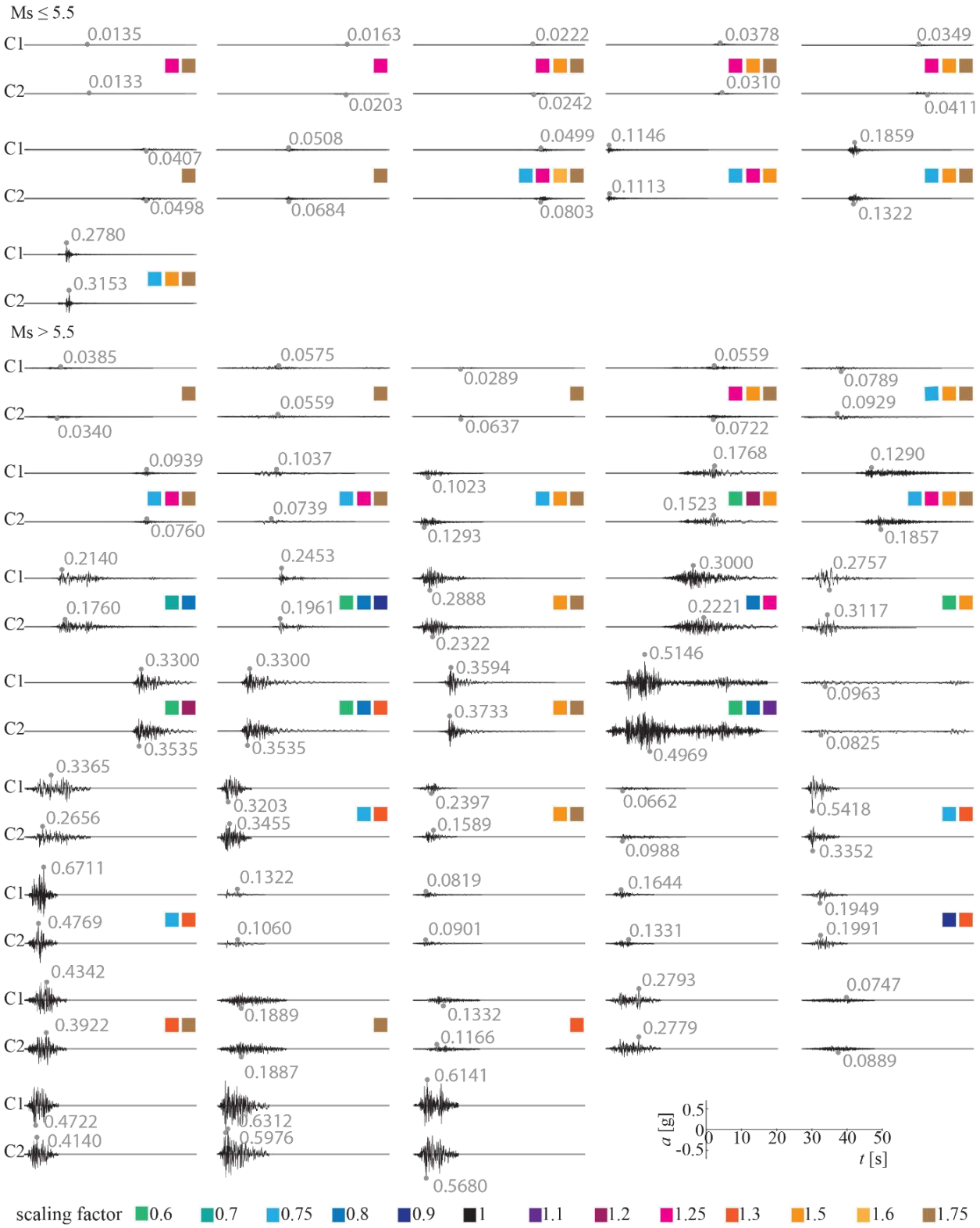

Figure 4.1.3. Time histories of the acceleration of the selected input motions.

Colours in Figure 4.1.3 indicate the scaling factors, when multiple colours are present, the same input motion was scaled more than once.

Figure 4.1.4 shows the mobilized G/G_0 (a) and hysteretic damping ratio (b) calculated in the four considered soil profiles through site response analyses under each event. The mean values mobilized in the soil volume, expected to be affect by the foundation motion (i.e. 1 m under foundation level)

are reported. As expected, the highest effects of nonlinearity are recognized: for the profile S3, characterized by the lowest initial stiffness; and the gravel soil profile S4, characterized by the earliest development of stiffness reduction (see Figure 4.1.2c). Conversely the lowest nonlinearity corresponds to the shallowest bedrock producing the highest natural frequency, *i.e.* the stiffest response (see Figure 4.1.2b). The actual soil profile, S1, at the school site shows an intermediate behaviour.

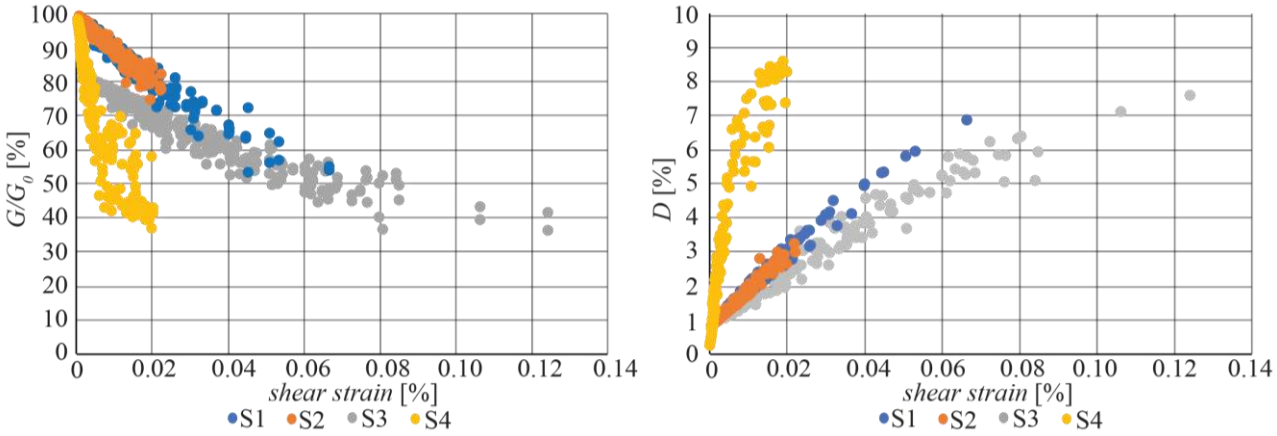

Figure 4.1.4. (a) G/G_0 and (b)hysteretic damping ratio mobilized in the four soil profiles in significant volume during each site response analysis.

Figure 4.1.5 groups the analyses according to different ranges of $Sa(T_1)$ of the free field motion resulting from the site response analyses and corresponding to the fixed-base period. The latter are reported in Table 4.1.1 together with the period of the CB models on the different soil profile, revealing that the different initial shear stiffness of the soil profiles significantly affects the CB C period.

Table 4.1.1: first period of each model.

Model	FB	CB -S1	CB -S2	CB -S3	CB -S4
T_1 [s]	0.1740	0.2580	0.2640	0.3050	0.2298

The comparison among the number of signals belonging to each group, reported in red on the top of Figure 4.1.5, shows that $Sa(T_1)$ values on surface of profile S4 are lower than 1.5 g and mainly concentrated in the lowest amplitude ranges. The ranges associated with the highest $Sa(T_1)$ are populated mainly by signals propagated in S1 and S3, highlighting that such profiles are more hazardous for the structural safety.
In the same Figure 4.1.5 the number of times in which $Sa(T_1)$ of the CB models exceeds that of the FB ones is reported in percentage on the Y-axis. Except for S2 showing a more irregular trend, such percentage increases with increasing $Sa(T_1)$ and is predominant (i.e. >50%) from $Sa(T_1)$>0.75 g. Hence, a detrimental effect of SFS interaction is shown on the seismic actions affecting the structure especially under the most severe input motions.

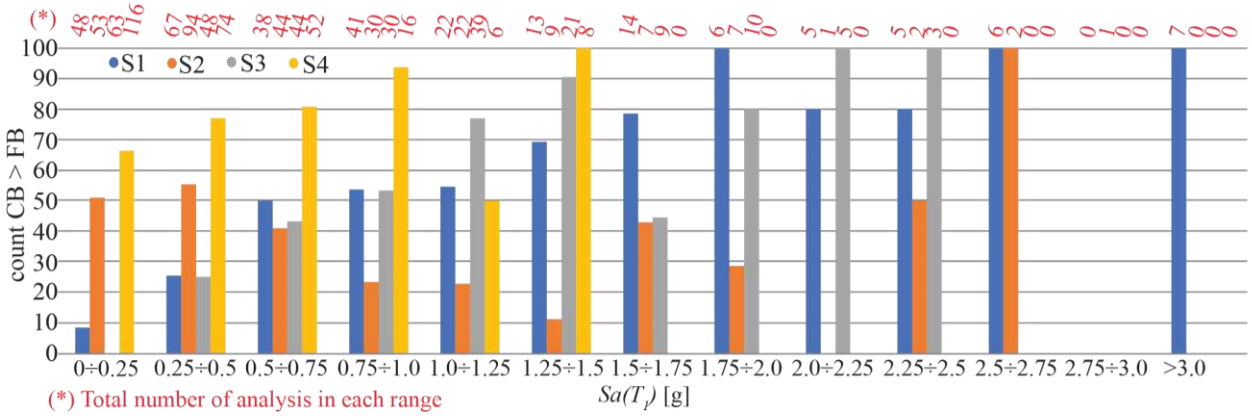

Figure 4.1.5. number of times in which Sa (T_1) of the CB model exceeds that of the FB.

2.3. Numerical model of the selected URM building

The 3D model of Visso school (Figure 4.1.6a) adopted for the execution of NLDA works according to the equivalent frame approach. It has been realized with the Tremuri software package (Lagomarsino et al. (2013) and has been calibrated in Brunelli et al. (2021a) thanks to the available data on the structure from the permanent monitoring and previous studies (ReLUIS (2018a)). The choice of adopting the equivalent frame model is justified by the regular pattern of openings in walls and by the evidence from the actual seismic response (Cattari and Magenes (2022)), that clearly highlighted the concentration of cracks in specific portions of the walls (namely, the piers and spandrels, respectively identified in orange and green in Figure 4.1.6a).The constitutive law used allows for describing the nonlinear response until very severe damage levels at element scale (i.e. DL_E from 1 to 5) through progressive strength degradation corresponding to assigned drift values; with the aim of executing NLDA (Cattari et al. (2018)), the constitutive law includes also a hysteretic response (Figure 4.1.6b). The latter is based on a phenomenological approach that allows also to differentiate the hysteresis loops in spandrels and piers and also varying the prevailing failure mode (e.g. if dominated by the flexural response or diagonal shear cracking). For further details on mechanical panel properties and modelling assumptions the interested reader may refer to Brunelli et al. (2021a).

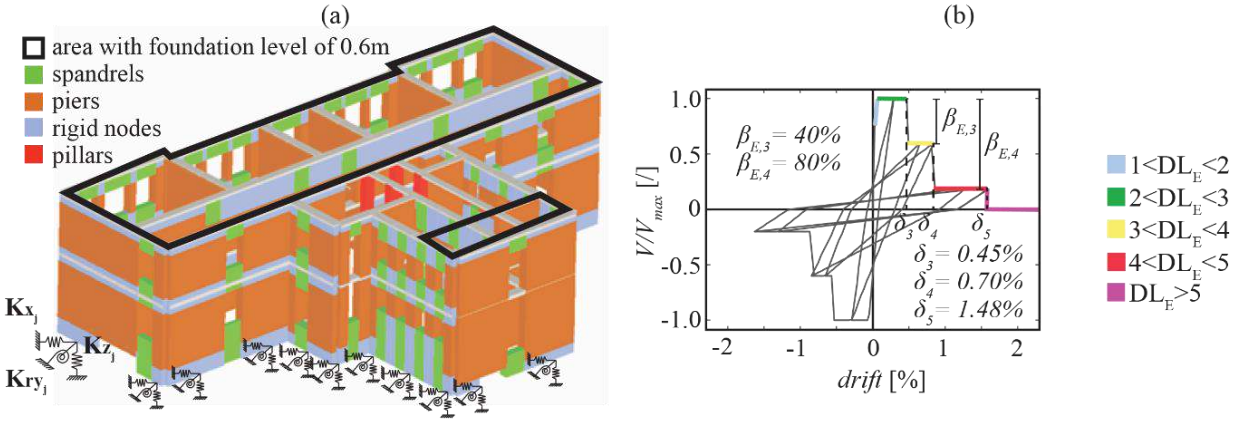

Figure 4.1.6. (a) 3D equivalent frame model with springs implemented in the CB model, (b) backbone and hysteretic response of masonry elements: piers under shear.

To simulate the base compliance, each foundation pier was equipped with springs (see Figure 4.1.6a), whose stiffness was calibrated through the real part of the soil-foundation impedances by Gazetas (1991). The foundation width was set equal to 0.90 m, while its length was defined by adding the half-length of the spandrel panel to the size of the load-bearing wall. The value of the embedment was set to 0.6 m, except for the area indicated in Figure 4.1.6a, where the embedment increases up to

2.95 m due to the presence of an underground level. The soil was modelled as an equivalent linear half-space with a shear modulus equal to that mobilized at the foundation depth under each input motion. A full soil-foundation contact was assumed.
Firstly, the periods along the X and Y directions (T^*_x and T^*_y) and the damping ratio (β_x and β_y) of the SFS system were estimated through the replacement oscillator by Maravas et al. (2014). To this aim, the building was approximated through a SDOF system with a viscous damping ratio equal to 3% and a lateral stiffness derived from the fundamental periods along the X and Y directions of the fixed base configuration (see Brunelli et al. (2021a)). To apply the formula by Maravas et al. (2014), the real and the imaginary parts of the monolithic foundation equivalent to the actual foundation systems were calculated from the sum of the real or imaginary parts of the impedances of the X-oriented (or Y-oriented) load-bearing walls. The contribution of the soil hysteretic damping mobilized at the foundation level (see Figure 4.1.6b) was added to the energy loss coefficients simulating the radiation damping ratio. Then the frequency-dependent dynamic coefficients of the impedances were computed as a function of the resulting T^*_x and T^*_y, through an iterative procedure. To simulate the additional energy dissipation due to SFS interaction, the mean value of β_x and β_y was introduced as a Rayleigh damping ratio into the equivalent frame model. The calculation was repeated for each input motion: consequently, the impedances and the resulting T^*_x and T^*_y as well as the mean value of β_x and β_y, were updated according to the mobilized soil shear stiffness and damping ratio during each seismic response analysis (see Figure 4.1.4).

3. DESCRIPTION OF RESULTS

3.1. Influence of site effects and SFS interaction on the fragility curves

Table 4.1.2 reports the number of analyses (N), the median value IM_{50} (in acceleration unit g) and the standard deviation (σ) used to generate the fragility curves of the fixed-base model analysed under the selected input motion (FB A).
Only few analyses, reported in brackets in Table 4.1.2, mobilize DL3, DL4 and DL5 for the FB A case; so the initial set of input motions described in Section 1.2 was integrated with the natural signals recorded on stiff soil and collected by Paolucci et al. (2020). However, the IM_{50} and σ resulting from the updated set of input motions are comparable with those obtained from the original selection (in brackets). There is only an increase, less than 10%, of the IM_{50} associated with DL5 in the case of PGA which results in a reduction of structural fragility.

Table 4.1.2: Median value (IM_{50}) and standard deviation (σ) associated with to the various damage levels for the FB A model.

FB A					
	PGA		$Sa(T_1)$		
	IM_{50}	σ	IM_{50}	σ	N
DL1	0.095	0.495	0.178	0.473	127
DL2	0.274	0.314	0.656	0.391	92
DL3	0.450 (0.413)	0.219 (0.255)	1.013 (0.969)	0.376 (0.423)	18 (10)
DL4	0.530 (0.488)	0.191 (0.147)	1.182 (1.156)	0.308 (0.299)	17 (7)
DL5	0.619 (0.562)	0.219 (0.178)	1.500 (1.428)	0.261 (0.314)	44 (12)

It is worth to remember that the IMs calculated for FB C and CB C refer to the bedrock. This implies that the IM_{50} values reduce moving from the FB A to FB C, independently of the soil profile. That highlights the expected increase of fragility for a fixed-base structure settled on soil type C with respect to that placed on soil type A, as shown in Figure 4.1.7 by way of example in the case of DL3.

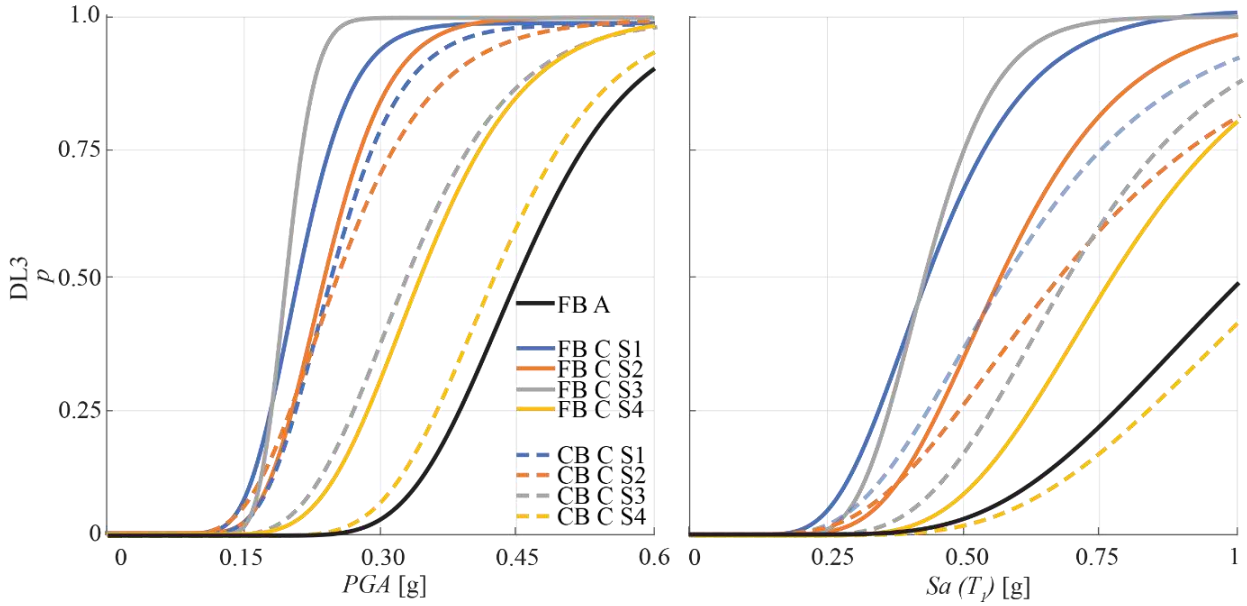

Figure 4.1.7. Comparisons between the curves obtained from the FB A, FB C and CB C assuming PGA and Sa (T_1) as IM in case of DL3.

The comparison with the CB C models reveals an increase of IM_{50} with respect to the FB C case. Such modification reduces the probability of failure on the building. Since the elongation of the CB C period produces an increment of the seismic actions with respect to the FB C case (see Figure 4.1.5 and Section 2.2), such beneficial effect is mainly due to the increase of damping ratio produced by the SFS interaction, as shown in Figure 4.1.7, referring to DL3. This general conclusion is however extendable to all DLs.

The same beneficial effect is evident by comparing the number of analyses that fall into the various DL_i for the FB C and CB C. There is in fact a reduction of the analyses in the more severe DLs for the CB C model, in particular for the profile S4 where the analyses in DL5 are only 3. Such reduced number of analyses reduces the reliability of the DL5 fragility curve for S4, hence this case will not be considered in the following interpretations. Obviously, the reliability of DL5 would have been improved by scaling through higher factors the signals originally selected, but such procedure would have led to unrealistically strong free field motions. Conversely, the low occurrence of DL5 for S4 (resulting from the numerical analyses) appeared much more realistic, because buildings settled on gravel are less prone to high damage since they are affected by lower seismic actions (see Figure 4.1.5) and benefit of higher soil damping.

The estimation of p_{DLi} through Equation 4.1.2 allows the computation of the mean damage μ_d expected to affect the structure, as follows:

$$\mu_d = \sum_{i=0}^{5}(p_{DLi}\, i) \qquad (4.1.2)$$

where p_{DLi} is weighted by i=0,1,2,3,4 or 5 passing from DL0 to DL5.

The calculation was performed by entering the curves of the case FB C and CB C with the values of PGA and Sa(T_1), at the bedrock of each selected input motion. The μ_d value may be conveniently converted into an equivalent discrete damage level by assuming a binominal distribution, leading to the following conversion intervals: 0-0.7 for DL0; 0.7-1.6 for DL1; 1.6-2.5 for DL2; 2.5-3.4 for DL3; 3.4-4.3 for DL4; 4.3-5 for DL5. The latter ones have been used to define the "square metric" in Figure 4.1.8. These comparisons are reported considering as IM: the PGA in (a); and the Sa(T_1) in (b). The grey fillings indicate a difference of 1, 2 or 3 DLs between the mean damage of FB C and CB C. In the case of the PGA, SFS interaction always leads to a reduction of the expected damage, independently of the soil profile and the greatest beneficial effects at DL3-4, specially for S3. Considering the Sa(T_1), the results are more dispersed. In any case there is a greater damage associated with the FB C model, but there are also some cases in which the CB C model leads to

greater damage, specially at lowest DL in S1 and S2. In this case, it is worth to remind that also the IM changes among the models, because the fundamental period changes as shown in Table 4.1.1. Despite these slight differences, the general conclusion on the SFS effects observed from the use of PGA and Sa(T_1) is the same.

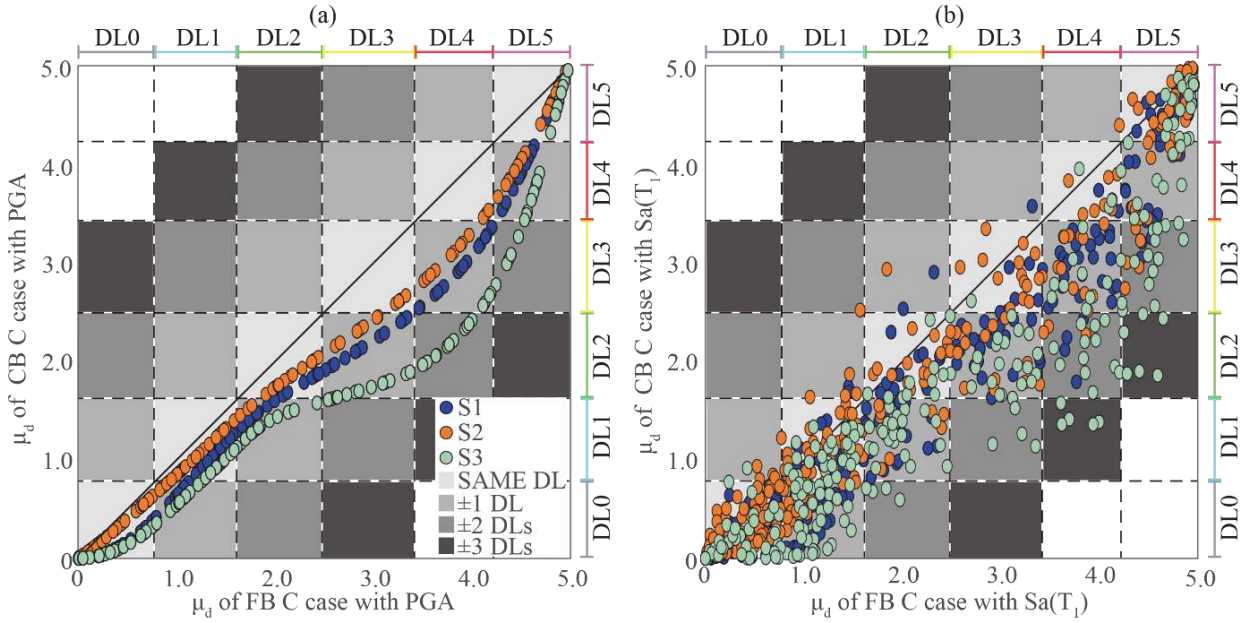

Figure 4.1.8. μ_d between FB C and CB C for S1, S2 and S3 in case of (a) PGA and (b) Sa(T_1).

3.2. Comparisons with the Eurocode previsions

In the most widespread cases of fragility curves generated for fixed base structures and stiff soil conditions (case FB A), site effects can be considered in the estimation of p_{DLi} in a simplified way, *i.e.* by entering in the curve with the IM amplified by the stratigraphic coefficient provided by Code. As an example, on the abscissa, Figure 4.1.9 shows the μ_d resulting from the fragility curve of FB A in which the terms p_{DLi} in Equation 2 alternatively corresponds to peak ground (PGA*) or the spectral (Sa(T_1)*) accelerations, amplified according to the coefficient proposed by CEN (2004). This is equal to 1.5 for events with a surface wave magnitude lower than 5.5; otherwise it is equal to 1.15 (see Figure 4.1.3). When only site effects are considered (FB C) (see Figure 4.1.9a and b), EC8 underestimates the damage in any case and up to three damage levels. Soil-structure interaction reduces the gap between the μ_d estimated through the Code conforming approaches and that estimated by explicitly accounting for the site effects joint to the soil foundation structure interaction (CB C) (see Figure 4.1.9c and d). However, a difference of one DL (very rarely of two DLs) still results also for CB C. Such underestimation arguably would increase if the increment of damping ratio induced by SFS interaction was considered in the computation of the IM*.

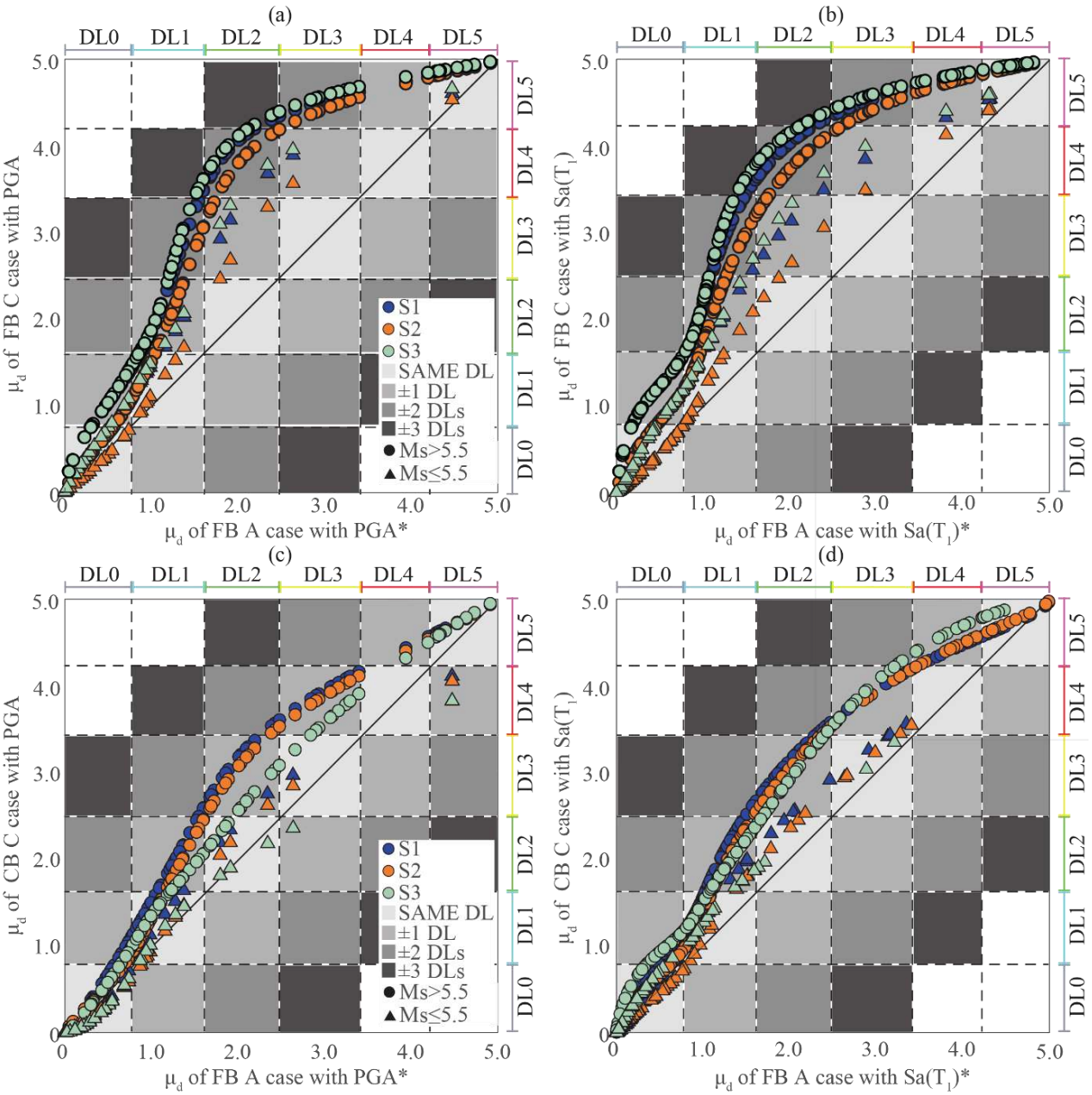

Figure 4.1.9. Comparison among the μ_d resulting for the different analyzed cases from the curves expresses as a function of (a) PGA and (b) Sa(T_1) for FB C model, (c) and (d) for CB C model. In the FB A case, the PGA* and Sa(T_1)* values - amplified according to the coefficients proposed in the Eurocode - were used.

4. CONCLUSIONS

The paper compares the fragility curves and the derived mean damages of a real URM structure ideally placed on stiff rock (FB A) or settled on four different soil profiles. The latter ones include its real foundation subsoil as well as other three with an equivalent shear wave velocity falling in the range of soil type C. The base of the structural model is alternatively assumed as fixed (FB C) or endowed with springs (CB C), simulating in that way the soil-foundation dynamic impedance. The comparison among the results of the FB A and FB C cases shows the expected increase of the probability of failure when site amplifications are considered.

The comparison among FB C and CB C highlights: i) a general increase in the spectral accelerations affecting the model on springs; ii) a reduction of the probability of failure. As expected, the first effect

(i) is due to the period elongation induced by the soil-foundation-structure interaction while the second (ii) is mainly ascribable to the increment of damping associated to the additional energy dissipated by the soil-foundation system.
The comparison among the results of models on the different soil profiles reveals that the highest damage levels are rarely achieved by structures placed on gravel. This is because they are affected by lower seismic actions and benefit of higher soil damping mobilized by the early development of nonlinearity in such soil types. Significant beneficial effects are also recognized for structures settled on soft clay again due to the significant damping mobilized by the considerable strain levels achieved in such profile.
Finally, the mean damages of FB C and CB C were compared with the values resulting from the probability of failures estimated by amplifying the intensity measure through the conventional coefficients proposed by Eurocode (CEN (2008)) to account for the site effects. The comparison shows that such simplified approach underestimates the damage up to two damage levels. Nevertheless, it is currently the most widespread procedure because fragility curves are mostly generated for fixed base structures and without considering site effects through site response analyses. Results achieved could be further developed in future works to improve also practice-oriented procedures.

CHAPTER 4.2

Influence of different building

Submitted to Bulletin of Earthquake Engineering.

FRAGILITY CURVES OF MASONRY BUILDINGS IN AGGREGATE ACCOUNTING FOR LOCAL MECHANISMS AND SITE EFFECTS

Michele Angiolilli[1], Andrea Brunelli[1], Serena Cattari[1]
[1]University of Genoa, Genoa, Italy
michele.angiolilli@edu.unige.it, andrea.brunelli@edu.unige.it, serena.cattari@unige.it

Abstract:

Masonry buildings in aggregate are largely diffused within the existing Italian and European building stock, especially in historical centres. Their seismic evaluation represents a difficult and open task that has not been exhaustively investigated so far. The study proposes a procedure aimed at evaluating the potential impact of the combination of local mechanisms and site-amplification in terms of fragility curves on an existing masonry aggregate. The latter consists of five adjacent structural units mutually interacting with each other during seismic sequences. The aggregate is inspired by the unreinforced masonry (URM) built heritage of the historic centre of Visso struck by the Central Italy 2016/2017 earthquakes. It was proved to be negatively affected especially by the site-amplification phenomena. The in-plane (IP) response of URM buildings was simulated through nonlinear dynamic analyses performed on a 3D equivalent frame model of the structure, whereas out-of-plane (OOP) mechanisms were analysed by adopting the rigid-block assumption but assuming as seismic input the floor accelerations derived from the post-processing of data derived from the global 3D model. Also an innovative procedure considering the pounding effect to the global response of the building was presented. Two soil conditions were assumed with (freefield) and without (bedrock case) site amplification. In the first case, a site response analysis based on a 1D soil model aimed to reproduce the actual soil profile under the examined aggregate has been carried out. The results showed that site effects strongly affected the seismic vulnerability of the aggregate, also possibly altering the combination between IP and OOP mechanisms with respect to what expected on basis of evidence from other historical centres. More specifically, for bedrock condition, the overall seismic response of the buildings in aggregate was strongly affected by such a combination, especially for medium-high damage levels where local mechanisms were prevailing with respect to the IP response. Conversely, for freefield condition, IP mainly governed the overall behaviour for all the damage levels, consistently with the field evidence. The result appears also affected by the architectural configuration of such buildings, characterized by quite large openings at ground floor.

Keywords: unreinforced masonry structures, building in aggregate, nonlinear dynamic analyses, equivalent frame model, site effects, out-of-plane mechanisms, structural pounding

1. INTRODUCTION

The seismic risk of existing unreinforced masonry (URM) buildings is particularly emphasized when they belong to historical centres of small municipalities, as testified by damage and losses produced by many seismic events (e.g. Decanini et al. (2004); Augenti and Parisi (2010); D'Ayala and Paganoni (2011); Cattari et al. (2012); Carocci (2012); Penna et al. (2014); Sextos et al. (2018); Sorrentino et al. (2019)). Such high seismic risk derives from a combined role of vulnerability and hazard. Vulnerability factors arise from the fact that small historical centres were often developed in a poor economic contest and without following a specific urban development plan. Indeed, they are usually the result of a process of building growth across centuries, leading to buildings in aggregate with interacting units characterized by different materials, construction techniques, heights, state of preservation and, often, improvised renovations. Buildings in aggregate are in fact one of their most distinctive features. In addition, the geomorphologic context in which such historical centres are built often highlighted the important role on the seismic response of local amplification phenomena associated with topographic and soil stratigraphic effects (e.g., Sextos et al. (2018); Stewart et al. (2018); Sorrentino et al. (2019); Brando et al. (2020); Chieffo and Formisano (2020)). This potential risk factor was confirmed by microzonation studies performed in various Italian areas after the aforementioned earthquakes (e.g. Lanzo et al. (2011); Monaco et al. (2014); Pagliaroli et al. (2020)).

The large diffusion of URM buildings in aggregate is confirmed by Figure 4.2.1a that depicts data available from the Da.Do. platform (Database of Observed Damage, see Dolce et al. (2019b)), referring to only residential URM buildings and neglecting mixed structures (i.e. R.C.-masonry buildings). In particular, one can see that the number of buildings in aggregate is about 3 times (i.e. 35261/12624) higher than the individual buildings by considering all municipalities and even higher, namely 4 (i.e. 26205/7045) focusing only on small municipalities (<2000 residents). The ratio is even larger only focusing on historical centres (e.g. Sisti et al. (2019)).

Figure 4.2.1b shows a comparison between the global damage level (DL) occurred for individual URM buildings and URM buildings in aggregate. That information was taken from Da.Do. that associates a DL to each surveyed building according to conversion criteria proposed in (Dolce et al. (2019b)) thanks to the availability of the respective AeDES forms (Baggio et al. (2007)). The DL are graduated in five levels consistently with the Macroseismic European Scale EMS98 (see Grünthal (1999)). From that figure, one can see that the DL tends to be statistically higher for buildings in aggregate than for individual ones.

Obviously, the results are merely qualitative since they refer to buildings located in zones with different seismic hazards and only struck by the L'Aquila earthquake in 2009. However, this outcome is confirmed by the results of the empirical fragility curves derived from the Da.Do data by (Penna et al. (2022b)) or from Norcia's survey data (Sista et al. (2019)). However, it is worth noting that isolated buildings are usually characterized by a structural typology and an architectural configuration different from buildings belonging to aggregate, that in general turn out less vulnerable (e.g. isolated buildings are often in peripheric area and belong to modern ones). This is important to be specified in light of the so-called "aggregate-effect" discussed in this study, meant as the effect that boundary conditions provided by adjacent structural units may have on the seismic response of an individual building belonging to an aggregate. Indeed, a proper comparison to assess such an effect may be carried out only if the isolated and in aggregate configurations are consistent one to each other (as examined in this study), circumstance that obviously is very difficult to be applied when referring to empirical observed data.

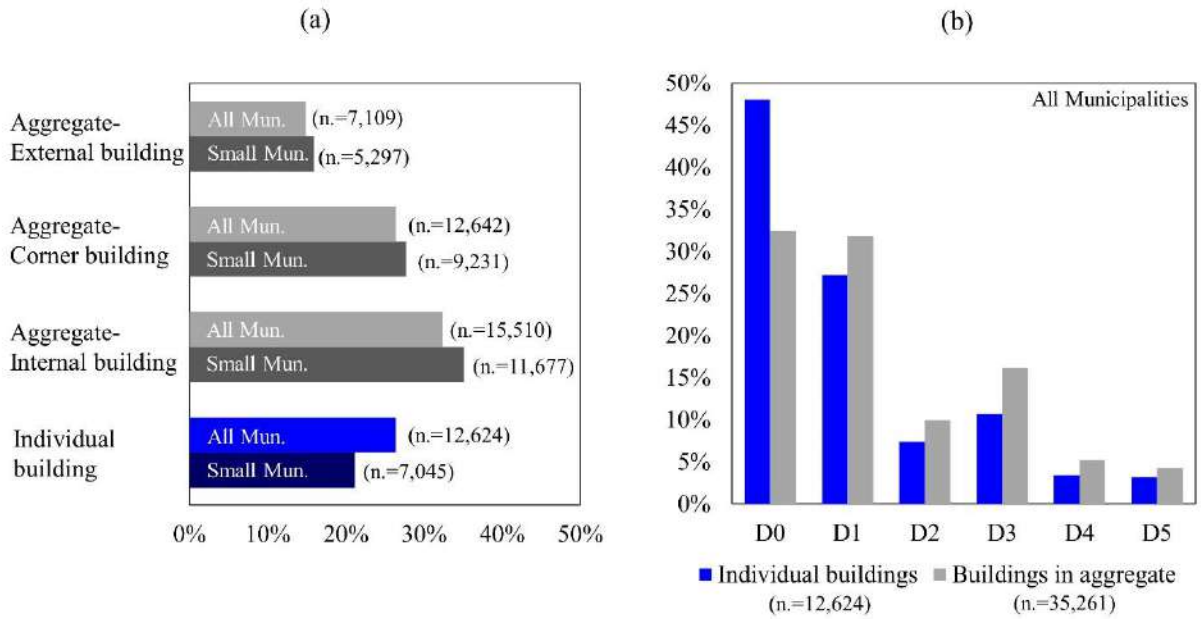

Figure 4.2.1. Comparison in terms of diffusion (a) or damage level (b) of URM buildings in aggregate or individual URM buildings among the data collected in the DaDo platform and related to surveyed buildings struck by the L'Aquila earthquake in 2009.

In recent years, some studies tried to overcome the issues related to the seismic vulnerability assessment of URM aggregates by adopting various approaches, i.e.: holistic approach (Cardinali et al. (2021)); heuristic approach (e.g. Vicente et al. (2014); Brando et al. (2017); Sandoli et al. (2022)); analytical-mechanical approach (Cocco et al. (2019); Cima et al. (2021); Nale at al. (2021)); analytical-numerical approach (Ramos and Lourenço (2004); Senaldi et al. (2010); Fagundes et al. (2017); Formisano and Massimilla (2019); Bernardini et al. (2019); Degli Abbati et al. (2019); Valente et al. (2019); Greco et al. (2020); Grillanda et al. (2020); Angiolilli et al. (2021); Battaglia et al. (2021); Valluzzi et al. (2021); Bernando et al. (2022)); large-scale approaches based on empirical evaluations obtained from post-earthquake data (Del Gaudio et al. (2019); Penna et al. (2022a); Sisti et al. (2019)); as well as hybrid methods (Kappos et al. (2006); Maio et al. (2015)) combining the previous approaches through the individuation of representative building classes. Comparisons between different approaches for specific case studies are reported in Chieffo et al. (2019) and Chiumiento and Formisano (2019).

Despite the efforts already made in literature, the following limitations are still recognized. For the pure empirical approach, only the position of the unit is considered as additional vulnerability factors with respect to ordinary residential buildings; moreover, there is the intrinsic difficulty aforementioned to clearly investigate the "aggregate effect". For heuristic approaches, vulnerability factors specific for buildings in aggregate are based only on expert judgment. For analytical-mechanical or analytical-numerical approaches, several studies account only for the in plane (IP) response - without explicitly considering local mechanism effects associated to the out of plane (OOP) response of walls - while other are conversely mostly addressed to OOP. Moreover, in most of the studies based on analytical-numerical models, the aggregate is modelled as an entire structure without explicitly considering the interacting effect among adjacent units. However, when aggregates are investigated as entire structures, an unreliable shear redistribution among the structural units may result since the presence of discontinuities between the adjacent buildings is neglected. The interaction effect of adjacent structural units was recently investigated in Angiolilli et al. (2021) through an analytical-numerical approach, by considering different connection level assumptions and by assessing the seismic response in terms of fragility curves; the study highlighted that the effectiveness of the structural link may affect the interaction between IP and OOP mechanisms, especially at the collapse performance state. Please refer also to RELUIS (2010) and Lagomarsino et

al. (2015) to consider, in a practice-oriented way, possible interaction effects when the accurate modelling of the entire aggregate is disregarded.

In addition to that, and focusing on the role topographic and soil stratigraphic effects, few literature studies specifically addressed the site-effect on URM study cases being able to provide clear evidence of the phenomenon together with data accurate enough for proceeding to a numerical simulation and model validation (e.g. Ferrero et al. (2020); Brunelli et al. (2021a); Brunelli et al. (2022a); Cattari et al. (2022a)). Actually, most fragility curves are derived without explicitly considering site effect and then simplistically considering it by entering into the fragility curves with an amplified value of the intensity measure (e.g. Formisano et al. (2021)). However, the amplification factor can be estimated too much roughly through ground motion prediction equations (e.g. Sabetta and Pugliese (1996)), roughly from studies at national scale (e.g. Falcone et al. (2021)), and more accurately from seismic microzonation studies at city-scale (e.g. Pagliaroli et al. (2020)). Thus, a rigorous approach would require site response analyses under numerous input motions.

Within this general context, the novelty of the present research regards the effect of the combined role of site amplification and the mutual interaction between adjacent structural units during seismic events in terms of fragility curves, explicitly accounting also for both out-of-plane and structural pounding. The case-study consists of five URM buildings inserted in an existing aggregate located in the historic centre of Visso (Italy) struck by the Central Italy 2016/2017 earthquakes (§2). A 3D Equivalent Frame model (fixed based assumption) was adopted to represent the IP behaviour of the structural units composing the aggregate (§3). Nonlinear dynamic analyses (NLDAs), according to the Cloud Method approach (e.g. Jalayer et al. (2017)), were performed by adopting sets of accelerograms considering either the bedrock and free-field conditions. Local mechanisms were evaluated separately, as usually done in the literature (see Simoes et al. (2014)) but based on the storey accelerations derived from the NLDAs performed on the 3D global model. That allows to implicitly consider the filtering effect provided by the nonlinear dynamic response of the structure, as proposed in Angiolilli et al. (2021) and further tested in Lagomarsino et al. (2022). The fragility curves derived for the IP global response and local mechanisms, in both the soil conditions, as well as their combinations are discussed in §4.

2. KEY-FEATURES OF THE SELECTED BUILDINGS IN AGGREGATE AND ADOPTED SOIL PROFILES

The case-study presented herein deals with an existing masonry aggregate located in the historical centre of Visso (see Figure 4.2.2).

The municipality of Visso was struck by several earthquakes in 2016 causing casualties and widespread damage to the built environment. The three mainshocks (E1, E2 and E3), occurred on 24th August, 26th October and 30th October, were characterized by low epicentral-distance with respect to the investigated case study (i.e. 16 km, 3 km and 11 km for E1, E2 and E3, respectively) and significative moment magnitude MW (i.e. 5.4, 5.9 and 6.5, for E1, E2 and E3, respectively).

Figure 4.2.2. The case study aggregate in the historical centre of Visso with the indication of the five structural units in the façades facing the municipality's square (U1 to U5 from right to left; picture bottom).

2.1. The investigated "row housing" aggregate

The type of the investigated aggregate is very widespread in Italian historical centres and is usually called "row housing" (consisting of a series of buildings aggregated in lines). In particular, the aggregate is composed of five-unit buildings dating back to different eras, each of them characterized by small and simple regular shapes. The openings are mainly present on the main façades, and the number of floors varies from three to four. Figure 4.2.3a,b depicts the elevations view (a) and the architectural plan (b) of the aggregate.

The geometric and structural details of the units were assumed on the basis of field survey and, in some cases, were also based on the characteristics of neighbouring damaged buildings that showed almost clearly the type of the masonry, the diaphragm system, and the distribution of the internal space, as illustrated in Figure 4.2.4. In particular, the load-bearing walls were characterized by two-leaf stone masonry, with rough stones sizing about 90-120 mm in height and 360-400 mm in length. Floor diaphragms were assumed to be composed of concrete slab (not reinforced) system 150 mm tick, whereas the foundation system was supposed to merely be a prolongation of the load-bearing walls, slightly embedded in the soil, as typically observed for existing URM buildings. The presence of sporadic tie-rods could be observed (see Figure 4.2.4 and Table 4.1.1) making some of structural units possibly susceptible to the activation of OOP mechanisms, especially at the upper building floor. Table 4.1.1 describes the main geometric features and the structural details of the five structural units.

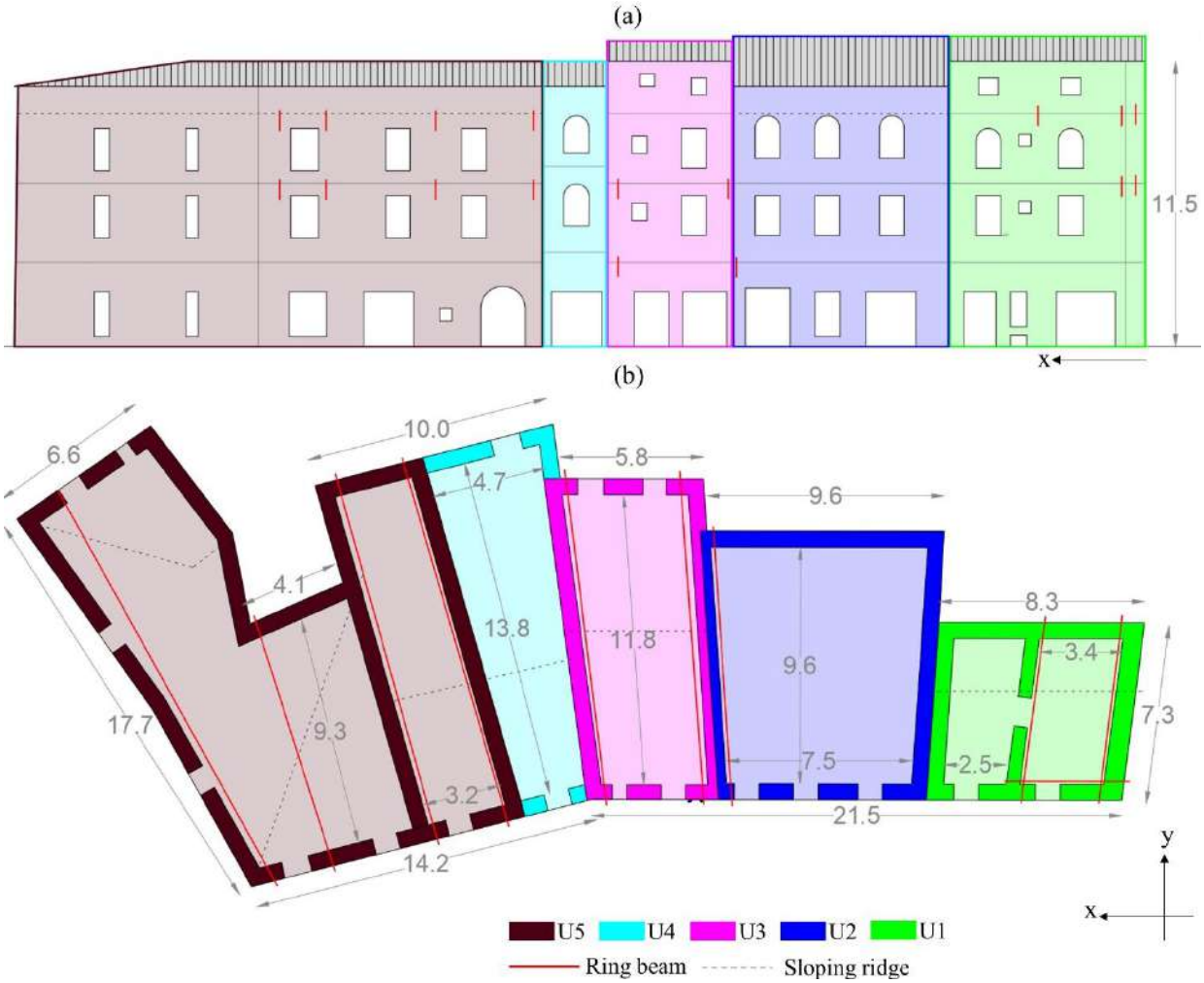

Figure 4.2.3. Front view facing the municipality's square (a) and architectural plan (b) of the Visso's aggregate.

Table 4.1.1: Geometric and structural features of the structural units composing the investigated aggregate. Note that the effective interstorey heights were slightly changed in the simulation to avoid numerical issues (i.e. *2.8m, **3.4 m, ***3.2m, ****2.8m.

structural unit	n. floors	plan configuration	interstorey heights [m]	total surface [m^2]	tie rods
U1	4	squared	3.4 - 3.2 - 2.8 - 2.1	58.6	2nd and 3rd diaphragm levels (both X and Y directions)
U2	3	squared	3.4 - 3.2 - 3.9*	100	1st diaphragm level (Y direction)
U3	4	rectangular	3.4 - 3.2 - 2.8 - 2.1	75.5	1st and 2nd diaphragm levels (Y direction)
U4	3	rectangular	3.8** - 3.45*** - 3.2*	57.1	no
U5	3	asymmetric "C"	3.4 - 3.2 - 3.9*	206.4	2nd and 3rd diaphragm levels (Y direction)

A detailed description of the five structural units is described in the following. The thickness of the external walls was 70 cm at the ground floor and 60 cm at the other levels. The only exceptions regard the thickness of the perimeter walls over the entire U1 height equal to 80 cm. The internal walls were supposed to be 5 cm lower in thickness than the perimeter walls of each specific floor.

Figure 4.2.4. Damage of different structural elements of the neighbouring masonry buildings located in the historical centre of Visso, useful also to understand structural details of the case study.

In particular, U1 is a 4-story building located on one edge of the aggregate and is the smallest structural unit. For this unit, the ratio between the total resistant wall section and the total surface (defined as RA in the following) is about 14% and 21% along X and Y directions, respectively. U2 is a 3-story building with RA of about 10% in both the directions due to its almost squared plan. The U3 is a 4-story building with RA of about 6% and 18% in X and Y directions, respectively, due to its rectangular shape in plan. U4 is a 3-story building presumably built in an earlier era with respect to the other structural units, sharing the pre-existing walls of U3 and U5 (see the plan configuration of Figure 4.2.3). Indeed, it is characterized by a different height with respect to U3 and presents a structural continuity with the U5 roof system. Actually, due to its structural configuration, U4 cannot be considered as a completely autonomous structural unit and, therefore, it was considered only for the analyses of the possible OOP mechanisms of the front façade because of the absence of tie rods and the scarce wall-to-wall connection with the adjacent structures. Finally, the U5 is located at the other end of the aggregate and is the biggest structural unit of the aggregate in terms of the total surface. For it, RA is about 6% and 17% in X and Y directions, respectively. Regarding the observed DL that occurred following the seismic events, according to EMS98 scale proposed by Grünthal (1998) (i.e. from DL0 to DL5) and on basis only of an external survey, U1 suffered DL3, both U3 and U4 suffered DL2, whereas U2 suffered a damage comprising between DL2 and DL3.

2.2. Topographic and soil stratigraphic features of Visso's municipality

The municipality of Visso is in a valley characterized by two main soil profiles and represents an interesting case for which a detailed study on the site and soil-foundation-structure interaction effects was already investigated in Brunelli et al. (2021, 2022a,c).

In particular, a soil profile representative of the central valley area corresponds to that under the Visso's school (see Figure 4.2.2), already in-depth studied by Brunelli et al. (2021a, 2022a). The other soil profile characterizes the historical center area (see Brunelli et al. (2022c)) and was characterized through two boreholes and a HVSR (Horizontal to Vertical Spectral Ratio) test (MZS3 (2018)). This profile is made of clayey silt for the first 4 m, overlaying a 11 m thick sandy gravel layer. The lack of exhaustive information about the soil stiffness necessitated the use of correlation functions between SPT data done for the Visso's School and the shear wave velocity (VS) of each layer of soil profile (see Brunelli et al. (2021a, 2022a)). In particular, V_S=162 m/s was obtained for the clayey silt soil and V_S=337 m/s for gravel layer. The consequent equivalent VS up to the bedrock depth is V_{Seq}= 272 m/s. For the Visso's school area, there is substantially no discrepancy between the punctual 1D subsoil model and the more detailed 2D analysis, while the valley-effect has resulted to be is beneficial for the historical center area as shown in (Brunelli et al. (2022c)). In the latter study, a validation of the numerical model adopted in this paper has been provided by comparing the actual damage with the simulated one. For the sake of simplicity, a 1D subsoil model was herein adopted

for the studied aggregate since the main purpose of this study was not to obtain the most reliable numerical model reproducing the real overall damage level (as done in Brunelli et al. (2021a) or Cattari et al. (2022a) for other cases study). Therefore, the seismic inputs under freefield condition were based on the stratigraphic amplification effects simulated in 1D condition with the STRATA software (Kottke and Rathje 2008). In particular, the ground motions used in this paper were recorded at stations located on stiff rock outcrop (i.e. V_{S30}>700 m/s) and selected from the SIMBAD database (Iervolino et al. (2014)). Definitively, freefield seismic signals were obtained by propagating the bedrock ones by considering soft soil profiles consistent with the real foundation subsoil of the aggregate. The complete list of used signals and their characteristics are illustrated in Brunelli et al. (2022a).

Note that 370 and 320 ground motions were adopted for bedrock and free-field soil conditions, respectively. In particular, for bedrock, it was necessary to use 50 additional seismic inputs to ensure a consistent derivation of the fragility curves also for high damage levels; these signals are characterized by a higher value of intensity measures and have been extracted by the selection made by (Manfredi et al. (2022)). Figure 4.2.5 illustrates the response acceleration - response displacement spectra (Sa-Sd) of the ground motions adopted for the two soil conditions. In the same figure, lines proportional to the fundamental periods of the buildings associated with their two main directions (X and Y) are also represented.

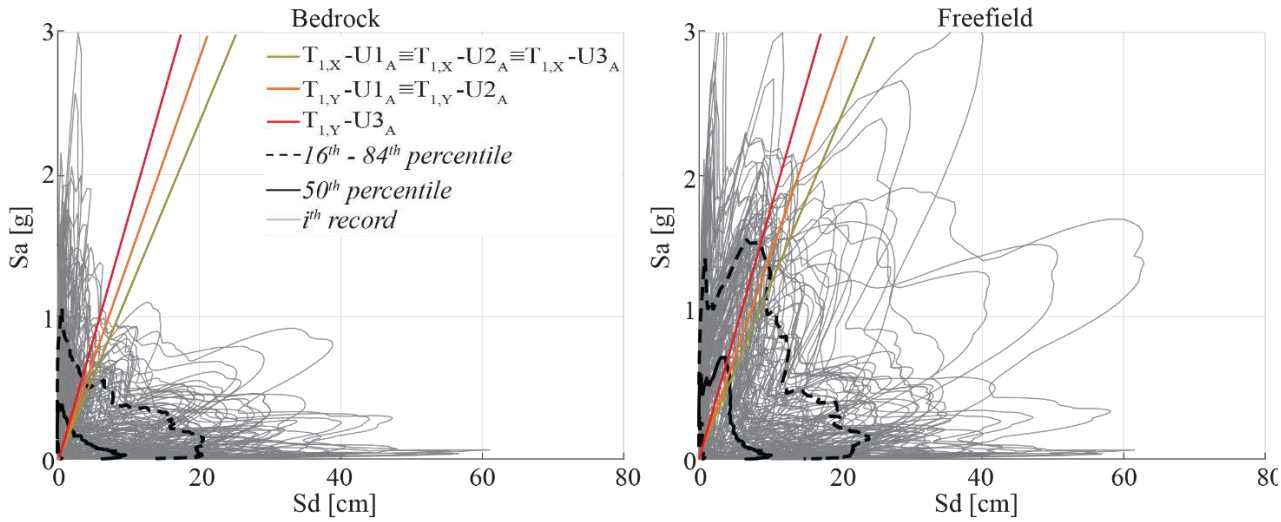

Figure 4.2.5. Displacement- and acceleration- response spectra (Sd-Sa) for bedrock and freefield with indication of the fundamental periods along the two directions (X and Y).

3. MODELLING AND ANALYSIS CRITERIA

3.1. Global in-plane response

The structural model of the URM aggregate was developed according to the equivalent frame modelling approach implemented in the Tremuri software (Lagomarsino et al. (2013)). Figure 4.2.6a-c illustrates the equivalent frame model constituted of piers (vertical elements), spandrels (horizontal elements) and rigid areas (nodes); the indication of the four units investigated in detail during the NLDAs is reported, too.

More specifically, the piecewise-linear beam model (i.e. NLBEAM) has been assumed to describe the nonlinear response of URM panels (Lagomarsino and Cattari (2013)). The NLBEAM features a constitutive law describing the nonlinear response until very severe damage levels (DL, from 1 to 5), through the definition of a relation between the drift value $\delta_{E,i}$ and the corresponding fraction of the

residual shear strength $\delta_{E,i}$ at the attainment of the i-th DL differentiated for piers, spandrels, flexural and shear behaviour (see for example Figure 4.2.6d).

Table 4.2.2: Mechanical parameters adopted in Tremuri.

	E (MPa)	G (MPa)	τ_0 (MPa)	f_m (MPa)
piers	2968	991	0.127	6.42
spandrels	2078	693	0.062	4.49
diaphragms	23333	9170	-	-

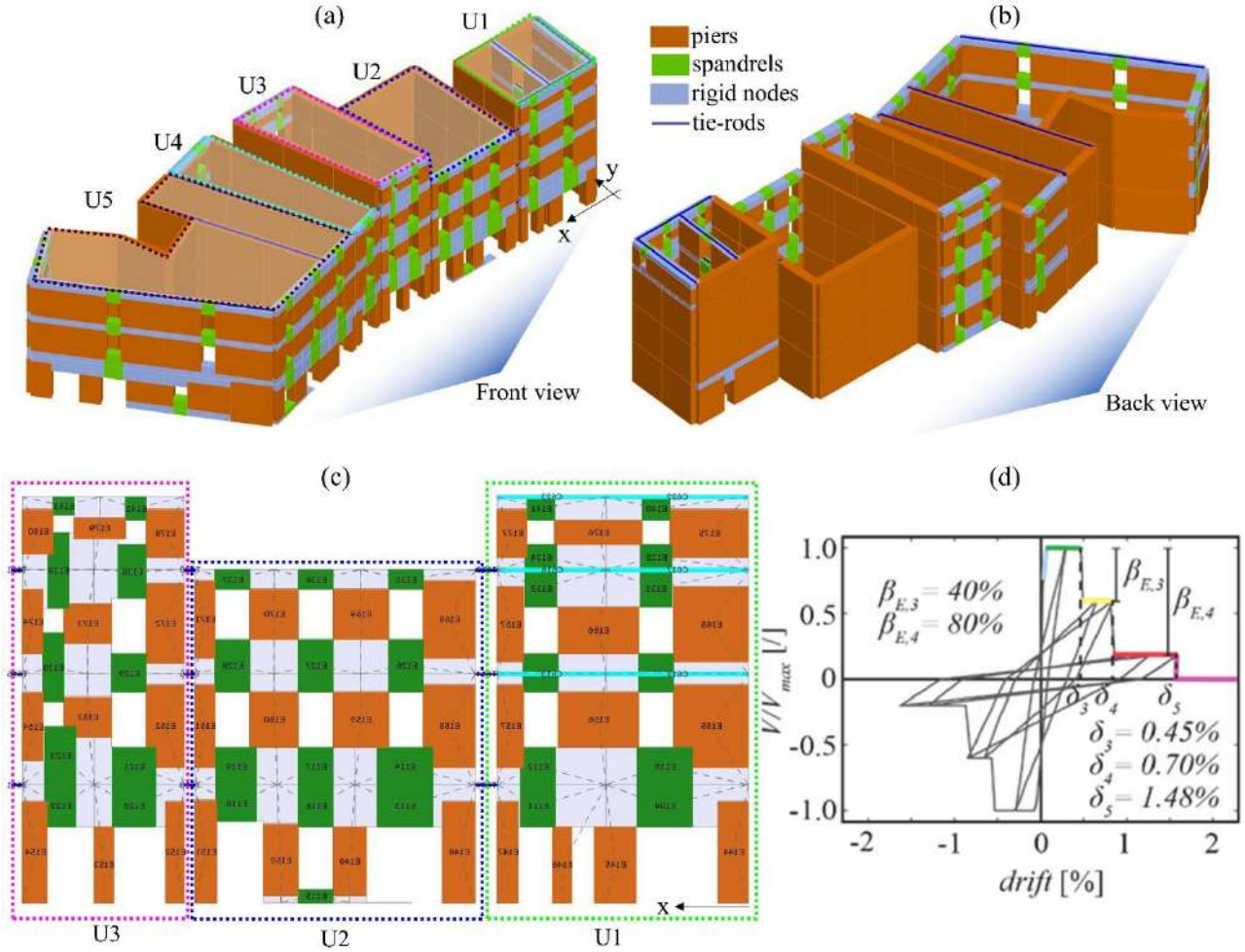

Figure 4.2.6. (a) and (b) 3D equivalent frame model of the aggregate: a) front view, (b) back view; (c) detail on the EF mesh obtained for the external walls of U1, U2 and U3; (d) backbone and hysteretic response of masonry elements: piers under shear.

The mechanical parameters adopted are listed in Table 4.2.2 and were based on those calibrated for the Visso's school (Brunelli et al. (2021a)) through a very accurate numerical simulation of the actual response of this monitored asset. The reliability of those values was also confirmed in Cattari and Angiolilli (2022) and Angiolilli et al. (2022b). The strength values (τ_0) are slightly higher than that used for the school (about 10%), but still consistent with the reference values proposed by MIT (2019) for analogous masonry type. Both the elastic properties (E, G) and the compressive strength (f_m) of spandrels were reduced by 0.7 with respect to that of piers, whereas tensile strength (τ_0) by 0.5, due to the anisotropic behaviour of masonry as well as the prevailing failure to vertical joints of spandrels.

Instead, the hysteretic response is controlled by parameters (c1…c4), defining the slope of unloading and loading branches of the hysteresis loops. Values of the parameters adopted in this study were calibrated to be consistent with experimental campaigns (Morandi et al. (2018), for piers, and

Beyer and Dazio (2012), for spandrels) and lists in Table 4.2.3. Please refer to Cattari et al. (2018) and Angiolilli et al. (2021) for further details on the formulation of NLBEAM and its potential in executing NLDA.

Table 4.2.3: Pier and spandrel parameters adopted for the model at the first and second rows, respectively.

Shear behaviour								Flexural behaviour							
Drift $\delta_{E,i}$ [%]			Res. Str $\beta_{E,i}$ [%]		Hyst. Res.			Drift $\delta_{E,i}$ [%]			Res. Str $\beta_{E,i}$ [%]			Hyst. Res.	
DL3	DL4	DL5	DL3	DL4	c1	c2	c3	DL3	DL4	DL5	DL4	c1	c2	c3	c4
0.45	0.7	1.48	0.6	0.2	0.8	0.8	0	0.60	0.80	1.81	0.85	0.9	0.8	0.6	0.5
0.50	1.5	2.0	0.7	0.7	0.2	0	0.3	0.50	1.5	2.0	0.7	0.2	0	0.3	0.8

In order to explicitly account for the interaction effect between adjacent units, the procedure proposed in Angiolilli et al. (2021) has been implemented. Thus, the units were modelled separately to each other introducing a finite-length gap and, then, connected by elastic truss elements (sectional area of 0.00164 m^2 and elastic modulus E of 210000 MPa with null tensile behaviour) as well as fictitious floors (thickness of 0.05 m, E=39420 MPa, G=13112 MPa). The finite-length gap represents the semi-length of the shared mid-wall, while fictitious floors limit openings along transversal directions and allow openings between units mainly along their longitudinal directions. Indeed, in the transversal direction, the effect of the fictitious floors strongly reduced the openings between buildings, as usually one can observe in existing units built separately but in contact with the pre-existing ones. The aggregate-effect was first investigated by modal analyses on both the entire 3D equivalent frame model of the aggregate (i.e. from $U1_A$ to U_{5A}) and the ones developed for the individual structural units ($U1_I$ and $U3_I$) to obtain a preliminary insight into their dynamic behaviour.

the fundamental period (T_1) values along the X and Y directions of the structure. All the buildings in aggregate were characterized by the same T_1 (i.e 0.172 s) along the X direction. On the other hand, in Y direction, $U1_A$ and $U2_A$ were characterized by T_1 = 0.144 s, whereas U3 and U5 (as well as U4) by T_1 = 0.117 s due to small "torsional" modes. Furthermore, T_1 associated with the individual buildings was higher (about 12% and 78% for $U1_I$ and $U3_I$, respectively) than that of the buildings in aggregate (i.e. $U1_A$ and $U3_A$) along the direction where the interaction takes place (i.e. X direction) due to the confinement that mutual interaction among structural units. On the other hand, T_1 was almost similar along the other direction (variation of 5% and -2% for $U1_I$ and $U3_I$ with respect to $U1_A$ and $U3_A$, respectively).

Table 4.2.4: Fundamental periods (values expressed in seconds) of the individual buildings and the buildings in aggregate (indicated respectively with the subscript I and A).

	$U1_A$	$U2_A$	$U3_A$	$U1_I$	$U3_I$
$T_{1,x}$ [s]	0.172	0.172	0.172	0.194	0.308
$T_{1,y}$ [s]	0.144	0.144	0.117	0.152	0.115

Figure 4.2.7 shows by way of example for some structural units the capacity curves of both the buildings in aggregate and individual buildings. The curves are expressed in terms of base shear coefficient (i.e. base shear over weight) versus roof drift, and have been obtained through nonlinear static analyses (NLSA) by applying a uniform force distribution proportional to the mass in X and Y directions and both verses.

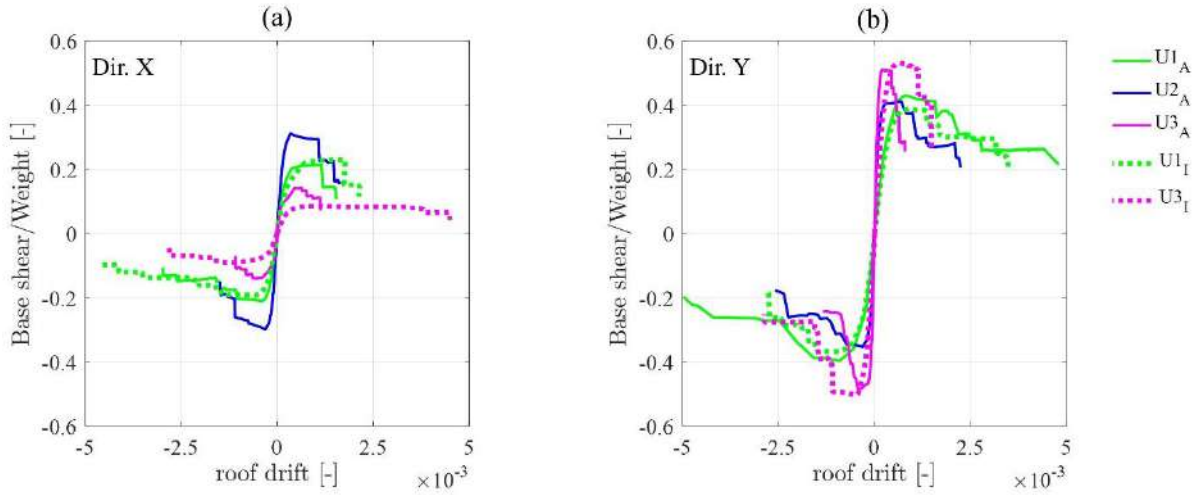

Figure 4.2.7. Dimensionless pushover curves obtained for the buildings in aggregate ($U1_A$, $U2_A$, $U3_A$) or individual buildings ($U1_I$, $U3_I$) along the X (a) or Y directions (b). The weights of $U1_A$, $U2_A$, $U3_A$, $U5_A$ are 5528 kN, 5375 kN, 4154 kN, 10371 kN, respectively. Note that the weight of $U1_I$ coincides with that of $U1_A$, whereas the weight of $U3_I$ is 5762 kN (in $U3_A$, the mass associated with the walls in contact with the adjacent unit was halved).

In particular, regarding the structural response of the buildings in aggregate, in both X and Y directions, a similar behaviour can be observed along the positive and negative directions due to the almost symmetric plan configuration of each structural unit (apart for the U1 in the X negative direction, where connections with adjacent structures are limited). Furthermore, the higher vulnerability of the buildings in aggregate can be observed along the X direction (where the interaction between structural units takes place), especially in terms of base shear coefficient. In particular, in that direction, $U3_A$ is characterized by the highest vulnerability, whereas $U2_A$ by the higher seismic response. Note that, in the Y direction, the $U3_A$ is instead characterized by the highest base shear coefficient although its response is very brittle (i.e. almost sudden drop in the shear strength), as compared to the others.

Regarding the aggregate-effect of U1, one can see that, along the X direction, drift capacity (both negative and positive directions) and base shear coefficient (positive direction) are negatively affected by about 5%. Instead, U1 is positively influenced by the aggregate-affect in both the shear strength (up to 10%) and drift capacity (up to 50%) along the Y direction (both negative and positive directions). On the other hand, the aggregate-effect positively affected the shear strength of the U3 in the X direction (about 65% and 55% in the positive and negative directions, respectively) and negatively affected that in the Y direction (about 5%). Moreover, for both X and Y directions, a clear reduction in the drift capacity can be observed for the $U3_A$ with respect to $U3_I$. Definitively, by observing the capacity curves obtained by NLSA, one cannot generalize whether the aggregate-effect positively or negatively affects the seismic behaviour of the individual buildings.

With the aim of deriving fragility curves, it is necessary to synthetically interpret the structural response data derived from each NLDA. In particular, the multiscale approach originally proposed in (Lagomarsino and Cattari (2015a)) and then further developed in (Sivori et al. (2022); Brunelli et al. (2022a)) was adopted to assign a specific damage level to the building compatible with the EMS98 scale (i.e. from DL1 to DL5). Please refers also to Cattari and Angiolilli (2022) for the description of a more accurate criterion aimed at evaluating the EMS98 global damage grade. In particular, the adopted multiscale approach combines two heuristic criteria at wall and global scale. The first (i.e. associated to the "wall scale") is based on the extension of the "minimum DL" occurred to piers ($DL_{min,P}$), weighted on their shear stress contribution. The concept of the "minimum DL" was originally proposed in (Marino et al. (2019)) to replace the adoption of the interstorey drift thresholds at the wall scale, as previously adopted in Lagomarsino and Cattari (2015a); in particular, such a

proposal assigns a damage level to the wall based on the minimum damage level attained by all the elements of a certain floor. The second (i.e. associated to the "global scale") is based on the top displacement associated with specific fractions of the overall base shear ($V_b/V_{b,max}$) of the building estimated on the pushover curves obtained through NLSAs. The multicriteria adopted are summarized in Table 4.2.5.

For each record, the worst criterion (i.e. the one that occurs at first) is then adopted to assign the final resulting global DL. According to this procedure, results of records can be properly grouped as those associated to the same DL.

Table 4.2.5: Multicriteria to define the global DL consistently with the EMS98 criteria (|δ =drift, δy = yelding drift).

DL	EMS98- description & quantification		wall scale criteria				global scale criteria	
1	Negligible to slight damage (no structural damage)	Hair-line cracks in a very few walls	$\sum_{DL_{min,P}\geq 1} \geq 0.2$				$\frac{V_b}{V_{b,max}} \leq 0.4$	$(\delta < \delta_y)$
2	Moderate damage (slight structural damage)	Cracks in many walls	$\sum_{DL_{min,P}\geq 2} \geq 0.35$				$0.4 < \frac{V_b}{V_{b,max}} \leq 0.8$	$(\delta < \delta_y)$
3	Substantial to heavy damage (moderate structural damage)	Large and extensive cracks in most walls	$\sum_{DL_{min,P}\geq 3} \geq 0.5$	or	$\sum_{DL_{min,P}\geq 4} \geq 0.1$		$0.7 \leq \frac{V_b}{V_{b,max}} < 1$	$(\delta > \delta_y)$
4	Very heavy damage (heavy structural damage, very heavy non-structural damage)	Serious failure of walls	$\sum_{DL_{min,P}\geq 4} \geq 0.35$	or	$\sum_{DL_{min,P}\geq 5} \geq 0.1$		$0.4 \leq \frac{V_b}{V_{b,max}} < 0.7$	$(\delta > \delta_y)$
5	Destruction (very heavy structural damage)	Total or near total collapse	$\sum_{DL_{min,P}\geq 5} \geq 0.5$				$0.2 \leq \frac{V_b}{V_{b,max}} < 0.4$	$(\delta > \delta_y)$

3.2. Local mechanism associated with OOP response

Among possible OOP collapse mechanisms usually observed in URM structures after post-earthquake scenarios (e.g. D'Ayala and Speranza (2003); D'Ayala and Paganoni (2017)), in this paper, the overturning of façades (i.e. the so-called one way cantilever mechanism) and that of tympanum (or gable) were considered.

The individuation of the walls susceptible to overturning was defined on the basis of building geometry, opening layout, constructive details and restraints given by the structure. In particular, it was reasonable to consider the OOP mechanisms involving the only upper level as well as the two upper levels of the façades facing the municipality's square, as illustrated in Figure 4.2.8, because of the wall slenderness and the amplification phenomena generally occurred for the upper building levels (e.g. Degli Abbati et al. (2018)). Those mechanisms were called one-floor cantilever mechanism (1FM) and two-floors cantilever mechanism (2FM), respectively. Note that those mechanisms were assumed only for the Y direction of the building (see Figure 4.2.8a). In addition it is also considered the overturning of the tympanum (or gable) mechanism (TM) in case of in elevation irregularities.

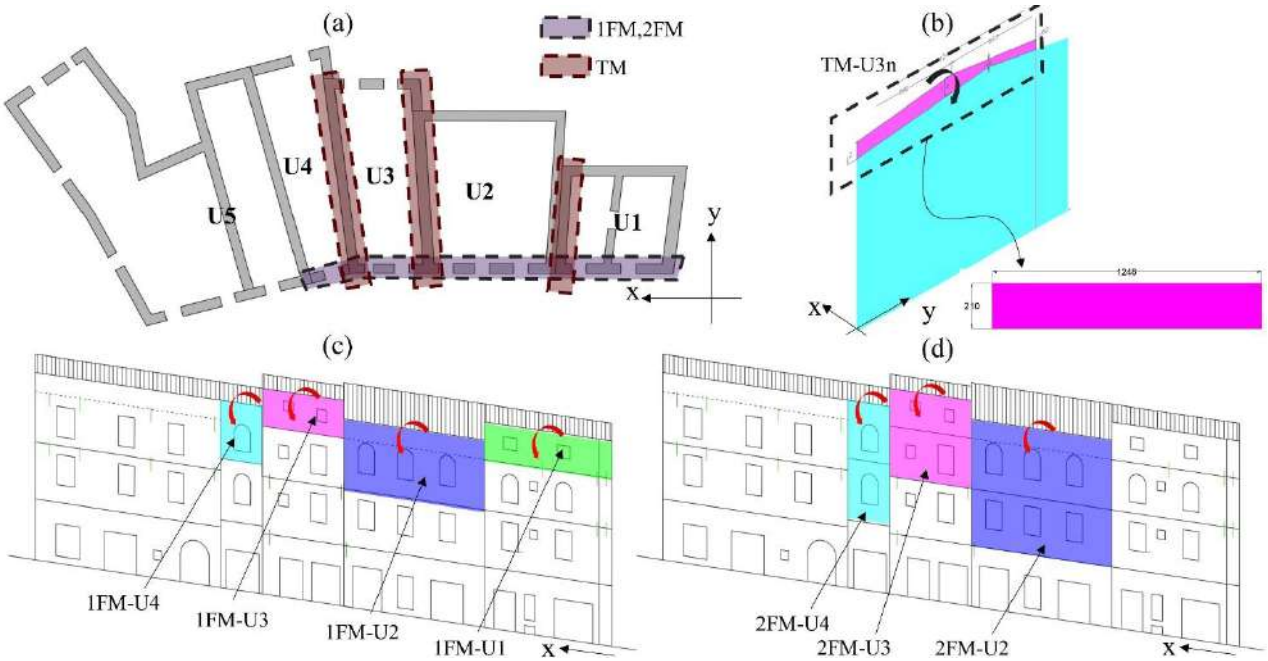

Figure 4.2.8. (a) Individuation of the walls investigated for the OOP analyses; (b) TM assumed for a portion of a U3 wall, with the indication of the equivalent walls considered in the OOP analyses, (c,d) walls for which the 1FM (a) and 2FM (b) were considered.

Furthermore, due to the different number of stories between U1 and U2, as well as between U3 and both U2 and U4, the tympanum (or gable) mechanism I of the wall portion taller than walls of the adjacent units was evaluated. Note that the TM-U3 regards OOP along the X direction of the building and both the positive and negative directions (i.e. TM-U3p and TM-U3n, respectively), whereas TM-U1 regards OOP only along the positive X direction.

Among possible criteria for numerically analyzing the aforementioned OOP mechanisms (Sorrentino et al. (2017); Abrams et al. (2017); Degli Abbati et al. (2021); Cattari et al. (2022b)), the engineering practice-oriented model based on the classic idealization of single-degree-of-freedom (SDOF) rigid block was adopted in this study. The legitimacy of the rigid-block assumption was proven also by the actual response of the aggregate under examination. More in general, in presence of poor quality of masonry with consequent scarce cohesion of stone/clay units with mortar, disintegration phenomena of the external leaf may also occur (De Felice (2011)); this circumstance must be carefully verified for filling units (like U4). In particular, the three-linear SDOF constitutive model proposed in Angiolilli et al. (2021) was adopted, In Figure 4.2.9, it is depicted in terms of OOP displacement (d^*) and pseudo-acceleration (α^*=g x_G/z_G). The latter is computed accounting also for the possible interlocking contribution (αi=g F 2h/(3W x_G)) provided by the internal orthogonal panels to the façade panels subjected to overturning.

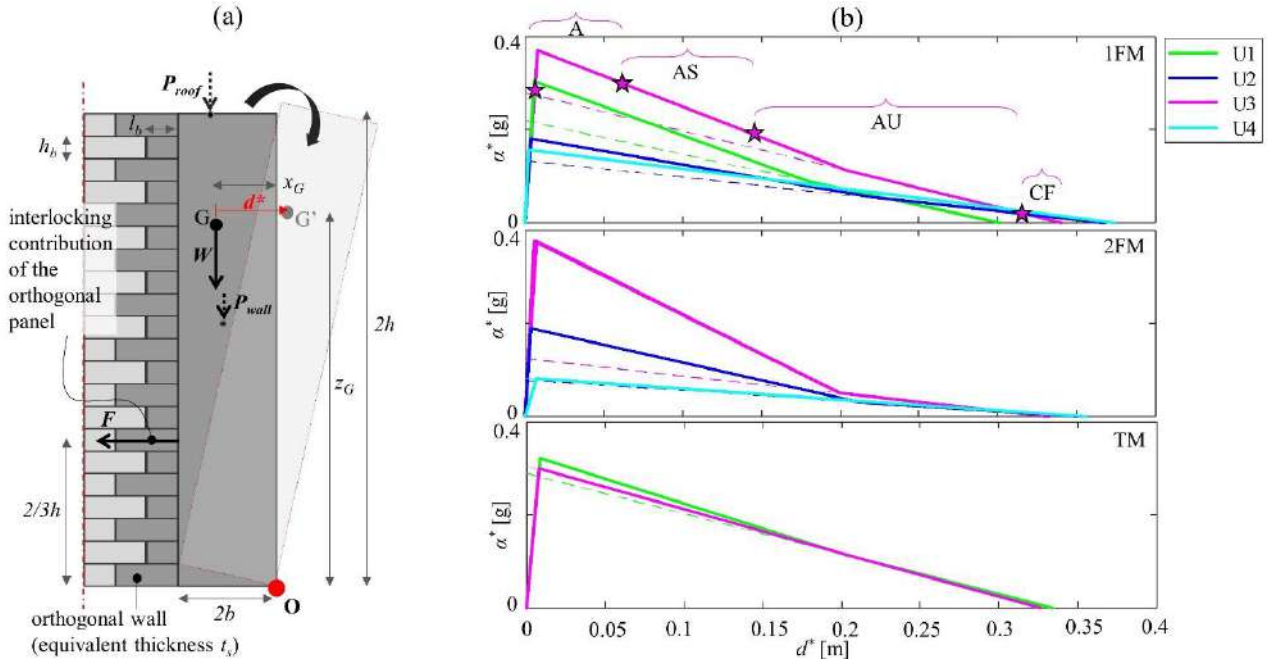

Figure 4.2.9. (a) idealization of the walls subject to OOP mechanisms; (b) SDOF model for the different units under the assumption of the mechanisms 1FM, 2FM and TM. For the sake of simplicity, in those curves are indicated the thresholds of the four limit states (A, AS, AU, CF) for the only U3 unit and 1FM.

It is worth noting that the roof structure is placed perpendicular to the walls located along the X direction of the building (see also Figure 4.2.4). However, because of the structural details of the roof system, it was assumed that 80% of the load was transferred to those walls, while the remaining part to the orthogonal walls placed along the Y direction (i.e. the ones for which TMs were considered). Differently from Simões et al. (2014), the possible restrain (i.e. stabilizing horizontal force) between the panels and the roof was neglected. Also the restrain between panels and diaphragms was neglected for the 2FMs. Table 4.2.6 lists all the geometric features and loads referred to walls belonging to U1, U2, U3 and U4 and to the mechanisms 1FM, 2FM and TM. Please see Figure 4.2.9a for the meaning of those parameters. Note that for all the cases, heights and overlap lengths of the masonry units (h_b and l_b) were assumed 0.11 m and 0.19 m according to the typology of the masonry. Moreover, wall density and friction coefficient were assumed 2100 kg/m3 and 0.577, respectively.

Table 4.2.6: Geometric features and loads needed for the definition of the OOP constitutive laws for the wall belonging to U1, U2, U3 and U4 regarding mechanisms 1FM, 2FM and TM.

	2h [m]	2b [m]	z_G [m]	P_{roof} [kN]	P_{Wall} [kN]	t_s [m]	interlocking
U1-1FM	2.10	0.55	1.05	63.80	159.7	1.90	yes
U2-1FM	3.90	0.65	1.94	256.8	398.7	1.00	yes
U3-1FM	2.10	0.65	1.05	22.10	134.9	1.30	yes
U4-1FM	3.25	0.65	1.61	76.70	93.05	0	no
U2-2FM	7.10	0.65	3.54	63.80	711.9	1.90	yes
U3-2FM	4.90	0.65	2.46	22.10	301.7	1.30	yes
U4-2FM	6.70	0.65	3.34	76.70	192.4	0	no
U1-TM	2.10	0.65	1.05	15.90	189.5	0.55	yes
U3-TMp	2.10	0.65	1.05	5.50	357.7	0	no
U3-TMn	2.10	0.65	1.05	5.50	357.7	0	no

As known, the OOP behaviour is ruled by the loss of equilibrium (sudden overturning phase of the panel after the initial rocking within the pseudo-elastic phase) rather than the attainment of the material strength limits or crack-band lengths. Hence, the difficult definition of specific DL thresholds related to OOP mechanisms can be established only in a conventional manner. However, their definition should ensure, as much as possible, a physical meaning similar to that associable with the

IP failure modes reported in the EMS98 and established in Table 4.2.5. To this aim, Table 4.2.7 defines four different phases of the OOP behaviour based on the maximum d* value computed during the NLDAs, namely from the activation of the mechanism (A) to the activated mechanisms with high probability of stable or unstable response (AS or AU, respectively), to certain failure (CF). That classification regards individual OOP mechanisms.

Table 4.2.7: Definition of the damage levels for OOP mechanisms.

name	description	quantification	DL_G
A	activation of the local mechanism with development of slight cracks to the panel	$0.05d_0<d^*\leq 0.2d_0$	1 (first mechanism among all the considered ones)
AS	activated mechanism characterized by high probability of stable response	$0.2d_0<d^*\leq 0.4d_0$	2 (first mechanism among all the considered ones)
AU	activated mechanism characterized by high probability of unstable response very close to evolving in a certain failure	$0.4d_0<d^*\leq 0.95d_0$	3 (first mechanism among all the considered ones) 4 (for all considered mechanisms) involving at least 25% of significant building volume)
CF	certain failure	$0.95d_0<d^*\leq d_0$	5 (for all considered mechanisms involving at least 25% of significant building volume)

Then, by considering the frequency and extension of the OOP mechanisms, it is possible to convert the four initial OOP phases in five OOP damage levels referred to the overall behaviour of the building and, therefore, ensure a comparison with the five DL defined for the IP behaviour. The "frequency and extension of OOP mechanisms" refer to the activation of all the potentially activable mechanisms for a specific wall or the activation of a single mechanism involving a portion associated to a significant building's volume. In particular, from DL1 to DL3 it is considered the higher d* among all the considered mechanisms for a specific wall, whereas DL4 and DL5 take into account the occurrence of all the considered mechanisms for a specific wall.

3.3. Local mechanism associated with structural pounding

As described in detail in §1, most existing buildings in aggregate are either with no separation distance or with insufficient separation with respect to the adjacent buildings. Therefore, an earthquake-induced structural pounding may occur, resulting in substantial damage or even total destruction of colliding portions. Typically, the buildings at the end of the "row" aggregate suffer the most severe damage because of the momentum transfer from the internal buildings as well as because of the larger openings that occur for the one-side free buildings; that was also noticed in Shrestha and Hao (2018), where it was also observed that a building sandwiched between two relatively massive buildings could be susceptible to a global crushing effect (Cole et al. (2012)). Depending on the dynamic characteristics of the buildings (e.g., fundamental period, mass, height, stiffness, orientation, geometry, etc.), during a seismic excitation, one can observe two phases: i) lateral displacements of adjacent buildings are synchronized (in-phase response) for which collision does not occur; ii) the adjacent buildings most likely develop different lateral responses (out-of-phase) due to the building-to-building variability, as such collisions between adjacent buildings with insufficient/null separation gap are inevitable. Hence, pounding could lead to more severe conditions in the case of adjacent buildings with very different dynamic characteristics because the out-of-phase response occurs more frequently.

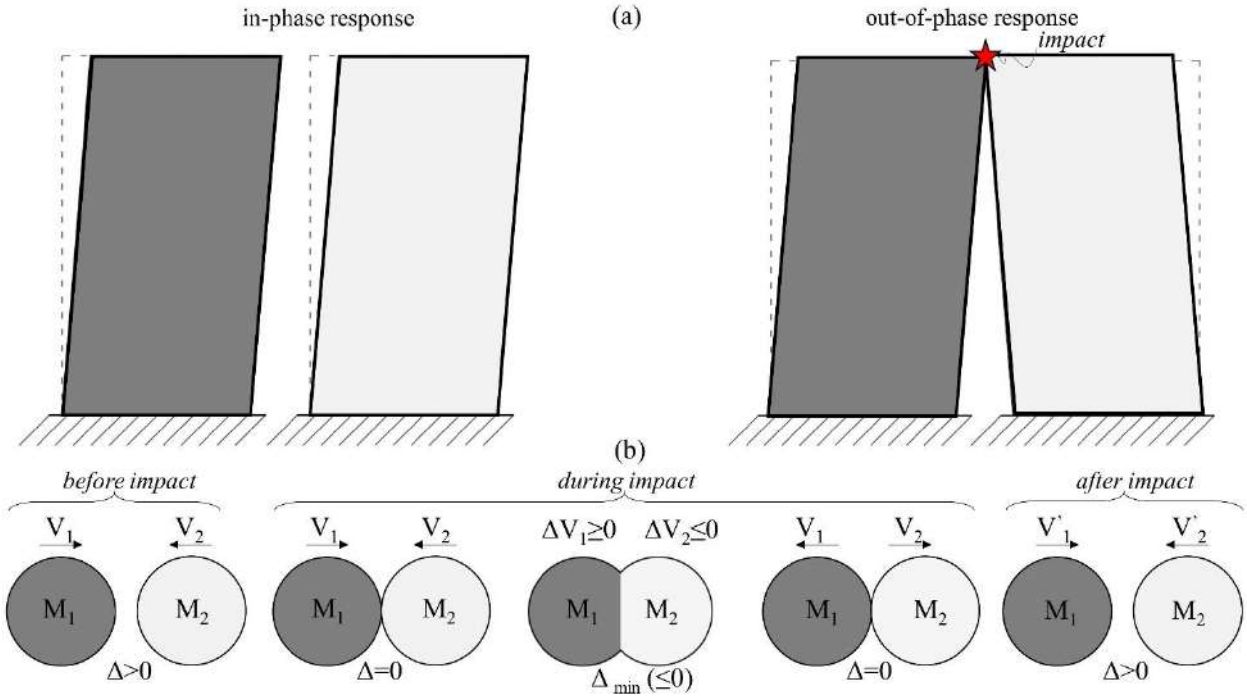

Figure 4.2.10. (a) Scheme of the possible responses of two adjacent buildings during seismic excitation; (b) impact phases within the out-of-phase response of two bodies schematized as spheres.

Furthermore, in the past earthquakes, it was observed that, generally for cases of adjacent buildings with same height, pounding location mainly took place at the top floors of the pounded buildings except for cases with relatively small gap distance, where pounding tended to take place at the middle or bottom floors (e.g. Naserkhaki et al. (2013)).

Structural pounding is a complex phenomenon involving plastic deformations, local crushing, fracturing, and friction at contact points. The process of energy transfer during impact is highly complicated, which makes the analytical/numerical analysis of this problem very difficult because of the high nonlinearity of the phenomenon that, in spite of its complexity, it has been intensively studied in the years, especially for RC buildings or bridges, by developing various models and using different models of collisions (e.g. Anagnostopoulos (1988); DesRoches and Muthukumar (2002); Lin and Weng (2001); Jankowski (2005); Jankowski (2008); Maison and Kasai (1990); Naserkhaki et al. (2013); Raheem (2006), among the other).

Here, a very simplified procedure was introduced to account for the effect of the structural pounding on the fragility curves of the studied buildings in aggregate. In particular, that phenomenon was analysed in the post-processing of the data derived from the global 3D model, similarly to what also performed for the investigation of OOP mechanisms. The pounding (impulsive) force P_f in an infinitesimal time *dt* (i.e. between the instant *i* and *i*') is equal to the momentum variation *M dv* (i.e. $P_f\ dt = M\ dv$, assuming a constant value for *M*). In finite terms become $P_f\ \Delta t = M\ \Delta v$, under the assumption that the P_f value remains constant during the impact. Furthermore, in this study, it was assumed that, at the collision instant, the final velocity was null (i.e. Vi'=0), so that ΔV=(Vi-Vi')=Vi; this is a conservative assumption. Based on the aforementioned considerations, the formulation adopted in this study to compute the pounding force P_f is described as:

$$P_{f,k} = \frac{M_n\ |V_{n,k}|}{\Delta t_{,k}} \tag{4.2.1}$$

where M_n is the total mass associated with the *n*-th node of the numerical model (representative of the building portion for which pounding was susceptible to occur), $V_{n,k}$ is the velocity of the *n*-th node during the *k*-th time history, and represents the estimation of the deceleration-time during the *k*-th time history. In particular, $\Delta t_{,k}$ is evaluated within the out-phase response (up to collision) and represents the time needed to pass from a certain value of axial force $N_{truss,k}$ different to zero (for

which pounding phase begin) to null axial force, for which opening between the adjacent units begins. Figure 4.2.11 illustrates an example of the evolution of both $V_{n,k}$ and $N_{truss,k}$ during the time of a specific NDA at the upper building level, between $U2_A$ and $U1_A$. From that figure, one can see also the procedure adopted to evaluate Δt,k during the time of the NDA. Therefore, it is possible to compute the variable $P_{f,k}$ (and its maximum value, $P_{f,max,k}$) for each *k*-th time history. It is important to observe that $P_{f,max,k}$ does not occur at the same instant of the maximum value of $N_{truss,k}$ needing the evaluation of $P_{f,k}$ for all the duration of the *k*-th time history to correctly estimate $P_{f,max,k.}$

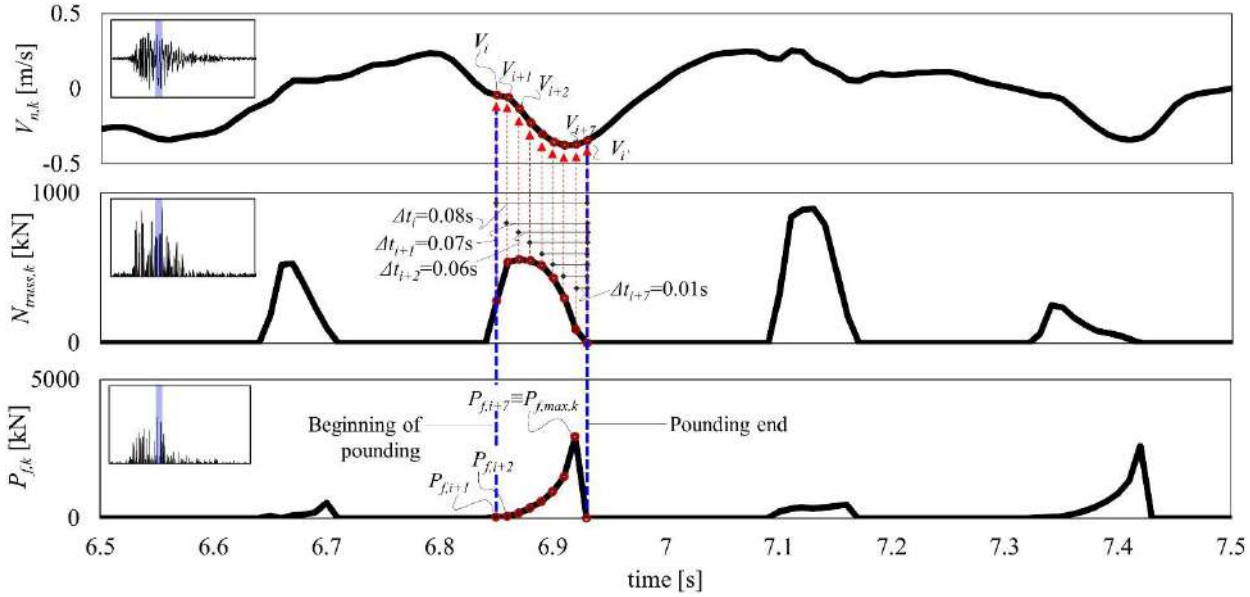

Figure 4.2.11. Graphical procedure to depict the estimation of the pounding force during a certain time history.

Among the possible pounding mechanisms between the investigated buildings, in this paper, that phenomenon was investigated between U2 and its adjacent units, namely U1 and U3. Furthermore, it was assumed that the effect generated by the pounding of U2 with respect to U1 and U3, was the same as that occurred from U1 to U2 as well as from U3 to U2 (i.e. by computing P_f, only by using V_n and Δt taken from U2). Obviously, this is a simplification because in real cases, pounding between buildings of different mass could result in more severe damage to the lighter building (Shrestha and Hao (2018)). Finally, it is worth specifying that the study of the structural pounding is here proposed only to the main façade of the aggregate, where pounding damage occurred in the real case. Table 4.2.8 lists the Mn values involving the structural pounding between U2-U1 and U2-U3 at the three building-levels.

Table 4.2.8: Values of the mass (Mn) involving the structural pounding between U2-U1 and U2-U3 at different building levels.

	level	M_n [kN]
U2-U3	1	53.4
U2-U1	1	5.8
U2-U3	2	38.7
U2-U1	2	5.6
U2-U3	3	34.1
U2-U1	3	79.0

Hence, one can compute the maximum P_f (i.e. P_{fmax}), evaluated during the entire duration of each time history (see Figure 4.2.11c), for each building level. Then, it is possible to verify if that force overestimates the compressive strength of the walls fm (see Table 4.2.2), namely if $P_{fmax}/Ap \geq fm$, where Ap is the pounding area. As depicted in Figure 4.2.12, for the definition of Ap, it was assumed a 45° load diffusion (in both longitudinal and transversal directions) from a wall portion of U2 to that of U1 or U3. This assumption is consistent with the typical one adopted for the tie-rods

design/verification. In particular, the impacting area of U2 depends on the height of the diaphragm (to which the higher mass is usually associated with respect to the other structural elements) as well as the thickness of the wall orthogonal to the façade where impact occurs (i.e. $t_{x,U2}$ in Figure 4.2.12).

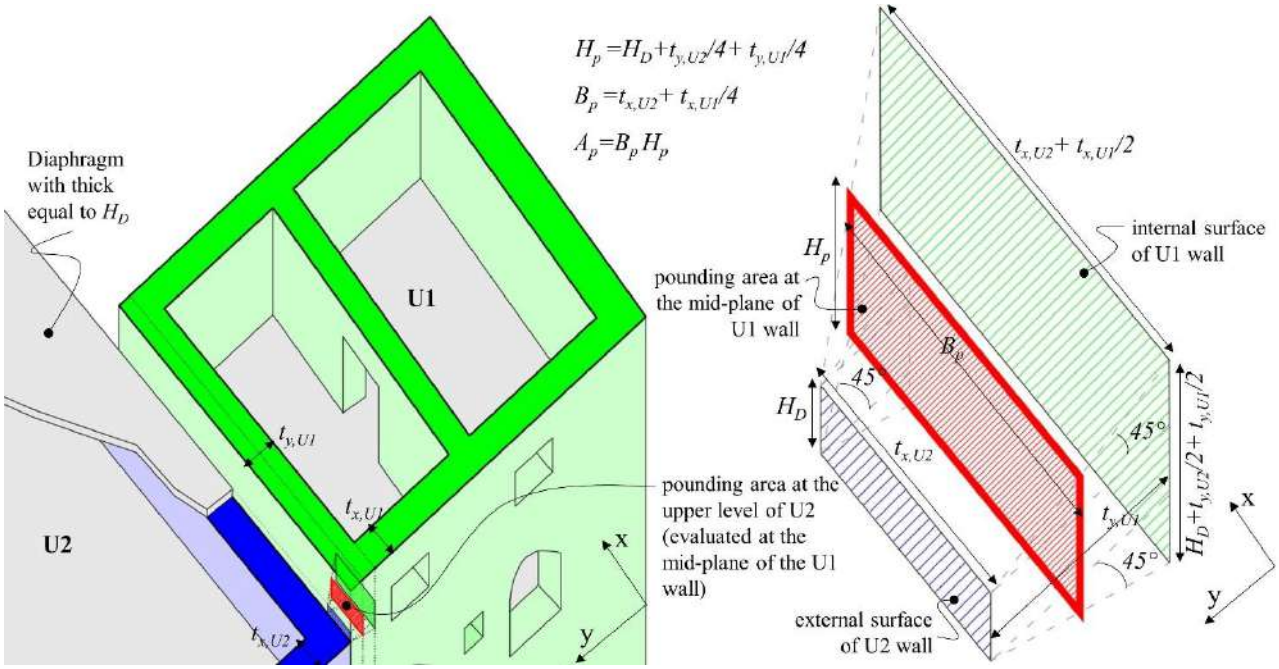

Figure 4.2.12. Graphical definition of the pounding area.

Then, assuming a 45° load diffusion and referring to the mid-plane of the wall belonging to the impacted building, one can compute the Ap. With a diaphragm thickness H_D of 0.15 m (for all the building levels) and wall thicknesses ($t_{x,U1}$, $t_{x,U2}$) equal to 0.70 m and 0.65 m, at the first and the two upper building levels, respectively, one can calculate for them Ap equal to 0.44 m^2 0.39 m^2.

Finally, from the checks made on the structural pounding for each time history, it is possible to know when compressive failure (i.e. overcoming of the fm) occurs because of that phenomenon. In that case, an increase by one grade of the in-plane DL for the interested pier was conventionally assigned. Note that a parametric analyses on the effect of this conventional method has been also performed by supposing an increase of two or more grades of DL due to pounding. Results of these preliminary analyses have shown an almost negligible effect on the number of grades assumed for such an increment. That was merely due to the DL assignment criterion adopted in this study, based on the "minimum DL" concept that consider the damage state of all the pier at a certain level (see §3.1) and not only a single peak of damage.

4. DERIVATION OF FRAGILITY CURVES

4.1. Adopted methodology

Among several procedures available in the current literature for characterizing the relationship between engineering demand parameter (EDP) and intensity measure (IM), in the present study, the Cloud Method (e.g. Jalayer (2017)) was adopted - so that at each record represents a single IM value and corresponds to a single EDP response. As introduced in §2.2, natural unscaled ground motions (i.e. 370 and 320 for rocky soil and free-field models, respectively), selected to be representative of a fairly large range of IMs, were adopted to model the record-to-record variability. Hence, fragility curves were computed by estimating the probability of exceeding (P_{DLi}) of different i-th DL given a

level of ground shaking quantified through the IM. As usual in risk analyses (Baraschino et al. (2019)), a lognormal cumulative distribution function was assumed for the fragility function, as following:

$$P_{DLi}(DL > DL_i|IM) = \Phi\left(\frac{\log(\mu|_{PGA})}{\sigma|_{PGA}}\right) \quad (4.2.2)$$

where $P(DL>DL_i|IM)$ is the probability that a ground motion with a certain intensity measure IM will cause the collapse, Φ is the standard normal cumulative distribution function (CDF), μ is the mean of the fragility function and σ is the lognormal standard deviation. The IM adopted in this work is the peak ground acceleration (PGA). representing also a quite common and robust choice for URM buildings. This choice reflects a quite common choice for URM buildings, but it is mostly related to the fact that previous works already testified results tend to be less or equally dispersed by considering, as IM, the PGA rather than, for example, $Sa(T_1)$ (see Kita et al (2020); Brunelli et al. (2021b)). Note that, for each k-th analyses, the geometrical mean of the PGA associated with the k-th accelerations in the X and Y directions was used. This choice may be inconsistent in the case of fragility curves derived for OOP mechanisms, for which the failure is mainly due to the PGA of a specific direction of the seismic acceleration (Y direction for 1FMs and 2FMS; X direction for TMs). However, aiming to compare and combine those curves (see §4.5), the authors reputed reasonable to assume for OOP mechanisms the same IM assumed also for the IP response. Furthermore, note that the not-amplified PGA values were considered for the computation of the fragility curves regarding the freefield model (i.e. the PGA values of the freefield condition coincide with the rocky-soil ones).

A description of the derivation of fragility curves, of each structural unit, combined between both IP behaviour and local mechanisms (i.e. OOP and pounding), defined in §4.5, is described in the following. Once IP fragility curves were evaluated directly on the DLs occurred for the NLDAs, due to the difficulty associated with the definition of different DL thresholds to derive opportune fragility curves specifically for structural pounding, the latter was taken into account by negatively affecting the IP response (see §3.3). That condition is considered as IP*. Then, to combine the IP* and OOP fragility curves, for each structural unit, in unique curves considering for both the behaviours, the most punitive condition between IP* and OOP is considered for each time-history. For example, for a specific time history, for which a certain PGA is associated, the worse among the OOP mechanisms of U1 led to DL4, whereas IP* led to DL2. Hence, for the combined fragility curves of U1, the reference PGA is treated to compute the mean and dispersion values of the fragility curve of DL4.

4.2. Bedrock associated with the global response

Figure 4.2.13a-c groups the 370 time histories as a function of the attained DL; each record is associated to its respective PGA. As expected, the DL tend to be higher for increasing PGA, especially from DL2 to DL3. A detail of the number of cases for which a certain DL occurred during the NLDAs is illustrated in Figure 4.2.13d, showing that $U1_A$ is characterized by the higher vulnerability. Indeed, DL4 and DL5 occurred more frequently for U1A with respect to $U2_A$ and $U3_A$; moreover, DL0 occurred in a very low number of cases for $U1_A$. Anyhow, those considerations are merely qualitative and results are better interpreted in terms of fragility curves in Figure 4.2.14a, where they are plotted for each structural unit in aggregate ($U1_A$, $U2_A$ and $U3_A$) for the different DLs (from 1 to 5). Table 4.2.9 summarizes the results of the fragility curves in terms of μ and $\ln(\sigma)$ values. In particular, one can see the increasing in the μ values of the curves associated with increasing DL values; furthermore, similar σ values can be observed for all the curves.

Table 4.2.9: Results of the IP fragility curves for the five DLs in terms of μ/ln(σ) values, under the rocky soil case.

	DL1	DL2	DL3	DL4	DL5
$U1_A$	0.091/0.390	0.222/0.318	0.368/0.185	0.457/0.200	0.592/0.215
$U2_A$	0.133/0.399	0.269/0.287	0.433/0.200	0.497/0.159	0.616/0.210
$U3_A$	0.125/0.448	0.257/0.288	0.450/0.201	0.482/0.196	0.606/0.219
$U1_I$	0.108/0.339	0.229/0.322	0.342/0.157	0.417/0.189	0.553/0.245
$U3_I$	0.099/0.425	0.187/0.360	0.254/0.457	0.361/0.327	0.441/0.383

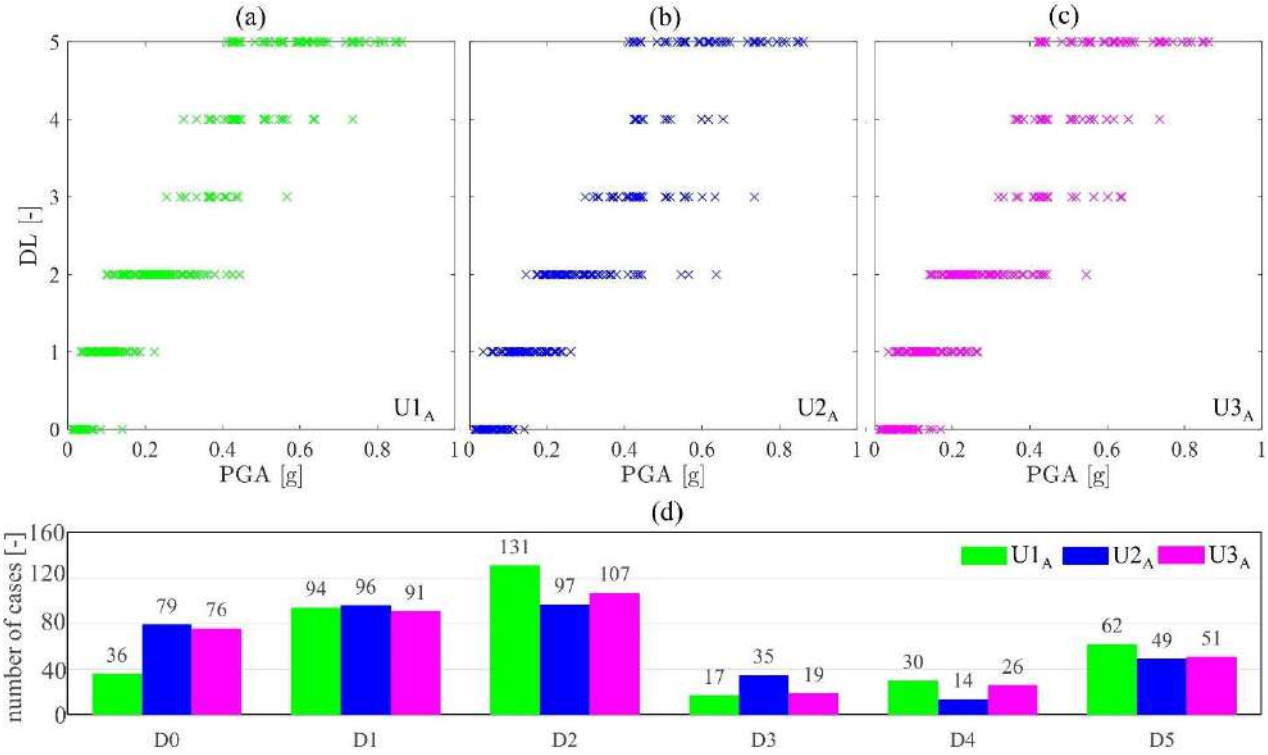

Figure 4.2.13. IP response of $U1_A$, $U2_A$ and $U3_A$ under the rocky soil assumption: (a, b, c) DL occurred for the 370 time histories as a function of their respective PGA geometrical mean (between the PGAs associated with the X and Y directions); (d) number of time histories for which a specific DL occurred.

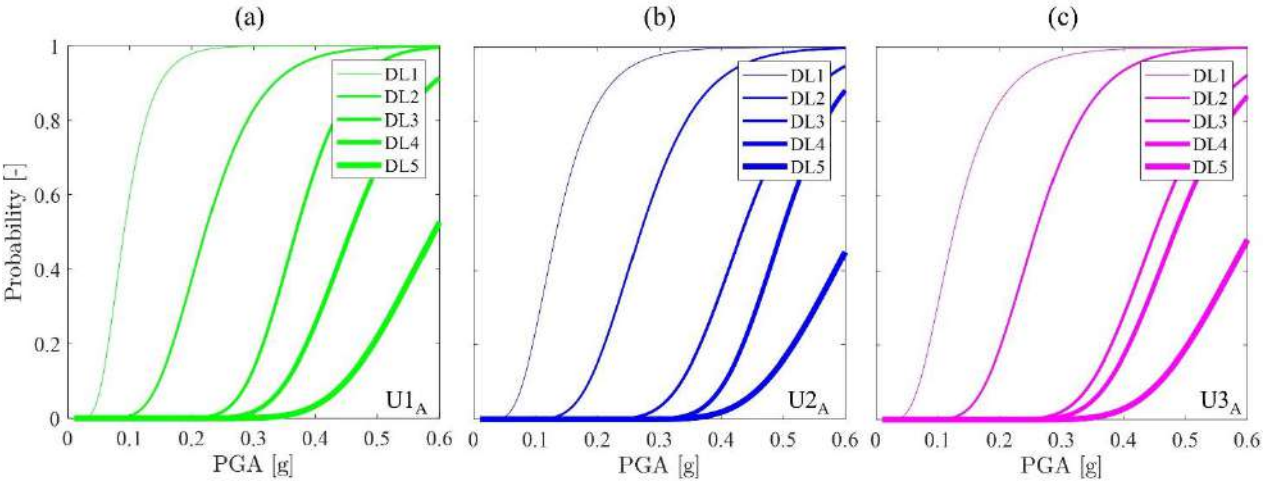

Figure 4.2.14. (a, b, c) Fragility curves of the IP behaviour (rocky soil assumption) in terms of the five DL for the three structural units.

Aiming to better compare the fragility curves reported above as a function of specific DL, one can observe Figure 4.2.15. In particular, results shows that $U1_A$ is characterized by the higher IP vulnerability as well as that $U2_A$ and $U3_A$ have similar seismic fragility. The higher vulnerability of $U1_A$ cannot be associated mainly with its structural features, as it presents a compact geometrical plan

as well as the high RA (with respect to the other units). The justification of this result can be searched in the dynamic response of the unit during seismic action. As also highlighted in Angiolilli et al. (2021), this trend confirms that pushover analyses describe in a quite rough way the actual seismic behaviour of buildings in aggregates. Indeed, the capacity curves of Figure 4.2.7 illustrated that $U1_A$ was not the most vulnerable unit for both the X and Y directions. On the other hand, the NLDAs expressed in terms of fragility curves show a different behaviour for $U1_A$. Furthermore, in Figure 4.2.15 one can observe the "aggregate-effect" for the only U3 cell by comparing the $U3_A$ and $U3_I$ curves (solid and dotted lines, respectively). In particular, it is clear the benefit offered by the confinement of the adjacent structural units to U3 especially for increasing DL values, as μ is decidedly lower for $U3_I$ with respect to that of U3A.

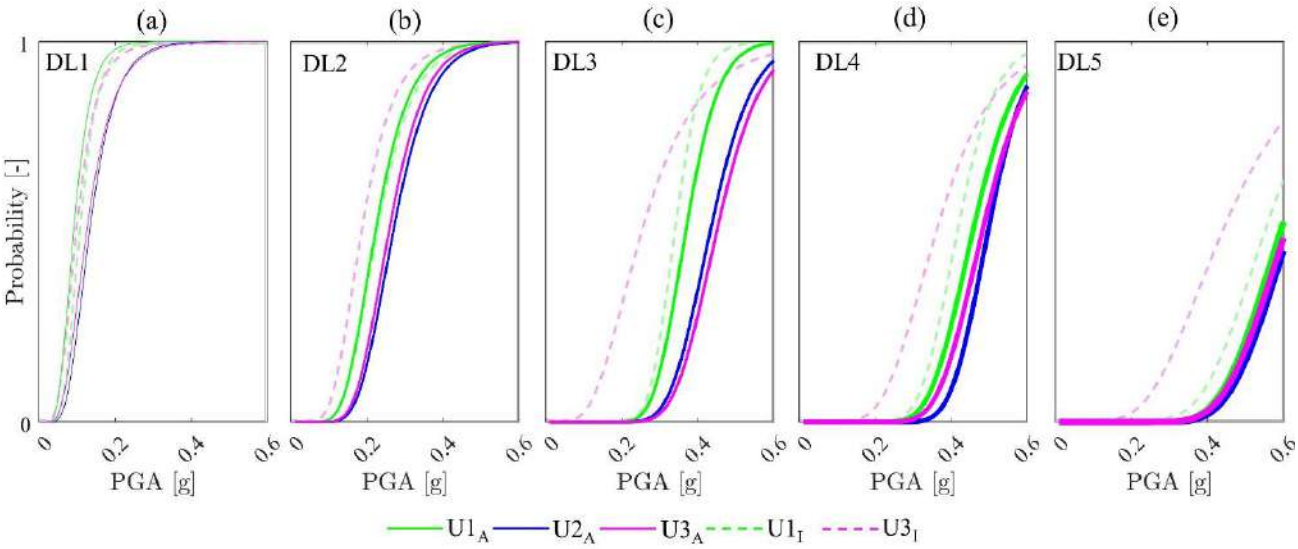

Figure 4.2.15. (a, b, c, d, e) Comparison between fragility curves obtained for specific DL (from 1 to 5) and different structural units ($U1_A$, $U2_A$ and $U3_A$) under the bedrock assumption. The dotted curves represent the response of $U1_I$ and $U3_I$.

4.3. Bedrock accounting for the local mechanisms

Figure 4.2.16 depicts the results in terms of maximum OOP displacement (d^*_{max}) occurred during the NLDAs for the four investigated structural units by only considering the 1FM; for the sake of brevity, the results considering 2FM and TM are discussed in the following directly in terms of fragility curves. Results of Figure 4.2.16 show that d^*_{max} value tends to increase for increasing PGA values, up to the attainment of the limit value d0 (for which the total overturning of the panel occurs). Furthermore, the results highlight the unstable OOP response, showing a consistent number of analyses ($d^*_{max,k}$ - PGA_k, points obtained for all the k time history) with d^*_{max} values lower than the A threshold or directly higher than CF threshold. Focusing only on the CF condition among the various units one can see that CF occurred more frequently for the façade of U1 (i.e. 79 times) although that case was characterized by a good OOP constitutive-law (it is worse only with respect to that associated with U3). This result is mainly due to the higher amplification in the floor accelerations occurred for that façade because of the higher structural height for which d* was evaluated (i.e. at base of the 3rd level for U3 and U1 - whereas for U2 and U4 it was evaluated at the base of the 2nd floor level) as well as the lower constrain level because of a free-side of the U1 building. Moreover, although U3 has the same structural height of U1, the best OOP constitutive-law and the lower floor accelerations occurred for U3 led to the lower number of certain failures (i.e. 26) with respect to that of U1. Finally, the consistent number of certain failures for U2 and U4 can be merely associated with their respective poor OOP constitutive laws since the amplification of the floor accelerations was lower for them (storey accelerations taken at the 2nd level).

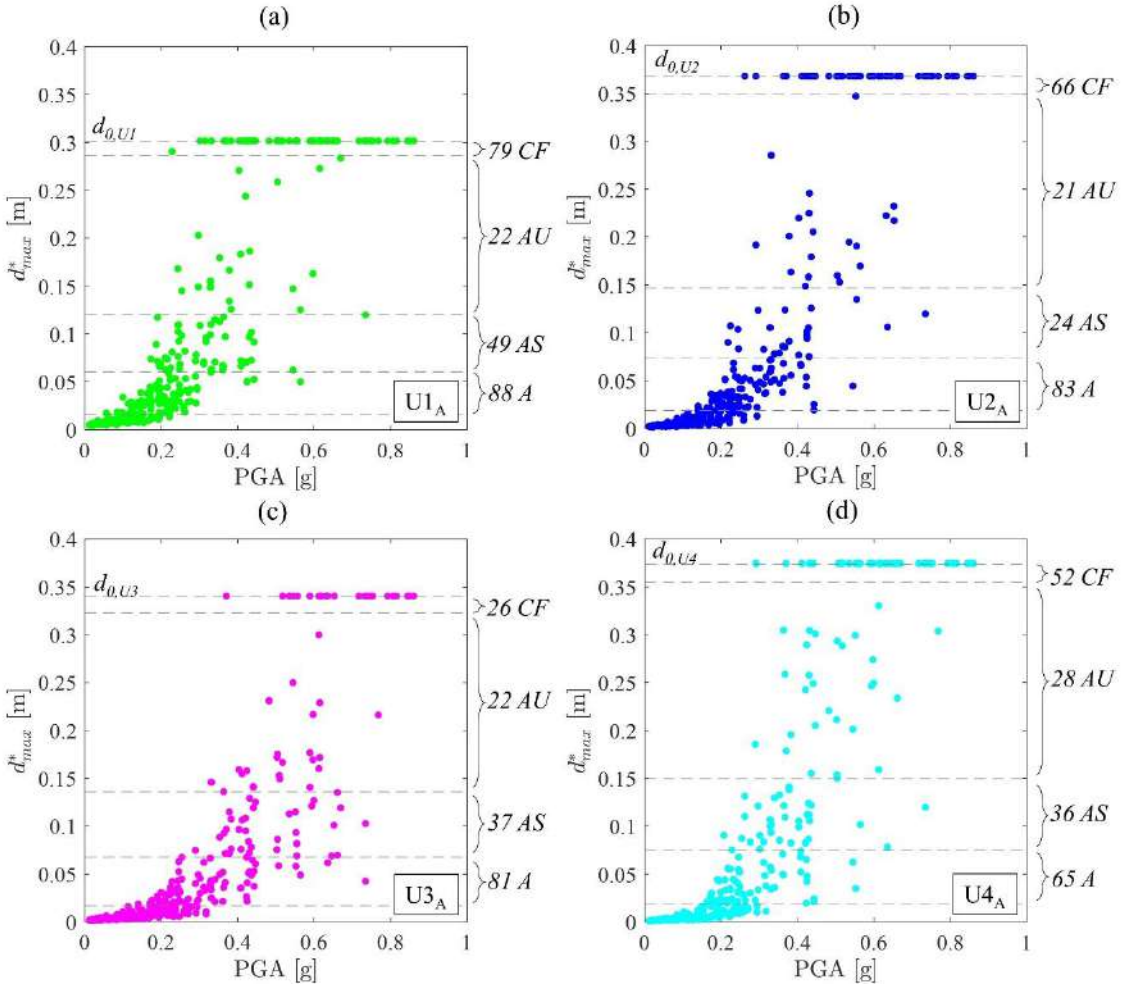

Figure 4.2.16. In that Figure 4.2.is also reported, for each structural unit, the number of time histories for which the various OOP limit states occurred.

Aiming to justify the consideration provided above related to the amplification of the floor accelerations, Figure 4.2.17a shows the comparison between the peak floor acceleration (PFA) (evaluated at the upper level of $U1_A$) and PGA values for all the 370 time histories, highlighting that PFA values are higher than the PGA ones, as usually observed in the dynamic response of structures under seismic actions. The PFA-PGA ratio (evaluated at the upper building levels) for all the structural units in aggregate are illustrated in Figure 4.2.17b. In particular, $U1_A$ and $U3_A$ (characterized by 4 stories) suffered higher floor amplification than $U2_A$ and $U4_A$ (characterized by 3 stories) confirming that filtering effect tends to be higher for increasing building levels (e.g. Degli Abbati et al. (2018)). Note that the $U1_A$ and $U3_A$ are characterized by 4 stories, whereas $U2_A$ by 3 stories. Note also that $U3_A$, being placed in the middle of the aggregate and, therefore, more confined in the seismic movement, is characterized by a slightly lower PFA-PGA ratio than $U1_A$, which has a free-side. It is important to observe how, in Figure 4.2.17b, the major amplification occurs for initial time histories (characterized by lower PGA values).

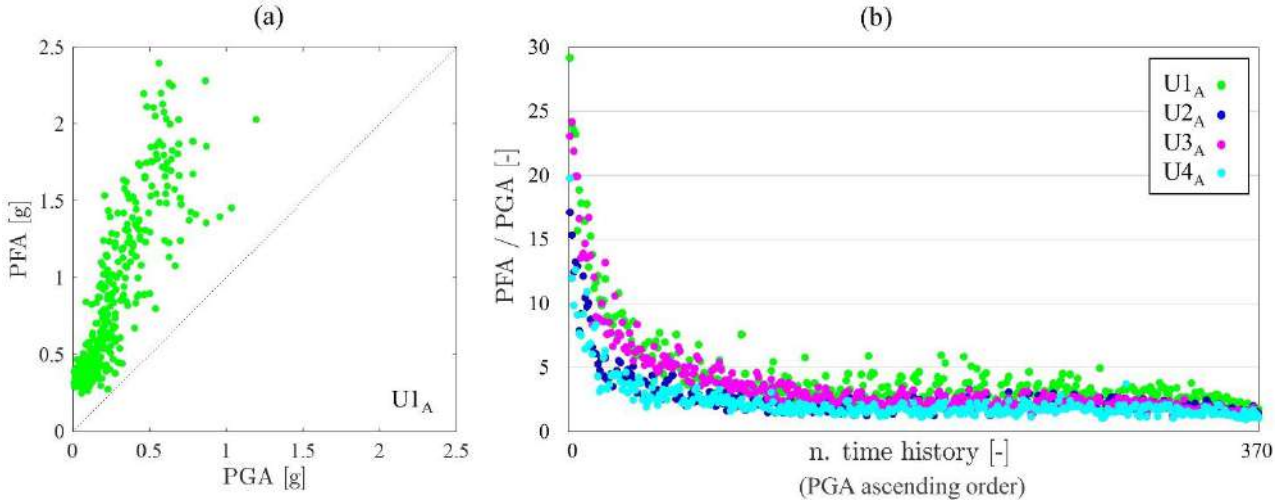

Figure 4.2.17. (a) PFA-PGA relations for U1A under bedrock condition; (b) PFA -PGA ratio for the 370 time histories at bedrock.

In general, results highlighted that OOP mechanisms were affected by the combination of PFA amplifications and constitutive law associated with that mechanism (based on the geometric-mechanical features and structural details of the wall subject to overturning).

Referring to fragility curves associated with OOP, due to the issue discussed above about the definition of DL thresholds, in Figure 4.2.19 a sensitivity analysis performed on this issue is reported. The figure focuses only to U1A under 1FM but similar effect of the sensitivity analysis was provided also for $U2_A$, $U3_A$ and $U4_A$, as well as for 2FM and TM mechanisms. In particular, results of Figure 4.2.19a-d regards the effect of different OOP thresholds (varied one by one with respect to those reported in Table 4.2.7): in Figure 4.2.19a the lower bound of A varied from $0.05d_0$ to $0.1\ d_0$; in Figure 4.2.19b the upper bound of A (and lower bound of AS) varied from $0.2d_0$ to $0.3d_0$; in Figure 4.2.19c the upper bound of AS (and lower bound of AU) varied from $0.4d_0$ to $0.5\ d_0$; in Figure 4.2.19d the upper bound of AU (and lower bound of CF) varied from $0.95d_0$ to $0.85d_0$. In general, the results show a moderate sensitivity of the fragility curves to the thresholds, especially to the upper bound of AS (or the lower bound of AU).

The OOP fragility curves of the four units are reported in Figure 4.2.19, by considering the three individual possible mechanisms (1FM, 2FM, TM). One can see that the most vulnerable condition for both A and AS regards the $U1_A$ under the 1FM assumption, especially for high PGA value. For low PGA values, $U1_A$ under 2FM assumption and $U3_A$ under TM assumption appear slightly more punitive. On the other hand, the most vulnerable condition for both AU and CF involve the $U4_A$ under the 2FM assumption. In general, one cannot see a clear trend among the different mechanisms, highlighting the importance of considering several mechanisms in the analyses of the OOP response.

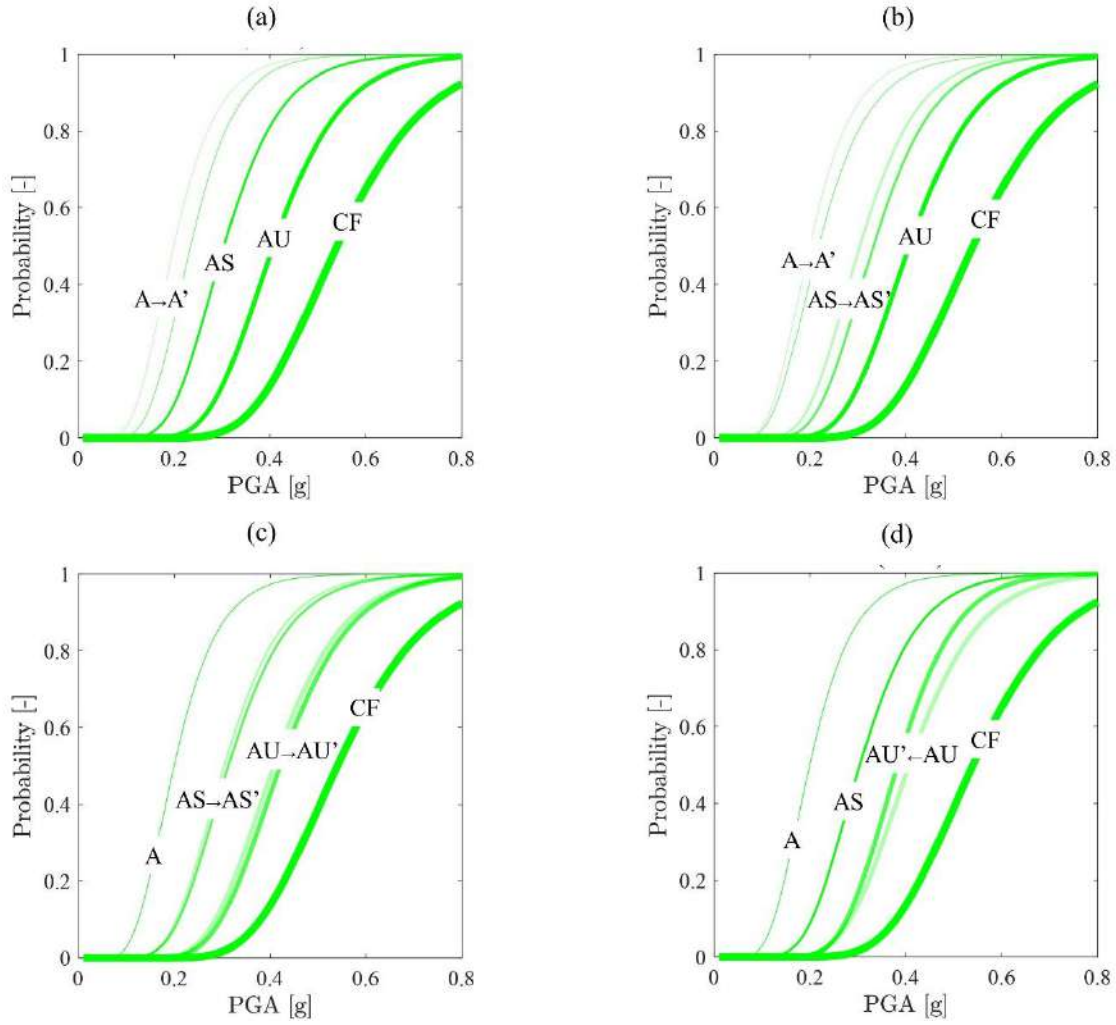

Figure 4.2.18. Sensitivity of the OOP fragility curves for the $U1_A$ on the different OOP thresholds (a) lower bound of A; (b) upper bound of A (and lower bound of AS); (c) upper bound of AS (and lower bound of AU); (d) upper bound of AU (and lower bound of CF).

Only for U4, one can see that 2FM is more severe than 1FM for all the four performance states. This is mainly because, in absence of interlocking, the 2FM is always characterized by a more severe constitutive law (see Figure 4.2.9) with respect to 1FM, due to disadvantageous geometrical conditions. Therefore, even if the storey accelerations taken into account for the 1FM (i.e at the 3rd floor) tend to be higher (because of the amplification effect) to those considered for the 2FM (evaluated at the 2nd floor), the constitutive law governs the overall OOP behaviour. Obviously, this statement is not always true for OOP mechanisms regarding walls characterized by good interlocking with the orthogonal walls, such as the U2 and U3 cases. Indeed, one can see that 1FM is always the prevailing governing mechanism for U2, whereas 1FM is more punitive than 2FM for U3 (except for the CF limit state). Furthermore, for U3, TM is the prevailing governing mechanism (also because 1FM and 2FM of U3 are characterized by a very good constitutive law).

Table 4.2.10: Results of the OOP fragility curves for the four OOP-DLs in terms of μ/ln(σ) values, under the rocky soil case.

	mechanism	A	AS	AU	CF
$U1_A$	1FM	0.199/0.363	0.304/0.310	0.407/0.277	0.540/0.274
	TM	0.200/0.454	0.322/0.423	0.434/0.344	0.539/0.295
$U2_A$	1FM	0.261/0.269	0.375/0.297	0.465/0.215	0.563/0.262
	2FM	0.297/0.298	0.417/0.225	0.521/0.210	0.589/0.230
$U3_A$	1FM	0.309/0.336	0.468/0.228	0.521/0.190	0.672/0.207
	2FM	0.351/0.317	0.492/0.196	0.587/0.189	0.539/0.226
	TM	0.213/0.482	0.319/0.399	0.461/0.378	0.510/0.269
$U4_A$	1FM	0.266/0.306	0.366/0.264	0.481/0.215	0.589/0.257
	2FM	0.219/0.291	0.319/0.267	0.370/0.288	0.492/0.366

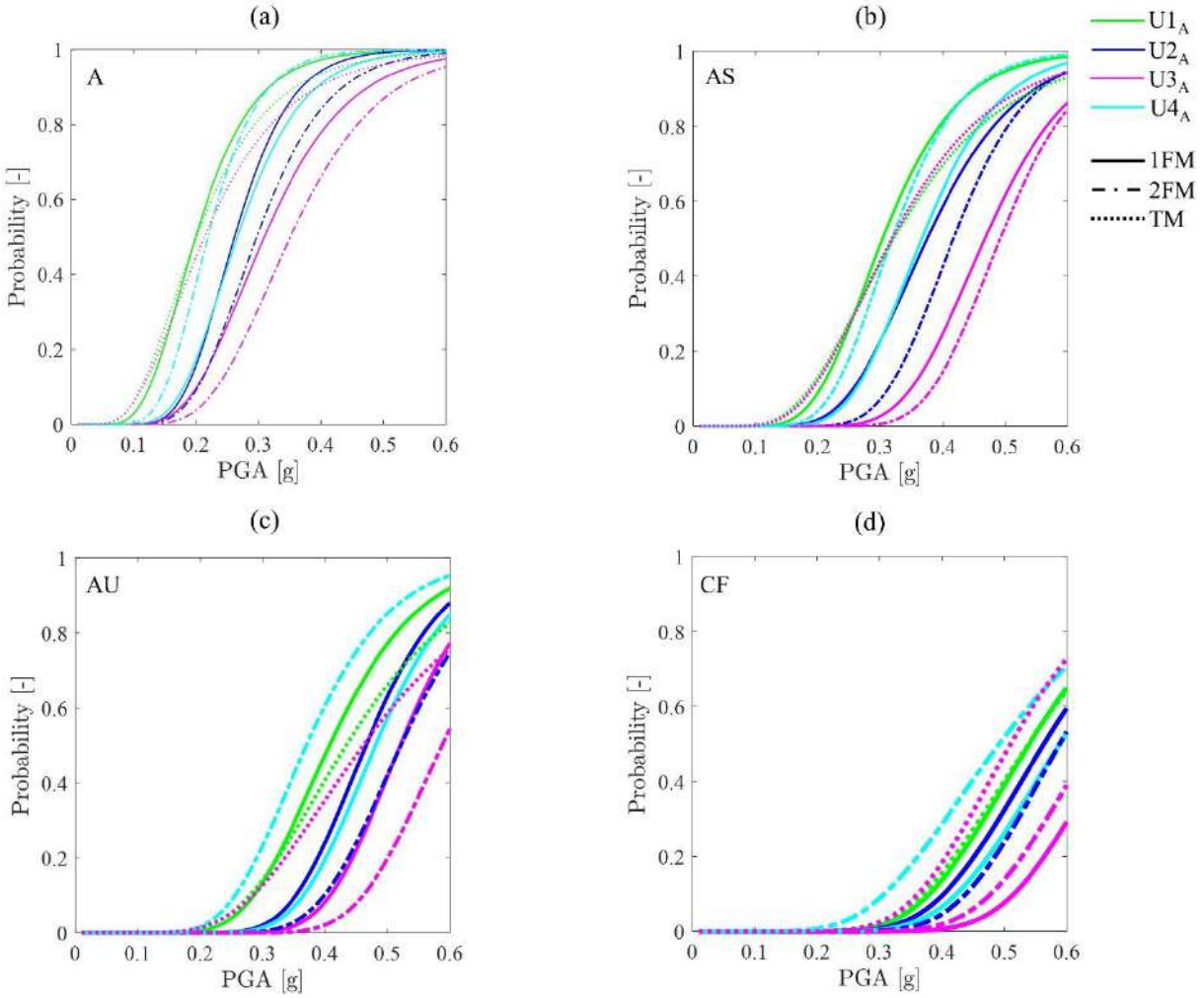

Figure 4.2.19. Fragility curves of individual OOP mechanisms at different performance states.

Aiming to statistically investigate the most severe OOP mechanism (1FM, 2FM or TM) occurred for the four structural units, Figure 4.2.20 shows their percentage of occurrence at the different performance states. This figure highlights that, as also commented above, it should be a good practice defining various possible mechanisms for each structure due to the difficulty in defining the prevailing mechanisms at priori when the record-to-record variability is explicitly accounted for. This is fundamental to derive fragility curves in a robust way, by taking into account the interaction between the various mechanisms. Indeed, the higher the percentage of occurrence for a specific mechanism (i.e. for U4 mainly governed by 2FM) the lower the effect in terms of fragility curves of combined mechanisms. The lower the prevalence of occurrence of a specific mechanism (i.e. for U1) the higher the effect in terms of fragility curves of combined mechanisms. This effect can be observed

in Figure 4.2.21, where the fragility curves of combined OOP mechanisms obtained through the criteria defined in Table 4.2.11 are illustrated.

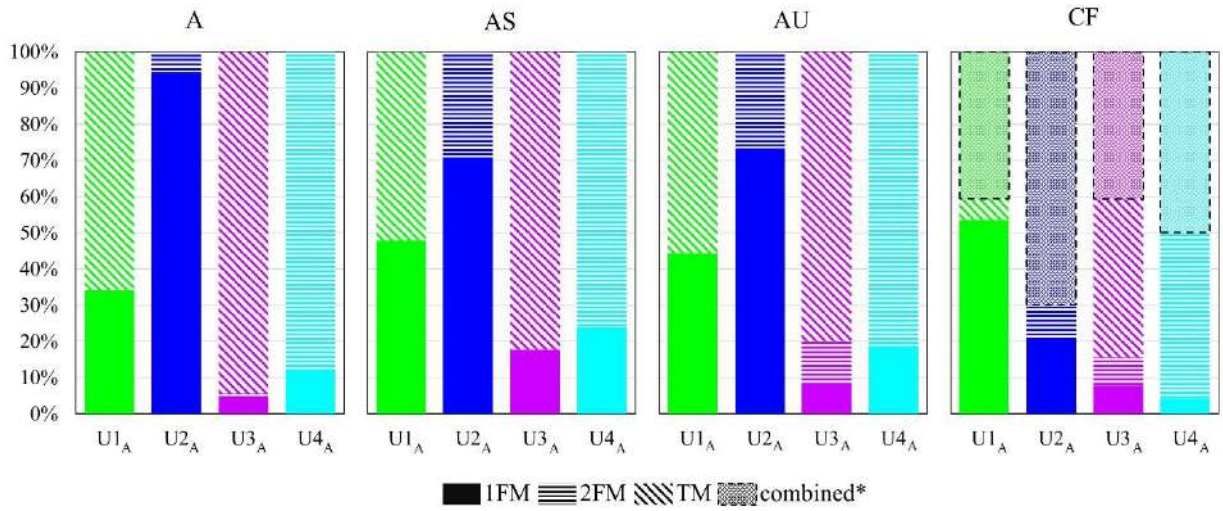

Figure 4.2.20. (a, b, c) Statistic investigation on the most severe OOP mechanism (1FM,2FM or TM) occurred for the four structural units at the differend DL. (* at least two mechanissms for which CF occurred).

Table 4.2.11: Results of the fragility curves of combined OOP mechanisms for the five DLs in terms of μ/ln(σ) values, under the rocky soil case.

	DL1	DL2	DL3	DL4	DL5
$U1_A$	0.175/0.392	0.266/0.311	0.404/0.384	0.495/0.274	0.557/0.259
$U2_A$	0.260/0.269	0.372/0.296	0.417/0.200	0.528/0.179	0.598/0.236
$U3_A$	0.193/0.398	0.309/0.358	0.444/0.292	0.647/0.208	0.700/0.181
$U4_A$	0.214/0.260	0.316/0.281	0.360/0.257	0.414/0.365	0.590/0.260

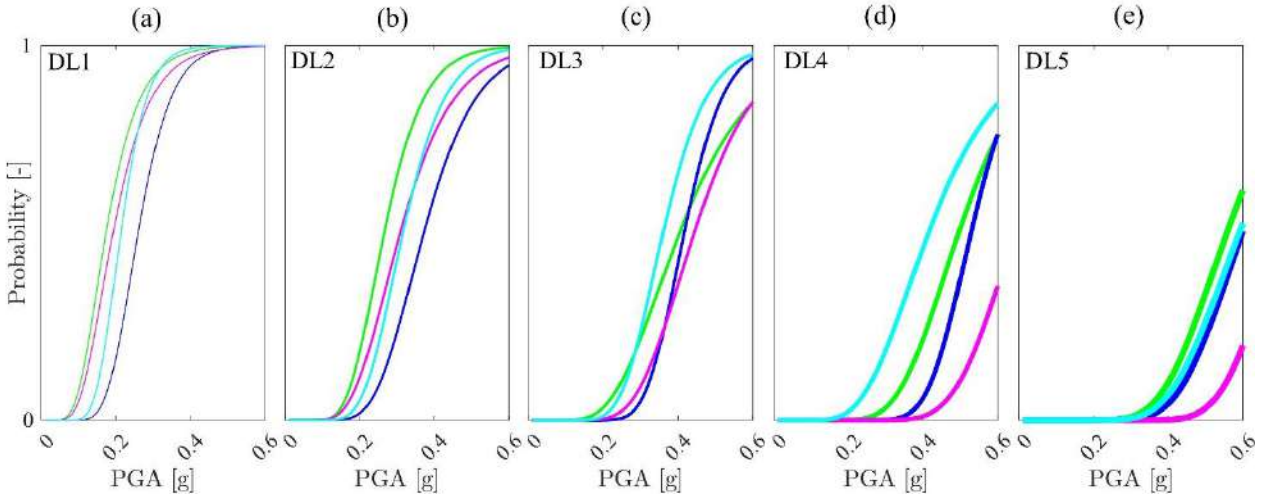

Figure 4.2.21. (a, b, c, d, e) Comparison between fragility curves of combined OOP mechanisms obtained for specific DL (from 1 to 5) and different structural units ($U1_A$, $U2_A$, $U3_A$ and $U4_A$) under the rocky soil assumption.

Finally, regarding the structural pounding, Figure 4.2.22a shows the pounding failure occurred between the adjacent structural units at the different building levels. In particular, between U2 and U1, pounding led to a consistent frequency of failure (about 32% of the 370 NLDAs) only at the third level (i.e. L3) because of the very small masses acting at the first two levels (see Table 4.2.8). On the other hand, between U2 and U3, failure occurred for only about 10% of the NLDAs, albeit with a failure diffusion among the three building levels. The effect of the pounding in terms of fragility curves can be observed in Figure 4.2.22b-d, where it is possible to see that the IP curves are negatively

affected (up to about 6% for $U3_A$) at the medium-high DL (i.e. DL3, DL4, DL5). Note that, the entity of negative effect could be more evident if a different method would have been adopted to define the building DL (i.e. not based on the minimum DL but on peak principles).

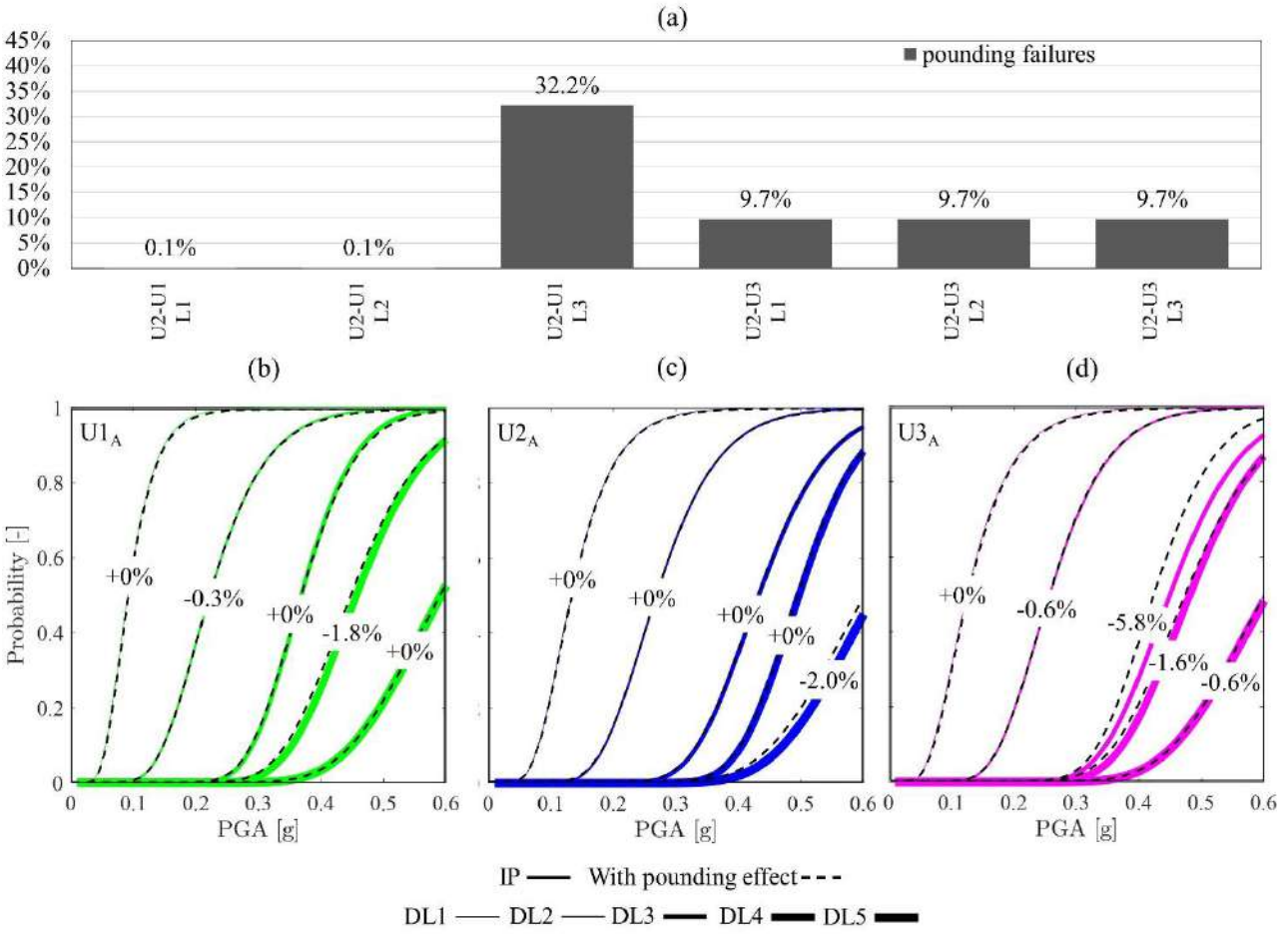

Figure 4.2.22. (a) Pounding failures occurred between U2-U1 and U2-U3 at the various building levels (L1, L2, L3), under rocky soil condition. (b, c, d) Effect of the consideration of the structural pounding on $U1_A$ and $U3_A$ (bedrock) (note that the percentage of variation are computed with respect to the μ value of the IP response).

4.4. Site amplification effects on both global and local behaviour

The site amplification effects on the vulnerability of the buildings in aggregate are here discussed. Regarding the IP response, that effect can be observed in Figure 4.2.23a in terms of fragility curves. In particular, it is possible to observe the strong reduction in the μ value in the case of freefield condition, as compared to those referred to bedrock condition. Moreover, for freefield and contrary to bedrock, the vulnerability of the different structural units is pretty similar to each other; $U1_A$ is not so much vulnerable as the other units as observed for bedrock condition (§4.2). The μ and σ values of the fragility curves are reported in Table 4.2.12. From Figure 4.2.23a one can see the response associated with individual buildings (dotted lines for $U1_I$ and $U3_I$) noting that the aggregate-effect positively influenced the nonlinear dynamic response of the buildings leading especially for $U3_I$ and medium-high DL. However, it is worth noting that the aggregate-effect is much more evident for bedrock than freefield.

Regarding the OOP response, first note that a not strong variation in the most severe OOP mechanisms (1FM, 2FM or TM) occurred for the four structural units at the four performance states, with respect to bedrock condition (see Figure 4.2.20). Hence, the site effect in terms of fragility curves is represented in Figure 4.2.23b. In particular, the curves representative of the freefield condition are more punitive with respect to the bedrock ones keeping almost the same trend observed for the

bedrock condition.

Table 4.2.12: Results of the IP fragility curves for the five DLs in terms of μ/ln(σ) values, under the freefield case.

	DL1	DL2	DL3	DL4	DL5
$U1_A$	0.066/0.500	0.136/0.405	0.217/0.200	0.246/0.243	0.367/0.364
$U2_A$	0.076/0.516	0.164/0.356	0.230/0.187	0.245/0.236	0.404/0.311
$U3_A$	0.076/0.519	0.148/0.370	0.204/0.248	0.239/0.209	0.392/0.321
$U1_I$	0.063/0.475	0.124/0.461	0.210/0.223	0.258/0.279	0.360/0.372
$U3_I$	0.060/0.508	0.114/0.429	0.156/0.302	0.202/0.323	0.314/0.415

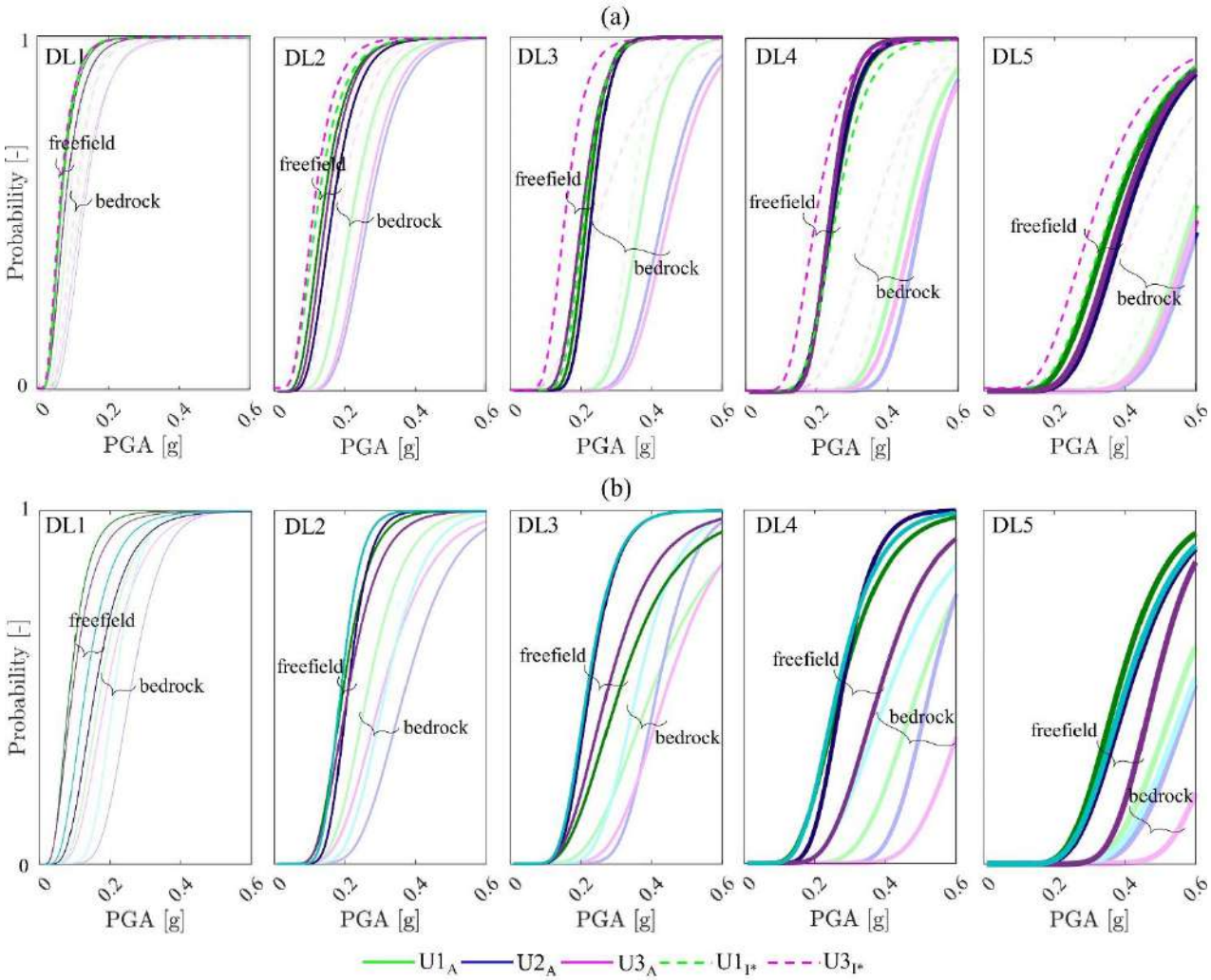

Figure 4.2.23. (a, b) Site effect (bedrock Vs freefield condition) on the IP (a) and OOP (b) fragility curves of the four structural units. (* not evaluated for OOP).

Regarding structural pounding, a higher effect of the site-amplification can be observed in Figure 4.2.24 with respect to the bedrock condition. In particular, pounding led up to 40% of failures (note that, for freefield, this value is computed on a small number of ground motions). Moreover, IP curves are negatively affected in a more diffused way (up to 5% for $U1_A$) at the different DL, as compared to the bedrock condition.

Table 4.2.13: Results of the fragility curves of combined OOP mechanisms for the five DLs in terms of μ/ln(σ) values, under the freefield case.

	DL1	DL2	DL3	DL4	DL5
$U1_A$	0.086/0.473	0.196/0.307	0.312/0.422	0.278/0.378	0.383/0.296
$U2_A$	0.158/0.439	0.210/0.231	0.226/0.281	0.280/0.258	0.413/0.303
$U3_A$	0.094/0.531	0.211/0.342	0.278/0.388	0.387/0.316	0.484/0.204
$U4_A$	0.131/0.458	0.190/0.237	0.220/0.294	0.267/0.341	0.404/0.309

Regarding structural pounding, a higher effect of the site-amplification can be observed in Figure 4.2.24 with respect to the bedrock condition. In particular, pounding led up to 40% of failures (note that, for freefield, this value is computed on a small number of ground motions). Moreover, IP curves are negatively affected in a more diffused way (up to 5% for $U1_A$) at the different DL, as compared to the bedrock condition.

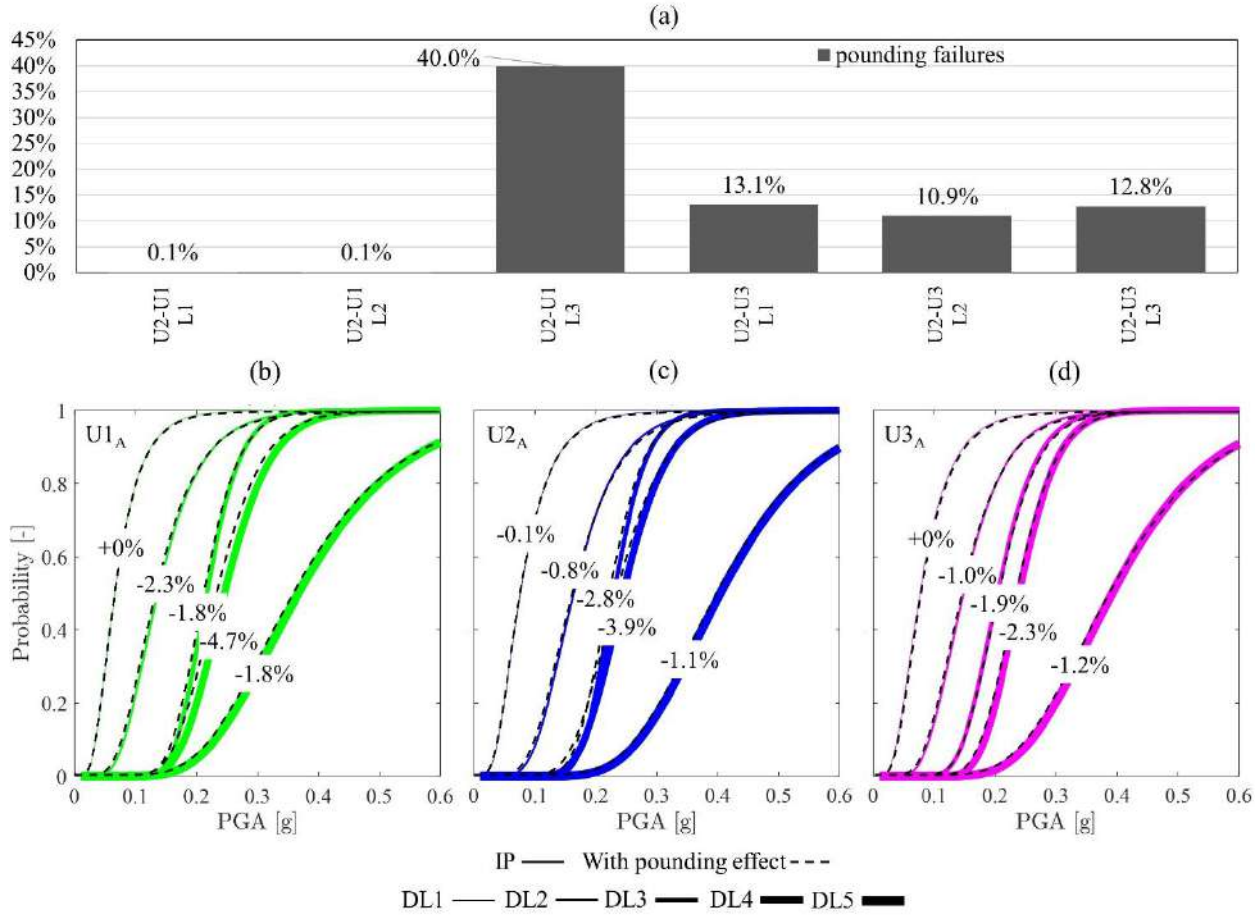

Figure 4.2.24. Effect of the structural pounding on $U1_A$, $U2_A$ and $U3_A$ (freefield). The percentage of variation is computed with respect to the μ value of the IP- freefield response.

Table 4.2.14: Results of the fragility curves of the combined IP-OOP mechanisms for the five DLs in terms of μ/ln(σ) values, under the freefield case (*only characterized by OOP behaviour).

	DL1	DL2	DL3	DL4	DL5
$U1_A$	0.066/0.500	0.127/0.394	0.214/0.215	0.230/0.238	0.364/0.362
$U2_A$	0.076/0.398	0.164/0.277	0.220/0.214	0.234/0.182	0.388/0.228
$U3_A$	0.074/0.504	0.137/0.362	0.200/0.213	0.239/0.209	0.392/0.321
$U4_{A*}$	0.131/0.458	0.190/0.237	0.220/0.294	0.267/0.341	0.404/0.309

4.5. Integration of the in-plane response with the local analysis

To derive fragility curves associated with combined global and local analysis, for each time history, the highest DL produced by them was considered (see also §4.1). Hence, giving a specific DL, if a prevailing failure mode is observed, the combined curve almost coincides with the most severe one. On the other hand, if one cannot observe a prevailing failure mode between IP or local mechanisms, the combined curve is much more severe than those associated with individual analyses.

Figure 4.2.25 shows the comparison between fragility curves of the four structural units under bedrock and freefield conditions, for each DL. Those curves are representative of individual mechanisms (IP* or OOP) as well as of combined analyses. Since pounding effect was already discussed in the previous section, here only IP* is reported for the sake of clarity. Note also that in the case of the filling structural unit $U4_A$, the combined curve coincides with the OOP one. The results show that DL1 is governed by the IP* response and, therefore, the combined fragility curve coincide exactly with it. Also for DL2, IP* prevails on OOP but, especially for U1A and U3A, the fragility curves of combined mechanisms are slightly more severe than the IP* ones. This means that for some time histories, OOP mechanisms led to higher DL as compared to IP*. The effect of the combined analyses could be better observed for the DL3 curves, especially for $U1_A$ and $U3_A$ under bedrock conditions, for which OOP prevails on the IP* response for low PGA values (up to about 0.4g). For freefield, the effect of the combined analyses is almost negligible as the IP* behaviour is much more severe than OOP. For DL4, one can observe similar trends commented for DL3 although less interaction between mechanisms can be observed. Finally, for DL5, one can observe that the IP* response tends to become as severe as (or even much more severe) the OOP one because a damage concentration usually occurs mainly on the elements located at the bottom building level, with a consequent strong reduction of the seismic amplification at the upper floor (where the OOP is evaluated). This result confirms the outcomes reported in (Angiolilli et al. (2021); Lagomarsino et al. (2022)) at the collapse performance state. In particular, for DL5, OOP prevails for $U1_A$ whereas IP* prevails for U2A and $U3_A$.

The same results of Figure 4.2.25 are illustrated in Figure 4.2.26a (focusing only to IP*+OOP mechanisms) by comparing the fragility curves of the structural units given a specific DL. This plot is important to understand which is the most vulnerable unit for each DL. In general, $U1_A$ tends to be the most vulnerable structural unit for all the DL and both soil conditions, although the extreme vulnerability of $U4_A$ prevails for DL4 (bedrock), due to its scarce OOP behaviour. Note that passing from bedrock to freefield, the high vulnerability of $U4_A$ is strongly reduced (at severe DL), as OOP is no longer the prevailing mechanism.

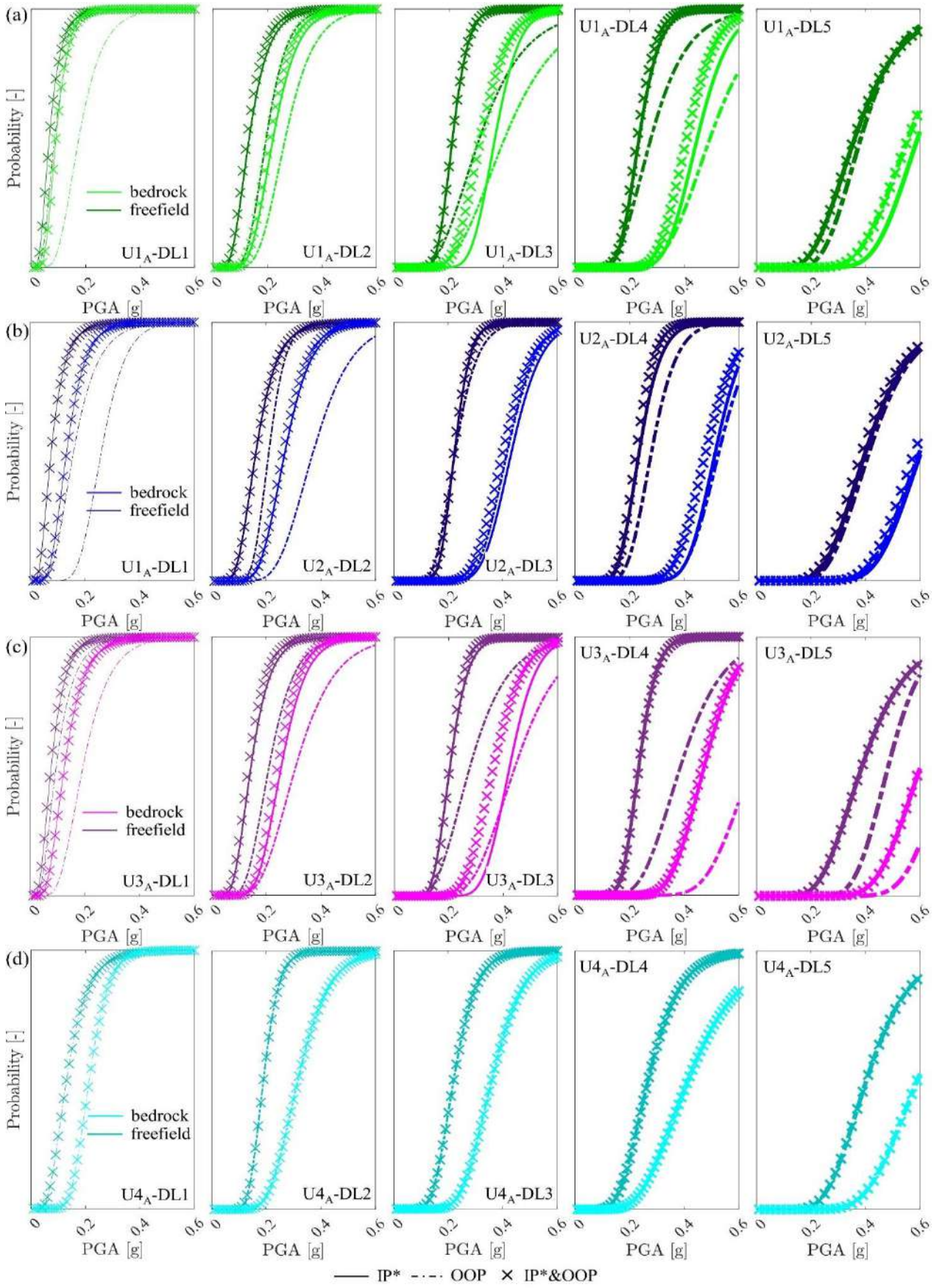

Figure 4.2.25. (a, b, c, d) Fragility curves related to IP* and OOP mechanisms as well as the combined ones (IP* represents the curve with pounding effect) for all the structural units.

Table 4.2.15: Results of the fragility curves of the combined IP*&OOP mechanisms for the five DLs in terms of μ/ln(σ) values, under bedrock and freefield conditions (IP*=in plane affected by pounding; *only characterized by OOP behaviour).

soil	unit	DL1	DL2	DL3	DL4	DL5
bedrock	$U1_A$	0.091/0.385	0.209/0.304	0.316/0.248	0.409/0.205	0.573/0.229
	$U2_A$	0.132/0.398	0.262/0.277	0.401/0.214	0.480/0.188	0.580/0.229
	$U3_A$	0.125/0.448	0.243/0.274	0.364/0.235	0.468/0.210	0.601/0.212
	$U4_{A*}$	0.214/0.260	0.316/0.281	0.360/0.257	0.414/0.365	0.590/0.260
freefield	$U1_A$	0.066/0.503	0.125/0.404	0.212/0.212	0.231/0.262	0.357/0.369
	$U2_A$	0.076/0.519	0.162/0.374	0.221/0.212	0.224/0.234	0.386/0.325
	$U3_A$	0.074/0.507	0.135/0.373	0.203/0.213	0.234/0.221	0.387/0.338
	$U4_{A*}$	0.131/0.458	0.190/0.237	0.220/0.294	0.267/0.341	0.404/0.309

Finally, from the results of Figure 4.2.26a it is possible to define the damage probability of each unit and each DL, as depicted in Figure 4.2.26b for both bedrock and freefield conditions. Therefore, it is possible to compute the mean damage $\mu_D=\sum_{i=1}^{5} DL_i P_{DL_i,\widehat{PGA}}$ (expressed as continuous values and depicted in Figure 4.2.26c) for each unit under both bedrock and freefield, where $P_{DL_i,\widehat{PGA}}$ is the probability associated with the ($\widehat{PGA}$ equal to 0.2604g) measured during the E2 seismic event and evaluated in Brunelli et al. (2021a) through an opportune deconvolutional study. It is worth noting that soil-foundation-structure (SFS) interaction was neglected in these comparison, while in the previous chapter and works (e.g. Brunelli et al. (2022a)) it was highlighted that SFS interaction combined with site-effect can also have a potential beneficial effect with respect to the only site-effect in terms of fragility curve. Therefore, only for greater completeness, it is reported in Figure 4.2.26c also the μ_D value in the case in which freefield is combined with SFS interaction by applying the corrective coefficients provided in Brunelli et al. (2022a) to the fragility curves obtained by fixed-base models. In general, results show a good consistency with the field evidence although a general overestimation of the DL with respect to the observed one can be noted, especially for U3, which represents the unit with the higher number of possible local mechanisms (thus strongly impacting the results obtained in this study). However, it is worth noting that the procedure proposed in this paper was not addressed to the simulation of the actual response of the aggregate to a specific event but instead to develop fragility curves.

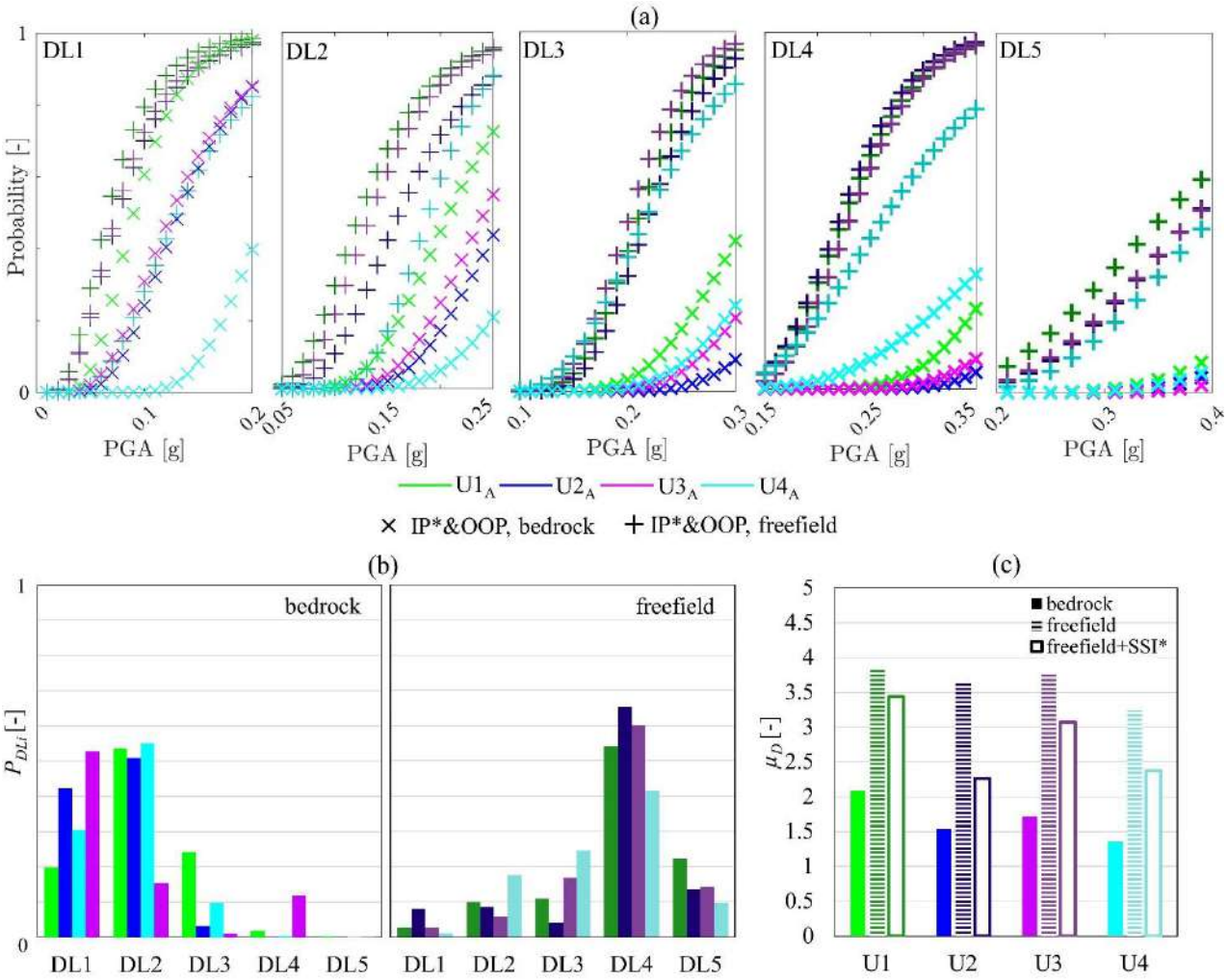

Figure 4.2.26. (a) Units by units comparison for each DL in terms of combined mechanisms (IP* and OOP) at both bedrock and freefield conditions; (b) DL probability density function of the four units under the two soil conditions; (c) DLμ of the four units under the two soil conditions, also in the case of freefield combined with SFS interaction (*estimated from Brunelli et al. (2022a))

5. CONCLUSIONS

This paper presents an integrated evaluation of both the in-plane (IP) behaviour and local mechanisms (out-of-plane, OOP, and structural pounding) within a procedure for deriving seismic fragility curves of mutually interacting existing URM buildings aggregated in a row layout. The procedure has been exemplified on a building aggregate located in Visso (Italy) and struck by the Central Italy 2016/2017 earthquakes.

The first important outcome of this study regards the inefficacy of capturing the actual seismic behaviour of masonry buildings in aggregate through nonlinear static analyses, at least with common load patterns proposed for ordinary isolated buildings. This outlines an important goal which future research efforts aim to be addressed especially for the development of practice-oriented seismic assessment procedures.

Therefore, the seismic behaviour of the aggregate was investigated performing nonlinear dynamic analyses (NLDAs), according to the Cloud Method approach, on the global 3D equivalent frame model of the aggregate accounting for the interaction effects among adjacent structural units, thus estimating more accurately their IP damage state. Then, storey accelerations derived from the 3D model - explicitly accounting for the filtering effect provided by the nonlinear response of the structure -provided more realistic seismic inputs to be used in the local mechanism assessment, which

is very sensitive to the record-to-record variability. Note that several plausible out-of-plane mechanisms, such as the overturning of the façades (the so-called cantilever mechanism) of both the upper level and the two upper levels of the buildings, as well as the tympanum mechanism, were investigated through the adoption of SDOF analytical models. Additionally, the structural pounding between adjacent structures was evaluated through a new simplified procedure, also based on the storey accelerations derived from the 3D model. According to that, the evaluation of the corresponding pounding force eventually may lead to additional IP damage level to the structural elements for which that phenomenon appeared.

The combination between IP and local mechanisms were then investigated also considering the site effects. Results highlighted that site-amplification may increase the failure probability associated with IP damage even if buildings, under the bedrock motion, appear vulnerable to local mechanisms. This result is obviously related to the investigated buildings, which are characterized by an inherent high IP vulnerability due to the low ratio between cross-section areas of masonry walls and openings. Note that the prevalence of the IP response for the investigated buildings is consistent with the field evidence.

On the other hand, under the bedrock condition, the results showed that, especially for medium damage levels (i.e. DL3), the overall seismic response of the buildings in aggregate was significantly affected by out-of-plane behaviour. For low damage level (i.e. DL1 and DL5), the overall seismic response of the buildings in aggregate was instead mainly governed by IP behaviour. In particular, for DL1, the IP behaviour prevails on the out-of-plane because of the effectiveness of the sporadic seismic strengthening system, preventing the OOP of the façades. For DL5, the IP response tends to become as severe as the OOP one because of the damage concentration that occurred mainly on the elements located at the bottom level, with a consequent strong reduction of the seismic amplification at the upper floor (where the out-of-plane is evaluated).

Especially at the bedrock condition, the combined fragility curve, considering the highest DL produced by the IP or OOP mechanisms, is much more punitive than those associated with individual mechanisms. Therefore, even if evaluated in a separate way, local and IP responses should be combined to obtain the actual response of the buildings under seismic action.

The study also highlights that it is fundamental to consider various OOP mechanisms to derive robust fragility curves. Indeed, although some geometric/mechanical configurations may suggest the prevalence of a specific mechanism rather than others, it is not recommended to consider only the most probable one because, within nonlinear dynamic analyses performed by using a large set of time histories, for some of them, it is possible that a less probable mechanism lead to the most severe response, thus negatively affecting the fragility curves.

Regarding the structural pounding, the simple engineering practice-oriented procedure introduced in this paper was a first attempt to consider this phenomenon in relation to seismic fragility curves, and obviously, further research into this methodology should be provided in future works. However, the proposed procedure could be easily introduced when explicit dynamic contact is not possible to introduce in the numerical model (as in the case of most of the current FEM software/framework available nowadays). The results showed that structural pounding could have a not negligible effect, especially for high-very high DL (i.e. DL3, DL4, DL5). Therefore, its evaluation must be encouraged in the seismic assessment of mutually interacting URM buildings in aggregate.

Finally, although some outcomes on the relationship between the IP and OOP response and its possible sensitivity to rocky/soft soil conditions may depend on the specific architectural/structural configuration of the examined aggregate, the procedure turned out quite effective in quantitively assessing such effects and could be conveniently replicated on other cases study.

CHAPTER 5

Large-scale risk assessment through the developed fragility curves

Summary:
Chapter 5 exploits the fragility curves calculated in Chapter §4 to generate damage scenario at urban scale in the village of Visso, including site and SFS interaction effects. The proposed approach leads to the definition of "site-specific" vulnerability studies conceived to be hopefully a useful support to mitigation policies at large scale.
The reliability of the results was checked by comparing the map of the damage estimated for the Visso village under the Central Italy earthquake through the use of developed numerical fragility curves to that deduced from the after-earthquake surveys.

A further deepening of the topic is investigated in Annex 5. In fact, currently, the intensity measure used to evaluate the on-site hazard in the seismic microzonation studies is different with respect to that adopted to derive structural fragility curves. So, hazard and vulnerability are both available for each site, but paradoxically cannot be combined. Trying to overcome such limitation, the effectiveness in the prediction of damage through the intensity measure typically adopted in the seismic microzonation studies was investigated in Annex 5.

Submitted to International Journal of Disaster Risk Reduction.

URBAN-SCALE SEISMIC DAMAGE SCENARIO OF URM BUILDINGS IN AGGREGATE SETTLED ON SOFT SOIL

Andrea Brunelli[1], Filomena de Silva[2], Serena Cattari[1]
[1]University of Genoa, Genoa, Italy
andrea.brunelli@edu.unige.it, serena.cattari@unige.it

[2]University of Naples Federico II, Naples, Italy
filomena.desilva@unina.it

Abstract:

The paper focuses on the seismic response of masonry buildings in the historical centre of Visso, severely hit by the 2016-2017 Central Italy earthquake. This represents an emblematic case of site effects and, also, of soil-foundation-structure (SFS) interaction. Maps of the observed damage at urban scale are compared with those derived using fragility curves calculated for the building stock that characterizes the Visso municipality. In particular, as quite recurring in typical small historical centres in Italy and Europe, the key feature of Visso municipality is to be mostly composed by building made by masonry (85%) of which the majority is in aggregate (93%).

Fragility curves were developed by a numerical procedure based on the execution of nonlinear dynamic analyses on 3D equivalent frame models, both fixed and compliant base accounting for site effects and SFS interaction. The numerical procedure was applied and validated in previous works to different archetypes representative either of an isolated school and buildings in aggregate. It aims balancing the computational effort with the potential of defining fragility curves customized for the built environment under investigation and, thus, hopefully capable to improve the reliability of risk assessment. Fragility curves for buildings in aggregate explicitly account for the recurring failure mechanisms that post-earthquake evidences have testified, i.e. in-plane and out-of-plane responses, interaction effects among adjacent units and pounding effects, as well.

In this work, these curves have been generalized to be applicable for a risk assessment at urban scale and the inventory of all data necessary to differentiate the vulnerability of the whole building stock has been finalized. The curves have been then applied for developing seismic damage scenario of the urban settlement. Results have shown that the match between the observed and simulated response is improved when the interaction between the structure and the soil is considered.

Keywords: seismic risk, fragility curves, masonry, buildings in aggregate, site amplification, dynamic soil-foundation-structure interaction, damage scenario.

1. INTRODUCTION

Earthquakes produced significant losses to urban historical centres as many Italian experiences emblematically testified (Sextos et al. (2018)), increasing the risk of their depopulation with detrimental social/economic implications. Such high seismic risk derives from a combined role of vulnerability and hazard. Vulnerability factors arise from the fact that urban centres were often developed in a poor economic contest and without following a specific urban development plan. Indeed, they are usually the result of a process of building growth across centuries, leading to buildings in aggregate with interacting units characterized by different materials, construction techniques, heights, state of preservation and, often, improvised renovations. In addition, the geomorphologic context in which urban centres are built often highlighted the important role on the seismic response of local amplification phenomena associated with topographic and soil stratigraphic effects.

That points out the need of effective procedures applicable at large scale to mitigate the risk. In this context, fragility curves represent an effective tool in predicting potential damage at urban scale. However, most of the literature works are addressed to residential buildings (e.g. Dolce et al. (2021a)) while very limited are those on buildings in aggregate, that constitute one of key feature of small urban centres. The majority of them are based on the heuristic approach (see Lagomarsino and Giovinazzi (2006); Vicente et al. (2014); Brando et al. (2017); Formisano et al. (2015)), while others are based on the analytical-mechanical (Leggieri et al. (2021)), analytical-numerical (see Angiolilli et al. (2021); Battaglia et al. (2021)), or pure empirical approaches (see Penna et al. (2022b)). However, for heuristic approaches, vulnerability factors specific for buildings in aggregate are based only on expert judgment; for analytical-mechanical or analytical-numerical approaches, the majority account only for the in-plane response without explicitly considering local mechanism effects (an exception is Angiolilli et al. (2021)); for the pure empirical approach, only the position of the unit is considered as additional vulnerability factors with respect to ordinary residential buildings. Moreover, most fragility curves are derived by neglecting site effects and soil foundation structure (SFS) interaction effects (e.g. Mosoarca et al. (2020)). To date, only the first effect (Formisano et al. (2021); Ademovic et al. (2022)) is sometimes considered by entering in the fragility curves with an amplified value of the intensity measure. The amplification factor can be estimated too much roughly through ground motion prediction equations (Sabetta and Pugliese (1996); Schiappapietra and Douglas (2020)), roughly from studies at national scale (e.g. Falcone et al. (2021)), and more accurately from seismic microzonation studies at city-scale (Pagliaroli et al. (2020)). A rigorous approach would require site response analyses under numerous input motions. The role of SE within the seismic risk at urban scale was for example investigated by De Risi et al. (2019). Recently, Abate et al. (2020) has shown an innovative seismic microzonation map based on a large-scale estimate of SFS interaction effects. Furthermore, Rovithis et al. (2017) proposed a methodology for assessing SFS interaction at large-scale using simple calculations within structural and geotechnical dynamics. Very few studies (see Brunelli et al. (2022a); Petridis and Pitilakis (2021)) - that explicitly included these effects in the computation of fragility curves - revealed that the so-estimated damage can be significantly higher than that associated with the current approximated approaches, emphasizing the importance of considering site and SFS interaction effects. Such evidence highlights the need of "site-specific" vulnerability studies, whose results can be exploited to generate simple but accurate maps of damage useful in the urban design, in the post-earthquake emergency and mitigation policies.

Within this context, the paper proposes the use of fragility curves derived in previous works from a numerical approach (Brunelli et al. (2022a); Angiolilli et al. (2022a))), that were customized for a specific built environment with the aim of balancing the computational effort with the desirable improvement of the reliability of risk assessment. More specifically, the demonstrative case study adopted in the study is the historical centre of Visso hit by the Central Italy 2016/2017 earthquake. The main features of Visso's municipality in terms of both subsoil condition and building types are

described at §2, together with the approaches adopted to collect all data necessary to fix the "inventory" phase of the risk analysis. Then, section §3 illustrates, firstly, the procedure adopted in the previous works to derive the fragility curves representative of specific archetypes (§3.1), and, then, how these curves have been generalized in this study to be presentative of building classes with homogenous behaviour, as typical of risk analyses at large scale (§3.2). Fragility curves were developed by a numerical procedure based on the execution of nonlinear dynamic analyses on 3D equivalent frame models, both fixed and compliant base accounting for site effects and SFS interaction. The archetypes which this paper focuses to are inspired by masonry buildings in aggregate, that constitute the key feature of Visso's historical centre, as well as most of Italian and European small historical centres. Finally, fragility curves on such specific archetypes were exploited to develop damage scenarios at urban scale (§4).

2. ANALYSIS OF SUBSOIL CONDITIONS AND BUILDING TYPES IN THE HISTORICAL CENTRE OF VISSO

2.1. Morphology, soil properties and site effects of the Visso valley

As shown in the map and cross section in Figure 5.1a, the Visso village is settled on an alluvial valley in which the three seismically homogeneous zones Mops 1041, 2001 and 2002 were identified during the 3rd level seismic microzonation studies (MZS3 (2018)). Mops 1041 is the outcropping of the geological bedrock, while the others pertain to deposits mainly made of sandy gravel soil alternated or joint to clayey silt and silty clay up to a depth from 2m to 15m in Mops 2001 and from 2m to 40m in Mops 2002. The historical URM built heritage lays closer to the valley edges on Mops 2001 and 2002, while the most recently urbanized area is located in the middle of the valley on Mops 2002.

During the seismic microzonation study, a borehole and a downhole test were executed in the centre of the valley down to 35 m. The corresponding soil layer and shear wave velocity, V_S, profile are indicated as DH in Figure 5.1b and were assumed as a reference for the subsoil model of the whole Mops 2001. The geotechnical model was validated by comparing the predominant frequency resulting from 1D and 2D (Cattari et al. (2019b); Brunelli et al. (2021a); Brunelli et al. (2022c)) site response analyses with that derived from records of ambient noise interpreted through the horizontal to vertical spectral ratio (HVSR).

The soil profile of Mops 2001 was inferred from the B4 and B5 boreholes. In lack of direct measurements, V_S was obtained through correlations with the number of blows of standard penetration tests (N_{SPT}) reported in Pietrantoni et al. (2013), Fabbrocino et al. (2015), Palmer and Stuart (1957), Kiku et al. (2001), Uma Maheswari et al. (2008), Fauzi et al. (2014), Fatehnia et al. (2015), Pérez-Santisteban et al. (2016), Gautam (2017), Thokchom e al. (2017) and Rezei et al. (2018). These correlations were calibrated on subsoil profiles all around the world; hence their reliability for the subsoil of Visso was firstly checked against the outcomes of the downhole tests. To this aim, they were applied to the N_{SPT} executed in the sandy gravel in the borehole DH, as well as in the clayey silt in the shallowest zone of B1, B2 and B3, leading to the V_S values plotted in Figure 5.1b through the light grey lines. The correlations by Imai and Yoshimura (1970) and Lee (1992) for clayey silt and by Ohta and Goto (1978) for Sandy gravels led to a closer match with the DH values and were consequently applied to the N_{SPT} measured in the borehole B4 to estimate the V_S profile reported in red in Figure 5.1b. Finally, the bedrock depth was set at 18 m after a calibration on the frequency measured through the HVSR2.

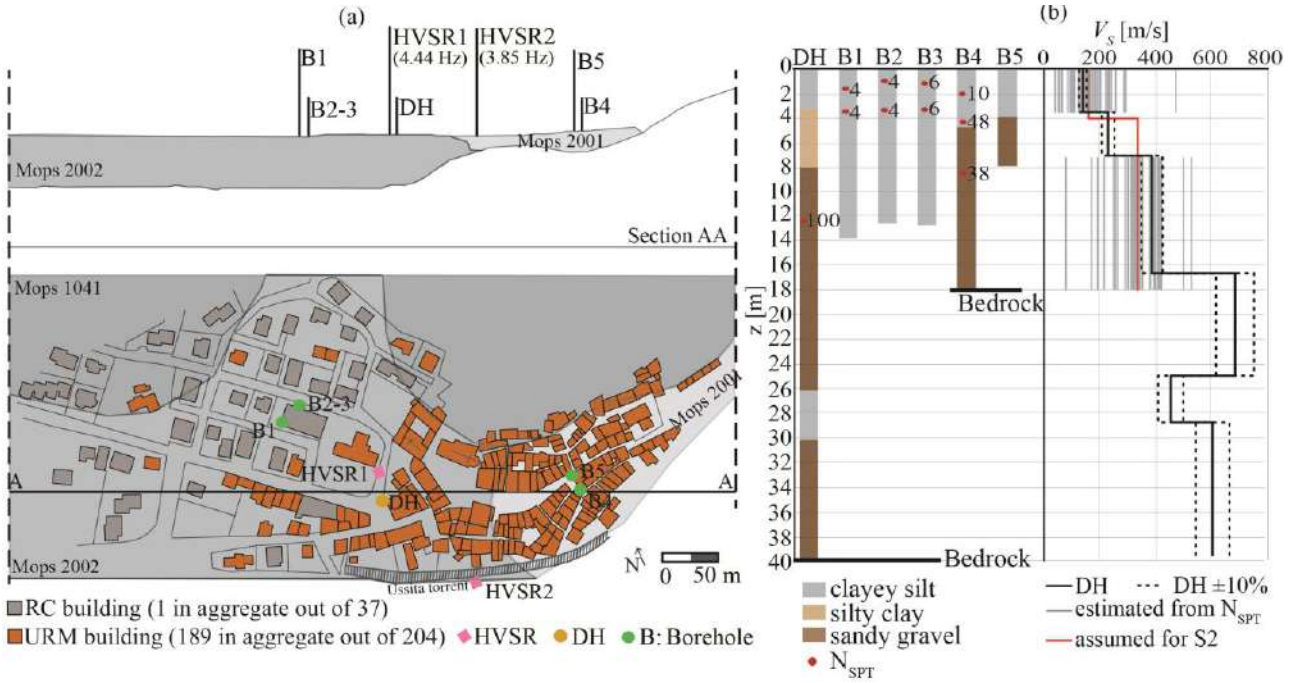

Figure 5.1. Map and cross section of the seismically homogeneous zones with location of on site surveys (a); soil and shear wave velocity profile used to generate the subsoil geotechnical model (b).

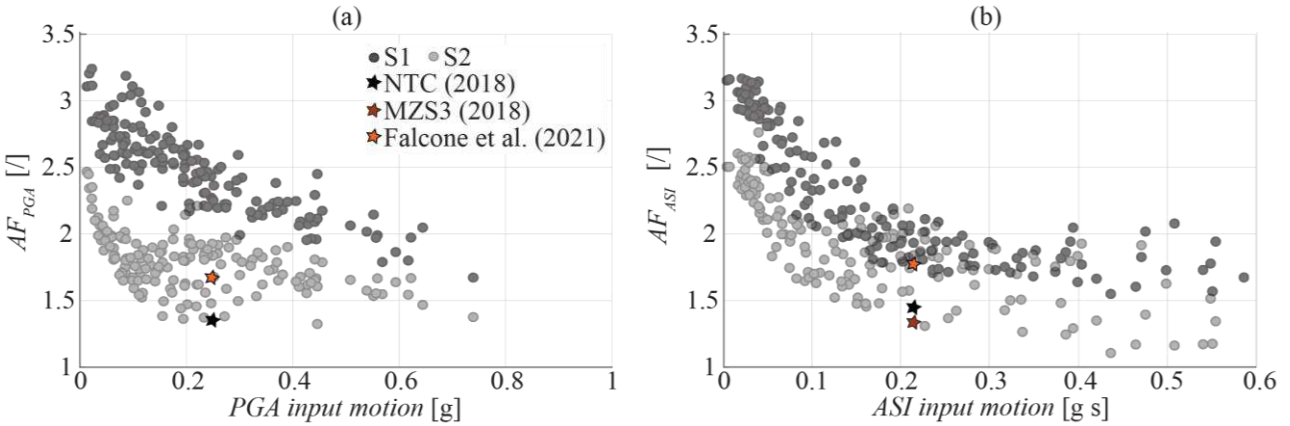

Figure 5.2. Amplification factors in (a) PGA and (b) ASI for the two soil profiles in Visso.

One dimensional linear equivalent seismic response analyses were executed on the defined soil profiles corresponding to the Mops 2001 and 2002, namely S2 and S1. The variation of the shear modulus and damping ratio with the shear strain was simulated through the properly calibrated relationship by Ciancimino et al. (2020) for the fine-grained soil and the curves suggested by Liao et al. (2013) for the coarse-grained soil. The bedrock was assumed to be linear visco-elastic with a damping of 0.5% and V_S=1300m/s, in agreement with the results obtained by MZS3 (2018).

The input motions employed in the seismic analyses are accelerograms of 49 natural events selected from the SIMBAD database (see Smerzini et al. (2013); Iervolino et al. (2014)) and recorded at stations located on stiff rock outcrop. All the parameters of the input motions together with the results of the site response analyses are reported in detail by Brunelli et al. (2021b) and Brunelli et al. (2022a). Figure 5.2 just shows the amplification factors of the intensity measures typically adopted in the simulations of the damage at urban scale, i. e. the peak ground acceleration, PGA, and the integral of spectral acceleration in the interval of period 0.1s-0.5s, ASI.

Both plots highlight the expected reduction of the amplifications with increasing amplitude of the input motion and higher amplifications for the deeper and softer S1.

In lack of site response analyses, the seismic fragility is estimated by applying an amplification factor to the bedrock intensity measure to obtain the free field value. The amplification factors provided by the Code (NTC (2018)), the microzonation studies (MZS (2018)) and the map by Falcone et al. (2021) are superimposed to the plots in Figure 5.2. The three approaches provide factors for hazard scenario with a return period equal to 475 years, corresponding to a PGA=0.24g and a ASI=0.21gs for the case of Visso. The values are equal for the two subsoil profiles and lower with respect to the prediction of the more accurate site response analyses. Only the prediction referred to the ASI by Falcone is intermediate between the results associated to S1 and S2.

The comparison clearly shows that the amplification can significantly vary with the amplitude of the input motion, hence the application of factors provided by NTC (2018), MZS (2018) or Falcone et al. (2021) to hazard scenario with different return period is arbitrary and unconservative especially for less severe and more recurrent earthquakes.

2.2. Overview on the structural features of masonry buildings

The collection of data necessary to describe the vulnerability of the building stock under examination constitutes an essential but at the same time tricky point of the risk assessment at large scale. In fact, it must balance the need of being not too much costly and time-consuming with that of being enough accurate to acquire all factors necessary to discriminate the possible seismic responses.

Usually, the large-scale built inventory relies on easily available information, such as the census data, eventually enriched by additional information based on on-site surveys of technicians. Usually, census data (e.g. the ISTAT census in Italy) provide basic information, e.g. number of floors, construction age and construction type, that however are aggregated at municipality scale. In Italy, CARTIS project (Zuccaro et al. (2015)) was aimed at integrating ISTAT information through an interview-based protocol on structural systems and material types. Various studies demonstrated how such an enrichment of inventory data may improve the reliability of final results (see for example Polese et al. (2021); Tocchi et al. (2022); Brando et al. (2021)). Recent studies attempt to implement algorithms that, based on open-access information, allow acquiring some basic geometrical information, namely in (Sousa et al. (2017)) by exploiting OpenStreetMap or CORINE initiative, and in (Rovithis et al. (2017)) by a LiDAR-based 3D city model. However, these experiences are limited to parameters, such as building height or plan dimension, that cannot properly characterize buildings in aggregate, key-feature of small historical centres as that examined in this study. In (Santa Maria et al. (2017)), the use of tools such as Street view and Apple Look Around Service was investigated to integrate such information by associating the structural typology (i.e. masonry, reinforced concrete,…) by a remote investigation made by the operator; then, in Pelizari et al. (2021) Deep Convolutional Neural Networks and street-level imagery where tentatively adopted with the same aim. Other studies address the interaction between data, acquired through remote sensing techniques, and point clouds acquired through laser scanner (see for example Bertocci and Bigongiari (2019); Predari et al. (2019)).

In this research, due to some restrictions imposed by the COVID19 emergency in performing direct on-site surveys and the fact that provisional interventions may have altered the actual state of buildings, all necessary data were collected by integrating the quite accurate documentation acquired by the team of University of Genoa during the post-seismic inspections just after the 2016/2017 seismic sequence (more than 350 photos) with the in-depth analysis of: photos from Google Street View and Google Earth; videos from YouTube made before and after the seismic event (including firefighter's drones); local and national newspaper and television news reports. Main goal was to associate to all buildings the main features which are expected to address their seismic behaviour. They have been defined referring to the common taxonomy proposed in literature for URM buildings

(Lagomarsino and Cattari (2015a); Silva et al. (2020); Crowley et al. (2020)) integrated with specific factors widely recognized as relevant in case of buildings in aggregate from both observed damage and vulnerabily models (Brando et al. (2017); Formisano et al. (2015); Mosoarca et al. (2020); Formisano et al. (2021)). Data - which are compatible within the scope of a large-scale vulnerability assessment- are mostly based on information that can be collected from an external visual inspection, then integrated with other parameters associated to the structural system (e.g. masonry typology, diaphragms and roof typology) deductible by the analysis of recurring features of Visso's municipality. In the examined case, the latter was possible through the details made visible by the seismic damage.

Figure 5.3 illustrates in a graphical way the synthesis of collected data in terms of: (a) number of stories; (b) presence of structural details like as tie-rods, reinforced concrete (RC) tie beams; (c) soaring portions. In particular, factors depicted in Figure 5.3a and 3b are indicators mainly associated to the potential activation of local mechanisms. Tie-rods configurations are differentiated in type A and B, consisting in the presence of tie-rods systematic at all levels or only at first two levels, respectively. In Figure 5.3b also the filling structural units are identified, which have been originated by the subsequent transformations which buildings in aggregate are typically subjected to. From Figure 5.3 it is observed that most of buildings are three-story (63.7%), without systematic tie-rods or RC tie beams at all levels (i.e. 39.9% without tie- rods and 24.1% with tie-rods of type B) and with tympanum potentially subjected to overturning due to irregularity in elevation. Moreover, from Figure 5.3 it is evident that most of buildings are ascribable to the "row housing" type, consisting of a series of buildings aggregated in lines.

Figure 5.3. Collection of data in the historical center of Visso in terms of: (a) number of storeys; (b) structural details and (c) soaring portions (i.e. in elevation irregularity). (d) Photos of typical buildings in aggregate present in Visso's municipality.

As far as the other parameters associated to the structural system are concerned, these may be summarized as follow:

- the age is ascribable to pre 1919 or 1919-1945 since the historical centre of Visso dates back to Middle age.
- the load-bearing walls are mostly characterized by two-leaf stone masonry, with rough stones sizing about 90-120 mm in height and 360-400 mm in length. The thickness of the external walls is approximately 70-80 cm at the ground floor and 55-60 cm at the other levels. The internal walls appear a bit thinner; more specifically, in the examined archetypes, they have been supposed to be 5 cm lower in thickness than the perimeter walls of each specific floor. Moreover, the ratio between the total resistant wall section and the total surface significantly differs from the longitudinal and transversal directions (being the longitudinal one, that parallel to the main direction of the aggregate), being higher in the transversal one mostly characterized by side walls. Conversely, façades oriented along the longitudinal direction are characterized by quite large openings at ground level;
- floor diaphragms are mostly characterized by brick and wooden decks. In some cases, a very thin concrete slab (not reinforced) is also present (presumably 15 cm thick, as deducted from photos). The main orientation of diaphragms is expected to develop perpendicularly to the transversal direction;
- the foundation system was supposed to merely be a prolongation of the load-bearing walls, slightly embedded in the soil, as typically observed for existing URM buildings.

3. DEVELOPMENT OF CUSTOMIZED FRAGILITY CURVES FOR BUILDINGS IN VISSO

Fragility curves have been developed according to the procedure illustrated in Brunelli et al. (2022a) by selecting archetypes representative of the buildings in the municipality of Visso.

The adopted procedure is based on a numerical approach and assumes a lognormal distribution for deriving the main parameters that define the fragility curves, as usual in risk analyses (Baraschino et al. (2019)).

The numerical approach consists of nonlinear dynamic analyses (NLDA) performed according to the Cloud method (see e.g. Jalayer et al. (2017)) and 3D numerical models that work according to the equivalent frame modelling approach (see Figure 5.4). Among possible alternatives (see D'Altri et al. (2020); Cattari et al. (2022)), the equivalent frame approach has been selected as the most suitable for balancing accuracy and computational effort and pursuing the main goal of developing customized fragility curves able to account for the distinctive features of the built under examination.

The influence of site effects and SFS interaction has been investigated by developing fragility curves derived under three different hypotheses:

- FB A case, that refers to fixed base (FB) structural models investigated by NLDA performed with records of natural earthquakes selected to be representative of seismic signals occurring on the rock or soil type A according to the Codes (e.g. NTC (2018) or CEN (2004));
- FB C case, according to which the fixed base structural model was analysed under accelerograms derived through linear-equivalent one-dimensional seismic response analyses of the soil profile recurrent in Visso (see §2.1);
- CB C case, in which the SFS interaction was considered by analyzing the compliant base (CB) model under the same free field input motions adopted in the FB C case. In this model, each foundation pier was equipped with springs, whose stiffness was calibrated through the real part of the soil-foundation impedances by Gazetas (1991). The structural period of CB model is predicted through the formula by Maravas et al. (2014) for the impedances calibrated on the initial soil stiffness. The same approach by Maravas et al. (2014) was adopted to estimate the

damping ratio of the compliant base system. The latter was introduced as a Rayleigh damping ratio into the structural model. Soil nonlinear response was considered by calibrating the foundation impedance functions and the analytical formula to estimate the damping ratio with the stiffness and the hysteretic damping mobilized in the soil volume affected by the foundation motion during each seismic response analysis. Fragility curves have been constructed for five damage levels (DLs) compatible with EMS98 (Grünthal (1998)). To this aim, a multiscale approach has been adopted for synthetically interpreting the huge amount of data provided by NLDA. It combines two main criteria: one that refers to the global response scale, and is based on the definition of proper thresholds of the displacement capacity of the building on the pushover curves estimated from nonlinear static analyses; the other that aims to monitor the spread of damage along the building, through the evaluation of the damage severity and diffusion on vertical walls on basis of the cumulative rate of walls that reached a given DL. Interested readers may refer to Brunelli et al. (2022a) and Sivori et al. (2022) for a more exhaustive description of such an approach.

A total of three case studies have been analysed: the school of Visso (Figure 5.4b); a first aggregate composed of five-unit buildings with a number of floors varying from three to four (Figure 5.4c); a second aggregate composed of five-unit buildings with a number of floors varying from two to three (Figure 5.4d).

The school and the second aggregate are set on soil profile S1, while the first aggregate on soil profile S2, according to section 2.1.

The geometric features, loads and all mechanical parameters have been assumed as deterministic and plausible for the specific features of buildings in Visso municipality. All details on that are reported in Brunelli et al. (2021a) and Angiolilli et al. (2022a).

Units of aggregates are characterized by small and simple regular shapes, as typical in this historical centre. Table 5.1 summarizes the main features of the two aggregates in terms of plan area, resistant area in longitudinal and transversal directions, number of storeys and interstorey height.

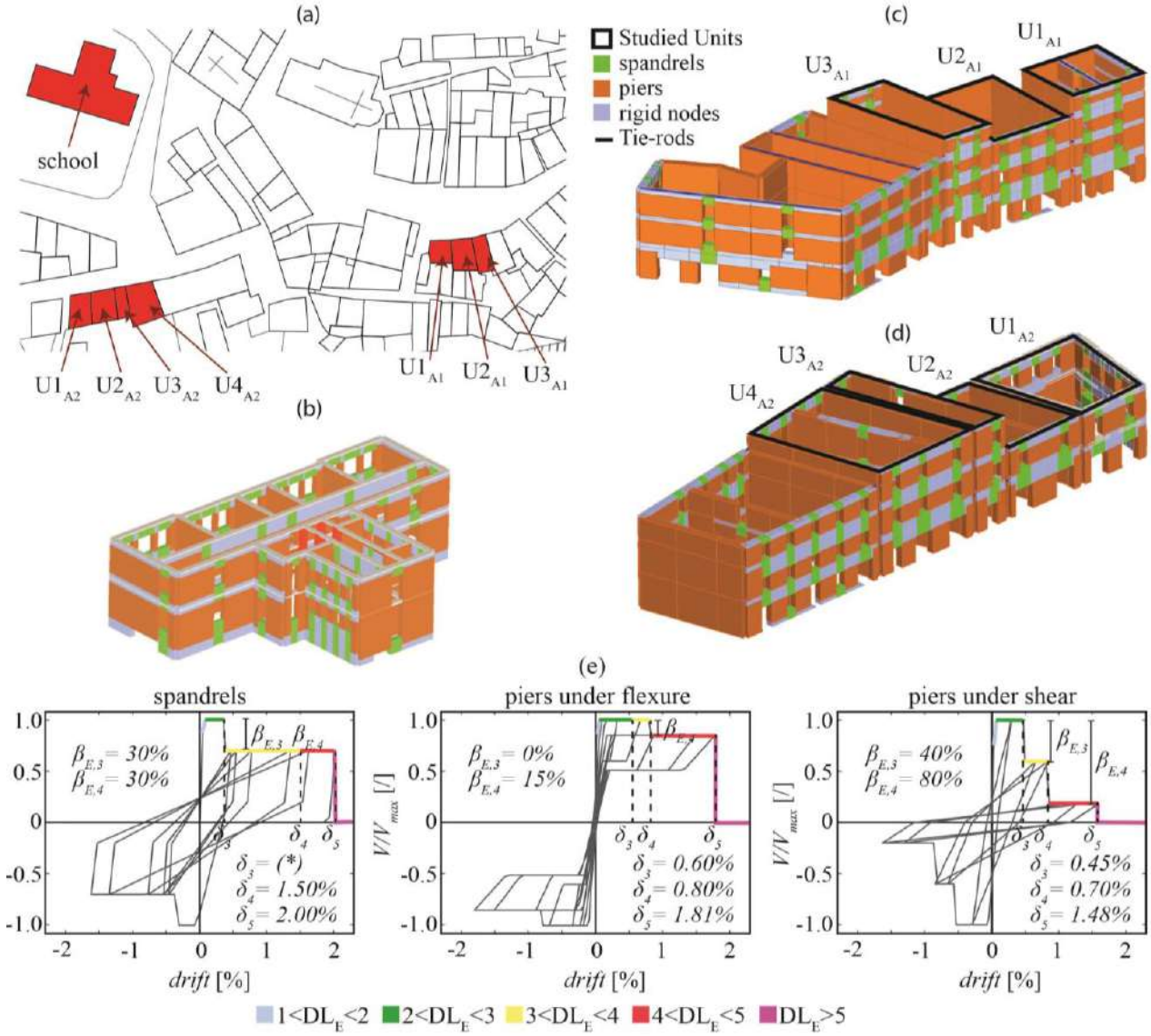

Figure 5.4. (a) Identification of selected cases studies in the plan view of Visso's Municipality; b) Visso's school; (c) aggregate no.1 examined in Angiolilli et al. (2022a); (d) aggregate no.2; (e) backbone and hysteretic response of masonry elements. For spandrels δ3 was defined starting from drift corresponding to the yielding point of the element and assuming a ductility factor equal to 4, similarly to what suggested in Beyer and Mangalathu (2014).

Table1: Characteristics of the buildings analysed: area, resistant area, number of floors, inter-storey height.

		Area [m^2]	Resistant Area		Storeys	Inter-storey height
			Long.	Transv.		
A1	U1	58.5	14.6%	27.7%	4	3.4-3.2-3.0-2.1
	U2	104.3	9.4%	10.3%	3	3.4-3.2-3.0
	U3	71.4	6.4%	12.1%	4	3.4-3.2-3.0-2.1
A2	U1	114.8	9.2%	9.5%	2	3.4-3.1
	U2	98.4	8.5%	14.9%	2	3.4-3.1
	U3	39.0	19.9%	39.8%	3	3.4-3.1-3.1
	U4	147.2	10.5%	16.5%	3	3.4-3.1-3.1

For example, Figure 5.5 summarizes the periods of FB and CB models for the aggregates together with the equivalent damping ratio assumed according to the aforementioned procedure. The periods are significantly modified especially for the aggregate 2 and the damping ratio is increased up to four times the fixed base value at the strongest PGAs.

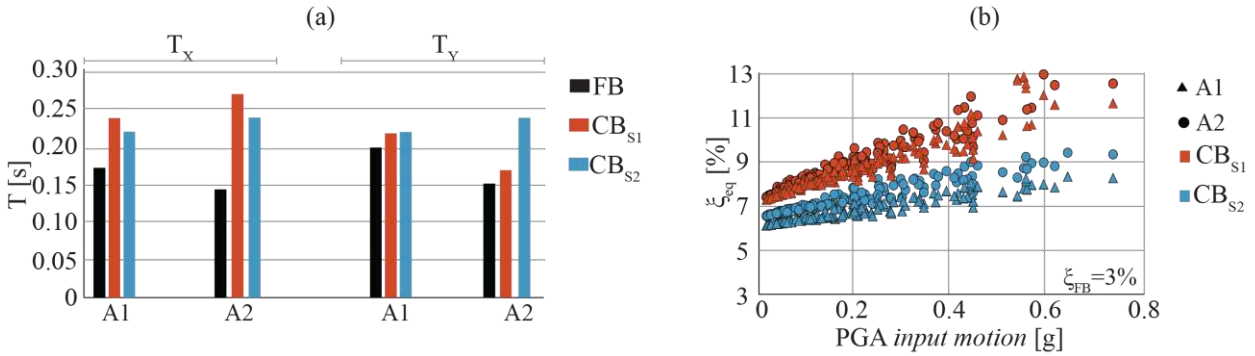

Figure 5.5. (a) Periods of FB and CB models of each structural units of two aggregates varying the two soil profiles considered; (b) equivalent damping estimated for each considered event.

The Visso's school, nowadays demolished due to the severe damage occurred, was permanently monitored by the Italian Seismic Observatory of Structures of the Civil Department of Civil Protection during the Central Italy 2016-2017 earthquake. Thus, it represents a very interesting, if not even singular, case-study that has been adopted for validating in a robust way the procedure through a quite accurate comparison of both qualitative (i.e. damage) and quantitative (i.e. accelerograms) parameters. Results are presented in Brunelli et al. (2021a).

Then, the first aggregate was in depth investigated in Angiolilli et al. (2022a) and validated in Brunelli et al. (2022c) through the qualitative comparison between the simulated and actual damage occurred after the 2016-2017 seismic sequence. For such a validation, the modification of the seismic motion expected along the valley of Visso (see §2.1) has been accounted for by performing some 2D site response analyses (Brunelli et al. (2022c)). The main results of such a comparison are summarized in Figure 5.6, which shows that the CB model in conjunction with the consideration of 2D effects is particularly effective in providing more consistent results with respect to the observed response. In the case of NLDA, the damage level at element scale (DL_E) is assigned as a function of the maximum drift (indicated in Figure 5.4e by the symbol δ) achieved during each analysis according to the constitutive law shown in Figure 5.4e. In particular, a different softening phase is modelled as a function of the main failure occurred (i.e., if flexural or shear) and the type of element (i.e., if pier or spandrel). Starting from the damage at element scale, according to the multiscale approach mentioned in §3 the damage level at scale of the whole structural unit is then assigned.

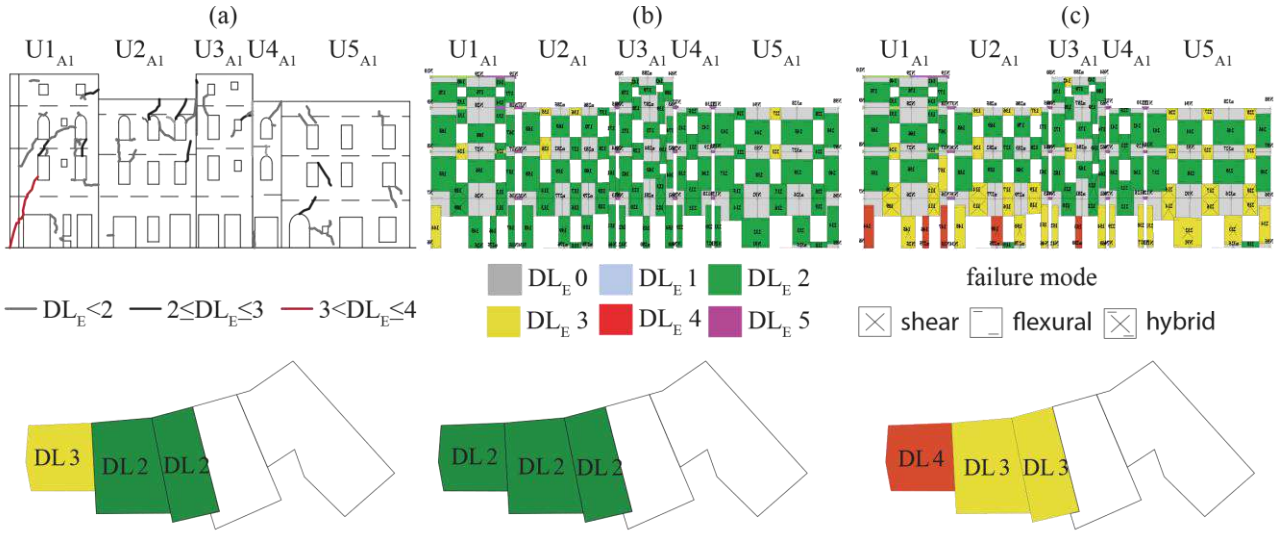

Figure 5.6. (a) Observed damage after the Central Italy earthquake and assignment of a global DL to each unit according to EMS98 scale; (b) simulated damage through the CB model after 26th October considering 2D site effects or (c) 1D site effects.

While for the Visso's school only the in-plane (IP) response was investigated (due to the presence of effective RC tie rods able to substantially prevent the activation of extensive local mechanisms), for the aggregate the tricky issues deriving from the combination of IP and out-of-plane (OOP) response as well as the pounding effects were addressed. As illustrated in detail in Angiolilli et al. (2022a), the OOP mechanisms were analysed in the post-processing of the data derived from the global 3D model by adopting the rigid-block assumption. The individuation of the walls susceptible to overturning was defined based on building geometry, opening layout, constructive details and restraints given by the structure. In particular, it was reasonable to consider the OOP mechanisms involving only the tympanum (TM) and upper level (FM1) as well as the two upper levels (FM2) of the external façades, because of the wall slenderness and the amplification phenomena generally occurred for the upper building levels (e.g. Degli Abbati et al. (2018)).The interaction effect among adjacent units has been modelled through the insertion of elastic truss elements and fictitious floors between the units; these elements allow the opening between buildings only along their longitudinal direction. To assess such interaction effect on the IP response, each structural unit has been also investigated as isolated. Moreover, also the pounding effect was considered in determining the actual damage level of each structural unit (see Angiolilli et al. (2022a)).

Such a procedure has been then replicated in this paper also on a second aggregate to enrich the representativeness of archetypes examined for the aim of the assessment at urban scale. Figure 5.7 presents the qualitative comparison between the observed and simulated damage. Results highlight that consideration of SFS interaction is beneficial, and it allows to obtain a damage pattern more consistent in terms of severity with respect to the real one.

The results of this second aggregate in terms of fragility curves are discussed in section 3.1 by comparing the outcomes also with the first aggregate; moreover, additional comments on the role of site and SFS interaction effects are provided too. Then results are generalized in section 3.2 to derive fragility curves representative of sub-types with homogeneous seismic behaviour to be applied for deriving the damage scenario presented in section 4.

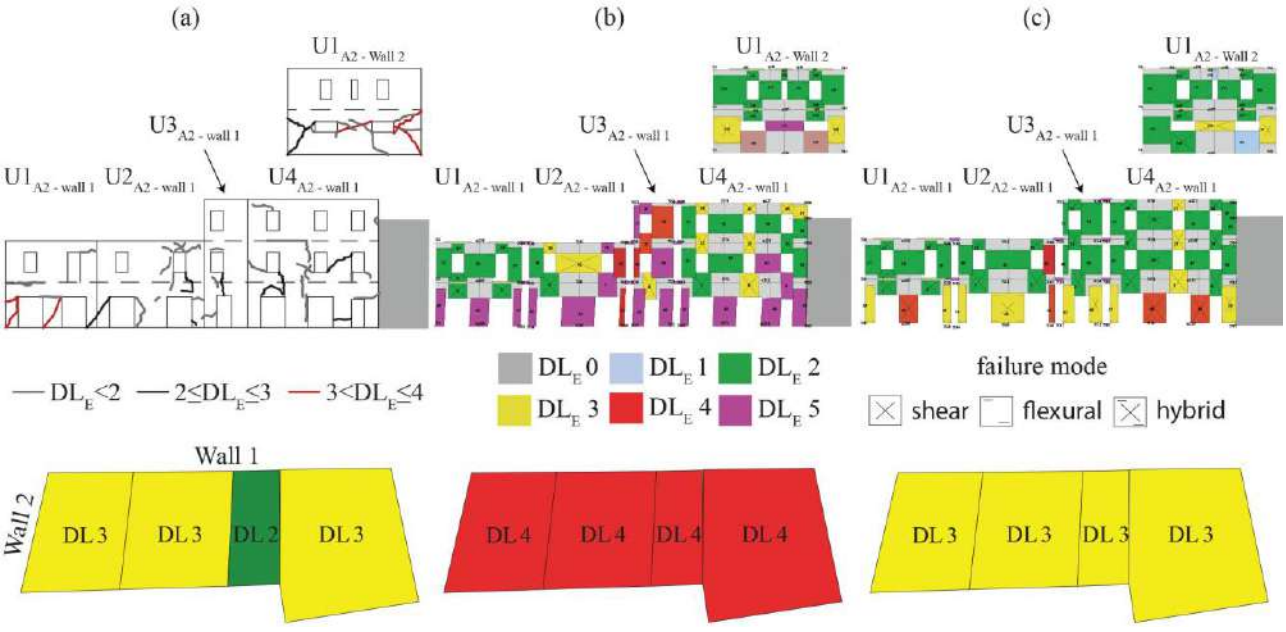

Figure 5.7. (a) Observed damage after the Central Italy earthquake and assignment of a global DL to each unit according to EMS98 scale; (b) simulated damage after 26th October through the FB model (b) or the CB model (c). For both models only 1D site effects are considered.

3.1. Fragility curves from NLDA of archetype buildings in aggregate

It is worth pointing out that the fragility curves represented in this section accounts only for the record-to-record variability uncertainty.

First of all, numerical models were adopted to quantitatively investigate the "aggregate effect", i.e. the effect that boundary conditions provided by adjacent structural units may have on the seismic response of an individual building belonging to an aggregate. To this aim, each structural unit has been investigated also as isolated. Figure 5.8 presents the results for fragility curves associated to DL2 and DL4 and for a 2/3 and 4-storeys structural units investigated by considering only the IP response. Independently of the FB or CB modelling, the effect revealed to be beneficial with respect to the isolated configuration. The same conclusion has been founded also for other DLs.

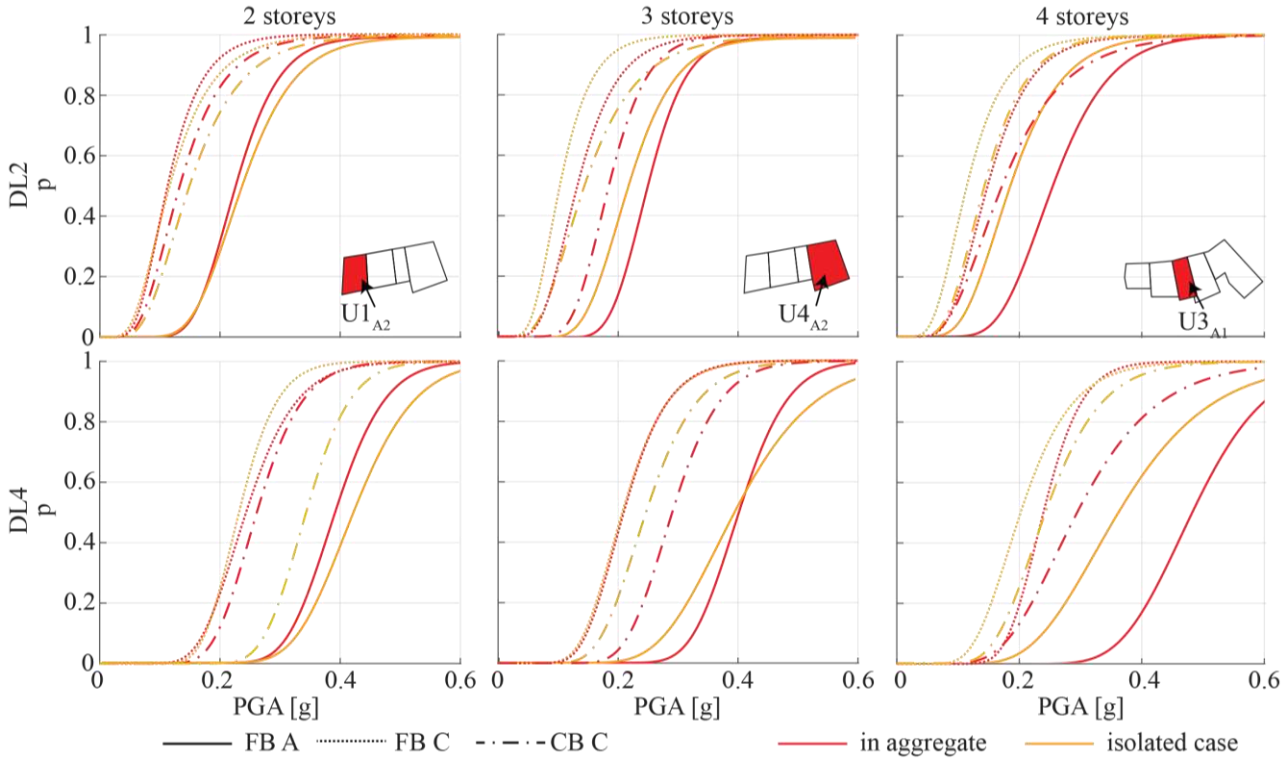

Figure 5.8. Effect on the fragility curves of aggregate interaction.

Then, for a wide set of structural units, Figure 5.9 highlights the role of site and SFS interaction effects on the IP response. Site effects always increases the probability of failure, while SFS interaction plays a beneficial role thanks to the additional contribution of soil and foundation to dissipate seismic energy.

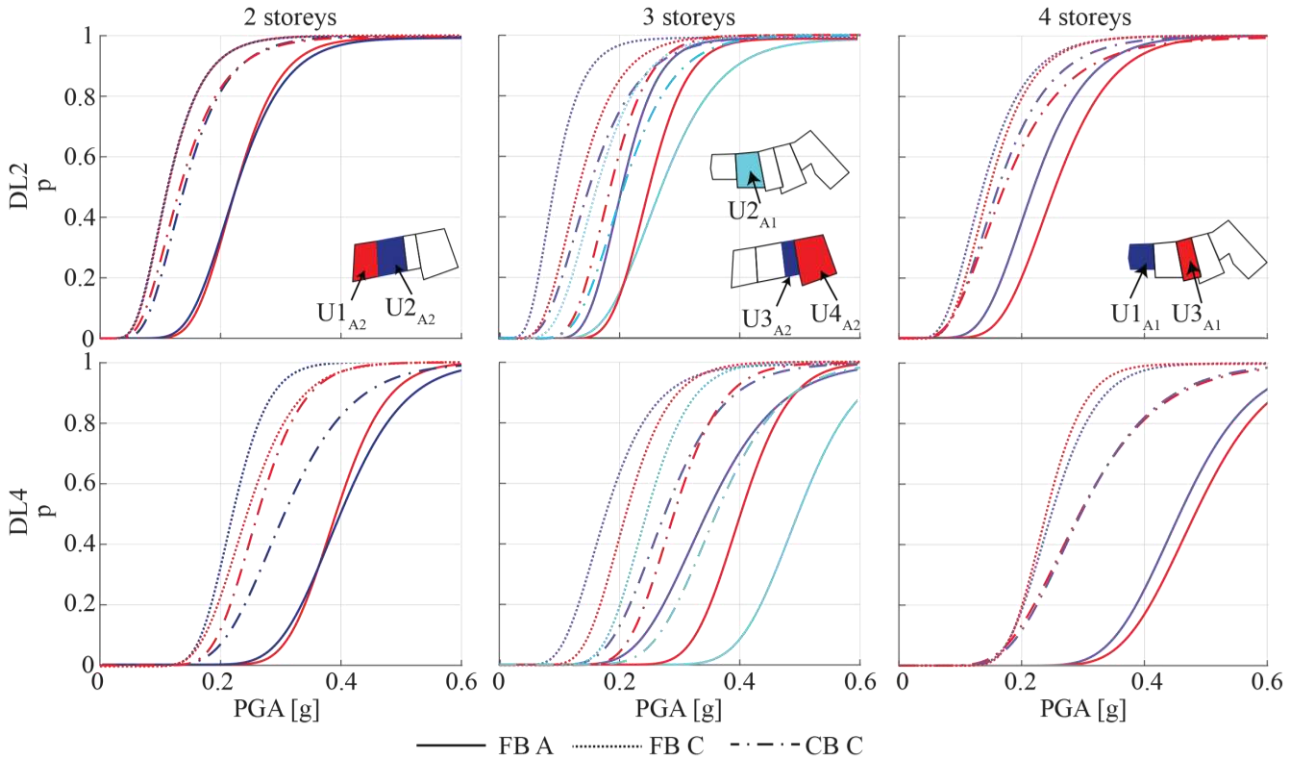

Figure 5.9. Effect on the fragility curves of SFS interaction.

Finally, Figure 5.10b illustrates the potential retreat of the fragility curve due to the activation of local mechanisms for the fixed base model together with the exemplification of the considered mechanisms for aggregate no.1 (Figure 5.10a). On that, it has to be pointed out that, according to Angiolilli et al. (2022a), such effect may be more or less significant since the filtering effect produced by the main structure varies with the damage level attained on walls (i.e. the amplification of floor spectra reduces with the increase of the IP damage).

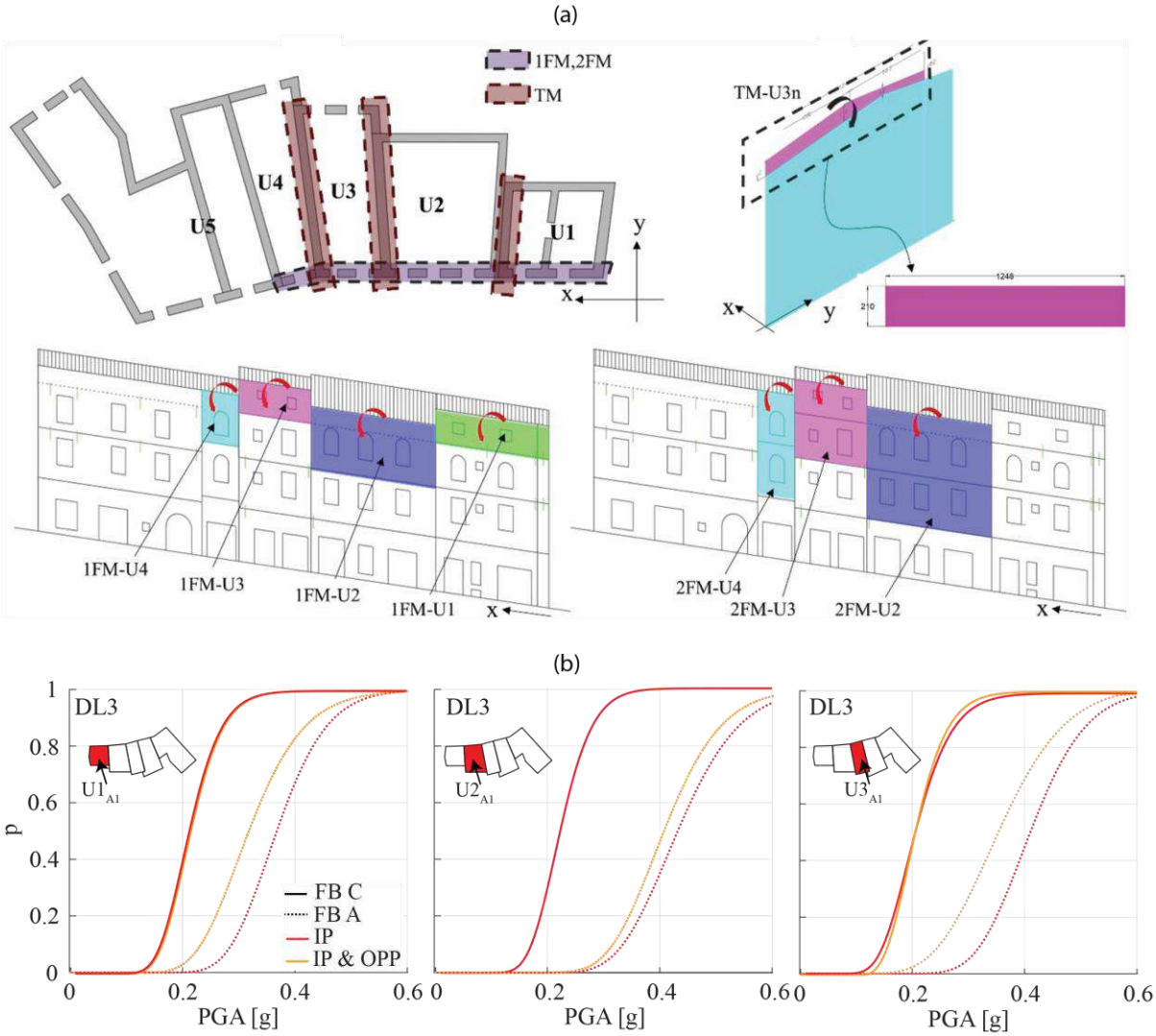

Figure 5.10. (a) Individuation of the walls investigated for the OOP analyses in the case of aggregate no.1 (adapted from Angiolilli et al. (2022a)); (b) effect on the fragility curves of activation of local mechanisms.

3.2. Fragility curves for homogeneous building classes

3.2.1. Derivation of the fragility curve parameters

The fragility curves described in the previous section and derived for specific archetypes are herein combined and integrated to obtain the corresponding one representative of sub-types of buildings with homogeneous behaviour, as usual for aims of risk analyses at large scale.

Thus, firstly, the parameters of fragility curves associated only to the IP response have been combined by considering all units characterized by the same number of stories. Available results have been further grouped according to the hypotheses made on site effects (SE) and SFS interaction effects (i.e. by differentiating results from FB A, FB C_{S1}, FB C_{S2}, CB C_{S1} and CB C_{S2} models). More specifically, for each group and each damage level (DLi, i=1÷5):

- the median value $IM_{50,IP,rec,DLi}$ has been obtained as the average of available values for each set;
- while the dispersion $b_{IP,rec,DLi}$ has been has been computed as:

$$\beta_{IP,rec,DLi} = \sqrt{\beta_{rec,DLi}^2 + c_{DLi}^2} \tag{5.1}$$

where $\beta_{rec,DLi} = \sqrt{\frac{\sum_{k=1}^{n} \beta_{DLi,k}^2}{n}}$ and $c = \sqrt{\frac{\sum_{k=1}^{n} ln^2(IM_{50,IP,DLi,k})}{n} - \frac{\sum_{k=1}^{n} ln(IM_{50,IP,DLi,k})^2}{n}}$

being k the counter that enumerates the number of examined structural units having a certain number of level (i.e. 2, 3 or 4) and n the total number of units in each group (i.e. two for 2 stories, three for 3 stories and two for 4 stories). In such a way, this dispersion accounts also for the inter-building variability.

Tables 2 and 3 summarize the obtained values for $IM_{50,IP,DLi}$ and $b_{IP,rec,DLi}$, respectively.

The values obtained for $b_{IP,rec,DLi}$ have revealed a negligible sensitivity to the number of levels or the boundary conditions of the unit (i.e. if isolated or in aggregate), while a more significant variation with the DL and the soil profile; the values obtained have been a bit standardized as reported in Table 5.3 by assuming equal reference values for DL1 and DL2 and DL>DL3.

Table 5.2: Fragility curves associated to the IP response: median values of $IM_{50,IP,DLi}$.

	2 storeys									
	Unit examined as isolated					Unit examined as in aggregate				
	FB A	FB C_{S1}	FB C_{S2}	CB C_{S1}	CB C_{S2}	FB A	FB C_{S1}	FB C_{S2}	CB C_{S1}	CB C_{S2}
DL1	0.117	0.050	0.068	0.063	0.087	0.102	0.048	0.064	0.060	0.071
DL2	0.236	0.115	0.148	0.149	0.192	0.226	0.112	0.136	0.136	0.166
DL3	0.320	0.204	0.234	0.262	0.281	0.325	0.205	0.206	0.211	0.232
DL4	0.420	0.232	0.256	0.344	0.331	0.393	0.231	0.246	0.283	0.293
DL5	0.560	0.390	0.399	0.490	0.484	0.565	0.360	0.379	0.408	0.430
	3 storeys									
DL1	0.101	0.050	0.058	0.077	0.082	0.124	0.057	0.072	0.080	0.088
DL2	0.217	0.104	0.117	0.145	0.143	0.239	0.118	0.142	0.173	0.188
DL3	0.285	0.165	0.183	0.202	0.203	0.328	0.182	0.191	0.227	0.255
DL4	0.394	0.208	0.211	0.247	0.243	0.409	0.208	0.234	0.313	0.321
DL5	0.506	0.335	0.356	0.403	0.405	0.552	0.339	0.361	0.421	0.431
	4 storeys									
DL1	0.104	0.046	0.061	0.061	0.069	0.107	0.049	0.071	0.077	0.084
DL2	0.206	0.107	0.119	0.132	0.134	0.239	0.116	0.142	0.153	0.167
DL3	0.297	0.172	0.181	0.196	0.200	0.407	0.186	0.210	0.257	0.237
DL4	0.384	0.197	0.228	0.253	0.273	0.469	0.238	0.242	0.358	0.295
DL5	0.496	0.326	0.336	0.345	0.360	0.599	0.357	0.379	0.477	0.451

Table 5.3: Values of various contributions considered to the dispersion of fragility curves.

	Soil A				Soil C			
	$\beta_{IP,rec,DLi}$	β_{cap}	$\beta_{TOT,IP}$	β_{OOP}	$\beta_{IP,rec,DLi}$	β_{cap}	$\beta_{TOT,IP}$	β_{OOP}
DL1	0.40	0.10	0.427	0	0.47	0.10	0.495	0
DL2	0.40	0.10	0.427	0.25	0.47	0.10	0.495	0.25
DL3	0.35	0.20	0.461	0.25	0.43	0.20	0.524	0.25
DL4	0.35	0.20	0.461	0.25	0.43	0.20	0.524	0.25
DL5	0.35	0.20	0.461	0.25	0.43	0.20	0.524	0.25

The values of dispersion so obtained account only for the record-to-record variability associated to the IP response and the inter-building variability, since mechanical properties and geometrical parameters have been assumed deterministic in the numerical analyses presented in section 3. Thus, to consider the effect of possible additional uncertainties associated to the variability of mechanical properties ($b_{m,DLi}$) and the sensitivity of the response associated to the local mechanisms ($b_{OOP,DLi}$), the values of dispersion have been modified as follow:

$$\beta_{TOT,DLi} = \sqrt{\beta_{IP,rec,DLi}^2 + \beta_{m,DLi}^2 + \beta_{OOP,DLi}^2} \quad with\ i = 1 \div 5 \tag{5.2}$$

by assuming the various sources of uncertainties as statistically independent.

Table 5.3 clarifies all the values adopted. In particular, values of $b_{m,DLi}$ have been defined on basis of previous works (Cattari et al. (2019a); Pagnini et al. (2011)) by considering also that masonry type in Visso municipality is quite homogeneous; the difference in values assigned to DL1/DL2 and DL3/DL4/DL5 reflects the role expected to be played by the uncertainty on drift thresholds that affect the displacement capacity of buildings at severe damage levels. In fact, as testified by various experimental campaigns (*e.g.*, Vanin et al. (2017); Morandi et al. (2018); Rezaie et al. (2020); Boschi et al. (2021)), such uncertainty may be dominant with respect to that associated to materials. Instead, as far the $b_{OOP,DLi}$ concerns, it has been quantified on basis of the numerical results carried out by Angiolilli et al. (2022a).

3.2.2. Simplified Modification factors to account for OOP, SE and SFS interaction effects

As far the $IM_{50,IP,DLi}$ concern, as already discussed in section 3.1, Table 5.2 shows the possible alteration of the median values expected when passing from Rock-like formations to soft soils, and, further, when accounting also for SFS interaction effects. With the aim of providing tools that may support a first quantitative estimate of such effects, results have been processed to define modification factors (MF) to be directly applied to $IM_{50,IP,A,DLi}$, analogously to what has been done by Peditris and Pitilakis (2020) for reinforced concrete structures; the suffix "A" specifies that reference is made to soil type A. Figure 5.11 shows the values of the MFs obtained from the results coming from the specific investigated units, while Table 5.4 summarizes the proposed reference values obtained as the average of all units associated to the same number of stories.

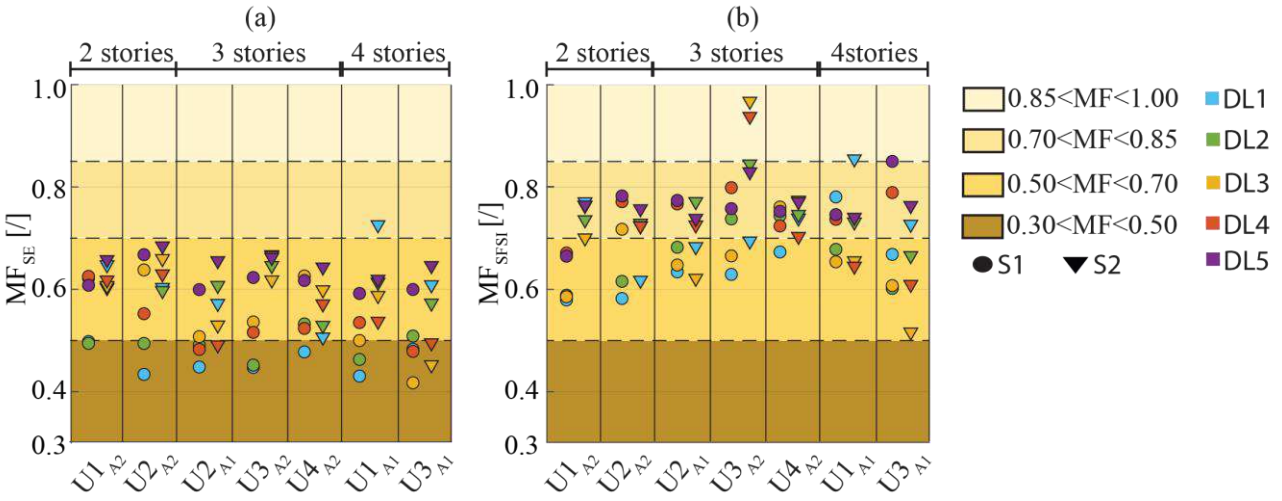

Figure 5.11. Modification factors associated to SE (a) and SFS interaction (b) effects computed from results derived from the specific examined archetypes.

Table 5.4: Reference values proposed for the MF_{SE} and MF_{SFSI} to be applied to $IM_{50,IP,A,DLi}$.

storeys		S1					S2				
		DL1	DL2	DL3	DL4	DL5	DL1	DL2	DL3	DL4	DL5
MF_{SE}	2	0.47	0.50	0.63	0.59	0.64	0.63	0.60	0.63	0.63	0.67
	3	0.46	0.49	0.56	0.51	0.61	0.58	0.60	0.58	0.58	0.65
	4	0.46	0.49	0.46	0.51	0.60	0.67	0.59	0.52	0.52	0.63
MF_{SFSI}	2	0.58	0.60	0.65	0.72	0.73	0.70	0.73	0.71	0.75	0.76
	3	0.65	0.72	0.69	0.76	0.76	0.71	0.79	0.79	0.79	0.78
	4	0.73	0.64	0.63	0.76	0.80	0.79	0.70	0.59	0.63	0.75

Analogously, proper MFs have been derived to account in a simplified manner for the effects associated to the local mechanisms. In this case the values have been derived processing all the results available from Angiolilli et al. (2022a) and briefly recalled in section 3.1. The resulting MFs are summarized in Table 5.5. They are differentiated as a function of the configuration in elevation, i.e. if regular (OOP_{reg}) or irregular (OOP_{irr}, i.e. with soaring portions). In general, in the case of irregularity in elevation, fragility curves tend to move back in a more significant way due to the possible activation also of the overturning of tympanum (see also Figure 5.8 for the identification of local mechanisms considered in this study). The differences in the values passing from soil A to soil C reflect the role of filtering effect made by the main structure that is altered also by the activation of the IP response, as already discussed in section 3.1.

Table 5.5: Reference values proposed for the MF_{OOP} to be applied to $IM_{50,IP,A,DLi}$. OOP_{irr} refer to case of irregularity in elevation potentially associated to the activation also of the tympanum's overturning.

	OOP_{reg}			OOP_{irr}		
	FB A	FB C	CB C	FB A	FB C	CB C
DL1	1	1	1	1	1	1
DL2	0.95	1	0.95	0.80	1	0.90
DL3	0.95	1	0.95	0.80	1	0.90
DL4	0.95	1	0.95	0.80	1	0.90
DL5	0.95	1	0.95	0.80	1	0.90

Finally, Figure 5.12 presents an overview of fragility curves obtained from the numerical approach adopted in this study compared with those recently derived for buildings in aggregate by Penna et al. (2022a) from a pure empirical approach. The latter are based on the fitting of damage data of L'Aquila 2009 earthquake, available from the Da.D.O. platform (Dolce et al. (2019b)) and extracting only the records associated to buildings in aggregate. In particular, in the figure, the fragility curves obtained by grouping the data associated to irregular layout masonry or poor quality of structural details (i) and those associated to regular layout masonry and good quality of structural details (ii) are reported, respectively; curves related to groups (i) and (ii) define the upper and lower bounds defined by the grey region in Figure 5.12. Although fragility curves derived from the pure empirical approach are not able to further discriminate the interaction among units or the predominance of the IP or OOP seismic response, they constitute a valuable reference to provide a preliminary validation of curves here derived. It is worth noting that in Figure 5.12 the latter refer to those derived for the rocky soil. This choice appears the most consistent for the aim of this comparison since the curves derived from the pure empirical approach doesn't explicitly distinguish for the possible seismic input amplification or the SFS interaction effects. The comparison shows a quite good agreement, in fact:

- in all cases (apart DL1), fragility curves from the numerical approach are within the zone delimited by the empirical approach and in general closest to the lower bound. This is consistent with the

masonry type that characterizes the Visso's historical centre, that is not assimilable to a regular layout (e.g. a brick mortar joints masonry) but neither to the worst irregular one;

- the dispersion of fragility curves from numerical approach is lower than that of curves from the pure empirical approach. Apart the intrinsic differences associated to the two alternative approaches, this is reasonable considering that the first ones are customized for a specific built while the second have been derived by grouping all together the buildings of almost an entire region.

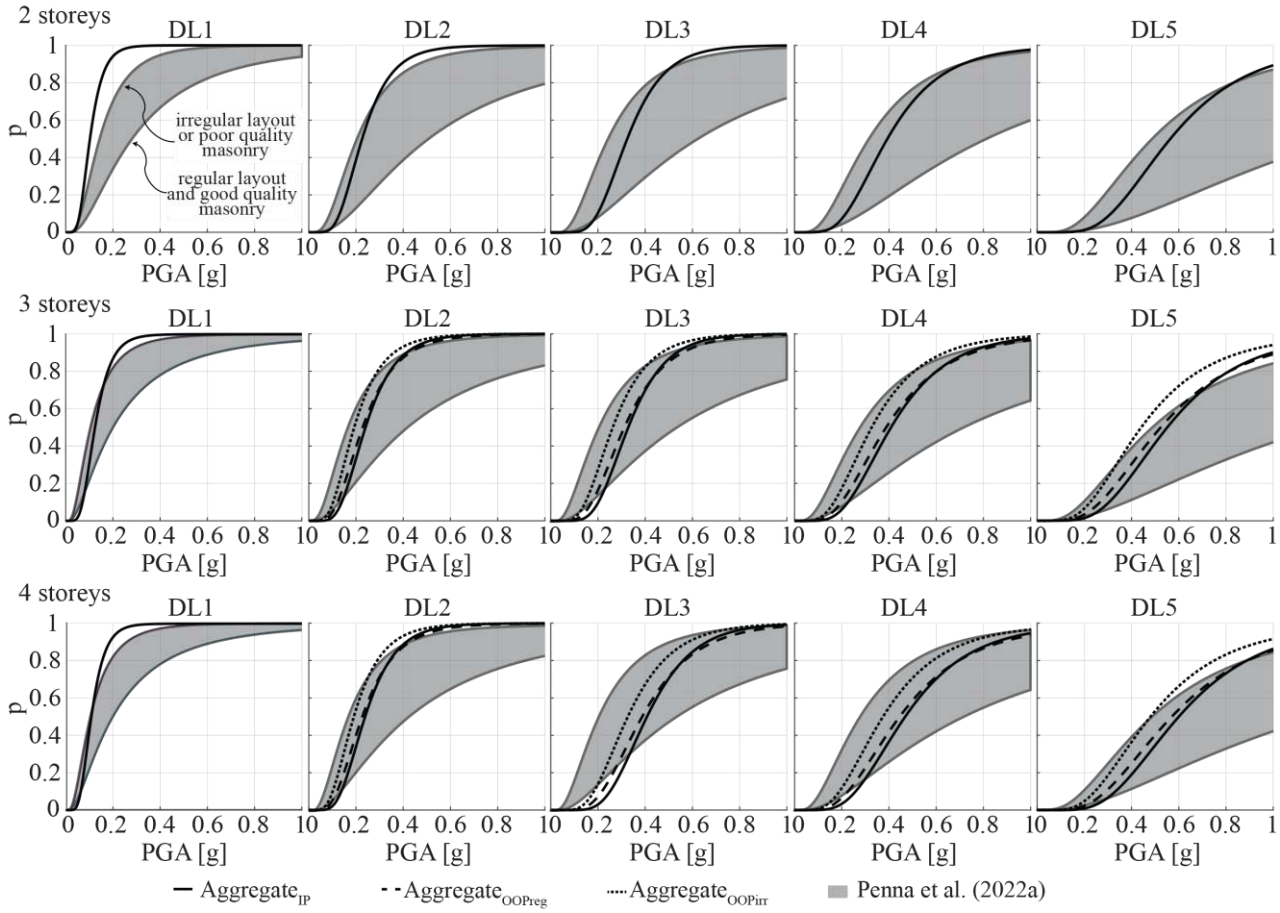

Figure 5.12. Comparison between the fragility curves derived in this study by neglecting SE and SFS interaction with those derived from a pure empirical approach by Penna et al. (2022a).

3.2.3. Application of the fragility curves to the built heritage of Visso

All modification factors and post-processing of data afore-discussed help to clarify the use of the data collected in the inventory phase (see section 2.2) for the association to each unit of the corresponding sub-type. Figure 5.13 clarifies through a logic tree such process, by way of example for the 3-stories units. The same applies for 4-stories units, while for 2-stories units the possible activation of local mechanisms has been neglected. The application of the MFs associated to the OOP follows the absence of tie-rods or the presence of tie-rods not systematic at all levels (type B), synthetically identified by the acronym LQD – Low Quality Details. Conversely, in the case where reinforced concrete (RC) tie beams are present or there are tie-rods at all levels (type A), the buildings are considered with High Quality Details (HQD); in this case, the MFs associated to the OOP are not applied.

As far the OOP response concerns, values presented in Table 5.5 highlights a role of OOP less pronounced than what testified by other numerical studies on different aggregates (e.g. Angiolilli et

al. (2021)) or experimental evidences (Carocci (2012); Penna et al. (2014); Sextos et al. (2018); Sorrentino et al. (2019)).

In Figure 5.14, a different colour is associated to each unit in order to clarify the attribution of the corresponding sub-type. In Figure 5.14, there is only one marker for two-story buildings because the possible activation of out-of-plane mechanisms for low-rise structures was neglected. This simplification appears to be justified also by the evidence in Visso historical centre.

To provide a first rough validation of the results achieved in this study, Figure 5.15 illustrates the actual local mechanisms activated in the historical centre of Visso after the Central Italy 2016/2017 earthquake. Indeed, it emerges how, compared to the high number of units characterized by vulnerability factors associated to the OOP (i.e. LQD or in elevation irregularities), the collapse of portions ascribable to loss of equilibrium is quite limited.

Moreover, it is worth highlighting that the MFs associated to OOP presented in Table 5.5 are based on the legitimacy of the rigid block assumption for masonry by neglecting the increase in the vulnerability due to the poor transversal connections among leaves or due to discontinuity produced by filled openings/filled flues, etc. Photos no.4 and 2 presented in Figure 5.15 testify how the activation of local mechanisms in some cases has been affected by this type of alterations; to investigate also these aspects was out of the scope of this study. Moreover, for this specific seismic sequence, also the damage accumulation phenomena have played a potential role (Sextos et al. (2018)). For example, in the case of school of Visso, the accurate reconstruction of data on damage made possible to ascertain that the local mechanism on the back façade (see photo no. 1 in Figure 5.15) occurred only after the shock of 26th October and after the IP response was already activated. All these considerations support the plausibility of the achieved numerical results.

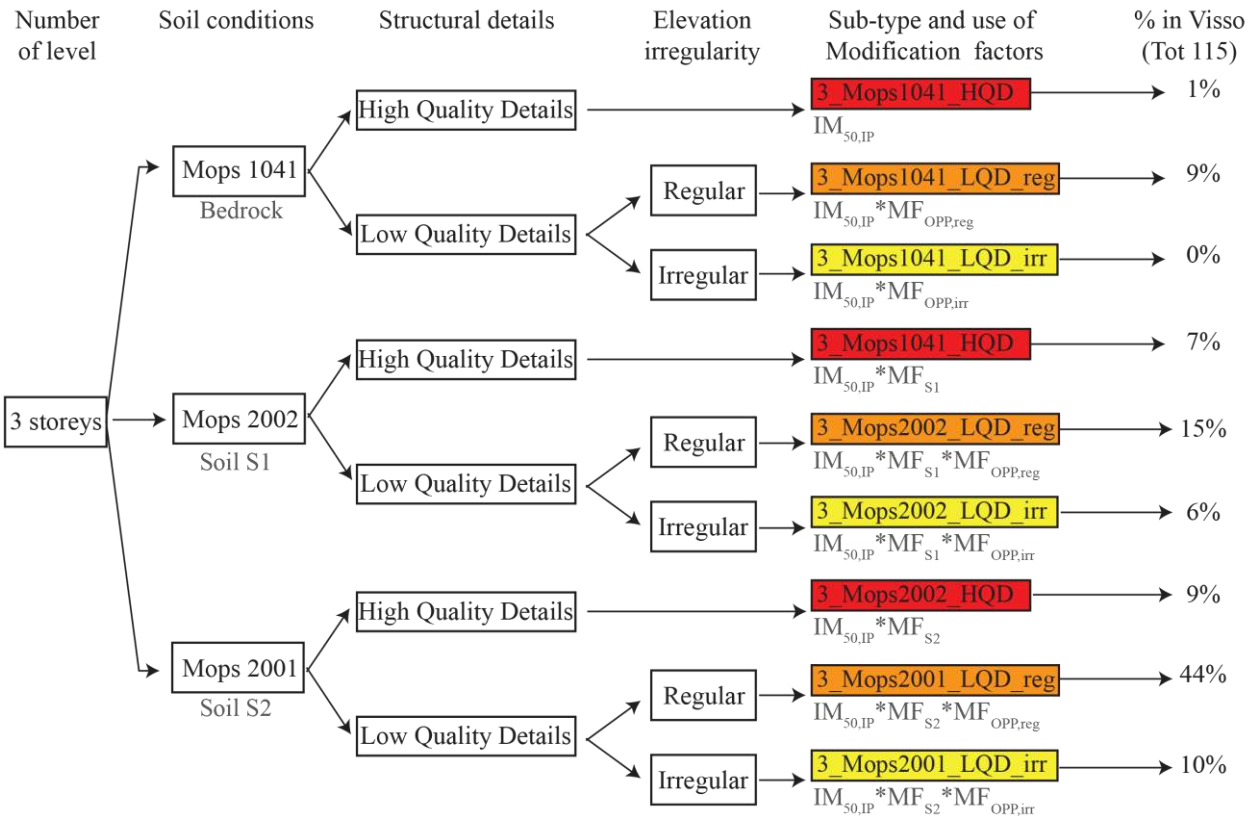

Figure 5.13. Logic tree aimed to clarify the use of data collected in the inventory phase for the association to the corresponding sub-type.

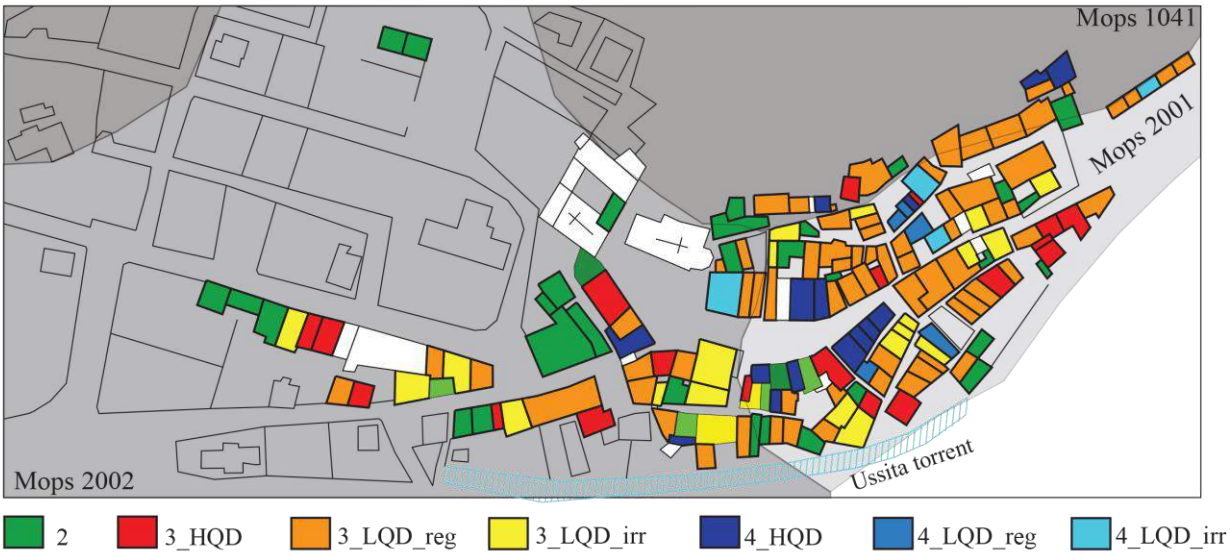

Figure 5.14. Association of sub-type building to structural units in Visso by adopting the classification of Figure 5.13.

Figure 5.15. Experimental evidence on the OOP occurrence in Visso's municipality after the Central Italy earthquake.

4. DEVELOPMENT OF DAMAGE SCENARIO AT URBAN SCALE

The results illustrated in previous sections are here used to develop damage scenario at urban scale.

In particular, Figure 5.16 shows the damage scenario estimated by entering in the fragility curves of section 3.2 with the PGA=0.26g, i.e. the one associated to the second mainshock occurred in October, 26th 2016; only for the school the damage was estimated through its proper fragility curves, as reported in Brunelli et al. (2022a). The comparison between the observed and simulated damage is limited to the units for which sufficient data to attribute the actual damage were available.

The DL associated to the actual response has been attributed on basis of criteria consistent to the EMS98 scale (DL0 ÷ 5); obviously, such an assignment is based only to the damage occurred on external façades. In particular, the damage from DL1 to DL4 was divided into two sub-classes of damage according to the severity of damage attributed to that DL. It was reconstructed from the data available from the on-site surveys and careful inspections of video and photos collected after the second mainshock (i.e. the information used also to proceed to the inventory phase). Instead, the discrete DL derived from numerical fragility curves has been defined on basis of following procedure. Firstly, the probability of reaching the five damage levels were weighted by 0,1,2,3,4 or 5 moving from DL0 to DL5 and summed to obtain the average damage μ_d (see Brunelli et al. (2022a)). The latter was then re-converted into an equivalent discrete damage level by assuming a binominal distribution (see also Brunelli et al. (2021a)), leading to the following conversion intervals: 0-0.7 for DL0; 0.7-1 for DL1; 1.6-2.5 for DL2; 2.5-3.4 for DL3; 3.4-4.3 for DL4; 4.3-5 for DL5. Coherently with what has been done in the assignment of actual damage, for each damage level the interval associated to the one very close to the next one has been defined, as clarified in the legend of Figure 5.17.

The different plots were derived by considering or not soil-foundation-structure interaction and site effects. The developed procedure allows to directly introduce in the calculation the stratigraphic amplification through 1D site response analyses, but even 2D site effects are expected to have occurred in the valley under investigation. For this reason, the PGA-amplification factors calculated by Brunelli et al. (2022c) from 2D site response analyses under the second mainshock were exploited to amplify the intensity measure on the x-axis of the fragility curves. More rigorously, the input motions of the structural analyses would be differentiated according to the location of the building along the valley.

From Figure 5.16 it emerges that if SE and SFS interaction are neglected, the damage is significantly underestimated. Conversely, it is overestimated when only SE are considered, even from 1 or 2D analyses. The match improves by introducing the SFS interaction. The difference between observed and simulated damage scenario was quantified by comparing the percentage of buildings suffering the different damage levels and the average damage. Figure 5.16b reports the outcomes for each modelling hypothesis. The statistics of damages revealed that the lowest observed DL_S are the worst reproduced. Since their weighted contributions to the average damage are the lowest, the final μ_d resulted in a satisfying comparison with reality especially when SE and SFS interaction are considered.

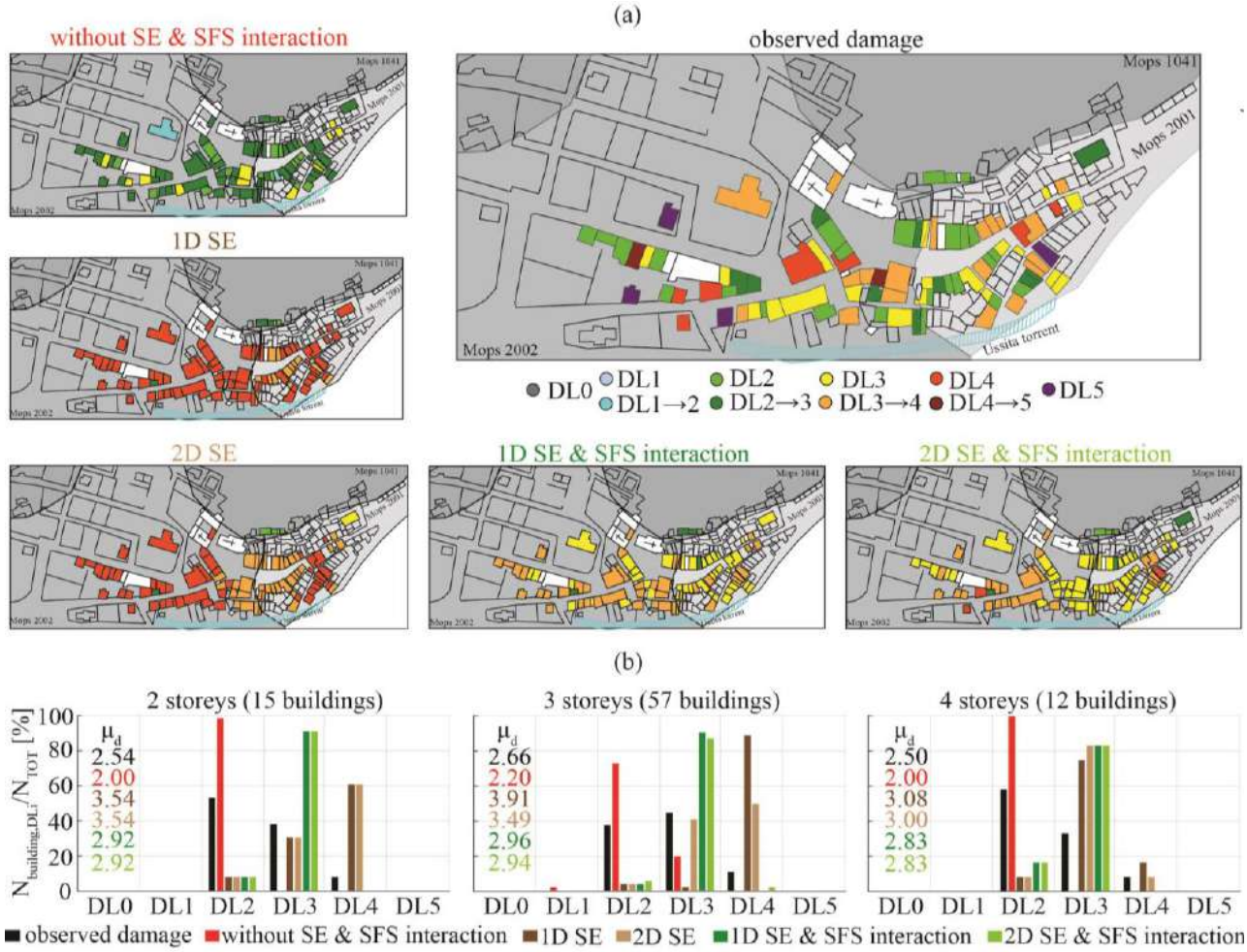

Figure 5.16. Maps (a) and statistics (b) of simulated and observed damage.

Once validated on the real observations, the same procedure was exploited to predict the damage expected under the earthquakes with a return period T_R=101 and 475 years, corresponding to PGA=0.136g and 0.260g as show in Figure 5.17. This application aims to show the potential of tools developed for also supporting mitigation policies at urban scale. The predictions were extended to the whole historical centre and site effects were neglected for buildings settled on Mops 1041, corresponding to the bedrock outcrop. Consistently with the simulation of the second mainshock, the predicted damage accounting for SE and SFS interaction is intermediate between that estimated neglecting and considering only site effects.

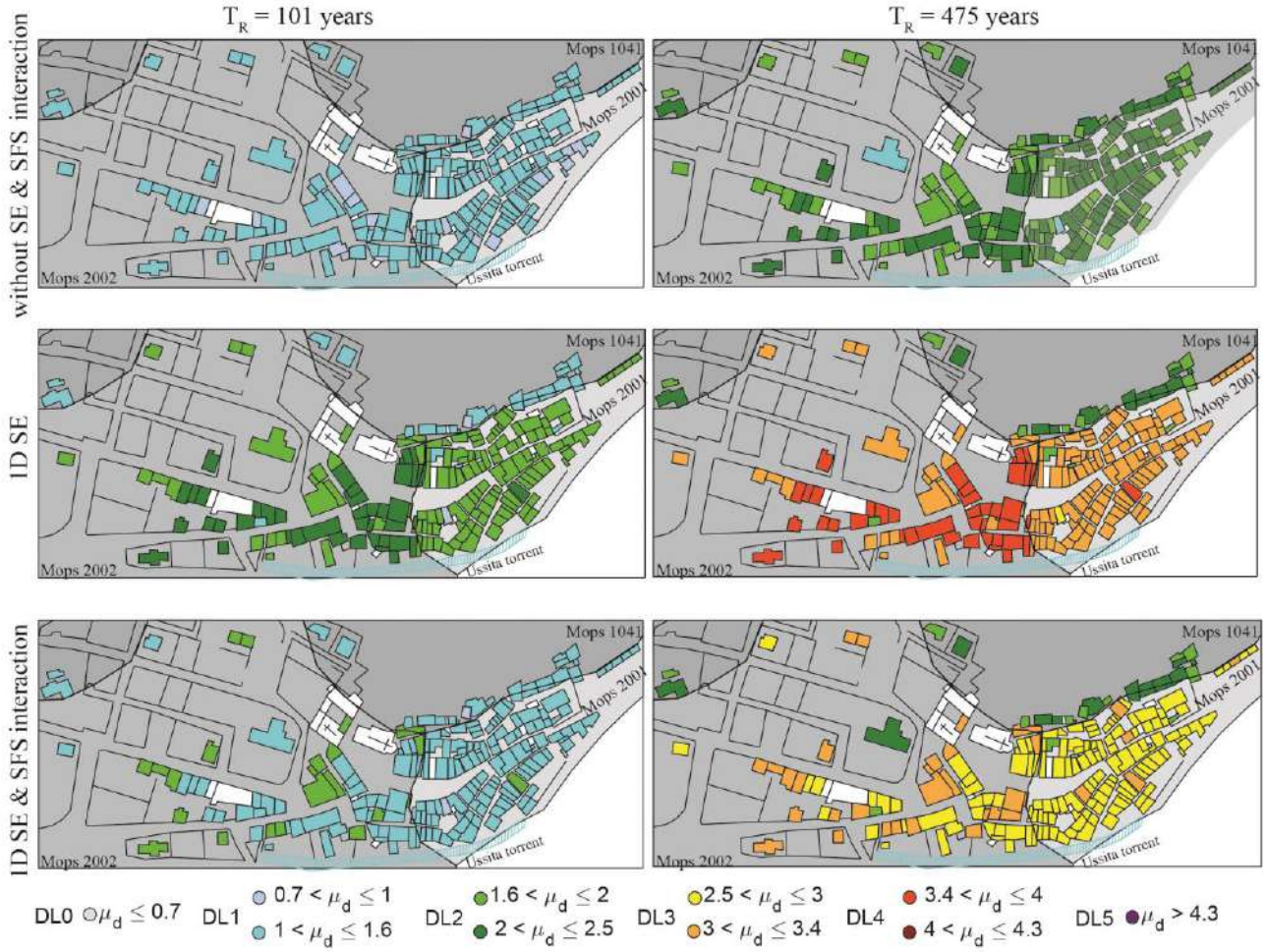

Figure 5.17. μ_d of buildings studied with only site effects, with SFS interaction and with the simplifying coefficients of the NTC (2018) code.

These damage scenario maps can be used for the purpose of estimating the impact produced by an earthquake also in terms of number of unusable and collapsed buildings as well as in terms of economic losses.

Several methodologies and tools for the estimation of unusable buildings and consequently evacuated population are available at international scale, e.g. Hazus-MH (FEMA (2003)), Syner-G (Khazai et al. (2012)), MCEER shelter model (Chang et al. (2008)). The approach use in this research is that proposed in Dolce et al. (2021b) based on the derivation from risk assessment methods previously carried out in Italy (Lucantoni et al. (2001); Bramerini and Di Pasquale (2008); Zuccaro and Cacace (2011)).

According to Dolce et al. (2021b), the buildings with very slight damage (D1) can be considered as usable buildings, all the buildings in D5 are considered collapsed buildings while the unusable ones can be distinguished in the two sub-categories, namely unusable buildings in the short term (UB_{st}) due to light or moderate damage and unusable buildings in the long term (UB_{lt}) due to more severe damage. For the computation of UB_{st} and UB_{lt}, the following equations has been adopted:

$$UB_{st} = \sum_{k=1}^{5} N_k u_{stk} \quad (5.3)$$

$$UB_{lt} = \sum_{k=1}^{5} N_k u_{slk} \quad (5.4)$$

where N_k are the number of URM buildings that experienced structural damage level D_k and u_{stk} and u_{ltk} are the percentage of unsafe buildings in the short and long term for each structural damage level D_k. The Table 5.6. illustrated the percentage adopted as proposed by Dolce et al. (2021b).

Table 5.6: Percentages adopted in Dolce et al. (2021b) for the estimation of short term and long term unsafe buildings.

% Unsafe buildings	D1	D2	D3	D4	D5
u_{stk}	0	40	40	0	0
u_{ltk}	0	0	60	100	0

This procedure was applied to the building stock composed by the 174 buildings in aggregate subjected to the three scenarios of Figure 5.17, by considering a return period of 475 years. The results obtained are reported in Table 5.7.

Consistently with what already shown by the damage scenario, the case without SE & SFS interaction would lead to have the majority of buildings still usable, while the other two scenarios lead to opposite consequences, with the majority of buildings unusable in the long term. The 1D SE simulation overestimates the damage by leading more buildings to be unusable for long-term.

Table 5.7: Values of the seismic risk in terms of consequences in terms of usable, unusable buildings in the short and long term, collapsed buildings and direct economic losses.

	Usable buildings	Unusable buildings in the short term	Unusable buildings in the long term	Collapsed buildings	Direct economic losses [million euro]
without SE & SFS interaction	104	70	0	0	9.80
1D SE	13	55	106	0	23.34
1D SE & SFS interaction	13	70	92	0	17.69

Finally, also the economic loss has been estimated by referring to equation proposed by Dolce et al. (2021b):

$$\text{economic loss} = \text{CU} \sum_{j=1}^{N} \sum_{k=1}^{5} A_j p_{j,k} c_k \qquad (5.5)$$

where N are the number of URM buildings, CU is the unit cost (Euro/m^2) of a building, including technical expenses and VAT, A_j are the built area of the j_{th} URM building; $p_{j,k}$ are the probability, in the considered time frame t for risk estimation, for the j_{th} URM building to experience structural damage state D_k; c_k is the percentage cost of repair or replacement (with respect to CU) for each structural damage state D_k.

These parameters are calibrated in Dolce et al. (2021b) on the basis of the actual repair costs that were monitored in the reconstruction process following recent Italian earthquakes (Di Ludovico et al. 2017a, b). However, these data were referred to residential buildings belonging to peripherical urban centres. More recent studies (Di Ludovico[1]) highlighted that in the case of buildings belonging to small historical centres the value of CU tends to be higher (due to higher technical difficulties in the reconstruction process and also to constraints made by the presence of artistic assets); more in general, it is expected that also the c_k factors would be recalibrated.

Since no literature works are yet available on that, in this research it has been decided to conventionally apply an increase of 30% to the CU cost considered by Dolce et al. (2021b). The updated values used in Equation 5.5 are given in Table 5.8.

Table 5.8: CU and cost parameters c_k (%) used to calculate the direct economic losses.

CU [€/m^2]	D1	D2	D3	D4	D5
1755	2	10	30	60	100

[1] Notes of the PhD Course "Seismic Losses and Consequences" offered by the University of Federico II of Naples and University of Genova in 2022, Teachers: Prof. M. Di Ludovico, Prof. S. Cattari and Prof. C. del Vecchio.

The resulting economic losses are shown in Table 5.7. The scenario without SE & SFS interaction leads to significantly smaller losses than the other two scenarios (2.4 times with respect to 1D SE and 1.8 times with respect to 1D SE & SFS interaction scenario). Finally, the 1D SE & SFS interaction scenario leads to a reduced loss (about 30%) with respect 1D SE.

5. CONCLUSIONS

The paper proposes a procedure based on low-demanding modelling strategies but accurate nonlinear dynamic analyses to consider such effects in the calculation of seismic fragility curves of masonry structures. Such procedure is intended to provide an effective tool merging the on-site hazard and the structural vulnerability applicable also to evaluate the seismic risk at urban scale.

The development of fragility curves specifically addressed to buildings in aggregate constitutes a first original contribution of the research. In fact, buildings in aggregate constitute one of key-feature of small historical centres present in Italy and, more in general, in Europe. Despite that, so far, the fragility curves proposed in the literature able to quantify the specific vulnerability factors that characterize them are very limited. The numerical procedure adopted revealed to be quite effective and the use of nonlinear dynamic analyses appears essential to investigate in a more reliable the interaction effects among units. The adopted integrated approach to analyse the interaction between the IP and OOP response is computationally efficient and allows to consider at least the filtering effect provided by the main structure on the seismic input that involves top portions of the aggregate. Results that account for the site effects and SFS interaction shows that the relationship between these two damage mechanisms may change if site effects are considered. Such relationship is expected depending on the actual vulnerability of aggregate to the IP response.

The effects of SFS interaction resulted in a reduction of the fragility for the analysed cases mainly due to the contribution to dissipate the seismic energy given by the foundation soil. Such aspect may suggest that the fixed base modelling is a conservative approach, but the damage estimated through such modelling strategy resulted higher and far from that observed. Conversely, a better agreement between simulation and reality is achieved when the SFS interaction is considered both at building and urban scale. The fixed-base model that simulates only the site amplification consequently also leads to heavier economic/social repercussions than the simulation with SFS interaction, as demonstrated by the latest analyses.

As far the future directions of the research, the following ones are identified.

Firstly, more rigorously, the input motions of the structural analyses would be differentiated according to the location of the building along the valley. Such approach is possible and will be exploited in the future, but requires a huge computational effort and so is poorly effective in large scale evaluation of risk.

Moreover, further work can be done to better differentiate the response among the aggregate types and improve the match at the lowest damage levels. In this frame, the cross interaction between foundations of adjacent buildings will be soon explored, since it may have a role in the response of buildings in aggregate.

Finally, the inventory phase - i.e. the collection of all data necessary to characterize the vulnerability of buildings - is today problematic, because it requires onerous campaigns in situ or to have, as in the case of Visso, a large amount of documentation. The use of automatic or semi-automatic procedures based on digital multi-scalar and multi-sensor surveys will be very useful in the future. This procedure can exploit also artificial intelligence algorithms. The objective is to define a user-friendly information acquisition system, appropriate for risk assessment at large scale but with the advantage of being automated.

Anyway, this work demonstrates that site-specific fragility curves computed through conventional modelling strategies for structures and subsoil are effective in the prediction of damage if they are carefully calibrated according to the recurrent soil and structure configurations.

Thanks to its flexibility, the proposed procedure may be integrated in a more complex process, based on the modelling of structures whose features are derived from onsite surveys through advanced technologies, joint to the outcome of seismic microzonation studies eventually integrated with additional analyses and aimed to the generation of risk maps at urban scale of the whole Italy.

CHAPTER 6

Conclusions and future developments

Main results achieved

The PhD thesis focuses on a scientific/technical problem requiring multidisciplinary expertise that involve two main fields: structural engineering and geotechnical engineering.

Starting from field evidence on the influence of site amplification and soil-foundation-structure interaction on the damage of an instrumented URM building and a historical centre under the Central Italy seismic sequence, this research proposes a procedure based on low-demanding modelling strategies but accurate nonlinear dynamic analyses to consider such effects in the calculation of seismic fragility curves of masonry structures.

So far, the specific studies addressed to this topic are quite limited in the literature and this PhD research attempts to contribute filling this gap. Such procedure is intended to provide an effective tool merging the on-site hazard and the structural vulnerability applicable also to evaluate the seismic risk at urban scale. Definitely, it aims to support the identification of most critical conditions and improving the planning of mitigation policies.

The research is focused on URM buildings isolated or in aggregate located on soft soil through shallow foundations, as usual for such building typology. Both the soil and structure types are inferred from the recurrent situations in the village of Visso, assumed as a benchmark for the validation of the procedure.

In the analysed cases, site effects are always detrimental leading to an increase in the damage with respect to the typical assumption of structures on rock.

Results achieved on the school of Visso have shown that such damage increment is underestimated if predicted by simply amplifying the intensity measure of the fragility curve of structures on stiff soil through Code-conforming factors, as usual in the current practice. Moreover, fragility curves of the same structure located on different subsoil may vary especially at high damage levels mostly influenced by the different nonlinear soil response. For this reason, the generation of fragility curves accounting for site effects through input motions directly recorded on soft soil need to be done by carefully selecting the accelerograms by matching the subsoil profile below the recording stations with that of the case under investigations. The comparison executed among the different analytical approaches for the evaluation of the foundation damping demonstrated that the results are poorly sensitive to the applied approach and changes significantly if the soil hysteretic damping is considered or not.

The development of fragility curves specifically addressed to buildings in aggregate constitutes another original contribution of the research. In fact, buildings in aggregate constitute one of key-feature of small historical centres present in Italy and, more in general, in Europe. Despite that, so far, the fragility curves proposed in the literature able to quantify the specific vulnerability factors that characterize them are very limited. In particular, such key factors are mostly identified in: i) the interaction effects between adjacent units and, more specifically, the pounding effects; ii) the integration between the in-plane (IP) and out-of-plane (OOP) response. The numerical procedure adopted revealed to be quite effective and the use of nonlinear dynamic analyses appears essential to investigate in a more reliable way such interaction effects. The adopted integrated approach to analyse the interaction between the IP and OOP response is computationally efficient and allows to consider at least the filtering effect provided by the main structure on the seismic input that involves top portions of the aggregate. Results that account for the site effects and SFS interaction are quite

interesting, showing that the relationship between these two damage mechanisms may change if site effects are considered. Such relationship is expected depending on the actual vulnerability of aggregate to the IP response.

The exploitation of the amplification factors of the integral of spectral amplitude provided by the seismic microzonation appears potentially useful for large scale evaluation, since they are derived for zones characterized by homogeneous subsoil profiles, but still unapplicable to the existing fragility curves expressed through the peak ground acceleration.

To explicitly considers the SFS interaction is generally beneficial, thanks to the contribution of soil and foundation in the dissipation of seismic energy. Only when the spectral acceleration is used as intensity measure, the expected damage of very stiff structure increases for the compliant base model. Such amplification occurs because the SFS interaction-induced increment of structural period moves the spectral amplitude on the ascending branch and up to the flat and highest zone of the spectrum.

Moreover, the comparison with the after-earthquake damage detection revealed that the damage is underestimated by fragility curves based on fixed base models, overestimated by considering only site effects and better captured only if site effects joint to SFS interaction are considered. Such beneficial effect may address researchers and practitioners to neglect SFS interaction in the vulnerability or risk assessment. Anyway, in a more recent resilience-based perspective, this contribution is worth to be considered since prevents or limit the irreversible structural damages, leading to a more resilient system.

This work demonstrates that site-specific fragility curves computed through conventional modelling strategies for structures and subsoil are effective in the prediction of damage if they are carefully calibrated according to the recurrent soil and structure configurations.

Future directions of the research

Three main possible directions for future developments are identified that involve:

- the procedure itself to account for site and SFS interaction effects;
- the results specifically achieved for masonry structures;
- the use of the procedure for developing damage and risk scenario at urban scale.

As the first point concerns, the so conceived procedure could be in the future enriched with more accurate evaluations of the impedance functions by considering the cross interaction among the closely spaced foundations of structures in aggregate, or by considering the eventual 2D site effects. Furthermore, the Rayleigh curve should be calibrated on the SFS damping ratio obtained for different frequencies, while in this research the Rayleigh curve was calibrated only to be enough flat around such a value of SFS damping ratio.

Moreover, although the uncoupled approach adopted in this research and the use of replacement oscillator are quite efficient in terms of computational effort, in future the development of a macroelement capable to describe in a more accurate way the dissipation provided by the foundation is desirable.

More specifically, regarding the simulation of the seismic behaviour of masonry structures, it is desirable to improve even more the explicit modelling integration of IP and OOP responses.

As the second point concerns, as well known the response of a compliant base structure depends on the structural pattern (period of vibration, strength and structural typology, foundation typology), on the subsoil configuration (stratigraphic profile, stiffness) and on the input motion (frequency and amplitude). For this reason, the analysed cases are not exhaustive to be conclusive on the beneficial or detrimental effects of the soft soil on the response of all URM building types. Additional parametric analyses will be very useful for deepening this issue.

As the third point concerns, thanks to its flexibility, the proposed procedure may be integrated in a more complex process, based on the modelling of structures whose features are derived from onsite surveys through advanced technologies, joint to the outcome of seismic microzonation studies eventually integrated with additional analyses and aimed to the generation of risk maps at urban scale of the whole Italy.

Indeed, the inventory phase - i.e. the collection of all data necessary to characterize the vulnerability of buildings - is today problematic, because it requires onerous campaigns in situ or to have, as in the case of Visso, a large amount of documentation.

New development of research could lead to an optimization of the data collection useful to provide the inventory of all the data necessary to characterize the structural response of the buildings in aggregate, enriching and streamlining the information provided by the only census databases existing today (see e.g. Zuccaro et al. (2015)), to capture the key features of buildings in and also ensure a comprehensive structural interpretation. The attention is focused both on geometrical data (e.g. not only total height and number of levels but also dimensions addressed to quantify the irregularity in elevation and percentage/distribution of openings in facades) and on structural details (e.g. masonry quality, presence of tie-rods, transformation of structural units like raising up, possible activation of out-of-plane mechanism, etc).

While in this research these data have been collected in a traditional way, the use of automatic or semi-automatic procedures based on digital multi-scalar and multi-sensor surveys will be very useful in the future. This procedure can exploit also artificial intelligence algorithms. The objective is to define a user-friendly information acquisition system, appropriate for risk assessment at large scale but with the advantage of being automated.

Even the identification of each structural unit in complex aggregate represents a big issue itself: the semi- and automatic procedures developed to identify the geometrical dimensions of units will contribute to support this preliminary but essential step of the risk assessment. The support given to such an identification by aerial images is fundamental, since these buildings are often characterized by complex irregularity in elevation and transformations involving the upper parts which are difficult to be detected only by terrestrial surveys.

ANNEX A 4.1a

Calibration of the real soil in Visso's historic center

To study the influence of the soil stiffness, four soil profiles were selected as explained in Chapter §4.1. They were selected so that the equivalent shear wave velocity up to the bedrock depth (V_{Seq}) falls in the range of values identifying the class C (as defined by NTC (2018); CEN (2004)). As explained in the Chapters §2 and 3, the first profile (S1) is the actual soil profile below the "Pietro Capuzi" School in Visso, made of alternations of sandy gravel layer (SG), covered and locally interbedded by clayey silt (CS) and silty clay (SC) lenses. Its V_S profile was directly measured through a Down-Hole test (DH) (see ReLUIS (2018a); MZS3 (2018)), which substantially confirmed the outcome of a previous MASW test (see Chapter §2). The V_{Seq} of S1 is equal to 281m/s. The details on the geotechnical characterization of this soil profiles S1 are reported also in Brunelli et al. (2021a), while the validation of the subsoil model is reported by Cattari et al. (2019a).
The second profile (S2) is representative of the soil profile in the historic centre of Visso. As explained in chapter 4.1 the information on such soil profile were collected during the third level microzonation studies MZS3 (2018). In this annex it is reported in detail the validation of the assumed stiffness for the S2 soil soils starting from the correlations that worked best for the DH test (see Figures 4.1.1 in Chapter 4.1). 40 correlations for coarse-grained soil and 50 correlations for fine-grained soil (see Table 1) were applied to the number of blows of SPT tests executed in the sandy gravel in the borehole close to the school, identified as DH1 in Figures 4.1.1 in Chapter 4.1, as well as in the clayey silt in the shallowest zone of B11 and B12. The cases are listed in Table 2 (validation). The tests used in the calibration are in Figures 4.1.1 in Chapter 4.1 coloured in red instead the unused tests are in black.

Table 1: V_S-N_{SPT} correlations applied in this study.

	Name	Formula Vs= [m/s]	Geographic area	Types of soil	N_{SPT} ranges investigated	r - R^2
1	Palmer and Stuart (1957)	$100.59\ N^{0.302}$				0.53
2	Kanai (1966)	$19\ N^{0.6}$		all soils	1-50	
3	Imai and Yoshimura (1970)	$76\ N^{0.33}$	Japan	all soils		
4	Ohba and Toriuma (1970)	$84\ N^{0.31}$	Osak (Japan)	alluvial soil (not gravel)	2-100	
5	Fujiwara (1972)	$92.1\ N^{0.337}$	Japan	all soils		
6	Ohsaki and Iwasaki (1973)	$81.4\ N^{0.39}$	Japan	all alluvial soil	2-100	0.886
7	Imai and Yoshimura (1975)	$92\ N^{0.329}$	Japan			
8	Imai et al. (1975)	$89.9\ N^{0.341}$	Japan	all soils		
9	Imai (1977)	$91\ N^{0.337}$	Japan	all soils		
10a	Ohta and Goto (1978)	$85.35\ N^{0.348}$	Japan	all alluvial soil	2-200	0.719
10b		$94\ N^{0.34}$	Japan	gravels	2-200	
11	Imai and Tonouchi (1982)	$96.9\ N^{0.314}$	Japan	all soils	1-400	0.868
12	Jinan (1987)	$116.1(N+0.3185)^{0.202}$	Shanghai (China)	all soils	10-40	0.7
13	Lee (1990)	$105.64\ N^{0.32}$	Taiwan	Silty Soils	1-50	0.73

14	Yokota et al. (1991)	$121\ N^{0.27}$	Japan	all soils	2-200	
15	Lee (1992)	$82.8\ N^{0.134}\ (z+1)^{0.333}$	Taiwan	Silty Soils	1-50	0.65
16	Kalteziotis et al. (1992)	$76.2\ N^{0.243}$	Greece	all soils	2-200	0.82
17a	Athanasopoulos (1995)	$107.6\ N^{0.36}$	Greece	all soils	6-200	0.75
17b		$121.7\ N^{0.33}$		alluvial soil (not gravel)		0.77
17c		$85.3\ N^{0.42}$		gravelly soil		0.68
18	Raptakis et al (1995)	$192.4\ N^{0.13}$	Greece	gravelly soil		
19	Sisman (1995)	$32.8\ N^{0.51}$				
20	Iyisan (1996)	$51.5\ N^{0.516}$	Turkey	Deep Alluvial deposits		0.81
21	Jafari et al. (1997)	$22\ N^{0.85}$	Teheran (Iran)	all soils	2-60	
22	Kiku et al. (2001)	$68.3\ N^{0.292}$	Adapazarı (Turkey)	all soils		
23	Jafari et al. (2002)	$22\ N^{0.77}$	Teheran (Iran)	Silty Soils	15-65	
24	Hasancebi and Ulusay (2006)	$90\ N^{0.308}$	Eastern Marmara Region (Turkey)	all soils	5-42	0.73
25a	Ulugergerli and Uyanik (2007)	$23.291\ Ln(N)+405.61$	Turkey	all soils	4-200	
25b		$52.999\ e^{0.011N}$		all soils	4-200	
26a	Hanumantharao and Ramana (2008)	$86.0\ N^{0.42}$	Delhi (India)	Sand - silt	2-50	0.94
26b		$82.6\ N^{0.43}$		all soils	2-50	0.95
27	Uma Maheswari et al. (2008)	$95.64\ N^{0.301}$	Chennaimcity (India)	all soils	1-80	0.835
28a	Dikmen (2009)	$58\ N^{0.39}$	Anatolia (Turkey)	all soils	2-50	0.75
28b		$60\ N^{0.36}$		silt	4-50	0.71
29	Akin et al. (2011)	$59.44\ N^{0.109} z^{0.426}$	Erbaa area (Turkey)	all alluvial soil	10-50	0.89
30a	Pietrantoni et al. (2013)	$263.6+2.878\ N$	region (Italy)*	all soils	4-100	0.15
30b		$158.97\ N^{0.224}$			4-100	0.15
30c		$306.97+2.011\ N$			4-100	0.09
30d		$195.01\ N^{0.179}$		gravels	4-100	0.09
30e		$199.47+2.188\ N+10.623\ z$			4-100	0.35
30f		$181.68+0.777\ N-0.777\ z$	Marche (Italy)	Silty - sandy silt Soils	4-100	0.36
31	Fauzi et al. (2014)	$105.03\ N^{0.286}$	Jakarta (Indonesia)	all soils	1-100	0.675
32	Fabbrocino et al. (2015)	$90.35\ N^{0.317}$	Molise (Italy)	all soils	2-95	0.865
33	Fatehnia et al. (2015)	$77.1\ N^{0.355}$	Florida (USA)	all soils	0-60	0.893
34a	Pérez-Santisteban et al. (2016)	$62.6\ N^{0.52}$	Madrid (Spain)	all soils	10-100	0.5
34b		$77.85\ N^{0.121}\ z^{0.619}$		all soils	10-100	0.76
35a	Gautam (2017)	$115.8\ N^{0.251}$	KathmanduValley (Nepal)	all soils	2-60	0.623
35b		$102.4\ N^{0.274}$		Silty Soils	3-34	0.355
36	Thokchom et al. (2017)	$4.778\ N + 135.7$	Dholera (India)	Silty Soils	1-80	0.776
37	Rezei et al. (2018)	$36.592\ N^{0.6787}$	Golestan (Iran)	all soils	5-50	0.75

*Sicilia, Calabria, Basilicata, Puglia, Marche, Toscana, Friuli region

The difference between the values of the Vs of the Down-Hole and those estimated from the number of blows of the SPT tests resulted minimum in six correlations for the gravels (10a, 10b, 17a, 17c, 26b, 30c) and five for the silts (10a, 3, 15, 24, 32). Correlation 10a therefore minimizes the difference for both types of soil. Figure 2 shows the value of Vs for each correlation for the several SPT test listed Table 2. Green (light and dark) colour indicates the correlations that best approximate

the value of Vs recorded by the Down-Hole test, the black dashed lines are representative of the minimum and maximum values calculated with formulations 25a and 25b (see Ulugergerli and Uyanik (2007)) which want to be representative of the maximum estimable variation of V_S for a soil. In the case of silt, the maximum value obtained is very large (always greater than 430 m/s) and therefore is not shown in Figure 2. Only these latter correlations were used to calculate the Vs of the soil below the historic centre. The average V_S values obtained from the two SPT tests in B4 was assigned to the gravel. The results for the silts obtained with correlations 3 and 15, or 24 and 32, are comparable and therefore the single value of 162 m/s, or 183 m/s, was assigned to the silts. Finally, also in the case of gravels the formulas 17a, 17c and 26b led to similar results and the single value of 416 m/s was assumed.

Table 2: SPT tests used for the validation of the correlation laws and the estimation of VS of the historical centre.

	Layer	N test	N_{SPT}	Test	Z [m]
Capuzi School area	sandy gravel	1	36	DH1	7
		2	100	DH1	12
	clayey silt	3	4	B11	1.6
		4	6	B12	1.2
		5	4	B10-B11	3.2
		6	6	B12	3.2
historic centre of Visso	sandy gravel	7	10	B4	1.9
	clayey silt	8	48	B4	4.4
		9	38	B4	8.3

The summary values are listed in Table 3 where cases from B to F are obtained by coupling each formulation best correlated for gravel with those for silt. These results are compared with Case A in which the values obtained from the Down Hole test are assumed. In any case the bedrock depth was assumed equal to 18m and the V_S equal to 1300 m/s. It can be noted that the V_{Seq} values are all very close (289.5±26)m/s.

Table 3: Cases considered for soil model (S2).

	Soil type	Formula	V_S [m/s]	V_{Seq} [m/s]	f1 [Hz]
Case A	Silty Soils	DH value	136	273	5.10
	gravelly soil	DH value	383		
Case B	Silty Soils	10a	190	275	4.33
	gravelly soil	10a	315		
Case C	Silty Soils	3-15	162	272	4.46
	gravelly soil	10b	337		
Case D	Silty Soils	3-15	162	309	5.58
	gravelly soil	17a-17c-26b	416		
Case E	Silty Soils	24-32	183	284	4.46
	gravelly soil	10b	337		
Case F	Silty Soils	24-32	183	324	5.70
	gravelly soil	17a-17c-26b	416		

A summary of the cases considered is also reported in Figure 3a where the V_S for the two layers of the soil profile S2 are compared in the six hypotheses of Table 3. In Figure 3b reports their amplification functions. The six subsoil profiles were modelled in the STRATA software (Kottke and Rathje (2008)) to execute linear site response analyses and calculate the predominant natural frequency from the amplification function. The latter were compared with the frequency 4.44 Hz associated with the peak of the amplification function obtained from the ratio between the horizontal and vertical component of the acceleration recorded under noise in the historical centre (HVSR in Figure 1). All the numerical values are reported in Table 3, while the amplification functions are shown in Figure 3b. The Case D and F led to a higher frequency than the target, the Case B, C and E have the same maximum frequencies close to the target value. The frequency obtained for the Case

A is intermediate among the numerical simulations, but higher than the experimental value. Among the three formulations that best approximated the target frequency, Case C was chosen as it was the one with the lowest V_{Seq}.

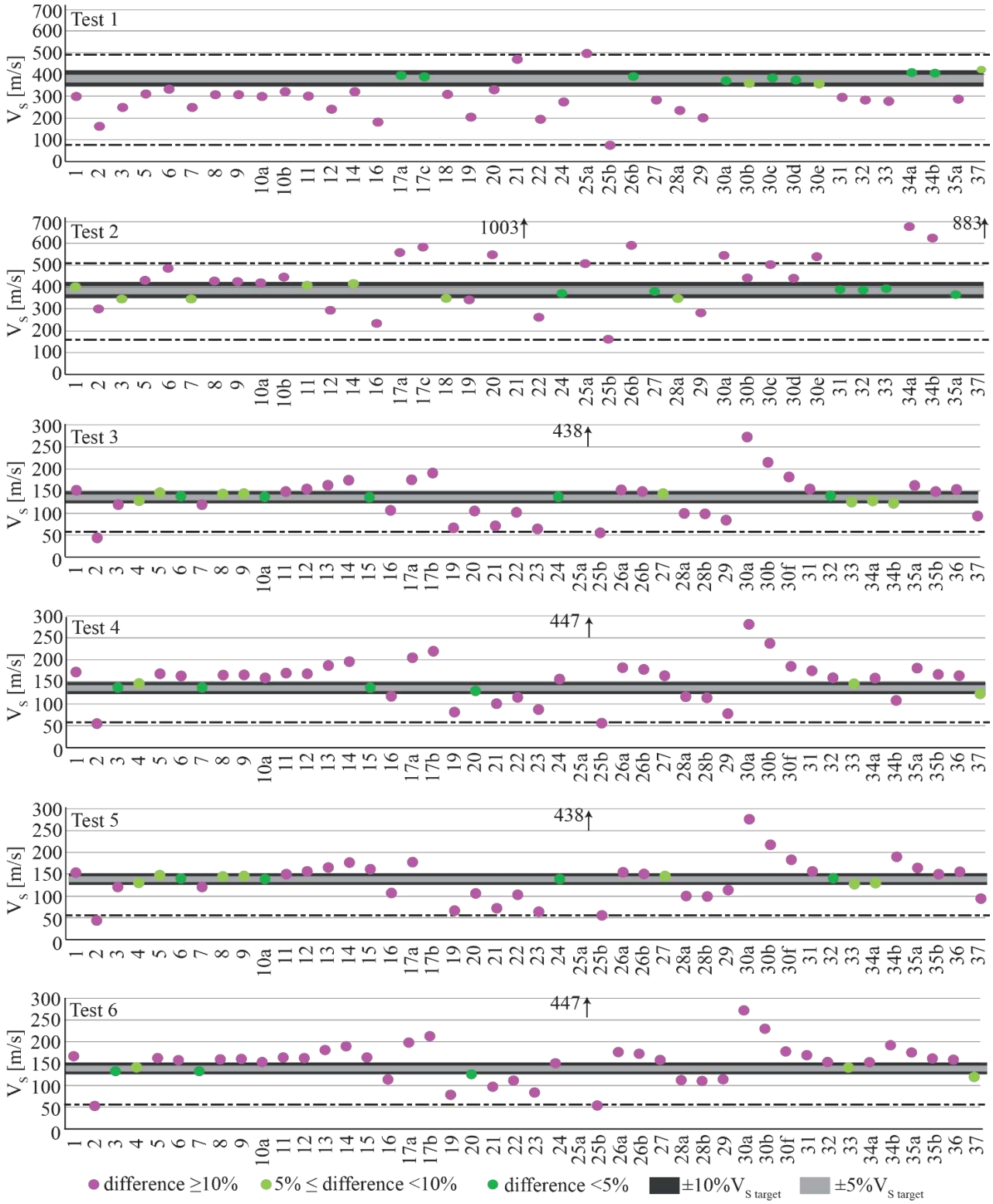

Figure 3. Calculation of the Vs for each correlation for the various SPT tests performed.

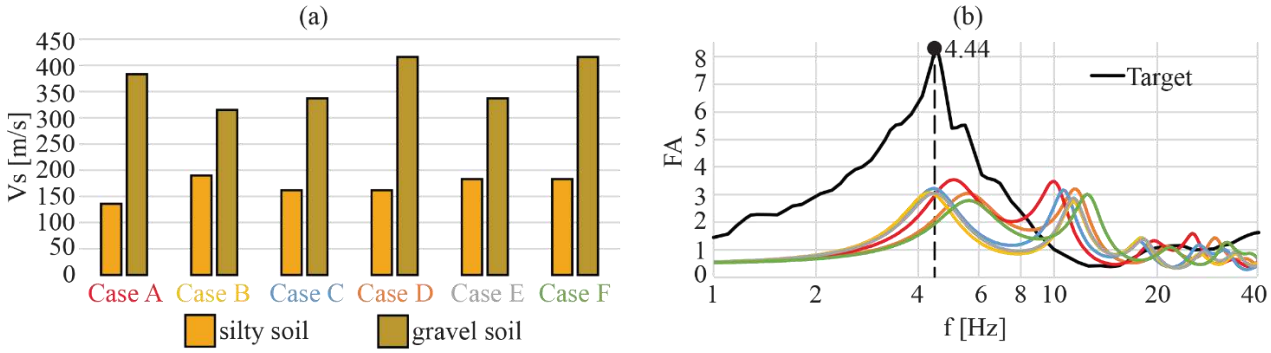

Figure 4. (a) variation of the V_S and (b) FA for the six cases considered.

ANNEX A.4.1b

Comparisons with fragility curves derived with a records selection compatible to soil C

The work carried out in Chapter §4.1 considers the specific site amplification for four soils (two real and two calibrated with literature formulations). To do this, a local seismic response was performed that requires different information about the soil. This is not always possible and would require carrying out boreholes on the site to be analysed to know the stratigraphy profile, and also MASW or Down Hole tests to know the stiffness of the soils.

Typically, studies aimed to derive fragility curves do not consider site amplification as Lagomarsino et al. (2021); Donà et al. (2020); Zuccaro et al. (2021); Rosti et al. (2021); Angiolilli et al. (2021a). The selection of works cited intentionally varied from numerical, empirical, analytical-mechanical hybrid or analytical-mechanical approaches. Other empirical works propose to consider site effects with corrective coefficients such as Chieffo and Formisano (2020) or Formisano et al. (2021).

Numerical approaches typically use selections of accelerograms recorded on rocky soil and use fixed base models. Therefore neither site amplification nor consequently the SFS interaction are investigated. New approaches propose to analyse the site amplification only with a selection of signals recorded by stations on soft ground and which are therefore representative of an input not at the bedrock but in the freefield. This Annex aims to compare the results obtained in fragility curves reported in Chapter 4.1 with those obtainable from non-linear dynamic analyses made with signals recorded directly from stations located on the soft ground. These signals would already include the site amplification obtained from the site where the signals were recorded. The work carried out up to now on the contrary had defined a selection of accelerograms recorded by stations placed on ground A or B with $V_{S,30}$ greater than 700 m/s precisely to try to have signals that did not already have site components inside them.

The new selection of signals recorded on deformable soils is obtained from Paolucci et al. (2020), and more recently published in Manfredi et al. (2022). These signals were recorded by stations placed on soils C and D and therefore consistent with the four of the previously described soil profiles which can be catalogued in type C soils according to NTC (2018) or CEN (2004). This comparison allows to evaluate what was the difference obtainable from analyses that consider the amplification of the specific site and that obtained from a wide selection of soils in that category.

With this new selection, non-linear dynamic analyses were made with the numerical model described in the Chapter §2. In this case, the comparison can only be done with the fixed base (FB) model as the stiffnesses and the damping mobilized by the soil are not available. These data were necessary to calibrate the impedances and equivalent damping of the complaint base (CB) model. To obtain this information, it would be necessary to deconvolve the signal recorded by the station placed on the deformable soil for that specific site and then do a site response analysis to obtain the mobilized stiffness and damping. This procedure was not always possible since the detailed information for all the stations in the selection of Paolucci et al. (2020) is not known. In any case, it would be inconsistent with the expeditious choice of directly considering signals recorded on deformable soils of the class of the first selection of this research. Therefore, considering signals recorded by stations placed on deformable soils, it is necessary to consider only possible site effects, but not the soil foundation structure interaction.

Figure 1 compare the acceleration spectra in freefield condition obtained from the local seismic response for each defined soil profiles with those of the Paolucci et al. (2020) selection. Furthermore,

the values of the structure period of the FB model in the two directions are reported (T_X = 0.148 s T_Y = 0.174 s as computed in Chapter 2). The differences in amplifications between the four soils was commented in Chapter §4.1, in Figure 1 was reported with the aim of considering the different amplifications with the selection Paolucci et al. (2020). It might seem that the Paolucci et al. (2020) amplify less than the first three soil profiles, since the maximum Sa is smaller, and would be greater only for soil S4. This is partially true for structural periods, as the 84th percentile of Paolucci et al. (2020) is greater than all other 84th percentiles. Therefore, overall the signals of Paolucci et al. (2020) have higher intensities than the freefield signals of other soils. There are only a few events of the first selection that have a greater amplification. Also, in peak ground acceleration (PGA) -first point of the spectrum-, it is noted how the 84th percentile for Paolucci et al. (2020) is greater.

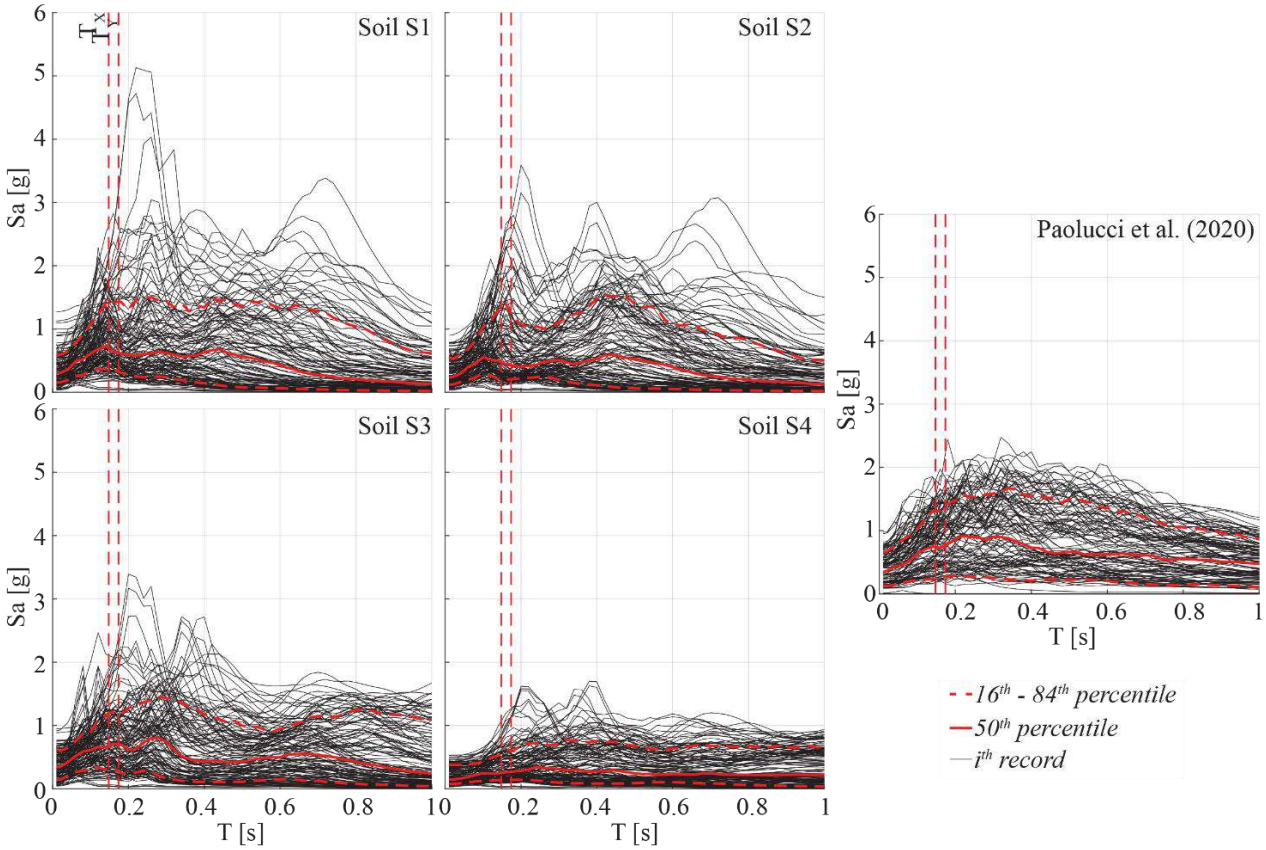

Figure 1. Acceleration response spectra of the resulting from site response analyses for the four soils and input of Paolucci et al. (2020).

The non-linear dynamic analyses with the selection signals of Paolucci et al. (2020) are also made considering the inversion of the direction of the signal. So 250 bi-directional analyses are carried out considering the first component in the X direction and the second in the Y direction and then vice versa. Since the comparison must be made with the same soil hypothesis, the fragility curves must be constructed not with the intensity measurement (IM) at the bedrock - as was done in the other chapters to obtain comparable results-, but in freefield, as those of selection Paolucci et al. (2020) already appear to be.

Table 1 and Table 2 report the number of analysis ($N_{records}$), the median value (IM_{50}) and the standard deviation (σ) for PGA; the spectral acceleration for the first period of structure (Sa (T_1)). Table 1 shows the analysis with the Paolucci et al. (2020) selection; Table 2 shows the results obtained for each soil considered. These tabulated values are obtained as the mean and deviation of the IM - in freefield - of the analysis that lead to that DL as already described in Chapter §3.

Table 1: Median value (IM_{50}) and standard deviation (σ) associated with the various DLs for the FB C model with the selection of Paolucci et al. (2020).

	PGA [g]		Sa(T_1) [g]		$N_{records}$
	IM_{50}	σ	IM_{50}	σ	
DL1	0.125	0.234	0.258	0.234	26
DL2	0.215	0.241	0.513	0.281	80
DL3	0.365	0.179	0.687	0.291	12
DL4	0.439	0.103	0.904	0.164	14
DL5	0.597	0.237	1.231	0.197	114

Table 2: Median value (IM_{50}) and standard deviation (σ) associated with the various DLs for the FB C model for the four soil profiles.

	PGA [g]		Sa(T_1) [g]		$N_{records}$
	IM_{50}	σ	IM_{50}	σ	
			S1		
DL1	0.126	0.395	0.310	0.301	54
DL2	0.258	0.315	0.608	0.397	99
DL3	0.380	0.108	0.793	0.289	14
DL4	0.443	0.151	0.952	0.222	27
DL5	0.659	0.305	1.370	0.379	72
			S2		
DL1	0.134	0.376	0.222	0.303	102
DL2	0.243	0.271	0.492	0.337	65
DL3	0.365	0.113	0.838	0.305	12
DL4	0.437	0.204	1.036	0.378	26
DL5	0.605	0.224	1.409	0.357	62
			S3		
DL1	0.127	0.436	0.254	0.298	55
DL2	0.267	0.330	0.553	0.347	92
DL3	0.417	0.184	0.894	0.283	17
DL4	0.510	0.184	1.101	0.367	18
DL5	0.597	0.228	1.120	0.318	84
			S4		
DL1	0.097	0.432	0.174	0.366	142
DL2	0.243	0.320	0.437	0.318	73
DL3	0.356	0.143	0.529	0.226	9*
DL4	0.374	0.086	0.571	0.257	8*
DL5	0.436	0.120	0.742	0.289	32

* data considered statistically unreliable.

Observing the number of records that end up in the various DL groups, it is confirmed that the selection by Paolucci et al. (2020) appears to be more punitive as it leads to large DLs. Furthermore, for soil S4 the results of DL3 and DL4 are not statistically valid as already described in Chapter §4.1. For this reason, the fragility curves for this soil are not constructed for these DLs.

Figure 2 shows the curves of the four soils and those obtained from the selection Paolucci et al. (2020) in PGA and Sa(T_1). For the PGA the Paolucci et al. (2020) curves for DL1 and DL5 are well correlated with those of the various soils, for DL2 it is more punitive, while for DL3 and DL4 the differences between the soils are more marked. For DL5 only S4 is different from the other three soils and from the formulation Paolucci et al. (2020) due to its dissipative behavior. In the case of Sa(T_1) the first two DLs the formulation Paolucci et al. (2020) brings results equal to those of other soils and some major differences are present in the higher DLs.

Since the signals of Paolucci et al. (2020) are obtained from amplifications obtained from many soils and have an inter soils statistic as well as record-to-records variability. While the curves of the four soils considered only the record-to-record variability. For this reason, it is necessary to combine the

curves of the four soils (only the first three for DL3 and DL4).

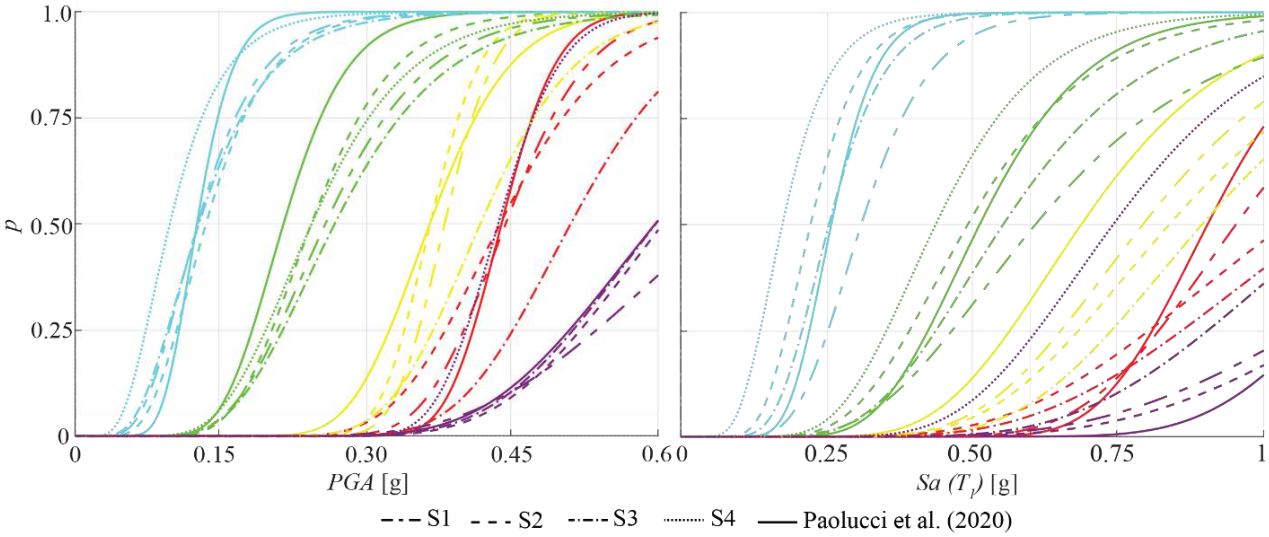

Figure 2. Comparisons between the fragility curves obtained by applying to the FB model the free field signal for the four soils or those resulting from the Paolucci et al. (2020) selection.

To combine the curves, The equations 1 and 2 are used to combine the curves for the average value of IM_{50} ($\overline{IM_{50}}$) and dispersion ($\bar{\sigma}$), respectively. These equations are used for each DL (from DL1 to DL5).

$$\overline{IM_{50}} = e^{\sum_{k=1}^{n} \ln(IM_{50,k})} \quad (1)$$

$$\bar{\sigma} = \sqrt{\sigma_m^2 + c^2} \quad (2)$$

where

$$\sigma_m = \sqrt{\frac{\sum_{k=1}^{n} \sigma_k^2}{n}} \quad (3)$$

$$c = \sqrt{b - a^2} \quad (4)$$

$$b = \frac{\sum_{k=1}^{n} ln^2(IM_{50,k})}{n} \quad (5)$$

$$a = \frac{\sum_{k=1}^{n} ln(IM_{50,k})}{n} \quad (6)$$

In Table 3 there are the value of $\overline{IM_{50}}$ and $\bar{\sigma}$ for the PGA e Sa(T_1) calculated with the equation 1 and 2. With these values, the fragility curves, called average fragility curves, are constructed to be compared with those of Paolucci et al. (2020).

Table 3: Median value (IM_{50}) and standard deviation (σ) associated with the various DLs for the average fragility curves between the four soil profiles value.

	PGA [g]		Sa(T_1) [g]	
	$\overline{IM_{50}}$	$\bar{\sigma}$	$\overline{IM_{50}}$	$\bar{\sigma}$
DL1	0.120	0.429	0.235	0.381
DL2	0.252	0.312	0.519	0.372
DL3	0.387	0.150	0.841	0.296
DL4	0.462	0.194	1.028	0.345
DL5	0.568	0.278	1.125	0.394

The comparison between the averaged curves of the Chapter §4.1 and those obtained with the signals of Paolucci et al. (2020) is reported in Figure 3. It can be noticed that for some DLs both for PGA and for Sa(T_1) there is a difference in the dispersion values rather than in the median values

(information can also be obtained by comparing Table 1 with Table 3). For other DLs there is a clearer difference also in the median value (for example for Sa(T_1) in DL3, 4 and 5). However, the comparison shows quite similar behavior between the two curves. This shows how well the selection of Paolucci et al. (2020) captures the pattern of C-type soils used in Chapter §4.1. But each soil amplifies in a different way as shown in Figure 2 and therefore the characterization of the response of that soil in Paolucci et al. (2020) was lost.

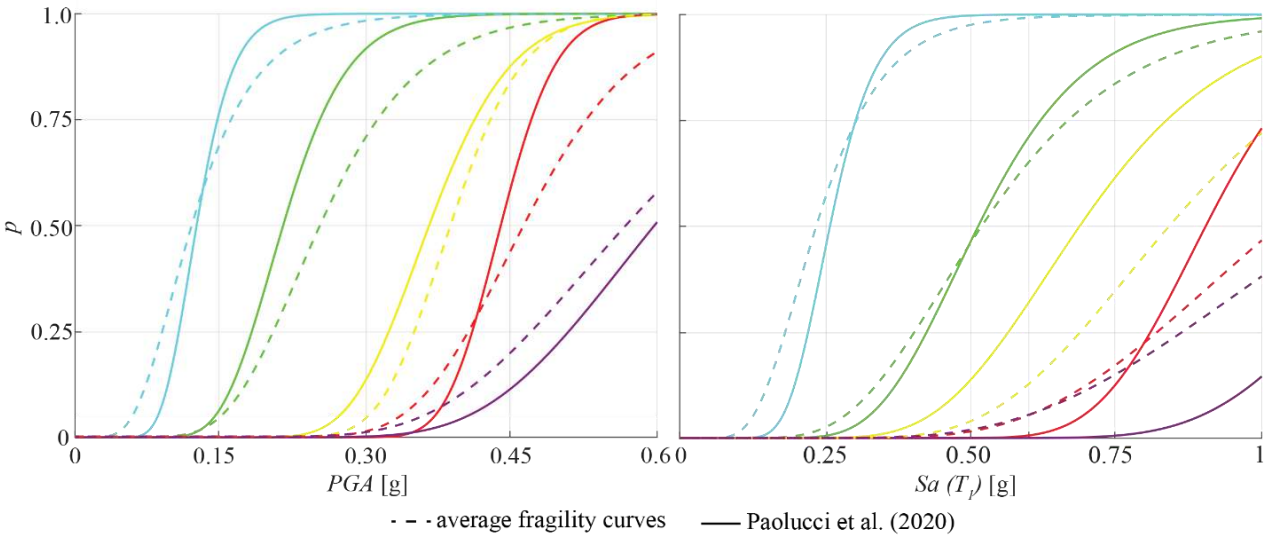

Figure 3. Comparisons between the fragility curves averaging on soils vs the Paolucci et al. (2020) selection.

A problem arises in the use of these curves, in fact the IM in freefield with which to calculate the probability of expected damage varies changing the characterizations of the stratigraphic profile. To obtain this data it is necessary to use an amplification approach of code (with all the issue shown in the other chapters of this PhD thesis), or to make a site response analyses. The latter consequently requires knowledge of the site in question, but the use of this type of selection proposed by Paolucci et al. (2020) and Manfredi et al. (2022) wanted to obviate the need to know the real characteristics of the soil profile, basing only on its macro characteristics (classification of soil in accordance with code). This comparison cannot be considered conclusive, but needs to be further analyzed in order to offer new simplified tools for site effects analyses.

ANNEX A.4.2a

2D valley effect and aggregate model validation

Published in *3rd International symposium on geotechnical engineering for the preservation of monuments and historic sites, 22-24 June 2022,* Naples, Italy.

SIMULATION OF DAMAGE OBSERVED ON BUILDINGS IN AGGREGATE AFTER THE 2016-2017 CENTRAL ITALY EARTHQUAKE ACCOUNTING FOR SITE EFFECTS AND SOIL-STRUCTURE INTERACTION

Andrea Brunelli[1], Giorgio Andrea Alleanza[2], Serena Cattari[1], Filomena de Silva[2], Anna d'Onofrio[2]
[1] University of Genoa, Genoa, Italy
andrea.brunelli@edu.unige.it, serena.cattari@unige.it

[2] University of Naples Federico II, Naples, Italy
giorgioandrea.alleanza@unina.it, filomena.desilva@unina.it, anna.donofrio@unina.it

Abstract:

The paper investigates the influence of site effects and soil-structure interaction on the response of buildings in aggregate in the historical centre of Visso, located in an alluvial valley in the Central Italy. The town was severely stricken by the Central Italy 2016/2017 seismic sequence and the subsequent inspections allowed the reconnaissance of damage suffered by the case study at hand. A monitoring system installed just out of the historical centre recorded the ground motion at Visso during the seismic sequence. Based on these records, the bedrock motion was then calculated through their deconvolution along the well characterized soil profile below the record station. The resulting signals were applied as input motions in linear equivalent site response analyses (i) of the 1D site effects due to soil stratigraphy amplification below the buildings in aggregate and (ii) of the whole 2D valley. In both cases, the subsoil model was inferred from the data gathered during the seismic microzonation study of the Visso village. The amplification of ground motion resulting from the 1D site response analysis is higher than that predicted by the 2D analysis along the same vertical. The whole aggregate was modelled in the Tremuri software through the equivalent frame approach and specific modelling strategies were adopted to account for the interaction among adjacent structural units. The model base was either completely restrained, to simulate the fixed-base conditions as typically assumed in the structural analysis, or endowed with springs, to simulate the effect of the soil compliance to the structural motion. Non-linear dynamic analyses were then performed on the fixed and complaint base models under the free-field motion obtained from the 1D and 2D site response analyses. The resulting damage patterns were compared to that detected on site. The comparison is satisfying only when the motion obtained from 2D site response is adopted as input motion and slightly improved when the compliant base conditions are considered.

Keywords: buildings in aggregate, observed seismic damage, 2D site effects, soil-structure interaction, substructure method.

1 INTRODUCTION

Ancient towns were often built to be isolated from the surroundings, mainly due to defensive strategies. Hence, they usually rise on flat-topped hills delimited by steep slopes or in valleys enclosed by mountains. Such complex geomorphological conditions influence the ground motion at surface (Pagliaroli et al. (2020)). This especially occurs in the case of valley, where also stratigraphic amplification effects are expected to be produced by soft covers. Moreover, the seismic response of structures founded on such covers is potentially also modified by the soil-structure interaction (Richart et al. (1970)). Such phenomena were recently investigated for unreinforced masonry (URM) buildings by Brunelli et al. (2021a) through the in-depth analysis of the response of the school of Visso (MC, Italy). The school constitutes an emblematic example hit by the Central Italy 2016/2017 seismic events and provided very precious and unique information, being permanently monitored by the Italian Department of Civil Protection. Other works based on evidence from recent earthquakes have already highlighted the detrimental effects of site-amplification in the damage of existing URM masonry buildings (for example: Sextos et al. (2018); Sorrentino et al. (2019); Brando et al. (2020)). Soil-foundation-structure (SFS) interaction is often not considered for URM buildings with shallow foundations, while Brunelli et al. (2022c) showed the role of the interaction and the susceptibility of the results to variation of different formulations in the literature. This paper numerically investigates the effect of site amplifications and SFS interaction on the response of a building in aggregate located in the historic center of Visso to the Central Italy 2016-2017 seismic sequence. Actually, studies on URM buildings in aggregate, that also consider the role of SFS interaction, are very few in literature (Caprili et al. (2015)). The aggregate is modelled taking advantage from the validation of the equivalent frame modelling strategy carried out by Brunelli et al (2021) on the Visso's school and refining the strategy with *ad hoc* solutions to account for the interaction between adjacent structural units, as recently investigated in Angiolilli et al. (2021). Being the case study settled not far from the border of the valley, an attenuation of the seismic motion is expected with respect to the 1D condition, due to the destructive interference among the refracted waves along the edges (Alleanza et al. (2019); Papadimitriou (2019)). Thus, an *ad hoc* study on this issue has been also performed in the paper. The agreement in terms of simulated damage is adopted as target to assess the role of various phenomena. Indeed, the influence of SFS interaction is expected to be beneficial, thanks to the contribution of damping associated to continuous and shallow foundation of such URM structure.

2 DESCRIPTION OF THE CASE STUDY

The investigated building in aggregate is made up of five units placed in rows having varying heights, from three to four floors. Due to the impossibility to make a detailed geometric survey of the buildings, their size was deduced from the photos and maps of Visso (see https://www.regione.marche.it/Regione-Utile/Paesaggio-Territorio-Urbanistica/Cartografia/Repertorio/Cartatecnica2000). The reconstructed geometry of the aggregate is reported in Figure 1.

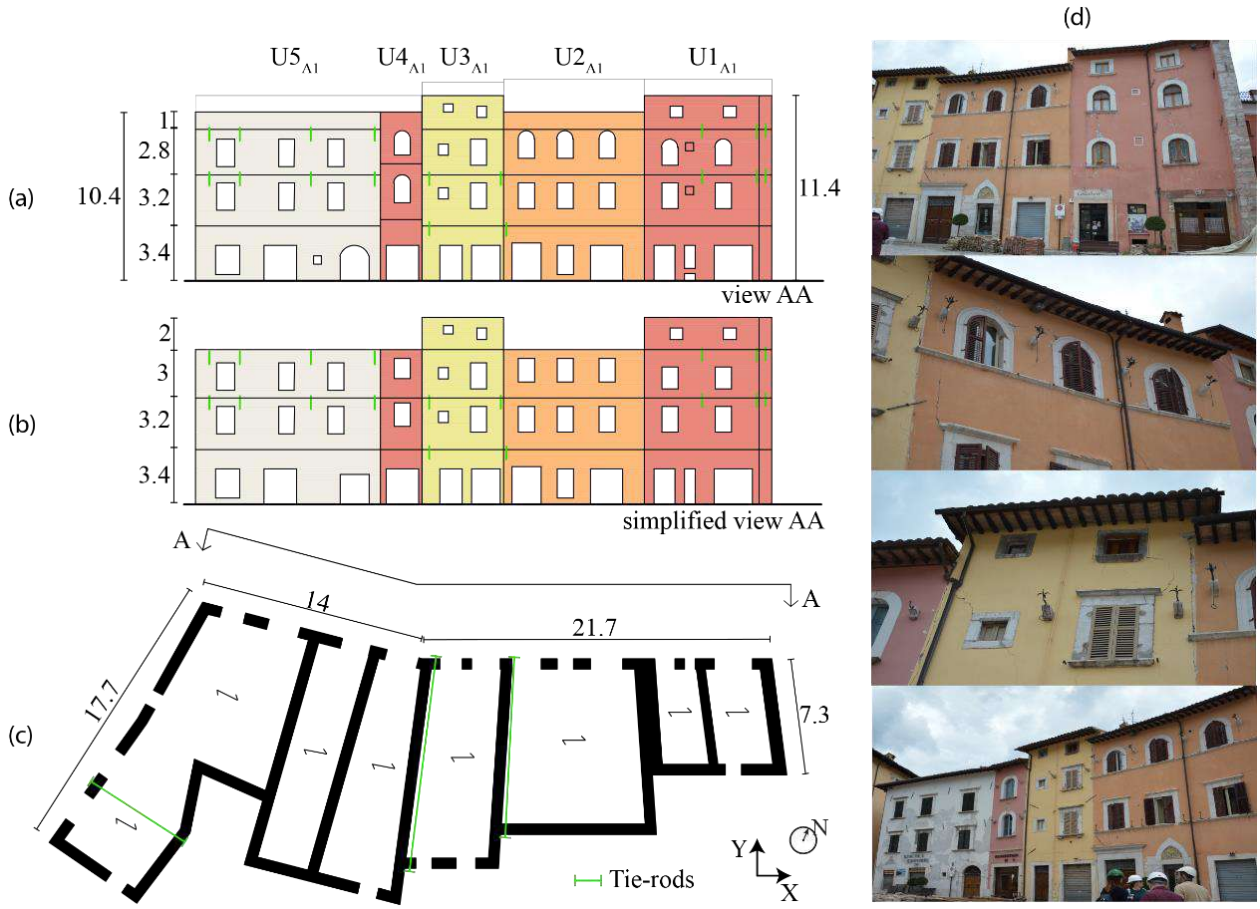

Figure 1. Geometric survey of building in (a) the real, (b) simplified elevation and (c) in plan of the ground floor; (d) photo of the aggregate following the seismic events in Central Italy 2016/17.

The height of the floors was inferred from the position of the openings and tie-rods visible from outside. Some structural features were deduced from other buildings where partial collapses, induced by out-of-plane mechanisms, occurred. Such collapses made these details visible, allowing to also verify their systematic recurrence (see Figure 2). Firstly, in such way, the transversal sections of URM walls were investigated by deducing the thickness and the masonry type. Indeed, the latter is mostly the same across the historical centre and is also consistent with that of the school of Visso (see Brunelli et al. (2021a)). Basing on such evidence, the walls were estimated 70 cm thick at the ground floor and 60 cm at the other levels. The only exceptions are the perimeter wall of unit $U1_{A1}$ (the right wall in Figure 1c) estimated 80 cm thick over the entire height of the building; and the walls of the last level in 55 cm. Moreover, the presence of internal walls was assumed in correspondence of the tie-rods visible in the external façades. The internal walls were supposed 5 cm lower as thickness than the relative perimeter walls. Basing on the position of the tie-rods and the typology of the single units, the units $U1_{A1}$ and $U2_{A1}$ are assumed to be sustained by autonomous load-bearing walls, while the other units to share the side transversal walls (i.e. those oriented in Y direction). In particular, the unit $U4_{A1}$ seems to be a filling unit built upon the two pre-existing orthogonal walls.

The main orientation of diaphragms is expected to develop perpendicularly to the Y-direction; all partition masonry walls were considered in the model as equivalent loads on the floors. From the photos of the other buildings in the historic center (see Figure 2), diaphragms are mostly characterized by brick and wooden decks. In some case, a very thin concrete slab (not reinforced) is also present. The same floor type was assumed in all units of the aggregate under examination since there is no evidence of any specific interventions and the units are considered substantially contemporary.

Figure 2. Example of walls and floors visible in other buildings of the historic center of Visso.

3 SITE EFFECTS IN THE VALLEY OF VISSO

3.1 Subsoil geotechnical model

The examined buildings in aggregate are on the border of an alluvial valley, whose 2D geological section is shown in Figure 3a (MZS3 (2018)). The soil stratigraphic sequence under the aggregate was defined thanks to the data of two boreholes and several Horizontal to Vertical Spectral Ratio (HVSR) of microtremors carried out within the third level microzonation studies, MZS3 (2018). The soil profile is constituted by clayey silt (CS), overlaying a sandy gravel layer (SG). In lack of experimental measurements, the shear wave velocity profile (V_S) was obtained through a correlation law between V_S and the number of blow counts of SPT tests performed in the boreholes. To validate the model, several correlations available in literature were checked and compared with the results of a Down Hole test (DH) carried out in a different site within the valley. In particular, the correlations by Imai and Yoshimura (1970) and Lee (1992) were used for CS and the one suggested by Ohta and Goto (1978) was adopted for SG, Figure 3b,c shows respectively the V_s profiles obtained for the two verticals V1 and V2, and used to define the geotechnical model for the seismic response analysis. The V1 profile (Figure 3b) was used to characterise the widest and thickest valley below the school, while the V2 (Figure 3c) profile was adopted for the shallow lateral valley below the aggregate. Each profile was extended to the entire section assuming a horizontal layering. The interface between the two valleys was established in accordance with the results of MZS3 (2018). The shear modulus decay ($G(\gamma)/G_0$) and the variation of damping ratio ($D(\gamma)$) curves (Figure 3d) were assigned based on Brunelli et al. (2021a). The relations developed by Ciancimino et al. (2020) for Central Italy soils was used to characterise the non-linear behaviour of CS and SC layers, considering an average value of plasticity index of 17% (measured on samples retrieved these formations). While for SG layers, the relationships suggested by Liao et al. (2013) were adopted, considering a confining pressure of 52 kPa for the superficial one and 207 kPa for the deeper, to reproduce the dependence of the nonlinear behaviour on the stress state. The bedrock was assumed to be linear visco-elastic with a damping of 0.5% and V_S=1300m/s, in agreement with the results obtained by MZS3 (2018).

The 2D analyses were carried out with the computer code QUAD4M (Hudson et al. (2003)), a finite element program that performs equivalent linear analysis in the time domain. The domain was laterally extended to minimize the effect of artificial reflections of the seismic waves due to lateral boundaries. The mesh consists of triangular elements, whose maximum size was defined according to Kuhlemeyer and Lysmer (1973) criterion. 1D seismic response analyses were also carried out along the vertical profiles V1 and V2 (Figure 3b,c) with the computer code STRATA (Kottke and Rathje (2008)) which performs equivalent linear analysis in the frequency domain.

The reliability of the obtained geotechnical model was checked by comparing the experimental fundamental frequency measured by the HVSR, at several sites along the cross-section of the valley, with that computed at the same site by 1D and 2D linear analyses. Figure 3a shows the comparison between the measured resonance frequencies (in black) and those obtained in the 1D (dark grey) and 2D (light grey) case. The agreement among the frequency values validates the numerical model.

Two-time histories of the Central Italy seismic sequence 2016-17, recorded near the school foundations (Figure 3a) were then used as reference seismic input motion. In particular, the main events of 24/08/2016 and 26/10/2016 were considered. They were deconvoluted at the bedrock through a 1D analysis and then applied to the 2D model of the valley, as well as to the 1D soil column V2 to obtain the ground motion at the base of the aggregate.

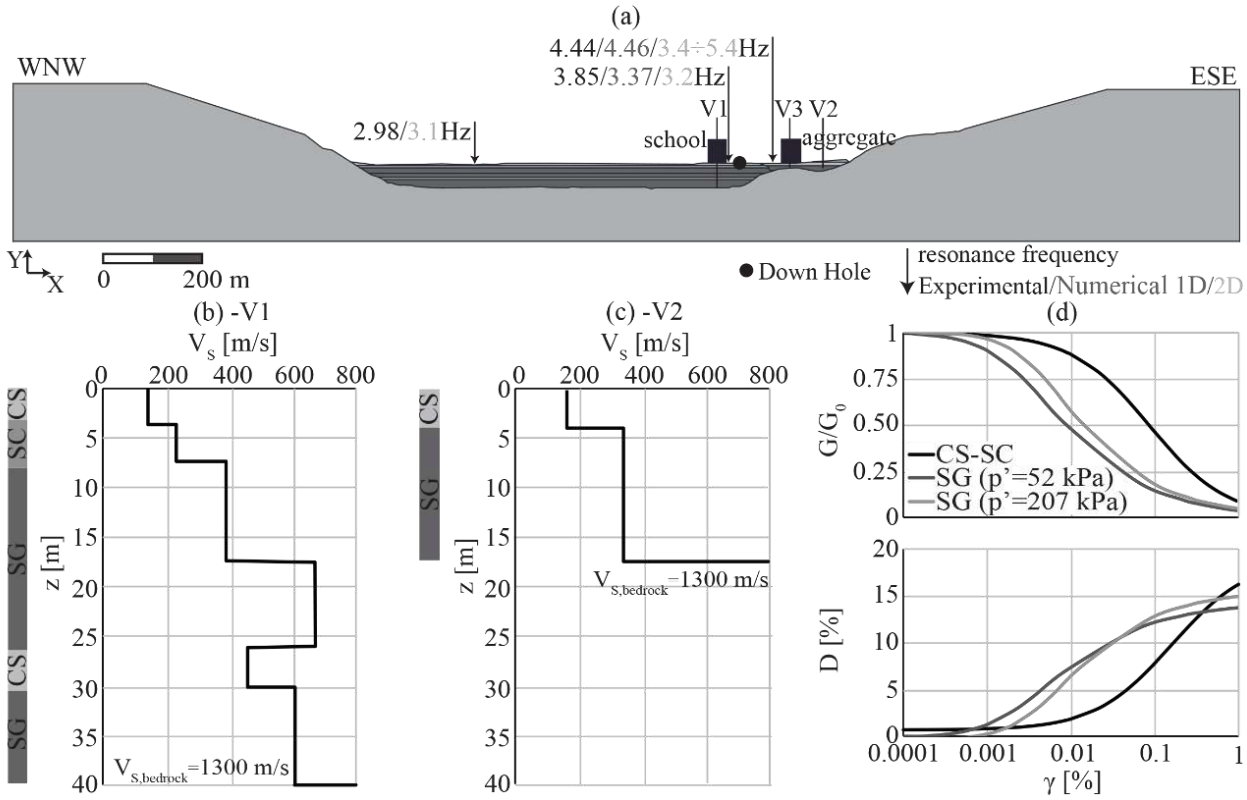

Figure 3. (a) 2D section adopted in the numerical analyses; (b) V_S profiles measured through the down hole test; (c) V_S profiles for the historical center of Visso and (d) G/G_0-γ and D-γ curves adopted in the analyses. Black and grey numbers along the cross-section in the upper portion represent experimental and numerical estimation of first natural frequency respectively (in 1D and 2D case).

3.2 Results of site response analyses

The results of the analyses were synthesized in terms of horizontal profiles of the amplification factors of spectral acceleration (AF) defined through equation 1:

$$AF_{T_a-T_b} = \frac{\int_{T_a}^{T_b} S_{a,s}(T)\,dT}{\int_{T_a}^{T_b} S_{a,r}(T)\,dT} \quad (1)$$

where $S_{a,s}(T)$, $S_{a,r}(T)$ are the spectral accelerations at the surface and at bedrock, and T_a, T_b were set equal to 0.1 and 0.5 s. The period range was defined in a way that is almost centred on the natural period of the aggregate. Furthermore, an amplification factor of peak ground acceleration, AF_{PGA}, was also calculated.

Figure 4 shows the profiles of $AF_{0.1\text{-}0.5s}$ (solid lines and full dots) and AF_{PGA} (dashed lines and empty dots), computed adopting the two input motions, obtained from both 2D (lines) and 1D (symbols) analyses. The trends of $AF_{0.1\text{-}0.5s}$ and AF_{PGA} between X= 600 m and 1400 m are comparable for the two events and characterized by two amplification peaks located close to the border of the

deepest valley. This behaviour is typical of very shallow valleys characterised by a shape ratio, H/B ≤ 0.1 (Alleanza (2022)). Furthermore, the amplification factors obtained from 1D analysis along V1 profile are close to those computed by 2D analysis, justifying the good agreement between the damage observed at the school and that simulated by Brunelli et al. (2021a) adopting the ground motion at surface, obtained from 1D analysis. On the other hand, the thin valley, between X=1400 m and 1600 m, shows a strong amplification of motion at the centre of the basin, leading to amplification higher than that computed by 1D analysis along the vertical V2. Indeed, a destructive wave field among the direct, refracted and surface waves close to the edges of the valley (e. g. V3 in Figure 4) attenuates the ground motion with respect to the centre (Alleanza et al. (2019); Alleanza (2022)). Consequently the spectral amplifications are lower than those predicted by 1D analyses along V2. Finally, nevertheless the differences in the soil profiles, 1D analyses along V1 and V2 lead to close values of the amplification factors, because their seismic response is mainly ruled by the shallowest (up to a depth of 18 m) and softest layers, characterised by similar dynamic properties.

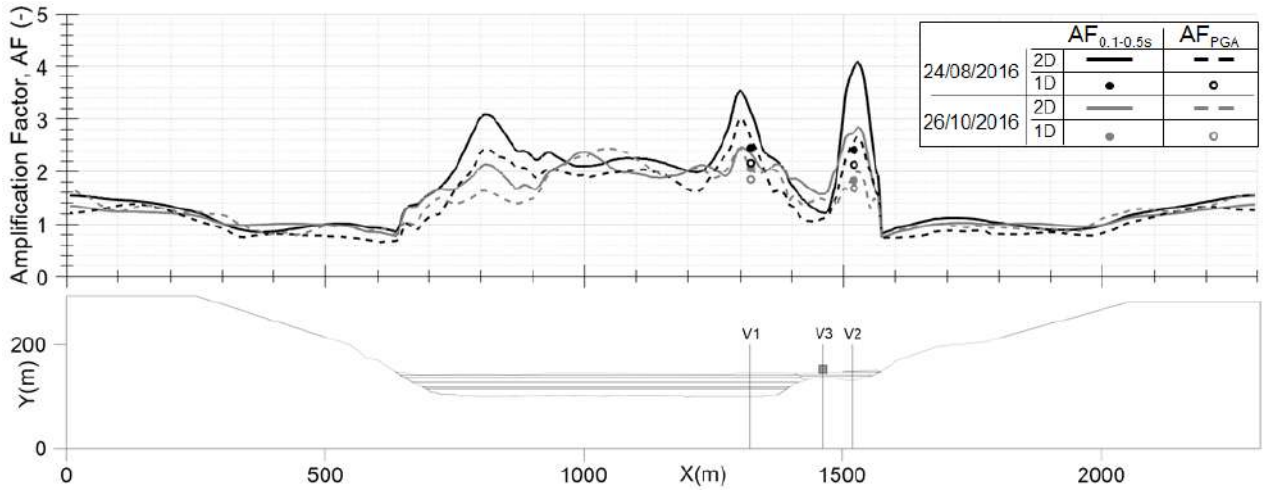

Figure 4. 2D amplification factors of the peak ground acceleration and of the spectral acceleration compared to those computed through 1D seismic response analyses along the verticals V1 and V2.

Figure 5 shows the comparisons among the accelerograms obtained on the surface from 1D (black line) and 2D (grey line) analyses for the events of 24/08/16 (continuous line) and 26/10/16 (dashed line). In details, Figure 5a compares the results at V1; in while Figure 5b compares the results obtained from the 1D analyses at V2 and from the 2D analyses at V3 (Figure 5b), where the aggregate is settled. The latter comparison is reported, because in the eventual lack of the 2D simulation, the ground motion resulting from 1D analyses along the vertical in the center of the valley is considered to be representative of the motion of the whole valley. In agreement with the above observations, the results obtained along the V1 profile by 1D and 2D analyses are very close, both in terms of amplitude and frequency content. On the other hand, accelerations and spectra computed along the V2 profile by 1D analyses show on average higher amplitudes respect to those obtained by 2D analyses.

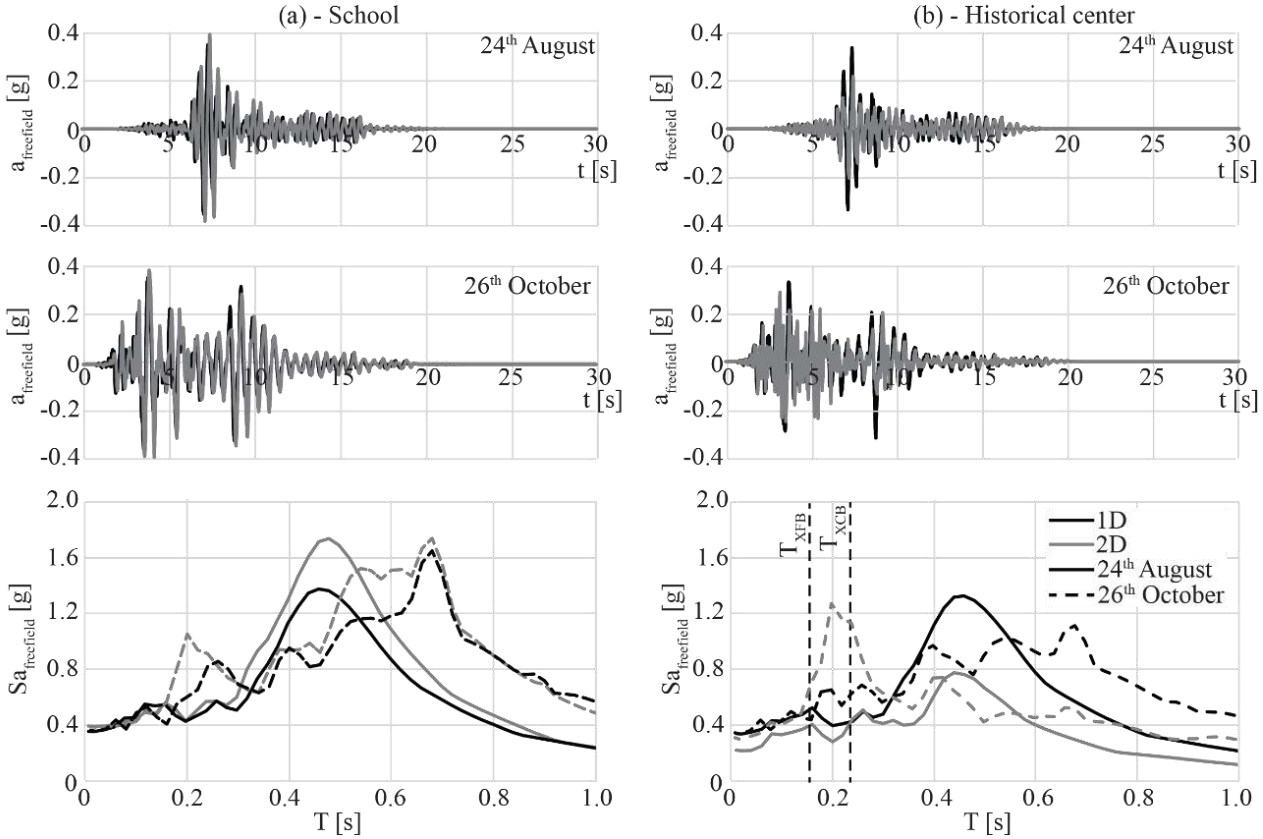

Figure 5. Comparison among the time histories and response spectra of the free field accelerations resulting in (a) school and (b) historical center from the 1D (in correspondence with V1) and 2D (in correspondence with V3) site response analyses under the events occurred on the 24th August and 26th October 2016.

4 EQUIVALENT FRAME MODEL OF BUILDINGS IN AGGREGATE

Among the modelling strategies available for URM structures (see D'Altri et al. (2020)), the 3D model here adopted is based on the equivalent frame approach. Accordingly, the nonlinear behaviour is assumed to be concentrated in masonry panels (the piers and spandrels, in orange and green respectively in Figure 6a) connected by rigid nodes (in cyan in Figure 6a). Piers constitute the main vertical structural elements able to equilibrate both vertical and horizontal actions, while spandrels play the main role of connecting the piers (like the beams in a corresponding reinforced concrete frame). For each URM wall, the geometry of piers and spandrels has been identified *a priori* according to the rules proposed in Lagomarsino et al. (2013), whose reliability has been recently validated in Cattari et al. (2021) and Ottonelli et al. (2021); indeed, the regular layout of openings justifies in this case to neglect such an epistemic uncertainty. The numerical model was realized with the Tremuri software package, developed by Lagomarsino et al. (2013). The model accounts only for the in-plane response of walls, but this simplification is justified in the case of the investigated aggregate that did not exhibit the activation of any local mechanism, differently from other in the historical center.

As far the geometry of the structural units concerns, few simplifications have been made with respect to the original configuration. In particular, the alignment of the floors between the units of the aggregate and the windows have been rectified, by neglecting some small misalignments in height (as shown in Figure 1a). The final view of the assumed geometry is illustrated in Figure 1b.

The adopted values of the Young's modulus (E) and shear modulus (G) are reported in Table 1, together with the strength mechanical parameters. These values have been derived starting from those used in the Visso school, whose reliability has been validated in Brunelli et al. (2021a) through a very accurate numerical simulation of the actual response of this monitored asset. The strength values (τ_0) are slightly higher than that used for the school (of a 10%), but still completely consistent with the

reference values proposed by Italian Building Code Commentary called MIT (2019) for the analogous masonry type. Both the elastic modulus (E,G) and the compressive strength (f_m) of the spandrels have been reduced by a multiplying factor equal to 0.7 with respect the piers; that is to account for the anisotropic behaviour of masonry and the fact the main mortar joints activated in spandrels are the vertical ones.

Table 1: Mechanical parameters adopted for piers, spandrels and diaphragms of floor.

	E (MPa)	G (MPa)	τ_0 (MPa)	f_m (MPa)	G_D (MPa)	E_D (MPa)
piers	2968	991	0.1268	6.42		
spandrels	2078	693	0.0625	4.49		
diaphragms of floor					9170	23333

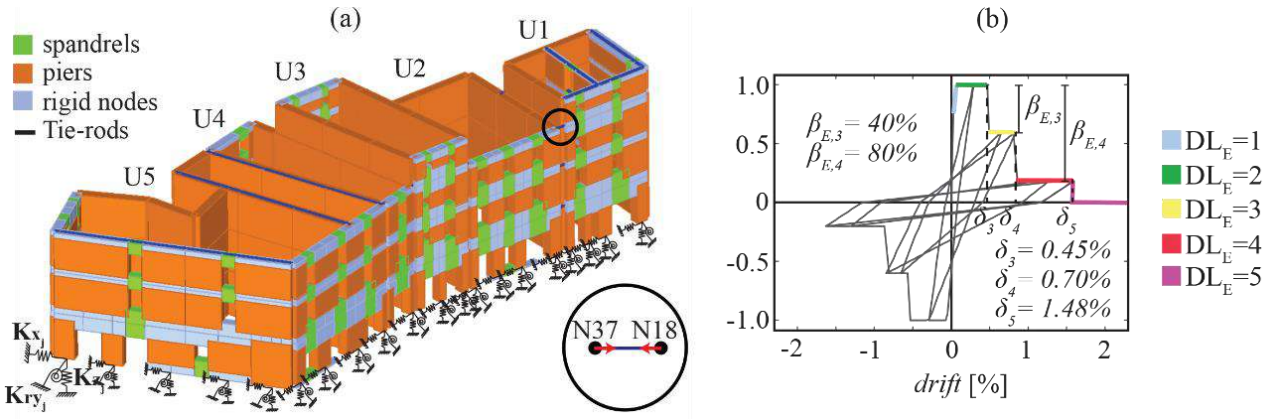

Fig 6. (a) Equivalent frame model; (b) backbone and hysteretic response of the masonry piers under shear.

Masonry panels are modelled according to the nonlinear beam piecewise-linear model proposed by Cattari and Lagomarsino (2013). This constitutive law allows for describing the nonlinear response until very severe damage levels at element scale (i.e. DL_E,i with i from 1 to 5), through progressive strength degradation (β_E,i), corresponding to assigned drift values (δ_i). The latter are differentiated as a function of most recurring failure modes that characterize URM panels (i.e. flexural, diagonal cracking shear or bed-joint sliding) and of their type (if piers or spandrels). They may be defined on basis of experimental dataset available in literature (e.g. Vanin et al. (2017); Rezaie et al. (2020)). In this case, the drift thresholds already validated in Brunelli et al. (2021a) have been adopted. By way of example, Figure 6b illustrates the response of a pier dominated by a shear failure mode.

The maximum shear strength of the panels has been computed according to the strength criteria already corroborated in the literature to interpret the aforementioned failure modes (see Calderini et al. (2009)). In particular, the flexural behaviour of piers was interpreted according to the criterion proposed in NTC (2018), whereas the shear behaviour according to the diagonal cracking failure mode proposed by Turnšek and2021 Sheppard (1980) and recommended also in MIT (2019) for existing irregular masonry.

As proposed by Angiolilli et al. (2021), the mutual interaction between the various structural units is considered through the insertion of elastic truss elements (see the circular zoom of Figure 6) and fictitious floors. These elements allow the opening between buildings only along their longitudinal direction (i.e. X direction). The truss element, able to react only in compression, are characterized by a transversal area of 0.00164 m^2 and elastic modulus E of 210000 MPa. The equivalent diaphragms instead are characterized by the following feature: thickness of 0.05 m, E=39420 MPa, G=13112 MPa.

As mentioned in the introduction, two models have been considered. A fixed based (FB) model and compliant base (CB) model to account for the SFS interaction. In the latter case, a series of springs were considered under each pier, as shown in Figure 6a. The details on the calibration of these springs and equivalent Rayleigh damping are given in the next paragraph. Figure 7 shows the fundamental

periods of two models together with the in-plan view of the mode shapes, that refer to the FB model. The first period mainly activates the longitudinal response, while the second and third modes the transversal one. More specifically, the second mode substantially involves the units $U1_{A1}$ and $U2_{A1}$, while the third mode the other ones. In the case of the CB model, the aggregate is idealized through the replacement oscillator approach proposed by Maravas et al. (2014), as better explained in section 4.1. Thus, in this case, two main modes are computed associated to the following periods: 0.221 s for the longitudinal direction; 0.2 for the transversal one.

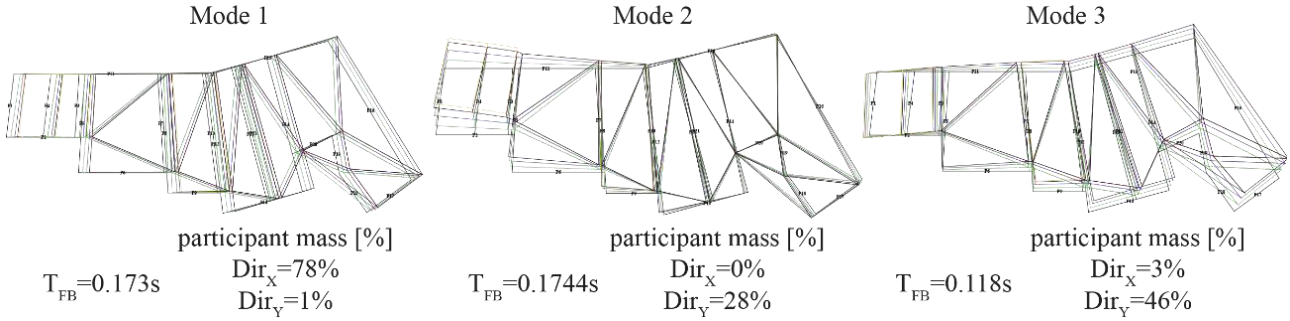

Figure 7. Modal shapes of the first three modes identified of the FB model, with period and participant mass.

4.1 Modelling of the foundation stiffness and damping

In the CB model, each foundation pier was equipped with springs, whose stiffness was calibrated through the real part of the soil-foundation impedances by Gazetas (1991). The foundation width was set constant and equal to 1 m, as results from the thickness of the load-bearing wall plus an enlargement of 0.15 m at each side. The length varies because it was defined by adding the half-length of the spandrel panel to the size of the load-bearing wall. The value of the embedment was set to 1 m, in according to the building typology and to the soil type.

The soil was modelled as an equivalent linear half-space. The half-space shear modulus was set equal to mobilized one, under each input motion, up to a depth equal to the foundation width below the foundation, and corresponding to the soil volume expected to be affect by the horizontal and rocking foundation motion (see Gazetas (1983)). As well known, the impedance functions are frequency dependent, hence they were calibrated iteratively until the supposed frequency resulted equal to the inverse of the period of the compliant-base aggregate. The latter was estimated through the replacement oscillator approach proposed by Maravas et al. (2014) for a Single Degree of Freedom (SDoF). To this aim, the building was approximated through a SDoF system with a viscous damping ratio equal to 3%, and a lateral stiffness derived from the fundamental periods along the X and Y directions of the FB configuration. The real and the imaginary parts of the impedance of the monolithic foundation, equivalent to the actual foundation systems, were calculated from the sum of the real or imaginary parts of the impedances of the X-oriented (or Y-oriented) load-bearing walls. Since the cumulative effects of the two mainshock was studied by applying the two input motions in cascade to the numerical model, the mean values of the impedances for each pier were introduced into the base springs of the numerical model.

Figure 8 shows for each foundation the values of the vertical (K_v), horizontal (K_x) and rotational (K_{ry}) impedances calibrated on the initial soil stiffness and on the mobilized one, obtained from the 1D and 2D seismic response analyses. The impedance calibrated on the soil stiffness mobilized into 1D analyses are slightly higher with respect to those associated with the soil stiffness resulting from the 2D analyses. The structural period of CB model is predicted through the formula by Maravas et al. (2014) for the impedances calibrated on the initial soil stiffness.

The same approach by Maravas et al. (2014) was adopted to estimate the damping ratio of the compliant base system. The contribution of the soil hysteretic damping, mobilized in the soil volume affected by the foundation motion, was added to the energy loss coefficients simulating the radiation damping ratio. The mean value of the damping ratio, resulting for the two directions and the two

mainshocks, was introduced as a Rayleigh damping ratio into the structural model. Table 2 shows the values for the X and Y direction (equal for the two-subsoil modelling) of the soil damping (D), of the equivalent damping for each direction and event (ξ_{eq}) and of the final value (ξ_{eqTOT}) used in the nonlinear dynamic analyses (NLDA). In general, the hysteretic damping mobilized in the 2D analyses, along the X direction, is slightly higher than that predicted through the 1D analyses, hence the final value of ξ_{eqTOT} is slightly higher. In both cases the whole damping ratio is more than twice the typical value of the fixed base assumption.

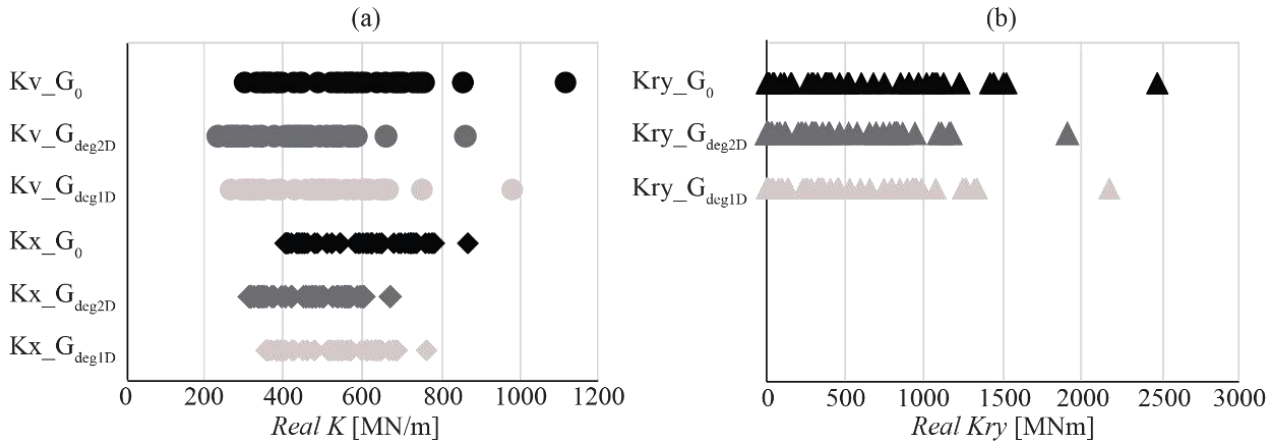

Figure 8. Range of variability of the real part of the foundation impedance, calibrated according to the initial soil stiffness (G_0) and the stiffness mobilized below the foundation according to the 1D (G_{deg1D}) and 2D (G_{deg2D}) site response analyses.

Table 2: Damping and equivalent damping of replacement oscillator, and final value used in the NLDA.

	D [%]				ξ_{eq} [%]				
	24th August		26th October		24th August		26th October		ξ_{eqTOT} [%]
	X	Y	X	Y	X	Y	X	Y	
1D	2.013	2.071	2.098	2.459	7.24	5.50	7.32	5.56	6.40
2D	3.597		3.029		8.59	6.72	8.10	6.27	7.42

5 COMPARISON AMONG THE SIMULATED AND OBSERVED DAMAGE

Since the aggregate is located at the edge of the valley, for a more accurate assessment of the damage, the acceleration time histories of the free field signals calculated along the X-axis in the vertical V3 through the 2D site response analyses, were applied together with the signals calculated through the 1D analyses in the Y-axis. The analyses were repeated also in the case in which, in both directions, the components of the input motion derived from 1D condition along V2 have been applied. Signals were thus applied to the FB model under free-field motions (named FB C case) and to the CB model under free-field motion (CB C case), to investigate the effects of the SFS interaction. In addition, the response of the FB model was also analysed under the bedrock motion, as a reference case, named FB A in the following, to evaluate only the effects of site amplifications. In all cases, the input motions relevant to the event occurred on the 24th August 2016 and 26th October 2016 were applied in cascade to simulate the cumulative damage.

Figure 9 compares the survey of the damage suffered by the main façade of the building with the outcomes of the NLDA at the end of the 26th October mainshock. This is the most vulnerable wall, due to the large openings at ground floor, while side perpendicular walls (being without openings and benefitting from the axial load transmitted by the diaphragms) are expected to be damaged lowly than the façade. As far the actual damage concerns, in Figure 9, the main pattern of cracks surveyed is reported together with a colour that indicated their severity (if lower than DL2, between DL2 and DL3 of higher). The damage level has been attributed on basis of the interpretation of available

photos. Since it was not possible to enter the buildings, the damage has been assigned only from outside.

The comparison among the observed and simulated damage highlights that the FB A model considerably underestimates the damage, as many structural elements remain in the elastic range. That firstly confirms the role of amplification site effects. Conversely, the analysis performed on the FB model, under the 1D free-field signal, overestimates the damage producing the attainment of DL5 on piers at the ground floor. The CB C model without valley effect appears less damaged than the FB C model in the same hypothesis, but in any case, more damaged than the actual building. When the free-field signals obtained from the 2D analyses are instead considered, the simulated damage is more close to the real one observed on the building both in the FB C and CB C model. As expected, both the valley effect and the SFS interaction have played a beneficial role in the seismic response of the aggregate

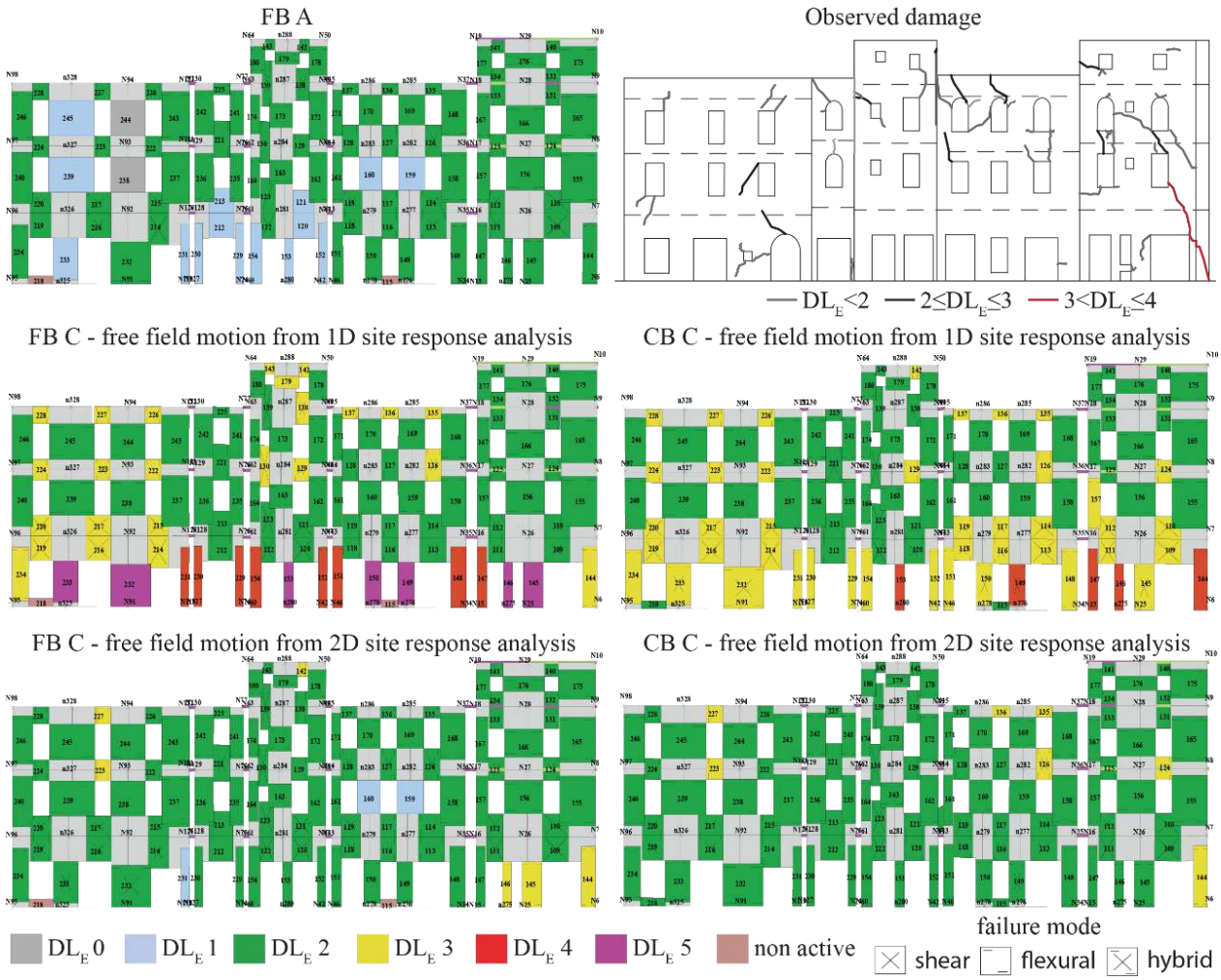

Figure 9. Comparison between observed and simulated damage on FB and CB model after the second mainshock.

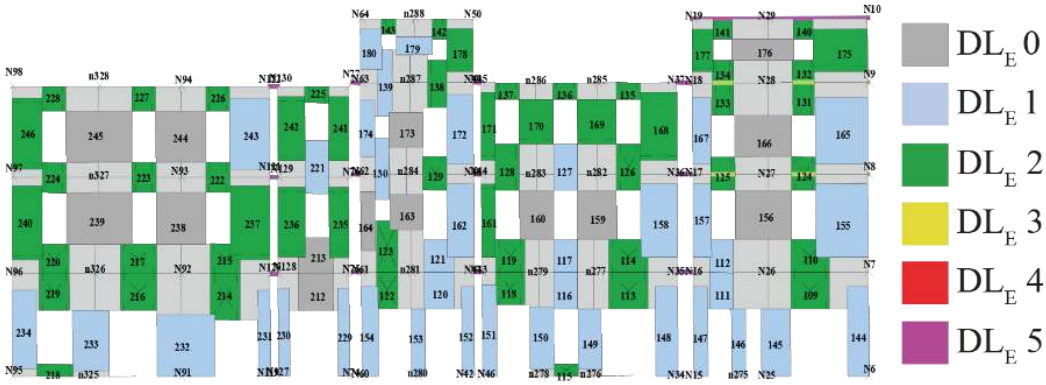

Figure 10. Simulated damage of CB model with valley effect before the peak of 24th August.

In fact, when the valley effect is considered, most of the structural elements are in DL2, apart the external ones in the unit U1 that already reached at least DL3, consistently with the observations. Despite that, in the real case there is a greater damage to the upper floors. This does not seem to be captured by the numerical model being everything in DL2. From Figure 6, DL2 of the numerical model corresponds to the attainment to the maximum shear strength of the panel, but the same DL may correspond to piers that just have been yielded or close to the attainment of DL3. In order to better investigate this aspect and discriminate to what condition the green colour actually corresponds to, Figure 10 shows the damage of the CB C model with the valley effect before the peak of 24th August. It is observed, consistently with the real damage, that the damage starts mostly on the upper floors and then spreads during the event on the lower floors.

6 CONCLUSION

The paper investigates the seismic response of URM building in aggregate. That architectural type is quite relevant being the one most recurring in small historical centres, in Italy but more in general in Europe. Moreover, the effects of site amplification and SFS interaction are analysed with reference to the emblematic study case of Visso municipality, hit by the Central Italy 2016/2017 event. The historical centre of Visso is particularly interesting since it is founded on an alluvial valley and the topographic and morphological shape of the valley make relevant also the 2D effect. The comparison between the numerically simulated and real damage showed that:

- in case of soft soils, the role of amplification phenomena needs to be accounted for;
- in this case, to neglect the 2D effect leads to excessively conservative results;
- for the investigated URM buildings in aggregate, the effects of SFS interaction leads to a beneficial contribute.

ANNEX A.4.2b

Extension of the procedure to more soils and more buildings

This Annex examines the response of the various buildings studied to the variation of the subsoil model. In particular, a first section it was defined the characteristic of another building in aggregate (called A2), instead in the second section was reported the results for the four profiles used in Chapter §4., comparing the results of the school of Visso (define in Chapter §2), the building in aggregate A1 (defined in Annex A.4.2a) and the building in aggregate A2. In this last case were considered only the first two soil profiles representative of soil in the historical center of Visso and the area of the school. For the definition of subsoil models, numerical models and the procedure adopted, please refer to the main text. It is only recalled that the fragility curves were constructed for five damage levels (DLi) and for different measurement intensities (IM): the peak ground acceleration (PGA); the spectral acceleration ($Sa(T_1)$); the cumulative absolute velocity (CAV); and the Housner P-Velocity Spectrum Intensity computed in the range of periods from 0.1 to 0.5 s ($IH_{0.1\ 0.5}$). Two other IMs are considered in Annex A.5: the H_{SM} and the A/V parameter.

1 DEFINITION BUILDING A2

As already done for Visso's school in Chapter §2 and for the first building in aggregate in Annex A.4.2a, also for this second building in aggregate a non linear dynamic analyses was performed with real events in central Italy to assess the reliability of the numerical model. The numerical model used as in the other cases the Tremuri software (see Lagomarsino et al. (2013)) according to the equivalent frame approach. For details on this approach and on the modelling hypotheses, please refer to the sections of the thesis relating to numerical modelling of the school of Visso or of the aggregate A1. The chosen building is located in via Giuseppe Rosi in Visso, about a hundred meters from the Visso school. The aggregate building consists of a row of units of two or three storeys as shown in Figure 1a. This section shows only in Table 1 the mechanical parameters used for the masonry and the floors of the building and an example of backbone and hysteretic response of masonry piers under flexure (see Figure 1b). The values of the mechanical parameters adopted for the masonry elements are consistent with those of the Italian code (MIT (2019)) for this type of masonry and are taken equal to those of the unconsolidated masonry of the Visso school. This choice is in line with the modeling assumptions described in Annex 4.2a for the first studied building in aggregate A1. The floors are considered flexible and with modules equal to those of aggregate A1 except for the $U1_{A2}$ unit because a reinforced concrete slab is visible (see Figure 2). For this reason, the model considered a slab at floor level and a reinforced floor which consequently has higher elastic modules (see Table 1). Figure 2 shows other details of the building in question.

Table 1: Mechanical parameters adopted for piers, spandrels and diaphragms of floor.

	E (MPa)	G (MPa)	τ_0 (MPa)	f_m (MPa)	G_D (MPa)	E_D (MPa)
cut stone	2574	858	0.0962	4.94		
diaphragms ofloor[1]					9170	23333
diaphragms of floor[2]					12500	50000

[1]unconsolidated floors; [2]consolidated floors

The building in adherence to the $U4_{A2}$ unit has undergone a partial out-of-plan mechanism. This part is modeled only to provide a constraint to the remaining part of the aggregate and thus simulate the real behavior of the first four units, but it is not expressly evaluated in this paper.

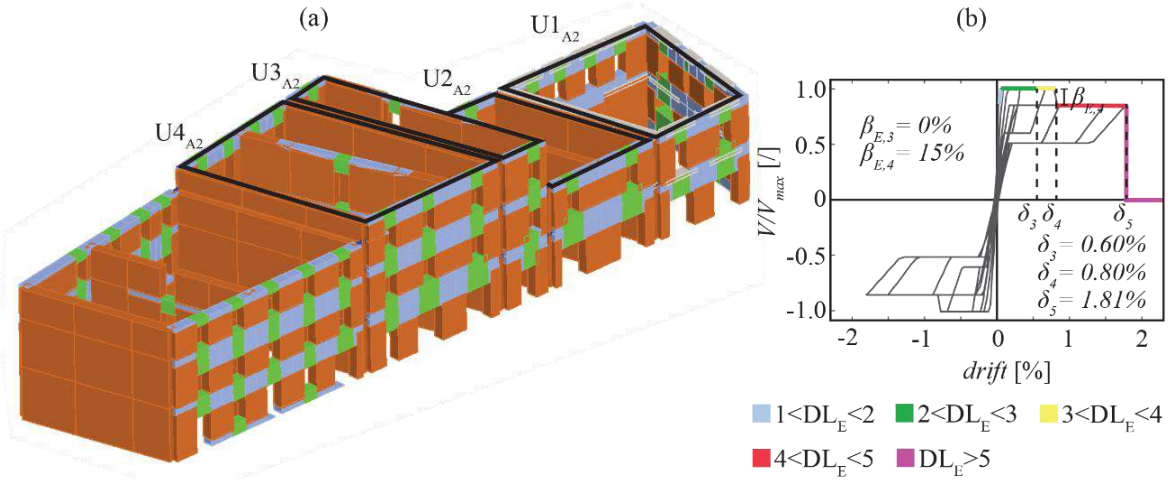

Figure 1. (a) Equivalent frame model; (b) backbone and hysteretic response of the masonry piers under flexure.

Figure 2. Photo of the building in aggregate, at the top main and side façade (unit $U1_{A2}$), at the bottom back façade.

As for the first building in aggregate, the aggregate effect was considered as Angiolilli et al. (2021a) to consider the mutual interaction among the various structural units. In particular, the paper considers a model (called Connected Buildings model) in which there are elastic truss elements sectional area of 0.00164 m^2 and elastic modulus E of 210000 MPa with null tensile behavior and fictitious floors (thickness of 0.05 m, E=39420 MPa, G=13112 MPa). These elements are used to allows opening between buildings only along their longitudinal direction.

Since this building is located near the Visso school, unlike aggregate A1, the soil profile below the building is the same of the school (called in this PhD thesis S1). As shown in Annex A.4.2a there are no significant valley effects for this area of Visso and therefore the signals recorded at the Visso school were used for the aggregate A2.

With these signals, non-linear dynamic analyses in cascade were performed considering the two main

events of the seismic sequence for the municipality of Visso: 24th August and 26th October 2016. The event of 30th October 2016 was not considered in this Annex because this third event does not lead to an increase in damage compared to that observed after the second main event, as shown in Chapters §2 and 3.

The role of the soil is analyzed by always considering a fixed base model (FB), that negate the soil foundation structure (SFS) interaction, and one with springs at the base called complaint base (CB) model, that accounts for the role of the SFS interaction.

The calibration of the real part of the impedances is always performed with the Gazetas (1991) formulation and the damping is implemented in the model as a damping equivalent to the Raleigh which also takes into account the hysteresis of the ground thanks to the replacement oscillator approach proposed by Maravas et al. (2014). No further details are provided as they are the same as already described for the Visso school (in Chapters §2 and 3) and for aggregate A1 in Annex A.4.2a. This Annex therefore directly reports the results of the formulation of the building on the real soil of Visso with a fixed base (FB C) and those with springs (CB C). As there is no other data available, the comparison between the numerical model and the real building is done by observing the actual damage.

However, it is important to underline that in order to take into account the cascade effect of the two events, the average values of both the impedances and the damping were considered and with these values the non-linear dynamic analysis were performed exactly in the same was as for both the school and the for the first aggregate.

As for aggregate A1, information on real damage is available only externally. The main facade as shown in Figure 2 shows greater damage than the rear facade which has suffered much less damage. While not having the damage of the internal walls, it can be assumed that the damage is less than the facades since in buildings of this type there are no large openings and therefore, they are normally more resistant walls. Figure 3 shows the damage simulated by the FB C model, the CB C model and finally what was observed.

The FB C model overestimates the damage since a mechanism of weak story is activated, actually activated, but which leads to a much higher damage than the real one in the portions of walls on the upper floors. The CB C model activates a weak story mechanism, but not so high and therefore the damage does not transfer to the portions of the above walls in line with the real damage. Almost all the masonry elements of the numerical model appear to have damage equal to or greater than DL2, while in the damage observed some portions have no visible lesions. This can in any case be consistent as DL2 damage begins to be visible and above all the assessment was made only from the outside. Furthermore, as for the Visso school, the DL2 damage can be, as defined, overestimated compared to the real one. For more details, refer to the Chapter §2 in which this aspect is analyzed for the school of Visso.

The numerical model both FB C and in particular CB C does not cause damage to the back portion of the building. This result is consistent with the actual damage. The numerical model working in the plane, this is a hypothesis of Tremuri software, so it can not grasp the mechanism out of the plane, but in any case, it is not the purpose of this numerical simulation since this mechanism is present in a portion not directly studied. In Figure 3 the body adjacent to the $U4_{A2}$ unit is not even directly reported, but only its profile is considered.

Furthermore, the type of recurring damage is also consistent with the real one. In fact, it can be observed that the damage is normally of the shear type, this is clearly recognizable in the real damage from diagonal lesion. In the simulation, the shear (indicated in the legend by the letter S) is the recurring mechanism on the first floor of the side wall of the $U1_{A2}$ unit and the main facade of $U1_{A2}$ and $U2_{A2}$.

For the few information, and for the purpose with which this numerical model is to be used, the numerical simulation obtained is considered satisfactory. Once again, the CB C model is better to represent the behavior of the real building.

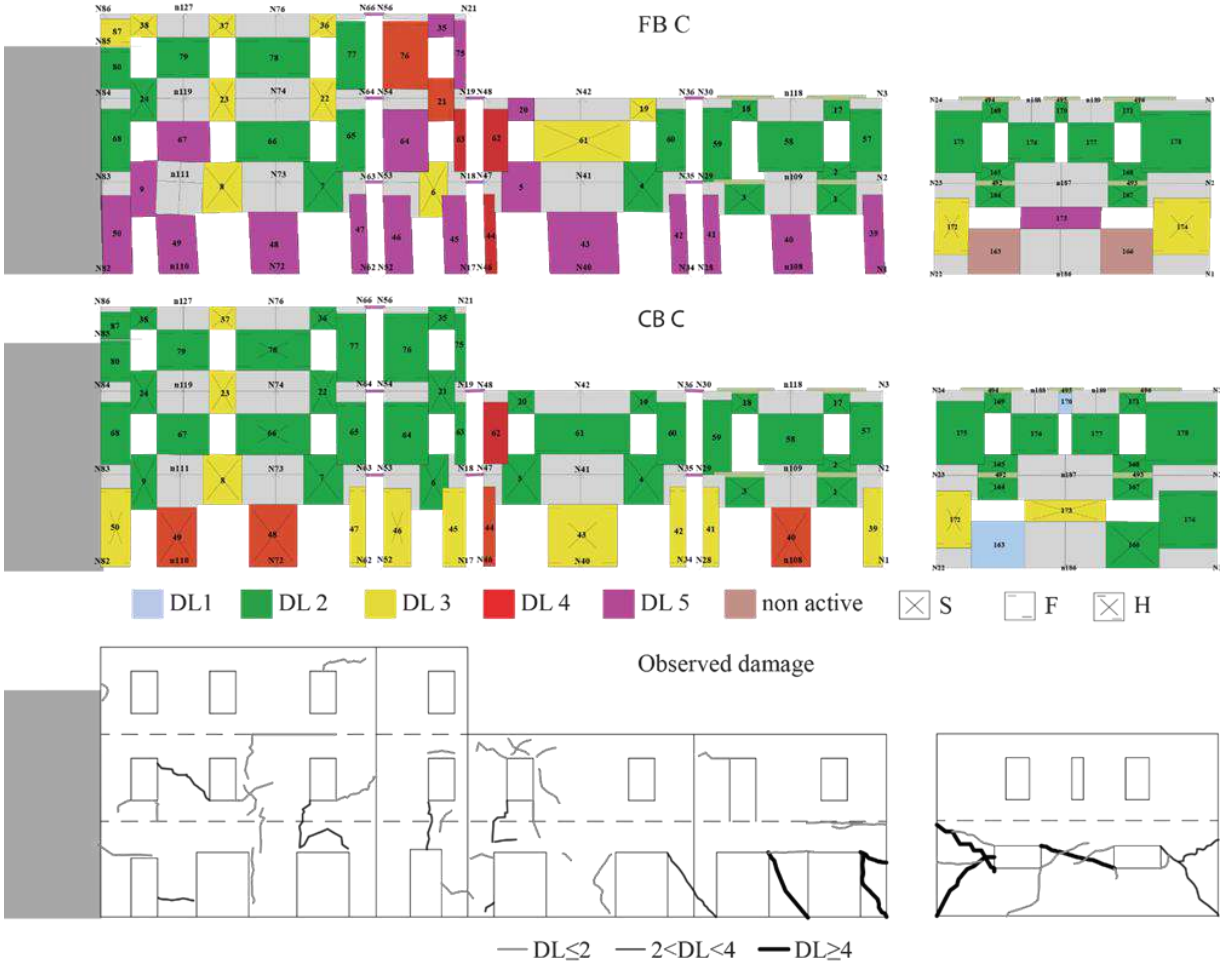

Figure 3. Comparison between observed damage after the second mainshock and the simulation results from FB and CB models.

2 RESULTS OF SITE RESPONSE ANALYSES UNDER RECORDS OF REAL EARTHQUAKES.

As already analyzed in the main text, three numerical models were considered for each building and the subsoil model was set, each representing a different hypothesis: the FB model A representative of the building on rigid ground A which therefore denies both site amplification and SFS interaction, the FB model C with the soil model C which evaluates only the specific amplification effects of that subsoil model, and finally the CB C model which considers the effects of both site amplification that of SFS interaction. The complete procedure is reported in Chapter § 3.

The response to the variation of the subsoil, fixed the seismic event, changes according to the stiffness and damping mobilized by each subsoil model which also amplifies different frequencies of the signal. Remember that the selection of signals is made by Selected Input Motions for Displacement-Based Assessment and Design (SIMBAD) database (see Smerzini and Paolucci (2013); Iervolino et al. (2014)) and the site response analyses through the STRATA software (Kottke and Rathje (2008)) adopting the soft soil profile representative of the subsoil from S1 to S4. The soil S1 is the soil below the school, the S2 of historical center of Visso, finally the soils S3 and S4 are respectively an ideal soil of clay and gravel.

The various selected soil profiles amplify different frequencies and therefore lead to having different freefield accelerograms. As a result, each soil involves different signal amplifications. Figure 4 shows the amplification factor of each selected event calculated as the ratio between the PGA of the freefield signal (ground motion) and that at bedrock (input motion).

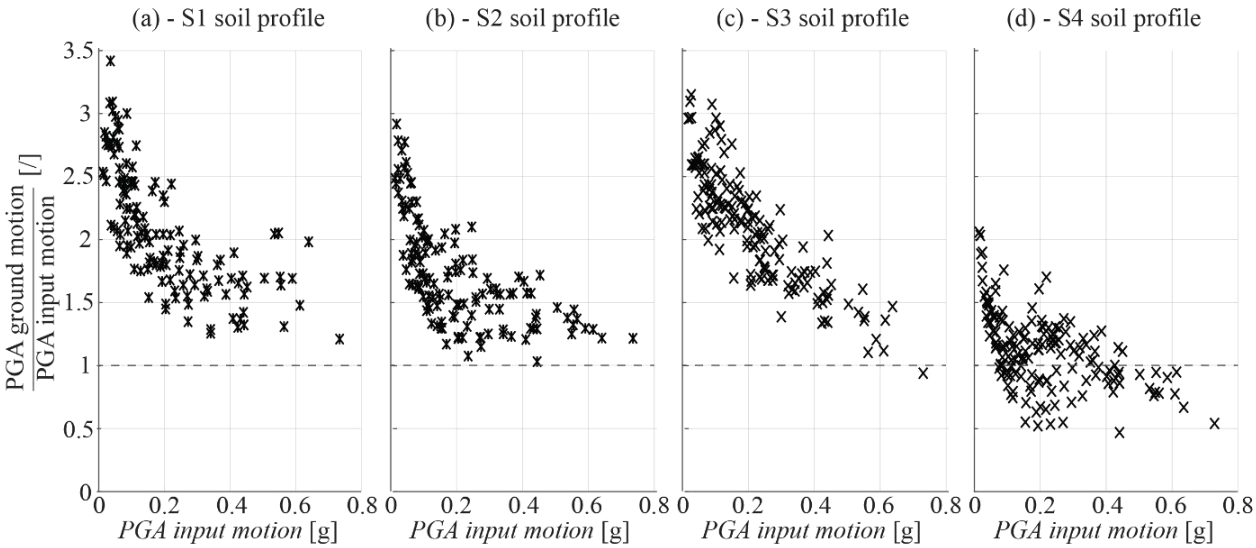

Figure 4. Amplification factors of PGA for soil (a) S1, (b) S2, (c) S3 and (d) S4.

First of all, this factor is greater for the events with a lower input's PGA. Moreover, in the case of the first three soil profiles there is always an amplification (in some cases the ratio is close to 1, value of non-modification of the seismic intensity), in the case of the S4 profile there are numerous analysis that lead to a contribution of deamplification of the signal in freefield. This is consistent with the results of the school of Visso for the soil S4 in the Chapter §4.1 and Brunelli et al. (2021b) that show a little number of analysis in the high DL. This same result occurs considering the other buildings studied with this soil profile.

The results in PGA are the same for all buildings, instead the value of $Sa(T_1)$ changes because the fundamental period of each studied buildings changes as well. These graphs were obtained by considering the geometric mean of the PGA in the two directions.

Furthermore, the fundamental period of the FB model does not vary by changing the subsoil model, while in the case of the CB model, in addition to varying the seismic input, the period of the structure also varies since at the base there are springs with different impedances calibrated with the formulation of Gazetas (1991). The period of the FB model is calculated through modal analysis with the TREMURI program (Lagomarsino et al. (2013)). The CB models estimated the period trought the Replacement Oscillator theory of Maravas et al. (2014), considering the initial stiffness of the soil (reported in Table 2).

Table 2: initial stiffness of four soil profile.

	S1	S2	S3	S4
G_0 [MPa]	37.69	53.50	29.54	97.06

Table 3 shows all the fundamental periods in the two directions for the FB and CB models as the soil profile varies. There are also period elongations passing from the FB model to the CB model: the ground S3 is the one that extends the period the most, while S4 is the one that extends it the least. This result is consistent with the initial stiffnesses shown in Table 2 since the soil S3 is the most deformable and S4 the most rigid. The X and Y directions do not have very different elongations, the Y tends to be the direction with the greatest elongation, this also depends on the geometry of the foundation.

Table 3: Comparison between all periods with varying stratigraphic profile.

		FB		CB		$T_{CB}/T_{FB}X$	$T_{CB}/T_{FB}Y$
		Tx	Ty	Tx	Ty		
School	S1	0.148	0.178	0.218	0.258	1.47	1.45
	S2			0.205	0.264	1.39	1.48
	S3			0.269	0.354	1.82	1.99
	S4			0.182	0.230	1.23	1.29
$U1_{A1,I}$	S1	0.194	0.152	0.346	0.303	1.78	1.99
	S2			0.312	0.270	1.61	1.78
	S3			0.356	0.311	1.84	2.05
	S4			0.266	0.225	1.37	1.48
$U3_{A1,I}$	S1	0.308	0.115	0.539	0.240	1.75	2.09
	S2			0.488	0.212	1.58	1.84
	S3			0.553	0.250	1.80	2.17
	S4			0.417	0.178	1.35	1.55
$U1_{A1,A}$ $U2_{A1,A}$	S1	0.173	0.144	0.239	0.219	1.38	1.52
	S2			0.221	0.200	1.28	1.39
	S3			0.220	0.195	1.27	1.35
	S4			0.202	0.178	1.17	1.24
$U3_{A1,A}$	S1	0.173	0.118	0.239	0.219	1.38	1.86
	S2			0.221	0.200	1.28	1.69
	S3			0.220	0.195	1.27	1.65
	S4			0.202	0.178	1.17	1.51
$U1_{A2,I}$	S1	0.112	0.079	0.190	0.154	1.70	1.95
	S2			0.171	0.136	1.53	1.73
$U4_{A2,I}$	S1	0.186	0.108	0.362	0.175	1.94	1.63
	S2			0.320	0.159	1.72	1.47
$U_{A2,A}$ (all Units)	S1	0.145	0.098	0.268	0.175	1.85	1.78
	S2			0.249	0.164	1.72	1.67

These period variations lead to a different spectral acceleration and therefore once the seismic event is fixed, the greater elongation compared to the FB period involves a different effect compared to the fixed base model (in some cases in amplification in others for de-amplification). Figure 5 shows the trends of the amplification factor of the spectral acceleration. The figure shows the amplification factors of the buildings in aggregate (A1 and A2) and those isolated for land S1 and S2. The trends of the amplification of the spectral accelerations for the Visso school on its real stratigraphy are present in Brunelli et al. (2022a), while the calculation of the different spectral accelerations as the terrain varies are present in Brunelli et al. (2021b).

Figure 5 shows both the FB and the CB model results. Also in this case the amplification is greater for lower seismic input values, up to some events that lead, especially for the fixed base model, to a de-amplification. Furthermore, it is observed that there is a significantly different behavior passing from the isolated model to the aggregate one. In fact, in the case of the building studied in the aggregate, all the structural units have the same period, the only exception is the $U3_{A1,I}$ in the Y direction which has a different period than the first two cells due to the torsional effects of the aggregate. As for the PGA, also in this case the representative value of the event is calculated as the geometric mean of the $Sa(T_1)$ in the two directions.

For this reason, there are some differences in behavior in terms of signal amplification that can lead to a variation in terms of damage achieved.

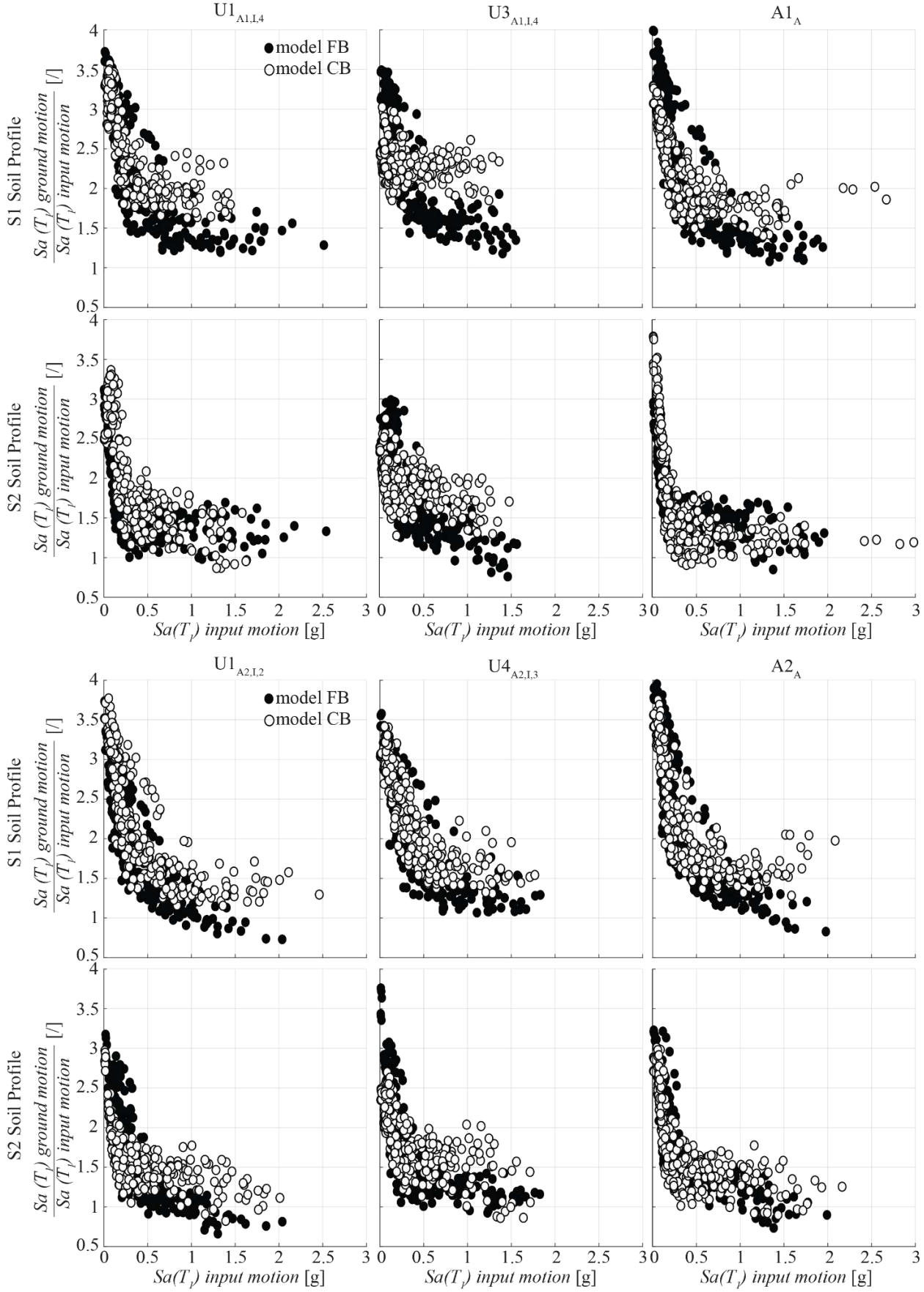

Figure 5. amplification factor in $Sa(T_1)$ for the building in aggregate and isolate for soil S1 and S2.

2.1 Influence of site and SFS Interaction effects on the fragility curves.

The tables from Table 4 to Table 8 show the average values (IM_{50}) and standard deviations (σ) for the FB A, FB C and CB C models for the four studied soil profiles. In particular, the values for the following IMs are reported: the peak ground acceleration (PGA); the spectral acceleration ($Sa(T_1)$) and the Housner P-Velocity Spectrum Intensity computed in the range of periods from 0.1 to 0.5 s ($IH_{0.1\ 0.5}$). The cumulative absolute velocity (CAV) is not reported as it was already observed for the Visso's school to have a behavior less correlated to the damage (greater deviations). This same result was obtained for the other buildings studied, for this reason it was not used to construct fragility curves. The values of IM_{50}s and deviations are calculated for the five groups of DL (from DL 1 to 5) as a function of the maximum damage achieved by each analysis as explained in Brunelli et al. (2022a). For the FB A case the initial set of input motions are integrated with additional natural signals recorded on stiff rock outcrop and collected by Paolucci et al. (2020) and Manfredi et al. (2022) to obtain a more robust statistic (as explained in Brunelli et al. (2022a) and Chapter §3). These new events are the same for all buildings. However, the updated parameters IM_{50} and σ are comparable with that resulting from the original selection as show in Brunelli et al. (2021b) and Brunelli et al. (2022a). In the tables of the FB A model, the values obtained from the complete selection are reported directly.

Table 4: Median value (IM_{50}) and standard deviation (σ) associated to the DLs for the FB A case.

Building	DLi	PGA [g]		$Sa(T_1)$ [g]		$IH_{0.1\ 0.5}$ [m]		$N_{records}$
		IM_{50}	σ	IM_{50}	σ	IM_{50}	σ	
school	DL1	0.095	0.495	0.178	0.473	0.024	0.625	127
	DL2	0.274	0.314	0.656	0.391	0.093	0.368	92
	DL3	0.450	0.219	1.013	0.376	0.174	0.186	18
	DL4	0.530	0.191	1.182	0.308	0.214	0.176	17
	DL5	0.619	0.219	1.500	0.261	0.249	0.221	44
$U1_{A1,I}$	DL1	0.108	0.339	0.201	0.316	0.029	0.461	72
	DL2	0.228	0.320	0.515	0.405	0.079	0.344	122
	DL3	0.342	0.156	0.852	0.403	0.135	0.219	19
	DL4	0.417	0.188	1.133	0.356	0.180	0.167	13
	DL5	0.553	0.245	1.330	0.336	0.214	0.282	84
$U3_{A1,I}$	DL1	0.099	0.425	0.171	0.370	0.025	0.403	60
	DL2	0.187	0.360	0.381	0.380	0.065	0.368	94
	DL3	0.254	0.457	0.582	0.424	0.099	0.427	13
	DL4	0.361	0.327	0.748	0.334	0.145	0.282	20
	DL5	0.441	0.383	0.961	0.433	0.169	0.415	132
$U1_{A1,A}$	DL1	0.091	0.390	0.168	0.338	0.023	0.543	94
	DL2	0.222	0.318	0.506	0.372	0.077	0.369	131
	DL3	0.368	0.185	0.985	0.177	0.138	0.145	17
	DL4	0.457	0.200	1.161	0.271	0.174	0.198	30
	DL5	0.592	0.215	1.455	0.267	0.237	0.225	62
$U2_{A1,A}$	DL1	0.133	0.399	0.273	0.366	0.041	0.498	96
	DL2	0.269	0.287	0.644	0.370	0.095	0.314	97
	DL3	0.433	0.200	1.081	0.304	0.165	0.214	35
	DL4	0.497	0.159	1.183	0.293	0.201	0.217	14
	DL5	0.616	0.210	1.529	0.235	0.246	0.211	49
$U3_{A1,A}$	DL1	0.125	0.448	0.261	0.403	0.037	0.540	91
	DL2	0.257	0.288	0.600	0.375	0.094	0.316	107
	DL3	0.450	0.201	1.029	0.292	0.158	0.306	19
	DL4	0.482	0.196	1.134	0.330	0.188	0.212	26
	DL5	0.606	0.219	1.391	0.258	0.242	0.226	51

$U1_{A2,I}$	DL1	0.117	0.432	0.237	0.340	0.031	0.685	118
	DL2	0.236	0.293	0.493	0.339	0.083	0.335	80
	DL3	0.320	0.227	0.678	0.353	0.108	0.333	19
	DL4	0.420	0.192	0.814	0.281	0.154	0.169	24
	DL5	0.560	0.291	1.119	0.309	0.220	0.273	80
$U4_{A2,I}$	DL1	0.101	0.383	0.204	0.359	0.027	0.489	81
	DL2	0.217	0.281	0.459	0.356	0.075	0.269	93
	DL3	0.285	0.308	0.601	0.505	0.115	0.267	19
	DL4	0.394	0.266	0.916	0.394	0.150	0.254	16
	DL5	0.506	0.340	1.125	0.391	0.195	0.341	103
$U1_{A2,A}$	DL1	0.093	0.437	0.187	0.401	0.023	0.614	123
	DL2	0.248	0.311	0.540	0.393	0.081	0.294	127
	DL3	0.382	0.233	0.833	0.254	0.127	0.373	16
	DL4	0.467	0.175	1.071	0.324	0.145	0.260	17
	DL5	0.597	0.211	1.336	0.231	0.218	0.276	63
$U2_{A2,A}$	DL1	0.105	0.408	0.211	0.374	0.030	0.553	103
	DL2	0.214	0.247	0.455	0.315	0.081	0.318	89
	DL3	0.329	0.200	0.728	0.311	0.107	0.300	30
	DL4	0.437	0.232	0.937	0.197	0.146	0.251	15
	DL5	0.541	0.244	1.234	0.284	0.225	0.251	88
$U3_{A2,A}$	DL1	0.104	0.348	0.211	0.256	0.027	0.586	81
	DL2	0.201	0.259	0.401	0.271	0.073	0.310	64
	DL3	0.266	0.303	0.508	0.210	0.094	0.342	15
	DL4	0.326	0.316	0.785	0.347	0.124	0.269	79
	DL5	0.560	0.282	1.254	0.292	0.201	0.361	74
$U4_{A2,A}$	DL1	0.164	0.368	0.338	0.355	0.040	0.626	124
	DL2	0.301	0.228	0.689	0.283	0.088	0.263	43
	DL3	0.331	0.220	0.741	0.287	0.112	0.243	14
	DL4	0.408	0.129	0.940	0.264	0.139	0.235	18
	DL5	0.568	0.230	1.278	0.264	0.207	0.287	79

Table 4 shows how the three IMs have the same behavior in terms of deviation for the FB A case. It is greater for the smaller DLs and then decreases (with some exceptions) for the higher DLs. Since $IH_{0.1\ 0.5}$ does not show a significantly better trend than the other two IMs and this measure of intensity is less correlated to the damage in the literature, only the results in PGA and $Sa(T_1)$ are considered in future representations.

Table 5: Median value (IM_{50}) and standard deviation (σ) associated to the DLs for the FB C and CB C cases for S1 soil profile.

Building	DLi	FB C					CB C				
		PGA [g]		$Sa(T_1)$ [g]		$N_{records}$	PGA [g]		$Sa(T_1)$ [g]		$N_{records}$
		IM_{50}	σ	IM_{50}	σ		IM_{50}	σ	IM_{50}	σ	
School	DL1	0.051	0.474	0.093	0.335	54	0.074	0.406	0.109	0.374	71
	DL2	0.120	0.430	0.237	0.469	99	0.158	0.439	0.317	0.452	87
	DL3	0.211	0.219	0.433	0.335	14	0.242	0.268	0.578	0.413	22
	DL4	0.240	0.248	0.595	0.338	27	0.357	0.274	0.794	0.426	37
	DL5	0.404	0.329	0.975	0.426	72	0.490	0.249	1.065	0.451	31
$U1_{A1,I}$	DL1	0.041	0.419	0.078	0.277	33	0.073	0.436	0.076	0.365	57
	DL2	0.105	0.486	0.203	0.531	106	0.162	0.494	0.272	0.482	121
	DL3	0.184	0.294	0.387	0.378	45	0.239	0.344	0.512	0.298	37
	DL4	0.209	0.254	0.427	0.350	16	0.335	0.349	0.705	0.377	10
	DL5	0.354	0.353	0.865	0.476	114	0.397	0.353	0.831	0.359	69

	DL1	0.050	0.521	0.081	0.321	49	0.050	0.521	0.050	0.354	49
	DL2	0.108	0.472	0.199	0.479	82	0.107	0.462	0.131	0.519	81
$U3_{A1,I}$	DL3	0.161	0.296	0.304	0.411	10	0.161	0.296	0.276	0.310	10
	DL4	0.186	0.331	0.356	0.354	18	0.191	0.339	0.295	0.289	19
	DL5	0.301	0.434	0.634	0.477	155	0.301	0.434	0.543	0.436	155
	DL1	0.039	0.398	0.073	0.229	30	0.071	0.404	0.102	0.304	61
	DL2	0.103	0.441	0.199	0.451	119	0.151	0.415	0.313	0.470	109
$U1_{A1,A}$	DL3	0.185	0.205	0.437	0.229	21	0.241	0.250	0.550	0.386	45
	DL4	0.245	0.232	0.564	0.333	32	0.337	0.264	0.885	0.474	21
	DL5	0.351	0.370	0.855	0.473	112	0.442	0.256	0.944	0.460	59
	DL1	0.060	0.441	0.107	0.349	69	0.084	0.399	0.132	0.376	71
	DL2	0.132	0.426	0.275	0.464	87	0.184	0.364	0.404	0.470	115
$U2_{A1,A}$	DL3	0.220	0.220	0.484	0.343	40	0.281	0.279	0.611	0.395	36
	DL4	0.240	0.280	0.525	0.300	19	0.381	0.199	0.791	0.273	16
	DL5	0.370	0.364	0.930	0.451	96	0.477	0.229	1.115	0.433	44
	DL1	0.061	0.475	0.119	0.390	72	0.084	0.395	0.126	0.372	59
	DL2	0.131	0.429	0.272	0.493	83	0.155	0.436	0.327	0.471	83
$U3_{A1,A}$	DL3	0.188	0.286	0.427	0.292	16	0.274	0.335	0.601	0.432	97
	DL4	0.231	0.206	0.523	0.331	39	0.381	0.341	0.862	0.476	16
	DL5	0.364	0.368	0.842	0.462	102	0.515	0.210	1.289	0.440	25
	DL1	0.050	0.517	0.099	0.408	42	0.063	0.455	0.106	0.313	62
	DL2	0.115	0.484	0.249	0.451	128	0.149	0.447	0.317	0.476	143
$U1_{A2,I}$	DL3	0.204	0.220	0.409	0.285	17	0.262	0.231	0.654	0.335	20
	DL4	0.232	0.215	0.468	0.323	32	0.344	0.169	0.890	0.349	40
	DL5	0.390	0.295	0.770	0.418	95	0.490	0.211	1.184	0.413	43
	DL1	0.050	0.484	0.101	0.352	47	0.077	0.423	0.106	0.361	70
	DL2	0.104	0.399	0.211	0.461	76	0.145	0.470	0.254	0.382	49
$U4_{A2,I}$	DL3	0.165	0.356	0.350	0.397	26	0.202	0.309	0.399	0.385	59
	DL4	0.208	0.283	0.430	0.388	42	0.247	0.268	0.515	0.429	35
	DL5	0.335	0.402	0.728	0.532	121	0.403	0.322	0.867	0.389	76
	DL1	0.043	0.538	0.083	0.582	53	0.057	0.477	0.083	0.316	59
	DL2	0.117	0.397	0.243	0.413	112	0.152	0.468	0.308	0.566	149
$U1_{A2,A}$	DL3	0.199	0.182	0.417	0.299	21	0.274	0.304	0.667	0.460	39
	DL4	0.242	0.231	0.517	0.356	29	0.355	0.252	0.758	0.406	17
	DL5	0.369	0.334	0.819	0.441	104	0.463	0.227	1.054	0.382	47
	DL1	0.044	0.489	0.085	0.446	44	0.071	0.430	0.105	0.377	75
	DL2	0.098	0.385	0.205	0.351	87	0.159	0.424	0.331	0.458	106
$U2_{A2,A}$	DL3	0.167	0.217	0.339	0.335	36	0.253	0.280	0.615	0.417	52
	DL4	0.203	0.131	0.431	0.239	19	0.389	0.245	0.894	0.394	20
	DL5	0.343	0.344	0.761	0.441	130	0.441	0.288	0.984	0.448	49
	DL1	0.043	0.415	0.091	0.394	39	0.060	0.435	0.086	0.312	59
	DL2	0.090	0.370	0.182	0.350	70	0.138	0.419	0.266	0.460	115
$U3_{A2,A}$	DL3	0.160	0.261	0.326	0.364	26	0.234	0.225	0.446	0.235	18
	DL4	0.196	0.335	0.413	0.402	64	0.301	0.338	0.719	0.350	64
	DL5	0.346	0.383	0.766	0.475	115	0.411	0.390	1.022	0.481	52
	DL1	0.076	0.477	0.150	0.399	99	0.103	0.378	0.184	0.349	71
	DL2	0.148	0.373	0.337	0.350	44	0.176	0.279	0.378	0.296	45
$U4_{A2,A}$	DL3	0.188	0.275	0.402	0.331	15	0.241	0.274	0.563	0.345	60
	DL4	0.221	0.222	0.445	0.329	16	0.309	0.253	0.769	0.417	21
	DL5	0.331	0.377	0.730	0.473	132	0.441	0.273	1.002	0.423	60

Table 6: Median value (IM_{50}) and standard deviation (σ) associated to the DLs for the FB C and CB C cases for S2 soil profile.

Building	DLi	FB C					CB C				
		PGA [g]		$Sa(T_1)$ [g]		$N_{records}$	PGA [g]		$Sa(T_1)$ [g]		$N_{records}$
		IM_{50}	σ	IM_{50}	σ		IM_{50}	σ	IM_{50}	σ	
School	DL1	0.070	0.551	0.126	0.457	102	0.080	0.545	0.127	0.564	118
	DL2	0.150	0.415	0.327	0.424	65	0.183	0.448	0.388	0.487	57
	DL3	0.240	0.230	0.562	0.333	11	0.252	0.328	0.651	0.474	13
	DL4	0.258	0.254	0.652	0.379	26	0.347	0.292	0.763	0.460	49
	DL5	0.426	0.282	1.024	0.401	62	0.496	0.246	0.972	0.451	25
$U1_{A1,I}$	DL1	0.041	0.419	0.078	0.277	33	0.073	0.436	0.076	0.365	57
	DL2	0.105	0.486	0.203	0.531	106	0.162	0.494	0.272	0.482	121
	DL3	0.184	0.294	0.387	0.378	45	0.239	0.344	0.512	0.298	37
	DL4	0.209	0.254	0.427	0.350	16	0.335	0.349	0.705	0.377	15
	DL5	0.354	0.353	0.865	0.476	114	0.397	0.353	0.831	0.359	69
$U3_{A1,I}$	DL1	0.050	0.521	0.081	0.321	49	0.050	0.521	0.050	0.354	49
	DL2	0.108	0.472	0.199	0.479	82	0.107	0.462	0.131	0.519	81
	DL3	0.161	0.296	0.304	0.411	14	0.161	0.296	0.276	0.310	14
	DL4	0.186	0.331	0.356	0.354	18	0.191	0.339	0.295	0.289	19
	DL5	0.301	0.434	0.634	0.477	155	0.301	0.434	0.543	0.436	155
$U1_{A1,A}$	DL1	0.066	0.500	0.119	0.417	85	0.078	0.480	0.126	0.423	92
	DL2	0.136	0.405	0.283	0.413	78	0.163	0.417	0.341	0.443	75
	DL3	0.217	0.200	0.462	0.179	18	0.242	0.281	0.533	0.445	60
	DL4	0.246	0.243	0.630	0.314	31	0.295	0.330	0.747	0.339	15
	DL5	0.367	0.364	0.903	0.464	100	0.439	0.252	1.027	0.497	63
$U2_{A1,A}$	DL1	0.076	0.516	0.139	0.455	116	0.091	0.456	0.158	0.465	104
	DL2	0.164	0.356	0.379	0.358	51	0.208	0.315	0.465	0.462	70
	DL3	0.230	0.187	0.524	0.327	38	0.269	0.334	0.622	0.539	52
	DL4	0.245	0.236	0.575	0.347	23	0.361	0.239	0.828	0.421	16
	DL5	0.404	0.311	1.005	0.413	83	0.456	0.254	0.986	0.486	46
$U3_{A1,A}$	DL1	0.076	0.519	0.148	0.471	108	0.091	0.472	0.152	0.490	93
	DL2	0.148	0.370	0.316	0.412	52	0.172	0.460	0.376	0.527	55
	DL3	0.204	0.248	0.470	0.233	18	0.233	0.336	0.596	0.613	20
	DL4	0.239	0.209	0.551	0.292	42	0.294	0.345	0.661	0.518	84
	DL5	0.392	0.321	0.918	0.424	90	0.463	0.284	0.987	0.533	34
$U1_{A2,I}$	DL1	0.068	0.556	0.136	0.491	91	0.087	0.409	0.160	0.340	97
	DL2	0.148	0.430	0.327	0.388	99	0.192	0.359	0.442	0.345	98
	DL3	0.234	0.251	0.403	0.384	16	0.281	0.207	0.706	0.315	23
	DL4	0.256	0.235	0.543	0.368	21	0.331	0.241	0.837	0.373	29
	DL5	0.399	0.296	0.788	0.410	87	0.484	0.212	1.198	0.355	45
$U4_{A2,I}$	DL1	0.058	0.515	0.117	0.444	71	0.082	0.414	0.126	0.396	78
	DL2	0.117	0.423	0.238	0.488	65	0.143	0.386	0.276	0.334	34
	DL3	0.183	0.285	0.384	0.352	32	0.203	0.272	0.409	0.352	54
	DL4	0.211	0.274	0.448	0.424	36	0.243	0.314	0.552	0.365	42
	DL5	0.356	0.363	0.773	0.498	110	0.405	0.302	0.918	0.390	78
$U1_{A2,A}$	DL1	0.063	0.573	0.122	0.528	86	0.070	0.521	0.115	0.463	102
	DL2	0.140	0.415	0.302	0.404	92	0.175	0.417	0.384	0.477	98
	DL3	0.221	0.238	0.436	0.325	17	0.259	0.296	0.600	0.466	39
	DL4	0.241	0.228	0.542	0.314	31	0.327	0.269	0.760	0.368	18
	DL5	0.391	0.321	0.876	0.426	90	0.436	0.280	1.045	0.404	56
$U2_{A2,A}$	DL1	0.065	0.507	0.130	0.435	86	0.076	0.532	0.128	0.510	120

	DL2	0.133	0.354	0.285	0.355	68	0.147	0.332	0.328	0.318	35
	DL3	0.199	0.177	0.411	0.281	27	0.210	0.196	0.419	0.276	26
	DL4	0.234	0.144	0.485	0.259	20	0.238	0.184	0.502	0.191	17
	DL5	0.366	0.332	0.820	0.430	110	0.354	0.358	0.868	0.443	115
$U3_{A2,A}$	DL1	0.065	0.489	0.131	0.424	68	0.076	0.493	0.128	0.495	113
	DL2	0.119	0.413	0.246	0.375	59	0.174	0.311	0.362	0.345	69
	DL3	0.186	0.169	0.375	0.281	20	0.231	0.160	0.495	0.230	15
	DL4	0.213	0.358	0.483	0.414	60	0.293	0.311	0.690	0.339	62
	DL5	0.369	0.353	0.810	0.470	98	0.456	0.248	1.167	0.374	51
$U4_{A2,A}$	DL1	0.093	0.461	0.185	0.412	121	0.132	0.442	0.256	0.459	98
	DL2	0.175	0.279	0.382	0.260	31	0.229	0.265	0.560	0.375	47
	DL3	0.215	0.173	0.414	0.230	17	0.277	0.314	0.689	0.434	16
	DL4	0.257	0.246	0.595	0.264	22	0.319	0.279	0.734	0.470	24
	DL5	0.363	0.349	0.824	0.428	105	0.433	0.288	1.020	0.419	58

Table 7: Median value (IM_{50}) and standard deviation (σ) associated to the DLs for the FB C and CB C cases for S3 soil profile.

		FB C					CB C				
Building	DLi	PGA [g]		$Sa(T_1)$ [g]		$N_{records}$	PGA [g]		$Sa(T_1)$ [g]		$N_{records}$
		IM_{50}	σ	IM_{50}	σ		IM_{50}	σ	IM_{50}	σ	
School	DL1	0.050	0.463	0.093	0.329	55	0.078	0.417	0.095	0.416	72
	DL2	0.116	0.393	0.228	0.426	92	0.174	0.406	0.317	0.439	99
	DL3	0.201	0.158	0.435	0.247	17	0.325	0.282	0.683	0.327	21
	DL4	0.246	0.284	0.545	0.383	18	0.437	0.223	0.833	0.341	29
	DL5	0.380	0.333	0.924	0.429	84	0.460	0.259	0.922	0.315	22
$U1_{A1,I}$	DL1	0.044	0.404	0.084	0.304	43	0.073	0.382	0.072	0.285	49
	DL2	0.105	0.408	0.200	0.439	90	0.138	0.437	0.216	0.422	93
	DL3	0.179	0.246	0.358	0.309	26	0.201	0.252	0.407	0.299	33
	DL4	0.210	0.277	0.513	0.438	23	0.270	0.195	0.510	0.239	16
	DL5	0.330	0.388	0.779	0.519	132	0.370	0.353	0.736	0.381	99
$U3_{A1,I}$	DL1	0.055	0.486	0.085	0.289	50	0.072	0.470	0.058	0.254	28
	DL2	0.094	0.425	0.171	0.366	51	0.113	0.478	0.153	0.457	83
	DL3	0.141	0.205	0.293	0.259	16	0.152	0.304	0.279	0.332	19
	DL4	0.196	0.378	0.400	0.429	26	0.193	0.271	0.353	0.305	16
	DL5	0.278	0.491	0.574	0.549	171	0.319	0.417	0.564	0.431	141
$U1_{A1,A}$	DL1	0.042	0.385	0.080	0.256	36	0.075	0.359	0.125	0.315	45
	DL2	0.108	0.430	0.209	0.452	109	0.152	0.386	0.312	0.473	102
	DL3	0.173	0.246	0.381	0.389	18	0.262	0.321	0.610	0.553	55
	DL4	0.212	0.309	0.509	0.378	31	0.339	0.290	0.727	0.476	39
	DL5	0.336	0.380	0.808	0.494	125	0.474	0.230	1.098	0.469	36
$U2_{A1,A}$	DL1	0.061	0.402	0.109	0.298	64	0.093	0.335	0.160	0.343	60
	DL2	0.126	0.376	0.255	0.392	79	0.182	0.338	0.385	0.428	91
	DL3	0.201	0.190	0.458	0.323	41	0.277	0.300	0.623	0.469	50
	DL4	0.216	0.202	0.526	0.276	15	0.353	0.320	0.824	0.480	16
	DL5	0.365	0.340	0.885	0.456	110	0.445	0.265	1.036	0.545	50
$U3_{A1,A}$	DL1	0.060	0.438	0.113	0.319	57	0.092	0.423	0.153	0.343	46
	DL2	0.124	0.404	0.255	0.413	96	0.168	0.370	0.360	0.439	93
	DL3	0.186	0.217	0.477	0.221	15	0.297	0.340	0.635	0.488	79
	DL4	0.235	0.197	0.546	0.284	31	0.340	0.315	0.772	0.400	14
	DL5	0.359	0.361	0.825	0.474	109	0.480	0.231	1.268	0.478	33

Table 8: Median value (IM_{50}) and standard deviation (σ) associated to the DLs for the FB C and CB C cases for S4 soil profile.

Building	DLi	FB C					CB C				
		PGA [g]		$Sa(T_1)$ [g]		$N_{records}$	PGA [g]		$Sa(T_1)$ [g]		$N_{records}$
		IM_{50}	σ	IM_{50}	σ		IM_{50}	σ	IM_{50}	σ	
School	DL1	0.086	0.589	0.160	0.551	142	0.098	0.571	0.180	0.564	128
	DL2	0.241	0.414	0.572	0.441	73	0.296	0.361	0.637	0.401	79
	DL3	0.344	0.262	0.772	0.309	9	0.423	0.230	1.082	0.378	13
	DL4	0.420	0.331	0.931	0.360	9	0.513	0.260	1.312	0.463	14
	DL5	0.480	0.205	1.301	0.281	32	0.526	0.153	1.389	0.104	3
$U1_{A1,I}$	DL1	0.102	0.481	0.178	0.429	88	0.099	0.520	0.179	0.494	73
	DL2	0.179	0.389	0.429	0.363	67	0.210	0.375	0.474	0.424	90
	DL3	0.241	0.260	0.569	0.389	18	0.321	0.328	0.690	0.462	43
	DL4	0.285	0.247	0.644	0.355	10	0.368	0.266	0.896	0.455	10
	DL5	0.387	0.327	0.954	0.463	89	0.445	0.302	0.993	0.435	39
$U3_{A1,I}$	DL1	0.086	0.558	0.144	0.497	82	0.091	0.522	0.124	0.453	68
	DL2	0.156	0.385	0.313	0.399	41	0.163	0.369	0.291	0.337	52
	DL3	/	/	/	/	0	0.213	0.291	0.455	0.210	5
	DL4	0.164	0.283	0.362	0.301	4	0.196	0.327	0.427	0.411	7
	DL5	0.290	0.457	0.609	0.509	162	0.308	0.441	0.621	0.514	142
$U1_{A1,A}$	DL1	0.090	0.560	0.164	0.516	124	0.109	0.517	0.213	0.467	83
	DL2	0.204	0.464	0.488	0.468	94	0.241	0.407	0.556	0.525	104
	DL3	0.310	0.288	0.803	0.397	19	0.377	0.284	0.868	0.499	51
	DL4	0.336	0.302	0.867	0.392	13	0.535	0.222	1.442	0.295	8
	DL5	0.435	0.252	1.071	0.394	52	0.567	0.058	1.206	0.320	4
$U2_{A1,A}$	DL1	0.115	0.531	0.230	0.538	116	0.146	0.427	0.287	0.467	97
	DL2	0.244	0.355	0.578	0.397	57	0.288	0.337	0.691	0.491	88
	DL3	0.321	0.314	0.843	0.408	33	0.413	0.270	0.951	0.498	34
	DL4	/	/	/	/	2	/	/	/	/	1
	DL5	0.436	0.254	1.071	0.397	51	0.535	0.206	1.311	0.340	9
$U3_{A1,A}$	DL1	0.113	0.554	0.232	0.550	107	0.140	0.427	0.282	0.453	80
	DL2	0.244	0.422	0.568	0.485	79	0.257	0.361	0.606	0.512	85
	DL3	0.290	0.244	0.718	0.405	13	0.395	0.293	0.897	0.496	56
	DL4	0.357	0.296	0.828	0.398	12	/	/	/	/	0
	DL5	0.438	0.260	1.000	0.413	47	0.532	0.220	1.391	0.311	8

Table 8 shows that the S4 profile involves few analyzes in high DLs (in particular DL3 and DL4) because of the highly dissipative behavior of the profile as already analyzed for the Visso's school in Brunelli et al. (2021b). This behavior is therefore also confirmed for the other buildings analyzed with this terrain profile. As Figure 4 showed there is indeed a reduction of the PGA for the S4 profile. Since this profile led to insufficiently reliable groups of DLs, the fragility curves for this soil were not constructed. It should be remembered that the analyzes carried out were 272 for the school of Visso (322 for FB A case), 320 for the other buildings (370 for the FB A case). The difference between the total sum of the analyzes performed and those reported in the previous tables corresponds to the analyzes ending in the DL0. These analyzes were not used to construct fragility curves.
Figure 6 shows for each building analyzed the modification factor (MF) carry out the site effects and SFS interaction starting from the FB A values. The MF_{SE} is the ratio between FB C values and FB A values, so corrects the IM_{50} of the fixed-base model on soil A to account for the site effects, while MF_{SFSI} is the ratio between CB C and FB A values to consider the effect of the interaction. In the case of the S4 profile, the results are reported only from the groups of DLs with a sufficient number of analyzes. The first result is that the SFS interaction has values closer to those obtained with the bedrock model. This means that the interaction leads to a benefit compared to the damage obtainable

from the model which only considers the site amplification. The multiplicative factor turns out to be very different when changing ground or building, in particular this factor is not constantly greater for lower or higher DLs, but has a wide variability. This variation doesn't depend on the number of stories or characteristics of buildings, in fact the MF changes in different way.
These multiplicative factors allow us to pass from the median value of the fragility curve of the fixed-base model to the bedrock (a value often available in the literature) to that which takes into account only the site effect or SFS interaction. Modifying the fragility curve as mentioned assumes that the deviation (therefore the gradient of the curve) does not change as the modeling changes. As reported in Chapter §5 (in this case only for S1 and S2 soils) there is a variability of the deviation that is reduced as the level of damage increases. Only in some rare cases (for DL2) this variation is greater than 8-10%. Other studies (see Petridis and Pitilakis (2020)) also propose this corrective factor only in IM_{50} to switch from the fragility curve of the FB A model to that of the model with the site effect or SFS interaction.

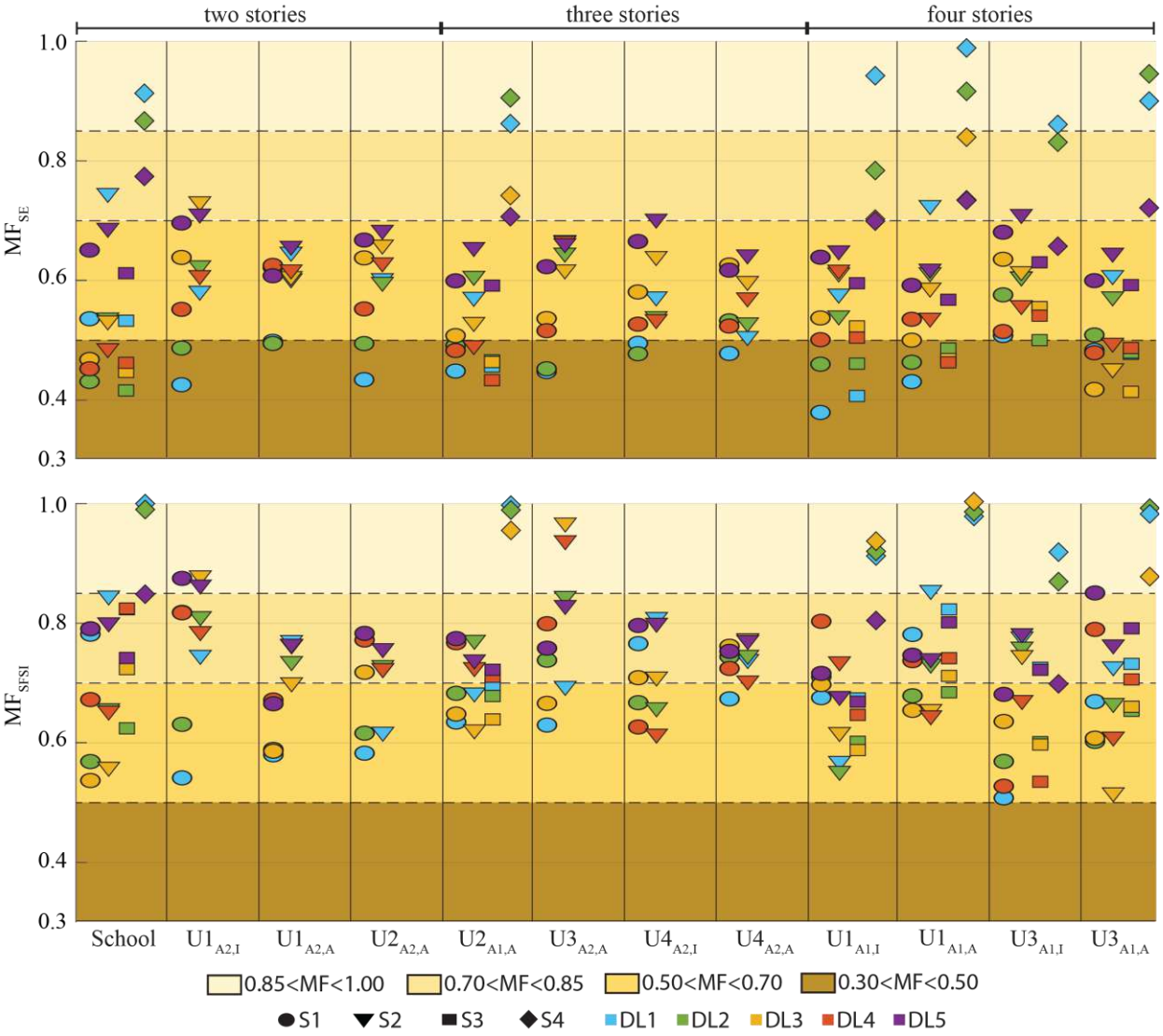

Figure 6. Modification factor for all building for site amplification and SFS interaction.

The effects expected to be caused on the analysed structure by an earthquake are quantitatively estimated in the following in terms of average damage (μ_d) computed through the fragility curves calculated with the values in table Table 5 to Table 7. As already explained in the main text, this parameter has been selected as an engineering demand parameter effective in synthetically comparing the results achieved from different approaches and various models. It is calculated as the sum of the

probabilities (p_{DLi}) weighted by 0,1,2,3,4 or 5 moving from DL0 to DL5. To try to be even more synthetic in the comparisons, the μ_d value is also converted into an equivalent DL according to the following ranges (Lagomarsino and Giovinazzi (2006)): 0-0.7 for DL0; 0.7-1.6 for DL1; 1.6-2.5 for DL2; 2.5-3.4 for DL3; 3.4-4.3 for DL4; 4.3-5 for DL5.
The Figure 7 shows the value of μ_d for the units of the building A1 and A2. The square elements are filled in light grey if the same DL is estimated by both models/approaches, and progressively darker when the estimation differs of one, two or three DLs. This figure allows to compare the results of the model in aggregate and in isolate case and to understand the difference between the model with only the site effects (on the abscissa axis) and the model with SFS interaction (on the ordinates axis).

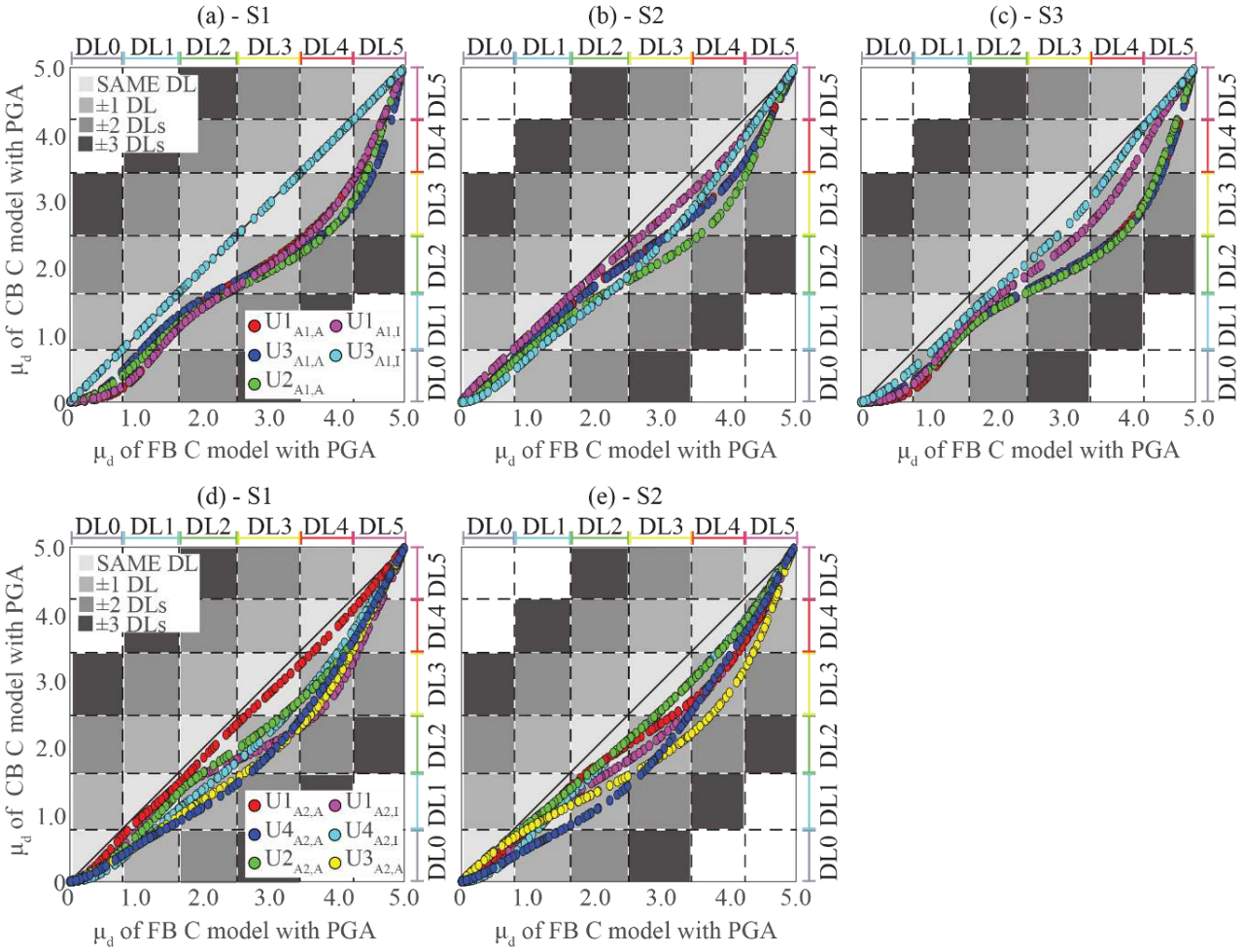

Figure 7. Comparison among the μ_d resulting for the different analysed cases from the curves expressed as a function of PGA (a,b,c) the building in aggregate A1 for soil S1, S2 and S3; (d,e) building in aggregate A2 for soil S1 and S2.

By observing only the trends of building A1, it can be observed that for all three soils, typically the response of unit 1 in the isolated and aggregate case is more similar to that of unit 3 where (with the exception of S2) a role is observed of the greatest SFS interaction in the aggregate case. In the case of building A2, the role of interaction is more present in the isolated units for both profiles studied. The overall differences between the FB and CB models on soil C are also significant for certain units up to 2 DL. Only for low damage levels for S2 there are some units with the highest trend for the CB C model for both buildings, but there is in any case a variation of the DL. The trends of the Visso school were not represented as they are contained in Brunelli et al. (2021a) and Brunelli et al. (2021b).
Figure 7 shows the μ_d results calculated for PGA values, as shown in Brunelli et al. (2021b) for the Visso school, also in this case it is confirmed that the trend in $Sa(T_1)$ is similar to that in PGA, but more dispersed and with some analysis that make the CB C model more punitive.

2.2 Comparisons with codes-conforming simplified approaches

As in the case of the Visso school, the results obtained from the FB C and CB C models were compared with those obtained from the simplified code method which considers the fragility curve of the FB A model and a new corrected value of IM (defined IM *) to keep account of the classification of the subsoil.
The details of the procedure are contained in Chapter §3.
In the case of the Visso school, the results were compared with four codes: the Italian Code (NTC (2018)); the Eurocode 8 -EC8 (CEN (2004); the American Code (ASCE7 (2016)); and the New Zealand Code (NZS (2017)). In this annex, the results are compared only for the first two codes, also considering that these structures are built in Italy.
Figure 8 shows the muds for the FB C and CB C model cases for building A1 for the three soil profiles analysed for NTC (2018). As in the case of Figure 7, the school results are not reported as they are reported for EC8 in Brunelli et al. (2021b). Also in this case, only the results for the PGA are reported as in the case of $Sa(T_1)$ there is a trend similar to that of the PGA, but only more dispersed.

In case of low levels of damage, the simplified code model (on the abscissas) well simulates the behavior of both the fixed-base and the complaint model. For the highest DLs (from DL2 to DL4) the code model greatly underestimates the damage of the fixed-base model (even of 2 DLs) for all A1 units except for the $U3_{A1,I}$ case where the code approach has substantially the same DL or at most the difference is one DL for all soil profiles. In the case of the CB model the differences become much lower: the maximum difference is 1 DL except for some points where it is 2. In some rare cases the code model cautiously overestimates the expected damage.

In the case of EC8 (see Figure 9), the points closest to the diagonal line are those with a magnitude (Ms) less than 5.5. In fact, the EC8 considers a different amplification depending on the magnitude, in particular this is equal to 1.5 for events with a surface wave magnitude lower than 5.5; otherwise, it is equal to 1.15.
No big differences are observed between the results with the NTC (2018) approach (Figure 8) and those with EC8 (Figure 9), the only differences are that in the case of the FB C model at low damage levels the EC8 underestimates the damage more, and that $U3_{A1,I}$ has a more similar behavior to the other cells for EC8.

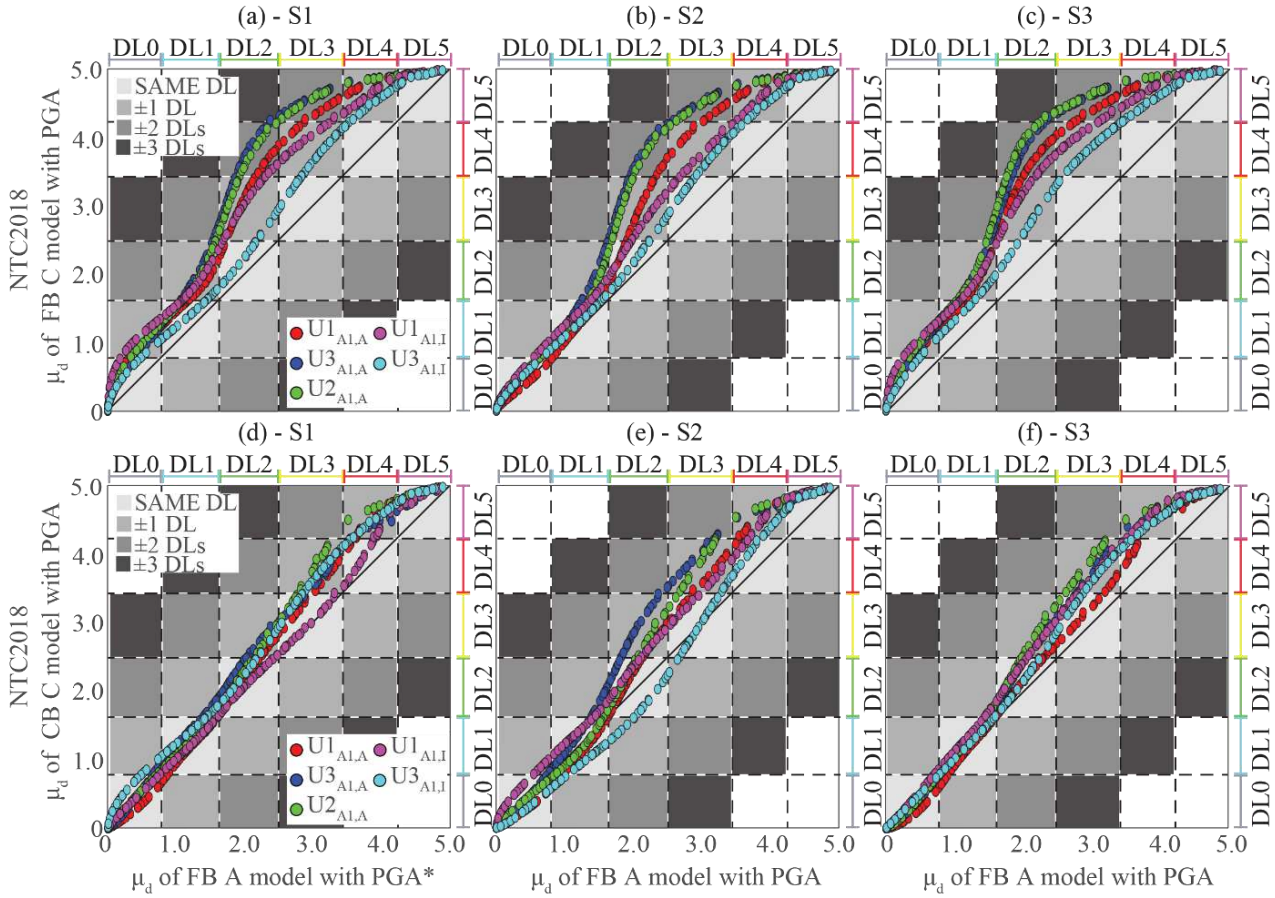

Figure 8. Comparison among the μ_d resulting for the different analysed cases from the curves expresses as a function of PGA for NTC (2018) in FB C case for (a) soil S1, (b) S2 and (c) S3 and for CB C case for (d) soil S1, (e) S2 and (f) S3.

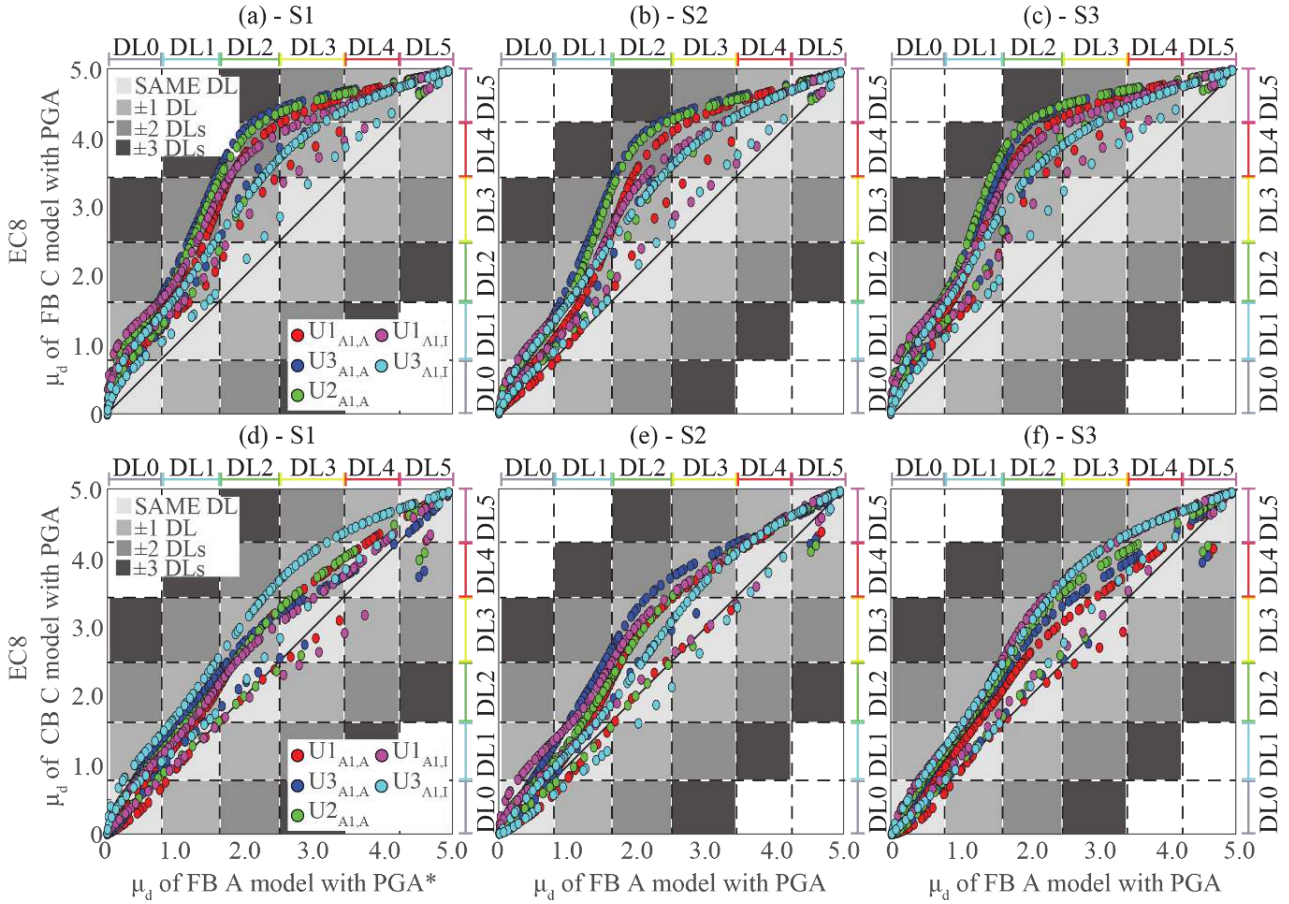

Figure 9. Comparison among the μ_d resulting for the different analysed cases from the curves expresses as a function of PGA for EC8 in FB C case for (a) soil S1, (b) S2 and (c) S3 and for CB C case for (d) soil S1, (e) S2 and (f) S3.

Finally, Figure 10 and Figure 11 respectively show the results of NTC and EC8 for building A2 (only for soil profiles S1 and S2). The results obtained for the first building (A1) can be considered similar for this second case study. It should be noted that in the case of the A1 there were only some units that appeared to have a more similar behavior between the numerical model and the simplified code approach in the case of the S2 profile. In the case of building A2, practically all structural units have a reduction in the gap between the two approaches (with the exception of cell $U4_{A2,A}$ which maintains the same trend as the soil changes). This implies that in the case of the CB model many units have pejorative (and therefore precautionary) behavior up to one DL with the code approach.

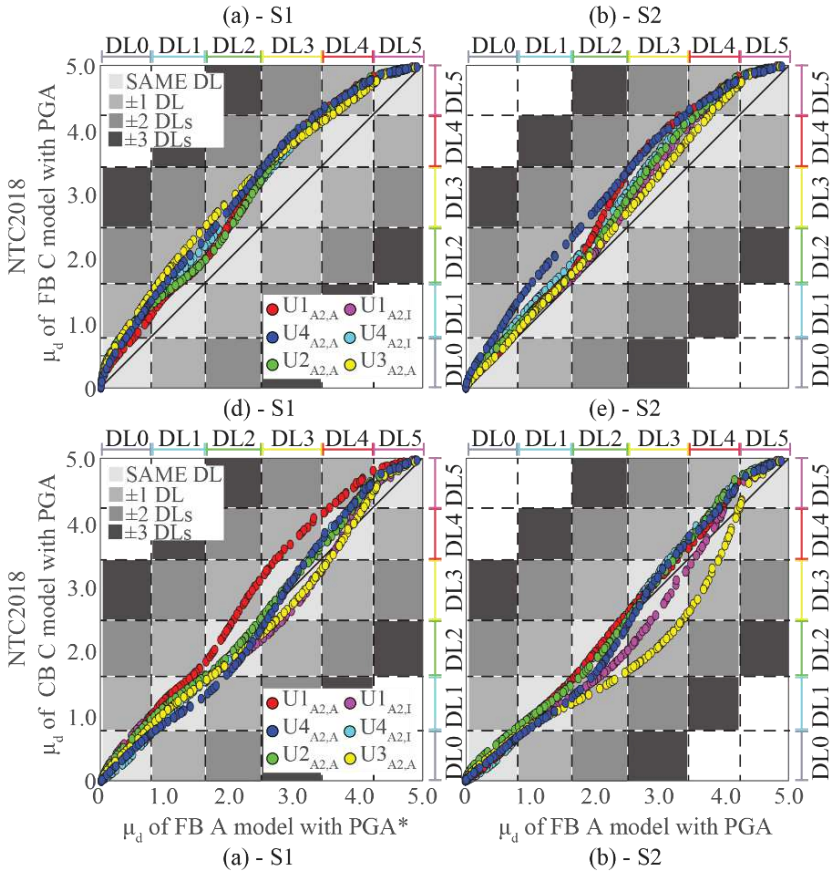

Figure 10. Comparison among the μ_d resulting for the different analysed cases from the curves expresses as a function of PGA for NTC (2018) in FB C case for (a) S1, (b) S2 and (c) S3 and for CB C case for (d) S1, (e) S2 and (f) S3.

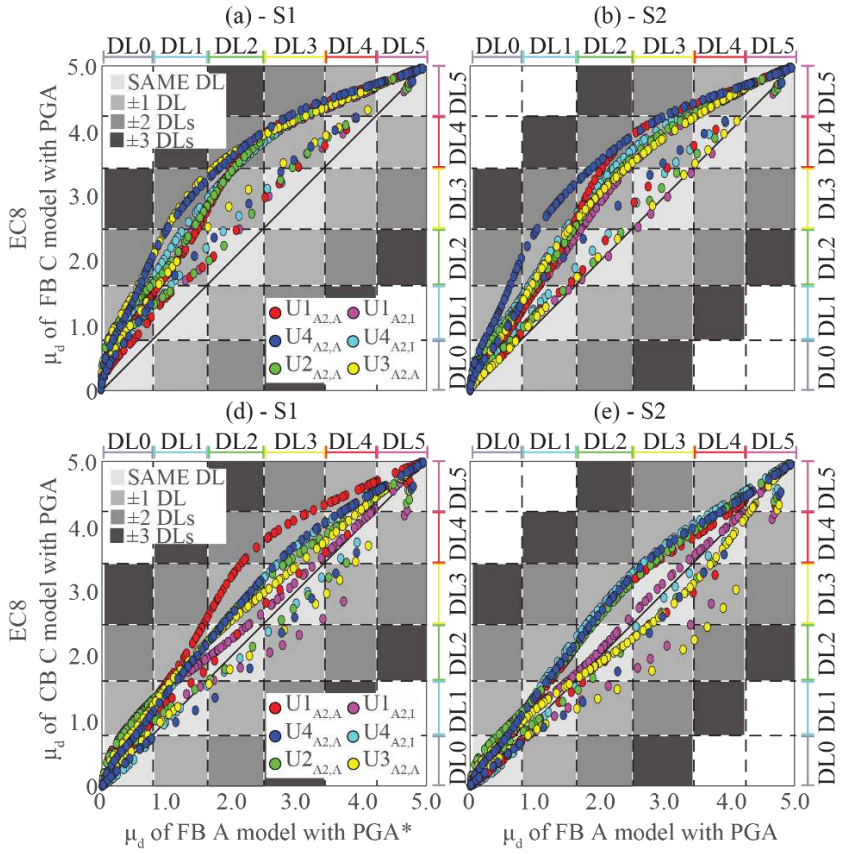

Figure 11. Comparison among the μ_d resulting for the different analysed cases from the curves expresses as a function of PGA for EC8 in FB C case for (a) S1, (b) S2 and (c) S3 and for CB C case for (d) S1, (e) S2 and (f) S3.

ANNEX A.5

Use of other intensity measures at urban scale

Several Intensity Measures (IM) were considered in this PhD thesis such as the peak ground acceleration (PGA), the spectral acceleration ($Sa(T_1)$), the cumulative absolute velocity (CAV) and the Housner P-Velocity Spectrum Intensity computed in the range of periods from 0.1 to 0.5 s ($IH_{0.1\ 0.5}$) as show in Chapter §3 and Annex A.4.2b.
This Annex analyses two other IMs: the H_{SM} and the A/V parameter.

1 H_{SM} PARAMETER: DEFINITION AND RESULTS.

The H_{SM} parameter (H = Hazard, SM = Seismic microzonation) was initially defined by Von Thun et al. (1988) and Naso et al. (2016) and most recently expanded by Mori et al. (2020). The purpose of this parameter is to consider several representative elements both of the signal (the input) and of the geographical area in which the analysed building is located. This is possible since the amplification factor used for the calculation of the H_{SM} considers the magnitude of the response spectrum due to the particular geological, geophysical and geotechnical characteristics of the considered area respected to the spectrum of code. The H_{SM} parameter is calculated with the following formula:

$$H_{SM} = ASI_{UHS}\left(\frac{AF_{T_n}}{\Delta T}\right) \qquad \text{with n=1,2,3} \qquad (1)$$

where:
- ASI_{UHS} is the Acceleration Spectrum Intensity (see Von Thun et al. (1988)), i.e. the integral value of the Uniform Hazard Spectrum (UHS) derived by seismic hazard studies (Seismic Hazard Map of Italy (MPS (2004)) in the relative period interval Tn (T_1 = 0.1-0.5 s; T_2= 0.4-0.8 s; T_3= 0.7-1.1 s) in this case, for the village of Visso;
- ΔT is the width of the integration interval (0.4 s, the same for all ranges);
- AF_{Tn} is calculated with the equation (2):

$$AF_{T_n} = \frac{\int_{T_a}^{T_b} Sa\ dT}{\int_{T_a}^{T_b} Sb\ dT} \qquad (2)$$

where:
- Sa is the pseudoacceleration elastic response spectrum at the study site (usually at the surface);
- Sb is the pseudoacceleration elastic response spectrum at the reference site (near site where the bedrock, i.e. type A ground, outcrops);
- Ta and Tb represent the extremes of the evaluated interval of T periods for each range Tn.

In particular, in this research all buildings have an elastic period in the first range of Tn (T_1 = 0.1-0.5 s) both in the case with fixed base (FB model) and complaint base model (CB model) and therefore only this interval has considered for the calculation of the H_{SM} parameter.
From the definition of the parameter and in particular in the equation 2 it is necessary to calculate the amplification factor as the ratio between the spectrum obtained from a local seismic response study and the input spectrum. This can only be done if the characteristics of the specific soil are known. It is not a parameter of immediate use (on the contrary, take for example the PGA), but it has the advantage of considering not only a peak effect of the input signal, but more characteristics of the

signal and of the soil. For this reason, recent studies are developing for Italy maps in amplification factors (or H_{SM}) (Falcone et al. (2021)).
In this research the Sb spectra are those selected from the SIMBAD database (Smerzini and Paolucci (2013); Iervolino et al. (2014)) as already explained in Chapter §3, while those on the surface defined Sa are the spectra obtained from the site response analyses with the program STRATA (see Kottke and Rathje (2008)) for the various subsoils considered.
The compatibility between the nine spectrum of code (see NTC (2018)) and input (S_b) spectra was defined as follows:

$$X_{bedrock} - \varepsilon \leq ASI_{UHS} \leq X_{bedrock} + \varepsilon \quad (3)$$

where:

- $X_{bedrock}$ is equal to the denominator of equation 2;
- ε is equal to 12% for all DLs except for DL1 where this error is 20%. This allowed for more values within this first level of damage. In fact, there were events that appeared to be close to ASIUHS with the shortest return period (TR = 30 years), but did not fall within the margin selected for the other DLs.

Having for each event the two components of the signal and their spectra on the surface (S_a) and at the bedrock (S_b), the geometric mean of the two components was calculated and compared with ASI_{UHS} to see their compatibility. The amplification factors (AF) in the two directions were calculated for the analyses with this compatibility. For this reason, not all analyses were useful for the calculation of the H_{SM} in case that the analyses not having a spectral value compatible with that of the ASI_{UHS} calculated for that range of periods (T_1).
Figure 1 compares the AF obtained using equation 2 (the black dots in the figure) with that obtained from Visso's seismic microzonation studies (see MZS3 (2018)). In particular, it can be seen that for the soil profile S1 (soil at the school of Visso) the average amplification factor obtained from the microzonation studies is practically always exceeded, in the case S2 (soil profile below historical centre) some rare signal decrease with respect to the proposed range which normally remains an underestimation of the real amplification obtained from the local seismic response with STRATA program (Kottke and Rathje (2008)). This indicates how less amplified signals would be obtained using the amplification factors of the microzonation for both areas of the municipality of Visso. The soil profile S1 amplifies bedrock signals more than S2.

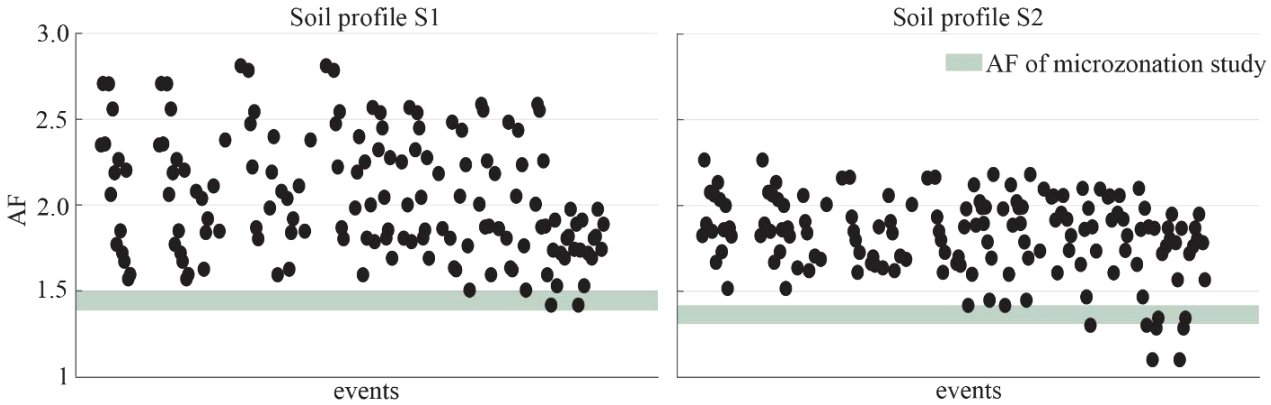

Figure 1. Confront between AF of microzonation study and that of each events by site response analyses from STRATA.

In the case of the soil profiles S3 (ideal homogeneous clay profile) and S4 (ideal homogeneous gravel profiles) it is not possible to make a comparison with the AF of the microzonation as they are soils defined in this research with a Vs that increases with the depth according to the formulation by d'Onofrio and Silvestri(2001) and Hardin and Kalinski (2005) respectively for S3 and S4 to have the V_{Seq} close to the first two profiles (as explained in Chapter §4.1). Figure 2 shows the amplification

factors obtained from the local seismic response in STRATA with the profiles S3 and S4. It is observed that the S4 profile is the soil that least amplifies of the four under examination and in some cases the AF value is equal to 1 (non-amplification) and in four events there is also a freefield signal deamplification. In the case of the S3 profile there is a greater amplification range than the other three profiles, in fact some events have maximum amplifications equal to almost 3, but the minimums lead to non-amplified events having an AF equal to 1.

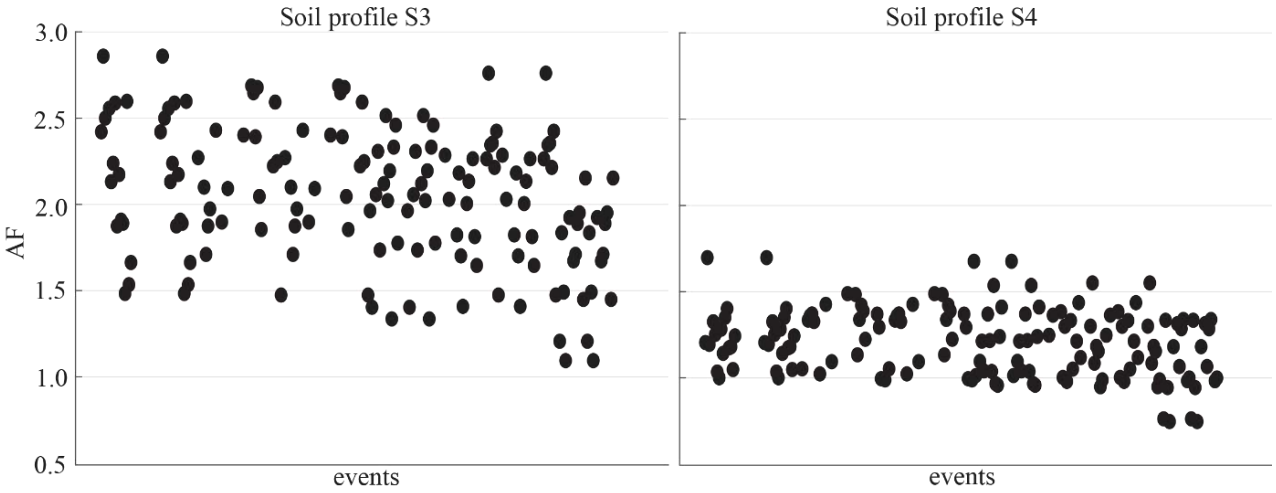

Figure 2. AF of each event by site response analyses from STRATA in case S3 and S4 profile.

These amplification values are consistent with the experimental ones obtained from Falcone et al. (2021) for the V_{Seq} of each medium reported in Table 1 for this range of periods and class of soil.

Table 1: V_{Seq} of the four soil profiles.

	S1	S2	S3	S4
V_{Seq} [m/s]	281	272	200	279

The gravelly soil profile led to have few analyses in the upper DLs (in particular DL4 and DL5) as already analysed in the Chapter §4.1 for the school and in Annex A.4.2b for the other building in aggregate. It has not been analysed in this annex because of the non-definable DLs and relative fragility curves.

Exactly as for the other IM, the fragility curves were calculated estimating the probability of exceeding (p_{DLi}) of the different damage levels (DLi) given a level of ground shaking quantified through the intensity measure, in this case H_{SM}. The p_{DLi} was computed from the lognormal distribution of IM causing the i^{th} DL and characterized by the median value IM_{mi} and the lognormal standard deviation σ:

$$p_{DLi}(DL > DLi|IM) = \Phi\left(\frac{\log IM|IM_{mi}}{\sigma}\right) \quad (4)$$

where Φ is the standard cumulative probability function.

Also in this case the effects of each event is calculated through the average damage (μd) computed with the fragility curves in H_{SM} as the sum of the probabilities (p_{DLi}) weighted by 0,1,2,3,4 or 5 moving from DL0 to DL5, according to equation 5:

$$\mu_d = \sum_{i=0}^{5}(p_{DLi}\ i) \quad (5)$$

To evaluate the reliability of this new parameter compared to the more common ones such as the PGA, the values of the μd obtained from the same earthquake were compared with one and the other IM.

Figure 3 shows the comparison obtained considering the Visso school as a building in the case of soil S1 (Figure 3a) and S3 (Figure 3b); fixed-base model (in black dots) and complaint base model (in

white dots). The trend is quite good, along the bisector of the graph, even if there are events that lead to an underestimation and an overestimation considering H_{SM}.

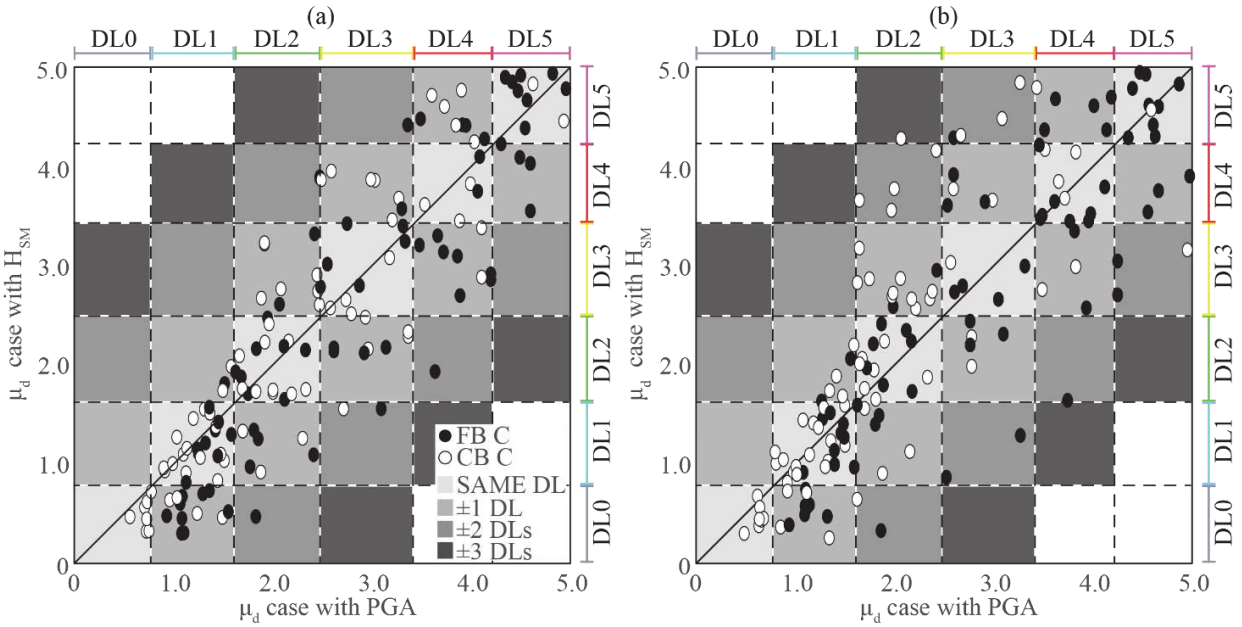

Figure 3. Correlation between the μ_d obtained with the curves calculated in PGA and with the H_{SM} parameter.

The covariance (CoV) between the μ_d obtained with the PGA and that with the H_{SM} was then calculated for all three soil profiles and for the various buildings analysed in this research. These values are reported in Table 2. The CoV always results on high values (the minimum CoV value is equal to 79.9% in the case of the school on S3). In two cases it was not possible to calculate the μ_d with the H_{SM} parameter as there were not enough analyses in the DL1. In other cases, this value is not available (abbreviation NP): the analyses with the building in aggregate (A2) were performed only with the first two soil profiles.

Table 2: CoV between the μd obtained with the curves in PGA and with HSM as the building and soil vary.

		S1		S2		S3	
		FB	CB	FB	FB	CB	FB
	School	88.8%	88.0%	86.5%	85.2%	85.8%	79.9%
Two storeys	$U1_{A2,I}$	88.5%	87.6%	86.8%	84.7%	NP	NP
	$U1_{A2,A}$	88.2%	88.5%	86.8%	86.4%	NP	NP
	$U2_{A2,A}$	88.9%	88.6%	87.2%	86.8%	NP	NP
Three storeys	$U2_{A1,A}$	88.6%	87.6%	86.9%	84.8%	85.2%	83.0%
	$U3_{A2,A}$	89.8%	89.2%	87.3%	85.5%	NP	NP
	$U4_{A2,I}$	89.6%	89.2%	87.7%	87.5%	NP	NP
	$U4_{A2,A}$	89.3%	88.1%	86.9%	86.0%	NP	NP
Four storeys	$U1_{A1,I}$	88.8%	88.1%	86.7%	86.4%	unavailable	84.6%
	$U1_{A1,A}$	unavailable	88.3%	86.9%	86.3%	86.2%	83.1%
	$U3_{A1,I}$	89.2%	89.2%	87.8%	87.1%	86.6%	86.5%
	$U3_{A1,A}$	89.0%	88.3%	87.2%	86.7%	85.5%	82.9%

NP: not performed

For previous considerations, the H_{SM} parameter is considered reliable for the evaluation of the calculation of the fragility curves and therefore the estimated average damage.

To try to be even more synthetic in the comparisons, the μ_d value is also converted into an equivalent damage level by conventionally referring to the binominal distribution, assuming the upper bounds of each membership corresponding to a probability of 0.5 in the corresponding cumulative distribution function (see Lagomarsino and Giovinazzi (2006)). This assumption leads to the

following ranges: 0-0.7 for DL0; 0.7-1.6 for DL1; 1.6-2.5 for DL2; 2.5-3.4 for DL3; 3.4-4.3 for DL4; 4.3-5 for DL5.

Figures 4,5 and 6 show the comparison between the μd estimated with the H_{SM} parameter with the fixed base model on the three analysed subsoils (on the abscissas axis) and that of the complaint base model (on the ordinates axis). In particular, Figure 4 shows the comparison of the two-storeys buildings, Figure 5 of the three-storeys ones and finally Figure 6 of the four-storeys buildings. It can be observed that also for this parameter the FB C model overestimates the damage, by a maximum of two DLs. The difference of DLs between the two models are expressed with squares elements in light grey if the same DL is estimated by both models, and progressively darker when the estimation differs of one, two or three damage levels. In some cases, totally comparable damage trends are obtained between the two models (for example in Figure 4 the building $U1_{A2,A}$ on soil S1 or in Figure 6 the building $U3_{A1,I}$ on soil S1 and S3). Very different behaviors are not observed varying the stratigraphy and fixing the building case. For some soil profile the difference between the two models increases (fixed base and base complaint), however there is no soil that is more (or less) punitive, this depends on the more amplified periods of the various events and the damage they cause.

The colors in the three figures indicate the correlation between the damage estimated from the fragility curves of each building with the H_{SM} parameter and those proposed by Mori et al. (2020). In fact, Mori et al. (2020) divided the building in five classes (see Table 3) in accordance with the vulnerability proposed by Lagomarsino and Giovinazzi (2006). In particular Mori et al. (2020) associates to each typological class of vulnerability an estimated damage as a function of the amplitude of the value of the H_{SM} parameter, four hazard classes (Low, Moderate, High and Very high). Table 2 and Table 3 shows on right side the estimated damage classes (indicated with letter D) for the range of periods under examination (T_1 = 0.1-0.5 s) for the vulnerability Class of building.

Table 3: Definition of building typology and H_{SM}–Damage grades associated with a 10% probability in 50 years hazard for the range of period T1.

Vulnerability Class	Building type	H_{SM}[g] Hazard Class			
		Low ≤0.21	Moderate 0.22-0.54	High 0.55-0.85	Very high ≥0.86
A	Adobe Rubble stone	D0-1	D1-D3	D3-D4	D4-D5
B	URM old bricks Simple stone	D0-D1	D1-D2	D2-D3	D3-D4
C	RC frame without ERD Massive stone URM with RC floors Shear walls without ERD	D0	D0-D1	D1-D2	D2-D4
D	RC frame moderate ERD Confined Masonry Shear walls moderate ERD	D0	D0-D1	D1	D1-D3
E	RC frame high ERD Shear walls high ERD	D0	D0	D0-D1	D1-D2

The school and $U1_{A2,I}$ and $U1_{A2,A}$ are considered into class C (since they are URM building with RC floors and RC slabs), while all the other buildings in class B. The green scale of the Figures 4,5 and 6 indicates the damage of the four Hazard Classes (from light green for the Low to darker for Very high Hazard Class).

The damage estimated from the fragility curves and that obtained with the Hazard classes of Mori et al. (2020) are well correlated especially in the first two Hazard classes. In the next two classes the correlation remains good, even if for some buildings both the High and Very high classes also bring less important damage level than those estimated by Mori et al. (2020), especially in the case of the complaint model (CB C). In the first case, see for example the buildings $U4_{A2,I}$, $U4_{A2,A}$ or $U2_{A1,A}$ in case of Soil S1, for the Very high class see the buildings $U3_{A1,A}$ for all soil profiles.

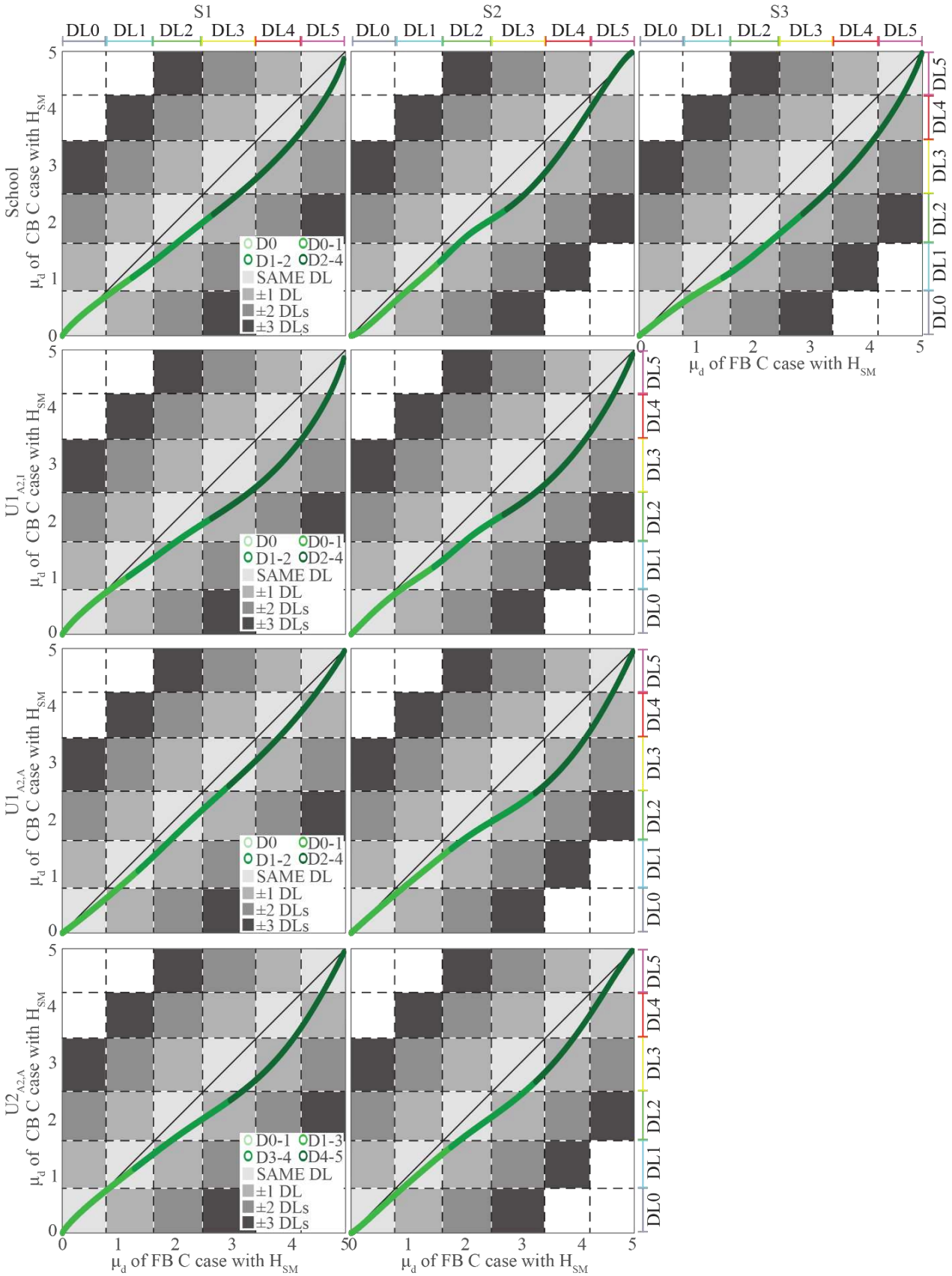

Figure 4. Comparison among the μ_d resulting for the different analyzed cases from the curves expresses as a function H_{SM} for FB C model and for CB C model for the building of two storeys.

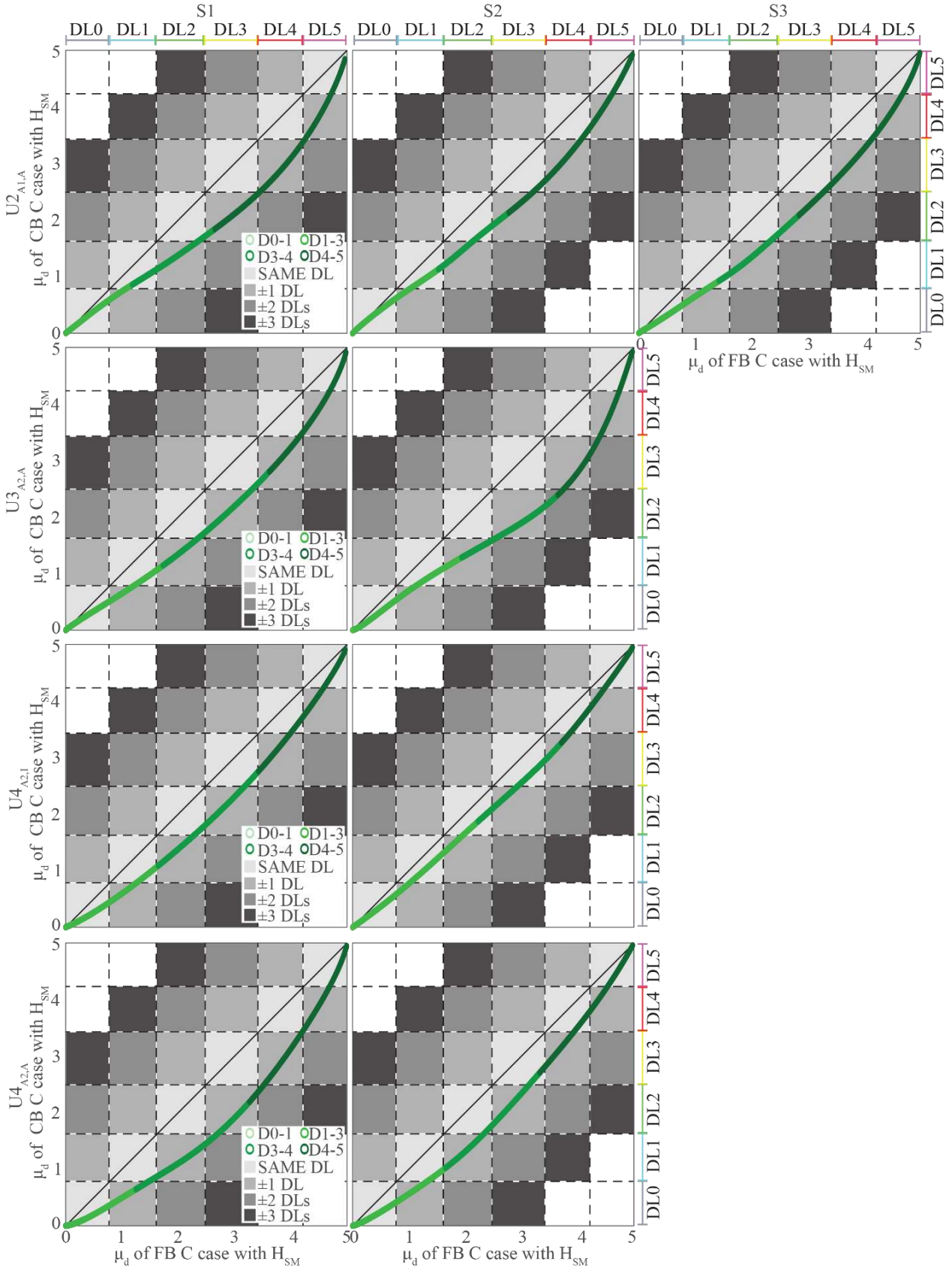

Figure 5. Comparison among the μ_d resulting for the different analyzed cases from the curves expresses as a function H_{SM} for FB C model and for CB C model for the building of three storeys.

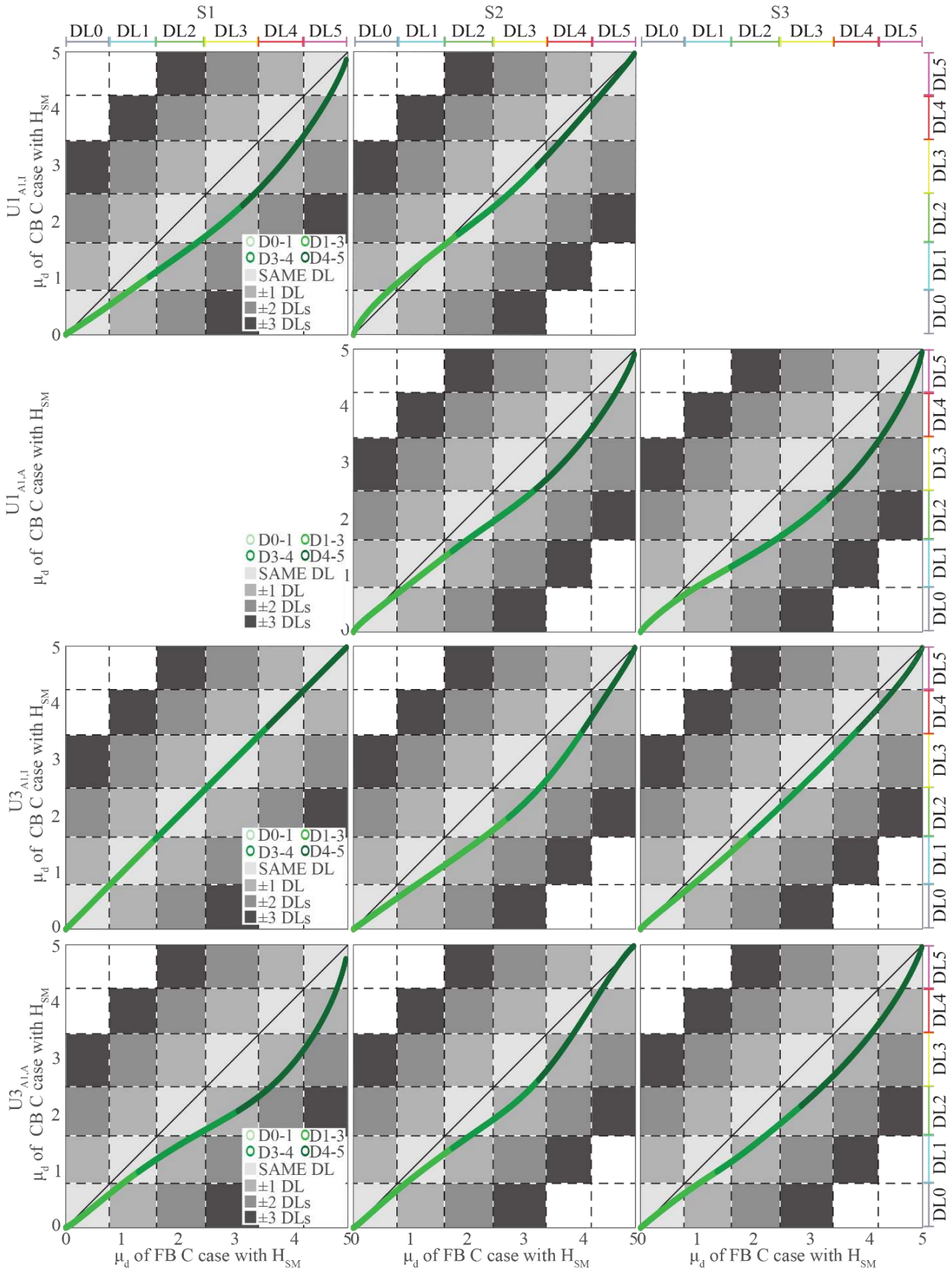

Figure 6. Comparison among the μ_d resulting for the different analyzed cases from the curves expresses as a function H_{SM} for FB C model and for CB C model for the building of four storeys.

The H_{SM} parameter is therefore a good alternative to the typical Intensity Measures. Also the comparison with the PGA in Figure3 and Table 3 shows how in some cases there is a different expected damage considering this new parameter. The current limit is, as already said, the not easy use of this parameter since there is no punctual mapping of the H_{SM} unlike the PGA or the amplification factors (AF) to quickly perform the calculation with the equation 1. To overcome these limits, Mori et al. (2020) proposes correlations between the PGA and the H_{SM} parameter, other studies instead propose the maps in H_{SM} (see Falcone et al. (2021)).

2 A/V PARAMETER: DEFINITION AND RESULTS

In this research the seismic events selected from the SIMBAD database (Smerzini and Paoluci (2013); Iervolino et al. (2014)) were obtained through many of their characteristics: peak ground acceleration (PGA), the spectral acceleration ($Sa(T_1)$), the cumulative absolute velocity (CAV), the Housner P-Velocity Spectrum Intensity computed in the range of periods from 0.1 to 0.5 s, the amplification factor (AF), H_{SM} parameter, etc. This made it possible to observe the effects that the site amplification produced on the seismic events for each of the soil profiles considered.

A further fundamental parameter that characterizes the ground motion is the frequency content as it influences the response of the long-period structures and inelastic structures. To consider this contribution is used the A/V parameter introduced by Newmark (1973) to indicate the dynamic characteristics of seismic ground motions on the basis of recorded earthquake accelerograms. This parameter is the ratio between the peak ground acceleration (PGA) and the peak ground velocity (PGV) as the equation 6 shows:

$$A/V = \frac{PGA}{PGV} \tag{6}$$

Newmark (1973) indicated the ratio for the rock site and the alluvium site. Seed et al. (1976) investigated the value of this ratio for more different type of soil (as rock, stiff soil, deep cohesionless soil, etc). More recently, Sawada et al. (1992) correlated this parameter with various representative of earthquakes such as the peak frequency, the average frequency, the magnitude, the epicentral distance and the significant duration of the event calculated according to the formulation of Trifunac and Brandy (1975). In particular, Sawada et al. (1992) shows an increasing linear regression for both the mean and peak frequency, while the A/V ratio has the negative interaction to magnitude and distance which means that the A/V ratio is lower as magnitude and distance are larger. Tso et al. (1992) reports three different ranges of A/V ratio:

$$A/V = \begin{cases} < 0.8\ g/m/s \quad low\ A/V\ range \\ 0.8 \div 1.2\ g/m/s \quad intermediate\ A/V\ range \\ > 1.2\ g/m/s \quad high\ A/V\ range \end{cases}$$

As already explained in Chapters §3 and 4.1, 49 real events recorded from stations on soil A were selected and then their direction reversal was first considered, bringing to 98 total real events and then scaled with small corrective coefficients to have a greater amplitude of seismic hazard. In Chapter §4.1 are reported the applied scale values for each real event. This signal modification was made only in amplitude and not in frequency. This choice is consistent with the small-scale values adopted, but makes the value of the A/V ratio constant between the real events and all those obtained by having scaled the real starting one. For this reason, only the selected real events are shown in Figure 7. Each black marker is associated with the bedrock event (and are therefore the same for the four soil profiles) while the red ones are associated with the freefield signals obtained from the local seismic response performed with the STRATA software. The red markers are obviously different for each soil profiles. The figure also shows the A/V ranges identified in the previous papers cited. It can be observed that the selected events are for the most part falling in the high frequency region (57

events), while 32 are in the intermediate region and only 9 in the low frequency region. Considering now the site effect, it can be observed that the S1 and S2 profile bring to a greater number of events falling back to high frequencies, while S3 and S4 lead to a greater number of events leading to lower frequencies.

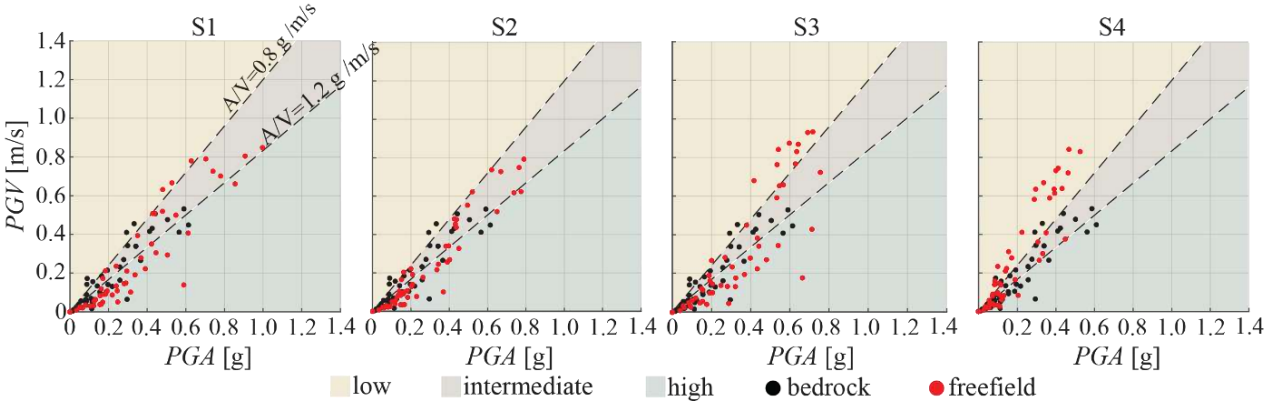

Figure 7. Peak acceleration versus peak velocity for the four soil profiles having low, intermediate, and high A/V ratios

Figure 8 reports the amplification factors of the A/V ratio ($AF_{A/V}$) expressed as the ratio between the value in freefield and that at bedrock. S1 and S2 soil profiles lead to an amplification of this ratio (values practically always greater than 1 with maximum values of 2 and 1.75 respectively), while S4 almost totally de-amplifies the A/V value (with values always less than 1, except in three cases, with minimum values reaching 0.4).

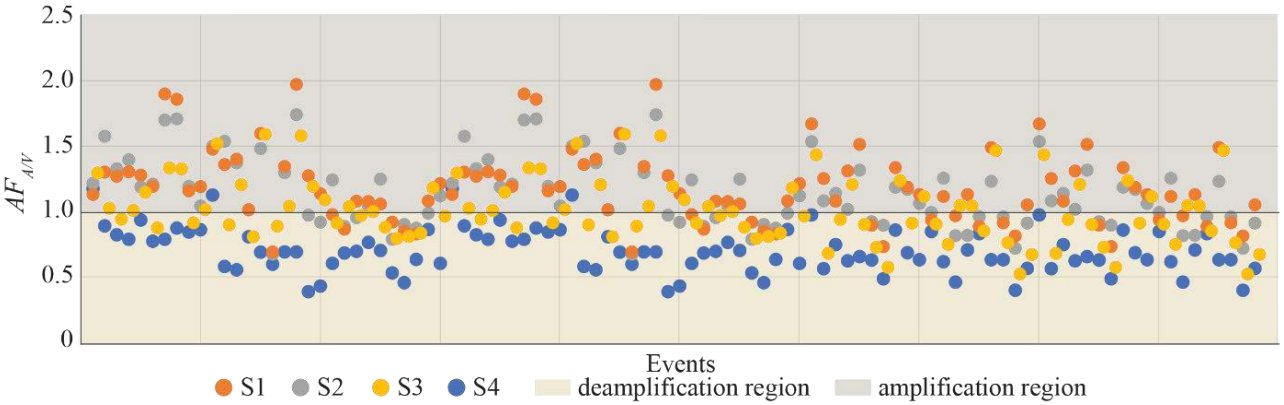

Figure 8. Amplification Factor of A/V ratio ($AF_{A/V}$) for the four soil profiles and for each events.

With this parameter it was not possible to calculate the fragility curves as considering only the real unscaled starting events did not allow to obtain a sufficiently large number of analyzes in each group of DLs, while considering all the signals (even the scaled ones) we had the same value of IM in A/V which led to different damage values as a function of the seismic amplitude of the signal. Therefore the same A/V ratio led to different damage values by staggering the calculation of the intensity curve.

However, two aspects are underlined. For low values of A/V it is highlighted how the ratio of the spectral accelerations calculated on the first elastic period ($Sa(T_1)$) of the base complaint structure compared to the fixed base one is greater and tends to decrease with increasing A/V until it is de-amplified. Figure 9a shows the trend of this ratio of spectral accelerations for the Visso school on S1 soil profile, but the same behavior with very similar trends results for the other structures and for the other soil profiles. This trend can be found both with the bedrock signals (black markers) and in the case of those propagated in freefield (in red). Figure 9b instead shows how for low input A/V values (on the abscissas there is the A/V value of the freefield signal used as input for non-linear dynamic analysis) the expected damage is greater and decreases as the value decreases. of the A/V ratio.

Therefore the damage appears to have an opposite trend with respect to the increase of the A/V parameter. The reported damage level (DLi) is that obtained from each dynamic analysis performed. Also in this case the figure refers to the school of Visso on S1 soil, but the same behavior can be found for the other buildings and soil profiles.

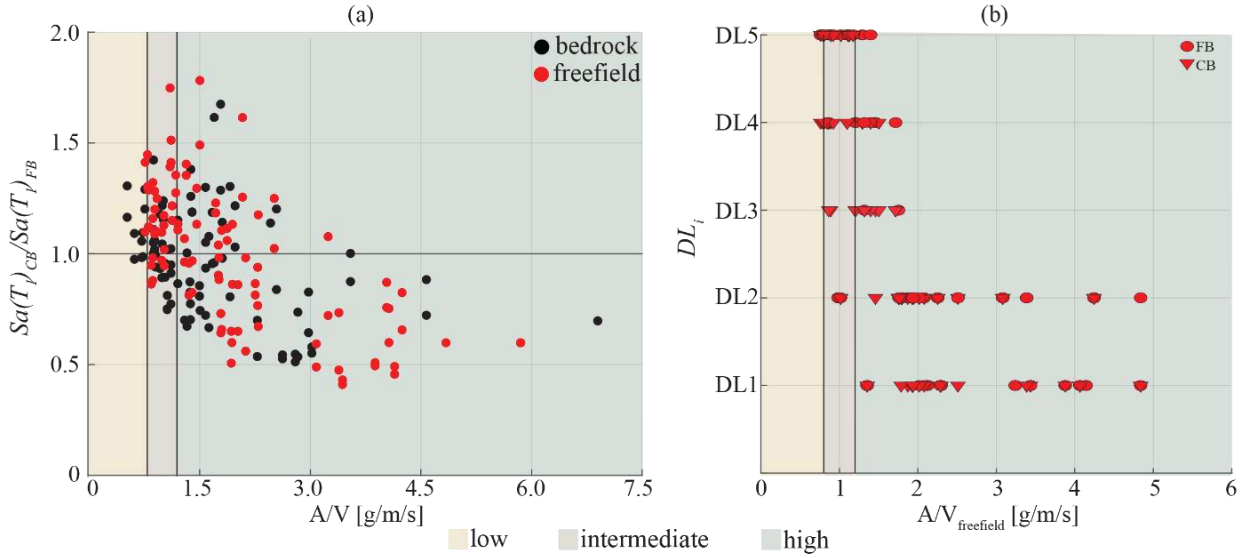

Figure 9. (a) spectral acceleration ratio as the A/V ratio varies for the bedrock (black) and freefield (red) signal; (b) variation of the expected damage as the A/V ratio increases.

Newmark (1973) proposed a further parameter (also used by Sawada et al. (1992)) as evolution of the A/V ratio: the parameter AD/V^2 (see the equation 7):

$$AD/V^2 = \frac{PGA\ PGD}{PGV^2} \qquad (7)$$

This parameter is not taken up by this research as it does not exceed the limits of the A/V ratio and is worse correlated to the other quantities analyzed by Newmark (1973) and Sawada et al. (1992) such as magnitude, frequency and duration.

ACKNOWLEDGEMENTS

The first due, but also heartfelt, thanks are for my supervisors who have followed me throughout these years: Serena Cattari and Filomena de Silva, then to the thesis reviewers, who made possible to bring improvements and additions with their valuable contributions.

Last, I left thanks for those who accompanied me during these years within the walls of DICCA, sharing moments of breaks and relax or hectic activity to friends, to my family and to Serena who put up with me even when I was stressed.

REFERENCES

Abate G, Bramante S, Massimino MR (2020) Innovative Seismic Microzonation Maps of Urban Areas for the Management of Building Heritage: A Catania Case Study. Geosciences 10(12), 480.

Ademovic N, Hadzima-Nyarko M, Zagora N (2022) Influence of site effects on the seismic vulnerability of masonry and reinforced concrete buildings in Tuzla (Bosnia and Herzegovina), Bull. Earthq. Eng., 20, 2643-2681.

Akin MK, Kramer SL, Topal T (2011) Empirical correlations of shear wave velocity (Vs) and penetration resistance (SPT-N) for different soils in an earthquake-prone area (Erbaa-Turkey). Engineering Geology, 119, 1-17.

Alleanza GA, Chiaradonna A, d'Onofrio A, Silvestri F (2019) Parametric study on 2D effect on the seismic response of alluvial valleys. Proc. of the 7th ICEGE, 17-20 June 2019. Rome, Italy.

Alleanza GA (2022) Two-Dimensional Amplification of Seismic Motion in Alluvial Valleys. Ph.D. dissertation. University of Napoli "Federico II", Napoli, Italy.

Anagnostopoulos SA (1988) Pounding of buildings in series during earthquakes. Earthq. Eng. Struct. Dyn., 16(3), 443-456.

Angiolilli M, Lagomarsino S, Cattari S, Degli Abbati S (2021) Seismic fragility assessment of existing masonry buildings in aggregate, Engineering Structures, 247, 113218.

Angiolilli M, Brunelli A, Cattari S (2022a) Fragility curves of masonry buildings in aggregate accounting for local mechanisms and site effects, Bulletin earthquake engineering, submitted.

Angiolilli M, Minkada ME, Di Domenico D, Cattari S, Belleri A, Verderame GM (2022b) Comparing the observed and numerically simulated seismic damage: a unified procedure for unreinforced masonry and reinforced concrete buildings. J. Earthq. Eng., under review.

ASCE7 (2016) American Society of Civil Engineers Minimum design loads and associated criteria for buildings and other structures. ASCE/SEI 7, 2016, Reston, VA.

Athanasopoulos GA (1995) Empirical correlations Vs-NSPT for soils of Greece: a comparative study of reliability. Proc. 7th Int. Conf. on Soil Dyn. Earthq. Eng., May, 1995, Chania, Crete, Greece.

Augenti N, Parisi F (2010) Learning from Construction Failures due to the 2009 L'Aquila, Italy, Earthquake. J Perform Constr Facil, 24(6), 536-555.

Avilés J, Pérez-Rocha LE (1996) Evaluation of interaction effects on the system period and the system damping due to foundation embedment and layer depth. Soil Dyn Earthq Eng.15, 11-27.

Baggio C, Bernardini A, Colozza R, Corazza L, Della Bella M, Di Pasquale G, Goretti A, Martinelli A, Orsini G, Papa F, Zuccaro G (2007) Field manual for post-earthquake damage and safety assessment and short term countermeasures (AeDES). European Commission-Joint Research Centre-Institute for the Protection and Security of the Citizen, EUR, 22868.

Baraschino R, Baltzopoulos G, Iervolino I (2019) R2R-EU: Software for fragility fitting and evaluation of estimation uncertainty in seismic risk analysis. Soil Dyn Earthq Eng. 132, 106093.

Bardet JP, Ichii K, Lin CH (2000) EERA: A computer program for Equivalent-linear Earthquake site Response Analysis of layered soil deposits, University of Southern California, Los Angeles, CA.

Battaglia L, Ferreira TM, Lourenço PB (2021) Seismic fragility assessment of masonry building aggregates: A case study in the old city Centre of Seixal, Portugal. Earthquake Engineering & Structural Dynamics, 50(5), 1358-1377.

Bayraktar A, Hökelekli E (2020) Influences of earthquake input models on nonlinear seismic performances of minaret-foundation-soil interaction systems. Soil Dyn Earthq Eng. 139, 106368.

Bernardini C, Maio R, Boschi S, Ferreira TM, Vicente R, Vignoli A (2019) The seismic performance-based assessment of a masonry building enclosed in aggregate in Faro (Portugal) by means of a new target structural unit approach. Engineering Structures, 191, 386-400.

Bernardo VMS, Campos Costa APDN, Candeias PJDOX, da Costa AG, Marques AIM, Carvalho AR (2022) Ambient vibration testing and seismic fragility analysis of masonry building aggregates. Bulletin of Earthquake Engineering, 1-25.

Bertocci S, Bigongiari M (2019) Digital survey for the analysis of the seismic vulnerability in Mexico City. In 14th Congress on graphic expression applied to building, 21-23 february 2019, Siviglia, Spain.

Beyer K, Dazio A (2012) Quasi-static cyclic tests on masonry spandrels. Earthq Spectra, 28(3), 907-929.

Beyer K, Mangalathu S (2014) Numerical study on the peak strength of masonry spandrels with arches. J Earthq Eng, 18(2), 169-186.

Bielak J (1971) Earthquake Response of Building-Foundation Systems, Ph.D. Thesis, California Institute of Technology, Pasadena, CA.

Bommer JJ, Magenes G, Hancock J, Penazzo P (2004) The Influence of Strong-Motion Duration on the Seismic Response of Masonry Structures. Bull. Earthq. Eng. 2, 1-26.

Borri A, Corradi M, Castori G, De Maria A (2015) A method for the analysis and classification of historic masonry. Bulletin of Earthquake Engineering, 13(9), 2647-2665.

Boschi S, Bernardini C, Vignoli A (2021) The tuscany masonry databasewebsite. Heritage, 4(1), 230-248.

Bournas DA, Negro P, Taucer FF (2014) Performance of industrial buildings during the Emilia Earthqyuake in Northen Italy and recommendation for their strengthening. Bull Earthq Eng, 12(5), 2383-2404.

Bramerini F, Di Pasquale G (2008) Updated seismic risk maps for Italy. Ing Sismica XXV, (2), 5-23 (in Italian).

Brando G, De Matteis G, Spacone E (2017) Predictive model for the seismic vulnerability assessment of small historic centres: application to the inner Abruzzi Region in Italy. Engineering Structures, 153, 81-96.

Brando G, Pagliaroli A, Cocco G, Di Buccio F (2020) Site effects and damage scenarios: The case study of two historic centers following the 2016 Central Italy earthquake. Engineering Geology 272, 105674.

Brando G, Cianchino G, Rapone D, Spacone E, Biondi S (2021) A CARTIS-based method for the rapid seismic vulnerability assessment of minor italian historical centres. International Journal of Disaster Risk Reduction, 63.

Brunelli A, de Silva F, Piro A, Parisi F, Sica S, Silvestri F, Cattari S (2021a) Numerical simulation of the seismic response and soil-structure interaction for a monitored masonry school building damaged by the 2016 central Italy earthquake, Bull. Earthq. Eng. 19, 1181-1211.

Brunelli A, de Silva F, Cattari S (2021b) On the Site-amplification and Soil-structure interaction in URM structures: use of fragility curves to assess the simplified code-approach. 8th COMPDYN, 27-30 June 2021, Athens, Greece.

Brunelli A, de Silva F, Cattari S (2022a) Site effects and soil-foundation-structure interaction: derivation of fragility curves and comparison with Codes-conforming approaches for a masonry school. Soil Dynamics and Earthquake Engineering 154(4), 107125.

Brunelli A, de Silva F, Cattari S (2022b) Urban-scale seismic damage scenario of URM buildings in aggregate settled on soft soil. Bulletin of Earthquake Engineering, in preparation.

Brunelli A, Alleanza G A, Cattari S, De Silva F, d'Onofrio A (2022c) Simulation of damage observed on buildings in aggregate after the 2016-2017 Central Italy earthquake accounting for site effects and soil-structure interaction. TC 301 Geotechnical engineering for the preservation of monuments and historic sites, 22-24 June 2022, Naple, Italy.

Calderini C, Cattari S, Lagomarsino S (2009) In-plane strength of unreinforced masonry piers, Earthquake Eng Struct Dyn, 38(2), 243-67.

Caprili S, Mangini F, Salvatore W, Scarpelli G, Squeglia N (2015) The influence of soil–foundation–structure interaction on the overall behaviour and diseases of a medieval building in Pisa. STREMAH 2015, 14th STREMAH, July 13-15 2015, La Coruna, Spain.

Cardinali V, Cristofaro MT, Ferrini M, Nudo R, Paoletti B, Tanganelli M (2021) A Multiscale Approach for the Seismic Vulnerability Assessment of Historical Centres in Masonry Building Aggregates: Cognitive Approach and Interdisciplinary Perspectives. International Journal of Architectural Heritage, 1-26.

Carocci CF (2012) Small centres damaged by 2009 L'Aquila earthquake: on site analyses of historical masonry aggregates Bull Earthquake Eng, 10, 45–71.

Casolo S, Diana V, Uva G (2017) Influence of soil deformability on the seismic response of a masonry tower. Bull. Earthq. Eng. 15, 1991-2014.

Cattari S, Degli Abbati S, Ferretti D, Lagomarsino S, Ottonelli D, Tralli AM (2012) The seismic behaviour of ancient masonry buildings after the earthquake in Emilia (Italy) on May 20th and 29th, 2012. Ingegneria Sismica, 29 (2-3), 87-119.

Cattari S, Lagomarsino S (2013) "Masonry Structures" in Developments in the field of displacement based seismic assessment. Edited by Sullivan TJ, Calvi GM, IUSS Press, Pavia, Italy, pp.151-200 and EUCENTRE, pp. 524, ISBN; 978-88-6198-090-7.

Cattari S, Degli Abbati S, Ferretti D, Lagomarsino S, Ottonelli D, Tralli A (2014) Damage assessment of fortresses after the 2012 Emilia earthquake (Italy). Bull Earthq Eng, 12(5), 2333-65.

Cattari S, Camilletti D, Lagomarsino S, Bracchi S, Rota M, Penna A (2018) Masonry Italian Code-Conforming Buildings. Part 2: Nonlinear Modelling and Time-History Analysis. J. Earthq. Eng. 22(2), 2010-2040.

Cattari S, Degli Abbati S, Ottonelli D, Marano C, Camata G et al. (2019a) Discussion on data recorded by the Italian structural seismic monitoring network on three masonry structures hit by the 2016-2017 Central Italy earthquake. COMPDYN, 24-26 June 2019, Crete, Greece.

Cattari S, Sivori D, Brunelli A, Sica S, Piro A, de Silva F, Parisi F, Silvestri F (2019b) Soil-structure interaction effects on the dynamic behaviour of a masonry school damaged by the 2016–2017 Central Italy earthquake sequence. 7th ICEGE conference, 17-20 June 2019, Rome, Italy, pp. 1655-1663.

Cattari S, Calderoni B, Caliò I, Camata G, de Miranda S, Magenes G, Saetta A (2021) Nonlinear modeling of the seismic response of masonry structures: critical review and open issues towards engineering practice. Bulletin of Earthquake Engineering, 1-59.

Cattari S, Angiolilli M, Alfano S, Brunelli B, De Silva F (2022a) Investigating the combined role of the structural vulnerability and site effects on the seismic response of a URM school hit by the Central Italy 2016 earthquake. Structures, 40, 386-402.

Cattari S, Calderoni B, Caliò I, Camata G, de Miranda S, Magenes G et al. (2022b). Nonlinear modeling of the seismic response of masonry structures: critical review and open issues towards engineering practice. Bulletin of Earthquake Engineering, 20,1939-1997.

Cattari S, Magenes G (2022) Benchmarking the software packages to model and assess the seismic response of URM existing buildings through nonlinear static analyses. Bull Earthq. Eng 20, 1901-1936.

Cattari S, Angiolilli M (2022). Multiscale procedure for the attribution of seismic damage levels in masonry buildings univocally applicable to real or numerical cases. Bulletin of Earthquake Engineering (under review).

Cavalieri F, Correia AA, Crowley H, Pinho R (2020) Seismic fragility analysis of URM buildings founded on piles: influence of dynamic soil–structure interaction models. Bull. Earthq. Eng. 18, 4127-56.

CEN (2004) EN 1998-1, Eurocode 8: Design of structures for earthquake resistance - Part 1: General rules, seismic actions and rules for buildings.

Chang S, Pasion C, Tatebe K, Ahmad R (2008) Linking lifeline infrastructure performance and community disaster resilience: models and multi-stakeholder processes. Technical Report MCEER-08-0004

Chieffo N, Formisano A (2019) Comparative seismic assessment methods for masonry building aggregates: a case study. Frontiers in Built Environment, 5, 123.

Chieffo N, Formisano A (2020) Induced seismic-site effects on the vulnerability assessment of a historical centre in the molise Region of Italy: Analysis method and real behaviour calibration based on 2002 earthquake. Geosciences, 10(1), 21.

Chiumiento G, Formisano A (2019) Simplified and refined analyses for seismic investigation of historical masonry clusters: Comparison of results and influence of the structural units position. Frontiers in Built Environment, 5, 84.

Ciancimino A, Lanzo G, Alleanza GA, et al (2019) Dynamic characterization of fine-grained soils in central Italy by laboratory testing. Bull Earthq Eng, 18, 5503–5531.

Ciancimino A, Lanzo G, Alleanza GA, Amoroso S, Bardotti R et al. (2020) Dynamic characterization of fine-grained soils in Central Italy by laboratory testing. Bull. of Earthq. Eng. 18, 5503–5531.

Cima V, Tomei V, Grande E, Imbimbo M (2021) Fragility curves at regional basis for unreinforced masonry buildings prone to out-of-plane mechanisms: the case of Central Italy. Structures, 34, 4774-4787.

Cocco G, D'Aloisio A., Spacone E, Brando G (2019) Seismic Vulnerability of Buildings in Historic Centers: From the "Urban" to the "Aggregate" Scale. Frontiers in Built Environment, 5, 78.

Cole GL, Dhakal RP, Turner FM (2012) Building pounding damage observed in the 2011 Christchurch earthquake. Earthquake Engineering & Structural Dynamics, 41(5), 893-913.

Conti R, Morigi M, Viggiani GMB (2017) Filtering effect induced by rigid massless embedded foundations. Bull Earthq Eng, 15, 1019-1035.

Cornell CA, Krawinkler H (2000) Progress and challenges in seismic performance assessment. PEER Center News, 3(2), 1-2.

Crowley H, Despotaki V, Rodrigues D, et al. (2020) Exposure model for European seismic risk assessment. Earthquake Spectra. 36(1), 252-273.

D'Altri AM, Sarhosis V, Milani G, Rots J, Cattari S, Lagomarsino S, Sacco E, Tralli A, Castellazzi G, de Miranda S (2020) Modeling strategies for the computational analysis of unreinforced masonry structures: review and classification. Arch. Comput. Methods Eng. 27, 1153-1185.

D'Ayala DF, Paganoni S (2011) Assessment and analysis of damage in L'Aquila historic city centre after 6th April 2009. Bulletin of Earthquake Engineering, 9(1), 81-104.

d'Onofrio A, Silvestri F (2001) Influence of Micro-Structure on Small-Strain Stiffness and Damping of Fine Grained Soil and Effects on Local Site Response. International Conferences on Recent Advances in Geotechnical Earthquake Engineering and Soil Dynamics, 2001.

da Porto F, Donà M, Rosti A, Rota M, Lagomarsino S, Cattari S, Borzi B, Onida M, De Gregorio D, Perelli FL, Del Gaudio C, Ricci P, Speranza E (2021) Comparative analysis of the fragility curves for Italian residential masonry and RC buildings. Bulletin of Earthquake Engineering 19, 3209-3252.

De Felice G (2011) Out-of-plane seismic capacity of masonry depending on wall section morphology. International Journal of Architectural Heritage, 5(4-5), 466-482.

De Risi R, Penna A, Simonelli AL (2019) Seismic risk at urban scale: the role of site response analysis. Soil Dyn. Earthq. Eng., 123, 320-336.

de Silva F, Pitilakis D, Ceroni F, Sica S, Silvestri F (2018) Experimental and numerical dynamic identification of a historic masonry bell tower accounting for different types of interaction. Soil Dyn Earthq Eng, 109, 235-250.

de Silva F, Piro A, Brunelli A, Cattari S, Parisi F, Sica S, Silvestri F (2019) On the soil-structure interaction in the seismic response of a monitored masonry school building struck by the 2016-2017 Central Italy earthquake. 7th ECCOMAS Thematic Conference on Computational Methods in Structural Dynamics and Earthquake Engineering, 24-26 June 2019, Crete, Greece.

de Silva F (2020) Influence of soil-structure interaction on the site-specific seismic demand of masonry towers. Soil Dyn Earthq Eng, 131, 106023.

Decanini L, De Sortis A, Goretti A et al. (2004) Performance of masonry buildings during the 2002 Molise, Italy, earthquake. Earthq Spectra 20, 191-220.

Degli Abbati S, Cattari S, Lagomarsino S (2018) Theoretically-based and practice-oriented formulations for the floor spectra evaluation. Earthquakes and Structures, 15(5), 565-581.

Degli Abbati S, D'Altri AM, Ottonelli D, Castellazzi G, Cattari S, de Miranda S, Lagomarsino S (2019) Seismic assessment of interacting structural units in complex historic masonry constructions by nonlinear static analyses. Computers & Structures, 213, 51-71.

Del Gaudio C, De Martino G, Di Ludovico M, Manfredi G, Prota A, Ricci P, Verderame GM (2019) Empirical fragility curves for masonry buildings after the 2009 L'Aquila, Italy, earthquake. Bulletin of earthquake engineering, 17(11), 6301-6330.

DesRoches R, Muthukumar S (2002) Effect of pounding and restrainers on seismic response of multiple-frame bridges. Journal of Structural Engineering, 128(7), 860-869.

Di Laora R, Rovithis E (2015) Kinematic Bending of Fixed-Head Piles in Nonhomogeneous Soil. J. Geotech. Geoenviron. Eng., 141(4).

Di Ludovico M, Prota A, Moroni C, Manfredi G, Dolce M (2017a) Reconstruction process of damaged residential buildings outside historical centres after the L'Aquila earthquake: Part I – "light damage" reconstruction. Bull Earthq Eng, 15(2) 667-692.

Di Ludovico M, Prota A, Moroni C, Manfredi G, Dolce M (2017b) Reconstruction process of damaged residential buildings outside historical centres after the L'Aquila earthquake: Part II - "heavy damage" reconstruction. Bull Earthq Eng, 15(2), 693-729.

Di Ludovico M, Santoro A, De Martino G, Moroni C, Prota A, et al. (2019) Cumulative damage to school buildings following the 2016 central Italy earthquake sequence. Boll Geofis Teor Appl, 60(2), 165-182.

Dikmen U (2009) Statistical correlations of shear wave velocity and penetration resistance for soils. Journal of Geophysics and Engineering, 6, 61-72.

Dolce M, Di Bucci D (2017) Comparing recent Italian earthquakes, Bull Earthq Eng, 15(2), 497-533.

Dolce M, Nicoletti M, De Sortis A, Marchesini S, Spina D, Talanas F (2017) Osservatorio sismico delle strutture: the Italian structural seismic monitoring network. Bull Earthq Eng 15(2), 621-641.

Dolce M, Speranza E, Giordano F, Conte C, De Martino G (2019a) The implementation of Italian National Seismic Program: a focus on seismic upgrading of critical buildings, XVIII ANIDIS conference, 15-19 September 2019, Ascoli Piceno (Italy) In Italian.

Dolce M, Speranza E, Giordano F, Borzi B, Bocchi F, Conte C, Pascale V (2019b) Observed damage database of past Italian earthquakes: the Da. DO WebGIS. Bollettino di Geofisica Teorica ed Applicata, 60(2).

Dolce M, Prota, A, Borzi B, da Porto F, Lagomarsino S et al. (2021a) Seismic risk assessment of residential buildings in italy. Bulletin of Earthquake Engineering, 19(8), 2999-3032.

Dolce M, Prota A, Borzi B, Da Porto F, Lagomarsino S, et al. (2021b) Seismic risk assessment of residential buildings in Italy, Bull. Earthq Eng 19, 2999-3032.

Donà M, Carpanese P, Follador V, Sbrogiò L, da Porto F (2020) Mechanics-based fragility curves for Italian residential URM buildings. Bull. Earthq. Eng, 1-34.

Douglas J, Seyedi DM, Ulrich T, Modaressi H, Foerster E, Pitilakis K, Pitilakis D, Karatzetzou A, Gazetas G, Garini E, Loli M. (2015) Evaluation of seismic hazard for the assessment of historical elements at risk: description of input and selection of intensity measures. Bull. Earthq. Eng. 13, 49-65.

Elsabee F, Morray JP (1977) Dynamic behavior of embedded foundations. Research Report R77-33, MIT, Cambridge, Massachusetts.

Fabbrocino S. Lanzano G, Forte G, Santucci de Magistris F, Fabbrocino G (2015) SPT blow count vs. shear wave velocity relationship in the structurally complex formations of the Molise Region (Italy). Engineering Geology 187, 84-97.

Fagundes C, Bento R, Cattari S (2017) On the seismic response of buildings in aggregate: Analysis of a typical masonry building from Azores. Structures, 10, 184-196.

Falcone G, Acunzo G, Mendicelli A, Mori F, Naso G, Peronace E, Porchia A, Romagnoli G, Tarquini E, Moscatelli M (2021) Seismic amplification maps of Italy based on site-specific microzonation dataset and one-dimensional numerical approach. Engineering Geology 289, 106170.

Fatehnia M, Hayden M, Landschoot M (2015) Correlation between Shear Wave Velocity and SPT-N Values for North Florida Soils. Electron. J. Geotech. Eng, 20(22).

Fathi A, Sadeghi A, Emami Azadi MR, Hoveidae N (2020) Assessing the soil-structure interaction effects by direct method on the out-of-plane behavior of masonry structures (case study: Arge-Tabriz). Bull. Earthq. Eng. 18, 6429-6443.

Fauzi A, Irsyam M, Fauji UJ (2014) Empirical correlation of shear wave velocity and N-SPT value for Jakarta. Int J GEOMATE. 7, 980-984.

Federal Emergency Management Agency (FEMA) (2003) Multi-hazard loss estimation methodology earthquake model, HAZUS-MH MR3 Technical Manual.

Ferrero C, Lourenco PB, Calderini C (2020) Nonlinear modeling of unreinforced masonry structures under seismic actions: validation using a building hit by the 2016 Central Italy earthquake. Frattura ed Integrità Strutturale, 14(51), 92-114.

Formisano A, Florio G, Landolfo R, Mazzolani FM (2015) Numerical calibration of an easy method for seismic behaviour assessment on large scale of masonry building aggregates, Advances in Engineering Software 80, 116-138.

Formisano A (2017) Theoretical and Numerical Seismic Analysis of Masonry Building Aggregates: Case Studies in San Pio Delle Camere (L'Aquila, Italy), Journal of Earthquake Engineering, 21(2), 227-245.

Formisano A, Massimilla A (2018) A novel procedure for simplified nonlinear numerical modeling of structural units in masonry aggregates. International Journal of Architectural Heritage, 12(7-8), 1162-1170.

Formisano A, Massimilla A (2019) Seismic numerical investigation on historical centres compounds: a new modelling technique of structural units. Journal of Building Pathology and Rehabilitation, 4(1), 1-14.

Formisano A, Chieffo N, Clementi F, Mosoarca M (2021) Influence of Local Site Effects on the Typological Fragility Curves for Class-Oriented Masonry Buildings in Aggregate Condition, Open J. Civ. Eng, 15, 149-164.

Fujiwara T (1972) Estimation of ground movements in actual destructive earthquakes. Proc. 4th European Symposium of Earthquake Engineering, 5-7 September 1972, London, England, pp. 125-132.

Gajan S, Kutter BL (2008) Capacity, settlement, and energy dissipation of shallow footing subjected to rocking. J Geotech Geoenviron, 134(8), 1129-1141.

Gaudiosi I, Vignaroli G, Sirianni P, Giallini S, Mori F, et al. (2016) Local seismic response studies in the north-western portion of the august 24th, 2016 Mw 6.0 earthquake affected area. The case of Visso village (central Apennines). Ann Geophys, 59(5).

Gautam D (2017) Empirical correlation between uncorrected standard penetration resistance (N) and shear wave velocity (VS) for Kathmandu Valley, Nepal. Geomat. Nat. Hazards Risk. 8(2), 496-508.

Gazetas G (1983) Analysis of machine foundation vibrations: state of the art. Soil Dyn Earthq Eng. 2, 1-41.

Gazetas G (1991) Formulas and charts for impedances of surface and embedded foundations. J Geotech Eng, 117(9), 1363-1381.

Gazetas G (2015) 4th Ishihara lecture: Soil-foundation-structure systems beyond conventional seismic failure thresholds. Soil Dyn Earthq Eng. 68, 23-39.

GEER (2016) Engineering reconnaissance of the 24 August 2016 Central Italy Earthquake: Ver 2, GEER Report 050, Geotechnical Extreme Events Reconnaissance Association, https://doi.org/10.18118/G61S3Z.

GEER (2017) Engineering Reconnaissance following the October 2016 Central Italy Earthquakes: Ver 2, GEER Report 050D, Geotechnical Extreme Events Reconnaissance Association Report, https://doi.org/10.18118/G6HS39.

Givens MJ, Mylonakis G, Stewart JP (2016) Modular Analytical Solutions for Foundation Damping in Soil-Structure Interaction Applications. Earthquake spectra, 32(3), 1749-68.

Graziotti F, Magenes G, Penna A (2012) Experimental cyclic behaviour of stone masonry spandrels. 15th World Conference on Earthquake Engineering, 24-28 September 2012, Lisbon, Portugal.

Graziotti F, Toninelli P, Solenghi M, Guerrini G, Penna A (2019) Numerical simulation of the earthquake response of a monitored URM school building. VII COMPDYN, 24–26 June 2019, Crete, Greece.

Greco A, Lombardo G, Pantò B, Famà A (2020) Seismic vulnerability of historical masonry aggregate buildings in oriental Sicily. International Journal of Architectural Heritage, 14(4), 517-540.

Grillanda N, Valente M, Milani G (2020) ANUB-Aggregates: a fully automatic NURBS-based software for advanced local failure analyses of historical masonry aggregates. Bulletin of Earthquake Engineering, 18(8), 3935-3961.

Grünthal G (1998) European macroseismic scale EMS-98. European Seismological Commission, Sub-commission on Engineering Seismology, Working Group Macroseismic Scales, Luxembourg, 1998.

Güllü H, Jaf HS (2016) Full 3D nonlinear time history analysis of dynamic soil–structure interaction for a historical masonry arch bridge. Environ Earth Sci. 75, 1421.

Hamidia M, Shokrollahi N, Nasrolahi M (2021) Soil-structure interaction effects on the seismic collapse capacity of steel moment-resisting frame buildings. Structures. 32, 1331-1345.

Hanumantharao C, Ramana GV (2008) Dynamic soil properties for microzonation of Delhi, India. J. Earth Syst. Sci. 117, S2, 719-730.

Hardin BO, Kalinski M (2005) Estimating the Shear Modulus of Gravelly Soils. J. Geotech. Geoenviron. Eng., 131(7).

Hasancebi N, Ulusay R (2007) Empirical correlations between shear wave velocity and penetration resistance for ground shaking assessments, Bull. Eng. Geol. Environ., 66, 203-213.

Homaei F (2021) Estimation of the ductility and hysteretic energy demands for soil–structure systems. Bull. Earthq. Eng. 19(3), 1365-1413.

Hudson M, Idriss IM, Beikae M (2003) QUAD4M: a computer program to evaluate the seismic response of soil structures using finie element procedures and incorporating a compliant base, rev. 2003. Center for Geotechnical Modelling Dept. of Civil and Environmental Engineering University of California, Devis.

Iervolino I, Galasso C, Paolucci R, Smerzini C (2014) Ground Motion Record Selection Based on Broadband Spectral Compatibility. Earthq. Spectra, 30(4), 1427-1448.

Iervolino I (2017) Assessing uncertainty in estimation of seismic response for PBEE. Earthquake Engineering & Structural Dynamics, 46(10), 1711-1723.

Iervolino I, Baltzopoulos G, Chioccarelli E, Suzuki A (2019) Seismic actions on structures in the near-source region of the 2016 central Italy sequence. Bull Earthq Eng, 17(10), 5429-5447.

Imai T, Yoshimura Y (1970) Elastic wave velocity and soil properties in soft soil. Tsuchito-Kiso 18 (1), 17-22 (in Japanese).

Imai T, Fumoto H, Yokota K (1975) The relation of mechanical properties of soil to Pand S-wave velocities in Japan. In: Proceedings of 4th Japan Earthquake Engineering Symposium. p. 89–96. (in Japanese).

Imai TP (1977) S-wave velocities of the ground in Japan. Proc. 9th Int. Conf. on Soil Mechanics and Foundation Engineering, 10-15 July, 1977, Tokyo, Japan, vol 2, 127-32.

Imai T, Tonouchi K (1982) Correlation of N-value with S-wave velocity and shear modulus. Proc. 2nd ESOPT, Amsterdam, Holland, 24-27 May, 1982, pp. 57-72.

Indirli MS, Kouris LA, Formisano A, Borg RP, Mazzolani FM (2013) Seismic damage assessment of unreinforced masonry structures after the Abruzzo 2009 earthquake: The case study of the historical centers of L'Aquila and Castelvecchio Subequo. International Journal of Architectural Heritage, 7(5), 536-578.

Iyisan R (1996) Correlations between shear wave velocity and in situ penetration test results (in Turkish), Chamber of Civil Engineers of Turkey, Teknik Dergi 7(2), 1187-1199.

Jabary RN, Madabhushi SPG (2017) Structure-soil-structure interaction effects on structures retrofitted with tuned mass dampers. Soil Dyn Earthq Eng, 100, 301-315.

Jafari MK, Asghari A, Rahmani I (1997) Empirical correlation between shear wave velocity (VS) and SPT Nvalue for south of Tehran soils, Proc. 4th Inter. Conf. on Civil Engineering, 1997, Tehran, Iran.

Jafari MK, Shafiee A, Ramzkhah A (2002) Dynamic properties of the fine grained soils in south of Tehran, J. Seismo. Earth. Eng., 4(1), 25-35.

Jalayer F, Ebrahimian H, Miano A, Manfredi G, Sezen H (2017) Analytical fragility assessment using unscaled ground motion records. Earthquake Engineering & Structural Dynamics, 46(15), 2639-2663.

Jankowski R (2005) Non-linear viscoelastic modelling of earthquake-induced structural pounding. Earthquake engineering & structural dynamics, 34(6), 595-611.

Jankowski R (2008) Earthquake-induced pounding between equal height buildings with substantially different dynamic properties. Engineering structures, 30(10), 2818-2829.

Jinan Z (1987) Correlation between seismic wave velocity and the number of blow of SPT and depth. Selected Papers from the Chinese J. Geotech. Eng., ASCE, 92-100.

Kalteziotis N, Sabatakakis N, Vasiliou I (1992) Evaluation of Dynamic characteristics of Greek soil formations. Proc. 2nd Hellenic Conference on Geotechnical Engineering, Oct. 1992, Thessaloniki, Greece,Vol. II, 239-246.

Kanai K (1968) Conf. on cone penetrometer The Ministry of Public Works and Settlement. Ankara, Turkey 1966, Presented by Sakai Y.

Kappos AJ, Panagopoulos G, Panagiotopoulos C, Penelis G (2006) A hybrid method for the vulnerability assessment of R/C and URM buildings. Bulletin of Earthquake Engineering, 4(4), 391-413.

Karapetrou ST, Filippa AM, Fotopoulou SD, Pitilakis KD. (2013) Time-dependent vulnerability assessment of RC buildings considering SSI and aging effects. COMPDYN, 12-14 June 2013, Kos Island, Greece.

Karapetrou ST, Fotopoulou SD, Pitilakis KD. (2015) Seismic vulnerability assessment of high-rise non-ductile RC buildings considering soil-structure interaction effects. Soil Dyn. Earthq. Eng. 73l, 42-57.

Karatzetzou A, Pitilakis D, Kržan M, Bosiljkov V (2015) Soil-foundation-structure interaction and vulnerability assessment of the Neoclassical School in Rhodes, Greece. Bull Earthq Eng, 13, 411-428.

Kaynia A M (2021) Effect of kinematic interaction on seismic response of offshore wind turbines on monopiles. Earthq. Eng. Struct. Dyn. 50(3), 777-790.

Khazai B, Vangelsten B, Franchin P, Daniell J, Cavalieri F, Plapp-Kunz T, Iervolino I, Esposito S (2012) A new approach to modeling post-earthquake shelter demand: integrating social vulnerability in systemic seismic vulnerability analysis. In: Proceedings of the $_{15}^{th}$ world conference on earthquake engineering, 2012, Lisboa, Portugal.

Khosravikia F, Mahsuli M, Ghannad MA (2018) The effect of soil–structure interaction on the seismic risk to buildings. Bull. Earthq. Eng. (Online), 16(9), 3653-3673.

Kiku H, Yoshida N, Yasuda S, Irisawa T, Nakazawa H, Shimizu Y, Ansal A, Erkan A (2001) In-situ penetration tests and soil profiling in Adapazari. Turkey. 15th ICSNGE/TC4 Satellite Conference on "Lessons Learned from Recent Strong Earthquakes", 2001, Istanbul, Turkey, pp. 259-265.

Kim S, Stewart JP (2003) Kinematic Soil-Structure Interaction from Strong Motion Recordings. J Geotech Geoenviron, 129(4), 323-335.

Kita A, Cavalagli N, Masciotta MG, Lourenco PB, Ubertini F (2020) Rapid post-earthquake damage localization and quantification in masonry structures through multidimensional non-linear seismic IDA. Engineering Structures. 219, 110841.

Kottke A, Rathje EMR (2008) Technical manual for Strata. Report 2008/10. Pacific Earthquake Engineering Research Center, University of California, Berkeley, 2008.

Kourkoulis SK (2007) Fracture and failure of natural building stones: applications in the restoration of ancient monuments. Springer Science & Business Media.

Kramer SL (1996) Geotechnical earthquake engineering. Prentice Hall, Upper Saddle River, New Jersey, 1996.

Kržan M, Gostič S, Cattari S, Bosiljkov V (2015) Acquiring reference parameters of masonry for the structural performance analysis of historical buildings. Bull Earthq Eng, 13(1), 203-236.

Kuhlemeyer RL, Lysmer J (1973) Finite element method accuracy for wave propagation problems. Soil Mechanics and Foundations, 99(5), 421–427.

Lagomarsino S, Giovinazzi S (2006) Macroseismic and mechanical models for the vulnerability assessment of current buildings. Bull. Earthq. Eng. 4(4), 415-443.

Lagomarsino S, Penna A, Galasco A, Cattari S (2013) TREMURI program: An equivalent frame model for the nonlinear seismic analysis of masonry buildings. Eng Struct, 56, 1787-1799.

Lagomarsino S (2015) Seismic assessment of rocking masonry structures, Bull Earthq Eng, 13(1), 97-128.

Lagomarsino S, Cattari S (2015a) PERPETUATE guidelines for seismic performance-based assessment of cultural heritage masonry structures, Bull Earthq Eng, 13(1), 13-47.

Lagomarsino S, Cattari S (2015b) Seismic performance of historical masonry structures through pushover and nonlinear dynamic analyses. Geotech. Geol. Earthq. Eng. 39, 265-292.

Lagomarsino S, Cattari S, Ottonelli D, Rossi M (2015) Buildings behaviour in urban fabric: the safety assessment issue in the post earthquake reconstruction plans. In Key Engineering Materials, 628, 96-101.

Lagomarsino S, Cattari S, Ottonelli D (2021) The heuristic vulnerability model: fragility curves for masonry buildings. Bull. Earthq. Eng. 4(4), 415-443.

Lagomarsino S, Cattari S, Angiolilli M, Bracchi S, Rota M, Penna A (2022) Modelling and seismic response analysis of existing URM structures. Part 2: case studies of Italian historical buildings, Journal of Earthquake Engineering, under review.

Lai C, Bozzoni F, Mangriotis MD, Martinelli M (2015) Soil liquefaction during the 20 May 2012 M5.9 Emilia earthquake, Northern Italy: Field reconnaissance and post-event assessment. Earthq Spectra, 31(4), 2351-2373.

Lanzo G, Silvestri F, Costanzo A, et al. (2011) Site response studies and seismic microzoning in the Middle Aterno valley (L'Aquila, Central Italy). Bulletin of Earthquake Engineering, 9(5), 1417-1442.

Lee SHH (1990) Regression models of shear wave velocities. Journal of the Chinese Institute of Engineers, 13, 519-532.

Lee SHH (1992) Analysis of the multicollinearity of regression equations of shear wave velocities. Soils and Foundations 32(1), 205-214.

Leggieri V, Ruggieri S, Zagari G, Uva G (2021) Appraising seismic vulnerability of masonry aggregates through an automated mechanical-typological approach. Automation in Construction, 132, 103972.

Liao T, Massoudi N, Mchood M, Stokoe KH, Jung MJ, Menq FY (2013) Normalized shear modulus of compacted gravel. 18th Int Conf Soil Mech Geotech Eng. Challenges and Innovations in Geotechnics, ICSMGE, 2-6 September 2013, Paris, France.

Lin JH, Weng CC (2001) Probability analysis of seismic pounding of adjacent buildings. Earthquake engineering & structural dynamics, 30(10), 1539-1557.

Lorenzoni F, Calabria A, De Conto N, da Porto F (2019) Assessment of the dynamic response of monitored masonry buildings after the Central Italy earthquake swarm in 2016. VII COMPDYN, 24-26 June 2019, Crete, Greece.

Lucantoni A, Bosi V, Bramerini F, De Marco R, Lo Presti T, Naso G, Sabetta F (2001) Seismic risk in Italy. Ing Sismica XVI, I(1), 5-36 (in Italian).

Magenes G, Penna A, Rota M, Galasco A (2014) Shaking table test of a strengthened full-scale stone masonry building with flexible diaphragms. Int J Archit Herit, 8(3), 349-375.

Maio R, Vicente R, Formisano A, Varum H (2015) Seismic vulnerability of building aggregates through hybrid and indirect assessment techniques. Bulletin of Earthquake Engineering, 13(10), 2995-3014.

Mair RJ (1993) Developments in geotechnical engineering research: application to tunnels and deep excavations. In: Proceedings of the institution of civil engineers. Civil engineering. 97(1), 27-41.

Maison BF, Kasai K (1990) Analysis for a type of structural pounding. Journal of Structural Engineering, 116(4), 957-977.

Manfredi V, Masi A, Özcebe AG et al. (2022) Selection and spectral matching of recorded ground motions for seismic fragility analyses. Bull Earthquake Eng, https://doi.org/10.1007/s10518-022-01393-0.

Maravas A, Mylonakis G, Karabalis DL (2014) Simplified discrete systems for dynamic analysis of structures on footings and piles. Soil Dyn Earthq Eng, 61-62, 29-39.

Marino S, Cattari S, Lagomarsino S, Dizhur D, Ingham JM (2019a) Post-earthquake Damage Simulation of Two Colonial Unreinforced Clay Brick Masonry Buildings Using the Equivalent Frame Approach. Structures. 19, 212-226.

Marino S, Cattari S, Lagomarsino S (2019b) Are the nonlinear static procedures feasible for the seismic assessment of irregular existing masonry buildings?. Eng. Struct. 200, 109700.

Mashhadi S, Asadi A, Homaei F, Tajammolian H (2021) Seismic response of mid-rise steel MRFs: the role of geometrical irregularity, frequency components of near-fault records, and soil-structure interaction. Bull. Earthq. Eng. 19, 3571-3595.

Masing G (1926) Eigenspannungen und Verfestigung beim messing. 2nd Int Congress of App Mech, 12-17 September 1926, Zurich, Swiss.

MIT (2019) Istruzioni per l'applicazione dell'aggiornamento delle Norme tecniche per le costruzioni di cui al Decreto Ministeriale 17/01/2018, Ministry of Infrastructures and Transportations, Rome, Italy. (in Italian).

Mitropoulou C, Kostopanagiotis C, Kopanos M, Ioakim D, Lagaros N (2016) Influence of soil-structure interaction on fragility assessment of building structures. Structures. 6, 85-98.

Moghaddasi M, Cubrinovski M, Chase JG, Pampanin S, Carr A (2011) Probabilistic evaluation of soil–foundation–structure interaction effects on seismic structural response. Earthq Eng Struct Dyn, 40, 135-154.

Monaco P, Totani G, Totani F, Grasso S, Maugeri M (2014) Site effects in the urban area of L'Aquila damaged by the April 6, 2009 earthquake. Earthquake-Soil Interaction; WIT Press: Ashurst, UK, 79, 71-86.

Morandi P, Albanesi L, Graziotti F, Piani TL, Penna A, Magenes G (2018) Development of a dataset on the in-plane experimental response of URM piers with bricks and blocks. Construction and Building Materials, 190, 593-611.

Mori F, Gaudiosi I, Tarquini E, Bramerini F, Castenetto S, Naso G, Spina D (2020) HSM: a synthetic damage-constrained seismic hazard parameter. Bull. Earthq. Eng. 18, 5631-5654.

Mosoarca M, Onescu I, Onescu E, Anastasiadis A (2020) Seismic vulnerability assessment methodology for historic masonry buildings in the near-field areas, Eng. Fail. Anal., 115, 104662.

Mouyiannou A, Rota M (2017) Selecting appropriate intensity measures for analytical state dependent fragility functions of URM buildings. 16th WCEE, 9-13 January 2017, Santiago, Chile.

MPS (2004) - Working Group MPS, Redazione della mappa di pericolosità sismica prevista dall'Ordinanza PCM del 20 marzo 2003 n.3274 All. 1. Rapporto conclusivo per il DPC, INGV, Milano-Roma, 2004, http://zonesismiche.mi.ingv.it/.

Mylonakis G, Nikolaou A, Gazetas G (1997)Soil-pile-bridge seismic interaction: kinematic and inertial effects. Part I: Soft Soil. Earthq. Eng. Struct. Dyn., 26(3), 337- 359.

Mylonakis G, Gazetas G (2000) Seismic Soil-Structure Interaction: beneficial or detrimental? J. Earthq. Eng. 4(3), 277-301.

Mylonakis G, Nikolaou S, Gazetas G (2006) Footings under seismic loading: Analysis and design issues with emphasis on bridge foundations. Soil Dyn Earthq Eng., 26(9), 824-853.

MZS3 (2018) Report of the 3rd level Seismic Microzonation of Visso village. Approved by the Working Group 29 May 2018. https://www.comune.visso.mc.it/documenti-cms/?cat-documenti=microzonazione-sismica.

Nale M, Minghini F, Chiozzi A, Tralli A (2021) Fragility functions for local failure mechanisms in unreinforced masonry buildings: a typological study in Ferrara, Italy. Bulletin of Earthquake Engineering, 1-31.

Naserkhaki S, El Rich M, ABDUL AF, Pourmohammad H (2013) Separation gap, a critical factor in earthquake induced pounding between adjacent buildings. Asian journal of civil engineering, 14(6), 881-898.

Naso G, Albarello D, Bramerini F, Castenetto S, D'Intinosante V, Moscatelli M (2016) Zone di amplificazione nelle carte di MS: una proposta di classificazione della pericolosità. XXXV Convegno Nazionale GNGTS, 22-24 November 2016, Lecce, Italy, section 2(2), 381-383.

Newmark NM (1973) A study of vertical and horizontal earthquake spectra, Directorate of Licencing, U.S. Atomic Energy Commission, Washington, D.C., USA, 1973.

NIST (2012) National Institute of Standards and Technology. Soil-structure Interaction for Building Structures, Report No. NIST GCR 12-917-21, U.S. Department of Commerce, Washington, D.C.

NTC (2018) Norme Tecniche per le Costruzioni. DM 17/01/2018, Italian Ministry of Infrastructure and Transportation, G.U. n. 42, 20 February 2018, Rome, Italy. (in Italian).

NZS (2017) New Zealand Society for Earthquake Engineering, the seismic assessment of existing buildings-technical guidelines for engineering assessments, Wellington.

Ohba S, Toriuma I (1970) Research on vibrational characteristics of soil deposits in Osaka, Part 2, on velocities of wave propagation and predominant periods of soil deposits. Technical Meeting of Architectural Institute of Japan.

Ohsaki Y, Iwasaki R (1973) On dynamic shear moduli and Poisson's ratio of soil deposits. Soil Foundations, 13, 61-73.

Ohta Y, Goto N (1978) Empirical shear wave velocity equations in terms of characteristic soil indexes. Earthq. Eng. Struct. Dyn, 6, 167-187.

Ottonelli D, Manzini CF, Marano C, Cordasco EA, Cattari S (2021) A comparative study on a complex URM building: part I - sensitivity of the seismic response to different modelling options in the equivalent frame models. Bull. Earthq. Eng. 20, 2115-2158.

Oz I, Senel SM, Palanci M, Kalkan A (2020) Effect of Soil-Structure Interaction on the Seismic Response of Existing Low and Mid-Rise RC Buildings. Appl. Sci. 10(23), 8357.

Pagliaroli A, Pergalani F, Ciancimino A, et al. (2020) Site response analyses for complex geological and morphological conditions: relevant case-histories from 3rd level seismic microzonation in Central Italy. Bulletin of Earthquake Engineering, 18(12), 5741-5777.

Pagnini LC, Vicente R, Lagomarsino S, Varum H (2011) A mechanical model for the seismic vulnerability assessment of old masonry buildings. Earthquake and Structures, 2(1), 25-42.

Pais A, Kausel E (1988) Approximate formulas for dynamic stiffnesses of rigid foundations. Soil Dyn Earthq Eng. 7(4), 213-227.

Palmer DJ, Stuart JG (1957) Some observations on the Standard Penetration Test and a correlation of the test with a new penetrometer. 4th Int. Conf. Soil Mech. Found. Eng., August 12-24, 1957, London, England.

Paolucci R, Ozcebe AG, Smerzini C, Masi A, Manfredi V (2020) Selection and spectral matching of recorded ground motions for earthquake engineering analysis. Internal report of RELUIS 2019 - WP4, Mappe di rischio e scenari di danno sismico (MARS).

Papadimitriou AG (2019) An engineering perspective on topography and valley effects on seismic ground motion', Proc. of the 7th ICEGE, 17-20 June 2019. Rome, Italy.

Parisi F, Augenti N (2013a) Earthquake damages to cultural heritage constructions and simplified assessment of artworks. Eng Fail Anal, 34, 735-760.

Parisi F, Augenti N (2013b) Seismic capacity of irregular unreinforced masonry walls with openings. Earthq Eng Struct Dyn, 42(1), 101-121.

Peduto D, Korff M, Nicodemo G, Marchese A (2019) Empirical fragility curves for settlement-affected buildings: Analysis of different intensity parameters for seven hundred masonry buildings in The Netherlands. Soils Found. 59(2), 380-397.

Pelizari PA, Geiß C, Aguirre P, Santa María H, Merino Peña Y, Taubenböck H (2021) Automated building characterization for seismic risk assessment using street-level imagery and deep learning, ISPRS Journal of Photogrammetry and Remote Sensing, 180, 370-386.

Penna A, Morandi P, Rota M, Manzini CF, Da Porto F, Magenes G (2014) Performance of masonry buildings during the Emilia 2012 earthquake. Bulletin of Earthquake Engineering, 12(5), 2255-2273.

Penna A. Senaldi IE, Galasco A, Magenes G (2016) Numerical Simulation of Shaking Table Tests on Full-Scale Stone Masonry Buildings. IJAH. 10(2-3), 146-163.

Penna A, Rosti A, Rota M (2022a) Seismic response of masonry building aggregates in historic centres: observations, analyses and tests. In: Bento R, De Stefano M, Köber D, Zembaty Z (eds). Seismic Behaviour and Design of Irregular and Complex Civil Structures IV. Geotechnical, Geological and Earthquake Engineering, 50, 19-36.

Penna A, Rota M, Bracchi S, Angiolilli M, Cattari S, Lagomarsino S (2022b) Modeling and seismic response analysis of existing URM structuress. Part 1: modern buildings, submitted to Journal of Earthquake Engineering.

Pérez-Santisteban I, Muñoz Martín A, Carbó Gorosabel A, Ruiz Fonticiella JM (2016) Empirical correlation of shear wave velocity (vs) with spt of soils in Madrid. first break, 34, 87-92.

Petridis C, Pitilakis D (2020) Fragility curve modifiers for reinforced concrete dual buildings, including nonlinear site effects and soil-structure interaction. Earthq. Spectra, 36(4), 1931-1951.

Pietrantoni M, Tagliaferri A, Petrangeli M (2013) Valutazione dell'affidabilità delle prove SPT per la caratterizzazione sismica dei terreni. Rivista Italiana di Geotecnica 1 (in Italian).

Piro A, de Silva F, Parisi F, Scotto di Santolo A, Silvestri F (2020) Effects of soil-foundation-structure interaction on fundamental frequency and radiation damping ratio of historical masonry building sub-structures. Bull Earthq Eng, 18, 1187-1212.

Pitilakis D, Karatzetzou A (2015) Dynamic stiffness of monumental flexible masonry foundations. Bull Earthq Eng, 13, 67-82.

Pitilakis D, Iliou K, Karatzetzou A (2018a) Shaking table tests on a stone masonry building: modeling and identification of dynamic properties including soil-foundation-structure interaction. Int. J. Archit. Heritage, 12(6), 1019-1037.

Pitilakis D, Rovithis E, Anastasiadis A, Vratsikidis A, Manakoua M (2018b) Field evidence of SSI from full-scale structure testing. Soil Dyn Earthq Eng, 112, 89-106.

Polese M, Di Ludovico M, Tocchi G, Prota A (2021) The use of an integrated approach for building inventory and effects on risk estimations at the territorial scale. 8th COMPDYN, 27-30 June 2021, Athens, Greece.

Predari G, Bartolomei C, Morganti C, Mochi G, Gulli R (2019) Expeditious methods of urban survey for seismic vulnerability assessments. Int. Archives of the Photogrammetry, Remote Sensing & Spatial Information Sciences

Puglia R, Vona M, Klin P, Ladina C, Masi A, Priolo E, Silvestri F (2013) Analysis of site response and building damage distribution induced by the 31 October 2002 earthquake at San Giuliano di Puglia (Italy). Earthq Spectra, 29(2), 497-526.

Raheem SEA (2006) Seismic pounding between adjacent building structures. Electronic Journal of Structural Engineering, 6(66), 155.

Rajeev P, Tesfamariam S (2012) Seismic fragilities of non-ductile reinforced concrete frames with consideration of soil structure interaction. Soil Dyn Earthq Eng. 40, 78-86.

Ramberg W, Osgood WR (1943) Description of stress-strain curves by three parameters. Natl Advis Comm Aeronaut, Washington DC.

Ramos LF, Lourenço PB (2004) Modeling and vulnerability of historical city centers in seismic areas: a case study in Lisbon. Engineering structures, 26(9), 1295-1310.

Raptakis DG, Anastasiadis SAJ, Pitilakis KD, Lontzetidis KS (1995) Shear wave velocities and damping of Greek natural soils; Proc. 10th ECEES, 1995, Vienna, Austria, pp 477-482.

ReLUIS (2010) Linee guida per il rilievo, l'analisi ed il progetto di interventi di riparazione e consolidamento sismico di edifici in muratura in aggregato. (in Italian).

ReLUIS – Task 4.1 Workgroup report, edited by Cattari S, Degli Abbati S, Ottonelli D, Sivori D, et al. (2018a) Report di sintesi sulle attività svolte sugli edifici in muratura monitorati dall'Osservatorio Sismico delle Strutture, Linea Strutture in Muratura, ReLUIS report, Rete dei Laboratori Universitari di Ingegneria Sismica (in Italian).

ReLUIS – WorkPakage 3, edited by de Silva F, Piro A, Silvestri F (2018b) Geotechnical characterization of Visso and Sant'Agata de'Goti, ReLUIS report, Rete dei Laboratori Universitari di Ingegneria Sismica.

ReLUIS – WorkPakage 1, Deliverable UniNa, (2018c) Modellazione delle curve di decadimento del modulo di taglio e del fattore di smorzamento di alcuni terreni dell'Italia Centrale, ReLUIS report, Rete dei Laboratori Universitari di Ingegneria Sismica (in Italian).

Rezaei S, Shooshpasha I, Rezaei H (2018) Empirical Correlation between Geotechnical and Geophysical Parameters in a Landslide Zone (Case Study: Nargeschal Landslide. Earth Sci. Res. J. 22(3), 195-204.

Rezaie A, Godio M, Beyer K (2020) Experimental investigation of strength, stiffness and drift capacity of rubble stone masonry walls. Construction and Building Materials, 251.

Rezaie A, Godio M, Beyer K (2020) Experimental investigation of strength, stiffness and drift capacity of rubble stone masonry walls. Constr Build Mater. 251, 118972.

Richart FE, Hall JR, Wood RD (1970) Vibrations of Soils and Foundations. Prentice-Hall.

Roesset JM (1980) Seismic Safety Margins Research Program (Phase I), Project III – Soil-Structure Interaction, A Review of Soil-Structure Interaction, UCRL-15262, Nuclear Test Engineering Division, Lawrence Livermore Laboratory, Livermore, CA, 1980.

Romis F, Caprili S, Salvatore W, Ferreira TM, Lourenco PB (2021) An Improved Seismic Vulnerability Assessment Approach for Historical Urban Centres: The Case Study of Campi Alto di Norcia, Italy. Applied Sciences 11(2), 849.

Rosti A, Rota M, Penna A (2021) Empirical fragility curves for Italian URM buildings. Bull Earthq Eng. 19, 3057-3076.

Rovithis E, Kirtas E, Bliziotis D, Maltezos E, Pitilakis D et al. (2017) A LiDAR-aided urban-scale assessment of soil-structure interaction effects: The case of kalochori residential area (N. greece). Bulletin of Earthquake Engineering, 15(11), 4821-4850.

Sabetta F, Pugliese A (1996) Estimation of response spectra and simulation of nonstationary earthquake ground motions. Bull. of the Seism. Soc. of America, 86(2), 337-352.

Sandoli A, Calderoni B, Lignola GP, Prota A (2022) Seismic vulnerability assessment of minor Italian urban centres: development of urban fragility curves. Bulletin of Earthquake Engineering, 1-30.

Santa María H, Hube MA, Rivera F, Yepes-Estrada C, Valcárcel JA (2017) Development of national and local exposure models of residential structures in Chile. Natural Hazards 86, S55-S79.

Sawada T, Hirao K, Yamamoto H (1992) Relation between maximum amplitude ratio (a/v, ad/v2) and spectral parameters of earthquake ground motion. Earthquake Engineering, X World Conferences, Balkema, Rotterdam, Netherlands.

Schiappapietra E, Douglas J (2020) Modelling the spatial correlation of earthquake ground motion: Insights from the literature, data from the 2016–2017 central italy earthquake sequence and ground-motion simulations. Earth-Science Reviews, 203

Seed HB, Murarka R, Lysmer J, Idriss IM (1976) Relationships of maximum acceleration, maximum velocity, distance from source, and local site conditions for moderately strong earthquakes. Bull. Seism. Soc. Am. 66(4), 1323-1342.

Senaldi I, Magenes G, Penna A (2010) Numerical investigations on the seismic response of masonry building aggregates. In Advanced Materials Research, 133, 715-720. Trans Tech Publications Ltd.

Senaldi IE, Guerrini G, Comini P, Graziotti F, Penna A, Beyer K, Magenes G (2020) Experimental seismic performance of a half-scale stone masonry building aggregate, Bull Earthq Eng, 18(2), 609-643.

Sextos A, De Risi R, Pagliaroli A, et al. (2018) Local site effects and incremental damage of buildings during the 2016 Central Italy earthquake sequence. Earthquake Spectra, 34(4), 1639-1669.

Shrestha B, Hao H (2018) Building pounding damages observed during the 2015 Gorkha earthquake. Journal of Performance of Constructed Facilities, 32(2), 04018006.

Silva V, Amo-Oduro D, Calderon A, et al. (2020) Development of a global seismic risk model. Earthquake Spectra. 36(1), 372-394.

Simões A, Bento R, Cattari S, Lagomarsino S (2014) Seismic performance-based assessment of “Gaioleiro” buildings. Engineering structures, 80, 486-500.

Sisman H (1995) An investigation on relationships between shear wave velocity, and SPT, and pressuremeter test results. M.Sc. Thesis, Ankara University, Geophysical Engineering Department.

Sisti R, Di Ludovico M, Borri A, Prota A (2019) Damage assessment and the effectiveness of prevention: the response of ordinary unreinforced masonry buildings in Norcia during the Central Italy 2016–2017 seismic sequence. Bulletin of Earthquake Engineering, 17(10), 5609-5629.

Sivori D (2021) Ambient vibration tools supporting the model-based seismic assessment of existing buildings. PhD dissertation, University of Genoa, Italy, 2021.

Sivori D, Cattari S, Lepidi M (2022) A methodological framework to relate the earthquake-induced frequency reduction to structural damage in masonry buildings. Bulletin of Earthquake Engineering, 1-36.

Smerzini C, Paolucci R (2013) SIMBAD: a database with Selected Input Motions for dis-placement Based Assessment and Design – 3rd release by Department of Structural Engineering, Politecnico di Milano, Italy. Research Project DPC RELUIS.

Sorrentino L, Cattari S, da Porto F, Magenes G, Penna A (2019) Seismic behaviour of ordinary masonry buildings during the 2016 central Italy earthquakes. Bull Earthq Eng. 17(10):5583-5607.

Sousa L, Silva V, Bazzurro P (2017) Using Open-Access Data in the Development of Exposure Data Sets of Industrial Buildings for Earthquake Risk Modeling. Earthquake Spectra, 33(1), 63-84.

Spence R, D'Ayala D (1999) Damage assessment and analysis of the 1997 Umbria-Marche earthquakes. Structural engineering international, 9(3), 229-233.

Stacul S, Rovithis E, Di Laora R (2022) Kinematic Soil–Pile Interaction under Earthquake-Induced Nonlinear Soil and Pile Behavior: An Equivalent-Linear Approach, 148(7).

Star LM, Tileylioglu S, Givens MJ, Mylonakis G, Stewart JP (2019) Evaluation of soil-structure interaction effects from system identification of structures subject to forced vibration tests. Soil Dyn Earthq Eng, 116, 747-760.

Stewart JP, Kim S, Bielak J, Dobry R, Power M (2003) Revisions to Soil-Structure Interaction Procedures in NEHRP Design Provisions. Earthq Spectra, 19(3), 677-696.

Stewart JP, Zimmaro P, Lanzo G, et al. (2018) Reconnaissance of 2016 Central Italy earthquake sequence. Earthquake Spectra, 34(4), 1547-1555.

Stucchi M, Meletti C, Montaldo V, Akinci A, et al. (2004) Pericolosità sismica di riferimento per il territorio nazionale MPS04. Istituto Nazionale di Geofisica e Vulcanologia (INGV). [dataset]. https://doi.org/10.13127/sh/mps04/ag.

Sundar A (2019) Time frequency distribution of a signal using S-transform (stockwell transform). (https://www.mathworks.com/matlabcentral/fileexchange/51808-time-frequency-distribution-of-a-signal-using-s-transform-stockwell-transform), MATLAB Central File Exchange.

Thokchom S, Rastogi BK, Dogra NN, Pancholi V, Sairam B, Bhattacharya F, Patel V (2017) Empirical correlation of SPT blow counts versus shear wave velocity for different types of soils in Dholera, Western India. Nat Hazards, 86, 1291-1306.

Tileylioglu S, Stewart JP, Nigbor RL (2011) Dynamic stiffness and damping of a shallow foundation from forced vibration of a field test structure. J Geotech Geoenviron, 137(4).

Tocchi G, Polese M, Di Ludovico M et al. (2022) Regional based exposure models to account for local building typologies. Bull Earthquake Eng 20, 193–228.

Tomeo R, Pitilakis D, Bilotta A, Nigro E (2018) SSI effects on seismic demand of reinforced concrete moment resisting frames. Engineering Structures 173, 559-572.

Trifunac MD, Brandy AG (1975) A study on the duration of strong earthquake ground motion. Bull. Seism. Soc. Am. 65(3):581-626.

Tso WK, Zhu TJ, Heidebrecht AC (1992) Engineering implication of ground motion ratio. Soil Dynamics and Earthquake Engineering 11, 133-144.

Turnšek V, Sheppard P (1980) The shear and flexural resistance of masonry walls. In Proc. Int. research conf earthq eng, June 30 - July 3, 1980, Skopje, Macedonia, pp. 517-573.

Ulugergerli UE, Uyanik O (2007) Statistical correlations between seismic wave velocities and SPT blow counts and the relative density of soils. J Test Eval, 35(2), 187-191.

Uma Maheswari R, Boominathan A, Dodagoudar GR (2008) Development of empirical correlation between Shear wave velocity and Standard Penetration Resistance in soils of Chennai City. Proc. in 14th WCEE, 12-17 October, 2008, Beijing, China.

Valente M, Milani G, Grande E, Formisano A (2019) Historical masonry building aggregates: advanced numerical insight for an effective seismic assessment on two row housing compounds. Engineering Structures, 190, 360-379.

Valluzzi MR, Sbrogiò L, Saretta Y (2021) Intervention Strategies for the Seismic Improvement of Masonry Buildings Based on FME Validation: The Case of a Terraced Building Struck by the 2016 Central Italy Earthquake. Buildings, 11(9), 404.

Vanin F, Zaganelli D, Penna A, Beyer K (2017) Estimates for the stiffness, strength and drift capacity of stone masonry walls based on 123 quasi-static cyclic tests reported in the literature. Bull Earthq Eng, 15(12), 5435–5479.

Veletsos AS, Nair VV (1975) Seismic interaction of structures on hysteretic foundations. J. Struct. Eng. 101, 109-129.

Vicente R, Ferreira TM, Varum H, Costa A, Silva JAR, Lagomarsino S (2014) Seismic vulnerability and risk assessment of historic masonry buildings. In Structural Rehabilitation of Old Buildings, Springer, Berlin, Heidelberg, pp 307-348.

Von Thun JL, Rochim LH, Scott GA, Wilson JA (1988) Earthquake ground motion for design and analysis of dams. In: Earthquake engineering and soil dynamics II-recent advance in ground-motion evaluation. Geotechnical Special Publication 20, ASCE, New York, 463-464.

Wolf J (1985) Dynamic soil-structure interaction. Prentice Hall, Englewood Cliff.

Yokota et al. (1991) Cited in Jafari MK, Shafiee A, Ramzkhah A. (2002) Dynamic properties of the fine grained soils in south of Tehran, J. Seismo. Earth. Eng., 4 (1), 25-35.

Zuccaro G, Dolce M, De Gregorio D, Speranza E, Moroni C (2015) La scheda CARTIS per la caratterizzazione tipologico-strutturale dei comparti urbani costituiti da edifici ordinari. Valutazione dell'esposizione in analisi di rischio sismico. Proc. of the GNGTS.

Zuccaro G, Perelli FL, De Gregorio D, Cacace F (2021) Empirical vulnerability curves for Italian mansory buildings: evolution of vulnerability model from the DPM to curves as a function of accelertion. Bull Earthq Eng. 19, 3077-3097.

Zuccaro G, Cacace F (2011) Seismic casualty evaluation: the Italian model, an application to the L'Aquila 2009 event. In: Spence R, So E, Scawthorn C (eds) Human casualties in earthquakes. Advances in natural and technological hazards research. Springer, Netherlands, 171-184.

Zucconi M, Ferlito R, Sorrentino L (2020) Validation and extension of a statistical usability model for unreinforced masonry buildings with different ground motion intensity measures. Bull. Earthq. Eng. 18, 767-795.